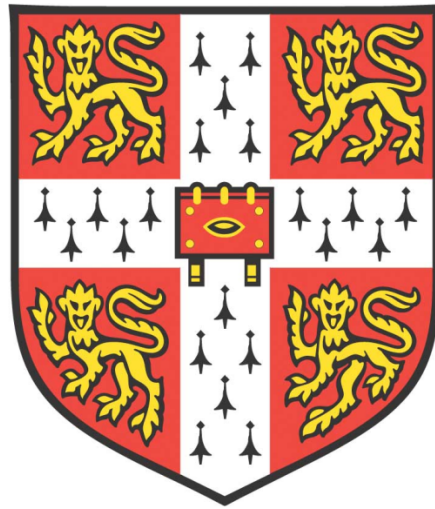


*MOLECULAR PHYSIOLOGY OF THE
CHLAMYDOMONAS PYRENOID*



Oliver Dominik Caspari

Wolfson College

Department of Plant Sciences

University of Cambridge

This dissertation is submitted for the degree of Doctor of Philosophy

September 2015

*I dedicate this thesis to you,
dear reader,
in the hope that you may find it useful*

Sapere aude!

DECLARATION

This dissertation is the result of my own work and includes nothing, which is the outcome of work done in collaboration except where specifically indicated in the text. It has not been previously submitted, in part or whole, to any university or institution for any degree, diploma, or other qualification.

In accordance with the Degree Committee for Biology guidelines, this thesis does not exceed 60,000 words.

Signed: _____

Date: _____

Oliver Dominik Caspari, MA

first submission (soft-bound): Cambridge, 30th September 2015

SUMMARY

Operation of the CO₂-concentrating mechanism (CCM) in the model green alga *Chlamydomonas reinhardtii* relies on confining Rubisco in a proteinaceous micro-compartment, the chloroplastic pyrenoid. Despite a long history of research, this enigmatic structure lacks a full definition both in terms of physiological function as well as molecular composition.

The work presented here used a unique set of pyrenoid-less mutants (which differ from wild-type only with respect to the genes coding for the small subunit of Rubisco) to address two key questions: (i) the function of the pyrenoid in photosynthesis in enabling the CCM to supply Rubisco with inorganic carbon under CO₂ limiting conditions; (ii) the mechanism of Rubisco aggregation underlying pyrenoid formation.

Firstly, cells that are unable to aggregate Rubisco were found severely limited by access to CO₂, yet fully able to compensate any structural changes within the chloroplast. Secondly, *in silico* and *in vitro* analyses of Rubisco protein interactions established that a linking agent is required for Rubisco aggregation. A Rubisco interactome was characterised using native gel electrophoresis and co-IP assays followed by mass spectrometry. In a complementary approach, a forward genetic screen based on high-throughput immunofluorescence localization of Rubisco aimed to identify key pyrenoid assembly factors.

The present study combined and developed a wide range of molecular, physiological and computational techniques, to show that Rubisco aggregation forming the pyrenoid is achieved through a complex network of protein interactions in order to effectively supply CO₂ via the CCM.

ACKNOWLEDGEMENTS

Firstly, I would like to thank my supervisor Howard Griffiths for giving me the opportunity to do this PhD and for his support during my various collaborative endeavours as well as completing this thesis; and also for taking me as demonstrator to the undergraduate field course which has been a yearly highlight. I would like to thank Moritz Meyer who has been a tremendous mentor throughout and whose advice and guidance I am indebted to. I will miss our half-secret conversations in German and our creative free-flow in front of the white-board. Further, I am grateful to all the members of the Griffiths lab for helpful discussions and practical advice, especially Madeline Mitchell and Cindy Chan with whom I shared the *Chlamydomonas* corner of the lab, and Chandra Bellasio for introducing me to the powers and mystique of chlorophyll fluorescence. I would like to extend this thanks to my students, in particular Charlie Whittaker who kindly allowed me to use some of his images and whom I wish all the best for his own PhD. Thank you also to Julian Hibberd and the members of his group for advice in shared lab meetings.

Much of the work presented in this thesis has been the result of some form of collaboration, and I am deeply grateful for all the help I have received. Of particular importance to me, both scientifically and personally, were my research visits to the Carnegie Institute for Science in Stanford, and I would like to thank my overseas mentor Arthur Grossman for inviting me and generously providing me with all the resources I needed. I am grateful to all the members of his lab for their help and company, in particular Dimitri Tolleter for his mentoring on the JTS-10, Tyler Wittkopp for all his help and Tingting Xiang for bringing a little sunshine into the lab every day. Furthermore, I thank Martin Jonikas and his lab for the collaboration on LCI5 and the CCM mutants, and in particular Leif Pallesen, Luke Mackinder, Liz Freeman Rosenzweig, Nina Ivanova and Greg Reeves not only for sharing their scientific expertise but also for making my time there truly a great experience.

I would further like to thank Tracy Lawson for giving me access to CFimager and FRRf equipment and teaching me how to use it, and Ruben Alvarez for sharing his R scripts for analysis of the data produced this way. Furthermore, I would like to thank Nik Cunniffe introducing me to the *AIC* and more generally for all his help on guidance with statistical data analysis, which actually has been one of the most enjoyable parts of my PhD experience.

I am grateful to Jeremy Skepper and his colleagues at CAIC for their equipment and help with TEM and IF, to Jonathan Lawson and his opera microscope at the Cambridge Department of Pathology, to Raymond Wightman for help with the microscopes at the Sainsbury Laboratory Cambridge, and to Heather Cartwright for her help with microscopy at Carnegie.

Furthermore, I am grateful to the *Studienstiftung des Deutschen Volkes* for giving me the opportunity to participate in a *Lebenswissenschaftliches Kolleg* on molecular dynamics by Helmut Grubmüller, Bernd de Groot and David Köpfer which inspired me to explore Rubisco docking *in silico*, to my Wolfson College mentor Pedro Ballester who encouraged me to keep it up, and to Ben Luisi and David de Sancho who offered valuable insight.

For all his advice and guidance on BN-PAGE, thank you to Steven Burgess. I am also grateful to the lab of Natasha Murzina, and especially Piotr Gierszewski, for allowing me to use their sucrose gradient fractionator in the department of biochemistry Cambridge. Furthermore I would like to thank Katherine Stott at the Cambridge Biophysics Facility for teaching me to use and interpret the AUC, and Katherine Lilley and her team at the Cambridge Centre for Proteomics for the LC-MS/MS and advice on how to analyse the data.

I further wish to gratefully acknowledge the Biotechnology and Biological Sciences Research Council for granting me a PhD studentship and the *Studienstiftung* for their stipend; further Wolfson College, the Cambridge Philosophical Society and the TH Middleton Fund (Department of Plant Sciences) for financial support toward conferences and research-related travel.

I thank my colleagues and friends for the experiences we shared over these past four year. I thank my parents for being there for me in the darkest hours, and also in the brighter ones. Thank you also to Shobana Sivanendran for making this last year the best period of my PhD. It was a pleasure and a privilege to share this journey with you.

Finally, thank you to Kayla Friedman and Malcolm Morgan of the Centre for Sustainable Development, University of Cambridge, UK for producing the Microsoft Word thesis template used to produce this document.

CONTENTS

1 INTRODUCTION	1
1.1 THE PHYSIOLOGY OF PHOTOSYNTHESIS REQUIRES ENERGY SUPPLY AND DEMAND TO BE BALANCED	2
1.2 CCMs ENABLE GREATER PHOTOSYNTHETIC EFFICIENCY BY INCREASING CO ₂ FIXATION CAPACITY	6
1.2.1 CCMs require compartmentalisation of Rubisco	6
1.2.2 Adaptive benefits of CCM operation depend on complex trade-offs	8
1.2.3 CCMs present a common solution to different problems arising from CO ₂ limitation.....	11
1.2.4 Genetic engineering of CCMs may provide a strategy to increase crop yield	12
1.3 CHLAMYDOMONAS AS MODEL GREEN ALGA.....	13
1.4 THE CHLAMYDOMONAS CCM GENERATES A HIGH CO ₂ ENVIRONMENT WITHIN THE PYRENOID	13
1.4.1 CCM induction is reflected by the Rubisco aggregation state	15
1.4.2 Key features associated with the Chlamydomonas pyrenoid	16
1.4.3 Pyrenoid features suggest functional involvement beyond the CCM.....	18
1.4.4 The mechanism of Rubisco aggregation in pyrenoid assembly has remained elusive	19
1.5 SSU SUBSTITUTION MUTANTS PROVIDE AN EXCELLENT EXPERIMENTAL PLATFORM FOR STUDYING THE PYRENOID.....	20
1.6 AIMS AND HYPOTHESES	21
2 PYRENOID LOSS ALTERS PHOTOSYNTHETIC ENERGY BALANCING .	23
2.1 INTRODUCTION	23
2.1.1 pETC and CBC activity must balance	23
2.1.2 NPQ indicates a mismatch in the energy balance	23
2.1.3 CCMs increase CCB turnover capacity	25
2.1.4 How does the Chlamydomonas pyrenoid affect the interaction between pETC and CBC?.....	25
2.2 MATERIALS AND METHODS	29
2.2.1 Strains.....	29
2.2.2 TEM	30
2.2.3 CF from algal colonies on agar plates	31

2.2.4	<i>JTS-10 and associated data</i>	36
2.2.5	<i>FRRf measurements</i>	42
2.3	RESULTS	42
2.3.1	<i>Thylakoids stack irrespective of pyrenoid occurrence despite coordination by the pyrenoid in WT</i>	42
2.3.2	<i>High throughput screen of ETR and NPQ demonstrates impact of pyrenoid occurrence under CCM inducing conditions</i>	44
2.3.3	<i>High-Resolution ECS and CF reveals Rubisco turnover feedback limitation</i>	48
2.3.4	<i>Elevated CO₂ restores photosynthetic performance in pyr- cells via CBC feedback</i>	49
2.3.5	<i>Expression of photosystems and accessory pigments undergoes physiological acclimation independent of pyrenoid phenotype</i>	51
2.3.6	<i>Pyrenoid occurrence alters functional association of PSII and chlorophyll in low CO₂</i>	54
2.3.7	<i>Demand for ATP is increased in the absence of a pyrenoid</i>	56
2.4	DISCUSSION	58
2.4.1	<i>Pyr- cells show a range of phenotypic differences from WT when grown in low CO₂</i>	58
2.4.2	<i>Pyrenoid absence has no discernable effect on the ultrastructural arrangement of photosynthetic membranes in mutant strains</i>	59
2.4.3	<i>Acclimation to different growth irradiances is identical in pyr- and WT</i>	60
2.4.4	<i>The way pyr- cells differ from WT is consistent with CO₂ starvation</i>	60
2.4.5	<i>Pyr- cells are rescued by high CO₂</i>	61
2.4.6	<i>Pyr- cells are limited through CBC feedback</i>	62
2.4.7	<i>The ATP cost of photorespiration is at least as high as that of CCM operation</i>	64
2.5	CONCLUSION.....	65
3	SSU SURFACE HELICES DRIVE PYRENOID FORMATION THROUGH A SPECIFIC RESIDUE INTERACTION PATTERN	66
3.1	INTRODUCTION	66
3.1.1	<i>Rubisco compartmentalization and the case for engineering protein compartments</i>	66
3.1.2	<i>Carboxysomes</i>	67
3.1.3	<i>The Chlamydomonas pyrenoid is dynamic</i>	67

3.1.4 Regulation can be informative about aggregation processes.....	67
3.1.5 Pyrenoid assembly hypotheses	68
3.1.6 The PTM hypothesis	68
3.1.7 The linker hypothesis	68
3.1.8 The Rubisco auto-docking hypothesis	69
3.1.9 Heterologous SSU expression lines fail to assemble a pyrenoid.....	70
3.1.10 Analysis of SSU interaction site reveals details of Rubisco packaging.....	71
3.2 MATERIALS AND METHODS	72
3.2.1 SDM.....	72
3.2.2 Analytical Ultracentrifugation (AUC).....	73
3.2.3 Bioinformatics.....	77
3.3 RESULTS	78
3.3.1 SDM of Rubisco small subunit surface helices identifies key residues necessary for pyrenoid formation.....	78
3.3.2 Forced in silico Rubisco auto-docking is more favourable in <i>Chlamydomonas</i> but the complexes are predicted not to be stable in solution.....	80
3.3.3 AUC demonstrates that Rubisco does not spontaneously homo-dimerize.....	84
3.3.4 Docking the SSU to the putative <i>Lci5</i> interface in silico reveals a crucial salt bridge between R20 (<i>LCI5</i>) and D23 (SSU).....	87
3.3.5 Forced in silico SSU protein docking reveals a specific interaction profile.	89
3.4 DISCUSSION	91
3.4.1 Site directed mutagenesis is a powerful tool to identify interface residues in vivo.....	91
3.4.2 Rubisco surface motifs were investigated in silico as likely interaction partners for the SSU helices	92
3.4.3 Rubisco auto-docking fails to account for pyrenoid formation in silico	92
3.4.4 Isolated Rubisco does not associate with but repels itself in vitro	93
3.4.5 Implications of in vitro findings for in vivo and in silico scenarios	94
3.4.6 In silico docking of <i>LCI5</i> shows promise to have identified the linker interface.....	95
3.4.7 <i>Spinacia oleracea</i> SSU as a negative control fails to identify bona fide interaction partners in silico but supports more general points about interactivity and mode of binding	96
3.4.8 An overall SSU interaction profile emerges	97

3.4.9 <i>Directions for future work</i>	98
3.5 CONCLUSION.....	99
4 A RUBISCO INTERACTOME PROVIDES INSIGHT INTO THE MECHANISM OF PYRENOID ASSEMBLY.....	100
4.1 INTRODUCTION	100
4.2 MATERIALS AND METHODS	102
4.2.1 <i>Strains and culture conditions</i>	102
4.2.2 <i>Protein extraction</i>	103
4.2.3 <i>First dimension (1D) BN-PAGE</i>	103
4.2.4 <i>Second dimension (2D) SDS PAGE</i>	104
4.2.5 <i>Western Blots</i>	104
4.2.6 <i>Figure generation</i>	105
4.2.7 <i>Co-IP</i>	105
4.2.8 <i>Mass spectrometry and computational analysis</i>	105
4.3 RESULTS	108
4.3.1 <i>Higher order complexes containing Rubisco can be resolved via BN-PAGE</i>	109
4.3.2 <i>BN-PAGE complex profile is highly reproducible</i>	109
4.3.3 <i>Features of interest are revealed by comparison with negative controls</i>	111
4.3.4 <i>Mass spectrometry identifies chaperonin 60 as the 60 kDa element of 720 kDa Rubisco-complex</i>	115
4.3.5 <i>The major proteins within the 720 kDa band are equally abundant in WT and pyr-</i>	118
4.3.6 <i>The 600 kDa band contains differentially abundant proteins of high abundance</i>	120
4.3.7 <i>Mass spectrometric analysis of co-IP experiments establishes a Rubisco interactome</i>	122
4.3.8 <i>The interactome is responsive to experimental treatments</i>	127
4.3.9 <i>Gene ontology informs a number of functional groups within the interactome</i>	131
4.3.10 <i>Remaining proteins are informative about a likely pyrenoid assembly mechanism</i>	135
4.4 DISCUSSION	137
4.4.1 <i>A large part of the Rubisco interactome is independent of the pyrenoid</i>	138

4.4.2 <i>Co-IP and BN-PAGE make specific contributions to the interactome analysis</i>	141
4.4.3 <i>A number of functional classes do show differences according to Rubisco aggregation state</i>	142
4.4.4 <i>The interactome supports Ca²⁺- and redox-regulation of Rubisco aggregation</i>	143
4.4.5 <i>The interactome offers mechanistic insight into pyrenoid assembly</i>	144
4.4.6 <i>The soluble protein interactome contains hints about the role of thylakoid membranes in pyrenoid formation</i>	146
4.5 CONCLUSION	147
5 IDENTIFICATION OF NOVEL PYRENOID MUTANTS THROUGH IF SCREENING	148
5.1 INTRODUCTION	148
5.2 MATERIALS AND METHODS	150
5.2.1 <i>IF mutant screen</i>	150
5.2.2 <i>IF optimisation</i>	151
5.2.3 <i>Image acquisition</i>	155
5.2.4 <i>Image quantification</i>	155
5.3 RESULTS	155
5.3.1 <i>IF can visualize pyrenoids with equal resolution to fluorescent-fusion techniques</i>	156
5.3.2 <i>IF can diagnose pyrenoid presence in canonical localisation</i>	157
5.3.3 <i>Mutants with large amounts of delocalized Rubisco</i>	159
5.3.4 <i>Mutants with a classical pyrenoid and additional Rubisco aggregates</i>	159
5.3.5 <i>Some mutants show Rubisco aggregation, but lack a classical pyrenoid</i>	159
5.3.6 <i>Quantitative measure of Rubisco aggregation</i>	163
5.4 DISCUSSION	165
5.4.1 <i>Assessing IF as high-throughput screening method</i>	166
5.4.2 <i>No pyrenoid-less mutant strains were recovered</i>	166
5.4.3 <i>Delocalized Rubisco mutants may include CCM induction regulators</i>	168
5.4.4 <i>The IF screen recovered a now well characterized pyrenoid factor</i>	168
5.4.5 <i>Mutant phenotypes indicate the presence of organization factors, including a protein misannotated as E3 ubiquitin ligase</i>	170
5.5 CONCLUSION	171

6 CONCLUSIONS.....	172
6.1 THE PYRENOID IS FUNCTIONALLY DEFINED AS AN ASPECT OF THE CCM.....	173
6.2 THE PYRENOID IS ASSEMBLED BY RUBISCO TETHERING MULTIPLE LINKER PROTEINS SUCH AS LCI5 VIA THE SSU HELICES	174
6.3 THE PYRENOID IS FUNCTIONALLY SELF-CONTAINED.....	177
6.4 TOWARDS A MOLECULAR UNDERSTANDING OF PYRENOID FORM AND FUNCTION .	178
7 REFERENCES	183
8 APPENDICES.....	198

LIST OF TABLES

TABLE 0.1: TABLE OF ABBREVIATIONS	XIX
TABLE 0.2: TABLE OF STRAINS	XXVI
TABLE 0.3: TABLE OF PARAMETERS.....	XXVII
TABLE 2.1: PARAMETERS OF THE MODEL BEST SUPPORTED BY CF SCREEN ϕ_{II} DATA ACCORDING TO AIC-BASED STATISTICAL ANALYSIS.....	46
TABLE 3.1: SDM PRIMERS	72
TABLE 4.1: MODELS FIT TO CO-IP DATA.	128
APPENDIX 8.3: COLONY POSITIONS FOR CF SCREEN PLATES IN APPENDIX 8.2.....	201
APPENDIX 8.27: TABLE OF PROTEINS DETECTED VIA LC-MS/MS IN CO-IP	226

LIST OF FIGURES

FIG. 1.1: LEF AND CEF PATHWAYS IN THE pETC.....	3
FIG. 1.2: CCMs ACCUMULATE CARBONATED TRANSPORT ACIDS TO RELEASE CO ₂ NEAR COMPARTMENTALIZED RUBISCO	7
FIG. 1.3: FIXATION OF EITHER 3 CO ₂ OR 4 O ₂ LEADS TO GENERATION OF 6 G3P VIA CBC OR PHOTORESPIRATION.....	10
FIG. 1.4: THE <i>CHLAMYDOMONAS</i> PYRENOID IS AN INTEGRAL PART OF CHLOROPLAST AND CCM	14
FIG. 2.1: AN ENERGY IMBALANCE BETWEEN pETC AND CBC CAN BE REBALANCED BY DECREASING SUPPLY VIA <i>NPQ</i> , OR INCREASING DEMAND USING A CCM.	24
FIG. 2.2: FLUORESCENCE (CF) AND SPECTROSCOPIC DATA (ECS, p700) ARE INFORMATIVE ABOUT pETC ACTIVITY.	27
FIG. 2.3: EXAMPLE SSU EXPRESSION VECTORS	29
FIG. 2.4: HIGH THROUGHPUT PHOTOSYNTHETIC ANALYSIS OF ALGAL COLONIES USING CF IMAGING	33
FIG. 2.5: PYRENOID ABSENCE HAS NO EFFECT ON THYLAKOID ARRANGEMENT.....	43
FIG. 2.6: HIGH THROUGHPUT CF SCREEN DEMONSTRATES IMPACT OF PYRENOID OCCURRENCE ON <i>ETR</i> UNDER CCM-INDUCING CONDITIONS	45
FIG. 2.7: HIGH THROUGHPUT CF SCREEN SHOWS HIGHER <i>NPQ</i> IN PYR- UNDER CCM- INDUCING CONDITIONS, SUGGESTING AN IMBALANCE BETWEEN pETC AND CBC. ..	47
FIG. 2.8: HIGH-RESOLUTION ECS AND CF MEASUREMENTS REVEAL FEEDBACK LIMITATION BY RUBISCO CATALYSIS.	48
FIG. 2.9: ELEVATED CO ₂ INSTANTANEOUSLY RESTORES PHOTOSYNTHETIC PERFORMANCE IN PYR- CELLS	50
FIG. 2.10: EXPRESSION OF PHOTOSYSTEMS AND ACCESSORY PIGMENTS UNDERGOES PHYSIOLOGICAL ACCLIMATION INDEPENDENT OF PYRENOID PHENOTYPE.	52
FIG. 2.11: PYRENOID OCCURRENCE ALTERS FUNCTIONAL ASSOCIATION OF PSII AND CHLOROPHYLL IN LOW CO ₂	55
FIG. 2.12: CEF IS LOWER IN ABSOLUTE TERMS BUT HIGHER RELATIVE TO <i>ETR</i> IN PYR-...	57

FIG. 3.1: LCI5 SEQUENCE CONSISTS OF 4 REPEATS WITH SHORT FLANKING REGIONS.....	69
FIG. 3.2: 14 AMINO ACIDS DIFFER BETWEEN <i>CHLAMYDOMONAS</i> AND <i>SPINACIA OLERACEA</i> SSU HELICES, ALTERING CHARGE DISTRIBUTION.....	70
FIG. 3.3: ANALYTICAL ULTRA-CENTRIFUGATION PILOT STUDY INFORMED METHOD DEVELOPMENT.....	75
FIG. 3.4: SDM IDENTIFIES KEY RESIDUES NECESSARY FOR PYRENOID FORMATION.....	79
FIG. 3.5: SSU HELIX <i>IN SILICO</i> AUTO-DOCKING IS MORE FAVOURABLE IN <i>CHLAMYDOMONAS</i> BUT CANNOT EXPLAIN PYRENOID FORMATION.	81
FIG. 3.6: SSU-LSU INTERACTION BASED ON CRYSTAL STRUCTURE INFORMATION IS MORE FAVOURABLE FOR <i>CHLAMYDOMONAS</i> SSU BUT PREDICTED NOT TO BE STABLE IN SOLUTION.....	83
FIG. 3.7: AUC REVEALS ISOLATED RUBISCO ACTUALLY REPELS ITSELF.	85
FIG. 3.8: LCI5 <i>IN SILICO</i> FOLDING AND DOCKING PREDICT INTERACTION PROCEEDS VIA LCI5 REPEAT HELIX RESIDUES W12, L16 AND R20 AND INVOLVES A SALT BRIDGE BETWEEN R20 AND SSU HELIX A RESIDUE D23.	86
FIG. 3.9: FORCING <i>SPINACIA OLERACEA</i> SSU TO BIND LCI5 REPEAT HELIX <i>IN SILICO</i> REVEALS A VERY DIFFERENT DOCKING PROFILE AND SHOWS R20 (LCI5) INTERACTION IS SPECIFIC TO <i>CHLAMYDOMONAS</i> SSU.....	88
FIG. 3.10: BIOINFORMATIC TOOLS GIVE INSIGHT INTO THE SSU HELIX INTERACTION PROFILE.....	90
FIG. 4.1: RESOLVING HIGH MOLECULAR WEIGHT COMPLEXES OF RUBISCO USING BN-PAGE IN A PILOT EXPERIMENT.	108
FIG. 4.2: BN-PAGE 1 ST DIMENSION PROFILE IS HIGHLY REPRODUCIBLE.	110
FIG. 4.3: BN-PAGE 2 ND DIMENSION PROFILE IS HIGHLY REPRODUCIBLE.	112
FIG. 4.4: PYR- SHOWS A SIMILAR BN-PAGE PATTERN AS WT.....	113
FIG. 4.5: SPINACH LEAF PROTEIN EXTRACT SHOWS A DIFFERENT BN-PAGE PROFILE WITH HIGHLY REDUCED RUBISCO HIGHER ORDER COMPLEXES.	114
FIG. 4.6: THE 720kDa/60kDa SPOT CONTAINS CHAPERONIN 60, A PROTEIN INVOLVED IN RUBISCO HOLOENZYME ASSEMBLY.....	116

FIG. 4.7: BESIDES CHAPERONIN 60, THE 720 kDa BAND CONTAINS COMPLEXES OF CBC COMPONENTS AND VACUOLAR ATPASE.	117
FIG. 4.8: THE 600 kDa BAND CONTAINS ABUNDANT RUBISCO.	121
FIG. 4.9: EXPRESSING CO-IP DATA AS % TOTAL PROTEIN BASED ON <i>EMPAI</i> VALUES REDUCES ERROR BY ACCOUNTING FOR DIFFERENCES IN CONCENTRATION.	123
FIG. 4.10: DIFFERENCES BETWEEN STRAINS AND CO ₂ TREATMENTS CAN INFORM CANDIDATE PROTEINS INVOLVED IN PYRENOID FORMATION.	126
FIG. 4.11: EXPERIMENTAL TREATMENTS RESOLVE DISTINCT PROTEIN BEHAVIORS IN CO-IP.	130
FIG. 4.12: THE MAJORITY OF THE RUBISCO INTERACTOME CAN BE GROUPED INTO FUNCTIONAL CLASSES ACCORDING TO GENE ONTOLOGY ANNOTATION.	132
FIG. 4.13: CANDIDATES UP IN WT MAY BE INVOLVED IN FORMING THE CONSTITUTIVE PYRENOID.	135
FIG. 4.14: CANDIDATES MOST ABUNDANT IN WT/AIR MAY BE INFORMATIVE ABOUT PYRENOID ASSEMBLY AND INCLUDE LINKER <i>LCI5</i>	136
FIG. 4.15: CANDIDATES UP IN AIR INCLUDE <i>LCIB</i> AND <i>LCIC</i>	137
FIG. 5.1: SCHEMATIC OF SCREENING PROCEDURE.	150
FIG. 5.2: HIGHEST QUALITY IF IMAGES ARE ACHIEVED WHEN OMITTING THE FORMALDEHYDE FIXATION STEP.	154
FIG. 5.3: IF LABELLING OF RUBISCO REVEALS PYRENOID PRESENCE AND ABSENCE IN CONTROLS.	156
FIG. 5.4: PYRENOID PRESENCE AND CANONICAL LOCALISATION IS EASILY IDENTIFIED VIA IF.	158
FIG. 5.5: MUTANTS WITH A LARGE PROPORTION OF RUBISCO DELOCALIZED OUTSIDE THE CANONICAL PYRENOID LOCATION.	160
FIG. 5.6: MUTANTS WITH MULTIPLE RUBISCO AGGREGATES, IN ADDITION TO A CANONICAL PYRENOID.	161
FIG. 5.7: SOME MUTANTS APPEAR TO CONTAIN RUBISCO AGGREGATES DISTRIBUTED ACROSS THE CHLOROPLAST, WHILE LACKING A CLEAR PYRENOID.	162
FIG. 5.8 RUBISCO IS QUANTIFIABLY DELOCALISED IN THE <i>LCI5</i> MUTANT.	164

FIG. 6.1: A PROPOSED MECHANISM FOR RUBISCO AGGREGATION WITHIN THE PYRENOID	179
APPENDIX 8.2: CF SCREEN COLONIES	200
APPENDIX 8.4: HIGH-THROUGHPUT SCREEN SHOWS HIGH CO ₂ RESCUES PYR- F _v /F _M ...	202
APPENDIX 8.5 HIGH CO ₂ RESCUES PYR- ϕ_{II} DURING FLUORESCENCE INDUCTION (20 MIN AT 106 μ E) AND DARK RELAXATION (5 MIN)	203
APPENDIX 8.6 HIGH CO ₂ RESCUES PYR- NPQ DURING FLUORESCENCE INDUCTION (20 MIN AT 106 μ E) AND DARK RELAXATION (5 MIN)	204
APPENDIX 8.7: ALTERED OXYGEN LEVELS (2%, 21%, 40%) HAVE LIMITED EFFECT ON ϕ_{II} BUT AFFECT NPQ DURING FLUORESCENCE INDUCTION (20 MIN AT 106 μ E) AND DARK RELAXATION (5 MIN).....	205
APPENDIX 8.8 ALTERED OXYGEN LEVELS (2%, 21%, 40%) HAVE LIMITED EFFECT ON ETR BUT AFFECT NPQ DURING A LIGHT RESPONSE CURVE	206
APPENDIX 8.9: THE MAJORITY OF NPQ IS FAST RELAXING Q _E	207
APPENDIX 8.10: HIGH-RESOLUTION JTS-10 DATA SHOWS PYR- F _v /F _M IS LOWER THAN WT WHEN GROWN AT 50 μ E IN AIR	208
APPENDIX 8.11: ECS PILOT STUDY SUGGESTS ORGANIC CARBON SUPPLY RESTORES PYR- LEF AT LEAST PARTIALLY	209
APPENDIX 8.12: BICARBONATE PILOT EXPERIMENT SHOWS AFTER 30S ECS IS UNRELIABLE DUE TO BACKGROUND DRIFT	210
APPENDIX 8.13: ACTIVITY OF THE WATER-WATER CYCLE (WWC) AROUND PSII IS NOT AFFECTED BY PYRENOID PRESENCE OR ABSENCE	211
APPENDIX 8.14: CEF IN PYR- CAN BE RESCUED BY LONG-TERM, BUT NOT INSTANTANEOUS, SUPPLY OF CARBON.....	212
APPENDIX 8.15: GROWTH AT HIGH CO ₂ BUT NOT ADDITION OF BICARBONATE RESCUES PYR- F _v /F _M	213
APPENDIX 8.16: NPQ OF PYR- IS RESCUED BY GROWTH AT LOW LIGHT OR HIGH CO ₂	214
APPENDIX 8.17: HIGH CO ₂ RESCUES PYR- CEF	215
APPENDIX 8.18: FRRF DATA ARE CONSISTENT WITH CFIMAGER AND JTS-10 DATA	216

APPENDIX 8.19: ADDITIONAL SDM CONSTRUCTS THAT DID NOT RECOVER PHOTOSYNTHETICALLY COMPETENT LINES	217
APPENDIX 8.20: 1 ST DIMENSION COOMASSIE STAINED GEL STRIPS AND RUBISCO WESTERNS FOR POSITIVE CONTROL WT STRAINS.	218
APPENDIX 8.21: 1 ST DIMENSION COOMASSIE STRAINED GEL STRIPS AND RUBISCO WESTERNS FOR THE PYR- STRAIN EXPRESSING <i>SPINACIA OLERACEA RBCS</i>	219
APPENDIX 8.22: 1 ST DIMENSION BN-PAGE PROFILE IS INDEPENDENT OF CELL LYSIS METHOD.....	220
APPENDIX 8.23: CHAPERONIN 60 IS THE SOURCE OF THE NON-REPRODUCIBLE, WT-SPECIFIC, HIGH-MOLECULAR WEIGHT BAND IMMUNO-LABELLED AS CONTAINING RUBISCO.....	221
APPENDIX 8.24: THE ~350 kDa BAND DOES NOT CONTAIN RUBISCO DESPITE IMMUNO-LABELLING IN A PRELIMINARY BN-PAGE SCREEN OF MEMBRANE PROTEINS FOR PYRENOID-RELEVANT COMPLEXES.....	222
APPENDIX 8.25: PAIRWISE COMPARISON OF CO-IP EXPERIMENTAL CONDITIONS.....	223
APPENDIX 8.26: THE STATISTICAL GROUPS INFORM WHICH CANDIDATES SHOW INTERESTING BEHAVIOUR.	224

LIST OF ABBREVIATIONS AND ACRONYMS

Table 0.1: Table of abbreviations

Abbreviation	Full description
2cPRX	<u>2</u> -cys peroxire <u>dox</u> in
3PGA	<u>3</u> -phosphoglycerate
α-KG	<u>α</u> -ketoglutarate (oxoglutarate)
AB	<u>A</u> ntib <u>o</u> dy
ABCC	<u>A</u> cetyl-coA biotin carboxyl carrier
abl	<i>Cr</i> mutants showing <u>a</u> berrant LCIB <u>l</u> ocalisation (Yamano et al., 2014)
aFDX	<u>a</u> po <u>fe</u> rred <u>o</u> xin
ANOVA	<u>A</u> nalysis of <u>v</u> ariance
ASCF1	<u>A</u> TP-syn <u>th</u> ase CF1 <u>α</u> -subunit
ATP	<u>A</u> denosine triphosphate
ATP syn.	<u>A</u> TP syn <u>th</u> ase
aTUB1	<u>α</u> - <u>t</u> ubulin 1
AUC	<u>A</u> nalytical <u>u</u> ltra <u>c</u> entrifugation
β-DM	n- <u>D</u> odecyl- <u>β</u> - <u>M</u> altoside
b₆f	Cytochrome <u>b</u> ₆ <u>f</u> complex
BF	<u>B</u> right <u>f</u> ield
BN-PAGE	<u>B</u> lue- <u>n</u> ative polyacrylamide gel <u>e</u> lectrophoresis
BPA	<u>B</u> isphosphoglycerate
BSA	<u>B</u> ovine <u>s</u> erum <u>a</u> lbumine
bTUB2	<u>β</u> - <u>t</u> ubulin 2
bya	<u>B</u> illion years ago
CA	<u>C</u> arbonic <u>a</u> nhydrase
CAH1	<i>Chlamydomonas</i> periplasmic <u>c</u> arbonic <u>a</u> nhydrase <u>1</u> (protein)
CAH3	<i>Chlamydomonas</i> thylakoid lumenal <u>c</u> arbonic <u>a</u> nhydrase <u>3</u> (gene)
CAH3	<i>Chlamydomonas</i> thylakoid lumenal <u>c</u> arbonic <u>a</u> nhydrase <u>3</u> (protein)

CAH4	<i>Chlamydomonas</i> mitochondrial <u>c</u> arbonic <u>a</u> nhydrase <u>4</u> (protein)
CAH5	<i>Chlamydomonas</i> mitochondrial <u>c</u> arbonic <u>a</u> nhydrase <u>5</u> (protein)
CAIC	<u>C</u> ambridge <u>A</u> dvanced <u>I</u> maging <u>C</u> entre
CAM	<u>C</u> rassulacean <u>a</u> cid <u>m</u> etabolism
CBC	<u>C</u> alvin <u>B</u> enson <u>c</u> ycle
CCM	<u>C</u> arbon <u>c</u> oncentrating <u>m</u> echanism
CDK	<u>C</u> almodulin- <u>d</u> ependent serine/threonine <u>k</u> inase
CEF	<u>C</u> yclic <u>E</u> lectron <u>F</u> low
CF	<u>C</u> hlorophyll <u>f</u> luorescence
chl	<u>C</u> hlorophyll
C_i	<u>I</u> norganic <u>c</u> arbon
CIA5/CCM1	<i>Cr</i> nuclear CCM ‘master regulator’ <u>C</u> _i <u>a</u> ccumulation <u>5</u> / <u>CCM</u> <u>1</u> (gene)
<i>cia5/ccm1</i>	<i>Cr</i> nuclear CCM ‘master regulator’ <u>C</u> _i <u>a</u> ccumulation <u>5</u> / <u>CCM</u> <u>1</u> (mutant)
CIA5/CCM1	<i>Cr</i> nuclear CCM ‘master regulator’ <u>C</u> _i <u>a</u> ccumulation <u>5</u> / <u>CCM</u> <u>1</u> (protein)
CIA6	<i>Cr</i> putative methyltransferase <u>C</u> _i <u>a</u> ccumulation <u>6</u> (gene)
<i>cia6</i>	<i>Cr</i> putative methyltransferase <u>C</u> _i <u>a</u> ccumulation <u>6</u> (mutant)
co-IP	<u>I</u> mmuno- <u>c</u> oprecipitation
CP12	Small protein associated with G3PDH and PRK; CBC regulator
CPI	<u>C</u> yclophilin-type peptidyl- <u>p</u> rolyl <u>c</u> is- <u>t</u> rans <u>i</u> somerase
<i>Cr</i>	<i>Chlamydomonas</i> <u>r</u> einhardtii
ΔpH	<u>p</u> H (proton) gradient between chloroplast stroma and thylakoid lumen
DCMU	3-(3,4- <u>d</u> ichlorophenyl)-1,1- <u>d</u> imethyl <u>u</u> rea (<i>alias</i> Diuron)
DHAP	<u>D</u> ihydroxy <u>a</u> cetone phosphate
DIC	<u>D</u> ifferential <u>i</u> nterference <u>c</u> ontrast
DNA	<u>D</u> eoxyribo <u>n</u> ucleic <u>a</u> cid
e.g.	<i>Exemplum gratiae</i> (latin: for example)
E4P	<u>E</u> rythrose <u>4</u> - <u>p</u> hosphate
ECS	<u>E</u> lectro <u>c</u> hromic <u>s</u> hift

EDTA	<u>E</u> thyl <u>e</u> diamine <u>t</u> etra <u>a</u> cetic <u>a</u> cid
eTEF1	<u>E</u> karyotic <u>t</u> ranslation <u>e</u> longation <u>f</u> actor <u>1</u> α 1
equiv	Molar equivalent
F1,6BP	<u>F</u> ructose-1,6- <u>b</u> isphosphate
F6P	<u>F</u> ructose <u>6</u> -phosphate
FBA	<u>F</u> ructose-1,6- <u>b</u> isphosphate <u>a</u> ldolase; Aldolase
FBP	<u>F</u> ructose-1,6- <u>b</u> isphosphate <u>p</u> hosphatase
FNR	<u>F</u> erredoxin- <u>N</u> ADP ⁺ <u>r</u> eductase
FPI	<u>F</u> KBP-type peptidyl-prolyl cis-trans <u>i</u> somerase
FRRf	<u>F</u> ast <u>r</u> epetition <u>r</u> ate <u>f</u> luorescence
G	<u>G</u> lycolate
G3P	<u>G</u> lyceraldehyde- <u>3</u> -phosphate
G3PDH	<u>G</u> lyceraldehyde- <u>3</u> -phosphate <u>d</u> ehydrogenase
Gc	<u>G</u> lycine
GDC	<u>G</u> lycine <u>d</u> ecarboxylase
GDH	<u>G</u> lycolate <u>d</u> ehydrogenase
GFP	<u>G</u> reen <u>f</u> luorescent protein
GGT	<u>G</u> lutamate/glyoxylate amino <u>t</u> ransferase
GI	NCBI <u>G</u> en <u>I</u> nf <u>o</u> ID
Glyc	<u>G</u> lycerate
GLYK	<u>G</u> lycerate 3- <u>k</u> inase
GOGAT	<u>G</u> lutamine <u>o</u> xoglutarate amino <u>t</u> ransferase
GOX	<u>G</u> lycolate <u>o</u> xidase
GrRb	<u>G</u> lycine-rich RNA-binding protein
GS	<u>G</u> lutamine <u>s</u> ynthetase
GTB1	<u>G</u> -strand <u>t</u> elomere <u>b</u> inding protein <u>1</u>
Gx	<u>G</u> lyoxylate
H⁺	Oxidized <u>h</u> ydrogen ion (proton)

HA	<u>H</u> ydroxylamine (<i>alias</i> Azanol)
HC	<u>H</u> igh <u>c</u> onfidence
HF	JTS-10 buffer (10% w/v <u>F</u> icoll in 20 mM <u>H</u> EPES/KOH, pH 7.2)
HLA3	<i>Cr</i> plasmalemma bicarbonate transporter <u>h</u> igh <u>l</u> ight- <u>a</u> ctivated <u>3</u> (protein)
HOP	<u>H</u> ydroxyp <u>yr</u> uvate
HPR	<u>H</u> ydroxyp <u>yr</u> uvate <u>r</u> eductase
HSP	<u>H</u> eat- <u>s</u> hock <u>p</u> rotein
ID	<u>I</u> dentifier
IP	<u>I</u> nterference (AUC detection method)
J1	<u>J</u> TTS-10 dataset 1
J2	<u>J</u> TTS-10 dataset 2
JGI	<u>J</u> oint <u>G</u> enome <u>I</u> nstitute
JTS	<u>J</u> oliot- <u>t</u> ype <u>s</u> pectrophotometer
LC-MS/MS	<u>L</u> iquid <u>c</u> hromatography- <u>m</u> ass <u>s</u> pectrometry with peptide mass fingerprinting
LCI1	<i>Cr</i> plasmalemma bicarbonate transporter <u>l</u> ow <u>C</u> O ₂ - <u>i</u> nduced <u>1</u> (protein)
LCI5	<i>Cr</i> pyrenoid linker protein <u>l</u> ow <u>C</u> O ₂ - <u>i</u> nduced <u>5</u> (gene)
lci5	<i>Cr</i> pyrenoid linker protein <u>l</u> ow <u>C</u> O ₂ - <u>i</u> nduced <u>5</u> (mutant)
LCI5	<i>Cr</i> pyrenoid linker protein <u>l</u> ow <u>C</u> O ₂ - <u>i</u> nduced <u>5</u> (protein)
LCIA	<i>Cr</i> chloroplast envelope bicarbonate transporter <u>l</u> ow <u>C</u> O ₂ - <u>i</u> nduced <u>A</u> (protein)
LCIB	<i>Cr</i> pyrenoid-associated <u>l</u> ow <u>C</u> O ₂ - <u>i</u> nduced <u>B</u> (protein)
lciB	<i>Cr</i> pyrenoid-associated <u>l</u> ow <u>C</u> O ₂ - <u>i</u> nduced <u>B</u> (mutant)
LCIC	<i>Cr</i> LCIB-associated <u>l</u> ow <u>C</u> O ₂ - <u>i</u> nduced <u>C</u> (protein)
LCR1	<i>Cr</i> transcription factor <u>l</u> ow <u>C</u> O ₂ - <u>r</u> egulator <u>1</u> (protein)
LEF	<u>L</u> inear <u>E</u> lection <u>F</u> low
LHCII	<u>L</u> ight- <u>h</u> arvesting <u>c</u> omplex <u>I</u> I
LSU	<u>L</u> arge <u>s</u> ub <u>u</u> nit of Rubisco (protein)
μE	μEinstein (equivalent to μmol photons m ⁻² s ⁻¹)
MA	<u>M</u> aster of <u>A</u> rts

MS	<u>M</u> alate <u>s</u> ynthase
mya	<u>M</u> illion <u>y</u> ears <u>a</u> go
NADH	<u>N</u> icotinamide <u>A</u> denine <u>D</u> inucleotide, reduced
NADPH	<u>N</u> icotinamide <u>A</u> denine <u>D</u> inucleotide <u>P</u> hosphate, reduced
NCBI	<u>N</u> ational <u>C</u> enter for <u>B</u> io <u>t</u> echnology <u>I</u> nformation
NDH	Chloroplastic <u>NAD(P)H</u> <u>d</u> e <u>h</u> ydrogenase
NPQ	<u>N</u> on- <u>P</u> hotochemical <u>Q</u> uenching
OEC	<u>O</u> xygen <u>e</u> volving <u>c</u> omplex
OEE3	<u>O</u> xygen <u>e</u> volving <u>e</u> nhancer protein 3
p700	reduced <u>PSI</u> reaction centre chlorophyll (absorbs at ~ <u>700</u> nm)
PBS	<u>P</u> hosphate- <u>b</u> uffered <u>s</u> aline
PC	<u>P</u> lastocyanin
pdb	<u>P</u> rotein <u>d</u> ata <u>b</u> ank (file format)
pETC	photosynthetic <u>E</u> lectron <u>T</u> ransport <u>C</u> hain
PEPC	<u>P</u> hospho <u>e</u> nolpyruvate <u>c</u> arboxylase
PG	2- <u>p</u> hosphoglycolate
PGK	<u>P</u> hosphoglycerate <u>k</u> inase
PGP	2- <u>p</u> hosphoglycolate <u>p</u> hosphatase
PPE	<u>P</u> entose <u>p</u> hosphate <u>e</u> pimerase
PPI	<u>P</u> entose <u>p</u> hosphate <u>i</u> somerase
PQ	<u>P</u> lastoquinone
PRK	<u>P</u> hosphoribulo <u>k</u> inase
PSI	<u>P</u> hotosystem <u>I</u>
PSIh	<u>P</u> hotosystem <u>I</u> subunit <u>h</u>
PSII	<u>P</u> hotosystem <u>II</u>
PTOX	<u>P</u> lastid <u>t</u> erminal <u>o</u> xidase
pyr-	<u>P</u> yreloid-less SSU substitution lines
qE	<u>E</u> nergy-dependent <u>q</u> uenching

qI	quenching due to acute photoinhibition
qT	quenching due to state transitions
RA	UV absorbance (AUC detection method)
Rbc	<u>Rubisco</u>
RBCS	<u>Rubisco</u> small subunit gene
RNA	<u>Ribonucleic acid</u>
RPM	<u>Rounds per minute</u>
rS28	Cytosolic <u>ribosomal</u> protein S28
Ru5P	<u>Ribulose 5-phosphate</u>
Rubisco	<u>Ribulose-1,5-bisphosphate carboxylase oxygenase</u>
RuBP	<u>Ribulose-1,5-bisphosphate</u>
R5P	<u>Ribose 5-phosphate</u>
S	<u>Svedberg</u> units for sedimentation rate [10^{-13} sec]
S1,7BP	<u>Sedoheptulose-1,7-bisphosphate</u>
S7P	<u>Sedoheptulose 7-phosphate</u>
SBA	<u>Sedoheptulose-1,7-bisphosphate aldolase</u> ; Aldolase
SBP	<u>Sedoheptulose-1,7-bisphosphate phosphatase</u>
SD	<u>Standard deviation</u>
SDM	<u>Site-directed mutagenesis</u>
SDS	<u>Sodium dodecyl sulphate</u>
SGT	<u>Serine/glyoxylate aminotransferase</u>
SHMT	<u>Serine hydroxymethyltransferase</u>
So	<i>Spinacia oleracea</i>
SP	<u>Saturating pulse</u>
SSU	<u>Small subunit</u> of Rubisco (protein)
ST	<u>Single turnover</u>
TBS	<u>Tris buffered saline</u>
TBS-TT	<u>Tris buffered saline</u> containing detergents <u>Tween20</u> and <u>Triton-X</u>

TEM	<u>T</u> ransmission <u>e</u> lectron <u>m</u> icroscopy
TPI	<u>T</u> riose phosphate <u>i</u> somerase
Tris	<u>T</u> ris(hydroxymethyl)aminomethane; (HOCH ₂) ₃ CNH ₂
TRK	<u>T</u> ransketolase
UV	<u>U</u> ltraviolet
v/v	<u>V</u> olume per <u>v</u> olume
v/w	<u>V</u> olume per <u>w</u> eight
VIPP1	<i>Cr</i> <u>v</u> esicle- <u>i</u> nducing <u>p</u> rotein in <u>p</u> lastids 1 (protein)
w/v	<u>W</u> eight per <u>v</u> olume
w/w	<u>W</u> eight per <u>w</u> eight
WT	<u>W</u> ild-type
WWC	<u>W</u> ater-to- <u>w</u> ater <u>c</u> ycle of electron flow around PSII
Xu5P	<u>X</u> ylulose <u>5</u> -phosphate

Table 0.2: Table of strains

Name used in text	Abbre- via- tion	<i>Chlamy- domonas</i> resource centre ID	alias	Description of strain	Reference
T-60	Q	CC-4415	$\Delta rbcS$ - T60-3 mt-	Cell-wall-less <i>RBCS</i> -knockout parent strain of SSU substitution lines	(Khrebtukova and Spreitzer, 1996)
Reciprocal (pyr-)	R		Rcpr	SSU-substitution line expressing chimeric <i>Chlamydomonas</i> SSU with <i>Spinacia</i> helices	(Meyer et al., 2012)
pyr-	S		SSSO	SSU-substitution line expressing <i>Spinacia oleracea RBCS</i> in T-60 background	(Genkov et al., 2010)
Arabidopsis (pyr-)	T		SSAT	SSU-substitution line expressing <i>Arabidopsis thaliana RBCS</i> in T-60 background	(Genkov et al., 2010)
(pyr-)	U		SSHA	SSU-substitution line expressing <i>Helianthus annuus RBCS</i> in T-60 background	(Genkov et al., 2010)
CC-3395	V	CC-3395	$cw_{arg-7-8} mt^-$	Cell-wall deficient, arginine-requiring parent strain of T-60	(Khrebtukova and Spreitzer, 1996)
WTint1,2 (WT)	W		SS1	SSU-substitution line expressing native <i>Chlamydomonas RBCS1</i> in T-60 background	(Genkov et al., 2010)
HelixAB (pyr+)	X		HAB	SSU-substitution line expressing chimeric <i>Spinacia</i> SSU with <i>Chlamydomonas</i> helices	(Meyer et al., 2012)
2137		CC-4886		Widely used walled WT control strain	(Mitchell et al., 2014)
cMJ030 (WT)				Cell wall-deficient WT parent strain used to generate genome-saturating mutant library (Jonikas research group, Carnegie, Stanford)	(Zhang et al., 2014)(Zhang et al., 2014)
137c	1	CC-124 CC-125		Walled WT parent strain of <i>cia5</i>	(Fukuzawa et al., 2001; Xiang et al., 2001)
<i>cia5</i>	2	CC-2702	<i>ccm1</i>	Strain carrying a knock-out in CCM “master regulator” <i>CIA5/CCM1</i>	(Fukuzawa et al., 2001; Xiang et al., 2001)

Table 0.3: Table of parameters

Parameter	Interpretation (typical values) [units]
% <i>emPAI</i>	% fraction of total protein content based on <i>emPAI</i>
a_{II}	Net PSII light interception factor ($\sim 0.83 \cdot 0.5$) [dimensionless]
A	<u>A</u> bsorbance [a. u.]
a/b	Ratio of chlorophyll abundances [mol mol ⁻¹]
a_I	Chl <u>a</u> associated with PSI core [mol mol ⁻¹]
a_{II}	Chl <u>a</u> associated with PSII core [mol mol ⁻¹]
a_{LHC}	Chl <u>a</u> associated with <u>l</u> ight- <u>h</u> arvesting <u>c</u> omplexes [dimensionless]
b_I	Chl <u>b</u> associated with PSI [mol mol ⁻¹]
b_{II}	Chl <u>b</u> associated with PSII [mol mol ⁻¹]
b_{LHC}	Chl <u>b</u> associated with <u>l</u> ight- <u>h</u> arvesting <u>c</u> omplexes [dimensionless]
b_m	<u>M</u> ean IF <u>b</u> ackground intensity [a. u.]
c	<u>C</u> oncentration [mol l ⁻¹]
c_A	IF image <u>c</u> ell <u>a</u> rea [μm^2]
c_D	Integrated IF image <u>c</u> ell fluorescence <u>d</u> ensity [a. u.]
CEF	<u>C</u> yclic <u>e</u> lectron <u>f</u> low (ST equivalents) [mol mol ⁻¹ s ⁻¹]
[<i>chl</i>]	Total (a+b) <u>chl</u> orophyll concentration [mol l ⁻¹]
$chl/PSII$	<u>Ch</u> lorophyll allocated to <u>PSII</u> [mol mol ⁻¹]
ε	Molar absorptivity [equiv ⁻¹ cm ⁻¹]
ε_{p700}	ε for p700 (64) [mequiv ⁻¹ cm ⁻¹]
EF	<u>E</u> lectron <u>f</u> low (ST equivalents) [mol mol ⁻¹ s ⁻¹]
<i>emPAI</i>	<u>e</u> xponentially <u>m</u> odified <u>P</u> rotein <u>A</u> bundance <u>I</u> ndex
ETR	<u>E</u> lectron <u>t</u> ransport <u>r</u> ate through PSII [$\mu\text{mol m}^{-2} \text{s}^{-1}$]
F_0	Minimal (<u>o</u> riginal) dark-adapted <u>CF</u> [a. u.]
F_m	<u>M</u> aximal dark-adapted <u>CF</u> [a. u.]

F_m'	Maximal light-adapted CF [a. u.]
F_s	Steady-state light adapted CF [a. u.]
F_v/F_m	(dark adapted) PSII quantum efficiency [dimensionless]
I	Light intensity received [$\mu\text{E} = \mu\text{mol m}^{-2} \text{s}^{-1}$]
I_0	Initial I received by spectrophotometer [μE]
I_2	I received by PSII [$\mu\text{E} = \mu\text{mol m}^{-2} \text{s}^{-1}$]
I_k	I where photosynthesis starts to saturate [μE]
I_x	I where ϕ_{II} is $0.5 \phi_m$ [$\mu\text{E} = \mu\text{mol m}^{-2} \text{s}^{-1}$]
J	Rate of electron transport in pETC [$\mu\text{mol m}^{-2} \text{s}^{-1}$]
J_{max}	Maximal J [$\mu\text{mol m}^{-2} \text{s}^{-1}$]
k	p700 dark relaxation decay rate constant [$\text{e}^{1/\text{sec}}$]
K_m	[S] where enzyme catalysis is $0.5 V_{max}$ [mol]
l	Light path length through cuvette (1) [cm]
LEF	Linear electron flow (ST equivalents) [$\text{mol mol}^{-1} \text{s}^{-1}$]
LEF/ETR	Ratio of ECS and CF-based LEF proxies (informs CEF)
$LHCs/PSII$	Number of light-harvesting complexes per PSII [dimensionless]
m_{ECS}	Slope of initial ECS dark relaxation decay [s^{-1}]
${}_n^f m_{ECS}$	m_{ECS} of exponential fit to normalized data [s^{-1}]
NPQ	Non-photochemical quenching [dimensionless]
ϕ_{II}	PSII operating efficiency [dimensionless]
ϕ_m	Maximal PSII operating efficiency [dimensionless]
$p\%$	% of cell IF signal arising from outside the pyrenoid [dimensionless]
p_A	IF image pyrenoid area (4.6) [μm^2]
p_D	Integrated IF image pyrenoid fluorescence density [a. u.]
P_m	Absorption of maximally oxidized p700 [a. u.]
P_s	Steady-state absorption of p700 [a. u.]

<i>[PSI]</i>	Concentration of <u>PSI</u> [mol l ⁻¹]
<i>[PSII]</i>	Concentration of <u>PSII</u> [mol l ⁻¹]
<i>PSI/PSII</i>	Ratio of photosystem abundances (1) [mol mol ⁻¹]
<i>p_x</i>	Fold-change of pyrenoid relative to cell IF intensity [dimensionless]
<i>red</i>	<u>Reduction</u> state of p700 (oxidized fraction) [dimensionless]
<i>σ_{II}</i>	Functional <u>PSII</u> absorption cross-section [nm ²]
<i>[S]</i>	<u>Substrate</u> concentration [mol]
<i>ST_{DH}</i>	<u>ST</u> of PSI (in the presence of <u>DCMU</u> and <u>HA</u>) [mol/mol]
<i>ST_n</i>	<u>ST</u> of PSI and PSII (<u>no</u> inhibitors) [mol e ⁻ / mol photon]
<i>t_{2/3}</i>	<u>Time</u> to reach <u>2/3</u> of <i>F_m</i> (in the presence of DCMU) [s]
<i>θ</i>	Empirical shape correction parameter (~0.7) [dimensionless]
<i>V_{max}</i>	<u>Maximum</u> rate of enzyme catalysis [mol s ⁻¹]

LIST OF APPENDICES

DERIVATION OF JTS-10 CORRECTION FACTOR.....	199
CHAPTER 2 SUPPLEMENTARY FIGURES.....	200
CHAPTER 3 SUPPLEMENTARY FIGURES.....	217
CHAPTER 4 SUPPLEMENTARY FIGURES.....	218
TABULARIZED RUBISCO INTERACTOME.....	226

1 INTRODUCTION

Human civilisation is contingent upon a sufficient production of food from crops. Over the course of the next century, increased demand for food by a burgeoning population is occurring at the same time as diminishing fossil fuel and fertilizer resources combined with increased climate change threaten harvests. Increasing crop yields is one key issue among many aspects of food production and distribution that needs to be considered to ensure food security. Understanding crop physiology has been crucial in enabling yield increases through breeding short-stalked varieties in what is called the “green revolution”, however, exploitation of this trait is reaching a biological limit. In order to enable a further increase in yield potential, other aspects of plant physiology need to be targeted.

One key aspect expected to support significant advances is the efficiency of photosynthesis, i.e. the amount of CO₂ fixed per light received. Attempting to increase the efficiency of a system that has been evolving for almost 3 bya may seem like a tall order, but a detailed understanding of the physiology can make possibilities apparent. Whereas the maximum quantum yield of the conversion of light into high energy metabolites via the photosynthetic electron transport chain (pETC) appears close to a theoretical maximum, fixation of CO₂ via Rubisco in the Calvin Benson Cycle (CBC) poses a major limitation for photosynthetic efficiency.

In addition to comparatively slow enzymatic catalysis, Rubisco not only catalyses the fixation of CO₂ but supports a reaction with O₂, leading to photorespiration which requires input of energy and resources. Energy supply via pETC must balance demand via CBC and photorespiration. Cells therefore dissipate energy that is received in excess of what can be

processed by the CBC as heat, actively reducing the efficiency of photosynthesis in order to avoid damage from reactive oxygen species.

Increasing the capacity of the CBC to process more energy supplied from the pETC would thus provide scope for improving the efficiency of photosynthesis overall. In evolution, this problem has been solved by the establishment of Carbon Concentrating Mechanisms (CCM). By expending energy on accumulating a high concentration of CO₂ around Rubisco, CBC capacity can be increased both relative to photorespiration and in absolute terms of increased CO₂ fixation per enzyme per unit time. As a result, significant effort is being invested to genetically engineer CCM operation in crop plants. From a crop-engineering point of view, there appears to be a trade-off between focusing on a highly complex mechanism from a closely related lineage such as C₄, compared to an apparently much simpler mechanism such as the cyanobacterial CCM which is associated with an evolutionary gap of ~2 bya.

In this divide, an algal CCM such as the one operated by model green alga *Chlamydomonas reinhardtii* appears as a good compromise between evolutionary distance and mechanistic simplicity. The work in this thesis contributes to a better understanding of the *Chlamydomonas* CCM by investigating a key aspect of this CCM, which is the aggregation of Rubisco in a proteinaceous micro-compartment called the pyrenoid. Specifically, the current study aimed to elucidate the mechanism of pyrenoid assembly, and provides insight into the interactions between pyrenoid, CCM and chloroplast ultrastructure. Over the following pages, key aspects of photosynthetic energy balancing, CCM operation and the *Chlamydomonas* CCM in particular will be introduced to set the work presented in later chapters into context. Over the following chapters, characterisation of photosynthetic and molecular physiology of *Chlamydomonas* mutant strains showing defects in the localisation of Rubisco are used to gain functional and mechanistic insight into the pyrenoid.

1.1 The physiology of photosynthesis requires energy supply and demand to be balanced

In photosynthesis, energy supply and demand are tightly regulated to balance at all times (Eberhard et al., 2008; Cardol et al., 2011; Foyer et al., 2012). Incoming energy in the form of light is processed by the pETC and converted into high-energy metabolites ATP and NADPH. Production of these metabolites is balanced against consumption with the majority being used in CO₂ fixation via the CBC. Getting the balance right is so crucial that it has been suggested to be the main reason for retention of genomes in the chloroplast (Allen,

2003; Lane, 2014). Physiological adjustments of photosynthesis can be understood as a constant rebalancing act as conditions shift between the supply of light or the supply of CO₂, which ever is more limiting (Von Caemmerer, 2013; McGrath and Long, 2014).

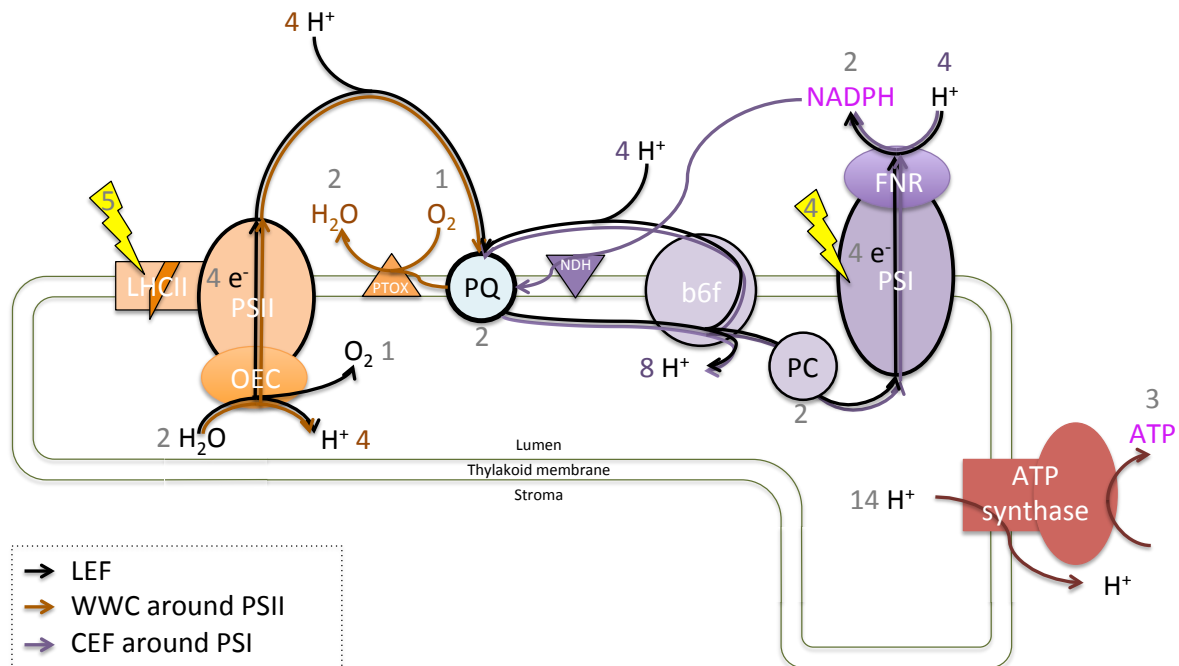


Fig. 1.1: LEF and CEF pathways in the pETC

As photosystem II (PSII) operates with a maximum quantum efficiency of 83%, for every 5 photons absorbed by the antenna system (symbolized here by the major constituent Light Harvesting Complex II: LHCII), 4 e⁻ are extracted from 2 H₂O via the Oxygen Evolving Complex (OEC) resulting in the release of molecular Oxygen as well as 4 H⁺ in the thylakoid lumen. The 4 e⁻ are passed on in pairs to 2 Plastoquinones (PQ), consuming 4 H⁺ on the stromal side of the thylakoid membrane in the process, thereby completing the process of pumping 1 H⁺ per e⁻ at PSII. Photosystem I (PSI) exhibits a quantum efficiency close to 100%, meaning only 4 protons are required to transfer 4 e⁻ from Plastocyanine (PC) to the Ferredoxin-NADP⁺ reductase (FNR) to produce 2 NADPH. For each e⁻ processed by PSI, 2 H⁺ are transferred from stroma to thylakoid lumen through the action of cytochrome b₆f (b₆f), as for every pair of e⁻ accepted (and thus 2 H⁺ released) from PQ at the thylakoid lumen, b₆f transfers 1 e⁻ to PC and recycles 1 e⁻ back to PQ at the stromal side, associated with the uptake of 1 H⁺. The two photosystems can work in series, resulting in linear electron flow (LEF) which requires 9 photons (5 at PSII, 4 at PSI) to transfer 4 e⁻ from H₂O to NADP⁺, associated with a transfer of 12 H⁺ (4 at PSII, 8 at b₆f/PSI) from stroma to thylakoid lumen. Alternatively, Photosystems can work independently: e⁻ extracted from H₂O by PSII can be donated from PQ to oxygen through the action of plastid terminal oxidase (PTOX) producing H₂O, hence the name water-water cycle (WWC). Cyclic electron flow (CEF) proceed by reinjecting electrons from the stromal side of PSI into the PQ pool, e.g. via NADPH dehydrogenase (NDH). Alternative CEF pathways have been omitted for simplicity but are functionally equivalent in terms of the H⁺ transferred per e⁻. Energy stored in the proton gradient is then used to drive ATP production via ATP synthase.

One important aspect of energy balancing is the distribution of light between photosystem I (PSI) and photosystem II (PSII). Light-driven oxidation of H₂O at the oxygen evolving complex (OEC) associated with PSII places biophysical constraints on the reaction centre, leading to a maximum quantum efficiency of ~83%. Thus PSII requires at least 5 photons for complete extraction of 4 electrons from water and production of 1 O₂ (Fig. 1.1). By contrast, PSI operates at nearly 100% quantum efficiency. When PSII and PSI work in series, linear electron flow (LEF) leads to the production of two NADPH as well as contributing the movement of 12 protons (H⁺) to the thylakoid pH gradient (Δ pH) per 9 photons (Eberhard et al., 2008; Raven et al., 2014). In the ATP synthase, 3 ATP are produced in one complete revolution driven by 14 proton-channelling CF₀ subunits, meaning ~2.6 ATP are produced per 12 H⁺ (Eberhard et al., 2008; Minagawa, 2013). Since CO₂ fixation via the CBC requires 3 ATP per 2 NADPH, the production of ATP from LEF alone is likely insufficient.

Cycling of electrons around a reaction centre may alleviate this imbalance, as such cyclic electron flow (CEF) would generate Δ pH but no NADPH. Several pathways for CEF around PSI have been suggested, such as via the Mehler reaction (Heber, 2002), via a PSI/cytochrome b₆f supercomplex (Iwai et al., 2010; Tolleter et al., 2011), or via chloroplastic NAD(P)H dehydrogenase (NDH) injecting electrons into the plastoquinone (PQ) pool (Eberhard et al., 2008). Either way, CEF likely contributes 2 H⁺ to Δ pH per photon, resulting in production of ~0.4 ATP (Minagawa, 2013). Thus equal distribution of light between the photosystems appears optimal to support CO₂ fixation, as 5 photons/PSII and 5 photons/PSI generate 3 ATP and 2 NADPH supporting fixation of 1 CO₂ via the CBC. As an alternative to CEF, electrons extracted from water by PSII can be cycled back to water from the PQ-pool via plastid terminal oxidase (PTOX), which may be particularly relevant in conditions where the availability of Iron is limiting PSI expression (Eberhard et al., 2008). As the Q-cycle in the cytochrome b₆f complex (b₆f) is bypassed, the water-water cycle around PSII (WWC) moves only 1 H⁺ per electron and thus has a lower efficiency than CEF around PSI.

A number of buffering systems exist to allow short-term energy storage when the supply of light suddenly exceeds CBC demand, such as reduction of the PQ-pool that donates electrons to cytochrome b₆f, or Δ pH. In this context, the recording of chlorophyll fluorescence (CF) has proved to be a very powerful tool to study photosynthesis, being quantitatively informative about the activity of PSII (Kautsky and Hirsch, 1931; Genty et al., 1989; Krause and Weis, 1991; Maxwell and Johnson, 2000; Papageorgiou and Govindjee,

2004; Cosgrove and Borowitzka, 2010). Using CF, the effect of short-term buffering systems has been well documented in fluorescence induction experiments when light is suddenly switched on and a pool of energy metabolites is built up even before the CBC is activated (Lazár, 1999; Papageorgiou and Govindjee, 2004).

In conditions where CBC activity is not sufficient to alleviate the imbalance between energy supply and demand, the efficiency with which incoming light is processed must be reduced. In this context, efficiency is meant as pETC output in terms of energy metabolites NADPH and ATP per input in terms of light received. Absorbing less of the incoming light and dissipating more of the absorbed light, rather than using the energy in the pETC, can reduce this efficiency. In contrast to PSI, PSII has only limited scope to dissipate excess energy as heat from within the reaction centre (Ivanov et al., 2008), and instead requires photoprotective mechanisms that limit the delivery of excess photons. An umbrella term for mechanisms effecting such a reduction in efficiency of energy transfer to PSII is non-photochemical quenching (*NPQ*), which describes the fluorescence quenching effect observed as a result (Horton et al., 2008; Lambrev et al., 2012).

The short term buffering systems mentioned above can play a role in feedback regulation of *NPQ*. For example, a high proton gradient leads to energy dependent quenching (qE) in the thylakoid membranes which involves the dissipation of excess energy as heat within the light harvesting complexes, often through the action of carotenoids (Holt et al., 2004; Jahns and Holzwarth, 2012). A highly reduced PQ-pool on the other hand can lead to redox-regulated phosphorylation of light harvesting complex II (LHCII) which then detaches from PSII in a process called state transitions (qT) (Haldrup et al., 2001; Finazzi, 2005; Ruban and Johnson, 2009; Minagawa, 2011).

By reducing the absorption cross-section of the light harvesting pigment bed, state transitions thereby lower the light energy channelled through PSII (Suggett et al., 2003; Iwai et al., 2007; Lambrev et al., 2011; Drop et al., 2014). Once dissociated, LHCII can form independent clusters that dissipate absorbed light as heat. Alternatively, LHCII can associate with PSI, altering the distribution of light between the photosystems and thus the balance between LEF and CEF (Haldrup et al., 2001; Finazzi et al., 2002; Eberhard et al., 2008; Minagawa, 2013). With ~80% of LHCII changing association during state transitions in *Chlamydomonas*, LHCII mobility is much greater in algae than in higher plants where only 20-25% move (Eberhard et al., 2008).

If excess energy is not sufficiently dissipated, accumulated reducing power leads to production of reactive oxygen species, resulting in acute photoinhibition (qI) when the rate of damage exceeds the rate of repair, and eventually chronic photoinhibition and photobleaching (Ivanov et al., 2008; Ruban and Murchie, 2012). In a scenario where energy supply exceeds demand, a reduction in the efficiency of photosynthesis via *NPQ* helps to prevent this accumulation of reducing power and is therefore often also referred to as photoprotection.

1.2 CCMs enable greater photosynthetic efficiency by increasing CO₂ fixation capacity

An alternative to reducing energy supply, and thus photosynthetic efficiency, would be to increase energy demand via a higher CBC turnover. In the low CO₂ atmosphere that we currently experience, the major limiting step in the CBC is the rate of CO₂ fixation by Ribulose biphosphate carboxylase/oxygenase (Rubisco). At 3 s⁻¹, Rubisco catalysis is slow compared to other enzymes, and with a K_m of ~10 μM only about every second active site is active at any given time at current atmospheric CO₂ concentrations of ≤400 ppm. Owing to mechanistic trade-offs between specificity to CO₂ compared to O₂ and speed of catalysis, Rubisco itself has only limited adaptive scope to support a higher fixation rate at a given CO₂ concentration (Tcherkez et al., 2006). Instead, multiple independent evolutionary events have generated mechanisms of energized inorganic carbon uptake leading to an elevated concentration of CO₂ in the vicinity Rubisco (Raven et al., 2012, 2014), allowing Rubisco to operate close to maximum enzymatic turnover and effectively suppressing oxygenation.

1.2.1 CCMs require compartmentalisation of Rubisco

An important aspect of such CCMs is the localization of Rubisco in a specific compartment where CO₂ is regenerated from previously captured inorganic carbon (C_i) to achieve high local concentrations. In aqueous solution such as in the cell cytoplasm, C_i is partitioned in a pH-dependent manner between CO₂, bicarbonate (HCO₃⁻) and carbonate (CO₃²⁻) with >90% present as HCO₃⁻ at physiological pH. Naturally occurring interconversion between C_i species can be rate limiting for biological processes in which case Carbonic Anhydrases (CA) are expressed. These bidirectional enzymes facilitate rapid interconversion of the equilibrium $H_2O + CO_2 \rightleftharpoons HCO_3^- + H^+$.

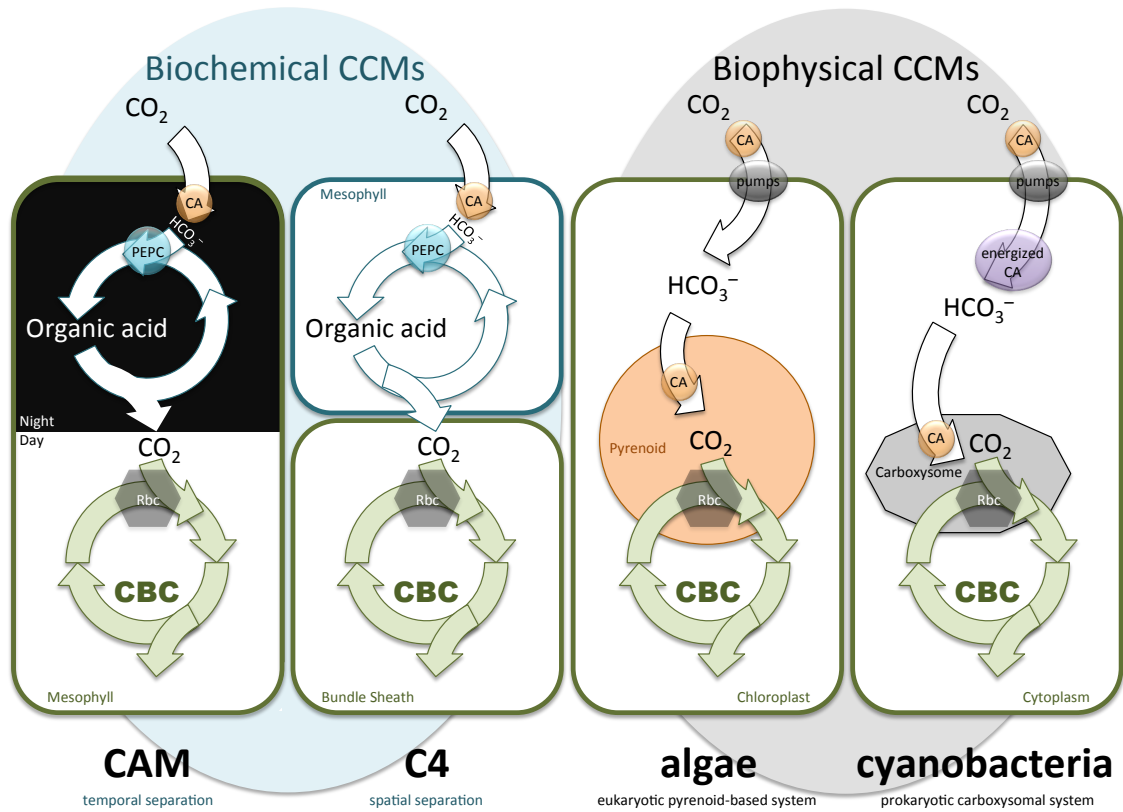


Fig. 1.2: CCMs accumulate carbonated transport acids to release CO₂ near compartmentalized Rubisco

Whereas Biochemical CCMs use organic acids generated from HCO₃⁻ by phosphoenolpyruvate carboxylase (PEPC), biophysical CCMs rely directly on inorganic HCO₃⁻ which is taken up actively via transmembrane pumps. As a result, carbonic anhydrases (CA) which speed up the interconversion of CO₂ and HCO₃⁻ is vital for both systems, but excluded from the HCO₃⁻ rich compartment of biophysical CCMs to prevent a short-circuiting of the carbon flux. An energized, unidirectional CA that specifically produces HCO₃⁻ from CO₂ has so far only been found in cyanobacteria. Compartmentalisation of Rubisco is crucial to enable transport acids to be accumulated and thus generate a high internal concentration of CO₂. This compartmentalisation can proceed via temporal separation of acid generation and Rubisco as in crassulacean acid metabolism (CAM), or via spatial separation as in C4 and biophysical CCMs. Whereas C4 uses the distinct cell type of the bundle sheath as compartment for Rubisco, biophysical CCMs proceed via the subcellular compartments of the eukaryotic pyrenoid or cyanobacterial carboxysomes. These subcellular structures regenerate CO₂ from HCO₃⁻ via internally localised CA to supply Rubisco; the remaining steps of the calvin benson cycle (CBC) are excluded from the Rubisco compartments to the surrounding algal chloroplast stroma or the cyanobacterial cytoplasm.

C_i capture can be via a “biochemical” CCM such as in higher plants, using phosphoenolpyruvate carboxylase (PEPC) to generate an organic acid from HCO₃⁻, which is then de-carboxylated in the spatially or temporally separated compartment containing Rubisco. Alternatively, a CCM is classed as “biophysical”, e.g. in cyanobacteria, eukaryotic algae and hornworts, when HCO₃⁻ itself is used as inorganic transport acid, to be converted

to CO₂ within a specialized subcellular structure where Rubisco is aggregated (Meyer et al., 2008; Villarreal and Renner, 2012). To aid C_i capture in this context, cyanobacteria use an energized unidirectional CA analogue to catalyse the production of HCO₃⁻ from CO₂, in addition to the involvement of bidirectional CAs important for rapid CO₂/HCO₃⁻ interconversion in both types of CCM.

Two types of higher plant “biochemical” CCMs can be distinguished by the mechanism of Rubisco compartmentalisation. In Crassulacean Acid Metabolism (CAM), many or all cells in a leaf may serve as the compartment for Rubisco and also provide an effective diffusion barrier for CO₂ in the absence of stomatal opening, with PEPC activity/organic acid sequestration and CBC operation separated temporally (Owen and Griffiths, 2013). C₄ metabolism works through spatial separation of the two carboxylases, with PEPC typically active in mesophyll cells and Rubisco sequestered in the specialized Bundle Sheath in Kranz Anatomy.

For a given “biophysical” CCM, Rubisco is generally aggregated in a specialized subcellular structure, which represents an effective way to achieve compartmentalisation within single-celled organisms. Packaging of Rubisco in cyanobacterial carboxysomes is a highly structured process that involves a number of well-defined scaffold proteins (Espie and Kimber, 2011; Rae et al., 2013). The outer boundary of carboxysomes is defined by facet-forming shell proteins like CSoS1 for α- and CcmK for β-carboxysomes. Protein facets assemble into an icosahedral-shaped organelle by lower-abundance variants forming the vertices, e.g. CSoS4 and CcmL for α- and β-carboxysomes respectively. Rubisco is packaged through linker proteins such as CcmM in β-carboxysomes, which is thought to replace individual small subunits from adjacent holoenzymes with a repeat motif connected by a disordered flexible linker region. In α-Cyanobacteria, CsoS2 has recently been suggested to play an analogous role using repeated motifs as binding interfaces connected by disordered flexible linker regions (Cai et al., 2015). By contrast, the much larger Rubisco aggregates found in eukaryotes, termed pyrenoids, are less-well defined and usually appear as amorphous protein clusters, sometimes involving thylakoid membranes (Griffiths, 1970).

1.2.2 Adaptive benefits of CCM operation depend on complex trade-offs

CCM operation leads to complex resource trade-offs. Firstly, and perhaps most importantly, the closer to CO₂ saturation Rubisco operates, the higher the rate of CO₂ fixation per unit time (Mettler et al., 2014). A second important aspect of CCM operation is that substrate oxygenation at Rubisco is effectively suppressed.

The reaction with O_2 , catalysed by Rubisco in a low CO_2 environment besides carboxylation, generates phosphoglycolate (PG) as a toxic waste product that needs to be expelled or recycled in a resource-intensive process called photorespiration (Foyer et al., 2009; Bauwe et al., 2010; Becker, 2013; Moroney et al., 2013). For every 4 O_2 fixed, photorespiration releases 2 CO_2 and 2 NH_3 , consuming 2 ATP in nitrogen re-fixation in addition to the 9 ATP and 6 NADPH consumed in the CBC to regenerate RuBP (Fig. 1.3). The impact is significant: on a global scale, photorespiratory nitrogen re-fixation exceeds primary nitrogen fixation by an order of magnitude.

As only 3 RuBP are regenerated for every 4 consumed via oxygenation, one RuBP needs to be regenerated from G3P that would usually be exported from the CBC to cellular metabolism, consuming an additional 1 ATP. While in higher plants the peroxisome hosts some of the photorespiratory enzymes, the entire pathway is located in the mitochondria in chlorophyte algae such as *Chlamydomonas* (Becker, 2013). Use of the mitochondrial glycolate dehydrogenase (GDH) instead of peroxisomal glycolate oxidase (GOX) allows *Chlamydomonas* to salvage energy by regenerating 4 NADH per 4 O_2 fixed in the conversion of Glycolate (G) to Glyoxylate (Gx). Every oxygenation event is thus associated with a loss of 0.5 CO_2 , 3 ATP and 1.5 NADPH in higher plants or 0.5 NADPH in *Chlamydomonas*.

The rate of oxygenation depends on the specificity of Rubisco for CO_2 , as well as the supply of CO_2 relative to O_2 , both of which decrease at higher temperatures resulting in increased rates of oxygenation. Costs of carbon accumulation on the other hand appears to be relatively fixed at around 1-2 ATP per CO_2 released in the vicinity of Rubisco (Foyer et al., 2009; Lucker and Kramer, 2013; Raven et al., 2014). A temperature sensitive energetic trade-off ensues between operating photorespiration in the absence of a CCM, and operating a CCM and thereby largely suppressing photorespiration. Both Photorespiration and CCM operation increase the ratio of ATP:NADPH consumed and thus generate a requirement for CEF.

In addition to altering the running costs of photosynthetic metabolism, CCM operation is thought to affect capital costs by changing the composition of protein machinery required for the task. As a result, energy and nutrient requirements such as nitrogen and phosphorus associated with RNA and protein synthesis may be reduced by the activity of a CCM (Raven et al., 2012). For higher plants, water use efficiency is increased.

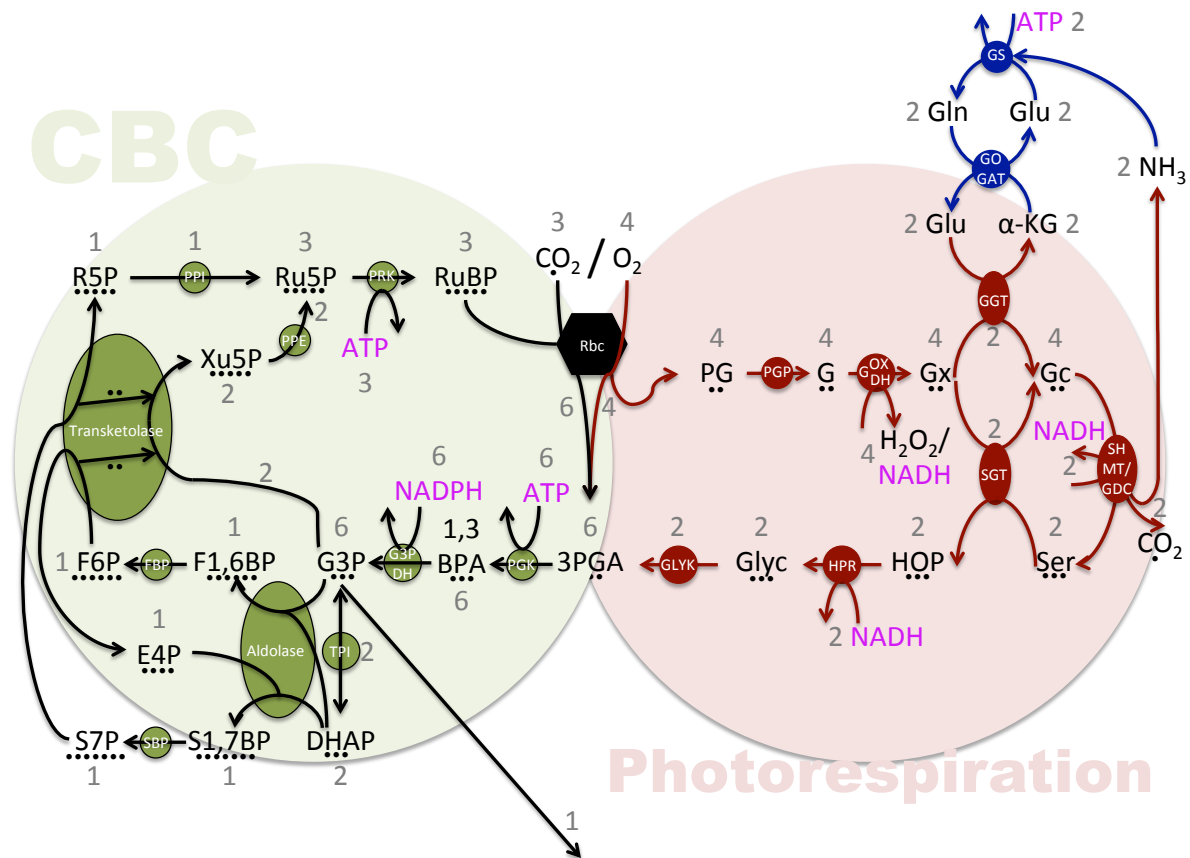


Fig. 1.3: Fixation of either 3 CO₂ or 4 O₂ leads to generation of 6 G3P via CBC or photorespiration.

Flux of carbon is highlighted as 1 point/C below metabolites. CBC (green) and photorespiratory nitrogen re-fixation (blue) occur in the chloroplast, photorespiratory enzymes (red) are localized in mitochondria in *Chlamydomonas* and in peroxisome/mitochondria in higher plants. For every 3 molecules of single-carbon CO₂ added to 3 five-carbon ribulose biphosphate (RuBP) substrates by Rubisco (Rbc), 6 molecules of three-carbon 3-phosphoglycerate (3PGA) are produced. Alternatively, Rbc can react with O₂, producing 4 molecules of 3PGA as well as 4 two-carbon 2-phosphoglycolates (PG) for every 4 RuBP consumed. In photorespiration, PG is processed by 2-phosphoglycolate phosphatase (PGP) to produce two-carbon glycolate (G). In higher plant peroxisomes, glycolate oxidase (GOX) turns G into two-carbon Glyoxylate (Gx), producing H₂O₂ as a side product. In *Chlamydomonas*, the generation of Gx is performed by mitochondrial glycolate dehydrogenase (GDH) which produces NADH instead of H₂O₂. Two out of every four Gx are processed by glutamate/Glyoxylate aminotransferase, generating 2 two-carbon glycines (Gc) as well as turning 2 glutamates (Glu) into 2 α-ketoglutarates (α-KG, *alias* oxoglutarate). 2 Gc are then combined to 1 three-carbon serine (Ser) via serine hydroxymethyltransferase (SHMT) and glycine decarboxylase (GDC), also producing 1 NADH, 1 CO₂ and 1 NH₃. The NH₃ is salvaged through nitrogen re-fixation in the chloroplast through a ATP-consuming reaction with Glu catalysed by glutamine synthetase (GS). Glu is regenerated from product glutamine (Gln) and the α-KG produced earlier via glutamine oxoglutarate aminotransferase (GOGAT). The remaining two out of every four Gx are turned into Gc via serine/Glyoxylate aminotransferase (SGT) which also processes Ser. The 2 three-carbon

hydroxypyruvates (HOP) produces in this way for every 4 oxygenation events are reduced to 2 three-carbon glycerates (Glyc) via NADH-consuming hydroxypyruvate reductase (HPR). Glyc is further processed by glycerate 3-kinase (GLYK), feeding 2 three-carbon 3PGAs into the calvin-benson cycle (CBC) in addition to the 4 produced by Rbc for every 4 O₂ fixed.

Whether from oxygenation or carboxylation, 3PGA is processed by ATP-consuming phosphoglycerate kinase to bisphosphoglycerate (BPA) and further by NADPH-consuming glyceraldehyde 3-phosphate dehydrogenase (G3PDH) into glyceraldehyde 3-phosphate (G3P). Of every 6 three-carbon G3P, 1 can be exported to cellular metabolism while the remaining 5 are processed into 3 five-carbon RuBP substrates for Rubisco. Triose phosphate isomerase (TPI) interconverts 2 G3P into dihydroxyacetone phosphate (DHAP), one of which reacts with a 3rd G3P in a reaction catalysed by the enzyme aldolase to form six-carbon fructose-1,6-bisphosphate (F1,6BP) which is then turned into six-carbon fructose 6-phosphate (F6P) by fructose-1,6-bisphosphate phosphatase (FBP). The enzyme transketolase uses F6P to donate two carbons to a 4th G3P, resulting in four-carbon erythrose 4-phosphate (E4P) and five-carbon xylose 5-phosphate (Xu5P) respectively. Aldolase then combines E4P with the 2nd DHAP produced earlier into seven-carbon sedoheptulose-1,7-bisphosphate (S1,7BP) which is then turned into seven-carbon sedoheptulose 7-phosphate (S7P) by sedoheptulose-1,7-bisphosphate phosphatase (SBP). Transketolase makes use of SBP again as a two-carbon donor to a 5th G3P, producing five-carbon ribose 5-phosphate (R5P) and a 2nd Xu5P. All three five-carbon species are turned into instances of five-carbon ribulose 5-phosphate (Ru5P), R5P via pentose phosphate isomerase (PPI) and Xu5P via pentose phosphate epimerase (PPE). Finally, Ru5P is phosphorylated into RuBP by phosphoribulokinase (PRK).

1.2.3 CCMs present a common solution to different problems arising from CO₂ limitation

The complex trade-offs involved in CCM operation highlight different aspects of the problem of conducting photosynthesis when CO₂ is limiting. Different aspects prevail in different environments. For example, beyond ~20°C CCM operation appears energetically more favourable than photorespiration (Ehleringer et al., 1997; Foyer et al., 2009). However, even at temperatures below this threshold, CCM operation may be advantageous in conditions where light is in excess and energy thus not limiting. By sustaining simultaneously a higher energy throughput and a higher rate of CO₂ fixation per unit time, CCM operators would be able to accumulate biomass more rapidly than non-CCM competitors. Where certain nutrients or water are limiting, a CCM could also provide an advantage at low temperatures despite a higher energy requirement. As a result, distinct driving forces have established CCM operation as part of separate evolutionary trajectories. For example, nitrogen homeostasis may have been a main driving force for early events in the evolution of C₄ in multiple clades with anatomical changes limiting loss of photorespiratory NH₃ release (Mallmann et al., 2014). For CAM evolution on the other

hand, water storage was possibly the most important initial driving force (Griffiths, 2013). In either case, CCMs only confer an advantage in a low CO₂ atmosphere, reflected by the rapid diversification of CAM and C4 lineages ~5-10 mya following a drop in atmospheric CO₂ (Williams et al., 2012; Givnish et al., 2014).

Diffusion of CO₂ is 10,000 times slower in water than in air. For terrestrial plants, this generates evolutionary pressure to minimize the aqueous phase diffusive path length and has led e.g. to large internal air spaces in most leaf architectures. Aquatic organisms on the other hand cannot escape a higher liquid boundary layer. As a result, CO₂ uptake can be limiting when photosynthetic drawdown exceeds the rate of diffusive supply. CCM operation enables the maintenance of high rates of CO₂ fixation, and can be more advantageous at higher CO₂ levels in an aqueous environment when compared with a terrestrial context. Accordingly, CCMs in aquatic organisms are much older than in land plant lineages (Badger et al., 2002; Leliaert et al., 2011) and generally only absent from some picoplankton species with cells small enough to allow diffusive supply of CO₂ to be sufficient.

After the advent of eukaryotic photosynthesis with the primary plastid endosymbiosis ~1.8 bya (Becker, 2013), pyrenoid-based CCMs may have evolved in response to lowered atmospheric CO₂ levels anywhere between close to the split of red and green lineages ≥ 1.1 bya (Raven et al., 2012; Becker, 2013) and a particularly low CO₂ period ~400 mya (Badger et al., 2002; Meyer and Griffiths, 2013). Pyrenoids are ubiquitous among photosynthetic eukaryotes as distantly related as hornworts and dinoflagellates suggesting analogous evolution, with well documented recent loss and regain of pyrenoids in closely related lineages supporting the idea that multiple independent evolution events may easily have been possible (Morita et al., 1998; Leliaert et al., 2011, 2012; Villarreal and Renner, 2012).

1.2.4 Genetic engineering of CCMs may provide a strategy to increase crop yield

Many of the most important crops, and especially those that feed most people such as rice and wheat, do not operate a CCM. By improving other aspects of plant physiology that also influence crop yield, such as the harvest index, it has been possible to considerably increase yields in the context of the green revolution; however, yield potential is now plateauing as genetic variation in these conventional traits reaches biological limits of exploitation (Long et al., 2015). One way to enhance Radiation Use Efficiency might be to introduce some form of CCM into these staples. This might be brought about either by means of the C4 biochemical CCM (IRRI, 2015) or by a biophysical CCM operating in every chloroplast.

Heterologous CCM operation is predicted to provide a growth benefit resulting in up to 50-60% higher yields on a large proportion of arable lands worldwide (Zhu et al., 2010; Long et al., 2011; Hibberd and Weber, 2012; Meyer and Griffiths, 2013; McGrath and Long, 2014).

The main factor that has limited the establishment of CCM operating varieties of rice and wheat is the sheer complexity of the mechanisms. C₄ requires coordination of a number of cell types, CAM is regulated on a diurnal cycle, and both show very dynamic responses to physiological challenges posed by the environment (Bellasio and Griffiths, 2014), which will be difficult to re-engineer (Hibberd and Weber, 2012; Borland et al., 2014). Aquatic CCMs seem much simpler by comparison but face a much wider phylogenetic gap to crop plants that may be difficult to bridge. A pyrenoid-based algal CCM, especially from a green lineage alga, may present a good compromise between the two sets of caveats in offering simple single-cell CCM operation while reducing the phylogenetic disparity from billions to hundreds of millions of years compared to Cyanobacteria (Leliaert et al., 2012; Becker, 2013).

1.3 *Chlamydomonas* as model green alga

The soil-dwelling single-celled green alga *Chlamydomonas reinhardtii* is an excellent model organism to study photosynthesis (Harris, 2001; Grossman et al., 2012). Fast generation times, ease of culture and a range of genetic tools, including a fully sequenced genome since 2007, make it a useful experimental platform (Grossman et al., 2007; Merchant et al., 2007). While the cells show ultrastructural differences to higher plants, e.g. in terms of thylakoid stacking, pETC and CBC are largely identical (Allen et al., 2011; Rochaix, 2011; Mettler et al., 2014). Important differences include details of photorespiration (Becker, 2013) and the mechanism of *NPQ* (Niyogi and Truong, 2013) as well as operation of a biophysical CCM (Wang et al., 2015). *Chlamydomonas* may thus be a good CCM donor organism, and for this reason is used here and elsewhere (Meyer and Griffiths, 2013; Mitchell et al., 2014; Mackinder et al., 2015) to identify a set of genes or mechanistic principles, capturing the complexity of the mechanism, that will allow establishment of a CCM in higher plants.

1.4 The *Chlamydomonas* CCM generates a high CO₂ environment within the pyrenoid

Despite the seeming simplicity of the single-celled system, and over 30 years of research, many aspects of the *Chlamydomonas* CCM still await further characterisation (Meyer and Griffiths, 2013). The CCM in *Chlamydomonas* employs a series of trans-membrane C_i

transporters and CAs (Fig. 1.4) to generate a high concentration of CO₂ around Rubisco within the single pyrenoid (Moroney and Ynalvez, 2007; Wang et al., 2015).

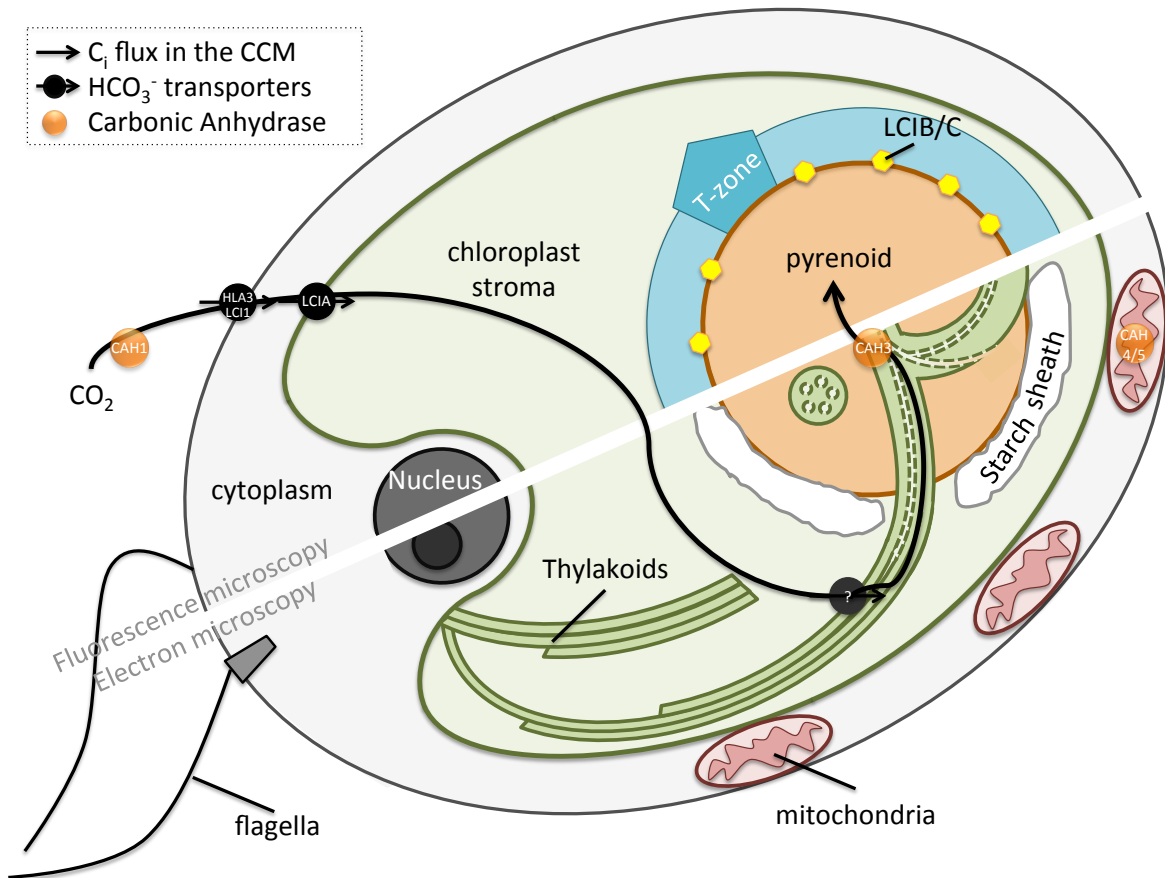


Fig. 1.4: The *Chlamydomonas* pyrenoid is an integral part of chloroplast and CCM

Cell features that have been determined by fluorescence and electron microscopy are shown in separate halves. Conversion equilibria between CO₂ and HCO₃⁻ have been omitted for clarity. Such interconversion is increased outside the plasma membrane by carbonic anhydrase 1 (CAH1) from where inorganic carbon (C_i), probably in the form of HCO₃⁻, is taken up through active pumps such as high light activated 3 (HLA3) and low carbon induced 1 (LCI1) across the plasma membrane and low carbon induced A (LCIA) across the chloroplast envelope. The existence of a bicarbonate transporter across the thylakoid membrane has been speculated but remains unconfirmed (?). Thylakoid luminal carbonic anhydrase 3 (CAH3) is thought to interconvert HCO₃⁻ and CO₂ within intrapyrenoidal thylakoid tubules, thus supplying CO₂ to Rubisco within the pyrenoid matrix. Diffusive loss of CO₂ from the pyrenoid may be limited through the action of a complex of low carbon induced B and C (LCIB/C). Carbonic anhydrases 4 and 5 (CAH4/5) that localize to the mitochondria are highly induced upon CCM induction and may thus feed respiratory CO₂ into the C_i flux of the CCM.

The pyrenoid is embedded at the base of the single cup-shaped chloroplast, at the opposite cell apex to two flagella. During photosynthesis, mitochondria appress between chloroplast and plasma membrane and mitochondrial carbonic anhydrases CAH4 and CAH5 are highly

upregulated under low CO₂, suggesting some recycling of respiratory C_i (Raven, 2001; Wang et al., 2015).

Candidate C_i transporters HLA3 and LCI1 identified across plasma membrane and LCIA in the chloroplast envelope support the notion of HCO₃⁻ as main transport acid in *Chlamydomonas*. Rapid interconversion between CO₂ and HCO₃⁻ is controlled through expression of CAs (Mitra et al., 2005; Moroney et al., 2011; Wang et al., 2015). Since CAs catalyse both equilibrium reactions, it is not immediately clear in which direction they will be operating. It is likely that periplasmic CAH1 will convert CO₂ at the cell surface into HCO₃⁻ for active transport. Release of CO₂ from HCO₃⁻ in the vicinity of Rubisco, and most likely from within the pyrenoid, is thought to be catalysed by CAH3 from within the thylakoid lumen (Wang et al., 2015). A mutant in *CAH3* has a strong CCM phenotype, and CAH3 has been shown to preferentially associate with intra-pyrenoid thylakoid membranes (Wang et al., 2015). It may be critical to avoid expression of CAs in cytoplasm and chloroplast stroma to avoid short-circuiting C_i accumulation (Price et al., 2011).

1.4.1 CCM induction is reflected by the Rubisco aggregation state

The CCM is not permanently active, but rather induced when required. Conventionally, the CCM is induced experimentally following transfer from high (0.5-5%) to low CO₂ (0.03-0.4%) using cells grown under continuous illumination (Borkhsenius et al., 1998; Yamano et al., 2010; Brueggeman et al., 2012). Alternatively cells can be grown in low CO₂ under an alternating dark-light regime, in which case cell division occurs in synchrony across the whole culture at the beginning of the dark phase. In this context, whole cell affinity for C_i exhibited by cells during the dark period is decreased, but increases shortly before subjective dawn to a similar level as measured for classically CCM-induced cultures (Mitchell et al., 2014; Tirumani et al., 2014). This apparent CCM induction coincides with a marked upregulation of putative CCM components at the dark-to-light transition, as well as re-localisation of Rubisco and CAH3 to the pyrenoid (Mitchell et al., 2014).

Two regulatory factors have been identified so far: Concerted action of a majority of CCM-related genes is regulated by CIA5/CCM1 (Fukuzawa et al., 2001; Xiang et al., 2001), a nuclear-localized putative transcriptional regulator which appears to lack direct DNA-binding capacities. Secondly, transcription factor LCR1 regulates a subset of low-CO₂ induced genes (Wang et al., 2015).

In CCM induced conditions, over 90% of Rubisco is localized to the pyrenoid (Borkhsenius et al., 1998; Ma et al., 2011; Mitchell et al., 2014). When the CCM is repressed, a significant fraction of cellular Rubisco is found delocalized throughout the stroma. The pyrenoid never fully disappears, however, and is split in half during cell division (Goodenough, 1970). Around 70% of Rubisco was found aggregated two hours before dawn, and ~50% remains in the pyrenoid at elevated CO₂ (Borkhsenius et al., 1998; Mitchell et al., 2014), making the fraction of Rubisco that is constitutively associated with the pyrenoid at least as large as the fraction that can be found dispersed throughout the stroma in certain conditions.

Classical CCM induction by switching asynchronously grown cells from high to low CO₂ takes up to four hours to aggregate the pyrenoid, judging from immunofluorescence targeting pyrenoid associated factor LCIB (Yamano et al., 2010). Most of this time, however, is probably due to the very gradual decline of Carbon in the medium upon switching gas supplies (Brueggeman et al., 2012). Sudden removal of dissolved inorganic Carbon by pelleting the cells and re-suspending in fresh medium results in a much quicker assembly within 20-60 minutes according to GFP-tagged LCIB, which seems to correlate well with overall pyrenoid structure according to DIC images (Yamano et al., 2010).

While Rubisco is fully aggregated 1h before subjective dawn, the partial aggregation state at 2h before dawn is essentially insensitive to a short light treatment of about 20 min (Mitchell et al., 2014). Thus aggregation of $\geq 90\%$ Rubisco in the pyrenoid takes up to 60 min and certainly more than 20 minutes, both pre-dawn and during low CO₂ CCM induction. This timescale may present a hint that *de novo* protein synthesis is required for the aggregation process, as regulation via post-translational modification is usually faster (Eberhard et al., 2008) as seen for CAH3, which fully completes preferential localization to the pyrenoid within 20 min upon a light treatment 2h before dawn, putatively following protein phosphorylation (Mitchell et al., 2014).

1.4.2 Key features associated with the *Chlamydomonas* pyrenoid

Beyond containing Rubisco, the *Chlamydomonas* pyrenoid displays a number of notable features (Vladimirova et al., 1982; Lacoste-Royal and Gibbs, 1987). Whilst not membrane-bound, the pyrenoid is surrounded by a starch sheath which thickens considerably in CCM-induced conditions, but is not required for the CCM to function (Villarejo et al., 1996). Thylakoid membranes penetrate the pyrenoid matrix and form an intra-pyrenoidal network of thickened thylakoid tubules that seem to coalesce at the centre of the pyrenoid

(Goodenough and Levine, 1969; Engel et al., 2015). The tubules are generated during the fusion of parallel thylakoid membranes, with invaginations forming internal mini-tubules that provide continuity between pyrenoid interior and the chloroplast stroma, and may play a role in metabolite exchange (Engel et al., 2015; Meyer and Griffiths, 2015).

This intricate arrangement of thylakoids and the presence of aggregated Rubisco in the pyrenoid may contribute to the differences in thylakoid organization that exist between green algae such as *Chlamydomonas* and higher plants (Chow, 1999; Chow et al., 2005; Kim et al., 2005). Higher plants exhibit thylakoids that stack in a helical fashion in distinct grana, with stromal lamellae providing connectivity (Mustárdy et al., 2008). Lateral heterogeneity between photosystems may have been a driving force for the evolution of this arrangement, with accumulation of PSII in appressed surfaces within granal stacks, and ensuing vertical connectivity of light harvesting pigment complexes and connectivity between PSII reaction centres to enhance the efficiency of light harvesting (Andersson and Anderson, 1980; Trissl and Wilhelm, 1993; Suggett et al., 2003; Mullineaux, 2005). By contrast, usually 2-4 *Chlamydomonas* thylakoid lamellae appress in thin stacks over long stretches parallel to the chloroplast envelope, with lumenal continuity provided at discrete thylakoid tip convergence zones (Engel et al., 2015).

Intra-pyrenoidal thylakoids have also been implicated in delivery of CO₂ to Rubisco from within the thylakoid lumen (Wang et al., 2015). The idea rests on two pieces of support: firstly a theoretical argument based around the low pH conditions in the thylakoid lumen during active photosynthesis favouring the production of CO₂ from HCO₃⁻ (Raven, 1997; Thoms et al., 2001), and secondly a severe high-CO₂ requiring phenotype of mutant with a knock-out in the luminal carbonic anhydrase *CAH3* (Karlsson et al., 1998). While not upregulated during CCM induction, *CAH3* shows preferential localization within the pyrenoid in CCM-induced conditions, possibly as a result of phosphorylation (Markelova et al., 2009; Sinetova et al., 2012; Mitchell et al., 2014). This arrangement would also require a thylakoid-localized bicarbonate transporter (Fig. 1.4), which has not been identified to date. The only other CA thought to be localized to the chloroplast, *CAH6* (Moroney et al., 2011), appears to actually associate with the flagella (Luke MacKinder, personal communication). A viable alternative to the thylakoid lumen hypothesis might be tethering of *CAH3* to the outside of the thylakoid membrane but inside the pyrenoid matrix, where a low pH environment favouring the production of CO₂ may be a direct result of protogenic CO₂ fixation by Rubisco.

A number of factors localize around the pyrenoid (Luke MacKinder, personal communication), such as the enigmatic LCIB/C complex (Yamano et al., 2010). A *lciB* mutant is lethal in air, but rescued both at elevated and very low CO₂, providing the best evidence to date that the CCM has several contributory levels of complexity (Wang and Spalding, 2014). Recently, LCIB/C has been suggested, by analogy to cyanobacteria, to act as energized, directional carbonic anhydrase (Wang et al., 2015). A mutation in *CAH3* is epistatic to *lciB* (Duanmu et al., 2009) suggesting LCIB acts downstream of CAH3. Interestingly, mislocalization of LCIB does not always lead to a severe CCM defect (Yamano et al., 2014), indicating that delocalized LCIB/C may still be able to at least partially fulfil the same function as when localized around the pyrenoid. Thus LCIB/C may play a role in CO₂ recapture, possibly through energized production of HCO₃⁻, limiting CCM leakage.

1.4.3 Pyrenoid features suggest functional involvement beyond the CCM

Originally thought to be a storage organ, e.g. for Rubisco (Griffiths, 1970), a role in the CCM became more and more apparent as the relationships outlined above were understood. A direct demonstration that the pyrenoid is a crucial part of the CCM was delivered through the first, and to date only, photosynthetically competent pyrenoid-less mutant strains produced in Rubisco small subunit (SSU) substitution experiments (Genkov et al., 2010; Meyer et al., 2012).

However, a number of observations suggest that the pyrenoid may play a role in several cellular processes in addition to the CCM. Firstly, the pyrenoid never fully disappears, and can be visualised clearly even when the CCM is repressed and up to 50% of Rubisco is distributed through the stroma (Goodenough, 1970; Borkhsenius et al., 1998; Mitchell et al., 2014). Secondly, the intricate arrangement of intra-pyrenoidal thylakoid tubules suggests that Rubisco aggregation may have an impact on thylakoid ultrastructure (Kim et al., 2005). Alternatively, thylakoid ultrastructure could be a determinant of Rubisco aggregation, e.g. with tubules acting as a seed around which the pyrenoid is formed, given that intra-pyrenoid-like thylakoid tubules are present even in the absence of Rubisco (Goodenough and Levine, 1970). Thirdly, chloroplast protein synthesis and complex assembly has been reported to be localized in distinct T-zones (see Fig. 1.4) around the pyrenoid in *Chlamydomonas* (Uniacke and Zerges, 2007, 2009). Finally, a small number of CCM-unrelated proteins have been localized to the pyrenoid, such as nitrite reductase and a DNA endonuclease expressed at night (Süss et al., 1995; Uniacke, 2009; Shukla et al., 2012).

These observations question whether the pyrenoid is solely a feature of the CCM, and possibly point towards a CCM-unrelated role in chloroplast homeostasis.

1.4.4 The mechanism of Rubisco aggregation in pyrenoid assembly has remained elusive

In analogous cyanobacterial carboxysomes, Rubisco aggregates via intrinsically disordered linker proteins within a highly structured protein shell (Espie and Kimber, 2011). While the pyrenoid is not bounded by a protein shell, involvement of a linker protein could explain how Rubisco is aggregated, and identification of linker candidates has formed a considerable part of the work presented in this thesis. Such a linker had thus far remained elusive, however, with early pyrenoid isolation experiments finding that the pyrenoid appears to be mostly composed of Rubisco itself (Kuchitsu et al., 1988). Only a few other proteins, such as Rubisco activase, have been localized to the pyrenoid (Süss et al., 1995; Mackinder et al., 2015), CBC enzymes on the other hand appear to be excluded (McKay and Gibbs, 1991b; Tabea Mettler, personal communication).

Alternatively, it seemed that aggregation of Rubisco could be driven by interactions between holoenzymes, possibly regulated through post-translational modifications. Rubisco is known to undergo a number of modifications during synthesis and complex assembly (Houtz et al., 2008), and mutation in a putative methyl transferase *CIA6* is among the few mutants with a partially defective pyrenoid characterized previously (Ma et al., 2011). As part of the current study, the affinity for Rubisco holoenzymes to bind each other in the absence of a mediator has been investigated for the first time.

From a close transmission electron microscopy (TEM) analysis, Rubisco appears to exhibit hexagonal close packing with a spacing of 2-4.5 nm between holoenzymes (Engel et al., 2015). A distance of this scale suggests either that holoenzymes bind each other with low affinity, resulting on average in large gaps between Rubisco units. Alternatively, a linker protein may be occupying that space. Rubisco aggregation occurs over a timescale of 20 – 60 min both during classical CCM induction as well as pre-dawn (Yamano et al., 2010; Mitchell et al., 2014), indicating that processes acting more slowly than post-translational modifications may be involved. The time lag could be accounted for by *de novo* synthesis of a linker protein.

Very recently, proteomic analysis of pyrenoid-enriched cell lysate fractions led to the identification of the intrinsically disordered protein *LCI5* as linker candidate (Mackinder et al., 2015). *LCI5* was first classified as CCM-associated gene due to being highly induced in

low CO₂ (Lavigne et al., 2001), and has since been suggested to associate with thylakoid membranes and be regulated via phosphorylation (Turkina et al., 2006). An interaction between Rubisco and LCI5 was confirmed by a reciprocal pull-down experiment (Mackinder et al., 2015). A *lci5* mutant has a high-CO₂ requiring phenotype, assembles a defective pyrenoid (Mackinder et al., 2015) and exhibits a whole-cell C_i affinity indicative of CCM dysfunction (Mitchell, 2014). Work presented in this thesis has contributed significantly to the characterisation of LCI5 as linker (Mackinder et al., 2015) through experimental analysis of the mutant strain, as well as investigating the potential for an interaction with Rubisco computationally.

1.5 SSU substitution mutants provide an excellent experimental platform for studying the pyrenoid

To date, the only mutant strains thought to be completely devoid of a pyrenoid whilst photosynthetically competent are Rubisco SSU substitution mutants (Genkov et al., 2010; Meyer et al., 2012). *Chlamydomonas* Strains expressing a higher plant SSU are photosynthetically competent and enzyme kinetic properties are virtually unchanged, as judged by *in vitro* measurements of isolated Rubisco, compared to wild-type (WT) control strain WTint1,2 that expresses *Chlamydomonas* native *RBCS1*. However, in contrast to WT no pyrenoid is assembled in the higher plant SSU-expressing strains, and the cells fail to operate a functional CCM (Genkov et al., 2010). These pyrenoid-less (pyr-) SSU lines were employed in this work as a formidable experimental platform to investigate the function of the pyrenoid, and how Rubisco aggregation or delocalisation interacts with pETC operation and chloroplast ultrastructure.

The site associated with facilitating pyrenoid formation was narrowed down to the SSU surface helices (Meyer et al., 2012): *Chlamydomonas* strain HelixAB expresses a chimeric SSU that matches *Spinacia oleracea* (Spreitzer, 2003) in amino acid sequence except in the helical parts where the sequence matches a *Chlamydomonas* SSU. This chimeric SSU results in aggregation of Rubisco in a pyrenoid, whereas a reciprocal construct with *Spinacia oleracea* helices on a *Chlamydomonas* SSU abolishes the pyrenoid. Generally, *Chlamydomonas* strains expressing higher plant SSUs, rather than chimeric SSUs, were used for experimental work. In addition to pyrenoid and CCM phenotypes, chimeric SSUs also show altered Rubisco enzyme kinetics, thus complicating the analysis. For example, HelixAB shows a ten-fold reduction in carboxylation rate compared to WT (Meyer et al., 2012).

Rubisco aggregation has to proceed via protein-protein interactions, either between Rubisco and a linker or directly between adjacent holoenzymes. That pyrenoid assembly is abolished in the absence of native SSU helices demonstrates that these helices are at the interface involved in the interactions that aggregate Rubisco. Any interaction between Rubisco holoenzymes, or with a linker, will thus have to involve the SSU helices. This observation was built upon in the current work to investigate both Rubisco auto-docking and a potential for interaction with linker candidate LCI5 computationally. Furthermore, SSU lines were used once more to investigate which proteins bind Rubisco specifically in the presence of the native SSU interface, to identify key pyrenoid assembly factors including linker protein candidates in addition to LCI5.

The host strain for these SSU substitution lines lacks the WT nuclear SSU genes. Both the *Chlamydomonas* and higher plant small subunit genes (*RBCS*) were expressed from cDNA copies via an identical construct, containing *Chlamydomonas RBCS1* introns 1 and 2 within the transit peptide to boost expression (Genkov et al., 2010). While the random insertion in the genome during transformation could theoretically affect protein expression, selection for photosynthesis reduced the variation and generated only high expression lines. Except for the sequence of *RBCS* and the insertion site, WT and pyr- strains are thus entirely isogenic, representing a uniquely excellent experimental platform for studying the pyrenoid.

1.6 Aims and hypotheses

Using SSU substitution mutants as a tool to characterize the *Chlamydomonas* pyrenoid, work presented in this thesis aimed to establish a number of key aspects.

The first aim was to establish whether the pyrenoid played a role in chloroplast homeostasis beyond a function in the CCM. In Chapter 2, a detailed analysis of the photosynthetic physiology is used to detect the presence of impairments in pyr- higher plant SSU lines that cannot be explained simply in terms of the CCM. Careful manipulation of light and CO₂ conditions enabled an unambiguous dissection of photosynthetic limitation, and the underlying rebalancing of energy.

The second aim was to characterize the nature of SSU interactions to gain mechanistic insight into the process of Rubisco aggregation in pyrenoid assembly. Key questions addressed in Chapter 3 include whether Rubisco is able to interact with itself and whether LCI5 may bind Rubisco via the SSU helices. A general interaction profile of the helices is

proposed to account for the lack of SSU interaction, and hence Rubisco aggregation, in pyr-lines.

Thirdly, the aim was to identify key pyrenoid assembly factors, such as linker protein candidates and regulatory factors, by comparing the Rubisco interactomes of WT and pyr-cells in Chapter 4. Since pyr- cells presumably lack a pyrenoid due to a disruption of the Rubisco interface, factors that are crucial for pyrenoid assembly must be among the proteins binding WT Rubisco SSU helices. Blue-native polyacrylamide gel electrophoresis (BN-PAGE) and immuno-coprecipitation (co-IP) are used as complementary approaches to establish a Rubisco interactome, using informative physiological conditions and an original analysis approach to maximize intelligibility of the data.

Finally, an independent forward genetic screen complemented the biochemical search for pyrenoid assembly factors. In a genome-saturating mutant screen, strains identified as CCM-deficient by collaborators were sub-screened for pyrenoid defects using indirect immunofluorescence (IF) localization of Rubisco in Chapter 5.

2 PYRENOID LOSS ALTERS PHOTOSYNTHETIC ENERGY BALANCING

2.1 Introduction

2.1.1 pETC and CBC activity must balance

In photosynthesis, high energy metabolite production via the pETC, and consumption in the CBC are constantly balanced (Allen, 2003; Eberhard et al., 2008; Joliot and Joliot, 2010; Cardol et al., 2011; Foyer et al., 2012; Lane, 2014). Light absorbed in the pigment bed is processed via the pETC resulting in the production of the reducing agent NADPH, as well as the cellular energy carrier ATP through chemiosmosis. A sudden drop in ATP and NADPH generation, e.g. due to shading, will lead to a substrate limited slowdown of carbon assimilation. If energy supply exceeds demand, a number of mechanisms come into play to readjust the balance either by decreasing pETC output or, where possible, increasing the capacity for CBC turnover (Fig. 2.1). Failure to readjust the balance leads to an excess of high energy reducing intermediates, which then results in the production of damaging reactive oxygen species.

2.1.2 *NPQ* indicates a mismatch in the energy balance

Most ways of reducing pETC turnover focus on limiting the amount of light that is processed by limiting light delivery to the photosystems or dissipating excess energy as heat.

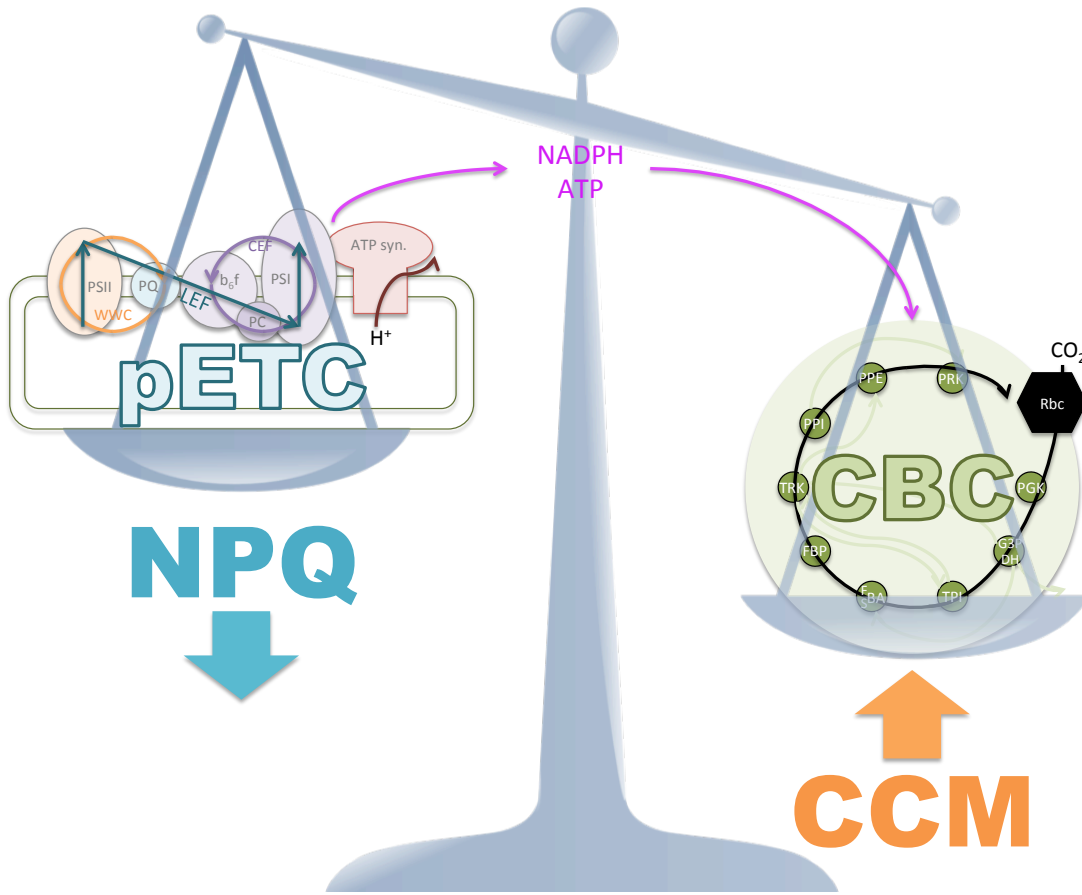


Fig. 2.1: An energy imbalance between pETC and CBC can be rebalanced by decreasing supply via *NPQ*, or increasing demand using a CCM.

Energy metabolites NADPH and ATP produced by the photosynthetic electron transport chain (pETC) are consumed almost exclusively by the calvin benson cycle (CBC). Non-photochemical quenching (NPQ) results in a decreased supply of energy metabolites, whereas operation of a carbon concentrating mechanism (CCM) increases CBC capacity and thus energy demand. Main components of the pETC are photosystem II (PSII), plastoquinone (PQ), the cytochrome b_6f complex (b_6f), plastocyanin (PC) and photosystem I (PSI). These components can be operated in series, resulting in linear electron flow (LEF) which contributes to the proton gradient as well as producing NADPH. Alternatively, the water-water cycle (WWC) around PSII or cyclic electron flow (CEF) around PSI result in proton pumping only. Energy stored in the proton gradient is converted into ATP by the ATP synthase (ATP syn.). The enzymes that make up the CBC are Rubisco (Rbc), phosphoglycerate kinase (PGK), glyceraldehyde 3-phosphate dehydrogenase (G3PDH), triose phosphate isomerase (TPI), fructose-1,6-bisphosphate or sedoheptulose-1,7-bisphosphate aldolase (FBA/SBA), fructose-1,6-bisphosphate phosphatase (FBP), transketolase (TRK), pentose phosphate isomerase (PPI), pentose phosphate epimerase (PPE) and phosphoribulokinase (PRK).

Whereas PSI is very effective at dissipating excess energy as heat from within the reaction centre, PSII is more liable to damage (Ivanov et al., 2008). Pathways that limit exciton delivery to PSII are often referred to as *NPQ*, as quenching can be observed as a result in chlorophyll fluorescence (CF) experiments.

In *Chlamydomonas*, the major component of *NPQ* is energy dependent quenching (qE) (Iwai et al., 2007). This qE is thought to act through dissipation of excess light as heat from within the antenna complexes in the thylakoid membranes, and is regulated directly by the ΔpH between lumen and stroma (Holt et al., 2004; Horton et al., 2008; Jahns and Holzwarth, 2012; Lambrev et al., 2012). As a build-up of energy intermediates leads to an increase in ΔpH , changes in *NPQ* can thus be directly informative about a mismatch between pETC and CBC turnover. A second major contribution to photoprotection in *Chlamydomonas* comes from state transitions. State transitions act through reducing the PSII absorption cross-section by removing LHCII complexes from the PSII antenna bed (Haldrup et al., 2001; Finazzi, 2005; Ruban and Johnson, 2009; Minagawa, 2011; Drop et al., 2014).

2.1.3 CCMs increase CCB turnover capacity

CCMs have arisen many times in the evolution of photosynthesis as a means of increasing carbon fixation in conditions where CO_2 availability is limiting CBC turnover (Raven et al., 2012). Energy derived from light is invested in accumulating a high concentration of CO_2 around Rubisco, allowing RuBP carboxylation to proceed at a faster overall rate as well as altering the balance between carboxylation and oxygenation to limit photorespiratory turnover. Because CCMs require some energy for operation and a faster CBC turnover consumes energy equivalents more rapidly, CCM operation gives scope for shifting the balance towards using more energy, and dissipating less, when light is plentiful (Fig. 2.1).

2.1.4 How does the *Chlamydomonas* pyrenoid affect the interaction between pETC and CBC?

In order for the CCM to be able to operate in *Chlamydomonas*, Rubisco needs to be aggregated in a pyrenoid. In SSU substitution strains expressing higher plant *RBCS* constructs, Rubisco fails to be recruited into assembly of a pyrenoid, rendering these pyrcells unable to operate a CCM (Genkov et al., 2010). As the pyrenoid is essentially an aggregate of Rubisco (Kuchitsu et al., 1988), it appears likely that the main function of the pyrenoid is to facilitate CO_2 fixation as part of the CCM. In this case, lack of a pyrenoid should lead to a CCM defect, which in turn should feedback limit pETC turnover and increase a requirement for *NPQ* to maintain a balance of energy flow (Fig. 2.1).

However, in addition to playing a role in the CCM, the pyrenoid has been implicated in a number of other functions, supported by the fact the pyrenoid does not fully disappear even when the CCM is repressed (Borkhsenius et al., 1998). Chloroplast protein translation,

import and complex assembly has been found to be localized specifically in certain T-zones around the periphery of the pyrenoid (Uniacke and Zerges, 2007, 2009). Several proteins not related to the CCM have been localized to the pyrenoid, including nitrite reductase (Süss et al., 1995; Uniacke, 2009) and a DNA endonuclease expressed in the dark (Shukla et al., 2012). Removing the pyrenoid may also have a disrupting effect on the distinct thylakoid membrane structures, which intersect and coalesce within the pyrenoid (Engel et al 2015). If, in addition to playing a part in the CCM, the pyrenoid is important e.g. for determining chloroplast ultrastructure, as suggested by structural associations with T-zones and thylakoid membranes, then defects exhibited by *pyr*- cells should go beyond a simple limitation in supply of CO₂.

Thus the SSU lines represent a unique experimental platform to investigate whether the pyrenoid can be functionally defined as simply a part of the CCM, or whether further roles need to be taken into account. If the role in the CCM fully describes the function of the pyrenoid, then *pyr*- cells should exhibit signs of being limited by supply of CO₂. This limitation can be removed by creating a high CO₂ environment for the cells experimentally, which will rescue any CCM defect and restore WT-like behaviour in CCM mutants (Fukuzawa et al., 2001; Xiang et al., 2001; Jungnick et al., 2014). However, if *pyr*- cells suffer defects in addition to CCM dysfunction, such as alterations in thylakoid ultrastructure, then these defects will prevail and addition of CO₂ will not be able to restore WT-like behaviour in *pyr*- cells.

The aim of the current study was thus to establish firmly whether there is any effect of pyrenoid loss on photosynthesis beyond a rebalancing of energy supply and demand due to CCM dysfunction. To this effect, differences between *pyr*- and WT were first characterized in detail for cells grown at low CO₂ (air, ~0.04% CO₂) when the CCM is induced in WT. To capture acclimation, cells were grown in low (10 μE), medium (50 μE) and high (≥ 100 μE) light intensities. The light intensities differ from classically defined low and high light intensities in the *Chlamydomonas* literature (Niyogi, 2009), owing to the comparatively high fragility of the strains used.

Any differences observed between WT and *pyr*- strains could indicate additional pyrenoid functions, or simply reflect regulatory processes that meet the challenge of performing photosynthesis with a lower CBC turnover in the absence of a CCM. To differentiate the two, addition of CO₂ was used as a tool to alleviate the CCM defect in *pyr*- cells. Of particular interest was the interplay between the pyrenoid and thylakoid ultrastructure, as

there did appear to be an effect on thylakoid arrangement judging from existing electron micrographs that had been taken to assess pyrenoid phenotype: thylakoid stacking was described as pronounced “hyperstacking” in pyr- cells (Meyer et al., 2012). Thylakoid architecture in *Chlamydomonas* differs from higher plants. In the absence of grana, thylakoid stacking is defined as lamellae lying parallel to each other in close proximity (Goodenough and Levine, 1969; Engel et al., 2015).

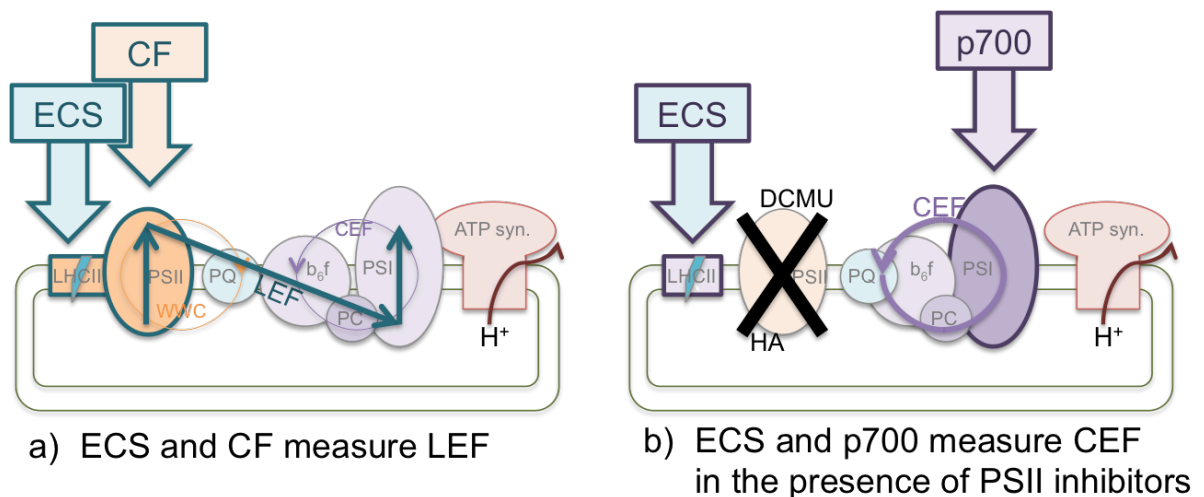


Fig. 2.2: Fluorescence (CF) and spectroscopic data (ECS, p700) are informative about pETC activity.

Main components of the electron transport chain are photosystem II (PSII) with an associated antenna system symbolized here by light harvesting complex II (LHCII), plastoquinone (PQ), the cytochrome b_6f complex (b_6f), plastocyanin (PC) and photosystem I (PSI). These components can be operated in series, resulting in linear electron flow (LEF) which contributes to the proton gradient as well as producing NADPH. Alternatively, the water-water cycle (WWC) around PSII or cyclic electron flow (CEF) around PSI result in proton pumping only. Energy stored in the proton gradient is converted into ATP by the ATP synthase (ATP syn.). Chlorophyll fluorescence (CF) measures the activity of PSII and is mostly informative about LEF (a) as the contribution of WWC is typically small. The electrochromic shift (ECS) method exploits the effect of the transthylakoid proton gradient on the light absorption characteristics of thylakoid membrane pigments such as the carotenoids in LHCII. While WWC, CEF and LEF all contribute to this proton gradient, LEF will be the largest component. This changes upon the addition of PSII inhibitors (b). Hydroxylamine (HA) disrupts the extraction of electrons from water, 3-(3,4-dichlorophenyl)-1,1-dimethylurea (DCMU) inhibits the donation of electrons to PQ, and together they stop PSII from contributing to electron transport. As a result, WWC and LEF cease, and all remaining activity measured by ECS can be attributed to CEF. Alternatively, the activity of PSI can be monitored by following the absorption of reduced reaction centre chlorophyll p700 at $\sim 700\text{nm}$ which is not possible in the absence of inhibitors due to interfering signals from PSII.

After revisiting thylakoid stacking using electron microscopy, the main focus was on functional analysis of photosynthetic responses using chlorophyll fluorescence (CF)

supported by associated spectroscopic data (Fig. 2.2). Activity of PSII can be inferred from CF (Fig. 2.2a), allowing the electron transport rate (*ETR*) through PSII to be estimated. As the water-water cycle (WWC) around PSII is usually assumed to be negligible, *ETR* is taken as a measure of LEF. However, WWC and PTOX activity can also be measured explicitly using CF by inhibiting electron flow through the cytochrome b_6f complex (Appendix 8.13).

Activity of PSI can be estimated from absorption data, as the reaction centre chlorophyll, p700, ceases to absorb at $\sim 700\text{nm}$ when oxidized to $p700^+$. In contrast to higher plants, PSII in *Chlamydomonas* absorbs significantly beyond 700nm , meaning PSI cannot be measured using a dual-PAM. Instead, PSI absorption can be measured at 705nm when PSII is inhibited (Fig. 2.2b), in which case the rate of *CEF* around PSI can be inferred.

The Electrochromic Shift (ECS) method generates a proxy for photosynthetically generated ΔpH by measuring changes in the absorbance of total thylakoid pigment content at $\sim 520\text{ nm}$ (Joliot and Delosme, 1974; Bailleul et al., 2010; Joliot and Joliot, 2010; Lucker and Kramer, 2013). Changes in the ΔpH have immediate consequences for the structure of antenna complexes such as LHCII: by altering the protonation state of crucial amino acids, the relative position of pigments within the complex is altered resulting in a lower absorptivity with increasing ΔpH . Exactly which pigments give rise to the ECS signal is still under debate, although given the wavelength it is likely that carotenoids play a major role. By following the initial relaxation of ΔpH in the dark after a period of illumination, the rate of H^+ transport through the ATP synthase can be inferred which must be equal and opposite to pETC H^+ pumping during steady state photosynthesis. As such, ECS can be used to infer *CEF* when PSII is inhibited (Fig. 2.2b), or total electron flow rates in the absence of inhibitors (Fig. 2.2a) which is usually taken as a measure of *LEF* as the dominating process.

Data will be shown initially as light response curves, which allow a differentiation between light acclimation and CO_2 limitation. The focus is then shifted to a detailed analysis of fluorescence induction, allowing effects of feedback from the CBC to be captured in real time. Finally, photosystem and pigment expression and functional association data were used to investigate structural changes in pyr- mutants on a molecular level.

2.2 Materials and Methods

2.2.1 Strains

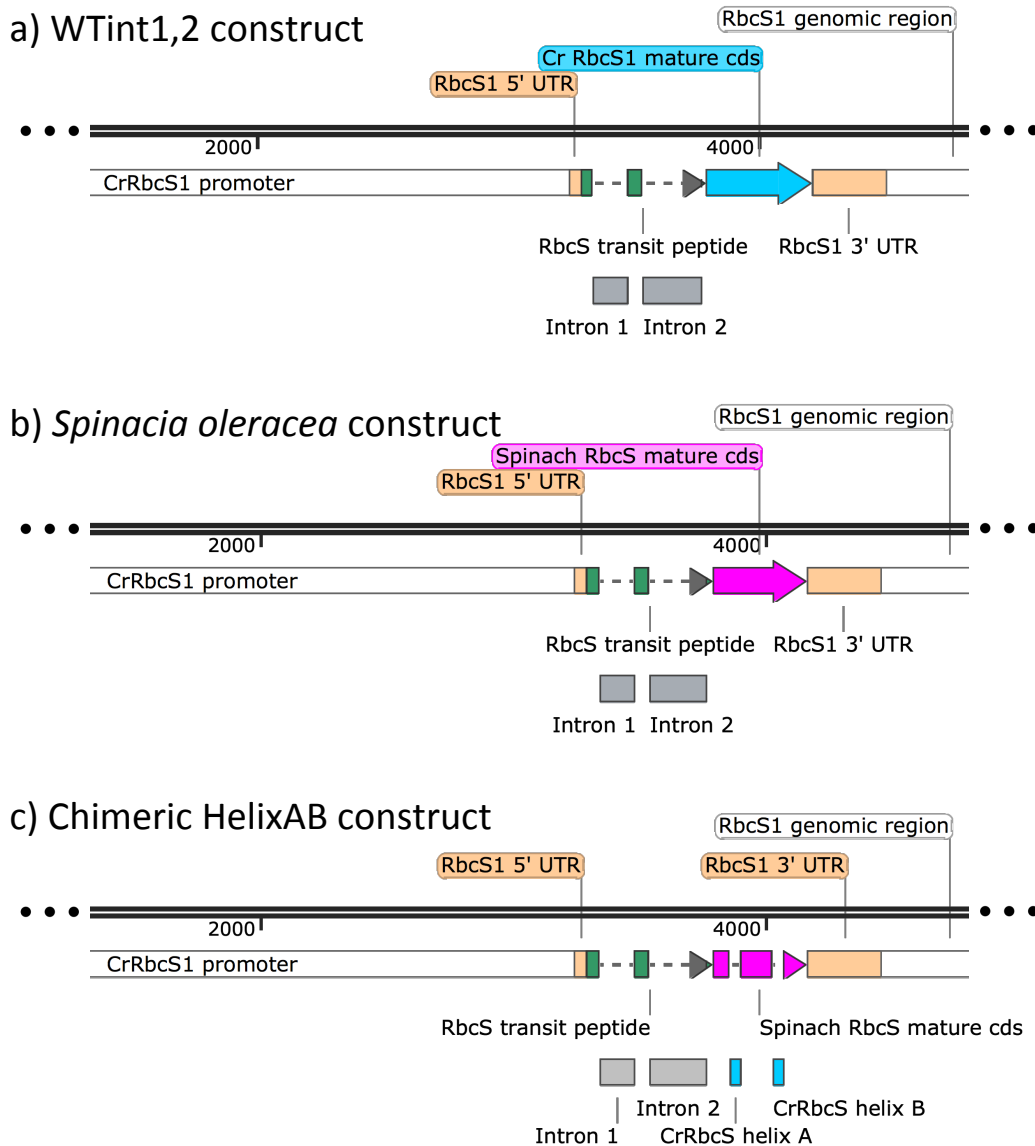


Fig. 2.3: Example SSU expression vectors

Vectors constructed by Genkov et al. (2010) for expression of different *RBCS* mature coding sequences such as (a) *Chlamydomonas* native *RBCS1* in strain WTint1,2, (b) *Spinacia oleracea* *RBCS* and (c) a chimeric construct where regions of *Chlamydomonas* *RBCS1* coding for SSU surface helices were combined onto *Spinacia oleracea* *RBCS* mature coding sequence (Meyer et al., 2012).

Experiments used *pyr-* lines generated through heterologous expression of higher plant *RBCS* cDNA versions from *Spinacia oleracea* (Fig. 2.3b), *Arabidopsis thaliana* and *Helianthus annuus*, and corresponding WT control strains WTint1,2 expressing native *Chlamydomonas* *RBCS1* cDNA (Fig. 2.3a) via a common expression vector that contains *Chlamydomonas* *RBCS1* introns 1 and 2 within the transit peptide (Genkov et al., 2010). In

addition, some experiments used strains expressing chimeric *RBCS* versions where *Spinacia oleracea* *RBCS* is combined with *Chlamydomonas* *RBCS1* sequences determining SSU surface helices in pyr⁺ strain HelixAB (Fig. 2.3c), or the reciprocal combination of *Spinacia oleracea* helices in the context of *Chlamydomonas* native SSU in pyr⁻ strain Reciprocal (Meyer et al., 2012).

2.2.2 TEM

2.2.2.1 Strains and culture conditions

WT strain WTint1,2 expressing *Chlamydomonas* native *RBCS1*, and a pyr⁻ strain expressing heterologous *Spinacia oleracea* *RBCS* were used (Genkov et al., 2010). Cells were grown in multiple cultures of 50 ml in minimal medium (based on Gorman and Levine (1965): Hutner's trace elements (Hutner et al., 1950) in 20 mM Tris, 15.1 mM HCl, 7.48 mM NH₄Cl, 815 μM K₂HPO₂, 533 μM KH₂PO₄, 406 μM MgSO₄, 340 μM CaCl₂) aerated with 5% CO₂ for 3 days at ~50 μE, normalized by chlorophyll content such that cell densities would be equivalent between strains at the point of harvest assuming a doubling time of 15h. After harvesting 50% of each culture, duplicate flasks were pooled, WT culture was diluted with minimal medium to normalized cultures to chlorophyll content such that densities of all cultures would be equal at the point of harvest assuming a doubling time of 35h at 50 μE, and cells were grown in 50 ml cultures aerated with air for 1 day at either 50 μE or 10 μE, at which point the remaining culture was harvested.

2.2.2.2 TEM preparation

At harvest, culture in excess of 50·10⁶ cells was transferred to 50ml Falcon tubes to which electron microscopy-grade I glutaraldehyde was added to 0.5% v/v. Cells were pelleted by centrifugation (3000 RPM, 4°C, 5 min). Pellets were re-suspended in 1 ml fixative (2.5% v/v glutaraldehyde and 1% v/v H₂O₂ in minimal medium), transferred to 1.5 ml conical screwcap microcentrifuge tubes labelled with carving marks, and incubated for 1 h at 4°C on a tube rotator. For the following incubation steps samples were kept at room temperature on a tube rotator, followed by centrifugation (5000 RPM, 5 min, room temperature). Cells were washed thrice with double distilled water for 5 min each and osmicated for 1 h at room temperature in 1 ml postfix (1% v/v OsO₄, 1.5% w/v K₃[Fe(CN)₆], 2 mM CaCl₂). Samples were washed 4 times for 5 min each in double distilled water and stained for 1 h in bulk stain (2% w/v uranyl acetate). After another 3 water washes, samples were subjected to serial dehydration by incubating for 5 min each in 70%, 95%, 100% ethanol followed by

two rounds of 100% acetonitrile. Samples were embedded overnight in 1ml 50% acetonitrile, 50% epoxy resin (34.15% w/w Quetol 651, 53.66 % w/w Nonenyl succinic anhydride, 9.76% w/w Methyl-5-norbornene-2,3-dicarboxylic anhydride, 2.44% v/w Dimethylbenzylamine). Samples were re-suspended in fresh 100% epoxy resin every 12 h for 4 times using toothpicks. After a final hard centrifugation (10,000 RPM, 10 min, room temperature) samples were overlaid with fresh resin, degassed overnight and cured at 60°C for 24 h. Pellets were halved, mounted orthogonally on resin stubs in araldite, cured for ≥ 2 h at 65°C and submitted to CAIC (Cambridge Advanced Imaging Centre, University of Cambridge, Cambridge, UK) for further processing.

2.2.2.3 TEM imaging

Grids were imaged at CAIC using a Tecnai G2 80-200kv TEM scope. 20 cells above $\sim 4.5\mu\text{m}$ in diameter were sampled randomly for each experimental condition. Smaller cells were excluded, as images of cells that appear very small are often actually derived from larger cells that were, by chance, cut close to the periphery of the cell, which distorts cells features and is therefore less useful for quantitative comparison of thylakoid stack widths.

2.2.2.4 Image quantification

Images of WT and pyr- grown under 5% CO₂ at 50 μE , or air at 50 μE or 10 μE , were indexed, pooled and presented in a random order, such that prior knowledge of experimental treatment would have minimal influence on the analysis. For each image, widths of 5 arbitrarily chosen thylakoid stacks were quantified using Fiji (Schindelin et al., 2012). Data was collated and plotted in Excel (Microsoft, Redmond, WA, USA), ANOVA testing for statistical significance was performed using R (The R Foundation, Vienna, Austria).

2.2.3 CF from algal colonies on agar plates

2.2.3.1 Strains and preparations for culturing

One independent insertion line of each of the three pyr- higher plant SSU lines *Spinacia oleracea*, *Arabidopsis thaliana* and *Helianthus annuus*, as well as two independent insertion lines of control WT *Chlamydomonas* native SSU line WTint1,2 were grown in the dark in 50ml liquid cultures containing acetate medium (2 mM sodium acetate in minimal medium) to a total chlorophyll concentration of 1.29-1.92 $\mu\text{g/ml}$, extracted in 100% methanol according to (Wellburn, 1994). Culture corresponding to 51.8 μg chlorophyll was harvested by centrifugation (2000 g, 3 min, room temperature) and re-suspended in 528 μl minimal medium to a final concentration of 100 μg chlorophyll/ml. For WT strains, three instances,

and for pyr- strains, two instances of 20 μ l were spotted on each of eight 24-well plates (Fig. 2.4, Appendix 8.2) of minimal agar (1.5% w/v agarose in minimal medium, solidified) in random positions (random.org, randomness, Randomness and Integrity Services Ltd, Dublin, Ireland).

2.2.3.2 Culture conditions

Spots were allowed to air-dry, plates were sealed with Parafilm[®] (Pechiney Plastic Packaging, Inc., Chicago, IL, USA) and placed in controlled gaseous environments within individual autoclave bags each containing 2.5 l of a specific gas mix. To generate gas environments, existing gas was removed from autoclave bags containing one plate each through the use of a vacuum pump, after which bags were refilled from gas cylinders (Appendix 8.2). Three plates were subjected to ordinary air, another three plates were subjected to 5% CO₂ from a custom-made cylinder balanced with air, each bag filled at a flow-rate of 0.03 l/sec for 84 sec. One plate was subjected to 40% O₂ and air-level CO₂, filled with a mix of pure O₂ at a flow rate of 0.5 l/min and air at a flow rate of 1.6 l/min for 72 sec. One plate was subjected to 400 ppm CO₂ in 2% O₂, by filling at 0.03 l/sec for 84 sec from a cylinder containing 2% O₂/balance N₂, and adding 1 ml pure CO₂ using a syringe. Plates in autoclave bags were subjected to different light levels in a growth cabinet: one air and one 5% CO₂ plate were grown at each of ~10 μ E, ~50 μ E and ~165 μ E. Plates in 2% and 40% O₂ were grown at ~50 μ E. Plates were subjected to these conditions for 4 days with gas removed and replaced by fresh gas daily.

2.2.3.3 CF analysis using CF imager

On the final day, lids were removed from the plates and gas was freshly replenished. Cells were dark adapted, by wrapping autoclave bags in aluminium foil, for several hours (during a drive from Cambridge to Colchester). Foil was removed and cells on plates within autoclave bags containing controlled gas environments were subjected to assessment of CF characteristics in CF imagers (Technologica Ltd., Colchester, UK) using the following protocol: 13 seconds after a saturating pulse to determine dark adapted F_v/F_m (Appendix 8.4), cells were subjected to fluorescence induction for 20 min and 3 sec at 106 μ E with probing saturating pulses after 20 sec, 1 min, 2 min, 5 min, 10 min, 15 min and 20 min (Appendix 8.5, Appendix 8.6, Appendix 8.7). Fluorescence relaxation in the dark was followed for 5 min and 3 sec with probing saturating pulses after 20 sec, 1 min, 2 min, 3.5 min and 5 min. Cells were subsequently subjected to a rapid light response curve with 2 min and 3 sec (probing saturating pulses after 2 min) at each light intensity under 22 μ E, 46 μ E,

106 μE , 170 μE , 251 μE , 356 μE , 509 μE and 679 μE (Fig. 2.6, Fig. 2.7, Appendix 8.8). Actual light intensities differed from nominal light intensities quoted in the CF imager protocol settings and were set to the quoted values using a light meter.

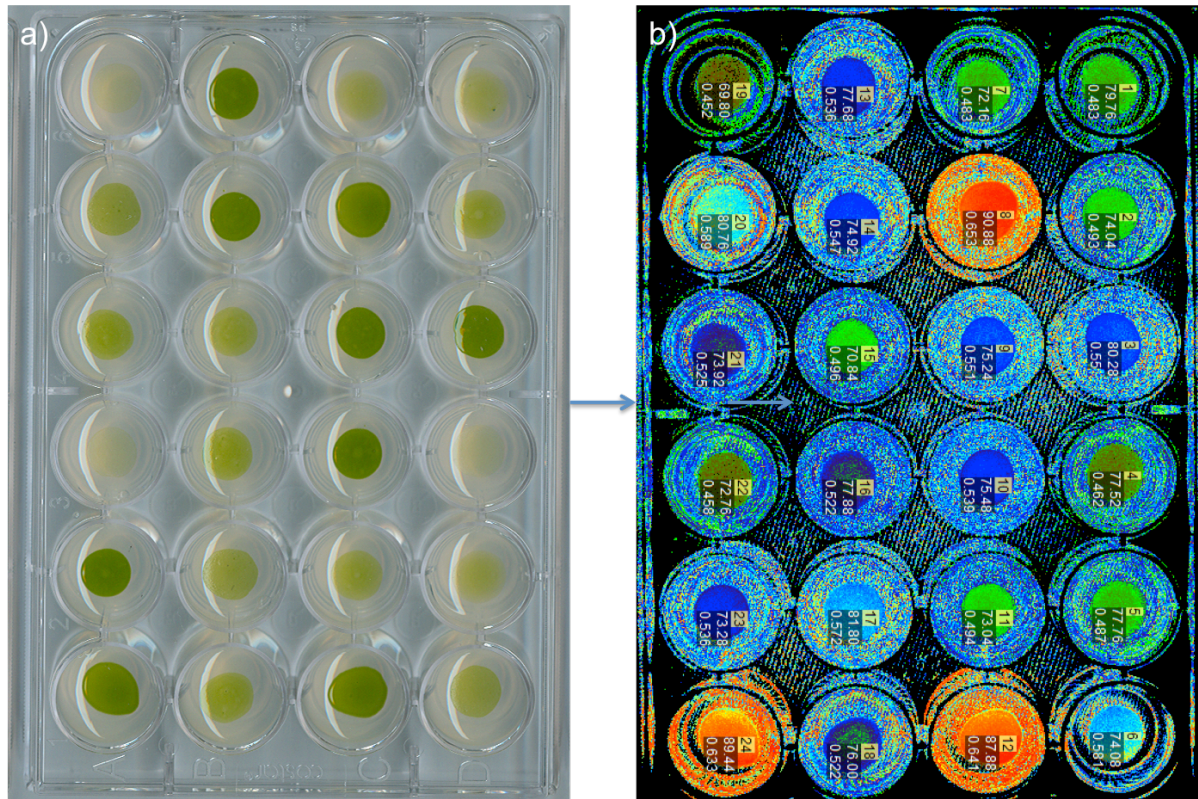


Fig. 2.4: High throughput photosynthetic analysis of algal colonies using CF imaging

Algal colonies spotted on 12-well tissue culture agar plates were screened using CF imaging. Colonies grown at air and 50 μE are shown as example in (a) with a corresponding ϕ_{II} measurement heatmap depicted as example CF image in (b).

2.2.3.4 Data analysis and figure preparation

Data was exported from the CF imager software in rich text format and converted into .txt files using Excel (Microsoft). Data was then analysed and plotted using the free statistical software package R (The R Foundation).

2.2.3.5 Mathematical models of light response curves

Based on photosynthesis literature, three mathematical models were adapted for description of CF derived light response data. Firstly, equation (2.1) shows a formulation suitable for CF data (Suggett et al., 2003) of an earlier model (Jassby and Platt, 1976; Platt et al., 1980) originally designed to describe O_2 evolution data.

$$\phi_{II} = \phi_m \frac{I_k}{I} (1 - e^{-\frac{I}{I_k}}) \quad (2.1)$$

Where ϕ_{II} is the instantaneous PSII operating efficiency calculated from CF data (Maxwell and Johnson, 2000), i.e. the data collected, I is the light intensity that the cells were subjected to, whilst ϕ_m and I_k are model parameters. ϕ_m is interpreted as maximal PSII operating efficiency and I_k is taken to be the light intensity at which photosynthesis starts to be light saturated.

Secondly, von Caemmerer (Von Caemmerer, 2013) developed equation (2.2) describing light-limited photosynthesis, designed for gas exchange data of CO₂ consumption:

$$J = \frac{I_2 + J_{max} - \sqrt{(I_2 + J_{max})^2 - 4\theta I_2 J_{max}}}{2\theta} \quad (2.2)$$

Where J is the rate of electron transport in the photosynthetic pETC, J_{max} is the maximum possible rate of electron transport, I_2 is the light received by PSII, and θ is an empirically derived parameter describing adjusting the shape of the curve and is reported to be approximately 0.7. A formulation of (2.2) suitable for CF data was developed using a number of assumptions common in CF literature (Maxwell and Johnson, 2000). Firstly, electron transport rate (ETR), or J , is determined by the light received by PSII (I_2) and the PSII operating efficiency (ϕ_{II}): $J = ETR = \phi_{II} \cdot I_2$. Secondly, how much light is received by PSII (I_2) is determined by the light intensity supplied to the organism (I) and net light interception by PSII (α_{II}): $I_2 = I \cdot \alpha_{II}$. The proportionality factor α_{II} is often assumed to be the product of the fraction of light absorbed by an organism, which has typically been reported as 0.83 for leaves (Von Caemmerer, 2013), and 0.5 accounting for an equal distribution of absorbed light between PSI and PSII. Alternatively, α_{II} can be understood as a ratio of the effective PSII absorption cross-section (σ_{II}) and maximal PSII operating efficiency (ϕ_m): $\alpha_{II} = \sigma_{II}/\phi_m$ (Suggett et al., 2003), from which it follows that $J = ETR = \phi_{II} \cdot I \cdot \sigma_{II}/\phi_m$. Assuming the electron transport rate that cannot be exceeded would be reached when a light intensity supporting saturated photosynthesis (I_k) were processed with maximal PSII operating efficiency (ϕ_m) allows J_{max} to be calculated as $J_{max} = ETR_{max} = \phi_m \cdot I_k \cdot \sigma_{II}/\phi_m = I_k \cdot \sigma_{II}$. Thereby (2.2) can be formulated in terms of the same parameters used for (2.1) as:

$$\phi_{II} \cdot I \cdot \sigma_{II}/\phi_m = \frac{I \cdot \sigma_{II}/\phi_m + I_k \cdot \sigma_{II} - \sqrt{(I \cdot \sigma_{II}/\phi_m + I_k \cdot \sigma_{II})^2 - 4\theta I \cdot \sigma_{II}/\phi_m \cdot I_k \cdot \sigma_{II}}}{2\theta} \quad (2.3)$$

Which can be simplified to:

$$\phi_{II} = \phi_{max} \frac{I + I_k - \sqrt{(I + I_k)^2 - 4\theta I \cdot I_k}}{2\theta I} \quad (2.4)$$

Finally, a version of the Michaelis Menten equation was formulated for description of CF data. Michaelis Menten was originally designed to describe enzyme kinetics dependent on substrate availability:

$$\frac{d[P]}{dt} = \frac{V_{max}[S]}{K_m + [S]} \quad (2.5)$$

Where t is time, P is a product, S is a substrate, V_{max} is the maximum rate of converting substrate into product, and K_m is the substrate concentration at which half the maximal rate of conversion is achieved. For the purposes of CF, the enzyme under investigation can be understood to be PSII. Since PSII processes photons, an appropriate substrate ($[S]$) term would be the net light interception by PSII (I_2): $[S] = I_2 = I \cdot \sigma_{II} / \phi_m$. As an excited electron is the “product” of light processing by PSII, the rate at which product is generated ($d[P]/dt$) can be thought of as equivalent to the rate of electron transport (ETR), thus: $d[P]/dt = ETR = \phi_{II} \cdot I \cdot \sigma_{II} / \phi_m$. As this is the same as J from (2.2), V_{max} can be understood as equivalent to J_{max} , thus: $V_{max} = J_{max} = ETR_{max} = I_k \cdot \sigma_{II}$. As K_m must be of the form $K_m = I_x \cdot \sigma_{II} / \phi_m$ where I_x is the light intensity at which $ETR = ETR_{max}/2$, it follows that:

$$\phi_{II} \cdot I \cdot \sigma_{II} / \phi_m = \frac{I_k \cdot \sigma_{II} \cdot I \cdot \sigma_{II} / \phi_m}{I_x \cdot \sigma_{II} / \phi_m + I \cdot \sigma_{II} / \phi_m} \quad (2.6)$$

Which can be simplified to:

$$\phi_{II} = \frac{I_k \cdot \phi_m}{I_x + I} \quad (2.7)$$

Considering the same case as mentioned above, where ETR_{max} is reached when $\phi_{II} = \phi_{max}$ and $I = I_k$, from the definition of K_m it follows that $I_x = I_k$:

$$\frac{\phi_m}{2} = \frac{I_k \cdot \phi_m}{I_x + I_x} \quad (2.8)$$

Which means that $K_m = I_k \cdot \sigma_{II} / \phi_m$, and that CF data can be described by the following version of the Michaelis Menten relation:

$$\phi_{II} = \frac{I_k \cdot \phi_m}{I_k + I} \quad (2.9)$$

2.2.3.6 Model choice and fit-based analysis

Three mathematical descriptions of light response curves, (2.1), (2.4) and (2.9), were fit to a subset of data (2% and 40% O₂ plates were excluded as less relevant for the chapter, see

Appendix 8.8. 165 μE data was excluded based on irregular behaviour not captured in any of the models, presumably caused by severe long-term photoinhibition, see Appendix 8.2c) using a nonlinear least squares algorithm. The data used probes the effect of three experimental variables: pyrenoid phenotype, light intensity experienced by the cells during growth, and CO_2 environment. Each of the three models contains two parameters, ϕ_m and I_k .

To establish whether experimental variables affected model parameters, parameters were either allowed to vary between experimental treatments or held constant during iterative model fits. For example, in one fit, a single number was approximated for ϕ_m to best describe all data. In a second fit, two ϕ_m values were approximated, one for cells in air and one for cells in 5% CO_2 . In a third fit, four ϕ_m values were approximated: one for pyr- cells in air, one for WT cells in air, one for pyr- cells in 5% CO_2 and one for WT cells in 5% CO_2 . This way, all combinations of experimental treatments for both parameters were described in 64 fits.

Which of these fits represented the best approximation of the underlying data was then established using the Akaike Information Criterion (*AIC*; Akaike, 1974), a mathematical method for balancing goodness of fit against the number of variables used. The process was repeated for each of the three models. Across all three models, the best fit was achieved by choosing an individual ϕ_m for each combination of pyrenoid phenotype, growth light and CO_2 conditions, and different values for I_k for each growth light condition (meaning the same value for I_k can be used across strains and CO_2 conditions at each light intensity). Of the three models, (2.1) put forward by Suggett et al. (Suggett et al., 2003) based on the work of Platt and co-workers (Jassby and Platt, 1976; Platt et al., 1980) was best supported by the data ($\Delta\text{AIC}: \geq 8.4$).

For this best model (2.1), parameter combinations were explored in more detail allowing for interactions between experimental treatments (now including 165 μE data). *AIC* was minimal for a model where ϕ_m was equal across WT and pyr- at 5% CO_2 but different at air, for each light intensity separately, which was thus used for Fig. 2.6.

2.2.4 JTS-10 and associated data

2.2.4.1 Culture conditions and preparative treatment

Cells were grown in 20 ml or 50 ml minimal medium liquid culture under continuous illumination and diluted every few days with fresh medium to keep cultures in mid-log phase. For the purposes of the first set of JTS-10 experiments (J1: Fig. 2.8, Fig. 2.12,

Appendix 8.10, Appendix 8.11, Appendix 8.12, Appendix 8.13, Appendix 8.14), cells were grown at 50 μ E without aeration. For the purposes of the second set of JTS-10 experiments (J2: Fig. 2.9, Fig. 2.10 b-f, Fig. 2.11 a-d, Appendix 8.15, Appendix 8.16, Appendix 8.17), cells were grown at ~10 μ E, ~50 μ E or ~100 μ E aerated with 5% CO₂/balance air at a flow rate of ~0.5 ml/min per ml culture, and aeration was switched to ordinary air for 1 day prior to harvest for experiments with air-adapted cells. Chlorophyll content was estimated by extraction in 100% methanol according to Wellburn (1994). Generally, around 10 ml culture was harvested by centrifugation (2,000 g, 3 min, room temperature) and re-suspended in usually 3.5 ml HF (10% w/v Ficoll in 20 mM HEPES/KOH, pH 7.2) in 15 ml Falcon tubes to a chlorophyll concentration of around 10 μ g/ml for J1, or precisely 12 μ g/ml for J2. Cells were dark adapted for \geq 20 min for J1, or \geq 40 min for J2 while shaking. For each set of JTS-10 measurements, 1.5 ml were added to a 4 ml cuvette. For J2, two replicate sets of JTS-10 measurements were done on the same sample, and 15 μ l of a 1M NaHCO₃⁻ stock was added to one of the two cuvettes prior to measurements (which one was chosen randomly using random.org).

2.2.4.2 JTS-10 protocol

Generally, the procedure of JTS-10 measurements was the following: firstly, an ECS trace (absorbance at 525 nm) of a Xenon bulb flash (J1), or alternatively three ECS traces of single turnover laser flashes (J1 & J2) were recorded. Secondly, a CF trace of a saturating pulse was recorded to estimate dark-adapted Fv/Fm.

After that, traces were recorded for estimation of linear electron transport rates. For J1, samples were sequentially subjected to 5 sec of actinic light at 32 μ E, 68 μ E, 156 μ E and finally 525 μ E, following firstly the decay of the ECS signal in the dark and secondly recording the effect of a saturating pulse on CF at the end of the light period. For J2, CF was traced while the sample was subjected to 30 sec of actinic light at 103 μ E followed by a saturating pulse. The trace was repeated at 21 μ E. Traces of 5 sec illumination were recorded at 21 μ E and 103 μ E. After that, fluorescence was traced during 2 min at 347 μ E with saturating pulses after 5 sec, 30 sec and 120 sec. Next, ECS traces were recorded for 5 sec actinic light treatments at 21 μ E, 103 μ E and 347 μ E.

Samples were subsequently treated with DCMU (20 mM 3-(3,4-dichlorophenyl)-1,1-dimethylurea, also known as Diuron, in 70% ethanol was used as 1000x stock). For J2, CF was recorded, to be used as proxy for PSII absorption cross-section, for one treatment of 5 sec at 347 μ E, followed by three repetitions of 5 sec at 103 μ E.

Next, HA (1 M hydroxylamine, also known as Azanol, in distilled water was used as 1000x-stock) was added to samples. After that, traces were recorded for estimation of *CEF* by firstly recording the decay of the p700 oxidation signal (absorbance at 705 nm) following a saturating pulse, and secondly following the decay of the ECS signal (absorbance at 525 nm), at the end of a 5 sec actinic light period at the same light intensities as above. Finally, an ECS trace of a Xenon bulb flash, or alternatively three ECS traces of single turnover laser flashes, were recorded.

2.2.4.3 Data analysis

For J1, data was analysed using Excel (Microsoft) by coping values over manually, whereas for J2, data was analysed using the free statistical software package R (The R Foundation). Briefly, raw data exported from the JTS-10 as .exp files was read into R, classifying the different traces by type (e.g. laser flash, F_v/F_m , ...) by making use of differences in the number of data points. Traces were first analysed internally for extraction of salient values, followed by two iterations of analysis where previously determined values from individual traces were combined for higher order Information gathering.

2.2.4.3.1 Fluorescence parameters

Minimal and maximal fluorescence were estimated from CF traces as values recorded 200 ms prior to, and 0.2 ms after saturating pulse application respectively, and used to calculate standard fluorescence parameters (Maxwell and Johnson, 2000). Dark adapted minimal (F_0) and maximal (F_m) fluorescence from F_v/F_m traces was used to calculate PSII quantum yield (F_v/F_m) as $F_v/F_m = (F_m - F_0)/F_m$, whilst steady state fluorescence (F_s) during actinic light treatments, and associated light adapted maximal fluorescence (F_m'), were used to calculate PSII operating efficiency (ϕ_{II}) as $\phi_{II} = (F_m' - F_s)/F_m'$. Assuming that of the light intensity (I) that samples were subjected to, 83% were absorbed by the cells of which 50% were distributed to PSII and the remainder to PSI, electron transport rate (*ETR*) was calculated as $ETR = I \cdot 0.83 \cdot 0.5 \cdot \phi_{II}$ (Von Caemmerer, 2013). Finally, *NPQ* was calculated from the reduction in maximal fluorescence compared to the dark-adapted state as $NPQ = (F_m - F_m')/F_m'$.

2.2.4.3.2 ECS-based ST values and PSI/II ratios

The ECS signal associated with a single turnover (ST) of photosystems was estimated from flash traces. Replicate ST values were averaged, and ST before (ST_n) and after addition of DCMU and HA (ST_{DH}) were used to calculate photosystem ratios (*PSI/PSII*) as $PSI/PSII = ST_{DH}/(ST_n - ST_{DH})$. For J1, the value recorded 5.05 ms after application of a laser flash

was used as best proxy for ST as use of this point resulted in the lowest variation between replicates for *PSI/PSII* values, compared to values recorded sooner or later after the flash. For Xenon bulb flashes, the value recorded 1.6 ms after application of the flash was used as best proxy for quasi-single turnover (*qST*: Xenon flashes are short enough to be ST for PSII, but long enough to result in more than one turnover per PSI) following standard lab practice (Dimitri Tolleter, personal communication). Assuming that samples assessed via Xenon flashes would have the same average *PSI/PSII* as samples assessed using a Laser, the number of PSI turnovers per *qST* was estimated as 1.74, which was then used to calculate ST from *qST* values. For J2, the value recorded in optimized ECS traces 0.65 ms after application of a laser flash was used as best proxy for ST.

2.2.4.3.3 ECS based electron flow rates

To estimate *LEF* and *CEF* from ECS traces (Joliot and Joliot, 2002; Bailleul et al., 2010; Lucker and Kramer, 2013) before and after addition of DCMU and HA respectively, traces were normalized to photosystem turnover equivalents via division by ST_n or ST_{DH} respectively. For J1, any background drift in the ECS signal was accounted for by subtracting a straight line fit through background recording points at the beginning (and, where dark relaxation had been fully recorded, at the end) of each trace, followed by ensuring dark decay values are positive by subtracting the minimal value recorded after switching the actinic light off. For J2, the value recorded 129 ms after switching the actinic light off was subtracted from the ECS trace, and the value at the exact time the light was switched off was estimated by fitting a straight line through 13 points recorded in 20 ms intervals up to 10 ms prior to the onset of darkness. For all data, exponential decay was fitted to the initial 20 ms of ECS decay in the dark, either using the GROWTH() function in Excel or by fitting a straight line through the natural logarithm of the data in R. From the slope ($\frac{f}{n}m_{ECS}$) between fitted decay values at 0 ms and 1 ms after the onset of darkness, per second electron flow rates (EF) were calculated as $EF = -1000 * \frac{f}{n}m_{ECS}$. Rather than estimating the slope directly from the data (m_{ECS}) as was standard lab practice (Dimitri Tolleter, personal communication), the slope was estimated from the fit to take the whole decay into account and thus minimize experimental error.

2.2.4.3.4 CEF estimated from p700

For J1, any background drift in the p700 signal was accounted for by subtracting a straight line fit through background recording points at the beginning (and, where dark relaxation had been fully recorded, at the end) of each trace (Alric, 2010; Johnson and Alric, 2012).

Steady state p700 oxidation signal (P_s) and maximal p700 oxidation (P_m) were estimated as values recorded 200-300 ms prior to, and 0.2 ms (Fig. 2.8) or 1 ms (J2) after saturation pulse application respectively, and used to calculate p700 light adapted reduction state (red) as $red = P_s/P_m$. Values detailing signal decay in the dark, recorded within 300 ms after saturation pulse application, were normalized to PSI turnover equivalents via division by P_m , and used to find the exponential decay rate (k), either using the LOGEST() function in Excel or by fitting a straight line through the natural logarithm of the normalized decay values in R. CEF was then calculated as $CEF = -1000 \cdot \ln(k) \cdot red$.

2.2.4.3.5 Chlorophyll per PSII based on JTS-10 measurements

Chlorophyll content of all cultures was estimated by extraction in 100% methanol (Wellburn, 1994) prior to harvest, and was used to calculate the concentration of chlorophyll of samples in HF ($[chl]$) based on a molecular weight of 893.49 g/mol. The concentration of PSI ($[PSI]$) was estimated from the JTS-10 (J2) absorbance measure of fully oxidized p700 (P_m) as follows (Johnson and Alric, 2012): The absorbance measure given by the JTS-10 is in a slightly unusual format, displayed as $\Delta I/I = (I_0 - I)/I$, where I_0 is the light applied to the sample, and I is the light transmitted by the sample. To achieve a classical measure of absorbance (A), defined as $A = \log_{10}(I_0/I)$, the JTS-10 value was corrected as $A = -(1/2.3) \cdot (\Delta I/I)$ (Appendix 8.1). Absorbance is proportional to length of the light path through the sample (l) and concentration of the absorbing species (c) as formulated in the Beer-Lambert Law: $A = l \cdot c \cdot \varepsilon$, where the proportionality constant ε is a material property of the absorbing species called molar absorptivity, which has been determined for PSI (ε_{p700}) to be 64 mequiv⁻¹ cm⁻¹ (Hiyama and Ke, 1972). Thus $[PSI]$ was calculated for a cuvette with a 1cm path length as:

$$[PSI] = \frac{\Delta I/I / -2.3}{\varepsilon_{p700} \cdot l} = \frac{P_m / -2.3}{64 \cdot 1} \quad (2.10)$$

The concentration of PSII ($[PSII]$) was calculated from $[PSI]$ using the ECS-derived $PSI/PSII$ ratio:

$$[PSII] = \frac{[PSI]}{PSI/PSII} = \frac{P_m}{-2.3 \cdot 64} \cdot \frac{(ST_n - ST_{DH})}{ST_{DH}} \quad (2.11)$$

Taking into account that ~240 molecules of chlorophyll are usually associated with each PSI reaction centre (Drop et al., 2014), the allocation of chlorophyll to PSII ($chl/PSII$) was calculated as:

$$\frac{chl}{PSII} = \frac{[chl] - 240 \cdot [PSI]}{[PSII]} = \frac{[chl] - 240 \cdot \frac{P_m}{-2.3 \cdot 64}}{-2.3 \cdot 64 \cdot \frac{(ST_n - ST_{DH})}{ST_{DH}}} \quad (2.12)$$

2.2.4.3.6 Chlorophyll per PSII based on chl a/b ratio

Alternatively, chlorophyll per PSII can be estimated from chlorophyll extraction data (Drop et al., 2014). Of the 240 chlorophylls (chl) coordinated by PSI, 196 are chl a (a_I) and 44 chl b (b_I). The core of PSII contains 35 chl a (a_{II}). A good approximation for light harvesting complexes, which consist of a mix of different protein complexes, was suggested to be 7.85 chl a (a_{LHC}) and 6.15 chl b (b_{LHC}) molecules per complex, on average. The chlorophyll ratio (a/b) must therefore be accounted by:

$$\frac{a}{b} = \frac{[PSI] \cdot a_I + [PSII] \cdot a_{II} + [LHCs] \cdot a_{LHC}}{[PSI] \cdot b_I + [LHCs] \cdot b_{LHC}} \quad (2.13)$$

Which can be rearranged to allow calculation of the number of light harvesting complexes per PSII ($LHCs/PSII = [LHCs]/[PSII]$) as:

$$\frac{LHCs}{PSII} = \frac{a_{II} + \frac{PSI}{PSII} \cdot (a_I - \frac{a}{b} \cdot b_I)}{\frac{a}{b} \cdot b_{LHC} - a_{LHC}} \quad (2.14)$$

Assuming $PSI/PSII$ to be unity (Drop et al., 2014) allows the number of chlorophyll molecules associated with PSII can thus be calculated as:

$$\frac{chl}{PSII} = \frac{LHCs}{PSII} (a_{LHC} + b_{LHC}) + a_{II} \quad (2.15)$$

2.2.4.3.7 DCMU saturation $t_{2/3}$ as proxy for functional PSII absorption cross-section

To get a measure of the functional absorption cross-section associated with PSII, fluorescence saturation was followed in samples treated with PSII inhibitor DCMU. Because of the sigmoidal shape of the saturation curve, the time taken to reach 2/3 ($t_{2/3}$) of maximal fluorescence (F_m) was used instead of saturation half-time. To calculate $t_{2/3}$, fluorescence recorded in the dark prior to actinic light treatment was subtracted from the original trace to give a zeroed trace. The maximum value recorded prior to application of the saturating pulse was taken as F_m . Data was transformed for each data point d_i at index i as: $d_i = (d_i - \frac{2}{3} F_m) \cdot (d_{i-1} - \frac{2}{3} F_m)$ which results in a negative number only at the i for which time t_i , at which point d_i was taken, obeys $t_{i-1} < t_{2/3} < t_i$. By fitting a straight line through d_i and d_{i-1}

in the zeroed trace, $t_{2/3}$ was then estimated as the time at which the value of the line is equal to $2/3$ of F_m .

2.2.5 FRRf measurements

For FRRf measurements (Fig. 2.11 d-f, Appendix 8.18), cells were grown in 50ml liquid culture in minimal medium for 4 days in continuous illumination, either at 50 μE and aerated with 5% CO_2 , or aerated with air at either 50 μE or 10 μE . Chlorophyll content was assessed daily (Wellburn, 1994), each time using the growth rates estimated this way (Fig. 2.5h) to normalize cultures (by adding fresh media, or excess culture from a different condition) such that chlorophyll content would be equal the following day. Cultures were decanted into 50ml Falcon tubes wrapped in aluminium foil and dark adapted for several hours (whilst driving from Cambridge to Colchester). For measurements, 50 μl culture was brought to 2 ml using fresh minimal medium. Cultures grown at 5% CO_2 were supplemented with 20 μl of a 1M NaHCO_3 stock. Saturating pulses (SP) were supplied every 20 sec, with 4 SP in the dark and 6 SP at every light intensity at 6 μE , 55 μE , 155 μE , 342 μE , 520 μE and 856 μE . For data analysis in R (The R Foundation), data from replicate SPs was averaged. For Fig. 2.11d, data was further averaged across light intensities for each sample before calculating averages and standard error between biological replicates, whereas Fig. 2.11 e&f show averages and standard error across biological repeats for each light intensity.

2.3 Results

2.3.1 Thylakoids stack irrespective of pyrenoid occurrence despite coordination by the pyrenoid in WT

Fig. 2.5 a&c&e show TEM images of median sections depicting WT cells grown contrasting physiological conditions. Flagella are missing, and since the cells are wall-less, the cell outline is irregular. The nucleus can be made out as dark grey nucleolus within a light grey nuclear sac, and the cup-shape of the chloroplast is clearly visible which can be easily identified by the presence of the string-like thylakoid membranes. Within the chloroplast, the pyrenoid can be seen as electron dense structure that is traversed by lighter grey intra-pyrenoidal thylakoid tubules (Engel et al., 2015) and surrounded by a sheath of white starch plates. Pyr- cells grown in the same conditions (Fig. 2.5 b&d&f) look remarkably identical except for the absence of the iconic pyrenoid structure.

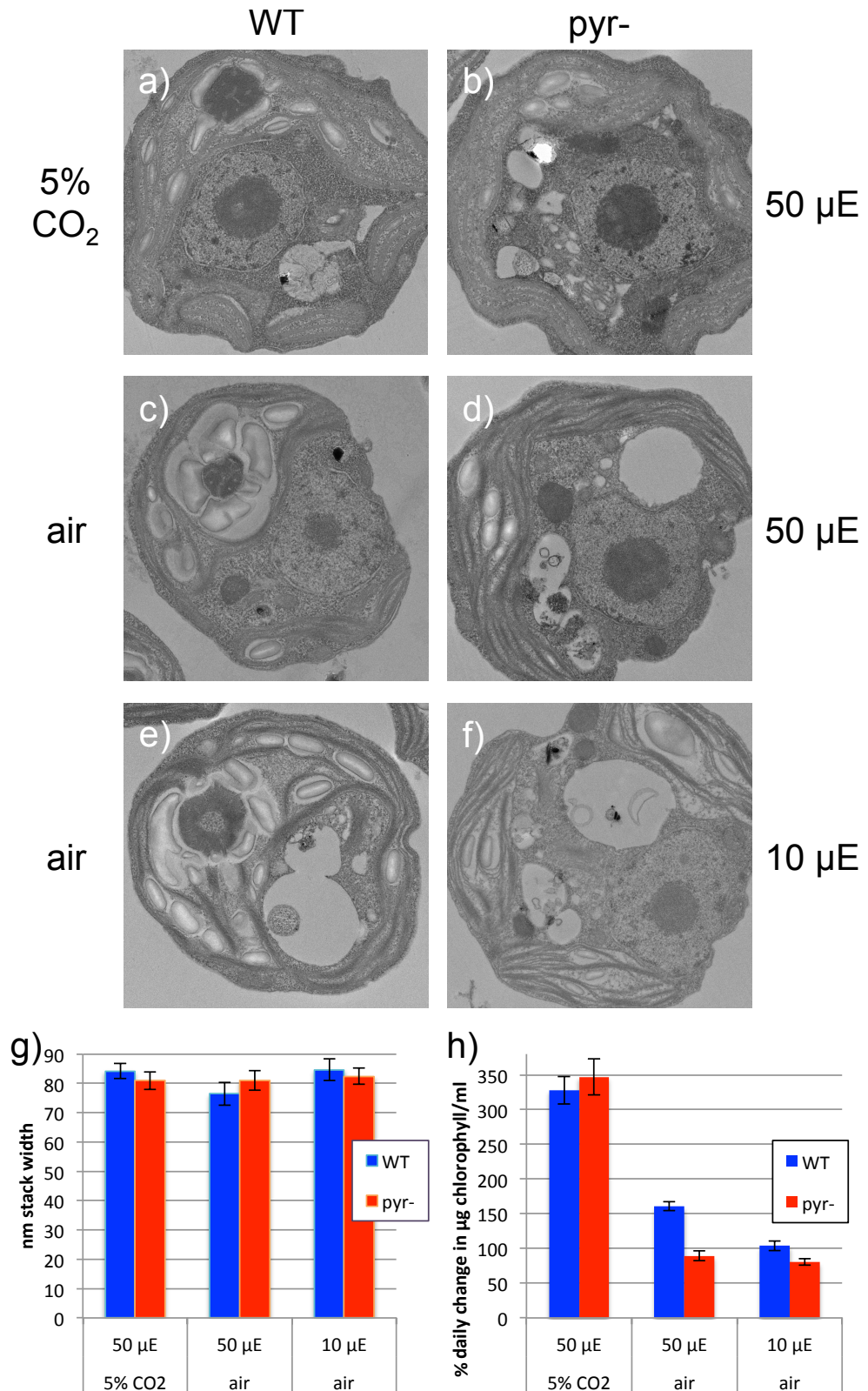


Fig. 2.5: Pyrenoid absence has no effect on thylakoid arrangement

TEM showing cells grown in contrasting conditions in (a)-(f), as per annotations. A quantification of thylakoid stacking is provided in terms of stack width (g) based on 20 cells per condition, and growth rates (h) are shown as % change in chlorophyll content over 24 hours (100% indicating no change) based on 4 independent cultures of 3 independent strains per condition, each reporting average \pm standard error.

The absence of any obvious difference in thylakoid stacking was corroborated by quantitative analysis (Fig. 2.5g) of stack width perpendicular to the orientation of lamellae which did not vary either between pyr- and WT ($p=0.912$) or between growth conditions ($p\geq 0.3$).

Such uniformity contrasts with stark differences in growth rates (Fig. 2.5h). When grown at 50 μE and aerated with 5% CO_2 , it takes ~ 14 h for the chlorophyll content of a culture to double, irrespective of whether it is a WT or a pyr- culture. At air, however, WT continues to grow at a slower rate with a doubling time of ~ 36 h at 50 μE or shows a stagnant chlorophyll content at 10 μE . By contrast, pyr- cultures grown in air show a decrease in chlorophyll content over time with an estimated half-life of ~ 110 h at 50 μE or ~ 72 h at 10 μE .

2.3.2 High throughput screen of *ETR* and *NPQ* demonstrates impact of pyrenoid occurrence under CCM inducing conditions

Photosynthetic characteristics of WT and pyr- strains were assessed using CF and spectroscopic proxies to obtain a range of informative parameters. As an initial screen, photosynthesis of SSU substitution strains was probed using colonies grown on agar plates in a range of physiological conditions using high-throughput CF imaging (Fig. 2.6, Fig. 2.7, Appendix 8.4, Appendix 8.5, Appendix 8.6, Appendix 8.7, Appendix 8.8).

To gain maximal insight into the Information contained in the data, a two-parameter model (Suggett et al., 2003) was fitted to the ϕ_{II} data underlying the *ETR* curves depicted in Fig. 2.6. This fit presents a powerful statistical analysis: using the *AIC* (Akaike, 1974), goodness of fit was weighed against number of parameters to establish which combination of parameters is best supported by the data (see Materials and Methods section 2.2.3.6). This approach established whether a particular experimental treatment (pyrenoid occurrence, light intensity or CO_2 concentration) had a significant effect on the shape of the curve, and which aspect of the curve (i.e. which model parameter) was most affected. The best fit is shown as solid lines through the averages with WT in blue and pyr- in red in Fig. 2.6, and parameters are listed in Table 2.1.

Fig. 2.6a shows a light response curve of cells grown in air-levels of CO_2 and a low light intensity of 10 μE . At experimental light intensities below 100 μE , *ETR* is low, increases almost linearly with light and is virtually identical between WT and pyr-. As experimental light intensity increases, the curvature of the lines increases as *ETR* reaches saturation, and the difference between WT and pyr- *ETR* becomes more pronounced.

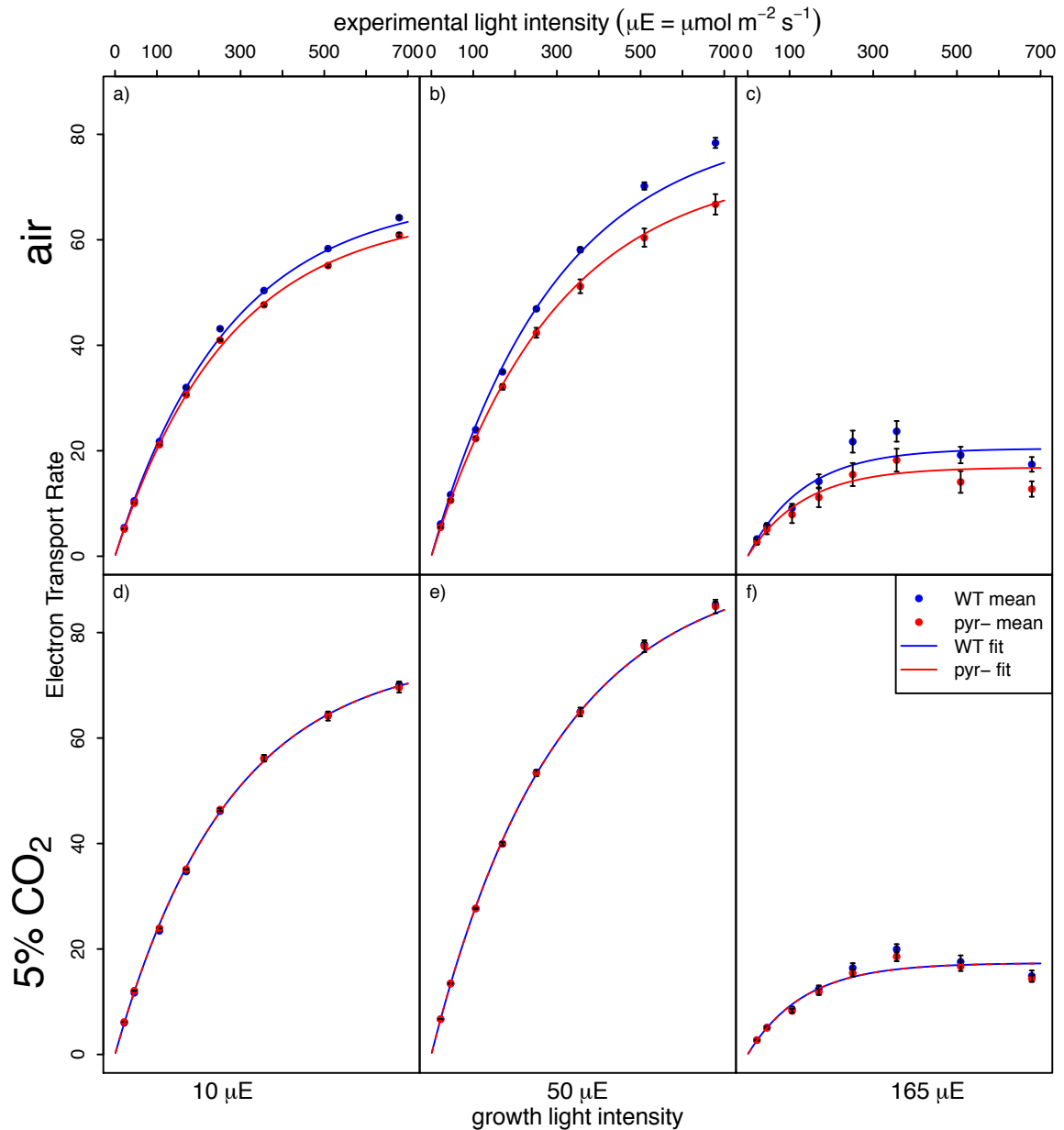


Fig. 2.6: High throughput CF screen demonstrates impact of pyrenoid occurrence on *ETR* under CCM-inducing conditions

Light response curves were collected using Technologica CFimager from algal colonies grown on agar plates in the growth light intensity detailed above and the CO_2 environment detailed on the left of the data panels. WT responses are shown in blue, pyr- mutant responses in red. *ETR* is shown as small dots between black error bars and overlaid with light response model (2.1) fit shown as solid lines. Data are the average of 6 biological replicates \pm standard error.

Fig. 2.6b shows the response of cells that were also grown in air, like those of Fig. 2.6a, but at a higher light intensity of $50 \mu\text{E}$. When grown at this higher light intensity, the difference in saturated *ETR* (ETR_{max}) between pyr- and WT increases and the values for ETR_{max} are higher than when grown in low light. Curvature of the light response curve is still identical between WT and pyr-. WT ETR_{max} is still higher than in pyr- but much lower than for cells

grown at lower light intensities. Fig. 2.6 d-f show the response of cells grown under 10 μE , 50 μE and 165 μE respectively as in Fig. 2.6 a-c, but in an atmosphere containing 5% CO_2 . In contrast to growth at air, cells grown and measured in elevated CO_2 have identical ETR in WT and pyr-. ETR_{max} is slightly higher than WT values at air for cells grown at 10 μE and 50 μE . Growth in very high light (165 μE , Fig. 2.6 c&f) is associated with a great reduction of ETR , consistent with visible photobleaching of the algal colonies (Appendix 8.2).

Fit parameters are detailed below the ETR graph. The saturation behaviour visible as curvature of the ETR line is captured in the model variable I_k . At each growth-light intensity, I_k values are identical for WT and pyr-, and are also identical across CO_2 environments. When grown at 50 μE , cells require more light to reach saturation than when grown at 10 μE , reflected by a higher I_k . At very high light, I_k is reduced again.

Table 2.1: Parameters of the model best supported by CF screen ϕ_{II} data according to AIC-based statistical analysis

parameters	10 μE		50 μE		165 μE		
	W	pyr-	W	pyr-	W	pyr-	
ϕ_m	air	0.61	0.58	0.67	0.61	0.37	0.30
	5% CO_2	0.68		0.76		0.31	
I_k (μE)	271		296		134		

ETR_{max} is captured mathematically by scaling the model parameters via $ETR_{max} = a_{II} I_k \phi_m$. The proportionality constant a_{II} represents light absorption by PSII and is generally assumed to be $0.5 \cdot 0.85$ (Maxwell and Johnson, 2000; Von Caemmerer, 2013). Given that I_k does not change between WT and pyr- at a given light intensity, ϕ_m is thus directly informative about differences in ETR_{max} . In contrast to I_k , ϕ_m is influenced by pyrenoid phenotype and CO_2 environment: Pyr- cells grown at air and 50 μE (Fig. 2.6b) show a reduction in ϕ_m compared to WT. Cells grown at 10 μE in air (Fig. 2.6a) show a similar response as those grown at 50 μE , however, WT cells show a greater reduction than pyr- cells. When grown at 165 μE (Fig. 2.6c), both WT and pyr- cells show significantly lower ϕ_m than at the other light intensities, yet WT is again considerably higher than pyr-. Cells grown at 10 or 50 μE (Fig. 2.7 d-f) show higher ϕ_m in 5% CO_2 than in air even for WT.

NPQ is shown in Fig. 2.7 a-c. For cells grown at low light in air, shown in Fig. 2.7a, NPQ starts off with values around 0.3 and then increases with experimental light intensity, tapering off slightly at very high experimental light. WT has consistently lower NPQ than pyr- at every stage of the light response curve ($p < 0.001$). For cells grown at 50 μE in Fig. 2.7b, initial NPQ is lower than in Fig. 2.7a and the difference between WT and pyr- ($p <$

0.001) over the whole curve is larger due to WT staying lower ($p = 0.018$) whereas *pyr-* is similar ($p = 0.903$). At the highest growth-light (Fig. 2.7c), *NPQ* starts off at slightly lower values than at lower growth-light again. However, WT and *pyr-* values are now very similar throughout. For cells grown at 5% CO_2 (Fig. 2.7 d-f), *NPQ* is lower than in air-equilibrated cells under all light regimes, and WT and *pyr-* are very similar. Like in air, lower initial *NPQ* values are observed for cells adapted to higher growth-light intensities.

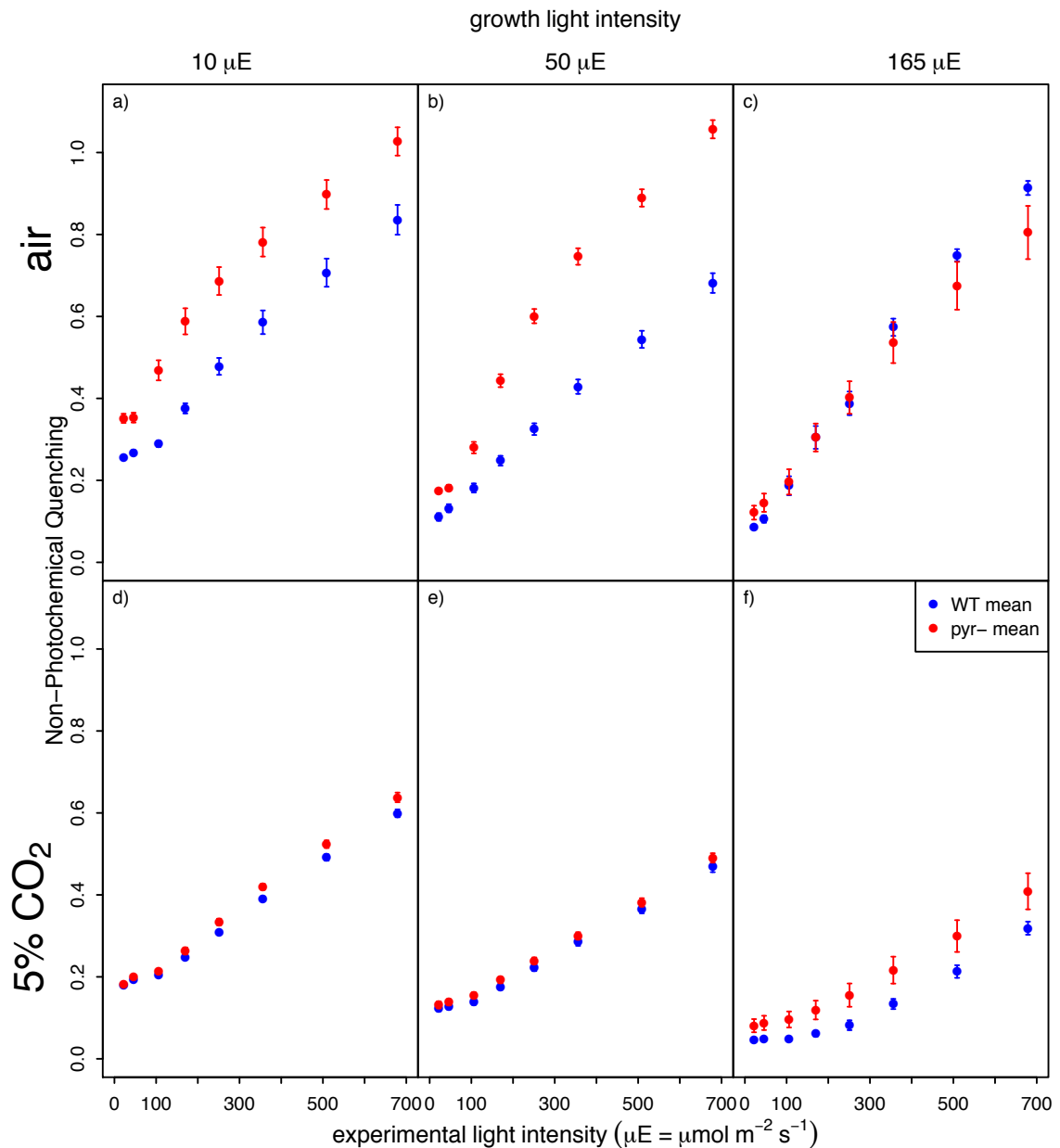


Fig. 2.7: High throughput CF screen shows higher *NPQ* in *pyr-* under CCM-inducing conditions, suggesting an imbalance between pETC and CBC.

Light response curves were collected using Technologica CFimager from algal colonies grown on agar plates in the growth light intensity detailed above and the CO_2 environment detailed on the left of the data panels. WT responses are shown in blue, *pyr-* in red. Data are the average of 6 biological replicates \pm standard error.

2.3.3 High-Resolution ECS and CF reveals Rubisco turnover feedback limitation

Using the high-resolution JTS-10 (Joliot and Joliot, 2002; Joliot et al., 2004), a more detailed investigation of the differences between WT and *pyr*⁻ when grown at air was then utilized to gain more insight into the behaviour of liquid cell cultures grown at 50 μE continuous illumination (Fig. 2.8).

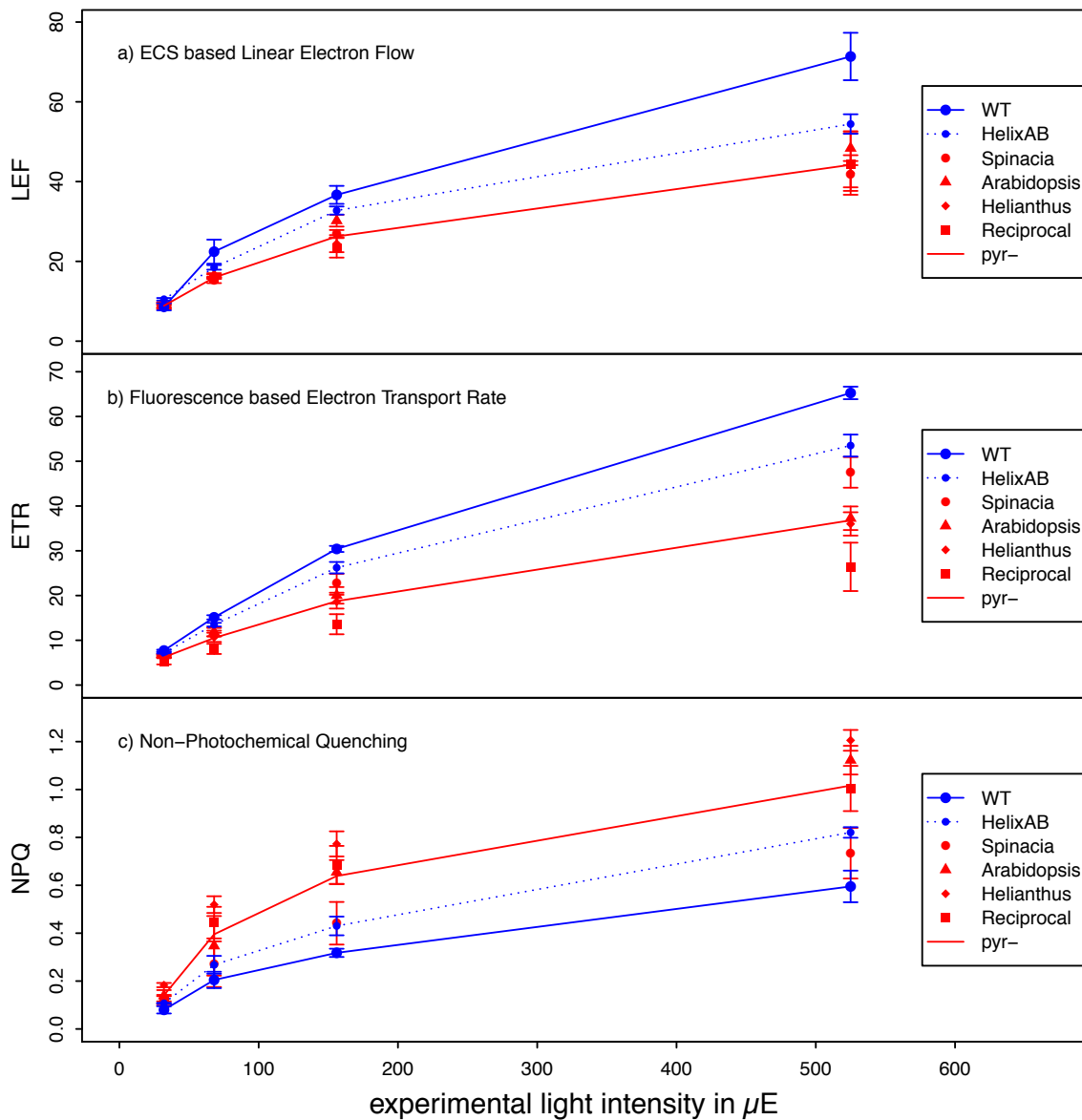


Fig. 2.8: High-Resolution ECS and CF measurements reveal feedback limitation by Rubisco catalysis.

Panels show JTS-10 data of (a) *LEF* estimated on the basis of ECS data, (b) *ETR* through PSII estimated on the basis of CF data and (c) *NPQ* estimated from CF. Lines show the average for WT (blue), *pyr*⁻ (red) and HelixAB (dashed, blue) while the symbols show the average for each strain \pm standard error based on ≥ 3 biological replicates for each strain. Cells were grown in liquid culture in the absence of aeration at a growth-light intensity of 50 μE .

The JTS-10 allows estimation of *LEF* (Fig. 2.8a) via the spectroscopic ECS method (Joliot and Delosme, 1974; Bailleul et al., 2010) in addition to *ETR* from variable CF (Fig. 2.8b). Like in Fig. 2.7, light response curves of WT (in blue) and pyr- cells (in red) is shown, with averages connected by solid lines. Data obtained from both proxies show that WT strains have higher rates of electron transport, and the difference between WT and pyr- is more pronounced at high light whereas at low experimental light intensities *LEF* and *ETR* are very similar.

In contrast to Fig. 2.6 and Fig. 2.7, strains carrying different *RBCS* constructs are resolved individually shown as average between coloured error bars. Pyr- strains cluster very tightly and have consistently lower values than WT. In addition to WT and higher plant SSU lines, chimeric SSU lines HelixAB and Reciprocal (Meyer et al., 2012) were included in this part of the study. HelixAB (dotted blue line) shows consistently lower *LEF* and *ETR* than WT but higher than pyr-. Finally, *NPQ* estimated from CF (Fig. 3c) shows higher values for pyr- strains than for HelixAB and WT, with WT showing the overall lowest *NPQ*.

2.3.4 Elevated CO₂ restores photosynthetic performance in pyr- cells via CBC feedback

To be able to differentiate between effects of carbon limitation and a structural impact of pyrenoid absence in CCM-induced cells, air-equilibrated cells were subjected to saturating levels of CO₂ during measurements. Addition of saturating (10 mM final concentration) bicarbonate to the JTS-10 cuvette was used as a tool to deliver high concentrations of CO₂ (equivalent to aeration with $\geq 1\%$ CO₂) to Rubisco even in cells that are unable to accumulate C_i by means of a CCM. The aim was to remove any differences in metabolic potential between the lines such that remaining differences could directly be attributed to a structural role of the pyrenoid in the chloroplast and pleiotropic effects of pyrenoid loss.

Fig. 2.9 no longer displays light response curves, instead the data are akin to a fluorescence induction time-course conducted at saturating light (350 μ E), with average PSII operating efficiency shown as a function of growth-light intensity. Fig. 2.9a thus shows the ϕ_{II} response of cells grown at low CO₂ exposed to 5 seconds of saturating light. WT (blue lines) has higher ϕ_{II} values than pyr- (red lines) throughout. After 30 seconds of saturating light (Fig. 2.9b), both WT and pyr- show a drop in ϕ_{II} in the absence of bicarbonate (solid lines), thus maintaining the difference between the two lines. A smaller drop for both lines is seen again at the 120 second time point (Fig. 2.9c) in the absence of bicarbonate (solid lines), still maintaining the difference between WT and pyr-. Thus cells grown and measured at air-

levels of CO₂ show a significant difference in ϕ_{II} between WT and pyr- (Fig. 2.9 a-c, solid lines, $p = 1.46 \cdot 10^{-5}$).

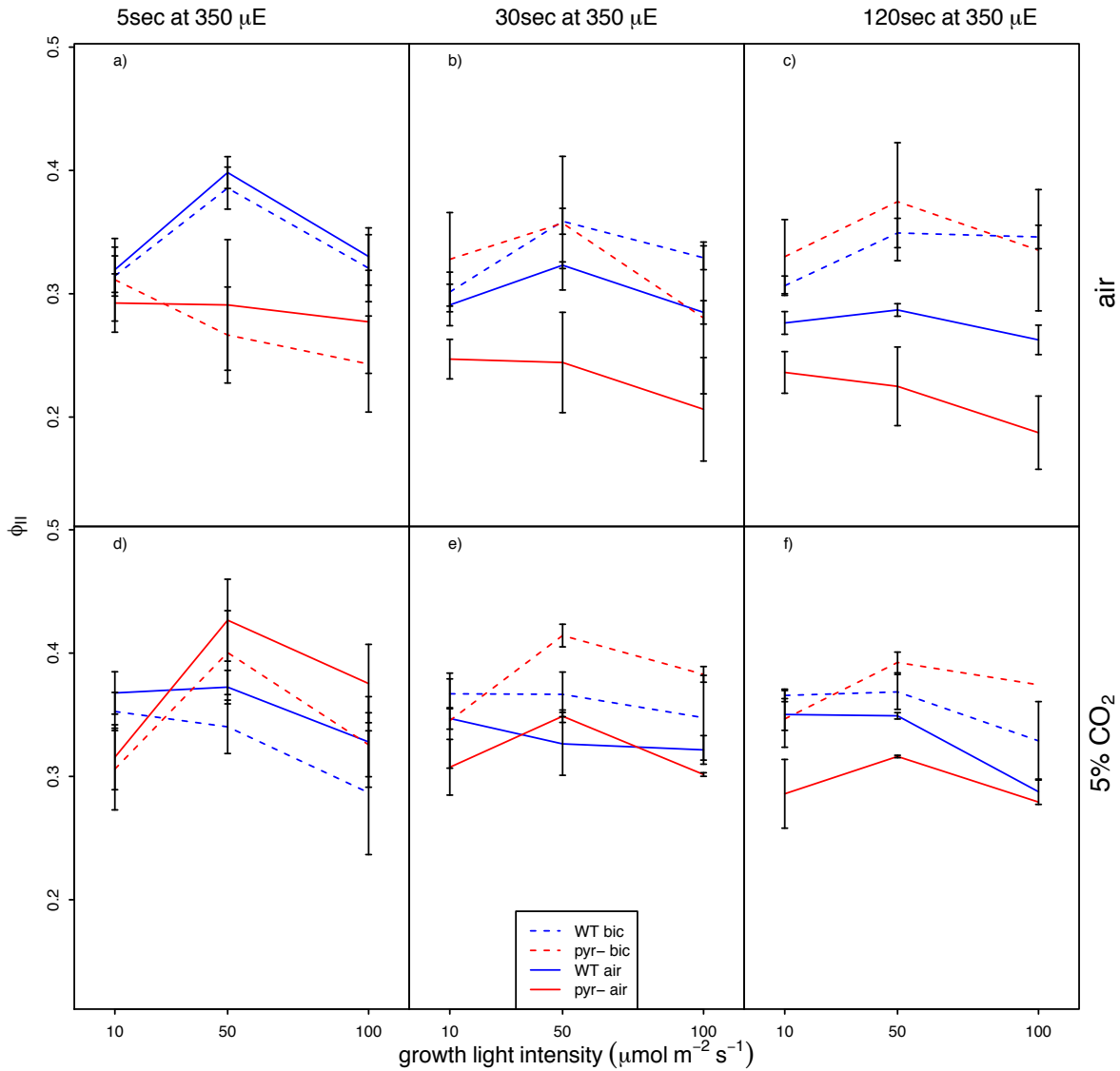


Fig. 2.9: Elevated CO₂ instantaneously restores photosynthetic performance in pyr-cells .

PSII operating efficiency (ϕ_{II}) was measured in the JTS-10 after 5s, 30s and 120s at $\sim 350 \mu\text{E}$ (to ensure saturation, informed by I_k in Table 2.1) as detailed above the data panels. Cells were grown at either air-levels or 5% CO₂ as detailed to the right of the panels, and at either low (10 μE), medium (50 μE) or high light intensity (100 μE) as shown on the x-axis. Strains supplemented with 10 mM bicarbonate directly before measurements are shown by broken lines. Untreated controls are shown by solid lines. WT responses are shown in blue, pyr- mutants in red. Data are the average of three biological replicates \pm standard error.

The presence of bicarbonate (broken lines) does not initially influence either WT or pyr- when probed after only 5 seconds of saturating light (Fig. 2.9a). After 30 seconds (Fig. 2.9b), however, bicarbonate treated samples show much higher ϕ_{II} values than untreated

samples. WT treated with bicarbonate stays at the same level as after 5 seconds, and pyr- ϕ_{II} values increase to the same level as WT. After 2 minutes, bicarbonate treated samples show a slight increase in performance compared to the 30-second time point, with pyr- ϕ_{II} values again being equivalent to WT. Thus the difference between pyr- and WT is removed by the addition of bicarbonate (Fig. 2.9 a-c, broken lines, $p=0.674$).

Cells grown at 5% CO₂, in contrast to air-grown cells, show no significant difference between WT and pyr- even in the absence of bicarbonate (Fig. 2.9 d-f, solid lines, $p = 0.998$). Similar to air-grown cells, ϕ_{II} values for both WT and pyr- drop over time in the absence of bicarbonate (solid lines). Despite this decrease compared to the 5-second time point, 5% CO₂ grown samples measured in the absence of bicarbonate (Fig. 2.9 d-f, solid lines) maintain high levels of ϕ_{II} that are equivalent ($p = 0.485$) to air-grown samples treated with bicarbonate (Fig. 2.9 a-c, broken lines).

Bicarbonate treatment (broken lines) of 5% CO₂-grown cells does not significantly alter ϕ_{II} values ($p=0.412$) after only 5 seconds of light (Fig. 2.9d). After 30 seconds (Fig. 2.9e), however, values for bicarbonate treated samples increase whereas untreated samples decrease, a pattern repeated after 2 min of light (Fig. 2.9f). This increase means that bicarbonate-treated 5% CO₂-grown cells (Fig. 2.9 d-f, broken lines) show higher ϕ_{II} values ($p=3.03 \cdot 10^{-3}$) than bicarbonate-treated air-grown cells (Fig. 2.9 a-c, broken lines). There is no difference between WT and pyr- when grown at 5% CO₂ and treated with bicarbonate ($p=0.897$).

2.3.5 Expression of photosystems and accessory pigments undergoes physiological acclimation independent of pyrenoid phenotype.

To capture any structural effect of pyrenoid loss on the regulation of pETC components, expression of photosynthetic pigments and photosystems was studied alongside functional electron transport rate measurements in the JTS-10 as shown in Fig. 2.10. As before, pyr- mutants are shown in red and WT in blue.

2.3.5.1 Chlorophyll / cell

Fig. 2.10a shows that total chlorophyll expression per cell is similar in pyr- and WT. Cells grown at 50 μ E at air, shown as red symbols for pyr- or blue symbols for WT and HelixAB, form a curved spread across the plot. Chlorophyll content is ~ 2 μ g chl/ml for cultures of ~ 1 million cells/ml compared to ~ 4 μ g chl/ml at ~ 2.5 million cells/ml, indicating that chlorophyll per cell decreases with increasing culture density.

Molecular Physiology of the *Chlamydomonas pyrenoid*

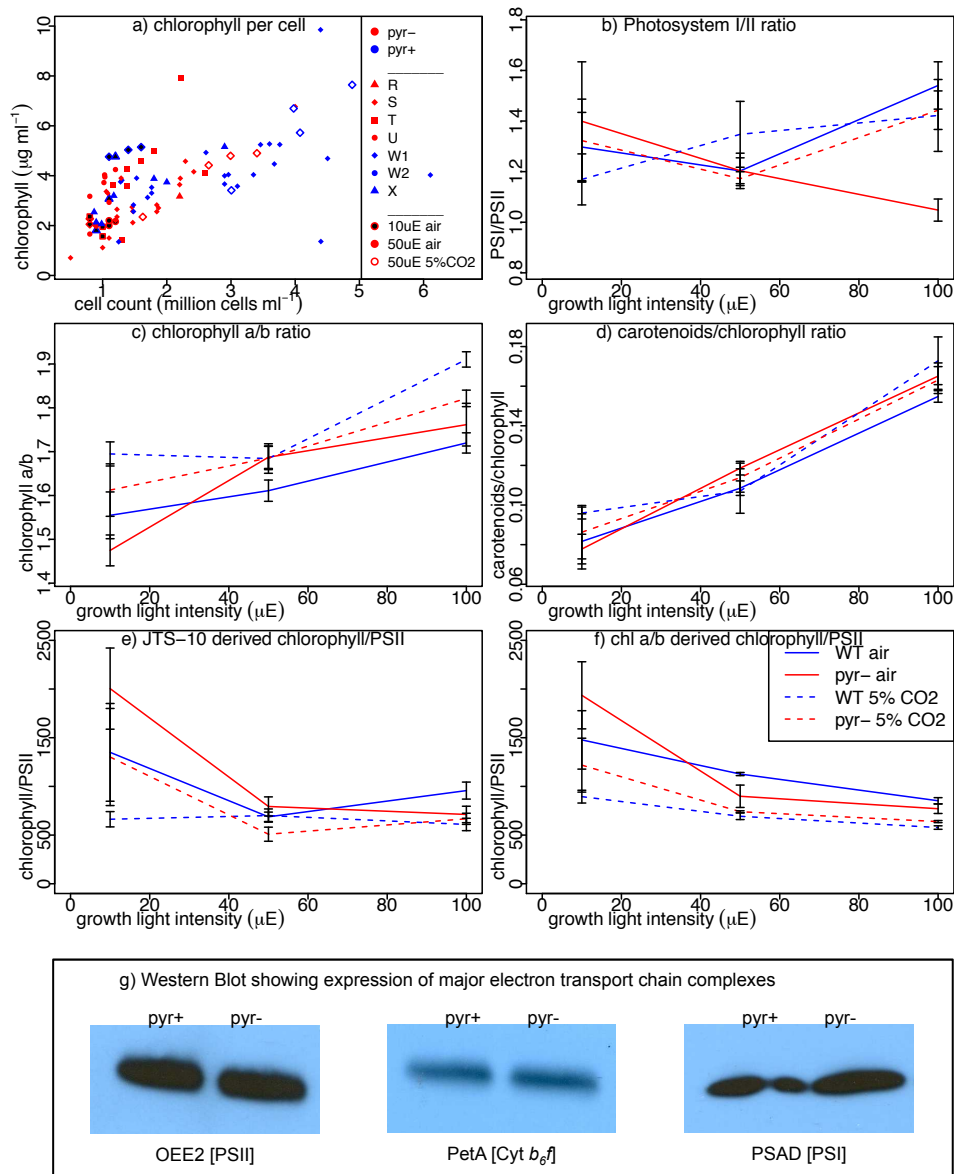


Fig. 2.10: Expression of photosystems and accessory pigments undergoes physiological acclimation independent of pyrenoid phenotype.

Chlorophyll expression on a per cell basis (a) is shown as scatterplot of individual measurements. Symbol outlines denote different strains by RBCS construct expressed (R – reciprocal, S- *Spinacia oleracea*, T- *Arabidopsis thaliana*, U- *Helianthus annuus*, W – native Wtint1,2 insertion lines, X – *Helix*AB). Red/blue colour coding refers to pyrenoid phenotype and symbol filling details growth conditions as per legend. The functional PSI/PSII ratio (b) is plotted against the light intensity that the cells were grown at. Data based on ≥ 3 biological replicates are shown as averages \pm standard error and are connected by solid lines if collected from cells grown in air, or broken lines when cells were grown at 5% CO_2 . Panel (c) shows chlorophyll a/b ratio and (d) carotenoid expression per chlorophyll depicted the same way. Chlorophyll allocation to PSII as estimated from JTS-10 data is shown in (e), estimates based on chlorophyll extraction data are shown in (f). Panel (g) shows a Western blot estimating relative protein expression of representative components of the major pETC complexes PSII, cytochrome b_6/f and PSI.

There are more data points for WT at high culture densities, owing to the slower autotrophic growth phenotype of *pyr-* lines at low CO₂, which makes it challenging to accumulate dense cultures. If total averages had been plotted rather than a spread, this bias in culture density could have generated a false impression of WT accumulating less chlorophyll per cell than *pyr-*, even though there is no significant difference between the two ($p = 0.232$). By plotting the spread of values the similarities are more visually compelling, as for culture densities between 1 - 2.5 million cell/ml where there is data for both WT and *pyr-* available, there is no discernable difference in chlorophyll expression: *pyr-* data points scatter above and below WT and HelixAB. The same equivalence between *pyr-* and WT was observed for cells grown at 5% CO₂ (white-bodied symbols) where higher *pyr-* culture densities could be achieved. Finally, the data available for cells grown at 10 μ E (black-bodied symbols) again supports equivalence, with HelixAB data points connecting *pyr-* and WT point clusters at different culture densities.

2.3.5.2 PSI/II

Fig. 2.10b shows the ratio of *PSI/PSII* as a function of growth light intensity. *PSI/PSII* ratios are equivalent between air and 5% CO₂ ($p > 0.96$) and across light intensities ($p > 0.3$). There is no difference between *pyr-* and WT ($p = 0.144$). Bicarbonate addition to the measurement cuvette did not affect the *PSI/PSII* ratio, as would be expected given that changes in these measures would require changes in protein abundance proceeding over much longer timescales than the JTS-10 measurements.

2.3.5.3 Photosynthetic pigments

In terms of chl *a/b* ratio shown in Fig. 2.10c, WT and *pyr-* behave identical to each other ($p = 0.503$) at both low and high CO₂. The chl *a/b* ratio increases with light intensity ($p = 1.5 \cdot 10^{-5}$), and there is a slight but significant shift towards a higher chl *a/b* ratio for both WT and *pyr-* when grown in high CO₂ ($p = 7.1 \cdot 10^{-3}$). Carotenoid expression, shown in Fig. 2.10d, shows a very clear increase with light intensity ($p = 2.85 \cdot 10^{-9}$) while pyrenoid occurrence or CO₂ environment do not have any effect.

2.3.5.4 Chl/PS

Two different proxies were collected concerning the relative expression of photosystems and associated antenna chlorophylls. Fig. 2.10e, combines p700 measurements of the JTS-10 with chlorophyll extraction data while Fig. 2.10f uses equations from (Drop et al., 2014) to calculate the same *chl/PSII* ratio from chlorophyll *a/b* data. The two proxies

agree that there are generally around 900 chlorophyll molecules allocated to each PSII centre, with JTS-10 data being somewhat lower and chlorophyll *a/b* ratio based estimates somewhat higher but in the same range ($p=0.114$). Both proxies show a decreased accumulation of chlorophyll per PSII with increasing light ($p=2.1 \cdot 10^{-14}$), whereby $10\mu\text{E}$ is significantly higher than $100\mu\text{E}$, and a slight increase when grown in air relative to 5% CO_2 ($p=4.19 \cdot 10^{-7}$), which is largest at $10\mu\text{E}$. Importantly, however, neither proxy shows a significant difference between WT and *pyr-* cells at either air or 5% CO_2 ($p=0.616$).

2.3.5.5 Western blots

For standard growth conditions, $50\mu\text{E}/\text{air}$, expression of the key pETC components PSII, cytochrome b_6f and PSI was probed via Western Blot analysis (Fig. 2.10g). All three pairs of bands show a very similar size band for *pyr-* as for WT, indicating the protein is accumulated to the same level in each case.

2.3.6 Pyrenoid occurrence alters functional association of PSII and chlorophyll in low CO_2

In addition to estimating the total presence of photosystems and accessory pigments, functional association between chlorophyll and PSII was probed. Fig. 2.11 a-c directly compare physical Photosystem antenna size in terms of chlorophyll molecules allocated to PSII on the x-axis with functional PSII absorption cross-section on the y-axis. Of the two proxies for *chl/PSII* presented in Fig. 2.10 e-f, here JTS-10 derived values are used for the x-axis for maximal comparability with simultaneously taken JTS-10 measurements on the y-axis. Shown is the time required to reach 2/3 of the fluorescence maximum in DCMU-treated samples, which is an inverse proxy for PII absorption cross-section: the longer it takes to reach saturation, the smaller the effective PSII absorption cross-section.

For low-light grown cells in Fig. 2.11a, functional absorption cross-section increases as physical antenna size increases: *pyr-* grown in air, shown as red symbol with solid-lined error bars, has the highest number of chlorophyll molecules associated with PSII whilst it also requires the least amount of time to reach saturation, indicating a larger absorption cross-section than in the other lines. On the other extreme, 5% CO_2 -grown WT cells, shown as white-bodied symbols with blue outline and broken-lined error bars, have the smallest physical and functional antenna size. The data is highly variable meaning that there is no statistically significant difference between *pyr-* and WT, although the data does suggest that air-grown cells have larger antennae than cells acclimated to a high- CO_2 environment.

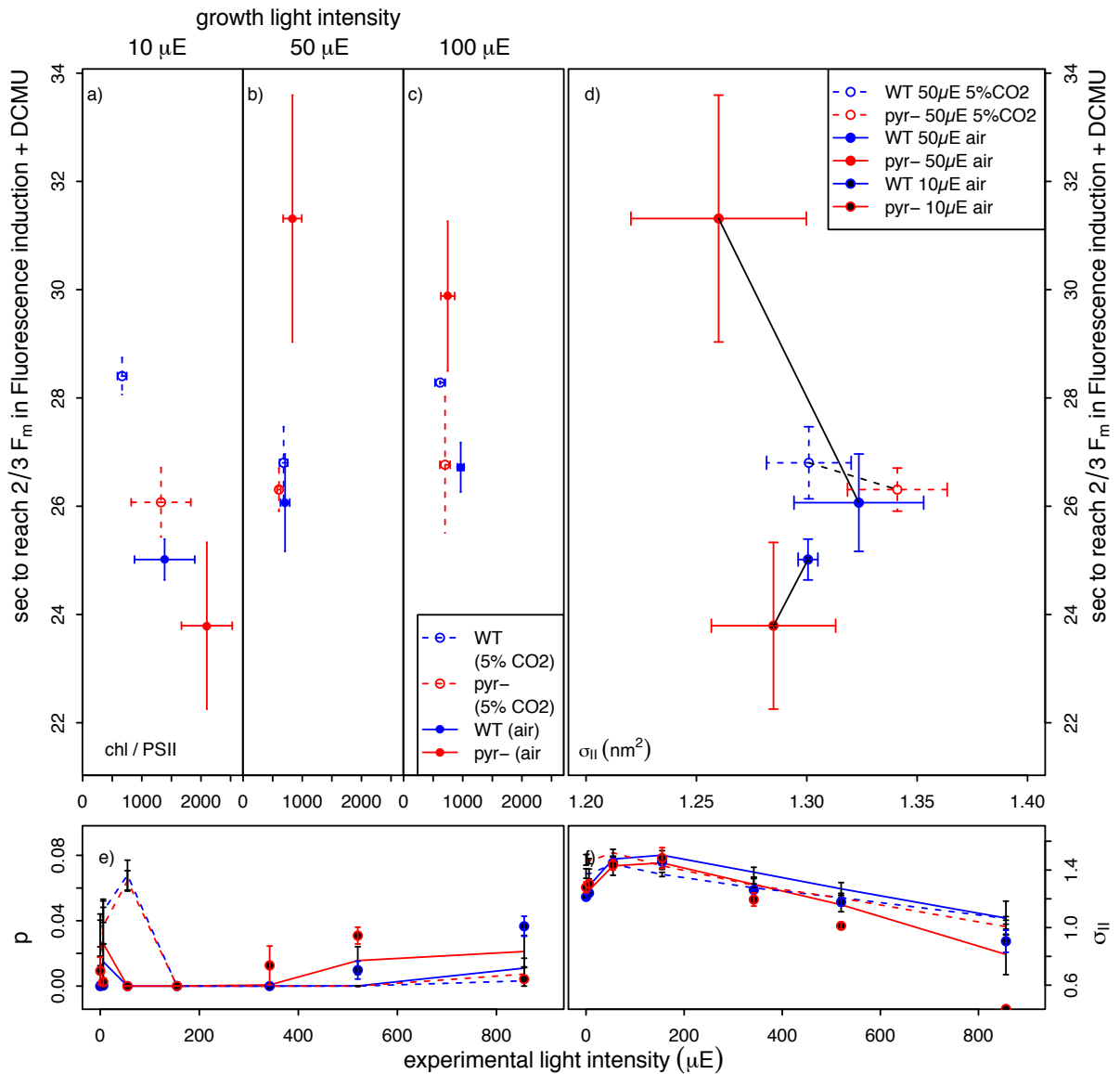


Fig. 2.11: Pyrenoid occurrence alters functional association of PSII and chlorophyll in low CO₂.

Panels (a)-(c) compare the physical PSII antenna size as *chl/PSII* (as in Fig. 2.10 e) on the x-axis with functional PSII antenna size measured as DCMU saturation kinetics on the y-axis. Some of the same DCMU saturation data is compared in (d) against an independent proxy for functional PSII antenna size, σ_{II} , derived from FRRf measurements. Depicted in (e) is p , a factor describing connectivity between PSII centres, which can take values between 0-1. Shown in (f) is the variation in the effective PSII absorption cross-section, σ_{II} , with changing light intensity. Averages across light intensities of (f) are used for the x-axis of (d). All data are based on at least three biological replicates shown as average \pm standard error.

The picture is drastically different ($p=6.96 \cdot 10^{-4}$) when the cells are grown at 50 μE , as shown in Panel b. All lines have very similar physical antenna sizes ($p>0.79$), however, pyr-cells grown at air show a large reduction in functional absorption cross-section, seen as increase in saturation time, compared to WT ($p=9.51 \cdot 10^{-4}$). Growth at 5% CO₂ does not

change WT absorption cross-section ($p > 0.999$), but it restores pyr- absorption cross-section to WT-levels ($p > 0.999$). The pattern is similar albeit less extreme at 100 μE ($p = 0.703$).

In Fig. 2.11d, the same JTS-10-derived DCMU saturation kinetics data on the y-axis are compared to σ_{II} , which is an independent proxy for PSII absorption cross-section derived from FRRf measurements (Kolber et al., 1998). Like the DCMU-measurements, σ_{II} data show that air-grown pyr- has a lower functional absorption cross-section than WT, but that growth at 5% CO_2 rescues pyr- to WT-levels. For cells grown at 10 μE in air, WT absorption cross-section is on average larger than pyr- according σ_{II} data. In the same condition, pyr- is on average smaller than WT according to DCMU saturation kinetics. This disparity confirms that the differences reflect random variation between samples that are not different biologically, as suggested by the lack of statistical significance in both cases.

A second disparity to DCMU-saturation data is that σ_{II} values for 10 μE grown cells suggest a lower absorption cross-section than for 50 μE -grown cells. DCMU saturation data on the other hand supports a larger absorption cross-section for low-light grown cells. This difference is likely a result of the light intensity used for measurements. Whereas DCMU saturation was recorded at around 100 μE , the σ_{II} values shown in Fig. 2.11d are the average of the σ_{II} light response curves shown in Fig. 2.11f. While there is considerable variation in the effective absorption cross-section of PSII with light intensity, the overall shape of the curves is represented well in the average as pyr- grown at 50 μE in air display consistently lower values than WT cells, while the traces for cells grown at 10 μE or 5% CO_2 have at least one crossover for WT and pyr-, signifying the variation around similar levels that is captured in Fig. 2.11d. At $\sim 100 \mu\text{E}$ in Fig. 2.11f, σ_{II} for 10 μE -grown cells is similar if not higher than for 50 μE grown cells, in line with DCMU saturation data. Finally, Fig. 2.11e shows that the connectivity between PSII centres, p , is near zero throughout all conditions.

2.3.7 Demand for ATP is increased in the absence of a pyrenoid

In addition to estimating LEF (Fig. 1.1), different proxies for CEF were measured. Both CCM operation in WT and photorespiration in the absence of a CCM in pyr- are expected to alter the ATP/NADPH requirement associated with each revolution of the CBC (Fig. 1.3). Therefore, *CEF* should be informative about the effect of the pyrenoid on the balance of energy metabolites. Absolute rates of *CEF* estimated from ECS in the presence of PSII inhibitors (Fig. 2.12a) as light response curve are higher in WT (W) and pyr+ strain HelixAB (X) than in pyr- strains when grown without aeration at 50 μE . The same pattern is found when *CEF* is measured using p700 absorbance (Fig. 2.12b).

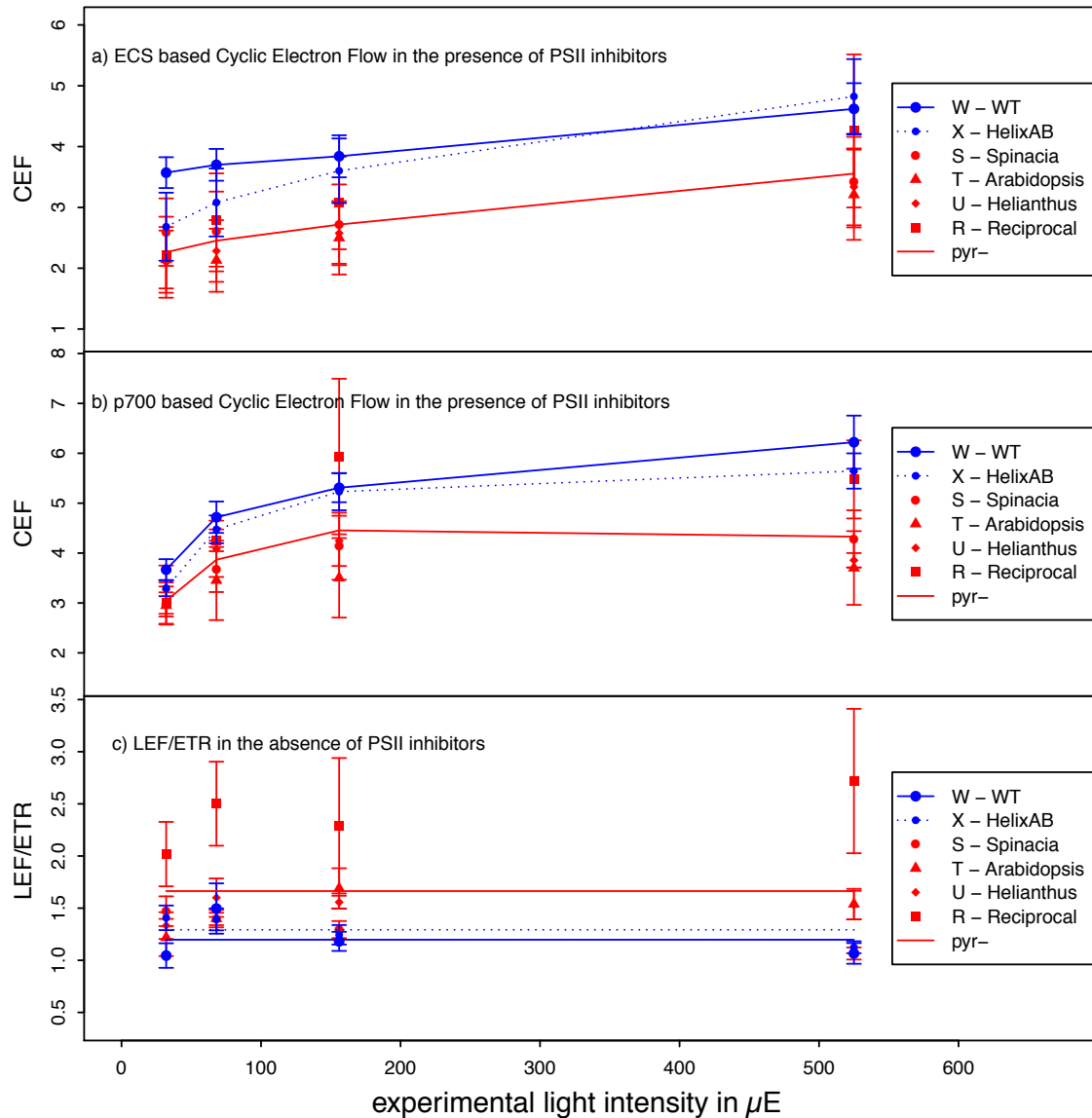


Fig. 2.12: CEF is lower in absolute terms but higher relative to *ETR* in *pyr*-

CEF in the presence of PSII inhibitors DCMU and HA was estimated on the basis of ECS (a) or p700 absorbance (b). The ratio of total electron flow based on ECS (*LEF*) to electron transport through PSII (*ETR*) (c) is shown as a proxy for the contribution of CEF to total electron flow in the absence of inhibitors. Data are shown as averages \pm standard error based on ≥ 3 biological replicates for each strain. Cells were grown in liquid culture in the absence of aeration at a growth-light intensity of 50 μE .

In the absence of PSII inhibitors (Fig. 2.2c), following the relaxation of ΔpH via ECS can be used to estimate total electron flow (Fig. 2.2). While this total flow is composed of WWC, CEF and LEF, the latter is generally thought to make up the greatest fraction, hence electron flow rates measured using ECS in the absence of PSII inhibitors are usually denoted *LEF* (Fig. 2.8a). Alternatively, *ETR* through PSII (Fig. 2.8b) can be estimated from CF and is informative about WWC and LEF (Fig. 2.2), but again is taken as an estimate of LEF as the contribution by WWC is very small (Appendix 8.13). Because CEF is captured by ECS but

not CF, ECS-based rates of *LEF* are higher than CF-based *ETR*. The ratio of *LEF/ETR* can therefore be used as a relative measure of CEF. This *LEF/ETR* (Fig. 2.12c) is relatively stable over a range of experimental light intensities, and levels in *pyr-* are at least as high as in WT.

2.4 Discussion

Photosynthetic Electron Transport must strike a fine balance (Fig. 2.1) between processing the incoming light, and matching the metabolic output with cellular demands (Allen, 2003; Cardol et al., 2011; Foyer et al., 2012; Lane, 2014). The latter will largely be governed by operation of the CBC: Unlike the mitochondria, the chloroplast does not contain export channels for ATP or NAD(P)H, and operation of a malate shuttle has been estimated to have a higher limit of ~10% of pETC output (Eberhard et al., 2008). The mutant lines used in this study are not only unable to aggregate Rubisco into a pyrenoid, these lines are also known to have a severe defect in the operation of the CCM as a direct result of pyrenoid loss (Genkov et al., 2010; Meyer et al., 2012). Unable to accumulate a high concentration of CO₂ around Rubisco, these cells should be expected to have lower rates of electron transport as a result of feedback from the CBC operating at a slower rate. In addition to metabolic feedback, however, there may be structural changes within the chloroplast resulting from the inability to assemble a pyrenoid.

2.4.1 *Pyr-* cells show a range of phenotypic differences from WT when grown in low CO₂

In CCM-inducing conditions (air), *pyr-* cells show a number of differences compared to WT diagnostic of photosynthetic impairment. Cultures of *pyr-* are slowly depleted of chlorophyll (Fig. 2.5h) as cells are dying, whereas WT cells continue to grow and divide (see also Appendix 8.2). In the mutants, PSII activity (ϕ_{II} , *ETR*) is lower (Fig. 2.6 a-c, Fig. 2.8 a&b, Fig. 2.9 a-c: solid lines; see also Appendix 8.5, Appendix 8.18; F_v/F_m : Appendix 8.4, Appendix 8.10; *LEF*: Appendix 8.11), *NPQ* is increased (Fig. 2.7, Fig. 2.8c; see also Appendix 8.6; Appendix 8.9; Appendix 8.16), and functional PSII absorption cross-section (σ_{II}) is decreased (Fig. 2.11). Absolute rates of *CEF* are decreased whereas the contribution of CEF to total electron flow is increased (Fig. 2.12; see also Appendix 8.17). These observations suggest there could be pleiotropic effects from pyrenoid absence. Alternatively, these differences could simply reflect altered metabolic demand and supply in the absence of a CCM experienced by *pyr-* cells. This study was designed to determine cause and effect of

photosynthetic impairment in cells where chloroplast structure and metabolism were perturbed by simply changing Rubisco SSU.

2.4.2 Pyrenoid absence has no discernable effect on the ultrastructural arrangement of photosynthetic membranes in mutant strains

Support for the idea of a pleiotropic, structural effect of pyrenoid loss comes from the fact that the pyrenoid has been implicated in organizing assembly of photosynthetic complexes (Uniacke and Zerges, 2007, 2009) and is known to interact with the thylakoid membrane system (Engel et al., 2015) as seen in Fig. 2.5, intra-pyrenoid tubules are continuous with single lamellae surrounding the starch sheath. In the stroma, 2-4 thylakoid lamellae form stacks over long distances running parallel to the envelope of the *Chlamydomonas* chloroplast (Goodenough and Levine, 1969). In further contrast to the arrangement in higher plant grana (Mustárdy et al., 2008), *Chlamydomonas* thylakoids are interconnected internally and with the chloroplast envelope at edge junction sites (Engel et al., 2015). The Rubisco aggregation state has been postulated to influence thylakoid stacking on theoretical grounds, based on the idea that solubilisation and hence uniform distribution of one would entropically favour aggregation or stacking of the other (Chow et al., 2005; Kim et al., 2005).

Thylakoid hyperstacking, defined as a higher number of lamellae per stack than in WT, had been reported before in pyr- lines (Meyer et al., 2012) in support of a structuring role of Rubisco aggregation in determining thylakoid architecture. This “hyperstacking” phenotype of pyr- strains was based on qualitative assessment of images that were taken, at different times, to assess pyrenoid phenotypes. A quantitative reassessment of cells that were grown in parallel in defined conditions and harvested and processed alongside each other, revealed no difference in thylakoid stacking either between pyr- and WT, or indeed between growth conditions. Thus the previously reported “hyperstacking” is not a phenotype of pyr- cells, but likely a result of some inconsistency in conditions.

For example, culture density affects chlorophyll expression and is easily skewed between pyr- and WT (Fig. 2.10a), suggesting different densities could lead to falsely interpreting thylakoid architectures as pyrenoid phenotype. Similarly, expression of photosynthetic pigments and complexes, the functional elements within the thylakoids, was found to be independent of pyrenoid presence or absence (Fig. 2.10). Thus a direct structural effect of pyrenoid loss that might account for the photosynthetic impairment in pyr- cells could not be detected.

2.4.3 Acclimation to different growth irradiances is identical in pyr- and WT

A more subtle pleiotropic effect of pyrenoid loss might be expected to interfere with acclimation to physiological conditions. However, pyr- cells were found to acclimate in the same way as WT to light. Cells limited by light express more chlorophyll per PSII (Fig. 2.10 c&e-f), whereas cells experiencing excess light express more photoprotective carotenoids (Fig. 2.10d). In light response curves (Fig. 2.6), pyr- cells show the same *ETR* saturation profile (I_k) as WT with low-light grown cells saturating at lower light intensities than high-light grown cells due to more efficient processing of light coupled with a lower-capacity CBC (Eberhard et al., 2008; Foyer et al., 2012; Von Caemmerer, 2013). The major fraction of photoprotective *NPQ*, *qE* (Appendix 8.9), depends on thylakoid membrane ΔpH (Holt et al., 2004; Iwai et al., 2007; Lambrev et al., 2012), thus the decrease in initial *NPQ* with growth light intensity (Fig. 2.7) reflects an underlying acclimation state. Low-light grown cells harvest light very effectively, achieving a high ΔpH and thus high *NPQ* even at low experimental light intensities (Fig. 2.5a), whereas cells acclimated to higher light (Fig. 2.5b) require more experimental light to reach the same ΔpH and thus *NPQ*. When the cells are grown for a prolonged period of time at very high light, long-term photoinhibition occurs (Fig. 2.6 c&f, see also Appendix 8.2c). Thus acclimation to light was seen to change the balance between harvesting and dissipating incoming photons (Eberhard et al., 2008; Foyer et al., 2012) and no sign of pleiotropic impairments due to pyrenoid absence was found. Acclimation was also seen to culture density, in cellular chlorophyll expression (Fig. 2.10a).

2.4.4 The way pyr- cells differ from WT is consistent with CO₂ starvation

When light is plentiful, photosynthesis is generally limited by CO₂ supply, whereas at low light the supply of photons becomes more rate limiting (Eberhard et al., 2008; Von Caemmerer, 2013; McGrath and Long, 2014). This effect can be seen in the solid lines of Fig. 2.9 a-c, where the difference between pyr- and WT is smallest for cells grown at 10 μE . Similarly, the difference in ETR_{max} between pyr- and WT is smaller for cells grown at 10 μE than at 50 μE (Fig. 2.7 a&b). The same effect of CO₂ limitation at high light can be seen within a light response curve, e.g. in Fig. 2.8 a-b. At the lowest experimental light intensity used, pyr- *LEF* or *ETR* are almost identical to WT, whereas at the highest intensity WT operates at about twice the average pyr- rate. Similarly in Fig. 2.7 a-c, pyr- and WT differ in ETR_{max} , which describes the CO₂ limited part of the curve, due to different ϕ_m at each growth light intensity. A similar light response curve behaviour is seen in Fig. 2.8 a-b for HelixAB. Like pyr- strains, pyr+ strain HelixAB shows a lower *LEF* and *ETR* than WT in

the CO₂ limited part of the curve. Due to the chimeric nature of the HelixAB SSU, Rubisco kinetics are impaired (Meyer et al., 2012). The HelixAB defect, and by analogy pyr-, thus originates in a feedback limitation due to the CBC turning over more slowly.

Cells feedback limited by CO₂ would experience more excess light. Consequently, functional absorption cross-section of PSII is decreased in pyr- cells in medium and high light (Fig. 2.11) and *NPQ* is increased (Fig. 2.7 a-c, Fig. 2.8c) compared to WT. Chlorophyll allocation to PSII remains high (Fig. 2.10 e-f, Fig. 2.11 a-c) as calculated assuming cells in state I (Finazzi, 2005; Minagawa, 2011; Drop et al., 2014). Thus state transitions, a known response to CO₂ limitation in *Chlamydomonas* (Iwai et al., 2007), could account for the disparity between physical and functional PSII antenna sizes. Higher qE as a major component of *NPQ* (Appendix 8.9) also indicates an increased ΔpH, suggesting an imbalance between fast electron transport and slow CO₂ fixation is backing up intermediates (Holt et al., 2004).

2.4.5 Pyr- cells are rescued by high CO₂

An impairment that is due to a pleiotropic effect of pyrenoid loss should persist even when any CCM defect is suppressed by the addition of CO₂. By contrast, a complete recovery of pyr- to WT levels was seen for cells grown at 5% CO₂ (see also Appendix 8.17). Growth rates match WT levels when cells are grown in elevated CO₂ (Fig. 2.5h, see also Appendix 8.2) and PSII activity (*ETR*: Fig. 2.6 d-f, see also Appendix 8.18; ϕ_{II} : Fig. 2.9 d-f, see also Appendix 8.4, Appendix 8.5, Appendix 8.15) as well as *NPQ* (Fig. 2.7 d-f, see also Appendix 8.6, Appendix 8.16) show no difference between WT and pyr-. Thus, in the absence of a requirement for a CCM, CBC turnover is no longer impaired. Hence equal demand drives equal pETC turnover, which generates a similar trans-thylakoid ΔpH and therefore qE, and requires similar PSII activity. To achieve the latter, PSII absorption cross-section is restored to WT levels (Fig. 2.11).

Growth at elevated CO₂, however, may mask more subtle pleiotropic effects of pyrenoid loss. During CCM repression in WT, a large fraction but not all of Rubisco is delocalized throughout the stroma (Borkhsenius et al., 1998; Mitchell et al., 2014). The remaining ‘minimal’ pyrenoid may play less of a role in coordinating photosynthesis than the full pyrenoid of CCM-induced conditions. To test for pleiotropic effects of pyrenoid loss in CCM-induced conditions, low CO₂-grown cells were measured in the presence of saturating bicarbonate (Fig. 2.9). This way, a high CO₂ environment was established only minutes before the measurements, ensuring the prior CCM induction state was maintained. Using

this technique, PSII activity of pyr- lines could be rescued to the same level as WT (Fig. 2.9 a-c, broken lines; see also Appendix 8.16). Thus even in CCM-induced conditions when pyrenoid size is maximal, photosynthetic impairment in pyr- lines is solely due to a limitation in the supply of CO₂. No evidence for a pleiotropic defect could be found.

The fact that WT cells still get a significant boost from added growth at high CO₂ (Fig. 2.7 d-f) or addition of bicarbonate (Fig. 2.9) suggests that CCM operation in these cells is unable to enrich CO₂ to saturating conditions. Most likely, this impairment of WT is an idiosyncrasy of the specific mutant strains used in this study, perhaps because WTint1,2 cells contain only *RBCS1*, or because the strains are highly cell wall deficient which might be associated with a decreased activity of CAH1. Parent WT strain CC-3395 generally outperforms WTint1,2 (Appendix 8.12). This comparative leakiness of WTint1,2, however, does not affect the validity of this study. The isogenic *RBCS* expression lines nonetheless present an ideal experimental platform for learning about the role of Rubisco localization in the pyrenoid.

2.4.6 Pyr- cells are limited through CBC feedback

The rescuing effect of bicarbonate was only observed for longer-term light exposures (Fig. 2.9 b-c; see also Appendix 8.12). For the very short exposure of only 5 seconds (Fig. 2.9a), there is no difference when probed in the presence and absence of bicarbonate. This behaviour is to be expected as part of fluorescence induction, as electron acceptors pools will be readily available to accept incoming energy after a short period of darkness (Lazár, 1999; Papageorgiou and Govindjee, 2004). After some time such short-term storage would have to be balanced with the turnover of the CBC as the ultimate electron acceptor. What the general disparity between bicarbonate presence and absence after 30 sec thus demonstrates, is that for our strains it takes more than 5 sec to activate the CBC, saturate internal electron acceptor pools and activate cross-talk between light and dark reactions of photosynthesis. The fact that bicarbonate addition does make a difference to pyr- cells, but only after CBC feedback has kicked in, thus signifies further that the mechanism of rescue operates through removing a limitation that had been imposed through the CBC.

The lag in bicarbonate rescue cannot, however, be due to a slow entering of bicarbonate into the cell. If that were the case, the lag would only appear in the first light treatment after bicarbonate addition and would not influence subsequent measurements. However, the lag in fact reappears in any light exposure that follows a brief period of intervening darkness. It is unlikely that the cell expels all bicarbonate between exposures, whereas the effect can be

explained if a cell containing bicarbonate reverts back to a fluorescence ground state with each short dark adaption (Krause and Weis, 1991; Maxwell and Johnson, 2000).

What is interesting is that the difference between WT and *pyr-* grown at air exists even at the 5 sec measurement (Fig. 2.8, Fig. 2.9a). This observation means that photosynthetic electron transport rates are lower in the *pyr-* lines despite no direct limitation from downstream carbon metabolism. This difference can be understood as reflecting a long-term acclimation status of the cells, resulting from prolonged growth in conditions where the CBC was limiting upstream light reactions due to a lack of accessible CO₂. Once the CBC starts syphoning off electrons in the presence of bicarbonate, *pyr-* is rescued to WT levels. This increase indicates that whatever acclimation has led to initially reduced photosynthetic activity in *pyr-* strains is second to the current metabolic performance of the cells. Thus *pyr-* cells are fully able to perform just as high rates of photosynthesis as WT once the CO₂ limitation has been removed.

Considering the bicarbonate addition data for cells grown at 5% CO₂ (Fig. 2.9 d-f), it is important to note that without bicarbonate, both WT and *pyr-* cells show high values of ϕ_{II} compared to when grown at air (Fig. 2.9 a-c). Growth under elevated CO₂ leads to the CCM being switched off even in WT (Wang et al., 2015). Thus cells grown under elevated CO₂ but measured in low CO₂ should be expected to display a non-CCM phenotype with low electron transport rates, akin to *pyr-*. Both WT and *pyr-* do indeed show some signs of being CO₂ limited. Values of ϕ_{II} drop between the 5sec measurement (Fig. 2.9d) and the later measurements (Fig. 2.9 e&f, solid lines), thus metabolic feedback from the CBC does limit electron transport when current CO₂ limitation starts overriding the long term acclimation to growth under elevated CO₂. CO₂ limitation is also reflected in the difference between bicarbonate presence (Fig. 2.9 d-f, broken lines) and absence (Fig. 2.9 d-f, solid lines) during later measurements. This difference suggests that bicarbonate addition does enable Rubisco to operate closer to saturation than is possible in the absence of bicarbonate.

However, ϕ_{II} values of cells grown at 5% CO₂ are closer to WT grown in air rather than *pyr-* grown in air, implying that the cells have a higher concentration of CO₂ internally than is present in air even in the absence of added bicarbonate. This internal CO₂ elevation in CCM repressed cells is most likely a consequence of higher rates of respiration as a result of acclimation to growth in high CO₂, increasing the inorganic carbon availability in the medium during dark adaptation. A very similar increase in performance was observed in *pyr-* cells grown in acetate when they were dark-adapted the same way in HEPES-Ficoll in

small Falcon tubes (Appendix 8.11), but not when grown on plates which have a larger air-space and probably pose less of a diffusion limitation to CO₂.

2.4.7 The ATP cost of photorespiration is at least as high as that of CCM operation

Operation of a CCM has long been thought to be associated with a cost in ATP for C_i accumulation, and hence with an increase in the ATP/NADPH ratio required for CO₂ fixation (Lucker and Kramer, 2013; Raven et al., 2014), which in turn should lead to increased CEF relative to LEF (Fig. 1.1). In the absence of a CCM, on the other hand, increased oxygenation leads to a demand of ATP in photorespiratory nitrogen re-fixation and, in *Chlamydomonas*, also to a production of NADH (Bauwe et al., 2012; Becker, 2013), thus equally increasing the ATP/NADPH ratio required for CO₂ fixation compared to CBC demand (Fig. 1.3).

That absolute rates of CEF are lower in *pyr*⁻ than WT (Fig. 2.12 a-b) is consistent with lower rates of LEF (Fig. 2.8) when grown in CCM-induced conditions. What determines the ratio of ATP/NADPH production is the rate of CEF (and WWC) relative to LEF in the pETC (Fig. 1.1). The relative rate of CEF was estimated by comparing the two proxies for linear electron transport, on the basis that ECS but not CF includes information about CEF (Lucker and Kramer, 2013). This contribution of CEF to total electron flow was found to be at least as high, or higher, in *pyr*⁻ compared to WT (Fig. 2.12c, see also Appendix 8.17), indicating that the supply ratio of ATP/NADPH is higher in *pyr*⁻. As supply and demand must balance, the ATP/NADPH requirement for operating a CCM in WT seems to be lower than the requirement for operating photorespiration in the absence of a CCM in *pyr*⁻. Consequently, the difference between *pyr*⁻ and WT disappears when cells are grown at high CO₂ (Appendix 8.17; for technical reasons it was not possible to establish the effect of bicarbonate addition, see Appendix 8.12).

Rates of photorespiration in *pyr*⁻ must therefore be high enough to generate a similar additional ATP demand per CBC revolution as does operation of a CCM in WT. This implies that some of the energy metabolites generated by photosynthetic electron transport in *pyr*⁻ is going towards photorespiration rather than carbon assimilation (see also Appendix 8.7, Appendix 8.8), which may explain why the difference in ETR between *pyr*⁻ and WT appears moderate compared to the difference in growth rates (Fig. 2.5h). Photorespiration thus acts to some extent as e⁻ valve, reducing the excess light burden on reaction centres by consuming some of the energy produced via the pETC (Bauwe et al., 2012; Moroney et al.,

2013). However, the effect is not sufficient to compensate for the loss of the CCM, hence the need for lower *ETR* and higher *NPQ* seen in *pyr-* to balance energy supply and demand.

2.5 Conclusion

The overall data presented here tells a very consistent story of photosynthetic regulation according to energetic supply and demand. Cells respond to changes in light intensity by adjusting pigments and photosystem antenna sizes (Fig. 2.10, Fig. 2.11), balancing maximum photosynthetic capacity against affinity for light (Fig. 2.7). High external CO₂ enables higher rates of LEF (Fig. 2.6, Fig. 2.9) and growth (Fig. 2.5). CO₂ fixation and electron transport are linked through feedback from the CBC (Fig. 2.9). A build-up of high energy intermediates that occurs when CBC turnover is low will result in an increase in ΔpH , thereby regulating *NPQ* via *qE* (Fig. 2.7, Fig. 2.8). In *pyr-* cells, failure to operate a CCM leads to a limitation in the turnover of Rubisco due to limited CO₂ supply. This limitation leads to impaired photosynthesis, similar to a mutant with impaired Rubisco kinetics (Fig. 2.8). Increased photorespiration leads to a high demand of ATP and hence *CEF* (Fig. 2.12), but does not present a sufficient energy sink to compensate for the lower energy demand as result of CCM loss. No evidence was found for a structural, pleiotropic defect of photosynthesis as a direct result of the inability to aggregate Rubisco into a pyrenoid (Fig. 2.5, Fig. 2.11). Rather all phenotypes seen in *pyr-* cells could be rescued through growth in high CO₂ (Fig. 2.5, Fig. 2.6, Fig. 2.7, Fig. 2.9, Fig. 2.11). PSII activity could be rescued with immediate effect through addition of bicarbonate (Fig. 2.9 b&c).

I therefore conclude that what limits photosynthesis in *pyr-* cells is limited access to CO₂ by Rubisco as a direct result of the inability of these cells to deliver CO₂ to Rubisco delocalized throughout the chloroplast, rather than aggregated in a pyrenoid. Additional differences observed between the strains, such as low initial electron transport rates (Fig. 2.9a), increased *NPQ* (Fig. 2.7 a-c, Fig. 2.8c) and altered PSII absorption cross-sections (Fig. 2.11), are a result of cellular regulation that deals with the consequences of lower photosynthetic turnover at a given light intensity, rather than themselves being causal in limiting photosynthesis in a way that is beyond cellular control. The notion that all phenotypes beyond pyrenoid and CCM loss are secondary results of cellular regulation and within cellular control is evidenced by the fact that such additional phenotypes are fully reversible in conditions where the primary limitation, that of CO₂ delivery to Rubisco, is relieved.

3 SSU SURFACE HELICES DRIVE PYRENOID FORMATION THROUGH A SPECIFIC RESIDUE INTERACTION PATTERN

3.1 Introduction

3.1.1 Rubisco compartmentalization and the case for engineering protein compartments

Boosting photosynthesis through operation of a CCM generally relies on sequestration of Rubisco in a specialized compartment. In higher plants, such compartmentalization is achieved through cellular differentiation leading to Kranz anatomy in C₄ plants, or temporal regulation over the diel cycle in CAM. In cyanobacteria and single celled algae, subcellular structures rather than multicellular organs must meet compartmentalization requirements. Rubisco packaging into cyanobacterial carboxysomes or algal pyrenoids form proteinaceous micro-compartments that are not defined by an external membrane. Genetically engineering an algal or cyanobacterial CCM to be expressed in C₃ plants has become a hot topic that is expected to offer large increases in yield (Zhu et al., 2010; Long et al., 2011; McGrath and Long, 2014). Understanding how Rubisco is packaged will be a key step towards this goal.

3.1.2 Carboxysomes

Cyanobacterial carboxysomes are a well-characterized example of a broader class of non-membrane-bound bacterial micro-compartments (Espie and Kimber, 2011). Encaged by an icosahedric shell comprised of dedicated proteins, Rubisco is tethered inside via specialized linker proteins, in close vicinity to CA providing CO₂ from the accumulated HCO₃⁻ (Badger and Price, 2003; Cai et al., 2015). In contrast to cyanobacterial carboxysomes, algal pyrenoids are much less well understood (Wang et al., 2015). Nonetheless, for higher plant engineering a pyrenoid may be the better option given that pyrenoid-bearing green algae such as *Chlamydomonas* bridge much of the >2bn year evolutionary gap between cyanobacteria and higher plants and operate in the context of a chloroplast (Badger et al., 2002; Leliaert et al., 2011).

3.1.3 The *Chlamydomonas* pyrenoid is dynamic

In *Chlamydomonas*, Rubisco is exchanged between stroma and pyrenoid, with a smaller fraction of ~50% in the pyrenoid in conditions where the CCM is inactive in high CO₂ (Borkhsenius et al., 1998) or ~70% in darkness 2 h before dawn (Mitchell et al., 2014). When the CCM is fully induced, at least 90% of Rubisco is found in the pyrenoid (Borkhsenius et al., 1998; Ma et al., 2011). Aggregated Rubisco is arranged less randomly than may be suggested by TEM images (Vladimirova et al., 1982; Lacoste-Royal and Gibbs, 1987; Borkhsenius et al., 1998). Using template matching, (Engel et al., 2015) were recently able to demonstrate that holoenzymes exhibits hexagonal close packing with a spacing of 2-4.5 nm within the pyrenoid.

3.1.4 Regulation can be informative about aggregation processes

Detailed knowledge of how Rubisco aggregation within the pyrenoid is regulated generates a set of constraints that can help to characterize the aggregation mechanism. During CCM induction through abrupt high to low CO₂ transition, aggregation of previously delocalized Rubisco takes more than 20 min but less than 1 h, and can take up to 4 h if CO₂ is depleted gradually within the medium (Yamano et al., 2010). Similarly during dark-light transition, the pyrenoid is fully assembled 1h prior to subjective dawn, yet a ~20 minute light treatment 2h before dawn fails to alter the Rubisco content of the pyrenoid (Mitchell et al., 2014). Such timescales hint that aggregation of Rubisco may require *de novo* protein synthesis.

3.1.5 Pyrenoid assembly hypotheses

Rubisco aggregation could either be achieved by direct physical interactions between holoenzymes, or involve other proteins. Such proteins may act as linkers, modify Rubisco to change binding affinities, or continually transport Rubisco into the pyrenoid. Given that the pyrenoid never fully disappears (Goodenough, 1970), the transport hypothesis seems unlikely as it would present a large energetic burden to pyrenoid maintenance (Raven et al., 2014).

3.1.6 The PTM hypothesis

Rubisco is known to be modified at a number of sites on both LSU and SSU during translation and holoenzyme assembly (Houtz et al., 2008). If similar modifications are used in *Chlamydomonas* to control the affinity with which Rubisco binds into the pyrenoid matrix, there should be modifiers that interact with Rubisco, and the modification should happen at the binding site or cause a conformational change of the protein that affects the binding site. Some evidence exists that such modifiers may be present. The only published mutant affecting pyrenoid formation to date, *cia6*, is a predicted methyl transferase, although no transferase activity could be detected *in vitro* (Ma et al., 2011). Another methyl transferase has been localized to the pyrenoid (Luke MacKinder, personal communication). However, control of aggregation through post-translational modifications would most likely involve low abundance modifying enzymes that elicit a quick repackaging response, which is at odds with Rubisco repackaging kinetics (Yamano et al., 2010; Mitchell et al., 2014).

3.1.7 The linker hypothesis

If a linker protein exists, it would be expected to be in fairly high abundance. Low abundance linking could be possible if the linker only existed in the outer layer of the pyrenoid, helping to form a shell within which Rubisco is trapped, similar to carboxysomes (Espie and Kimber, 2011). However, no evidence of any such shell is visible in electron micrographs, instead the pyrenoid matrix appears very uniform (Genkov et al., 2010; Meyer et al., 2012; Engel et al., 2015). The starch sheath surrounding the pyrenoid is not necessary for pyrenoid formation or function, as known from analysis of a starch-less mutant (Villarejo et al., 1996). In lieu of a sheath, a linker would be expected throughout the Rubisco matrix. Such a linker would have to be fairly small to account for the 2-4.5 nm holoenzyme separation reported by (Engel et al., 2015).

3.1.9 Heterologous SSU expression lines fail to assemble a pyrenoid

The only photosynthetically competent mutant lines existing today that completely lack a pyrenoid express a higher-plant version of the small subunit of Rubisco in a background strain lacking *RBCS* (Genkov et al., 2010). Heterologous SSUs assemble into functional holoenzymes with the *Chlamydomonas* native LSU.

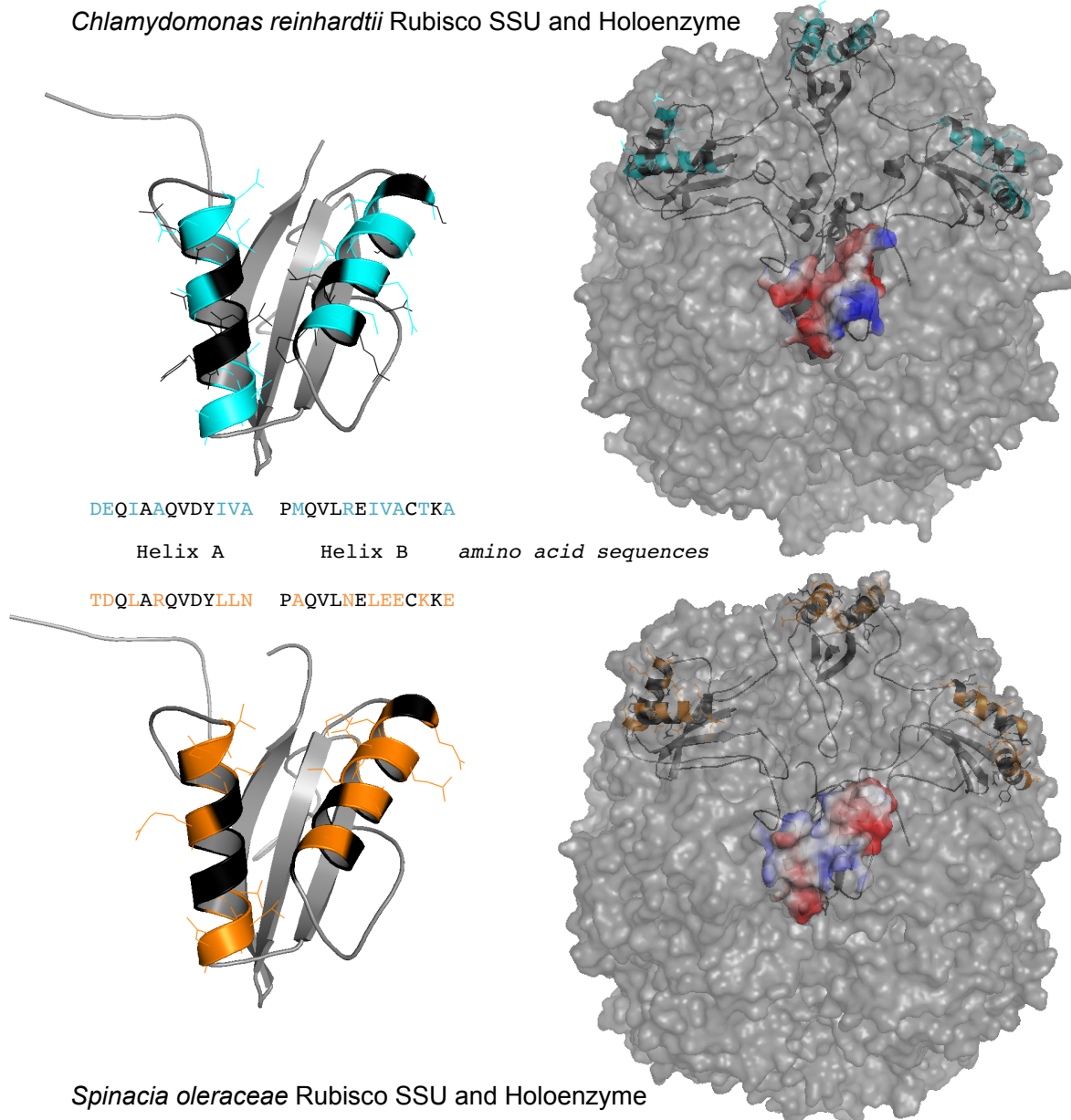


Fig. 3.2: 14 amino acids differ between *Chlamydomonas* and *Spinacia oleracea* SSU helices, altering charge distribution.

Chlamydomonas and *Spinacia oleracea* Rubisco SSUs are shown in isolation, highlighting residues that differ between the helices, and in the context of a holoenzyme. In protein contact heat maps of SSU helices, red areas favour binding of positively charged residues, whereas blue areas bind negative charges.

The resulting enzyme is as capable of carbon fixation as the native *Chlamydomonas* holoenzyme *in vitro* and supports growth of cell cultures at a rate equal to isogenic WT strains when grown at elevated CO₂ (Genkov et al., 2010; Fig. 2.5h). The protein, however, fails to be recruited into forming a pyrenoid *in vivo*, and as a result SSU mutant lines fail to operate a functional CCM.

The region of the SSU that governs Rubisco aggregation was pinned down to the *Chlamydomonas* SSU surface helices (Meyer et al., 2012). About half the residues are conserved between *Chlamydomonas* SSU helices, which support pyrenoid formation, and *Spinacia oleracea* SSU helices, which do not (Fig. 3.2). The 14 residues that differ, however, have a striking effect on protein interaction potential of the helices based on vacuum electrostatics. Whilst *Chlamydomonas* shows a negatively charged cleft between the helices showing up red in Fig. 3.2, and a hydrophobic ridge on helix B next to a positively charged cleft shown in blue, the *Spinacia oleracea* SSU shows a very different pattern with alternating charges along both helices and a hydrophobic cleft instead of a hydrophobic ridge.

3.1.10 Analysis of SSU interaction site reveals details of Rubisco packaging

In order to establish how Rubisco is packaged into the pyrenoid, the work presented here builds on the finding that Rubisco SSU surface helices are necessary for pyrenoid formation. Site-directed mutagenesis (SDM) altering specific helix residues was used to characterize this putative protein interaction site. Building on SDM findings, the Rubisco-Rubisco docking hypothesis was investigated both *in silico* and *in vitro*. In addition to SSU auto-docking across the helices, a SSU-LSU interface was identified based on crystal contacts in the structure of *Chlamydomonas* Rubisco (Taylor et al., 2001). After using Analytical Ultracentrifugation to refute Rubisco auto-docking, *in silico* analysis focused on interactions between SSU helices and the recently discovered linker candidate LCI5. Priority was given to exploring the Rubisco-Rubisco docking and linker hypotheses as they were deemed more likely to be able to explain pyrenoid formation than PTM and transport hypotheses given current knowledge about pyrenoid regulation as detailed above. The combined set of *in silico*, *in vitro* and *in vivo* data reveals a specific interaction profile that allows *Chlamydomonas* SSU surface helices to support pyrenoid formation, and informs future experimental approaches.

3.2 Materials and Methods

3.2.1 SDM

3.2.1.1 Plasmids and Host Transformation.

Vector pSS1-ITP (Genkov et al., 2010), containing *Chlamydomonas RBCS1* cDNA under the control of the *Chlamydomonas RBCS1* promoter and introns 1 and 2 (Fig. 2.3a), was modified using QuikChange Lightning Kit (Agilent, Santa Clara, CA, USA) with primers designed using primer3 (Rozen and Skaletsky, 2000) as listed in Table 3.1.

Table 3.1: SDM primers

Primer	α change	Templates	Constructs generated
CTG CCT CCT CTG ACC ACC GAC CAG CTC GCC GCC CAG GTC GAC TAC	D23T, E24D, I26L	pSS1-ITP; V94E/A95E	D23T/E24D/I26L; -"/V94E/A95E
GAC GAG CAG ATC GCC CGC CAG G TC GAC TAC ATC	A28R	pSS1-ITP; 94-EE	A28R; -"/V94E/A95E
gC CAG GTC GAC TAC CTC CTC AAC AAC GGC TGG ATC CCC TG	I33L, V34L, A35N	A28R	A28R/I33L/V34L /A35N
C TGC CGC GAC CCC GCG CAG GTG CTG AAC GAG ATC GTC	M87A, R91N	A28R/I33L/ V34L/A35N	A28R/I33L/V34L /A35N/ M87A/R91N
TG CTG CGC GAG ATC GAG GAG TGC ACC AAG GCC TTC C	V94E, A95E	pSS1-ITP; A28R/I33L/ V34L/A35N	V94E/A95E; A28R/I33L/V34L /A35N/ V94E/A95E

Mismatches introduced are shown as underlined bases. Where the template differs from the native *RBCS1* cDNA, lower case letters are used. Reverse complements were used as reverse primers. Multiple templates or constructs written in the same cell of the table are separated by semicolons.

Constructs were verified by sequencing (Department of Biochemistry, University of Cambridge). Host cells of *RBCS*-deletion strain T-60 (Khrebtukova and Spreitzer, 1996) were transformed via electroporation (generally NEPA21, Nepagene, Chiba, Japan; Gene Pulser Xcell, Biorad, Hercules, CA, USA for Quadruple and the 28-R/94-EE strain used for TEM) followed by multiple rounds of selection for restored photosynthesis on minimal medium in the light.

3.2.1.2 Phenotype characterization

Spot tests were used to screen strains by plating dark-grown cells in minimal medium in the light under 5% CO₂ or air to test respectively for photoautotrophy or CCM defects as

relative reduction of growth after 7 days. Preparation for TEM on air-equilibrated cells grown at medium light intensity was conducted as described in Chapter 1. For immunofluorescence (IF), cells grown at 5% CO₂ in 96-well format (Quadruple in 50ml culture) were air-equilibrated overnight and 200µl were affixed to a poly-L-lysine coated 96-well imaging plate (microscope slide for Quadruple). Cells were fixed for 20 minutes at 4°C using 2% v/v formaldehyde in minimal medium, washed in TBS (Tris-Buffered Saline: 10 mM Tris pH 7.6, 148 mM NaCl, 2.7 mM KCl), permeabilized at Room Temperature for 30 minutes using TBS-TT (0.05% Triton X-100 and 0.05% Tween20 in TBS) and blocked for 30 minutes using 1% BSA in TBS-TT. Samples were treated at 4°C overnight in a 1:5000 dilution of 1° AB (Rabbit antibody raised against Rubisco purified from wheat) in TBS-TT, washed thoroughly using TBS and treated with 2° AB (1:500 dilution of goat anti-rabbit Alexa 488 in TBS) for 1 hour at room temperature. After washing thoroughly with TBS, samples were embedded in ProLong® Gold Antifade Mountant (Life Technologies, Thermo Fisher Scientific, Paisley, UK). An Opera System (PerkinElmer, Waltham, MA, USA) was used to collect confocal z-stacks using a 488nm laser to excite fluorophore and chlorophyll and a 561nm laser for chlorophyll auto-fluorescence only (SP2 – Leica microsystems GmbH, Wetzlar, Germany – for Quadruple using 488nm only with filters to distinguish label and CF). Composite images of label- and auto-fluorescence stack maxima were generated using Fiji (Schindelin et al., 2012).

3.2.2 Analytical Ultracentrifugation (AUC)

3.2.2.1 Experimental Procedure

Cells bulked up at 5% CO₂ and air-equilibrated over night were normalized to $8 \cdot 10^8$ cells/ml in protein extraction buffer (50 mM Tris/HCl, 5mM MgCl₂, pH 7.0 with cOmplete™ Mini EDTA-free protease inhibitors – Roche, Basel, Switzerland). Soluble proteins were extracted by sonication (2 pulses of 40 seconds for wall-less cells or 6 pulses of 30 seconds for walled cells, Soniprep 150, MSE, London, UK) followed by centrifugation (12,000 RPM, 15 minutes, 4°C, Hawk 15/05, MSE) to pellet membranes. Proteins were separated on 200 ml 10-30% w/v continuous sucrose gradients by ultracentrifugation (32,000 RPM, 17 hours, 4°C, Beckman Coulter, Brea, CA, USA) followed by gradient fractionation to isolate Rubisco holoenzyme fractions (Spreitzer and Chastain, 1987). Several rounds (2x 2h at Room Temperature, then over night at 4°C) of dialysis (Slide-A-Lyzer™ G2, 3.5K MWCO, 3mL, Life Technologies) were used for exchange into AUC

buffer (50mM Bicine pH 8.0, 10mM NaHCO₃, 10mM MgCl₂, 1mM DTT) which was chosen for its suitability in enzyme kinetic assays (Genkov et al., 2010). Rubisco isolate was concentrated (Amicon Ultra-15, 100k MWCO, Merck Millipore, Billerica, MA, USA), quantified (Bradford, Biorad) and run on the AUC (20 000 RPM, Beckman Coulter) blanked against buffer from the last dialysis round. Continuous c(s)/S spectra were fit using sedfit (Schuck, 2000) and normalized to the holoenzyme peak (S=18).

3.2.2.2 Method Development

3.2.2.2.1.1 removing ambiguity

AUC optimization was focused on removing ambiguity stemming from impurities in Rubisco isolates, aiming to provide a definitive answer to whether Rubisco multimerization in WT and not pyr- can account for pyrenoid formation. Fig. 3.3a shows a comparison of WT and pyr- c(s)/S profiles. Strain cMJ030 was chosen as WT rather than WTint1,2 for expressing both *RBCS1* and *RBCS2*. The pyr- strain expressing *Arabidopsis thaliana RBCS* (*Arabidopsis*) was intended to be used alongside the standard pyr- strain expressing *Spinacia oleracea RBCS*, however, Rubisco extracted from the latter was lost during preparation. WT shows two medium sized peaks at S<10, one main peak at S=18 which represents single Rubisco holoenzymes (Gurevitz et al., 1985), and a number of minor peaks at S>20 representing high molecular weight species. Pyr- shows a similar profile with a main holoenzyme peak at S=18, two slightly lower intensity peaks at S<10 slightly shifted about S relative to WT, and a very minor peak around S=29. The peaks at S<10 demonstrate the presence of contaminating species in the sample, thus calling into question whether the high molecular weight species present in WT and largely absent in pyr- represent Rubisco multimers or simply further contaminants.

3.2.2.2.1.2 Comparing RA (UV absorption) and IP (interference) methods

Comparison of RA and IP data can be informative about the identity of unassigned peaks since non-proteinaceous species will have similar interference but different UV absorption characteristics as proteins. Fig. 3.3b shows that RA intensity of pyr- peaks at S<10 is lower than IP intensity, suggesting low molecular weight contaminants may not be proteins. The peak at S>20 on the other hand has a similar intensity in RA and IP, suggesting high molecular weight species are proteinaceous. Thus the presence of Rubisco multimers cannot be ruled out, nor confirmed, on the basis of RA/IP comparison.

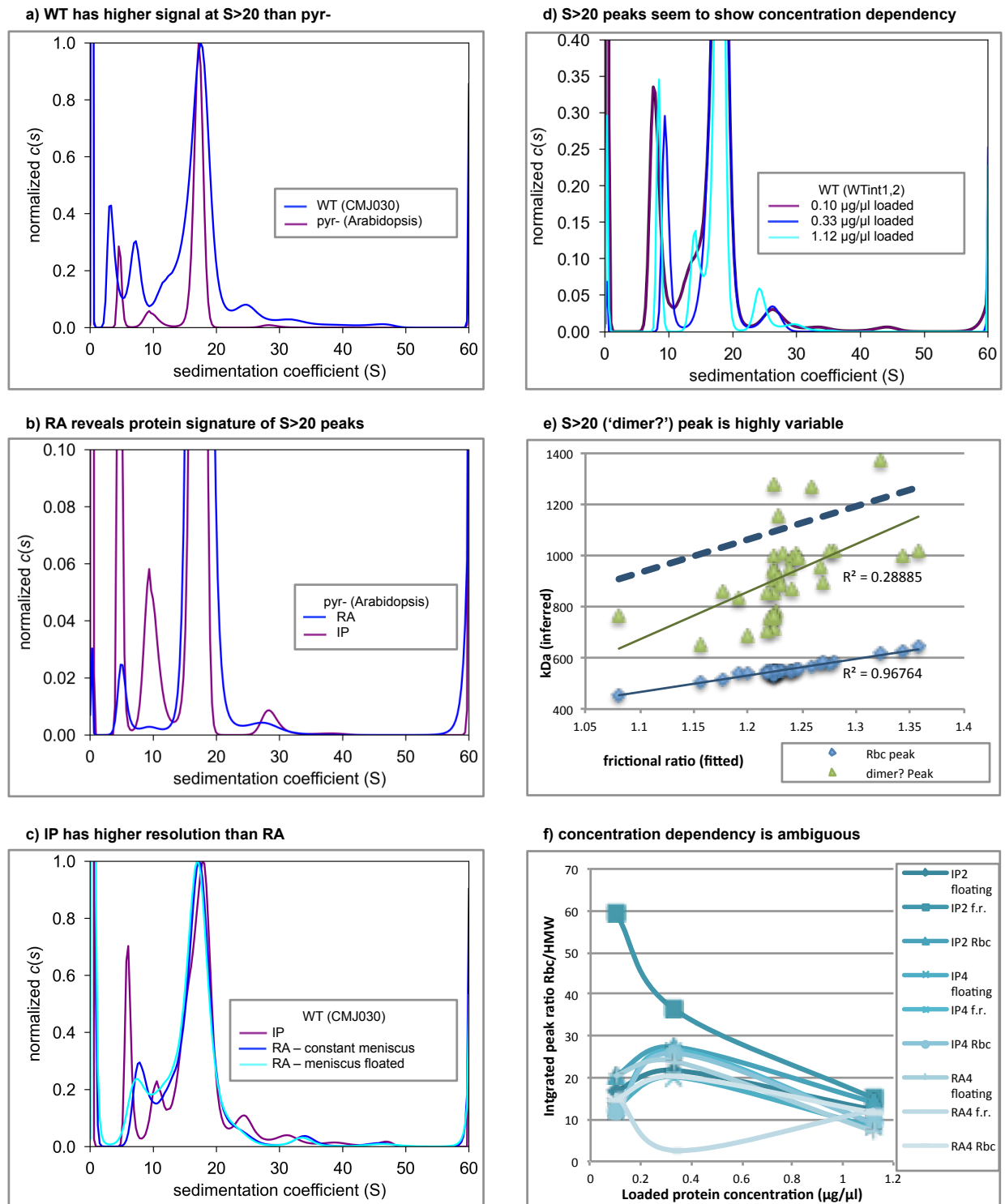


Fig. 3.3: Analytical Ultra-Centrifugation pilot study informed method development.

Continuous c(s)/S spectra normalized to single holoenzymes are shown in (a) comparing WT and pyr-, (b) comparing RA and IP, (c) demonstrating higher IP resolving power and (d) showing concentration dependency. A sensitivity analysis about the frictional ratio is shown in (e) comparing holoenzyme and possible dimer molecular weight estimates and (f) analysing concentration dependency.

In Fig. 3.3c, WT RA profiles show only 1 peak at $S < 10$ and fewer peaks at $S > 20$ than IP, demonstrating the lower resolving power of the noisier RA method. Resolution could not be improved by altering fit parameters, as indicated by the meniscus settings. Higher resolution IP profiles are shown in other figures.

3.2.2.2.1.3 Using a dilution series to alter monomer/dimer equilibrium

Fig. 3.3d shows that in a dilution series of WT Rubisco isolate, high molecular weight peaks seem to show a clear increase at the highest concentration which also leads to a split of the 26 S peak visible at lower concentrations into two distinct peaks around 23 S and 30 S. In an association-dissociation equilibrium between monomers and multimers, an increase in concentration should push the system towards a higher degree of association. Fig. 3.3d shows a sensitivity analysis of estimated molecular weights. Frictional ratios fitted to 20,000 RPM Interference (IP2), 40,000 RPM interference (IP4) and 40,000 RPM Absorbance (RA4) data were allowed to vary (“floating”), held constant at 1.223199 (the value that yields 550kDa according to linear regression, “f.r.”) or chosen to yield a holoenzyme size of 550kDa (“Rbc”). Estimated Rubisco holoenzyme size varies around the expected value of 550kDa. The main high molecular weight peak (tagged “dimer?”) stays below the size expected from a dimer (indicated by the dashed blue line), which could nonetheless be consistent with a dimer since the model assumes that all sedimenting species have the same frictional ratio, which is used together with the sedimentation coefficient to estimate molecular weight. Fig. 3.3f shows the concentration dependency of the peak ratio calculated as integrated Rbc peak divided by the integrated HMW (“dimer?”) peak.

Overwhelmingly the graph reports the highest ratio of holoenzyme to high molecular weight species at a total protein concentration of $0.33 \mu\text{g}/\mu\text{l}$. However, when the frictional ratio is kept constant at 1.223199 there is a consistent decline of the ratio with increasing concentration. This ambiguity generating variability between fits seen in Fig. 3.3 e&f is due to very low peak intensities for species at $S > 20$. Hence concentrations used to generate definitive results in Fig. 3.7 were tenfold higher. For this dataset, strain 2137 was used as WT rather than WTint1,2 for expressing both *RBCS1* and *RBCS2*, and rather than cMJ030 for higher comparability within the research group (Mitchell et al., 2014).

3.2.3 Bioinformatics

3.2.3.1 Rubisco auto-docking

Chlamydomonas (1GK8, Taylor et al., 2001) and *Spinacia oleracea* (8RUC, Andersson, 1996) Rubisco holoenzyme crystal structures were retrieved from the protein data bank (pdb; www.rcsb.org, Berman et al. 2000). SSU and LSU structures were extracted using PyMOL (Schrödinger, New York, NY, USA). The HADDOCK webserver (Dominguez et al., 2003; de Vries et al., 2010) easy interface was used to dock SSUs *in silico*, specifying helix residues 23, 24, 87, 91, 94 and 95 as active based on SDM results and >40% solvent accessibility (Fig. 3.10) as determined by NACCESS (Hubbard and Thornton, 1993), whereas PDBePISA (Pisareva et al., 2011) interface NN32 informed active residues for SSU-LSU docking.

3.2.3.2 Analysis of LCI5

In the absence of a protein structure for LCI5, the second of four repeats, which represents a minimal consensus sequence (Fig. 3.1), was analysed for secondary structures using 9 secondary and 12 tertiary structure predictions (Geourjon and Deléage, 1995; Jones, 1999; Shi et al., 2001; Sen et al., 2005; Söding, 2005; Cheng et al., 2005; Jayaram et al., 2006; Eswar et al., 2007; Kelley and Sternberg, 2009; Lobley et al., 2009; Kaufmann et al., 2010; Yang et al., 2011, 2014; Xu and Zhang, 2012; Källberg et al., 2012; Blaszczyk et al., 2013; Buchan et al., 2013; Kumar, 2013; Drozdetskiy et al., 2015). Tertiary structures were screened for interacting residues using the Cport webserver (de Vries and Bonvin, 2011). From the 11 tertiary structures that contained side-chain information, an ensemble containing predicted helical repeat 2 residues 8-22 was generated in PyMOL which was then used to dock against Rubisco SSUs via the HADDOCK prediction interface.

3.2.3.3 Figure generation

For display, PyMOL was used to render docked structures and to align holoenzyme structures. Cluster statistics were averaged across represented classes, and energies and HADDOCK scores were multiplied by (-1) in Excel. For Fig. 3.8a, Fig. 3.9 b&f and Fig. 3.10a, the percentage of structure, Cport or HADDOCK predictions that report an involvement in helix or interface formation, retrieved from HADDOCK structures using a PyMOL script (Vertrees, 2009), is shown for each amino acid. The LSU profile in Fig. 3.10a shows buried surface area reported by PISA as percentage of the highest. Amino acid conservation profiles shown as WebLogos (Crooks et al., 2004) in Fig. 3.10b are based on

Chapter 3: SSU surface helices drive pyrenoid formation through a specific residue interaction pattern

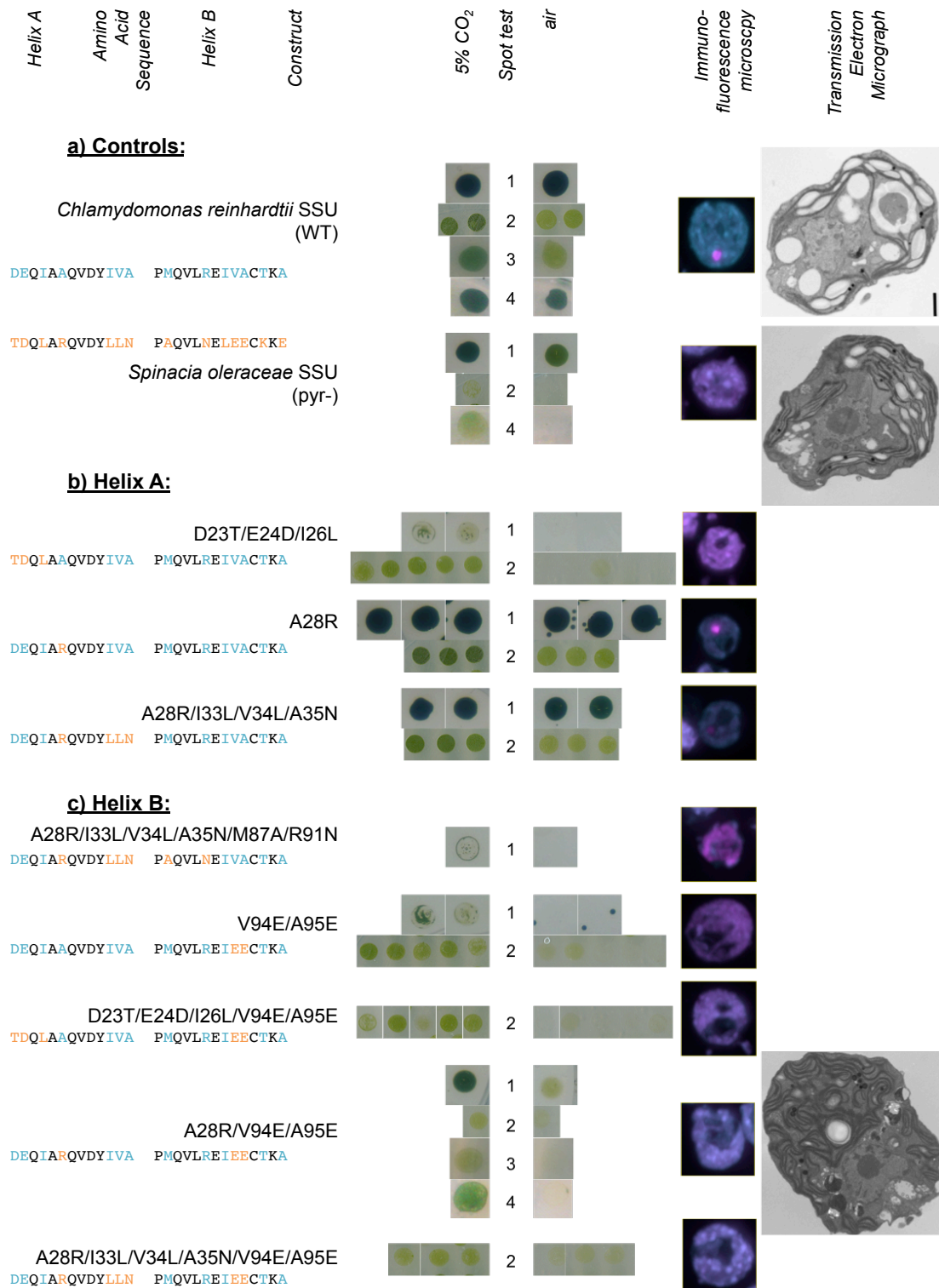


Fig. 3.4: SDM identifies key residues necessary for pyrenoid formation.

Data is arranged in columns detailing the amino acid sequences of helices A and B, the construct, up to four independent spot tests arranged vertically showing algal growth under 5% CO₂ or air, followed by IF images and TEM demonstrating pyrenoid phenotype. Horizontally arranged colonies in spot tests represent independent insertion lines. WT and pyr⁻ controls are shown in (a), mutants informative about helix A in (b) and helix B in (c). TEM credit: Dr. Moritz Meyer.

The pyrenoid further presents itself as electron dense structure embedded in a thick starch sheath in electron micrographs. By contrast, expression of *Spinacia oleracea* SSU gives rise to pyr- cells (Genkov et al., 2010). While pyr- cells grow to a similar extent as WT at 5% CO₂, growth in air is highly reduced. Rubisco is delocalized throughout the chloroplast leading to a mixed purple colour in a composite IF image, and the conspicuous pyrenoid structure is absent from electron micrographs.

Mutating the N-terminus of helix A (Fig. 3.4b) in construct D23T/E24D/I26L gives rise to *Spinacia oleracea* SSU-like behaviour: cells are unable to grow in air and show delocalized Rubisco in IF. Mutating the central A28R on the other hand allows cells to exhibit a normal WT-like phenotype in air and a pyrenoidal IF signal. Extending the latter mutation to include the C-terminal half of helix A in construct A28R/I33L/V34L/A35N does not prevent cells from aggregating Rubisco and growing in air.

A28R/I33L/V34L/A35N can be turned pyr- by further mutating residues M87A/R91N of helix B (Fig. 3.4b). Resulting cells show very weak growth even in 5% CO₂ and no sign of Rubisco aggregation. Moving further along in helix B, substitution of hydrophobic residues by negatively charged residues in V94E/A95E abolishes air growth and Rubisco aggregation. Constructs D23T/E24D/I26L/V94E/A95E, A28R/V94E/A95E and A28R/I33L/V34L/A35N/V94E/A95E that combine mutations in helix A with V94E/A95E all show similar defects in Rubisco aggregation and growth at air-levels of CO₂, as well as absence of a pyrenoid in TEM for A28R/V94E/A95E. Further constructs D23T/E24D/I26L/M87A/R91N, D23T/E24D/I26L/V94E/A95E/T97K/A99E and A28R/I33L/V34L/A35N/V94E/A95E/T97K/A99E were generated but did not recover any photosynthetically competent lines (Appendix 8.19).

3.3.2 Forced *in silico* Rubisco auto-docking is more favourable in *Chlamydomonas* but the complexes are predicted not to be stable in solution.

Using the information from SDM experiments, SSUs were forced to interact *in silico* to assess the role such an interaction may play in aggregating Rubisco *in vivo*. Fig. 3.5 shows an analysis of the structures predicted by HADDOCK (Dominguez et al., 2003). Auto-docking of two *Chlamydomonas* SSUs (Fig. 3.5a) results in helix B being wedged between the two SSU helices of an adjacent holoenzyme, stabilized through a salt bridge between D23 on helix A of one partner and R91 on helix B of the other. The interaction shows rotation symmetry around a central vertical axis between the two parallel helix B partners.

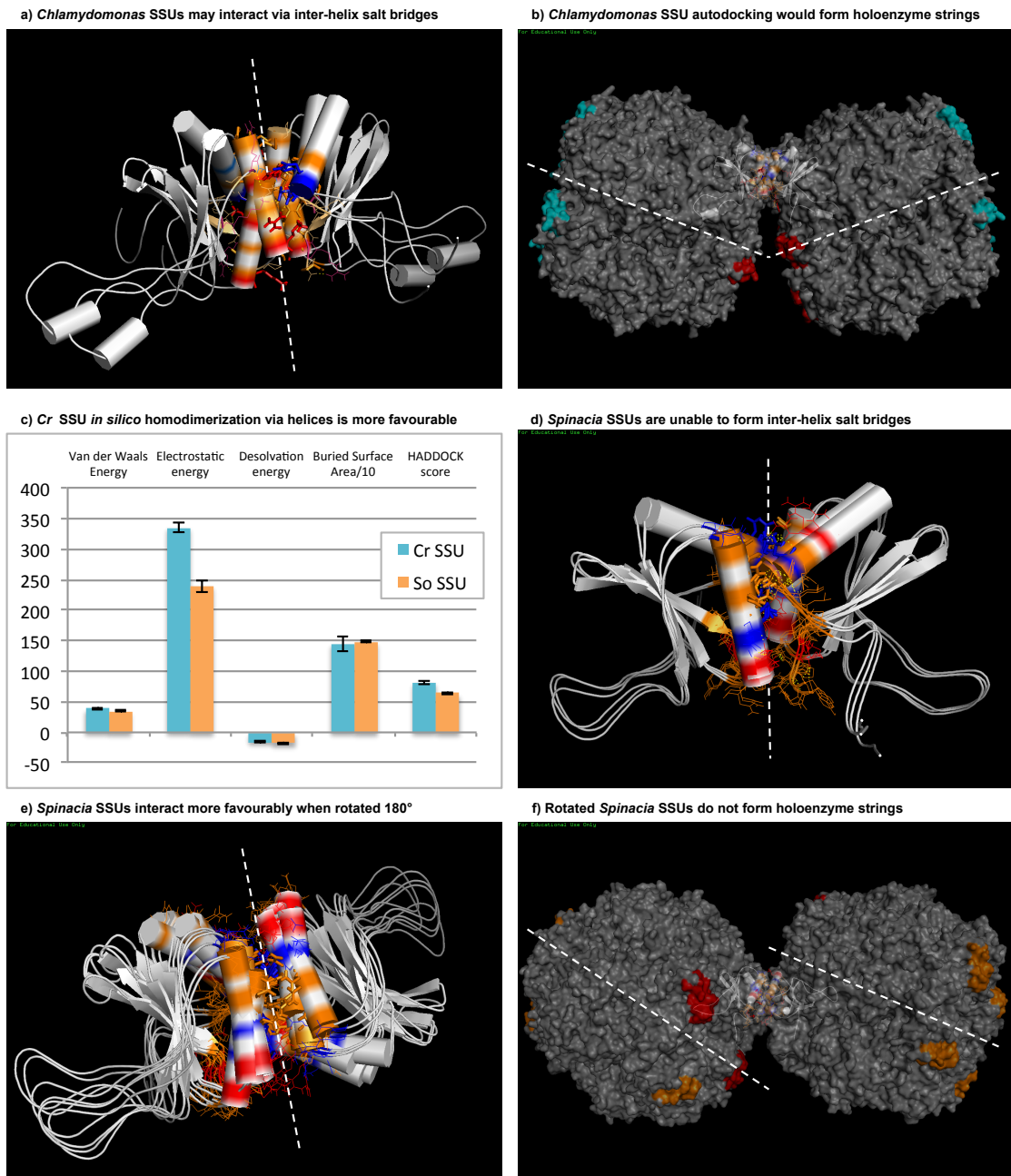


Fig. 3.5: SSU helix *in silico* auto-docking is more favourable in *Chlamydomonas* but cannot explain pyrenoid formation.

An overlay of *Chlamydomonas* SSU interactions predicted by HADDOCK is shown in a). Charged interface residues are shown in red if positive or blue if negative. Orange highlights further interacting residues. Polar contacts along the interface are indicated as yellow dashes. Residues are shown as lines when part of the interaction only in one structure, or sticks if participating in all interfaces. Holoenzymes aligned to the highest confidence structure are shown in (b). Sites able to accept further interacting partners are shown in cyan, sites obscured by the depicted interaction are shown in red. Interface statistics are shown in (c). *Spinacia oleracea* SSU interactions are shown in (d), or (e) if rotated relative to WT. Holoenzymes aligned to best *Spinacia oleracea* structure are shown in (f) with free interaction sites highlighted in orange. Dashed white lines show axes of symmetry (for holoenzymes through the solvent channel).

HADDOCK retrieved only two clusters of structures with almost identical relative positions of the SSU proteins, indicating high confidence in the predicted 3D arrangement. Such an interaction in the context of a holoenzyme implies a slightly angled end-to-end joining of the Rubisco complexes (Fig. 3.5b). SSUs that are located on the same face as the interacting SSU within a holoenzyme cannot recruit further interaction partners since the existing partner is in the way. Thus each Rubisco could bind a total maximum of two holoenzymes.

By contrast, forcing the *Spinacia oleracea* SSU to dimerize across the surface helices results in interactions without inter-protein salt bridges, leading to a much lower release of free energy through electrostatic interactions than in *Chlamydomonas* (Fig. 3.5c). Consequently the HADDOCK score, an overall measure for goodness of the predicted complex, is lower for *Spinacia oleracea* despite a similar buried surface area and only slightly decreased Van der Waals and de-solvation energies. De-solvation is associated with a free energy cost even for *Chlamydomonas*. While some of the predicted *Spinacia oleracea* docking complexes show the same interaction symmetry as was seen in WT (Fig. 3.5d), the more favourable interaction proceeds with a 180° rotated interaction partner, placing the axis of symmetry perpendicular to helix B (Fig. 3.5e). This rotation results in a very different dynamic of the holoenzyme (Fig. 3.5f).

A second potential Rubisco-Rubisco interface involving the *Chlamydomonas* SSU helices docking to an interface on the LSU was identified using PDBePISA (Fig. 3.6a). No such interface was found for *Spinacia oleracea* Rubisco. Despite the LSU interface being comprised almost exclusively of charged residues, the *Chlamydomonas* interaction does not contain any inter-protein salt bridges. A HADDOCK model based on the PISA residues yields a single cluster of structures which do form inter-protein salt bridges and show a rotation of the SSU about the LSU helices (Fig. 3.6b).

In contrast, HADDOCK modelled LSU-binding by the *Spinacia oleracea* SSU across the PISA-suggested residues does show some capacity to bind in PISA-suggested 3D arrangement (Fig. 3.6c), however the highest confidence model is rotated again (Fig. 3.6d). Multimerization across the PISA-suggested site would lead to solvent channel axes lining up parallel (Fig. 3.6e). In contrast to the SSU-SSU interaction, holoenzymes are not stacked on top of each other but edge-on. As every interaction precludes a further interaction from happening on the adjacent LSU and SSU interfaces, a maximum of two partners can be contacted from each face of the holoenzyme, meaning four interactions per Rubisco.

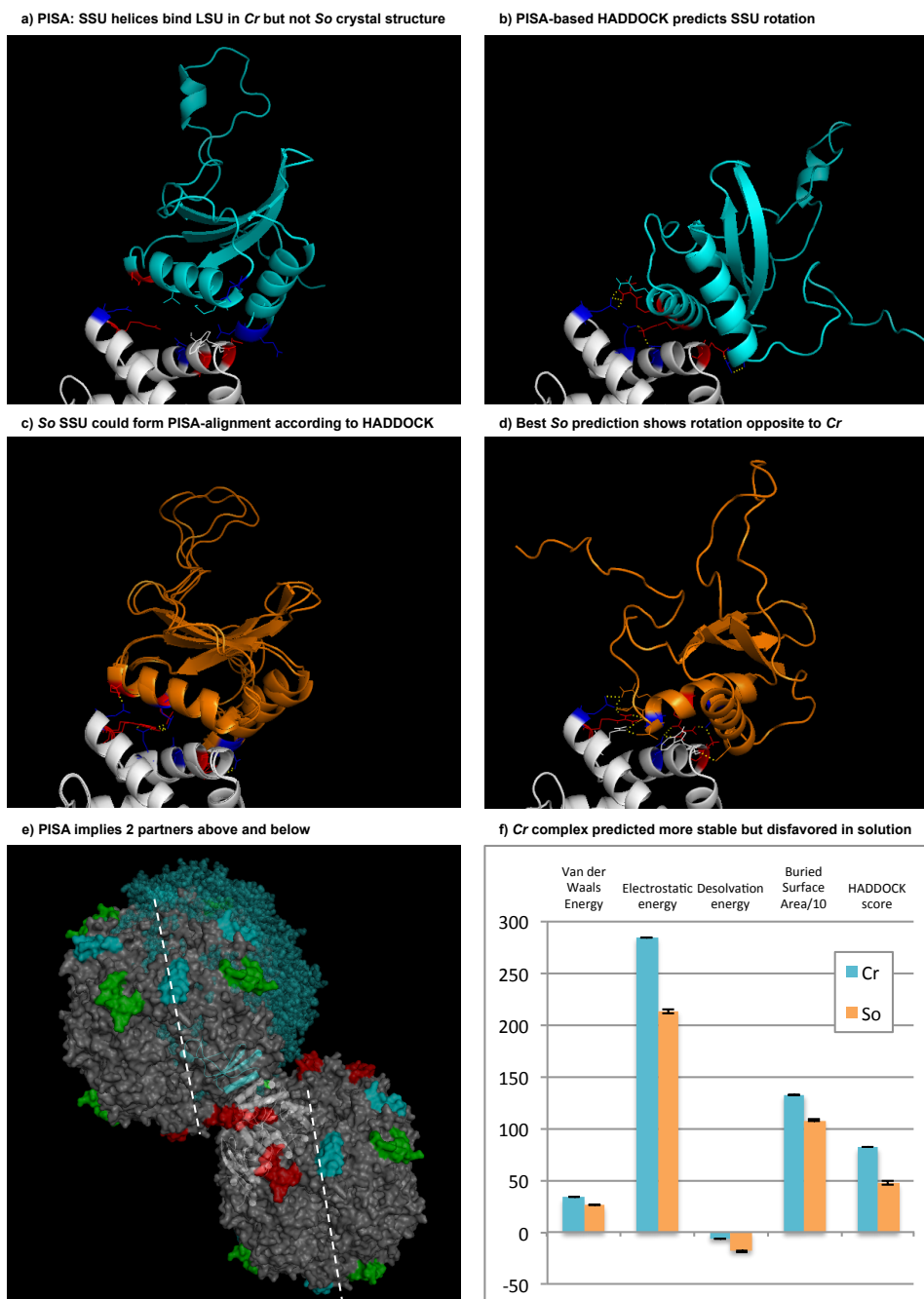


Fig. 3.6: SSU-LSU interaction based on crystal structure information is more favourable for *Chlamydomonas* SSU but predicted not to be stable in solution.

PDBePISA *Chlamydomonas* SSU-LSU interface is shown in (a). HADDOCK generated SSU interactions with *Chlamydomonas* LSU based on PISA interface residues are shown in (b) for *Chlamydomonas* SSU and (c)-(d) for *Spinacia oleracea* SSU. LSU is shown in white, *Chlamydomonas* SSU in cyan and *Spinacia oleracea* SSU in orange. Interacting residues are shown in red if positively charged or blue if negatively charged, polar contacts are depicted as yellow dashes. Holoenzymes aligned to the PISA structure are shown in (e). Free SSU interaction sites are shown in cyan, LSU sites in green, and sites obscured by the current interaction in red. A cyan holoenzyme demonstrates how the alignment is altered by the HADDOCK-suggested rotation of *Chlamydomonas* SSU. Interface statistics are shown in (f).

The SSU rotation suggested by HADDOCK does not drastically change this overall holoenzyme behaviour, as it results only in a slight rotation shown as cyan overlay. The energy profile of the docking shows greater free energy release for *Chlamydomonas* compared to the three *Spinacia oleracea* clusters, mostly due to greater electrostatic energy, but also to larger Van der Waals forces, all over a greater surface area, resulting in an overall better HADDOCK score. As for SSU auto-docking, de-solvation energy disfavours an interaction proceeding via the SSU-LSU interface even in *Chlamydomonas*, in line with a warning reported by PDBePISA that the complex may not be stable in solution.

3.3.3 AUC demonstrates that Rubisco does not spontaneously homo-dimerize

In order to test the Rubisco-Rubisco docking hypothesis experimentally, sedimentation velocity profiles of isolated holoenzymes were recorded in an AUC. AUC is a powerful tool for detecting multimers as fast-sedimenting, high-molecular weight species. AUC association analyses are often based on shifting the balance of the dynamic equilibrium between monomers and multimers by changing protein concentration. Fig. 3.7a shows a dilution series for Rubisco isolated from WT *Chlamydomonas* cells, displayed as detected protein signal plotted against the sedimentation coefficient in Svedberg units (S) estimated from the data. The profiles at each concentration show one or two minor peaks at low S values representing preparation impurities, one major peak towards the centre of the spectrum which represents single Rubisco holoenzymes, and another minor peak at high S values representing high molecular weight species (see Materials and Methods for assignment justification). The dilution series shows no concentration dependent increase in peak size for high molecular weight species, rather peaks are seen to vary within fitting error.

Rubisco isolated from a pyr- *Chlamydomonas* strain expressing *Spinacia oleracea* SSU (Fig. 3.7b) shows peaks for high molecular weight species that are higher than in WT and again show no sign of concentration dependence. Both WT (Fig. 3.7a) and pyr- (Fig. 3.7b) Rubisco sedimentation profiles do show a concentration dependent shift of the main holoenzyme peak about S which is explored in Fig. 3.7c: weighted averages of S scale linearly with the protein concentration accessed as the area under the curve.

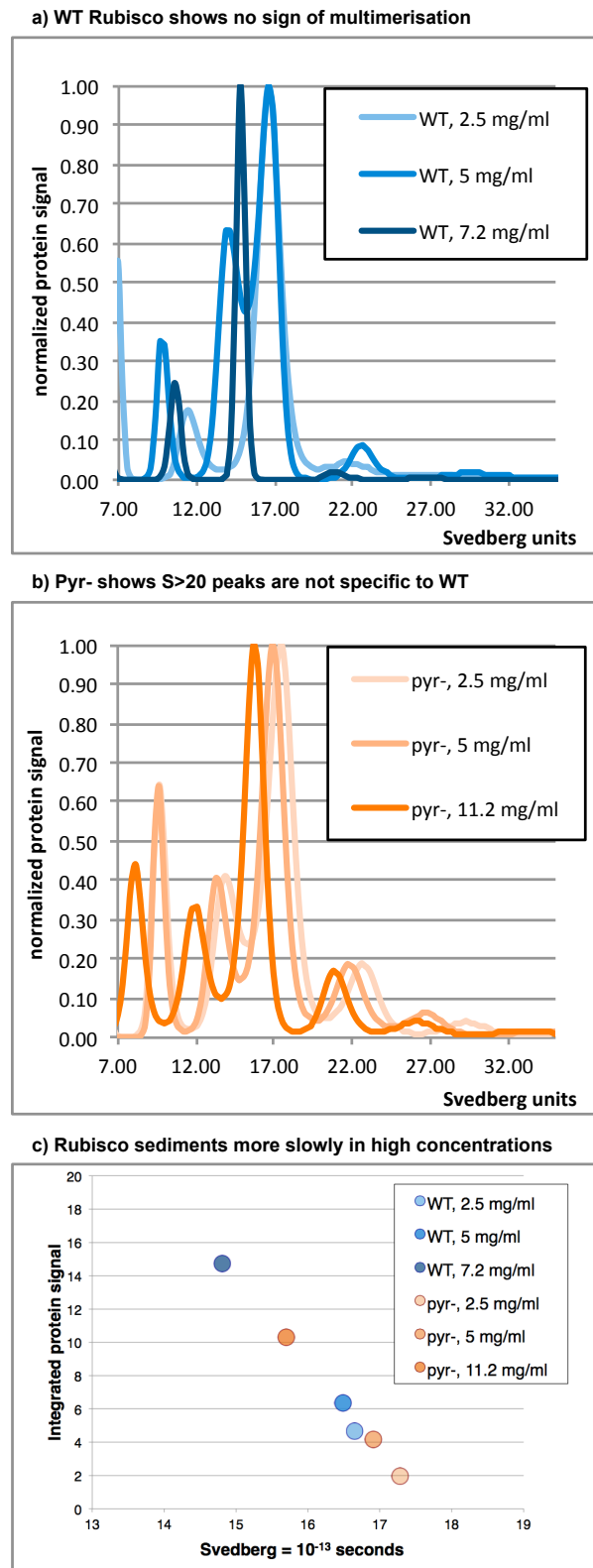


Fig. 3.7: AUC reveals isolated Rubisco actually repels itself.

Continuous $c(s)/S$ profiles are shown for Rubisco isolated from a) WT and b) pyr-cells. The relationship between the sedimentation coefficient and the concentration of Rubisco in the sample is shown in c).

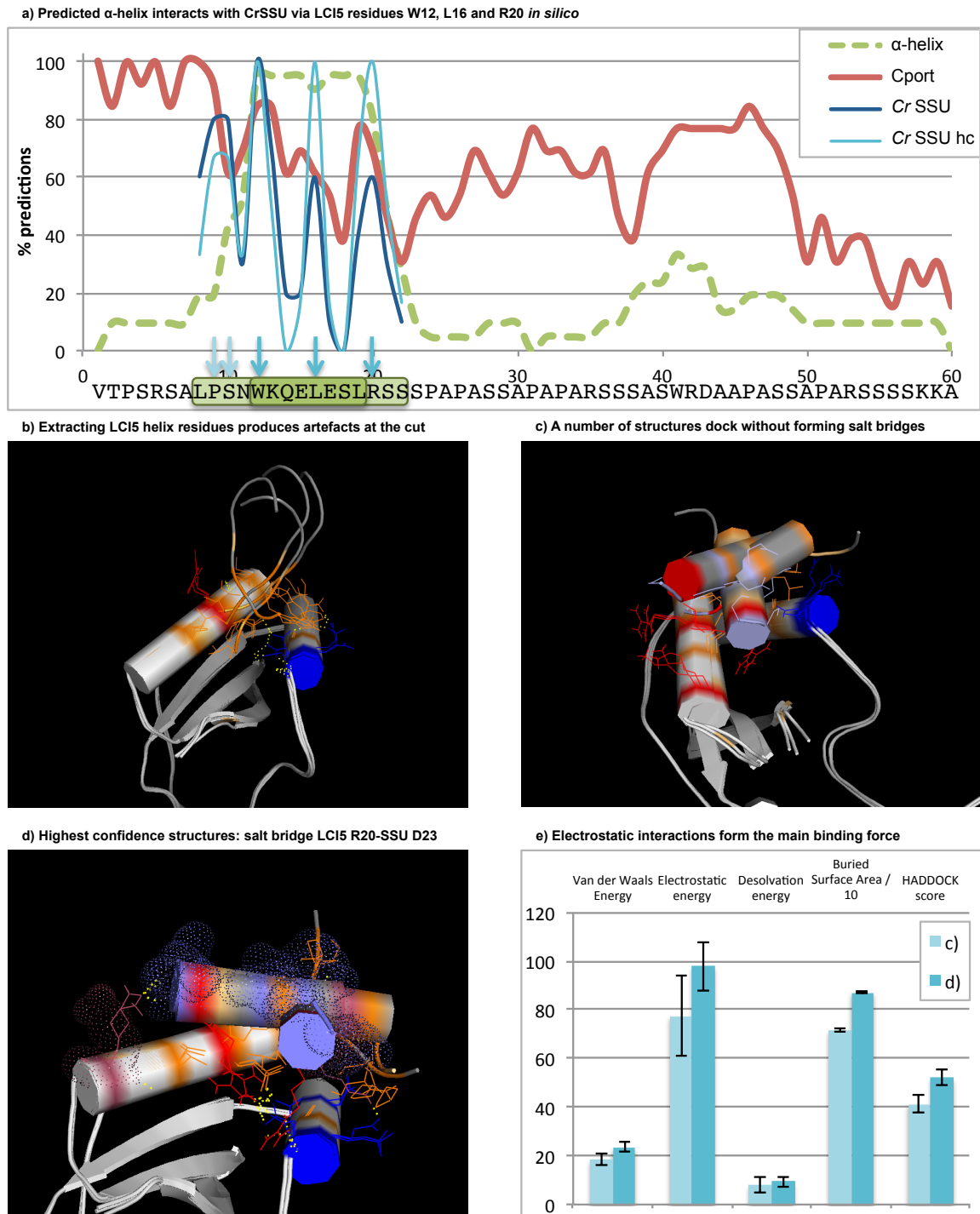


Fig. 3.8: LCI5 *in silico* folding and docking predict interaction proceeds via LCI5 repeat helix residues W12, L16 and R20 and involves a salt bridge between R20 and SSU helix A residue D23.

An analysis of LCI5 repeat 2 (a) shows what percentage of prediction tools report involvement of a residue in forming an α -helix, or an interaction according to Cport, or interaction with *Chlamydomonas* SSU (*Cr* SSU) according to HADDOCK. A high confidence (HC) subset of docked structures has had artificial structures (b) removed but includes structures in (c) and highest confidence structures in (d). Interacting residues are shown as lines and are highlighted orange, or blue if negatively or red if positively charged, and in lighter colours if part of a subset of interactions only. Interface statistics are shown in (e).

3.3.4 Docking the SSU to the putative Lci5 interface *in silico* reveals a crucial salt bridge between R20 (LCI5) and D23 (SSU)

Besides Rubisco, currently the best and only candidate for a linker protein is LCI5 (Mackinder et al., 2015). LCI5 contains 4 near-identical sequence repeats (Fig. 3.1) of which here only repeat 2 is analysed. Over 90% of predictions agree that repeat residues between W12 and L19 form an α -helix, and at least 10% of the predictions support helix formation for residues between L8 and S22 (Fig. 3.8a). In the region around W41 a second short helix is predicted with low confidence. The predicted interaction profile obtained by screening predicted folds for interacting residues using Cport (de Vries and Bonvin, 2011) starts out very high, shows large sinusoidal variation across the predicted helical stretch and climbs to a plateau between residues 38 and 50, coinciding with the second possibly helical stretch.

On the basis of this analysis, the LCI5 helical region stretching from L8 to S22 was deemed the most likely interface candidate, and docked against Rubisco SSU using HADDOCK. Predicted interactions with the *Chlamydomonas* SSU all contained LCI5 repeat residue W12 in the interface, with interaction peaks otherwise broadly in line with Cport predictions but shifted by one amino acid. Removing artificial complexes (Fig. 3.8b) from the HADDOCK prediction set results in absolute agreement of the remaining structures that the interaction proceeds via residues L16 and R20 in addition to W12. Furthermore P9 and S10 in the less confidently helical part are involved in a majority of structures.

Four of the ten HADDOCK predictions were classed as artefacts (Fig. 3.8b) on the basis that the interface includes the artificial Lci5 C- and N-termini produced by cutting the helical stretch out *in silico*, which do not exist *in vivo*. Of the remaining structures, half interact without forming salt bridges (Fig. 3.8c) whereas the other half all form a salt bridge between R20 and SSU helix A residue D23 (Fig. 3.8d). Of these two sets, the latter scores more highly according to HADDOCK (Fig. 3.8e) signifying a more probable formation of the complex with slightly higher Van der Waals, substantially higher buried surface area and a large increase in the free energy released through electrostatic interactions. De-solvation energies suggest the interaction is stable in solution.

Docking the LCI5 helix stretch to the *Spinacia oleracea* SSU results in a set of complexes that receive only slightly lower HADDOCK scores than the best *Chlamydomonas* complexes (Fig. 3.9a), show a similar release of free energy upon binding and have only somewhat smaller buried surface areas.

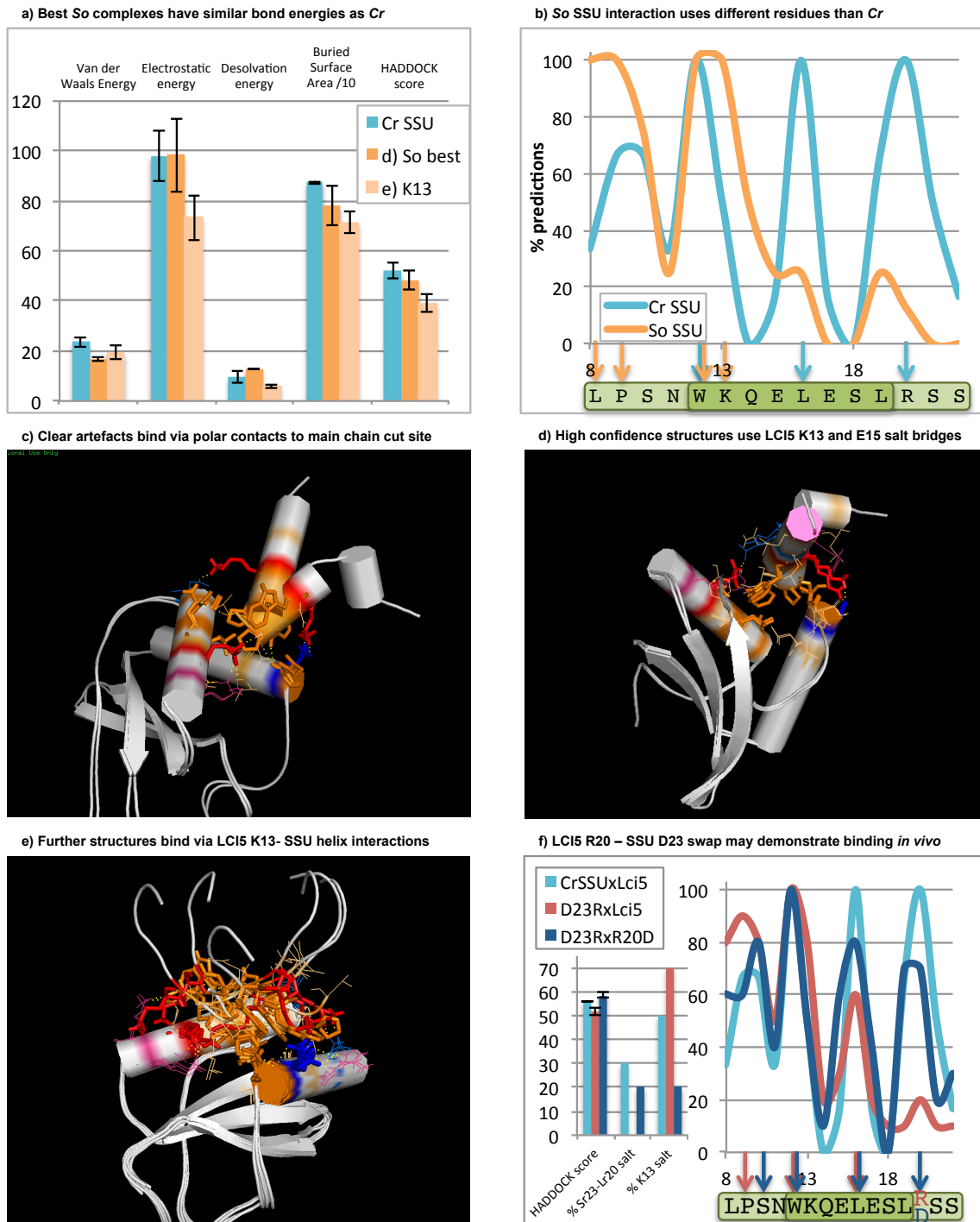


Fig. 3.9: Forcing *Spinacia oleracea* SSU to bind LCI5 repeat helix *in silico* reveals a very different docking profile and shows R20 (LCI5) interaction is specific to *Chlamydomonas* SSU.

HADDOCK interface statistics are shown in (a). For each LCI5 putative helix residue, (b) shows how many interactions are formed as percentage of predicted interfaces after removing obvious artefacts shown in (c) but including high confidence structures in (d) and structures in (e). Interacting residues are shown as sticks and highlighted orange, or blue if negatively or red if positively charged, or are shown as lines highlighted in lighter colours if part of a subset of interactions only. The effect of mutating *Chlamydomonas* SSU D23R and LCI5 R20D *in silico* is explored in (f) showing interaction statistics and residue profiles.

However, the interaction now proceeds via a very different set of residues (Fig. 3.9b). Only W12 interacts in all *Chlamydomonas* and all *Spinacia oleracea* complexes. Key *Chlamydomonas*-interactive residues L16 and R20 only play a very minor, if any, role in interactions with *Spinacia oleracea* SSU, instead L8, P9 and K13 play a major role.

Two structures (Fig. 3.9c) were regarded as clearly artificial on the basis that polar contacts were formed involving the artificial N-terminus of the cut. Highest confidence structures (Fig. 3.9d) are wedged between the helices by way of W12, forming a salt bridge between K13 and *Spinacia oleracea* SSU helix A D24 and another electrostatic interaction involving E15 and *Spinacia oleracea* SSU helix B. For the remaining structures, K13 also plays a crucial role, either through salt bridges with D24 or D31 on helix A or polar contacts with helix B (Fig. 3.9e).

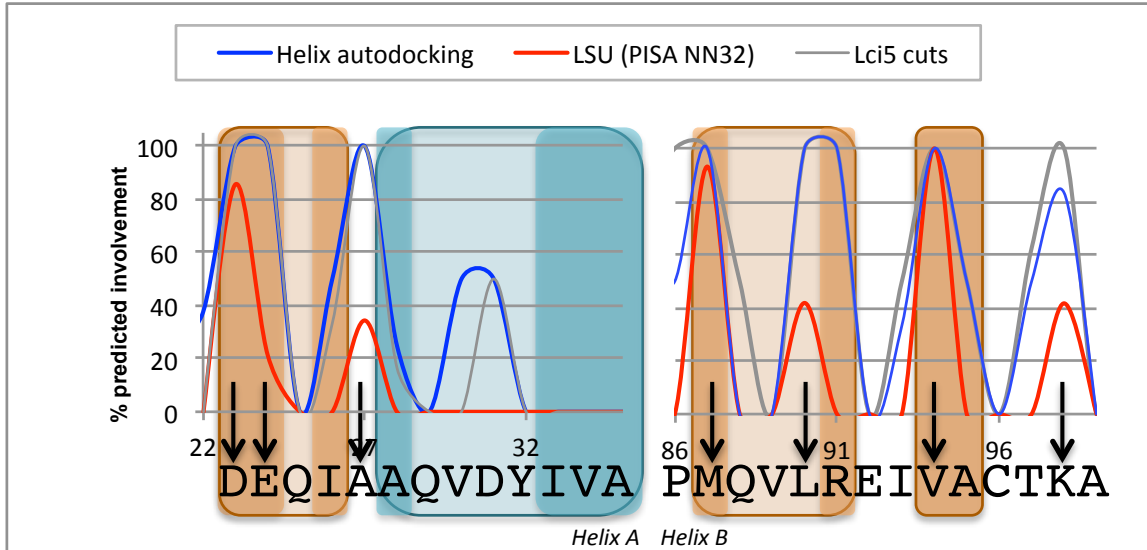
The final panel shows the results of mutating *Chlamydomonas* SSU residue D23R *in silico* and the effect this has on docking the LCI5 repeat helix (in red). The overall score of the best complex is somewhat lower, the mutation completely abolishes any salt bridges between SSU residue 23 and LCI5 residue 20, and at the same time salt bridges are more often formed through residue K13 than in the interaction with *Chlamydomonas* SSU. The interacting residue profile is reminiscent of the interaction with *Spinacia oleracea* SSU insofar residues L8 and P9 near the artificial N-terminus play a role in a larger number of HADDOCK predictions. L16 and especially R20 are much less involved than with *Chlamydomonas* SSU.

Docking a D23R SSU against a LCI5 helix carrying the complementary mutation R20D leads to a recovery of the HADDOCK score actually slightly above WT levels. A salt bridge between SSU residue 23 and LCI5 helix residue 20 are found in two of the ten HADDOCK models including the second-best complex. At the same time, salt bridges formed by K13 (LCI5) are reduced to 20% of models. The residue interaction profile does not quite match the trusted WT set, although it is reminiscent of the WT data before removal of obvious artefacts, and importantly L16 and D20 (LCI5) regain importance for sustaining complex formation whereas L8 and P9 go down closer to WT levels.

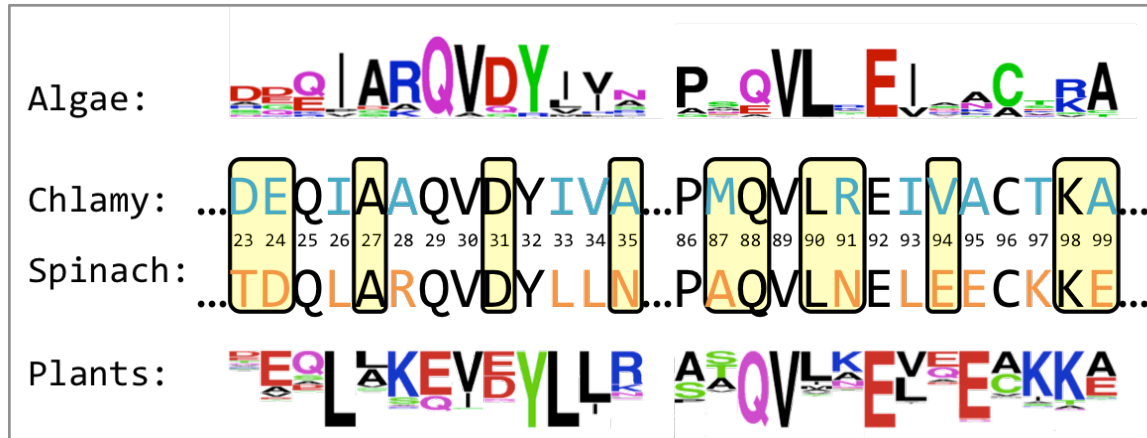
3.3.5 Forced *in silico* SSU protein docking reveals a specific interaction profile

The information about which SSU residues are predicted to interact in either SSU-SSU, SSU-LSU or SSU-LCI5 was pooled (Fig. 3.10a) and compared to SDM results shown as coloured highlights.

a) *In silico* docking and SDM agree on seven key interaction residues



b) Hypervariable surface residues allow interaction site evolution



c) Consensus residues are not sufficient to drive pyrenoid formation

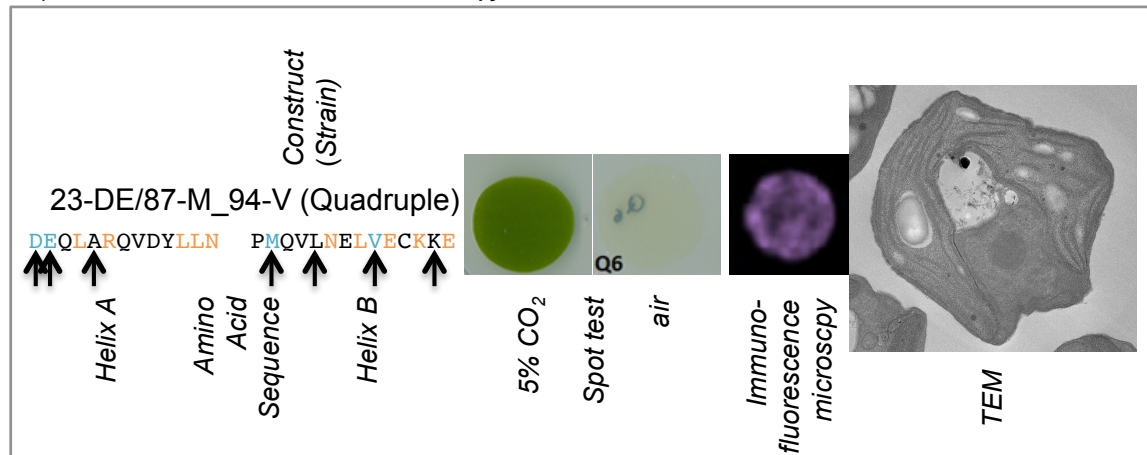


Fig. 3.10: Bioinformatic tools give insight into the SSU helix interaction profile.

SDM, HADDOCK predictions for SSU-SSU and SSU-LCI5, and PDBePISA-based SSU-LSU interaction profiles are compared in (a). *Chlamydomonas* and *Spinacia oleracea* sequences with surface exposed residues highlighted in yellow are set against algal and higher plant amino acid conservation profiles in (b). Results of SDM altering *Spinacia oleracea* SSU by introducing consensus interaction residues highlighted with arrows are shown in (c).

The interface residue peaks overlap for SSU helix A residue D23 and for helix B residues M87, V94 which are also supported by SDM data. *In silico* docking further supports an involvement of residues A27, L90 and K98 for which no SDM data exists. SDM and HADDOCK predictions, but not PDBePISA, further suggest R91 as interacting partner. The second half of helix A is unlikely to play a role according to both SDM and *in silico* data.

Looking at the consensus interface residues in a wider context (Fig. 3.10b), firstly predicted interaction peaks coincide directly with surface exposed residues highlighted in yellow. Residues 87 and 94, and to a lesser extent also 23, 24, and 98 show high variability among different pyrenoid-positive algal species. Of the 7 consensus residues, three residues (A27, L90, K98) are identical in the *Spinacia oleracea* sequence that does not support pyrenoid formation. In a wider plant sequence context, *Chlamydomonas* residues M87 and V94 are furthest removed from their higher plant equivalents, although there is a fair amount of variation at these residues among plants.

Consensus predicted interaction residues are however not sufficient to drive pyrenoid formation: a strain expressing a *Spinacia oleracea* SSU carrying mutations T23D, D24E, A87M and E94V is unable to grow in air, has a delocalized IF signal and lacks a pyrenoid in TEM (Fig. 3.10c).

3.4 Discussion

The work presented uses the key finding that Rubisco SSU surface helices are involved in pyrenoid formation (Meyer et al., 2012) to explore protein-protein interactions underlying Rubisco aggregation in *Chlamydomonas*. A detailed survey of the surface helix residues using SDM as well as bioinformatics allowed identification of key residues and goes some way towards understanding important features of how the helices engage in any interaction. The Rubisco-Rubisco docking hypothesis is refuted on the basis of *in silico* and *in vitro* evidence, and a possible interaction with proposed linker protein LCI5 is dissected bioinformatically generating specific hypothesis testable through mutagenesis.

3.4.1 Site directed mutagenesis is a powerful tool to identify interface residues *in vivo*

As shown in prior SSU SDM studies, Rubisco aggregation into a pyrenoid is necessary for the CCM to function (Genkov et al., 2010; Meyer et al., 2012). Thus CCM operation tested through spot tests and pyrenoid presence or absence established using IF and TEM therefore

present different aspects of equivalent information in this set of mutants. As shown in Fig. 3.4 and summarized in Fig. 3.10a, SDM thus established one site on helix A (D23, E24, I26) and two sites on helix B (M87, R91 and V94, E95) that are necessary for pyrenoid formation, whereas a second site on helix A (A29, I33, V34, A35) was found not to play a role. As amino acids were mutated simultaneously for each site, the SDM data do not support conclusions about which residues are required for pyrenoid formation.

3.4.2 Rubisco surface motifs were investigated *in silico* as likely interaction partners for the SSU helices

Building on SDM insights, protein interactions involving the SSU helices were explored *in silico*. While a role for transport of Rubisco or post-translational modifications in pyrenoid formation cannot be ruled out, current knowledge about pyrenoid regulation (Yamano et al., 2010; Mitchell et al., 2014) suggests slower acting agents are key drivers. It thus seems most likely that Rubisco aggregation is achieved either through docking some form of protein linker, or Rubisco binding to itself. Using Ockham's razor, the simplest explanation would be to postulate SSU auto-docking via the helices (Fig. 3.5). Extending the idea of Rubisco multimerization led to the identification of a further interaction target site, informed by the crystal packing of Rubisco via PDBePISA (Fig. 3.6a). Since crystallization represents a specialized multimerization event, crystal-packing contacts make good candidates for interaction sites.

3.4.3 Rubisco auto-docking fails to account for pyrenoid formation *in silico*

SSU auto-docking by itself supports at best holoenzyme strings, but not interconnected networks (Fig. 3.5b). The interaction between *Chlamydomonas* SSUs is reportedly more stable than for *Spinacia oleracea*, a hallmark characteristic required of an interface to account for pyrenoid formation according to existing mutant phenotypes (Genkov et al., 2010). However, de-solvation incurs a free energy penalty (Fig. 3.5b), meaning that in aqueous solution, each component is entropically more stable in isolation than in the complex.

SSU-LSU interactions connect holoenzymes end-on (Fig. 3.6e), thus it is unlikely that this SSU-LSU interaction could complement the SSU-SSU interactions by interconnecting Rubisco strings. However, the PISA interaction does support formation of an interconnected network, as one Rubisco can coordinate up to four partners. This 3D arrangement is in disagreement with the findings of (Engel et al., 2015) who report hexagonal close packing

on the basis of electron microscopy data. Their model reports six interaction partners, three on either side and a ring of six further partners around Rubisco with the distance between holoenzymes of 2 - 4.5 nm.

An arrangement similar to hexagonal close-packing might be possible across the PISA site if the interaction can pivot between that predicted by PISA (Fig. 3.6a) and that predicted by HADDOCK (Fig. 3.6b). The binding of one partner in one conformation and the next partner in the other would free up one of the interaction sites marked in red in Fig. 3.6e, thus allowing up to four partners to bind to the same protein face. If on average every holoenzyme actually binds three partners with medium affinity such that the interactors continuously disengage and re-engage in every single interaction, an average profile like the one seen by (Engel et al., 2015) could be the result.

However, such an arrangement is not very well supported *in silico*. HADDOCK returned a single cluster with an interaction model where the SSU is turned by about 90° relative to the PISA site, suggesting the PISA site does not present a viable interface arrangement outside the specific confinements of a crystal. In the PISA model itself, interaction partners are too far apart from each other for any interacting residues to be retrieved in PyMOL. Thus it seems likely that while crystallization may have occurred across this site, *in vivo* an interaction involving the implicated residues would at best collapse to the HADDOCK model. For the HADDOCK model, de-solvation is again associated with a free energy penalty, consistent with PISA reporting that the complex is not stable in solution.

3.4.4 Isolated Rubisco does not associate with but repels itself *in vitro*

A classic AUC experiment to characterize the association-dissociation equilibrium between monomers and multimers is to analyse a dilution series. Where multimers would be expected to show up increasingly as high molecular weight species when loading concentrations are high, isolated Rubisco shows no concentration dependency in peak sizes (Fig. 3.7). High molecular weight peaks are also not specific to WT, as pyrenoid formation via Rubisco oligomerization would require. Thus high molecular weight peaks visible in the AUC profiles represent preparation impurities, and not Rubisco multimers.

There is, however, an effect of increasing concentration resulting in a lower weighted average S-value associated with the holoenzyme peak (Fig. 3.7c). A lower Svedberg value here signifies that the protein sedimented more slowly when there was more protein present. Such a slowdown could be attributed to an increased viscosity of the buffer, however, the

concentrations used are still too low for molecular crowding to have a large impact on protein behaviour (Ellis, 2001). Moreover, Fig. 3.7c clearly shows that S-retardation of the Rubisco peak is governed by the actual concentration of Rubisco itself (assessed as area under the peak) and not the total loading concentration. Because in this case the WT Rubisco preparation contained fewer impurities than the pyr- preparation, the total amount of Rubisco was actually higher in the former despite greater total protein loading in the latter. Therefore the slowdown of Rubisco sedimentation seems to originate in holoenzymes interacting in a way that generates a force opposite to sedimentation: Rubisco repels itself.

3.4.5 Implications of *in vitro* findings for *in vivo* and *in silico* scenarios

The protein concentrations used here are still a long way below *in vivo* protein concentrations of around 300-400 mg/ml (Ellis, 2001). However, given that Rubisco makes up <6% of total protein in microalgae (Losh et al., 2013), the highest concentrations used here would be on the same order as delocalized Rubisco concentrations in the chloroplast. Thus any small affinity by Rubisco to bind to itself that might be revealed by the use of much higher concentrations would not be able to account for pyrenoid formation through the spontaneous aggregation of Rubisco dispersed throughout the chloroplast.

But more than simply not aggregating, Rubisco was found to actually repel itself at least in certain conditions, like the ones present in the AUC. Thus a factor that promotes aggregation will be necessary to drive pyrenoid formation. It is of course possible that a different buffer composition may neutralize repelling forces, similar perhaps to the effect of cations on thylakoid stacking (Daum et al., 2010). Such a mechanism might allow the extent of Rubisco aggregation in the pyrenoid to be controlled by chloroplast stroma ionic composition. An obvious candidate, pH, may vary quite considerably depending on the local environment in an actively photosynthesizing *Chlamydomonas* chloroplast: thylakoid membranes importing protons should lead to an overall alkaline stroma. Within a pyrenoid on the other hand, proton release associated with active CO₂ fixation should acidify the pyrenoid interior. Thus HCO₃⁻ might be better a candidate, as it is accumulated by an active CCM and thus could be exploited as a signal. However, given that (Engel et al., 2015) posit a gap of 2-4.5 nm between holoenzymes in the pyrenoid, a macromolecular linker seems more likely than ionic agents: the van der Waals radius of HCO₃⁻ is only around 0.5 nm (Batsanov, 2001).

3.4.6 *In silico* docking of LCI5 shows promise to have identified the linker interface

Whilst no candidate linker protein was known when the work was initiated, very recently the protein LCI5 has been found to fulfil this role (Mackinder et al., 2015). A major limitation in using bioinformatics tools to assess binding of LCI5 was the lack of a crystal structure. To get around this problem, a number of different tertiary fold predictors were used to get a reasonable approximation of what may be the real fold. LCI5 is a highly disordered protein, which contains four almost identical sequence repeats (Fig. 3.1). These repeats may work autonomously, possibly each docking a separate holoenzyme with disordered regions acting as flexible tethers between the helical interfaces. Therefore the fold of a single repeat was retrieved. The various fold predictions differ drastically for the most part, except around the helical part of the protein. The predicted helical stretch is the one region within the repeat with a low frequency of Prolines, Serines and Alanines that promote disorder within the rest of the protein. As the sole structured part of LCI5, the confidently predicted helical stretch was docked in isolation as an ensemble of all fold predictions.

In contrast to Rubisco auto-docking predictions, the SSU interaction with the LCI5 helix does appear stable in solution, judging from de-solvation energies (Fig. 3.8e, Fig. 3.9a). *Chlamydomonas* SSU-LCI5 complexes predict an interaction involving W12, L16 and R20 with a high degree of confidence. That a salt bridge between R20 (LCI5) and D23 (SSU helix A) can form irrespective of the 3D alignment of the LCI5 helix relative to the SSU helices makes this specific prediction likely hold true, whatever the actual fold of the rest of LCI5 may be. Furthermore, the fact that R20 (LCI5) is involved in almost none of the predicted interactions with the *Spinacia oleracea* SSU lends further support to the idea that R20 may play an important role in realizing pyrenoid formation *in vivo* through docking to the Rubisco SSU.

In the context of the full LCI5 repeat, the interaction may be supported by the region around W41 which shows a high ability to interact according to CPORT (Fig. 3.8a) and shows some propensity to form a helix, possibly as a result of having a short stretch without disorder-inducing residues. The remainder of the protein may remain flexible *in vivo* instead of adopting a specific rigid fold. LCI5 is known to be phosphorylated in conditions that promote CCM activity (Turkina et al., 2006) which may regulate the interaction with Rubisco. Reported LCI5 phosphorylation target residues T2, S22 and S23 are very close to

either side of the helix stretch, thus negatively charged phospho-residues might contribute to the interaction by binding positively charged helix B (Fig. 3.2).

High-level testing for protein interaction between Rubisco and LCI5, similar to the AUC test for Rubisco auto-docking, are currently underway (Mackinder et al., 2015). Should docking be confirmed *in vitro*, then the *in silico* analysis presented here could inform a SDM strategy to demonstrate binding *in vivo*. A strain that expresses a *Chlamydomonas* SSU carrying the mutation D23R should be unable to form the salt bridge to LCI5 helix residue R20, leading to a loss of binding and a pyrenoid-deficient phenotype. If heterologous expression of an *LCI5* gene carrying the mutation R20D at every sequence repeat is able to rescue the pyrenoid deficiency of above strain, this would very neatly demonstrate *in vivo* interaction across the *in silico* predicted site.

An *in silico* mimic of the described SDM strategy (Fig. 3.9f) rescues salt bridge formation across the mutated residue, and restricts *Spinacia oleracea* SSU-like salt bridge formation via K13. In both *Spinacia oleracea* and the single mutant D23R, the modelled interaction may require the arbitrary cut as N-terminal residues are heavily involved whereas C-terminal residues lose importance. Adding the restoring mutation R20D shifts the binding profile back to a more *Chlamydomonas* SSU-like profile. Thus, at least *in silico*, both the destructive and restorative mutations behave as expected.

3.4.7 *Spinacia oleracea* SSU as a negative control fails to identify *bona fide* interaction partners *in silico* but supports more general points about interactivity and mode of binding

As a principal strategy for testing the relevance of a predicted interaction, docking to *Chlamydomonas* SSU helices was compared to *Spinacia oleracea* SSU docking. Since the *Spinacia oleracea* SSU is unable to support Rubisco aggregation when in expressed in *Chlamydomonas*, a predicted complex would seem more relevant if the interaction between a candidate and *Spinacia oleracea* was weaker than with *Chlamydomonas* helices. All three candidates, however, show better overall docking to *Chlamydomonas* according to HADDOCK, as reported in the lower HADDOCK scores for complexes with *Spinacia oleracea* SSU (Fig. 3.5c, Fig. 3.6f, Fig. 3.9a). Moreover there is no PISA predicted interface across SSU helices in the crystal structure of *Spinacia oleracea* Rubisco (Andersson, 1996) suggesting crystal formation proceeded via a different protein surface than for *Chlamydomonas*.

Thus rather than *Spinacia oleracea* being a good negative control that allows identification of the “real” interaction partner, it seems that the *Chlamydomonas* SSU helices generally present a surface locus that is more favourable for forming protein-protein interactions than *Spinacia oleracea*. In both SSU auto-docking (Fig. 3.5c) and PISA-based SSU-LSU interactions (Fig. 3.6f), differences in electrostatic interactions play a major role in allowing *Chlamydomonas* SSU to bind more favourably. Docking to LCI5 shows no difference in electrostatic free energy release (Fig. 3.9a) because the salt bridge between R20 on LCI5 and D23 on SSU helix A (Fig. 3.8d) is replaced by a salt bridge formed through LCI5 residue K13. In any case, electrostatic interactions are important to drive the interaction here too. Therefore the simple arrangement of charges along the *Chlamydomonas* helices with a negative helix A juxtaposed to a positive helix B across a hydrophobic ridge (Fig. 3.2) appears to create a good protein interaction interface. The more complex charge pattern on the *Spinacia oleracea* helices seems less amenable to support binding.

In addition to lower complex formation abilities, *in silico* docking suggests that an altered mode of binding may contribute to disrupting Rubisco aggregation in *Spinacia oleracea* SSU lines. In SSU auto-docking (Fig. 3.5), the altered charge profile on the *Spinacia oleracea* SSU requires helix A to bend backwards a lot more than in the *Chlamydomonas* structure. Perhaps as a result, the most favourable interactions by *Spinacia oleracea* proceed across a rotated interface in both SSU-SSU and SSU-LSU interactions (Fig. 3.5e-f, Fig. 3.6d). When docking LCI5, all of the predicted *Spinacia oleracea* SSU complexes place a major interactive burden on the end residue L8. The artificial N-terminus likely generates more degrees of freedom at that site *in silico* than the LCI5 helix has *in vivo*. Therefore none of the predicted *Spinacia oleracea* complexes would probably be able form in the context of an unsevered LCI5 protein. By contrast, LCI5 interaction with the *Chlamydomonas* SSU proceeds via the entire length of the LCI5 helix with little reliance on the end residues, thus making the present *in silico* docking a credible model for LCI5 behaviour.

3.4.8 An overall SSU interaction profile emerges

In addition to generating highly specific, testable hypotheses about protein interactions, analysis of the SSU helices agrees on an overall interaction pattern independent of the specific *in silico* interaction partner. Since SDM knowledge is required for specifying some interface residues, the most interesting HADDOCK result is the importance of residues A27, L90 and K98 that were not assigned *a priori*. Similarly, A95 was assigned but is not

involved in the majority of HADDOCK models, suggesting it plays only a minor role in interface formation. Simply searching for interaction sites on involving the SSU helices retrieved the PDBePISA interface, which is based on crystal contacts and thus independent of SDM data. Thus the overall consensus interaction site presented in Fig. 3.10a combines SDM data, HADDOCK information about further residues that is implied by the SDM data, and publically available experimental data about the behaviour of the SSU helices in crystal formation.

The fact that a number of key residues are hyper variable among pyrenoid-containing green algae suggests that the interaction site has arisen recently. If these residues are indeed crucial for the interaction that aggregates Rubisco into the pyrenoid, and the pyrenoid was an evolutionary ancient trait, then selection should act to minimize variation at these residues between descendents of an original pyrenoid-bearing alga. This idea does not match up with the high variation seen (Fig. 3.10b), meaning in turn that other pyrenoid-bearing algae likely employ a different mechanism for pyrenoid assembly while the *Chlamydomonas* mechanism of interacting SSU surface helices likely has arisen recently in this lineage: Surface residues would only be under low selective pressure if not involved in an interaction, as a mutation would then be unlikely to disrupt the quaternary structure. This also means that highly conserved residues on the higher plant side, such as E95 and K97, might hint at underlying selective pressures. Should genetic manipulation of these residues be necessary for establishing a pyrenoid in a higher plant, then co-expression of different SSU versions including some that contain the original 95E and 97K may be necessary to allow endogenous SSU roles to be performed.

3.4.9 Directions for future work

The 7 consensus interaction residues are not, however, sufficient for pyrenoid formation (Fig. 3.10c). The next best candidate that may be required for interface formation but that is missing from the Quadruple construct 28-DE/87-M_94-V would be R91. R91 is surface exposed and implicated in interactions by both SDM and HADDOCK, but did not appear in the consensus set as it does not participate in the PISA interface. Secondly, the region around K98 in helix B is confidently predicted to play a role *in silico* but is not resolved in the current SDM dataset. While K98 itself is present in both *Spinacia oleracea* and *Chlamydomonas*, the surrounding two residues may interfere with the behaviour of K98. Thirdly, buried residue 95 could be important as it is a drastic change from *Chlamydomonas reinhardtii* Alanine to negatively charged *Spinacia oleracea* Glutamate that may alter local

residue arrangement. Least likely to play a role are residues 26 and 93 which interchange Isoleucine for Leucine.

3.5 Conclusion

Rubisco aggregation involving the SSU surface helices presents itself as an evolutionarily recent protein-protein interaction site made possible through a simple arrangement of charges combined with hydrophobic surface residues (Fig. 3.2). Key residues include D23, E24, A27, M87, L90, V94 and K98, however, further residues are required for pyrenoid reconstitution and may include R91 (Fig. 3.10). In isolation, holoenzymes fail to form stable complexes in solution (Fig. 3.5, Fig. 3.6) but positively repel each other (Fig. 3.7) and require a linking agent to facilitate an interaction. Whether LCI5 is such a linking agent could be tested by expressing an R20D-carrying *LCI5* gene in a strain that is pyrenoid-deficient due to a D23R-mutation in the SSU (Fig. 3.9).

4 A RUBISCO INTERACTOME PROVIDES INSIGHT INTO THE MECHANISM OF PYRENOID ASSEMBLY

4.1 Introduction

Proteins have an inherent propensity to interact. Facilitated by the crowded environment present inside cells (Ellis, 2001), aggregations of proteins can lead to debilitating disease when unchecked (Ross and Poirier, 2004), but also enable the operation of large scale complexes with fascinating functions, ranging from decision making in prokaryotic motility (Stock and Zhang, 2013) to light harvesting in photosynthetic membranes (Nelson and Ben-Shem, 2004; Kirchhoff, 2008; Drop et al., 2014). In the majority of aquatic microbial photosynthetic organisms, aggregation of Rubisco into micro-compartments not bound by membranes forms an essential part of any CCM. Whereas a well-defined protein casing encloses cyanobacterial carboxysomes with Rubisco tethered inside (Espie and Kimber, 2011), eukaryotic pyrenoids are less well defined (Wang et al., 2015). Understanding the mechanism of Rubisco aggregation in the pyrenoid is essential for gaining insight into the evolution of this enigmatic organelle, and a key requirement for genetically engineering an algal CCM into crop plants (McGrath and Long, 2014).

In contrast to carboxysomes, the pyrenoid of the model green alga *Chlamydomonas* lacks an outer casing. The starch sheath which usually delineates the pyrenoid is not required for

Chapter 4: A Rubisco interactome provides insight into the mechanism of pyrenoid assembly

pyrenoid function in the CCM (Villarejo et al., 1996). The single pyrenoid localizes to the centre of the chloroplast at the cell apex. A number of proteins are localized specifically around the pyrenoid, including the entire plastid protein translation machinery, believed to be organized in coordination with plastid protein import in so-called T-zones (Uniacke and Zerges, 2009). The enigmatic LCIB/C complexes also localize around the pyrenoid (Wang and Spalding, 2014). The pyrenoid is further traversed by an intricate system of thylakoid membranes. Intra-pyrenoidal thylakoids differ drastically from stromal lamellae, fusing to form large tubules, containing internal mini-tubules which provide stromal continuity between the exterior and interior of the pyrenoid (Engel et al., 2015).

Rubisco itself forms a major component of the pyrenoid (Lacoste-Royal and Gibbs, 1987; Kuchitsu et al., 1988), showing hexagonal close packing with a spacing of 2-4.5 nm between holoenzymes (Engel et al., 2015). While over 90% of cellular Rubisco is localized inside the pyrenoid under CCM-induced conditions, Rubisco delocalizes to the chloroplast stroma when the CCM is repressed in elevated CO₂ (Borkhsenius et al., 1998) or at night in recently divided, synchronized cells (Mitchell et al., 2014). However, the pyrenoid never fully disappears, not even during cell division when each daughter cell inherits one half (Goodenough, 1970).

The composition of isolated *Chlamydomonas* pyrenoids was recently analysed by mass spectrometry (Mackinder et al., 2015). Pyrenoid enriched fractions were found to contain in high abundance a low-CO₂ inducible protein, LCI5, and this protein is now considered to be a likely molecular linker of Rubisco holoenzymes. Rubisco and LCI5 have been shown to bind to each other in reciprocal pull-down experiments (Mackinder et al., 2015). An *lci5* knock-down mutant exhibits a defective pyrenoid and a severe CCM-phenotype. The only other mutation found so far to affect pyrenoid morphology is in a putative methyltransferase called *CIA6* (Ma et al., 2011). In addition to linker proteins, the pyrenoid structure implies the presence of thylakoid membrane organization proteins as well as molecular tethers between thylakoids and pyrenoid matrix. The specific localization of the pyrenoid at the heart of the chloroplast should require structuring elements, and the mobility of Rubisco indicates the presence of factors regulating the aggregation state.

A major insight into the mechanism of Rubisco aggregation was the finding that *Chlamydomonas* strains expressing a higher plant Rubisco SSU lack pyrenoids (Genkov et al., 2010). Using SDM it was possible to show that the *Chlamydomonas* SSU surface helices are necessary for pyrenoid formation (Meyer et al., 2012). These helices most likely are

involved in a key protein-protein interaction that enables Rubisco to aggregate in the pyrenoid (see Chapter 3).

To find the key elements involved in pyrenoid assembly, the present study therefore aimed to identify Rubisco interaction partners. BN-PAGE (Schägger and von Jagow, 1991; Swamy et al., 2006; Wittig et al., 2006; Järvi et al., 2011) and co-IP (Heide et al., 2009; Simeoni et al., 2013), were used to establish a comprehensive Rubisco interactome in *Chlamydomonas*. The principle behind identifying factors that play a role in Rubisco aggregation relied on making a comparison between a WT strain and a pyr- strain that expresses *Spinacia oleracea* Rubisco SSU. Since the only difference between otherwise isogenic strains is the version of Rubisco SSU expressed, key pyrenoid assembly factors should be among the proteins that bind to Rubisco in WT but not in pyr-. A second comparison between cells grown in CCM-repressive (5% CO₂) as well as CCM-inductive (air) conditions was used as an additional analytical tool to dissect the co-IP data.

Given that even when the CCM is repressed, ~50% of Rubisco remains aggregated, proteins that consistently bind to Rubisco in WT independently of CO₂ conditions for growth may be informative about maintenance of this constitutive pyrenoid. Factors specific to WT grown in air on the other hand should provide insight into the mechanism of full pyrenoid assembly in the context of a CCM, including low CO₂-induced linker candidates like LCI5. Some of the proteins binding Rubisco in WT cells grown at 5% CO₂ could be delocalisation-promoting factors. Factors binding Rubisco in pyr- on the other hand could present aggregation-promoting factors, especially in air where the pressure for pyrenoid assembly should be maximal. A suite of proteins would also be expected to interact with Rubisco independently of pyrenoid presence, for example folding chaperones such as chaperonin 60 (Liu et al., 2010; Vitlin Gruber et al., 2013) and Rubisco activase (McKay et al., 1991; Portis et al., 2008). The interactome reported in this chapter gives the first biochemical support for the association of the pyrenoid with chloroplast protein translation complexes, suggests a role for the cytoskeleton in pyrenoid organization and identifies key linker and regulatory protein candidates.

4.2 Materials and Methods

4.2.1 Strains and culture conditions

To define the interactome, wall-less SSU substitution strains used were WTint1,2 (WT) and the pyr- strain expressing a *Spinacia oleracea* RBCS construct. For BN-PAGE experiments,

Chapter 4: A Rubisco interactome provides insight into the mechanism of pyrenoid assembly

walled WT strain 2137 was used in a pilot study (Fig. 4.1) and as positive control (Appendix 8.20), in one case supplemented by CC-3395 (alias *cw_darg-7-8 mt⁻*) which is the WT parent strain of SSU substitution lines (Khrebtukova and Spreitzer, 1996). Protein was extracted by grinding spinach leaves (Marks and Spencer, London, UK) in liquid nitrogen was used as negative control (Fig. 4.5). In the optimized protocol, cells were inoculated from fresh (1-2 week old) dark-grown acetate-containing agar plates into 50 ml minimal medium aerated with 5% CO₂. After 2-3 days, cultures were normalized based on total chlorophyll content (Wellburn, 1994) assuming a doubling time of 15h (Fig. 2.5h), such that mid-log (ca. 3 µg chlorophyll/ml, see Fig. 2.10a) would be reached one day prior to scheduled protein extraction, at which point aeration was switched to ambient CO₂ over night. Where high-CO₂ samples were required, proteins were also extracted before switching aeration.

4.2.2 Protein extraction

Culture in excess of 1 mg chlorophyll was harvested by centrifugation (2,000 RPM, 5 minutes, 4°C, Eppendorf 5804R, Germany) in 50ml Falcon tubes and re-suspended in 1ml protein extraction buffer (50 mM Tris/HCl, 5mM MgCl₂, pH 7.0 with cOmplete™ Mini EDTA-free protease inhibitors, Roche). Proteins were extracted by sonication (2 pulses of 40 seconds for wall-less cells or 6 pulses of 30 seconds for walled cells, Soniprep 150, MSE, London, UK) followed by centrifugation (12,000 RPM, 15 minutes, 4°C, Hawk 15/05, MSE) to separate soluble and membrane fractions. Total soluble protein in the supernatant was quantified using the Bradford method (Bio-Rad). Pellets containing membrane proteins were washed in storage buffer (50 mM HEPES/KOH, 100 mM Sorbitol, 10mM MgCl₂, pH 7.5), re-suspended to 1 mg chl ml⁻¹ in re-suspension buffer (25 mM BisTris/HCl pH 7.0, 20% w/v Glycerol with cOmplete™ Mini EDTA-free protease inhibitors, Roche) and solubilized by adding equal volume solubilisation buffer (2% w/v n-Dodecyl-β-Maltoside, or β-DM, in re-suspension buffer) to give final concentrations of 0.5 mg chl ml⁻¹ and 1% β-DM.

4.2.3 First dimension (1D) BN-PAGE

For soluble fractions, one volume of sample was mixed with 0.25 volume of glycerol prior to loading 40 µg protein per lane. For membrane fractions, one volume of sample was mixed with 0.25 volume of 5x BN sample buffer (100 mM BisTris/HCl pH 7.0, 37.5% w/v sucrose, 0.5 M ε-amino caproic acid, 2.5% weight per volume Coomassie Brilliant Blue G) prior to loading 8 µg chlorophyll (=20 µl) per lane. Precast native gels (NativePAGE™

Novex® 3-12% Bis-Tris Protein Gels, 1.0 mm, 10 well, Life Technologies) were run using 6 µl standards (NativeMark™ Unstained Protein Standard, Life Technologies) with blue cathode buffer (0.02% w/v Coomassie Brilliant Blue G in 50 mM Tricine, 15 mM Bis-Tris/NaOH, pH 7.0) and blank anode buffer (50 mM BisTris/HCl pH 7.0) in 4°C at 150 V for 90 minutes. Lanes were cut into individual 1D strips and if necessary stored at -20°C between plastic sheets. 1D strips were stained overnight in staining solution (0.2% w/v Coomassie Brilliant Blue R in 40% by volume ethanol, 10% by volume acetic acid), destained for 15 minutes in Destain 1 (40% by volume ethanol, 10% by volume acetic acid) followed by successive rounds in Destain 2 (10% by volume acetic acid), rehydrated in distilled water and photographed on a gel illumination box. Where applicable, bands were cut for mass spectrometry from the stained gel strips, or equivalent strips in the case of 850 kDa bands (Appendix 8.20, Appendix 8.21).

4.2.4 Second dimension (2D) SDS PAGE

To run the 2nd dimension, 1D strips were activated by incubation at 37°C for 1h in 9.5 ml BN-strip activation buffer (0.5 M Tris, 6 M Urea, 23% by volume glycerol, 20% weight per volume SDS, pH 6.8) supplemented with 0.5 ml β-mercaptoethanol, and fixed into the well space of precast 2nd dimension gels (NuPAGE® Novex® 10% Bis-Tris Protein Gels, 1.5 mm or 1 mm, 2D well, Life Technologies) using 1% Agarose in 1x SDS running buffer (NuPAGE® MOPS SDS Running Buffer, Life Technologies). Using 5µl protein standards (Novex® Sharp Pre-Stained Protein Standard, Life Technologies), gels for staining and Western blotting were run in parallel at room temperature in either a XCell SureLock® Mini-Cell or a Bolt® Mini Gel Tank (Life Technologies) placed on ice at 100 V for 140 minutes using a Bio-Rad power pack 200. Gels were stained using a Silver stain kit (Pierce™, Life Technologies).

4.2.5 Western Blots

Western blotting was performed in a Bio-Rad Mini Trans-Blot Electrophoretic Transfer Cell, according to the manufacturer's instructions, using transfer buffer A (25 mM Tris pH 8.3, 192 mM glycine, 20% by volume methanol, 0.025% w/v SDS). SDS-PAGE separated proteins were transferred onto PVDF blotting membrane (Amersham™ Hybond™, GE Healthcare, Chalfont St Giles, UK), either overnight in 4°C at 30 V or 70 minutes at room temperature at 100 V. The membrane was incubated overnight at 4°C or 1h at room temperature in blocking buffer (2.5% w/v dried milk powder in standard Tris Buffered

Chapter 4: A Rubisco interactome provides insight into the mechanism of pyrenoid assembly

Saline, or TBS, containing 137 mM NaCl, 15.4 mM Tris/HCl, pH 7.6). Incubation in 1° AB (Rabbit AB raised against wheat Rubisco in the research group of John Gray, 1:5,000 in blocking buffer) was either overnight at 4°C or 1h at room temperature, followed by 1h at room temperature in 2° AB (ECL™ peroxidase-labelled anti-rabbit, 1:50,000 in blocking buffer) with TBST (0.1 % by volume Tween20 in TBS) washes in between. Blots were developed using Western Lightning® *Plus*-ECL (PerkinElmer) in a Compact X4 developer (Xograph, Stonehouse, UK).

4.2.6 Figure generation

Images of gels and Westerns were rotated and contrast, brightness and saturation adjusted for maximal visibility of features using iPhoto (Apple, Cupertino, CA, USA). Figures containing such images were assembled in PowerPoint (Microsoft).

4.2.7 Co-IP

Immuno-precipitation of Rubisco from total soluble protein extracts was performed using commercially available Seppro® Rubisco Spin Columns (Sigma Aldrich, St. Louis, MO, USA). Eluted proteins were concentrated and buffer was exchanged into PBS (Phosphate-buffered saline: 137mM NaCl, 10mM Na₂HPO₄, 2mM KH₂PO₄, 2.7mM KCl) using ultrafiltration spin columns (Vivaspin 500 or Vivaspin 2, Sartorius Stedim Biotech GmbH, Göttingen, Germany) [use of Vivaspin 500 is recommended based on 2-fold higher yield].

4.2.8 Mass spectrometry and computational analysis

4.2.8.1 Data collection and transformation

Sample analysis via liquid chromatography-mass spectrometry with peptide fingerprinting (LC-MS/MS) was performed at The Cambridge Centre for Proteomics (University of Cambridge, UK). The NCBI database for *Chlamydomonas reinhardtii* proteins was used to fit detected peptides, creating a Mascot (Matrix Science, London, UK) .csv file for each submitted 1D gel band, 2D gel spot or co-IP protein eluate. Using the open source software R (The R Foundation), NCBI protein GenInfo Identifier (GI) numbers and *emPAI* values were retrieved from each mascot file. Serving as a proxy for protein abundance, *emPAI* values are calculated as

$$emPAI = 10^{\frac{N_{observed}}{N_{observable}}} - 1$$

(Ishihama et al., 2005), where $N_{observed}$ is the number of peptides detected in LC-MS/MS, and $N_{observable}$ is the number of theoretically observable peptides per protein (see Results section 4.3.4). Missing *emPAI* values were estimated using a regression of $\log_{10}(emPAI + 1)$ against $peptide-spectrum\ matches / protein\ mass$. For each experiment, abundances of individual proteins (i) were normalized to the sum of protein abundances and expressed as pseudo-concentration protein contents (% *emPAI*) in terms of a % fraction to remove biases arising from different total protein concentrations between experiments (equivalent to Eq.3 in Ishihama et al., 2005):

$$\% emPAI_i = \frac{100 \cdot emPAI_i}{\sum_{i=1}^n emPAI}$$

For each experiment (1D bands at 600 kDa, 720 kDa, 850 kDa, 2D spots at 720/60 kDa, co-IP), proteins and associated % *emPAI* values from different replicates were collated. In replicates where a protein had not been detected, % *emPAI* was set to 0.

4.2.8.2 Statistical model fitting

The `nls()` function in R was then used to calculate least squares associated with different models for each protein. Each model defines a number of classes and fits a single value to all replicates within each class, converging towards the average. For 600 kDa and 720 kDa 1D bands, two models were fit: one model with one variable describing the average of all replicates, and a second model with two separate variables for WT and pyr- replicates.

For co-IP data, 15 different models were fit (see Table 4.1): one model with four independent variables describing averages of WT at air, WT at 5%CO₂, pyr- at air and pyr- at 5%CO₂ separately (Table 4.1 model 1), six models with three parameters describing all permutations of pooling two conditions (Table 4.1 models 2-7), seven models with two parameters describing all permutations of two sets of pooling two conditions (Table 4.1 models 8-10) and all permutations of pooling three conditions (Table 4.1 models 11-14), and one model with one variable describing the total average across all conditions (Table 4.1 model 15). A nonlinear model was used to get information about which treatment is associated with highest abundance for a given protein, instead of using a linear model to establish whether a treatment had a significant effect.

4.2.8.3 Model selection and protein classification

Least squares associated with each model were then used to decide which model was best supported by the data on the basis of the *AIC* (Akaike, 1974). The best model informed

Chapter 4: A Rubisco interactome provides insight into the mechanism of pyrenoid assembly

classification of a protein as equally abundant or differentially abundant. If differentially abundant, the condition with the highest abundance was chosen as most informative to classify the protein. For 600 kDa and 720 kDa 1D bands this creates three classes of proteins (Fig. 4.7, Fig. 4.8): those that are more abundant in WT (coloured blue), those that are equally abundant (coloured grey) and those that are more abundant in pyr- (coloured red). For co-IP, 15 classes are generated (Appendix 8.26): one class where proteins are equally abundant in all conditions (h), four classes where proteins are most abundant in one of the conditions (a)&(c)&(m)&(o), two classes where proteins are equally abundant in WT and pyr- but responsive to CO₂ (g)&(i), two classes where proteins are equally abundant in air and 5% CO₂ but differ between WT and pyr- (b)&(n), four classes where proteins are equal amongst three of the condition but are less abundant in the fourth (d)&(f)&(j)&(l), and two (biologically unintuitive) classes where proteins are equal between WT/air and pyr-/5% CO₂ or WT/5% CO₂ and pyr-/air and higher than in other conditions (e)&(k).

4.2.8.4 Gene Ontology analysis

NCBI protein GI numbers reported by mascot were submitted to DAVID (Huang et al., 2009b) for functional enrichment analysis (Huang et al., 2009a) and gene ID conversion into Genbank IDs which were submitted to the Algal Functional Annotation Tool (Lopez et al., 2011) for gene ID conversion into Phytozome identifiers, and subsequent enrichment and functional annotation analysis based on JGI.v3.IDs. Terms from both sources were combined with the mascot protein descriptions and converted into a list of functional annotations for each protein. Throughout this chapter, proteins are identified by their latest Phytozome JGI.v5 identifiers where possible.

4.2.8.5 Identification of candidates

Information was considered not reliable for a subset of proteins (Fig. 4.12a), based on rare appearance (in only 1 or 2 out of 12 replicates) or low abundance, calculated in trade-off with appearance as:

$$\frac{\text{relevant abundance}}{\text{abundance of Rbcl}} / \text{absence count} < 0.01$$

Remaining proteins were sorted into functional categories based on annotation terms.

4.3 Results

The only difference between otherwise isogenic WT and *pyr*⁻ strains is the expression of distinct Rubisco SSUs. Resolving complexes of Rubisco experimentally should thus allow the identification of factors that enable pyrenoid formation by binding to the *Chlamydomonas* SSU. Rubisco complexes were firstly resolved using BN-PAGE. Fig. 4.1 highlights the experimental strategy: as a 1st dimension, total soluble protein is separated by molecular weight of native protein complexes, as shown by the Coomassie Blue stained 1D gel strips. A single lane of a 1st dimension gel is then analysed further on a 2nd dimension gel, separating individual polypeptides via denaturing SDS-PAGE. Rubisco subunits are then identified using a Western blot, indicating which high molecular weight complexes contain Rubisco.

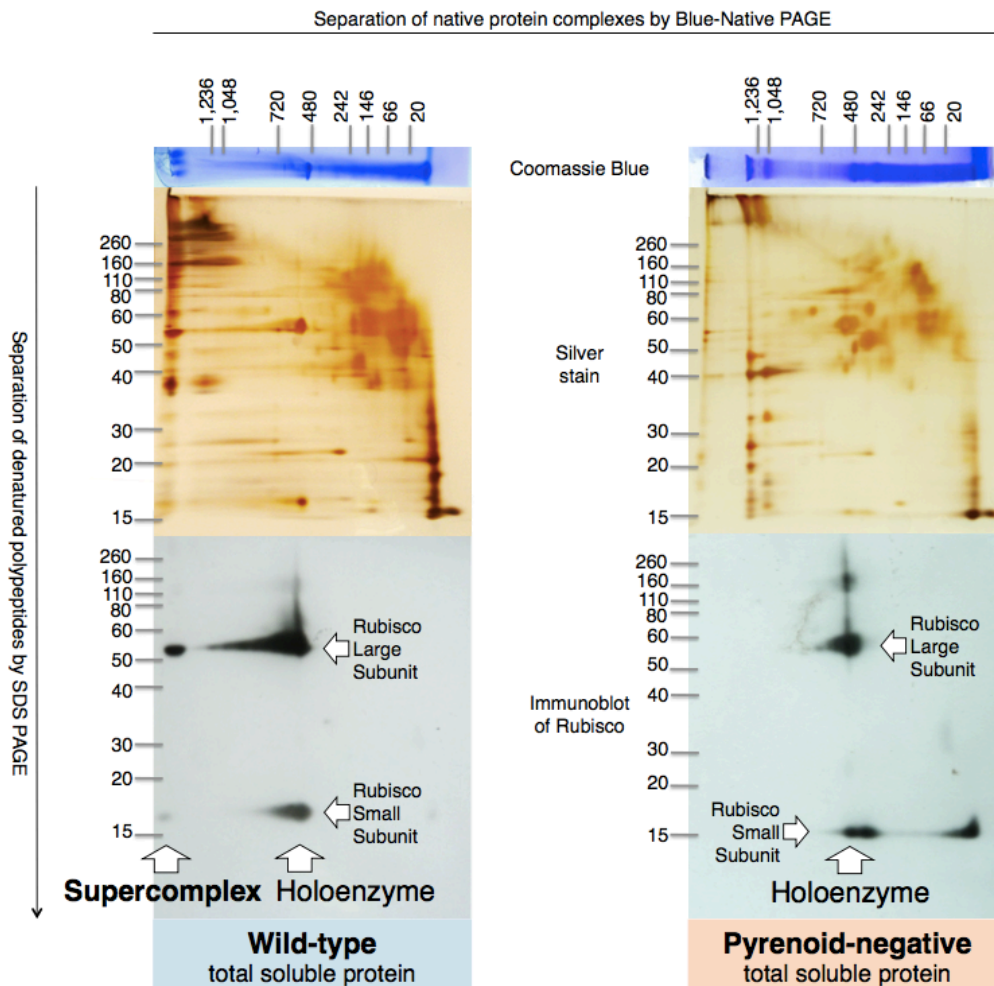


Fig. 4.1: Resolving high molecular weight complexes of Rubisco using BN-PAGE in a pilot experiment.

WT strain 2137 is compared to a *pyr*⁻ strain expressing *Spinacia oleracea* *RBCS*.

4.3.1 Higher order complexes containing Rubisco can be resolved via BN-PAGE

In the 1st dimension, the majority of Rubisco is present in a complex of ~500 kDa in both samples. At a theoretical weight of 14.7 kDa, the *Spinacia oleracea* SSU is slightly smaller than the *Chlamydomonas* counterpart of 16.3 kDa (Genkov et al., 2010). As a result, the Rubisco holoenzyme band travels at a larger molecular weight in the 1st dimension in WT than in pyr-. Rubisco subunits individually show molecular weights of ~55 kDa for the LSU, ~17 kDa for WT SSU and ~15 kDa for pyr- SSU in the 2nd dimension separation. In WT, the Western signal of the large subunit shows a high molecular weight tail, as well as a discrete spot to the very left labelled as “Supercomplex”, both of which are absent from pyr-. Pyr- shows a second SSU spot on the far right, traveling at the buffer front of the 1st dimension at <20kDa.

4.3.2 BN-PAGE complex profile is highly reproducible

Fig. 4.2 demonstrates the high reproducibility of 1st dimension gels and associated Rubisco Western blots in seven representative experiments using total soluble WT protein. The major feature seen in Western blots is a dark band travelling just above the 480 kDa marker, corresponding to a conspicuous band in the centre of each Coomassie gel. Rather than a discrete band such as in Fig. 4.2b, this ~500 kDa Western band shows in most replicates some diminishing straining towards higher molecular weights, hereafter referred to as high molecular weight tail, visible most clearly in Fig. 4.2 a&e and to a lesser extent in the remaining replicates. Fig. 4.2 b&d-f also show a second Rubisco band just below the 66 kDa marker. Equivalent gels for pyr- (Appendix 8.21) and positive control strains (Appendix 8.20) are shown in the appendices. Some gels also show faint labelling at ~720 kDa (Fig. 4.2 a&e&g, Appendix 8.20 a&e&g, Appendix 8.21 b&e&g).

After establishing the reproducibility of the soluble protein complex profile in 1st dimension BN-PAGE between experiments (Fig. 4.2, Appendix 8.21) and across cell lysis methods (Appendix 8.22), three of the replicates (Fig. 4.2 e-g) were analysed further via 2nd dimension SDS-PAGE and mass spectrometry of specific bands. Fig. 4.3 shows 2nd dimension gels and westerns of these three replicates. Like the 1st dimension strips, the 2D gels show a highly reproducible pattern. Each protein complex that was present in the 1st dimension strip is separated into individual polypeptide components.

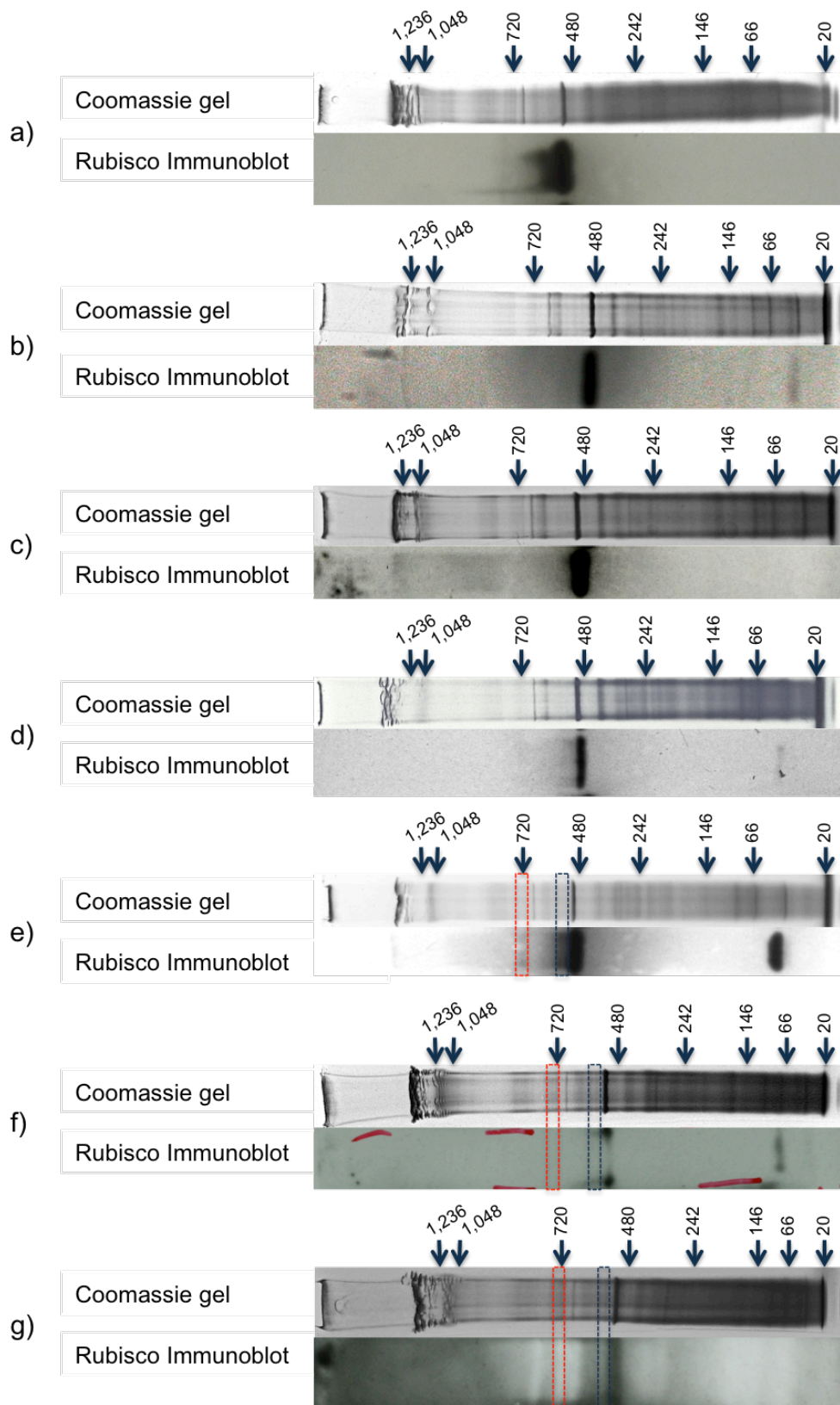


Fig. 4.2: BN-PAGE 1st dimension profile is highly reproducible.

Shown are Coomassie stained gel strips and Rubisco Westerns for WT strain WTint1,2 expressing *Chlamydomonas* *RBCS1*. Bands highlighted in red and blue boxes were cut out for further analysis via mass spectrometry.

As a result, proteins of different sizes that had been associated in a single complex line up along the vertical axis, whereas lines appearing along the horizontal axis can be informative about the involvement of a single protein in multiple complexes (Kügler et al., 1997). Proteins that do not participate in any complex travel at the same molecular weight in both the 1st and the 2nd dimension and give rise to the hyperbolic silver stain pattern towards the right of 2nd dimension gels.

2nd dimension Westerns of Fig. 4.3 predictively resolve most Rubisco at a complex size of ~500 kDa horizontally along the 1st dimension, and subunit sizes of ~55 kDa and <20 kDa vertically along the 2nd dimension. The large subunit shows a horizontal high molecular weight tail. This high molecular weight tail of the LSU in the 2D Western is consistent with the high molecular weight tail of the ~500 kDa band observed in 1D Westerns (Fig. 4.2, Fig. 4.3). On the other hand, the 1D Rubisco band close to the 66 kDa marker (Fig. 4.2 b&d-f, Fig. 4.3 a&b), the size of which suggests the labelled entity could be dissociated LSU, does not correspond to any labelling on the 2D Westerns.

Salient features of the LSU high molecular weight tail can be made out as points where the labelling intensity increases in a stepwise fashion, appearing as a minor shoulder of the tail at ~720 kDa and a major shoulder at ~600 kDa complex size. At a native complex size of ~720 kDa there is also a discrete spot formed by a ~60 kDa peptide labelled by the Rubisco antibody.

The part of the 2nd dimension gel corresponding to the ~720 kDa shoulder, highlighted in red in Fig. 4.3, contains a large discrete spot corresponding to the ~60 kDa immuno-labelled protein. In addition, there is a major band at ~40 kDa and minor bands at ~70 kDa, ~50 kDa and ~25 kDa as well as a band connecting to the Rubisco large subunit spot at ~55 kDa.

The region of the 2nd dimension gel that corresponds to the ~600 kDa shoulder, highlighted in blue in Fig. 4.3, contains a wide band upwards of ~80 kDa, a tail from the Rubisco LSU at ~55 kDa, a weak band at ~50 kDa, a second major band at ~40kDa, a somewhat diffuse band at ~25 kDa and a smear near the buffer front <20 kDa.

4.3.3 Features of interest are revealed by comparison with negative controls

Equivalent gels and Westerns analysing pyr- protein (Fig. 4.4) show the same major features as seen for WT. The most striking difference is the presence of a low molecular weight tail for the Rubisco large subunit in 2nd dimension Westerns. As in Fig. 4.1, pyr- SSU also shows a 2nd spot on the far right corresponding to the 1st dimension buffer front (Fig. 4.4b).

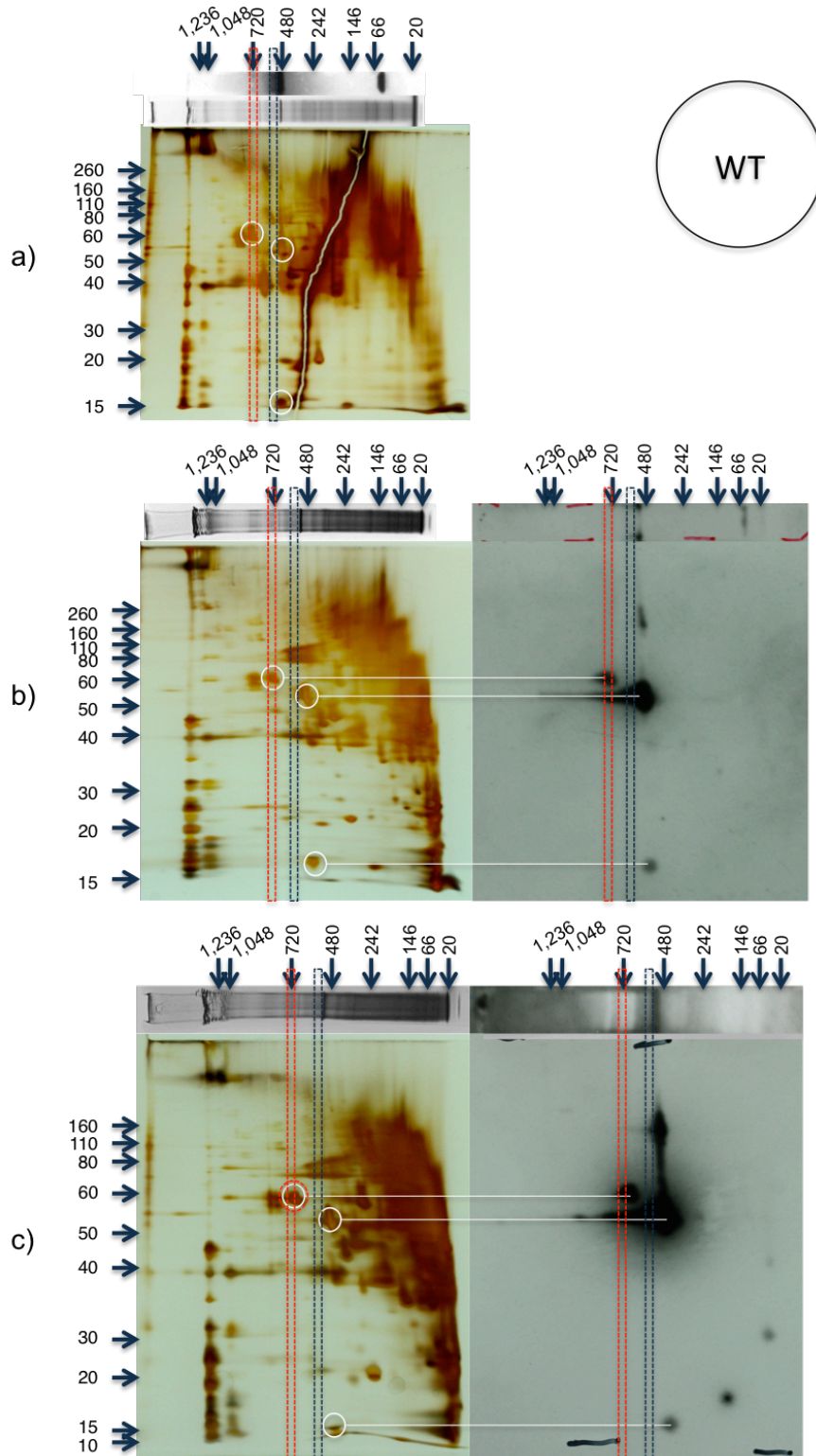


Fig. 4.3: BN-PAGE 2nd dimension profile is highly reproducible.

Coomassie-stained 1st dimension gel strips are depicted above silver stained 2nd dimension gels, each separating soluble protein extracted from WT (strain WTint1,2). Corresponding 1st and 2nd dimension Rubisco Western Blots are shown to the right of the gels, except for (a) where a 1D Western is shown above the 1D gel strip. White circles highlight parts of gels corresponding to major Western features. 1D Bands highlighted in red and blue boxes, and the 2D spot highlighted in a red circle, were cut out for further analysis via LC/MS-MS.

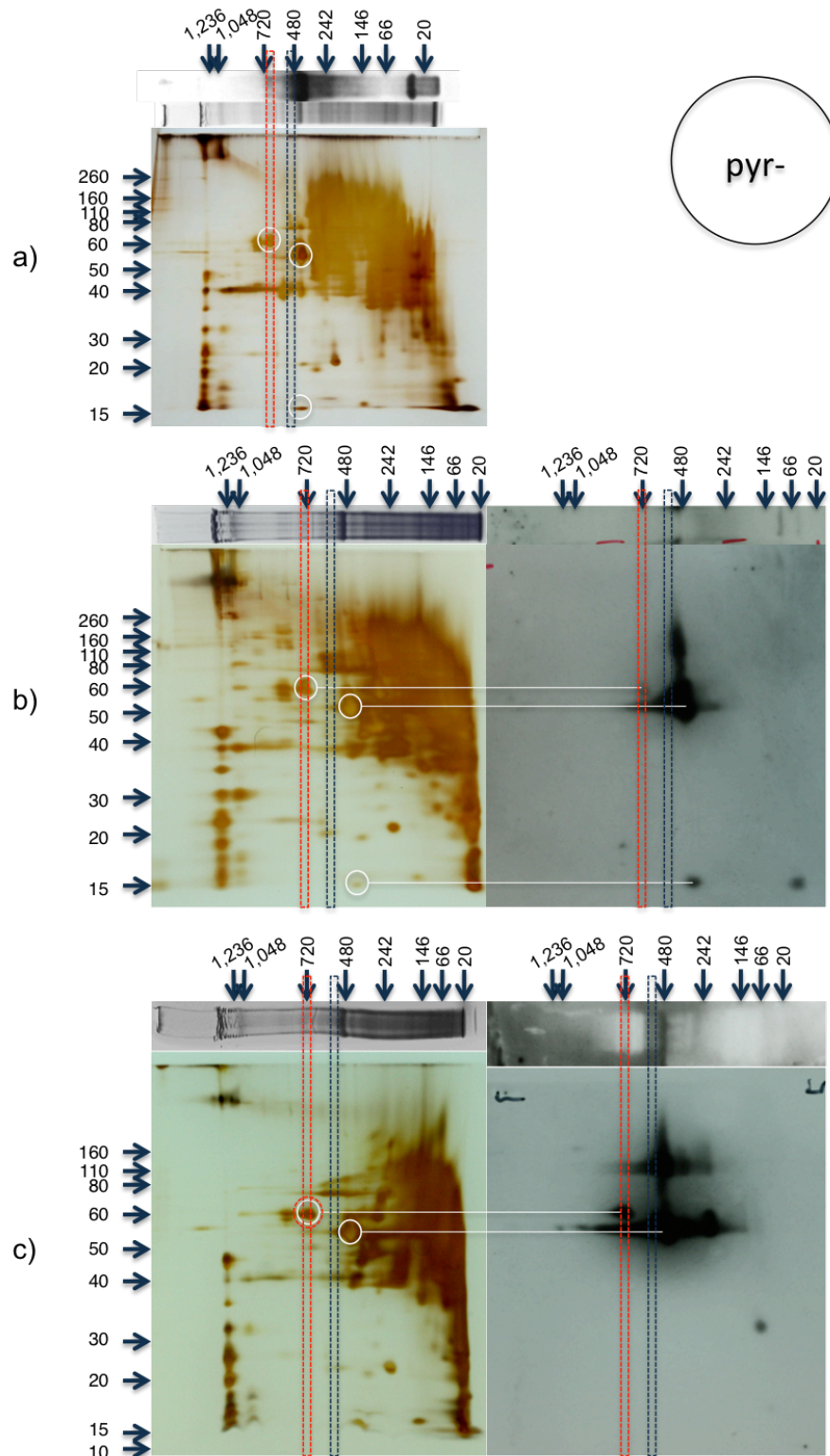


Fig. 4.4: pyr- shows a similar BN-PAGE pattern as WT.

Coomassie-stained 1st dimension gel strips are depicted above silver stained 2nd dimension gels, each separating soluble protein extracted from pyr- (*Spinacia oleracea* SSU-expressing line). Corresponding 1st and 2nd dimension Rubisco Western Blots are shown to the right of the gels, except for (a) where a 1D Western is shown above the 1D gel strip). White circles highlight parts of gels corresponding to major Western features. 1D Bands highlighted in red and blue boxes, and the 2D spot highlighted in a red circle, were cut out for further analysis via LC-MS/MS.

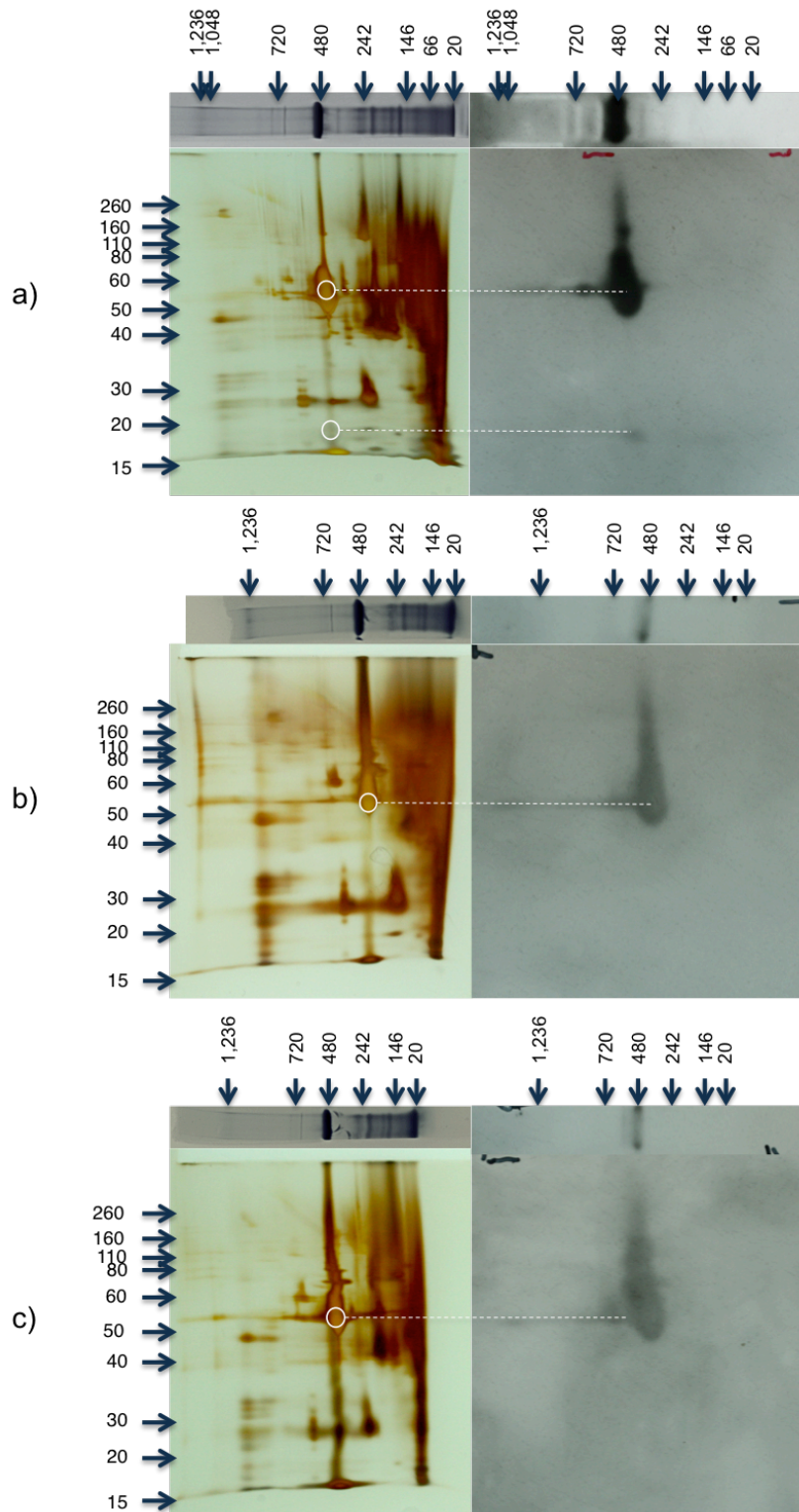


Fig. 4.5: Spinach leaf protein extract shows a different BN-PAGE profile with highly reduced Rubisco higher order complexes.

Coomassie-stained 1st dimension gel strips are depicted above silver stained 2nd dimension gels, each separating soluble protein extracted from spinach leaves. Corresponding 1st and 2nd dimension Rubisco Western Blots are shown to the right of the gels. White circles highlight parts of gels corresponding to major Western features.

The large subunit high molecular weight tail and the ~60 kDa subunit of the ~720 kDa complex are also labelled, although with somewhat lower intensity than in WT.

Protein extracted from spinach leaves on the other hand shows a very different overall BN-PAGE profile (Fig. 4.5). Rubisco comprises a much larger fraction of total soluble protein, reflected in a wider band at ~500 kDa. Despite this higher abundance of Rubisco, only a highly reduced high molecular weight tail is seen for the large subunit, and no labelling of any 60 kDa polypeptide could be observed.

4.3.4 Mass spectrometry identifies chaperonin 60 as the 60 kDa element of 720 kDa Rubisco-complex

For further insight into the protein composition of BN-PAGE features of interest, gel spots were submitted to LC/MS-MS mass spectrometric analysis. In the following figures, mass spectrometry data is displayed by comparing protein abundances in WT on the x-axis against pyr- on the y-axis. LC/MS-MS detection is semi-quantitative, with the exponentially modified Protein Abundance Index (*emPAI*) being one of the most reliable proxies for quantitative protein abundance assessment (Ishihama et al., 2005).

Briefly, the *emPAI* value corrects the number of identified peptides by the number of identifiable peptides for a given protein, which depends on the digestion method (here: trypsin) and the size of the protein: larger proteins result in more peptides. To minimize the effect of experimental error accumulating during sample preparation, measured *emPAI* values for each protein were normalized by the sum of all *emPAI* values in an experiment, thus reporting individual protein abundances as a percentage of total measured protein content (Ishihama et al., 2005) within a sample (denoted % *emPAI*).

To establish the identity of the *Chlamydomonas*-specific 60 kDa species immuno-labelled as Rubisco, spots (labelled with red circles) from one 2nd dimension WT gel (Fig. 4.3c) and the corresponding pyr- gel (Fig. 4.4c) were submitted to mass spectrometry. Fig. 4.6 shows the abundances of the 183 detected proteins. A number of proteins were detected only in WT or only in pyr- at <0.1% of total protein, appearing parallel to either axis on the plot below the -1 marks. The 77 proteins shared between both samples show a linear relationship close to a 1:1 correlation, which means that pyr- protein abundances are very similar to WT. Over 97% of total protein in each sample is made up of the four isoforms of chaperonin 60 (in decreasing order of abundance: chaperonin 60C / Cre06.g309100.t1.2, chaperonin 60B2 / Cre07.g339150.t1.1, chaperonin 60B1 / Cre17.g741450.t1.2, chaperonin 60A /

Cre04.g231222.t1.1). Other proteins form only minor fractions of <1% total protein each, including Rubisco LSU (gi|41179049).

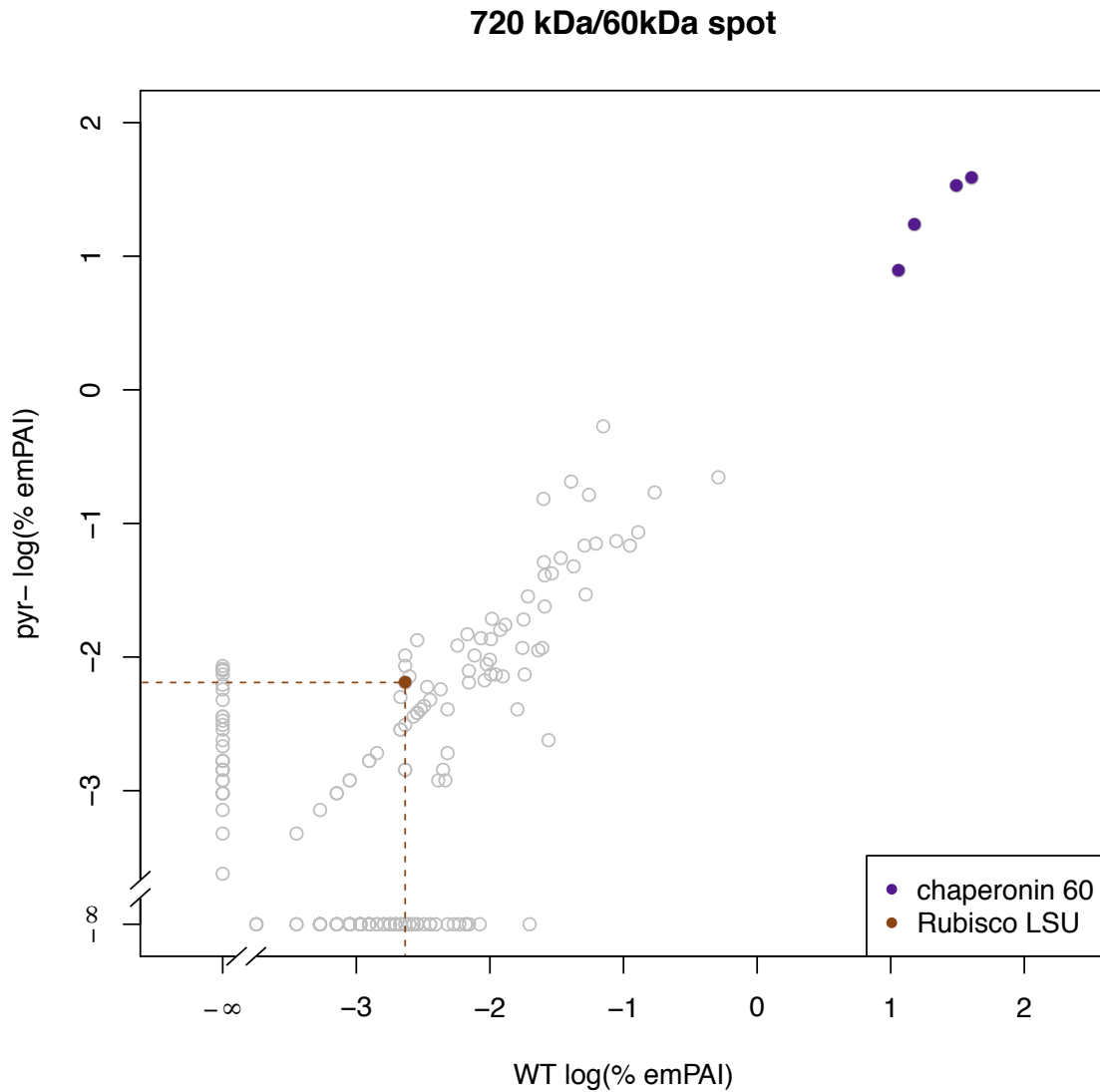


Fig. 4.6: the 720kDa/60kDa spot contains chaperonin 60, a protein involved in Rubisco holoenzyme assembly.

Abundances of all detected proteins are shown for WT and pyr- samples, expressed as base 10 logarithm of the percentage of total protein content within a sample based on *emPAI* values. Rubisco LSU is highlighted in brown.

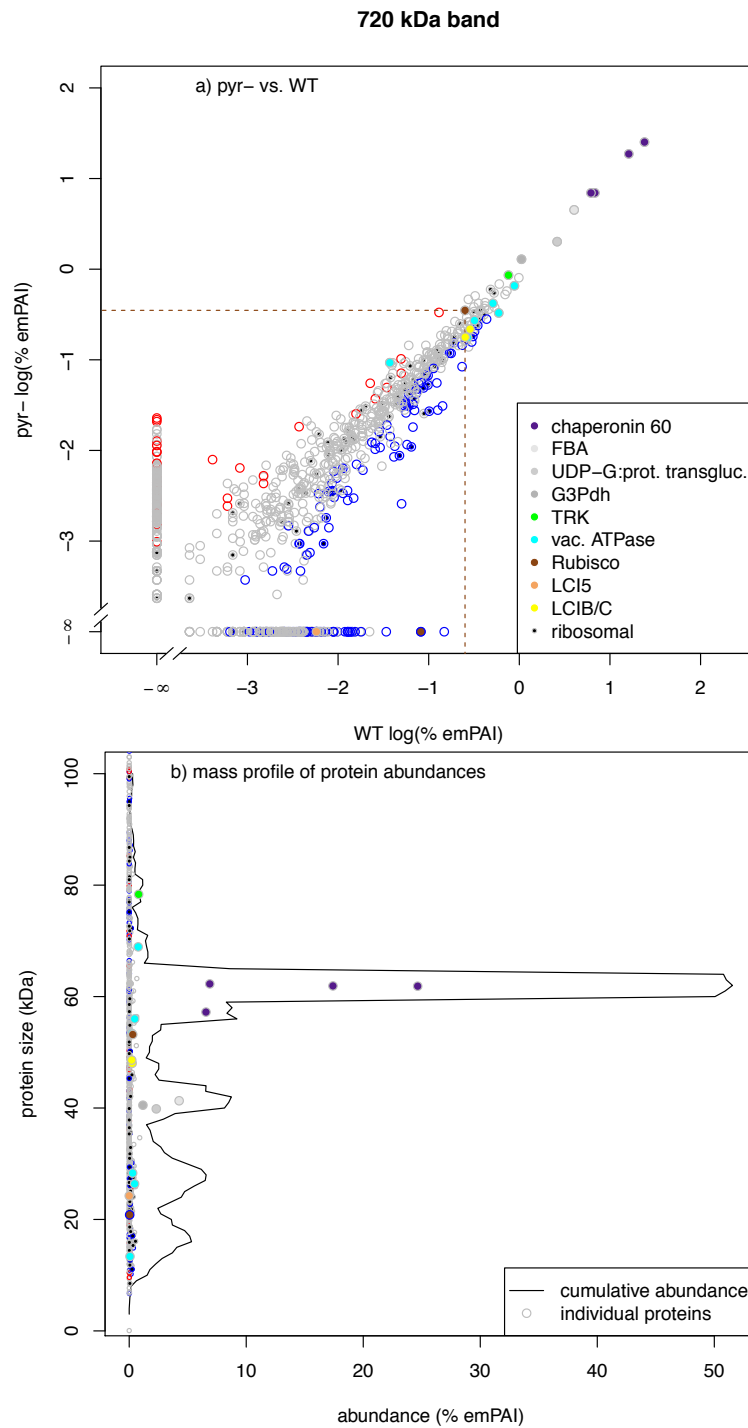


Fig. 4.7: Besides chaperonin 60, the 720 kDa band contains complexes of CBC components and vacuolar ATPase.

Graph (a) shows average abundances of all detected proteins in pyr- compared to WT across three replicates each, as base 10 logarithm of % *emPAI*. Rubisco LSU is highlighted in brown. Proteins significantly more abundant in WT are shown as blue, those up in pyr- as red circles. Graph (b) shows protein abundances averaged across pyr- and WT, plotted against molecular size for individual proteins as well as cumulative over 5 kDa bins.

4.3.5 The major proteins within the 720 kDa band are equally abundant in WT and pyr-

A complex of ~720 kDa cross-reacts with Rubisco antibody in several 1st dimension westerns blots (Fig. 4.2 a&e&g, Appendix 8.20 a&e&g, Appendix 8.21 a&e&g) and generates a minor shoulder in the 2nd dimension Western LSU high-molecular weight tail (Fig. 4.3) as well as a ~60 kDa spot containing chaperonin 60 (Fig. 4.6).

Rubisco labelling at ~720 kDa seems less pronounced in pyr- 2D westerns (Fig. 4.4). Based on these findings, the ~720 kDa band was selected as an interesting feature of the BN-PAGE profile that could potentially be informative about Rubisco interactions underlying pyrenoid formation. As such, ~720 kDa bands were cut out from three replicate 1D gels of WT and pyr- (highlighted in red in Fig. 4.2 e-g, Fig. 4.3 for WT and Appendix 8.21 e-g, Fig. 4.4 for pyr-) and submitted to mass spectrometry, with the aim of establishing whether certain proteins appear specifically in WT.

In Fig. 4.7a, abundances of all detected proteins are compared between WT and pyr-. Of the 1,080 proteins detected, 557 are shared between WT and pyr-. Most of these shared proteins show similar abundances in the two strains, forming a diagonal point cloud that depicts a 1:1 correspondence. In contrast to the data shown in Fig. 4.6, three replicates from WT and pyr- each form the basis for Fig. 4.7, allowing for statistical analysis. Differentially abundant proteins are mostly low abundance proteins, in combination accounting for only ~5% of total protein. Similarly, proteins that were only ever detected in one of the two strains, depicted as forming lines parallel to the axes in the plot clustering at $\log(0) = -\infty$, are at $\leq 10^{-1}$ % *emPAI* mostly of low abundance only.

At such low abundances, LC/MS-MS detection can become unreliable, meaning that some of the differences observed between WT and pyr- may be artefacts. That these low abundance proteins may still be biologically meaningful, however, is suggested by the fact that Rubisco itself is present at fairly low abundance: The LSU is at $\sim 10^{-0.5}$ % *emPAI* equally abundant in WT and pyr-, the *Chlamydomonas* SSU (Cre02.g120100.t1.2) is even less abundant at $10^{-1.1}$ % *emPAI*, and is only present in WT consistent with the fact that pyr- expresses *Spinacia oleracea* RBCS and lacks the *Chlamydomonas* SSU. It is therefore interesting to note that the pyrenoid linker candidate LCI5 (Cre10.g436550.t1.2) is among the proteins only present in WT, albeit at a low abundance of $10^{-2.2}$ % *emPAI*.

The majority of detected protein content, however, is equally abundant in WT and pyr-. Approximately 55.5% of total protein in both strains is made up exclusively of the four

Chapter 4: A Rubisco interactome provides insight into the mechanism of pyrenoid assembly

isoforms of known Rubisco interactor chaperonin 60, which is therefore the major contributor to the ~720 kDa band. CBC cycle enzymes fructose-1,6-bisphosphate aldolase (FBA / aldolase / Cre05.g234550; 4.3 % *emPAI*), glyceraldehyde-3-Phosphate dehydrogenase (G3PDH / Cre01.g010900.t1.2; 1.2 % *emPAI*) and transketolase (TRK / Cre02.g080200.t1.2; 0.8 % *emPAI*) form a second high abundance fraction potentially relevant as Rubisco interaction partners. Further high abundance components shared between WT and *pyr*- less obviously connected to Rubisco are UDP-Glucose protein transglucosylase (Cre13.g565800.t1.2), accounting for 2.3%, and vacuolar ATPase subunits, jointly making up 2.3% also. Of lower abundance, but interesting as known CCM-candidates, are LCIB (Cre10.g452800.t1.2) and LCIC (Cre06.g307500.t1.1), which share a similar abundance and an equal presence in WT and *pyr*- with Rubisco LSU.

In order to be able to compare the mass spectrometry data with the 2nd dimension gel profile of the ~720 kDa band (highlighted in red Fig. 4.3 and Fig. 4.4), protein abundances were plotted against molecular weight in Fig. 4.7b. Given the high similarity of WT and *pyr*-, protein abundances were averaged across both strains for the purposes of Fig. 4.7b. Polypeptide size in kDa was plotted on the vertical axis to give maximal comparability with 2nd dimension gels that separate polypeptides vertically. Since silver staining of SDS-gels indicates the total amount of protein in a particular part of gel independent of how many different proteins contribute, individual protein abundances were summed over 5 kDa moving bins to generate a total protein profile for direct comparison with the gels (Fig. 4.7b black line). With peaks at ~80, ~70, ~60, ~50, ~40, ~25 and <20 kDa, the distribution of protein abundances in the mass spectrometry data is consistent with the band pattern of 2nd dimension gels at ~720 kDa complex size (highlighted in red Fig. 4.3 and Fig. 4.4).

Fig. 4.7b. also shows individual protein abundances, which were plotted in the same graph to make the main contributors of each peak easily identifiable. Major contributing factors of the two minor peaks at ~70 kDa and ~80 kDa are vacuolar ATPase subunit A and TRK, respectively. The highest peak at ~60 kDa is composed of the four chaperonin 60 subunits. At ~50 kDa, only a minor peak could be observed, which includes LCIB and LCIC. The second highest peak at ~40 kDa can be attributed jointly to FBA, G3PDH and UDP-Glucose protein transglucosylase. The two peaks at ~25 and <20 kDa do not contain a single main contributing factor but instead are composed of many low abundance proteins, with LC15 contributing to the ~25 kDa band.

4.3.6 The 600 kDa band contains differentially abundant proteins of high abundance

In addition to the ~720 kDa band, the band at ~600 kDa was selected as potentially informative about Rubisco interactions underlying pyrenoid formation based on the presence of a major shoulder in the LSU high molecular weight tail more pronounced in WT (highlighted in blue in Fig. 4.3 and Fig. 4.4). Just slightly heavier than a holoenzyme travelling in isolation, the ~600 kDa band could be informative about a small linker protein remaining attached to Rubisco during migration in the BN-PAGE. Fig. 4.8 shows the results of analysing the ~600 kDa bands cut out of the 1st dimension gel slices by mass spectrometry.

Abundances of the 1,022 detected proteins are compared between WT and pyr- in Fig. 4.8a. The 569 proteins shared between WT and pyr- show good correlation of abundances, indicating that the majority of complexes are equally present in both strains, like in the ~720 kDa band. Three out of the four highest abundance components are not significantly different between WT and pyr-, being FBA (23.4 % *emPAI*), Rubisco LSU (4.9 % *emPAI*) and G3PDH (3.8 % *emPAI*), all three of which were also present at lower abundances in the ~720 kDa band.

In contrast to the ~720 kDa band, differential abundance is seen not only for low abundance proteins: highly abundant TRK is among the 87 proteins significantly more abundant in pyr- (WT: 3.4 % *emPAI*, pyr-: 6.5 % *emPAI*), as is the high abundance glutamine synthetase (WT: 1.2 % *emPAI*, pyr-: 1.9 % *emPAI*). Rubisco LSU and TRK are so close together that the points overlap.

The 58 proteins more abundant in WT include CCM-candidate LCIC (WT: 1.4 % *emPAI*, pyr-: 0.75 % *emPAI*) and the *Chlamydomonas* SSU (WT: 0.8 % *emPAI*, pyr-: 0.06 % *emPAI*). As in the ~720 kDa band, candidate linker protein LC15 was detected only in WT (0.06 % *emPAI*).

The protein size profile shown in the bottom graph of Fig. 4.8 shows 6 major peaks corresponding to the main silver stain features of the ~600 kDa slice in Fig. 4.3 and Fig. 4.4. The ~80 kDa peak is mostly composed of TRK. Rubisco LSU is the main contributor to the ~55 kDa peak. There is a peak around 50 kDa to which LCIB and LCIC contribute. The ~40 kDa peak is composed jointly of FBA, G3PDH, and glutamine synthetase versions. The two peaks either side of 20 kDa lack major components and instead are composed of a large number of low abundance proteins, including the majority of detected ribosomal proteins.

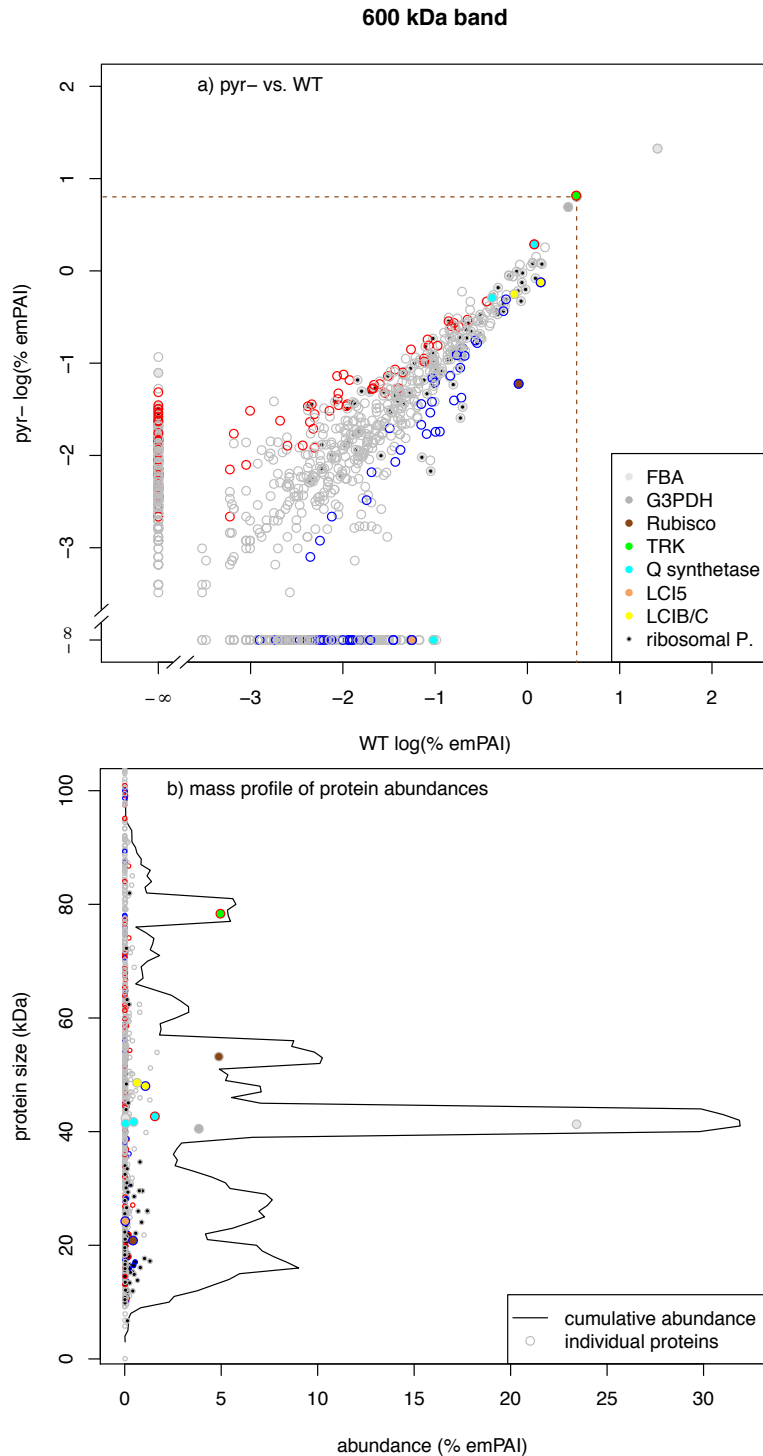


Fig. 4.8: The 600 kDa band contains abundant Rubisco.

Graph (a) shows average abundances of all detected proteins in pyr- compared to WT across three replicates each, as base 10 logarithm of % *emPAI*. Rubisco LSU is highlighted in brown. Proteins significantly more abundant in WT are shown as blue, and those up in pyr- as red circles. Graph (b) shows protein abundances averaged across pyr- and WT, plotted against molecular size for individual proteins as well as cumulative over 5 kDa moving bins.

4.3.7 Mass spectrometric analysis of co-IP experiments establishes a Rubisco interactome

Complementing BN-PAGE, co-IP (Heide et al., 2009; Simeoni et al., 2013) was used as a separate and independent way to investigate Rubisco protein interactions with the aim of identifying interaction partners involved in pyrenoid formation. In co-IP, soluble protein extract is passed through a column, where antibodies coated on beads precipitate a protein of interest, in this case Rubisco. Proteins that bind to Rubisco will be retained whilst the remainder of the extract is washed out. The identity of the putative Rubisco interaction partners retained in this way was then established via LC-MS/MS. In order to gain maximal insight into the physiological role of the different proteins, the effect of growth at 5% CO₂ repressing the CCM was investigated in addition to probing WT and pyr- grown at air. As a result, the Rubisco interactome is compared between four conditions based on three replicate co-IP experiments for each condition: WT/air, WT 5% CO₂, pyr-/air and pyr- 5% CO₂.

4.3.7.1 Normalisation of the data by total protein content minimizes experimental error and generates a good basis for quantitative comparisons

Given that the analytical approach is based on identifying quantitative differences in abundances of individual proteins between conditions, it was imperative to minimize experimental error between replicates in the absence of experimental treatments to make quantitation more intrinsically reliable (Ong and Mann, 2005; Heide et al., 2009; Mühlhaus et al., 2011). For this purpose, *emPAI* values (Ishihama et al., 2005) were used as the most reliable proxy for protein abundances based on available mass spectrometry data. A major potential source of error was the fact that total protein concentration differed between co-IP experiments owing to technical inaccuracies of the antibody and concentration columns used (see Materials and Methods section 4.2.7 for details).

Two ways of normalizing *emPAI* data were investigated to see whether this error arising from differences in total protein concentration could, at least partially, be accounted for *in silico* (Fig. 4.9a). Firstly, individual protein abundances were normalized as percentage of total protein content detected within each experiment, giving % *emPAI* values that were already used for BN-PAGE mass spectrometry analysis. Alternatively, protein abundances were normalized by the abundance of Rubisco LSU detected in the same experiment, resulting in an indication of how much protein was present relative to Rubisco in each co-IP sample.

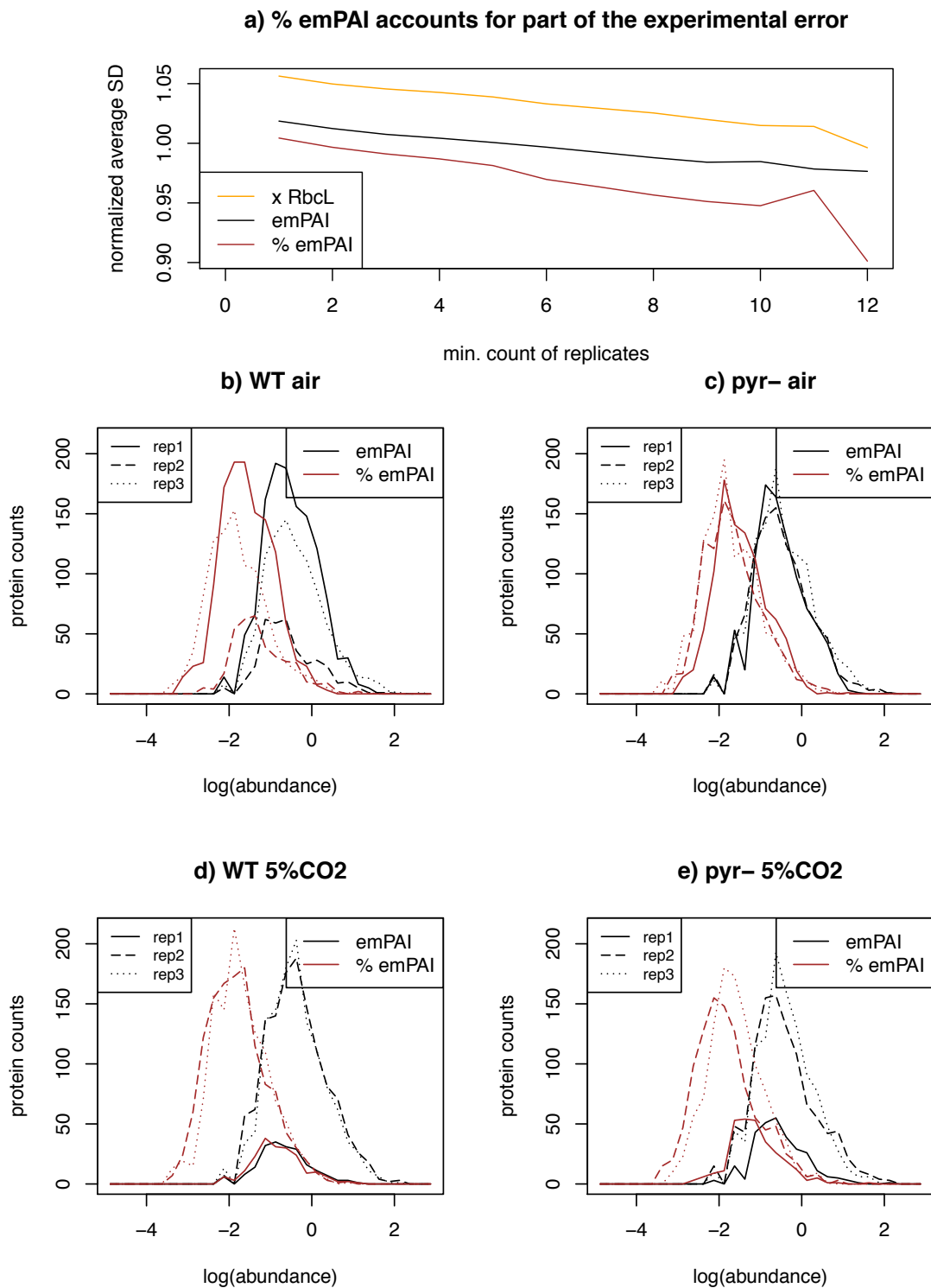


Fig. 4.9: Expressing co-IP data as % total protein based on *emPAI* values reduces error by accounting for differences in concentration.

In order to establish whether normalization by the abundance of Rubisco LSU (*xRbcL*) or total protein content (*% emPAI*) would minimize variation between replicates compared to raw abundance data (*emPAI*), average SD was investigated in (a) as function of how reliably proteins were detected. For the best normalization, the effect of on the distribution of protein abundance values between replicates was investigated further in (b)-(e) separately for each experimental condition.

In each case, the effect on the variation between replicates was taken as benchmark for whether or not the normalisation was accounting for experimental error. This variation between replicates is plotted on the y-axis in Fig. 4.9a as normalized average standard deviation (SD): SD was calculated for each of the 2,689 detected proteins in each of the four conditions across the three biological replicates. The resulting 10,756 SD values were averaged to yield a single number for each normalization. To account for the different ranges of values for each normalisation, average SD values were then normalized by the total average protein abundance across all proteins and all replicates of all conditions. The thus calculated normalized average SD serves as a measure of variation between replicates and a proxy for experimental error.

The x-axis of Fig. 4.9a depicts the effect on this error proxy of limiting the dataset to an ever more high-confidence subset of proteins. Not all 2,689 proteins were detected in all 12 co-IP experiments (conducted as three replicates in four experimental conditions): some proteins even only ever appeared in a single experiment. At a *minimum count of replicates* of 1, all 2,689 proteins are thus considered, whereas if only those proteins are taken into account that were consistently detected in all 12 experiments, the number of proteins shrinks to 57. The rationale for this consideration was that proteins that consistently appear are most likely to be true Rubisco interactors, whereas proteins that appear only in one or two experiments may be contaminants that had not sufficiently been washed out.

As shown in Fig. 4.9a, normalization by total protein content as % *emPAI* reduces the variation between replicates compared to raw *emPAI* values. The effect is particularly pronounced for proteins that were detected 12 times, i.e. in all replicates of each condition. Normalization by Rubisco LSU on the other hand leads to increased variation, possibly due to an inflation of the error associated with LSU detection with existing experimental error in the *emPAI* dataset.

Fig. 4.9 b-e show the effect of the % *emPAI* normalization on the distribution of protein abundances for each dataset. Each of the 12 co-IP experiments is presented as a histogram of protein abundances in four graphs comparing the three replicates of a particular experimental condition. Raw *emPAI* values (black lines) vary between 10^{-2} and 10^2 . Each sample contains a small number of high abundance proteins toward the right of the spectrum, and an increasing number of lower abundance proteins. Histogram peaks are aligned at an *emPAI* value of around $10^{-0.5}$, below which distributions show a rapid decline reflecting the detection limit of LC/MS-MS. This detection limit means that samples with a

low total protein concentration, such as WT/air replicate 2 and replicate 1 of WT and pyr- at 5% CO₂, show lower numbers of proteins at all abundances, but a histogram peak that is aligned at the same abundance as samples with a high protein concentration.

The effect of the % *emPAI* normalization (red lines) is to shift histograms such that it is no longer the histogram peaks that are aligned between replicates, but rather the high-abundance tail. Samples that are very similar in distribution of protein abundances even before normalisation, such as pyr-/air replicates in Fig. 4.9c, remain very similar in distribution after normalization. However, for samples that suffered from a low total protein concentration, such as replicate 1 of WT 5% CO₂ (Fig. 4.9d), the % *emPAI* normalisation means that highly abundant proteins are now recorded with similar abundance values as highly abundant proteins in the other replicates. In this way, the % *emPAI* normalisation is able to account for some of the experimental error between replicates that arises simply from differences in total protein concentration of co-IP samples.

A second effect of the normalisation is to shift the entire histogram profile to the left with most protein abundances now falling between 10¹ and 10⁻⁴. This effect results from the arbitrary choice of representing abundances as percentage of total protein content; for example if abundance had been recorded as ‰ *emPAI* instead of % *emPAI*, histograms would be shifted to the right by 1 point on the log₁₀ scale without any effect on the relative variation in abundance between proteins.

4.3.7.2 The Rubisco interaction profile is altered by the experimental treatments

As a first step towards understanding the interactome data, the effect of the experimental treatments on individual protein abundances was plotted out in Fig. 4.10. In direct analogy with BN-PAGE mass spectrometry data depiction, Fig. 4.10a shows protein abundances in pyr- plotted against WT. To present the % *emPAI* data in this way, protein abundances were averaged across air and 5% CO₂ replicates for each strain.

Most proteins cluster along the diagonal line of equivalence, indicating abundances are similar in pyr- and WT. Rubisco LSU, highlighted in brown, shows fairly high and equal abundance in pyr- and WT at ~0.3 % *emPAI*. The four most abundant proteins calmodulin (Cre03.g178150.t1.1; ~17 % *emPAI*), G-strand telomere binding protein 1 (Cre01.g032300.t1.2; ~14 % *emPAI*), eukaryotic translation elongation factor 1 α 1 (gi|159476938; ~11 % *emPAI*) and cytosolic ribosomal protein s29 (Cre08.g358556; ~9 % *emPAI*) are also equally present in WT and pyr-.

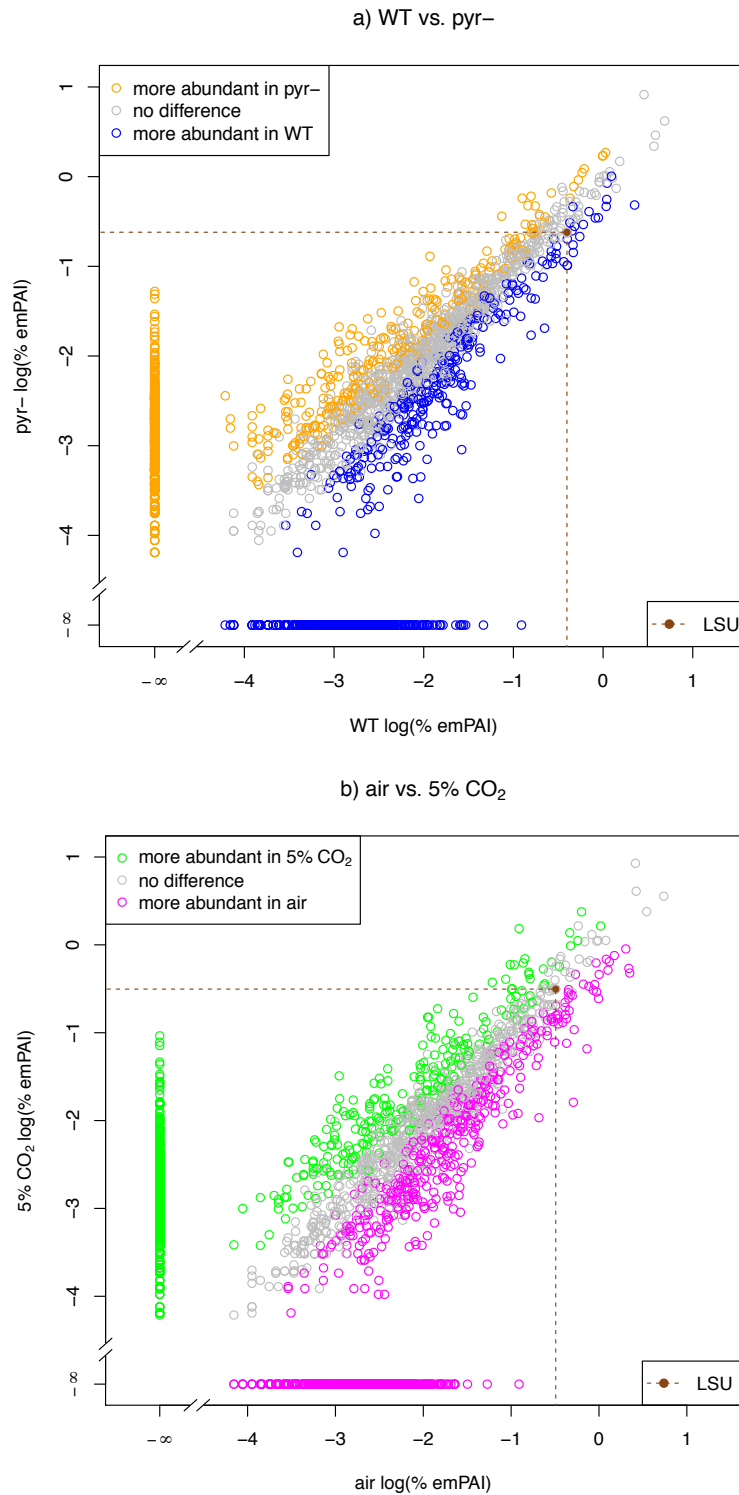


Fig. 4.10: Differences between strains and CO₂ treatments can inform candidate proteins involved in pyrenoid formation.

Base 10 logarithm of averages across CO₂ treatments are shown for WT and pyr- in (a), averages across strains for air and 5% CO₂ are shown in (b), with the position of Rubisco LSU highlighted. Significant differences were established using AIC-based model fitting with colour coding corresponding to Table 4.1 and Fig. 4.11 as $\circ = \text{orange}$, $\circ = \text{grey}$, $\circ = \text{blue}$ for (a) and $\circ = \text{green}$, $\circ = \text{grey}$, $\circ = \text{magenta}$ for (b).

Chapter 4: A Rubisco interactome provides insight into the mechanism of pyrenoid assembly

Statistically significant differences in abundance are present among low as well as high abundance proteins, as visible through the colour coding. Proteins that were completely absent from one of the two strains, on the other hand, are generally of low abundance, with the majority below 10^{-2} % *emPAI*.

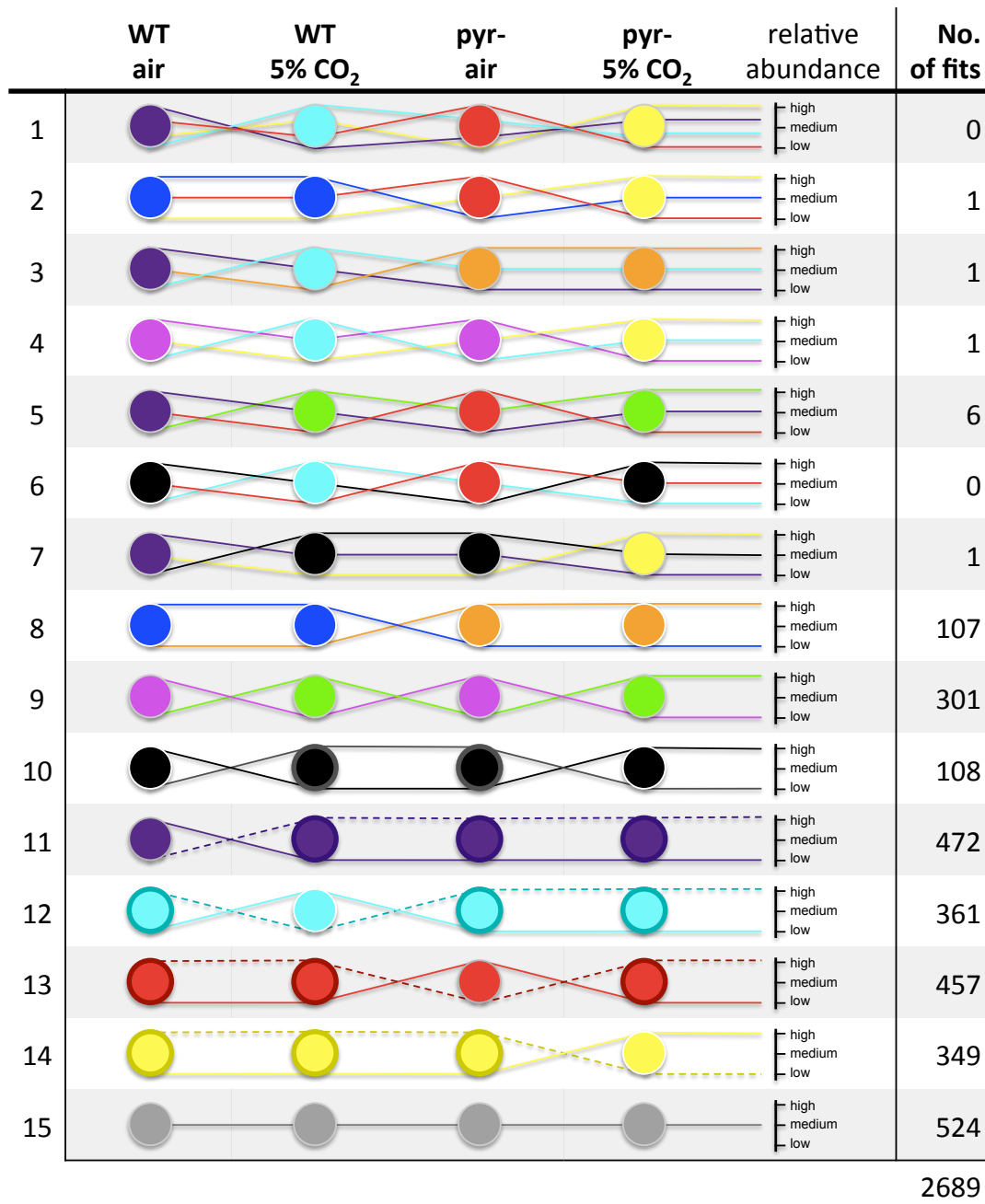
Fig. 4.10b shows an equivalent analysis of the differences between 5% CO₂ and air, for the purpose of which protein abundances were average across strains. The pattern is similar as in Fig. 4.10a: Generally, protein abundances are similar between air and 5% CO₂, with Rubisco LSU as well as the four most abundant proteins mentioned above showing no significant difference. At the same time, differences are present even among highly abundant proteins, whereas proteins that are completely absent from a particular CO₂ condition are of low abundance only. Log-log plots equivalent to Fig. 4.10 detailing all possible pairwise comparisons of the four experimental conditions confirm this same pattern (Appendix 8.25).

4.3.8 The interactome is responsive to experimental treatments

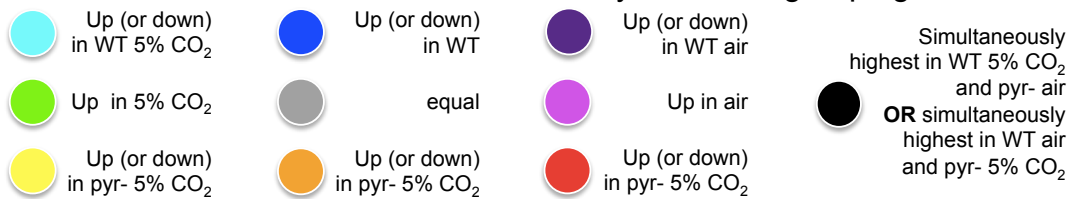
The abundance of any single protein may be different between conditions depending on CO₂ concentration, or strain, or a particular combination of the two. In order to capture the effect of the experimental treatments on the abundance of each individual protein, different statistical models were fit to the data (Table 4.1) and the model best supported by the data was determined using the Akaike Information Criterion or AIC (Akaike, 1974). By weighing the number of parameters against the goodness of fit, the use of the AIC allows selection of the simplest model that best describes the data. This approach represents a powerful statistical analysis which was used to identify for each protein in which set of conditions abundance was highest.

Each model describes the data as sets of conditions among which protein abundance is equal, but different from other conditions. For example, model 8 (Table 4.1) assumes that protein abundance is determined by pyrenoid phenotype, fitting a single parameter to WT/air and WT 5% CO₂ and a second parameter to pyr-/air and pyr- 5% CO₂. During the fitting, the two parameters will converge towards the average of all data within the two groups, thus reporting the average abundance in WT and pyr- respectively. If protein abundances are indeed similar within but different between strains, then this model will be better supported by the data than any of the other models, signified by a lower AIC. On the basis of this statistical framework, each protein was then sorted into a particular statistical grouping depending on which experimental condition was associated with the highest abundance.

Table 4.1: Models fit to co-IP data.



Parameters are colour coded by statistical grouping:



A statistical grouping is assigned based on the condition(s) where protein abundance is higher (or, if all else equal, lower) than in the other conditions.

The models describe protein abundances in the different experimental conditions (columns) as identical (same colour) or different (different colours) to each other. Depending on which condition or set of conditions has the highest abundance (represented by lines), a protein is attributed a particular statistical grouping (colour).

Chapter 4: A Rubisco interactome provides insight into the mechanism of pyrenoid assembly

In Table 4.1, levels of protein abundance are represented symbolically by lines, colour coded according to the statistical grouping that a particular pattern would result in. Thus for model 8, a protein would be classed as “up in WT” (blue) if the equal protein abundance in WT/air and WT 5% CO₂ was higher than the equal abundance in pyr- across CO₂ conditions (see Appendix 8.26).

A number of proteins were found to be equally abundant in three out of four conditions (models 11-14, Table 4.1), in which case the important piece of information was considered to be which condition differed for the purposes of colour coding. For example, a protein with equal abundance across WT and pyr-/air, but different in pyr- 5% CO₂ (model 14, Table 4.1) would be colour coded yellow, signifying that the condition with the most notable difference in abundance is pyr- 5% CO₂, irrespective of whether the abundance in this condition was higher (solid line) or lower (dashed line). In the latter case, the protein was attributed the statistical grouping of being “down in pyr- 5% CO₂” (yellow).

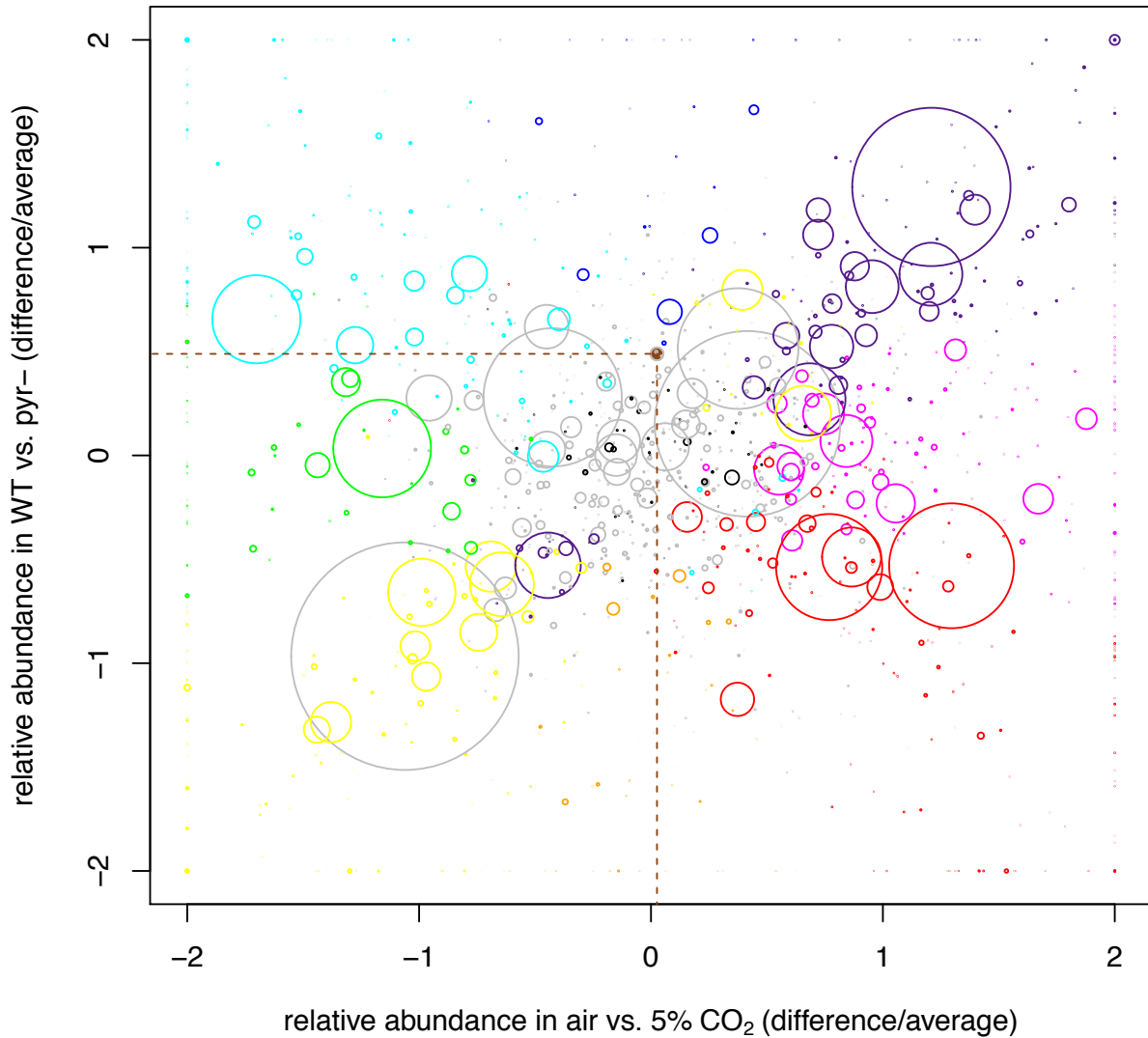
While models allowed up to four parameters to be fitted (models 1-7, Table 4.1), only 10 out of 2,689 were best described by three (models 2-7, Table 4.1) and none by four parameters (model 1, Table 4.1). For the majority of proteins, the fitting of two parameters thus determined the single most divisive difference between sets of similar abundances in the data (models 8-14, Table 4.1).

To be able to visualize this complexity of responses to experimental conditions, it was imperative to come up with a way of plotting the effect of strain and CO₂ simultaneously within the same graph. This was achieved through a relative abundance plot in Fig. 4.11. In this relative abundance plot, variation along the y-axis captures the differences in protein abundance across strains that was depicted as log-log plot in Fig. 4.10a.

For this purpose, relative abundance is calculated as the difference between WT and pyr-, normalized by the average across the two strains ($\frac{[WT]-[pyr-]}{[WT]+[pyr-]}$). Proteins that were only detected in one of the two strains thus appear at a relative abundance value of ± 2 , whereas a relative abundance ± 1 indicates that the difference between strains is as big as the average, i.e. a fold-change of 3. A relative abundance of 0 indicates exact equality between WT and pyr-. In the same way, the x-axis depicts variation with CO₂ condition.

By depicting differences across strain and CO₂ conditions simultaneously, statistical grouping as per Table 4.1 can be visualized effectively. Proteins can be affected by only one of the experimental treatments, i.e. they differ between strain but show no difference with

CO₂ concentrations (blue and orange), or differ between CO₂ conditions but show equal abundance across strains (green and magenta).



colour key:			size key:	
■ up (or down) in WT 5% CO ₂	■ up in WT	■ up (or down) in WT air	· 0.1	protein abundance relative to RbcL
■ up in 5% CO ₂	■ equal	■ up in air	· 0.25	
■ up (or down) in pyr- 5% CO ₂	■ up in pyr-	■ up (or down) in pyr- air	○ 1	
■ up in the diagonal WT 5%CO ₂ / pyr- air OR up in the diagonal WT air / pyr- 5%CO ₂			○ 4	
			○ 10	

Fig. 4.11: Experimental treatments resolve distinct protein behaviors in co-IP.

Axes show relative abundances as the difference in % *emPAI* divided by the average % *emPAI*. The circle size indicates protein abundance as an average across replicates of conditions where abundance is simultaneously highest according to the statistical grouping (indicated through colour coding). Rubisco LSU is highlighted in brown.

Alternatively, proteins can be most differentially abundant in a particular condition, e.g. be more abundant in WT/air than any of the other conditions (purple in top right quadrant), or be lowest in WT/air whilst equal among the other three conditions (purple in bottom left quadrant). Finally, proteins coloured black are equally abundant in WT/air and pyr- 5% CO₂ whilst at the same time more abundant than in the other two conditions, or vice versa most abundant at the same time in WT 5% CO₂ and pyr-/air.

In addition to relative abundance across conditions, the absolute abundance of each protein is of diagnostic importance, and is indicated by the size of the circle. Absolute abundance is calculated as an average across relevant conditions, for example if a protein is statistically significantly more abundant in air but equal across strains (magenta), then WT/air and pyr-/air replicates were averaged.

The vast majority of proteins were of low abundance and appear as background scatter. Only a small number of abundant (>0.1 % *emPAI*) proteins differ between WT and pyr-irrespective of CO₂ conditions (7 in WT: blue, 10 in pyr-: orange). A larger number of abundant proteins are responsive to CO₂ but equal across strains (20 in 5 % CO₂: green or 47 in air: magenta). Proteins differentially abundant in pyr- 5% CO₂ (yellow) or WT/air (purple) form a diagonal connecting the edges of the plot, indicating protein behaviour is uniquely affected by these conditions. By contrast, proteins most abundant in WT 5% CO₂ (cyan) stay below 1 on the y-axis, indicating that the CO₂-effect weighs more heavily than the effect of strain differences. Similarly, abundant pyr-/air (red) proteins are close to 0 on either axis.

4.3.9 Gene ontology informs a number of functional groups within the interactome

In order to distinguish those proteins that may be relevant for pyrenoid formation from factors that associate with Rubisco for other reasons, such as holoenzyme assembly or regulation, a functional analysis of the interactome was carried out on the basis of gene ontology annotations. Functional annotation was performed using the two separate online tools DAVID (Huang et al., 2009b) and Algal Functional Annotation Tool (Lopez et al., 2011). Both tools supply annotation terms based on a number of sources such as gene ontology, KEGG (Kanehisa et al., 2012) and mapman (Thimm et al., 2004) which were compiled into a list of annotations for each protein.

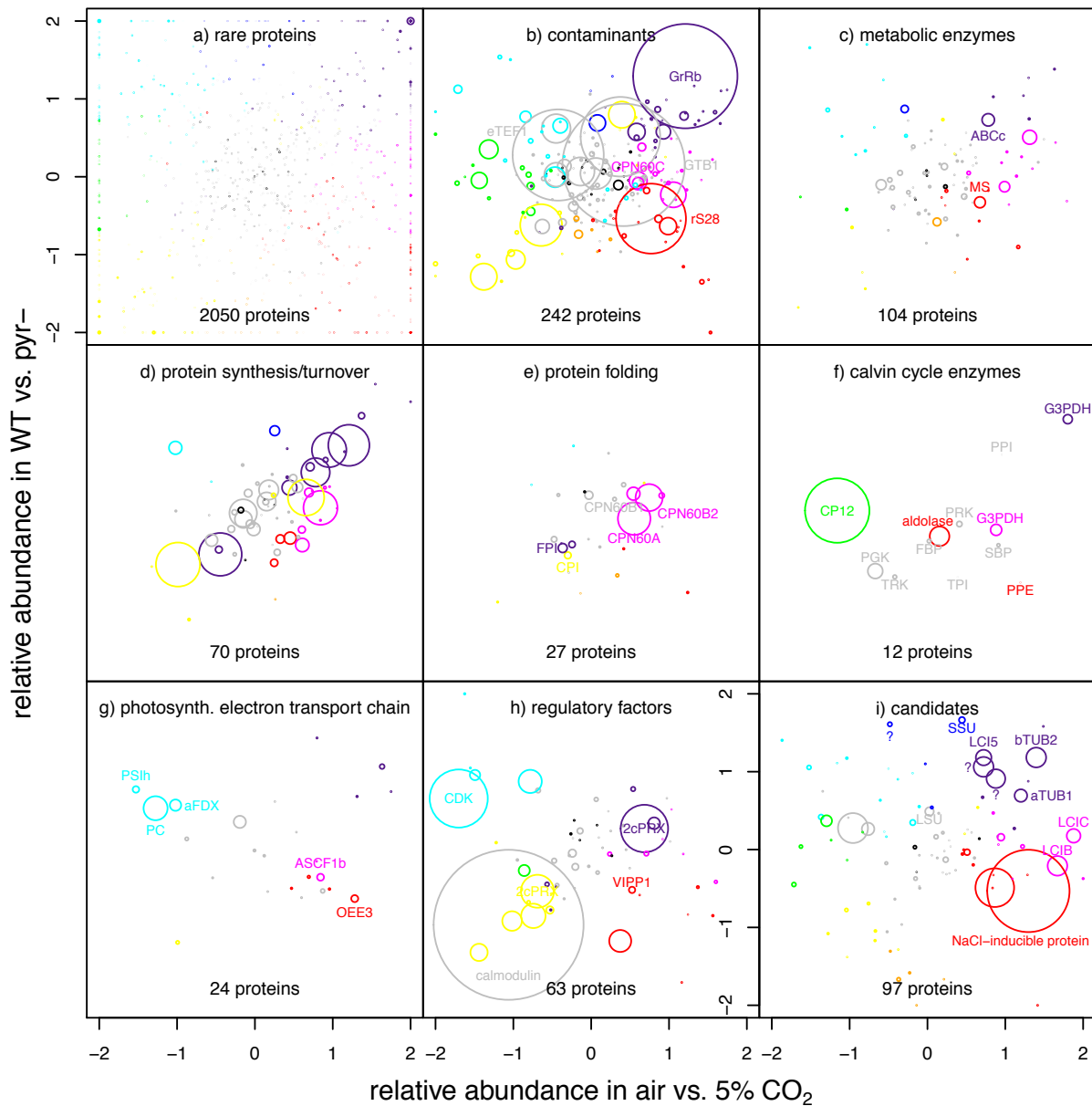


Fig. 4.12: The majority of the Rubisco interactome can be grouped into functional classes according to gene ontology annotation.

Low confidence proteins (a) are either detected rarely or of extremely low abundance. Proteins were classed as contaminants (b) if known to localize to a cellular compartment other than the chloroplast. Gene ontology annotation was used for functional assignment of classes (c)-(i). Colour coding denotes statistical grouping as per Table 4.1 and Fig. 4.11. Abbreviations: (b) GrRb = glycine rich RNA-binding protein, eTEF1 = eukaryotic translation elongation factor 1 α 1, CPN60 = chaperonin 60, GTB1 = G-strand telomere binding protein 1, rS28 = cytosolic ribosomal protein S28; (c) ABCc = acetyl-coA biotin carboxyl carrier, MS = malate synthase; (e) FPI = FKBP-type peptidyl-prolyl cis-trans isomerase, CPI = cyclophilin type peptidyl-prolyl cis-trans isomerase; (f) CP12 = calvin cycle protein CP12, PGK = phosphoglycerate kinase, G3PDH = glyceraldehyde 3-phosphate dehydrogenase, TPI = Triose phosphate isomerase, FBP = fructose-1,6-bisphosphate phosphatase, TRK = transketolase, SBP = sedoheptulose-1,7-bisphosphate phosphatase, PPI = pentose phosphate isomerase, PPE = pentose phosphate epimerase, PRK = phosphoribulokinase; (g) PSIIh = photosystem I subunit h, aFDX = apoferreredoxin,

Chapter 4: A Rubisco interactome provides insight into the mechanism of pyrenoid assembly

PC = plastocyanin, ASCF1b = ATP synthase CF1 α -subunit, OEE3 = oxygen evolving enhancer protein 3; (h) CDK = calmodulin-dependent serine/threonine kinase, 2cPRX = 2-cys peroxiredoxin, VIPP1 = vesicle inducing protein in plastids 1; (i) LSU = Rubisco large subunit, SSU = Rubisco small subunit, LCI = low CO₂ induced, bTUB2 = β -tubulin 2, aTUB1 = α -tubulin 1, ? = uncharacterized protein.

Proteins that were detected in only a small minority of replicates, or that were present at very low abundance were discarded as in the low confidence set (Fig. 4.12a). These proteins span the entirety of the plot. In particular, this set includes almost all of the proteins framing the edges, which indicates presence in only a subset of conditions. Based on functional annotation terms, high confidence proteins within the Rubisco interactome were then grouped into 8 functional classes (Fig. 4.12 b-i).

Proteins that were tagged with functional annotation terms indicating a localisation to cellular compartments other than the chloroplast (Fig. 4.12b) were classed as contaminants as they are unlikely to interact with Rubisco *in vivo*. Many proteins of this set are relatively abundant with 29 proteins that are more abundant than Rubisco, including G-strand telomere binding protein 1 (GTB1, largest grey circle) and a mitochondrial glycine rich RNA-binding protein (GrRb / Cre09.g392350.t1.2, largest purple circle) that is significantly most abundant in WT/air, where it accounts for 12 % of total protein content. Around 20% of the proteins classed as contaminants are involved in cytosolic protein synthesis according to annotation terms. Cytosolic protein synthesis machinery includes some of the most abundant apparent contaminants, such as eukaryotic translation elongation factor 1 α 1 (eTEF / gi|159476938, 2nd largest grey circle) and cytosolic ribosomal protein S28 (rS28 / Cre12.g510450.t1.2, largest red circle).

Metabolic enzymes (Fig. 4.12c) show low to medium abundances clustering in the centre of the plot, indicating invariance across experimental treatments. A number of factors are shifted to the right, however, being significantly more abundant in low CO₂ (e.g. lipid metabolic acetyl-coA biotin carboxyl carrier / ABCc / Cre01.g037850.t1.1, the largest purple circle, or carbohydrate metabolic malate synthase / MS / Cre03.g144807.t1.1, the largest red circle).

Proteins associated with gene ontology terms like “ribosome”, “translation” or “proteasome” were classed as involved in protein synthesis and turnover (Fig. 4.12d). Plastid localized protein synthesis and turnover factors cluster along the diagonal between WT/air and pyr-5% CO₂. The most abundant proteins of the set that are driving this behaviour are all plastid ribosomal proteins differentially expressed in WT/air (purple circles).

Protein folding factors (Fig. 4.12e) cluster mostly in the centre of the plot. Two of the four chaperonin 60 isomers (CPN60A and CPN60B2) are among the most abundant proteins of the set (largest purple circles) and significantly more abundant in air, a behaviour mirrored by the mitochondrial paralogue (CPN60C, Fig. 4.12b). The protein folding set also contains a large number of peptidyl-prolyl cis-trans isomerases, many of which are down in WT/air (e.g. FKBP-type isomerase FPI / Cre16.g675550.t1.2, largest purple circle) or up in pyr-/5% CO₂ (e.g. cyclophilin type isomerase CPI / Cre12.g495951.t1.1, largest yellow circle).

Out of 11 CBC enzymes (Fig. 4.12f), 9 are more abundant in pyr- on average, two of which are statistically grouped as up in pyr-/air including Aldolase (Cre05.g234550.t1.2) which is the most abundant member of the set. Enzymes close to Rubisco in the pathway are more abundant than those further away with phosphoglycerate kinase (PGK / Cre11.g467770.t1.1), glyceraldehyde 3-phosphate dehydrogenase (G3PDH / Cre01.g010900.t1.2) and Aldolase detected at up to twice the abundance of Rubisco LSU, and fructose-1,6-bisphosphatase (FBP / Cre12.g510650.t1.2), transketolase (TRK / Cre02.g080200.t1.2) and phosphoribulokinase (PRK / Cre12.g554800.t1.2) at about half the LSU abundance. CP12 (Cre08.g380250.t1.2) is present at a higher abundance than Rubisco in all conditions, but is ~4-fold more abundant in elevated CO₂ compared to air.

Elements of the pETC recovered in the Rubisco interactome lie across a diagonal between WT 5% CO₂ and pyr-/air (Fig. 4.12g). Variation with CO₂ is more pronounced than variation between strains, yet a clear influence of strain is visible. Elements up in pyr-/air include subunits of PSII (e.g. oxygen evolving enhancer protein 2 / OEE2 / Cre08.g372450.t1.2, the largest red circle) and ATP synthase (e.g. CF1 α -subunit / ASCF1b / gi|41179050). WT/5% CO₂ factors are PSI-associated elements plastocyanin (PC / Cre03.g182551.t1.2), apoferrredoxin (aFDDX / Cre14.g626700.t1.2) and PSI subunit H (PSIh / Cre07.g330250.t1.2).

Regulatory factors (Fig. 4.12h) show large variation between conditions and are particularly abundant in 5% CO₂. The two most abundant proteins calmodulin (largest grey circle) and a calmodulin-dependent serine/threonine kinase (CDK / Cre07.g327350.t1.2, largest cyan circle) are involved in Ca²⁺-dependent signalling. Redox factors appear as important group with the most abundant factors in WT/air (2cPRX / Cre02.g114600.t1.2, largest purple circle) and pyr-/5%CO₂ (2cPRX / Cre06.g257601.t1.2, largest yellow circle) both 2-cys peroxiredoxins, and further redoxins abundant in each of the four conditions. Other regulatory proteins include post-translational modification and transcription factors. The

most abundant protein up in pyr-/air is vesicle-inducing plastid protein 1 (VIPP1 / Cre13.g583550.t1.2, largest red circle), a known regulator of thylakoid membrane organization.

Proteins not included in one of the functional groups (Fig. 4.12i) mostly are uncharacterized proteins, some of which may be key pyrenoid assembly factors. This shortlisted set of candidates contains 97 proteins, which are reasonably close in abundance to Rubisco subunits. For this set of candidates, statistical grouping was explored further (Appendix 8.26).

4.3.10 Remaining proteins are informative about a likely pyrenoid assembly mechanism

The following figures highlight different groups in an arrangement that reproduces their positions in relative abundance plots like Fig. 4.11. In each case, a relative abundance plot is overlaid with a spider plot of four axes, arranged in a cross-shape, showing the measured abundances (% *emPAI*) of an example protein for each of the four conditions.

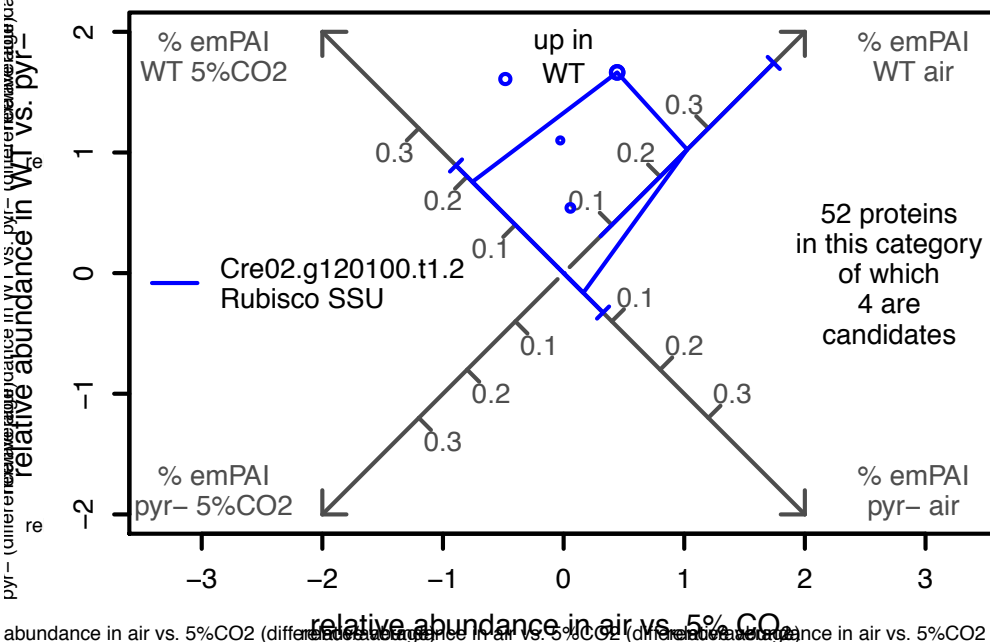


Fig. 4.13: Candidates up in WT may be involved in forming the constitutive pyrenoid

Of the proteins functionally annotated as “candidates” (Fig. 4.12i), only those proteins that were statistically grouped as “up in WT” are shown. A spider plot is overlaid across the graph, showing % *emPAI* values from each experimental condition explicitly as average \pm standard error based on three biological replicates for the Rubisco SSU.

The rationale for showing the spider plots is to visualize directly how the position of a protein on the relative abundance plot is determined by the measured abundances in each

experimental condition. Furthermore, the spider plots present an opportunity to show variation explicitly as error bars, which were omitted from previous figures for the sake of clarity.

Only 4 candidates were more abundant in WT than in pyr- (Fig. 4.13), independent of CO₂ environment, of which *Chlamydomonas* Rubisco SSU (effectively acting as a control) is the most abundant. The 2nd most abundant (Cre16.g659700.t1.2) has about half the abundance of LSU and is >9 fold higher in WT than in pyr-. Keeping in mind that at least 50% of Rubisco remains aggregated in WT regardless of CO₂ conditions, these candidates that are consistently associated with WT Rubisco may play a role in the maintenance of the constitutive pyrenoid.

As the pyrenoid is fully assembled only in WT/air, proteins most abundant in this condition form perhaps the most interesting candidates (Fig. 4.14). As an example, LCI5 (Cre10.g436550.t1.2) is shown. Of the two circles close to LCI5 on the plot, the closest is a completely uncharacterized protein (Cre02.g084000.t1.2), whilst the one overlaying the cross-axis contains an iron-sulphur-cluster binding domain (Cre01.g050550.t1.2). The remaining two circles of similar size are α -tubulin 1 (aTUB1 / Cre03.g190950.t1.2) and β -tubulin 2 (bTUB2 / Cre12.g549550.t1.2).

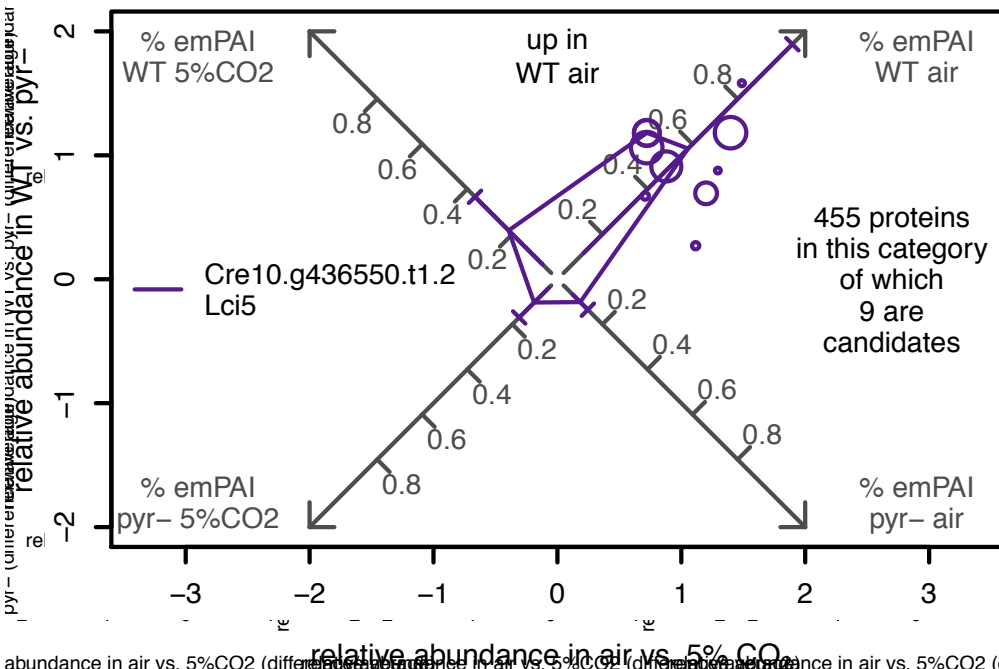


Fig. 4.14: Candidates most abundant in WT/air may be informative about pyrenoid assembly and include linker LCI5

Candidates (Fig. 4.12i) statistically grouped as “up in WT/air” are shown, with a spider plot overlaid across the graph explicitly showing % *emPAI* average \pm SE from each experimental condition based on three biological replicates for LCI5.

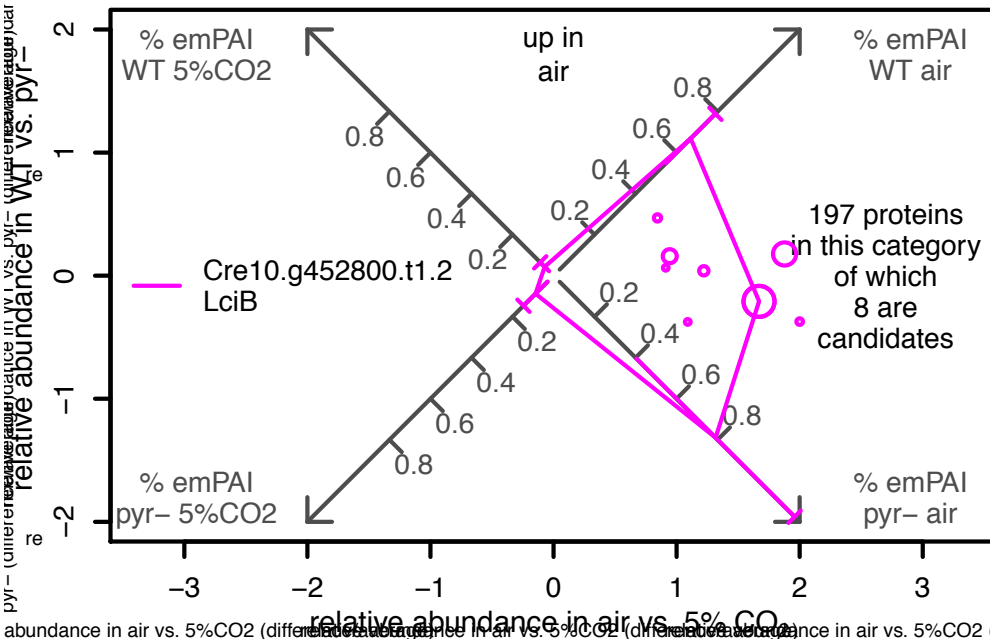


Fig. 4.15: Candidates up in air include LCIB and LCIC

Candidates (Fig. 4.12i) statistically grouped as “up in air” are shown, with a spider plot overlaid across the graph explicitly showing % *emPAI* average ± SE from each experimental condition based on three biological replicates for LCIB.

Appendix 8.26i shows candidates significantly more abundant in air but equal between WT and pyr-. Proteins associating with Rubisco specifically in low CO₂ may play a part in the CCM. Indeed, the most abundant proteins in this set were the CCM factors LCIB and LCIC, which are present at very low abundances in 5% CO₂ samples, shifting the circles to the far right in the relative abundance plot.

4.4 Discussion

The aim of the current study was to characterize a Rubisco interactome in *Chlamydomonas* strains that are able and unable to aggregate Rubisco into a pyrenoid, in order to identify key pyrenoid assembly factors. The most likely explanation for how expression of heterologous Rubisco SSUs leads to pyrenoid absence would be that key protein interactions require native SSU surface motifs to establish (Chapter 2). The approach was thus aimed at identifying SSU interaction partners that establish high molecular weight complexes containing Rubisco. While the methods used could not differentiate whether an interaction proceeded via SSU or LSU, those interactions that are relevant for pyrenoid formation could be identified by occurring only in WT but not pyr-. Because neither BN-PAGE nor co-IP would be able to resolve entire pyrenoids, the strategy was based on breaking the pyrenoid apart during cell lysis, and resolving sub-complexes in which components of the pyrenoid

remain associated. That the pyrenoid disassembles during lysis is supported by the fact that the majority of Rubisco holoenzymes, visible as a complex of ~500 kDa in BN-PAGE, is present as soluble protein (Fig. 4.2, Fig. 4.3, Fig. 4.4, Appendix 8.20, Appendix 8.21) rather than pelleting with membrane proteins (Appendix 8.24).

4.4.1 A large part of the Rubisco interactome is independent of the pyrenoid

Both co-IP and BN-PAGE show a number of features that are shared between WT and pyr-, despite clear differences in pyrenoid and associated CCM phenotypes (Chapter 2). 1st dimension (Fig. 4.2) and 2nd dimension gels (Fig. 4.3, Fig. 4.4) are virtually identical and lack any obvious differences between the strains. Consistently, the most abundant proteins of gel bands and co-IP were equally present in WT and pyr- (Fig. 4.6, Fig. 4.7, Fig. 4.8, Fig. 4.10). Expression and assembly of protein complexes thus appears highly similar between strains and is only very subtly affected by the localisation of Rubisco within the chloroplast.

In fact, similarities between WT and pyr- stretch so far that, in contrast to initial expectations (Fig. 4.1), no discrete Rubisco supercomplexes could be found using BN-PAGE (Fig. 4.2). A high-molecular weight band containing Rubisco identified initially (Appendix 8.20) was composed mostly of chaperonin 60 proteins (Appendix 8.23). As Gro-EL homologue, chaperonin 60 proteins are involved in folding and assembly of Rubisco subunits (Liu et al., 2010; Vitlin Gruber et al., 2013). While expressed constitutively, plastid chaperonin 60B expression is increased up to three-fold in a heat shock scenario (Schroda et al., 2015) and thought to be required for sustained activity of Rubisco (Salvucci, 2008), e.g. by aiding refolding of denatured subunits. Thus this non-reproducible band may have been due to an event of incubator overheating as a result of a fault in the ventilation that occurred shortly prior to extraction.

Instead of a discrete complex, a range of low abundance, high molecular weight complexes were found, as indicated by the high-molecular weight tail of the Rubisco LSU in 2nd dimension Western blots (Fig. 4.3). In a spinach leaf protein extract, a similar tail is highly reduced (Fig. 4.5) despite the much higher abundance of Rubisco in higher plants compared to microalgae (Losh et al., 2013). Thus in *Chlamydomonas* a much larger proportion of Rubisco forms part of high molecular weight complexes than in Spinach. A high molecular weight tail is present, if perhaps somewhat reduced, in pyr- protein extract (Fig. 4.4), suggesting a large proportion of these Rubisco complexes are not to do with pyrenoid assembly.

Chapter 4: A Rubisco interactome provides insight into the mechanism of pyrenoid assembly

As far as Rubisco itself is concerned, the LSU was recovered as an abundant and equally present component of all conditions in the co-IP (Fig. 4.10, Fig. 4.11) and equal between strains in BN-PAGE (Fig. 4.6, Fig. 4.7, Fig. 4.8), consistent with previously reported equal expression (Genkov et al., 2010; Meyer et al., 2012). The *Chlamydomonas* SSU was recovered almost only in WT as expected from the fact that *pyr-* expresses a *Spinacia oleracea* SSU. That traces of *Chlamydomonas* SSU were detected in only one out of six *pyr-* co-IP samples indicates that cross-contamination is minimal, despite the fact that the same column was used for all samples (see Section 4.2.7).

A significant fraction of proteins that invariantly associated with Rubisco are factors involved in synthesis, folding, localization and degradation of proteins. Ribosomal proteins form a considerable fraction of 600 kDa and 720 kDa BN-PAGE bands (Fig. 4.7, Fig. 4.8), and synthesis proteins include some of the most abundant components of the co-IP (Fig. 4.12 b&d). High abundance in the co-IP may be due to the formation of large translational complexes, multiple copies of which sitting along a single mRNA could be pulled out with a single partially translated Rubisco subunit. The lack of differential abundance is consistent with an equal abundance of Rubisco itself, requiring a similar suite of Rubisco synthesis and turnover factors across conditions.

Following protein synthesis, another set of proteins equally associated with Rubisco in both WT and *pyr-* are chaperones aiding protein folding, including most notably chaperonin 60. A homologue of bacterial GroEL, chaperonin 60 proteins form a double-ring structure inside which proteins, especially ones that have large buried surface areas like Rubisco LSU, can fold correctly (Schroda, 2004; Vitlin Gruber et al., 2013). In the co-IP dataset, some bias towards a higher abundance in air-grown cells was found, perhaps in line with stress-related expression of chaperonin 60. The majority of 60 kDa chaperonin subunits was found in a complex with an apparent weight of ~720 kDa (Fig. 4.3, Fig. 4.6, Fig. 4.7). Chaperonin 60 subunits form two rings of seven members, meaning the complex should be >800 kDa in size. The discrepancy may be due to the shape of the complex influencing the passage through the gel. The fact that chaperonins were much more highly abundant than other proteins in the ~720 kDa 1st dimension band suggests that the complex migrated either binding a number of different proteins, of which the Rubisco LSU may have been one, or empty. The latter is supported by the fact that in the 720 kDa band, mitochondrial chaperonin 60C (Schroda et al., 2015) migrates alongside plastid chaperonin 60B, and that in a presumed heat shock scenario, Rubisco associated with chaperonin 60 migrated as complex much larger than 720 kDa (Appendix 8.20, Appendix 8.23).

While protein folding and turnover factors would bind Rubisco independently of pyrenoid presence or absence, a further set of proteins appeared at similar levels in WT and *pyr-* due to not binding to Rubisco *in vivo*. Proteins known or predicted to localize in compartments other than the chloroplast (Fig. 4.12b) that appear in the co-IP may have interacted non-specifically with either Rubisco, the antibody or some other component of the co-IP columns *in vitro*. Such non-specific binding offers another explanation for how some proteins can be much more abundant than Rubisco itself in a Rubisco co-IP. Whilst for the most part equally abundant in WT and *pyr-*, these contaminants do show variation with CO₂ conditions. It thus seems likely that the abundance of these contaminants reflects expression within the cell, with some of these proteins differentially regulated according to CO₂ environment. By the same logic, the glycine rich RNA-binding protein (Cre09.g392350.t1.2) annotated as mitochondrial that was found to be most abundant in WT/air may be upregulated in this condition, for example as a result of CCM operation.

Whilst turnover, folding and metabolic (Fig. 4.12c) proteins form an insightful part of the Rubisco interactome, equal abundance in WT and *pyr-* suggests that none of these factors are important for pyrenoid assembly. Therefore it was intriguing to find LCIB and LCIC not only present in the Rubisco interactome in both BN-PAGE (Fig. 4.7, Fig. 4.8) and co-IP, but also equally associated in WT and *pyr-* (Fig. 4.15). LCIB and LCIC are well-characterized crucial components of the CCM. Highly induced in low CO₂, the two proteins associate in a hexameric complex, which is known to localize around the pyrenoid in CCM-induced conditions (Yamano et al., 2010; Wang and Spalding, 2014). Mutants in *LCIB* are lethal in air-levels of CO₂ but viable in both elevated and very low CO₂.

The fact that both LCIB and LCIC are present at high abundance in the co-IP dataset strongly suggests that at least one of the two proteins interacts with Rubisco. While the association is much stronger in low CO₂, consistent with the expression profile of the proteins, the interaction with Rubisco is independent of pyrenoid presence. This interaction offers a simple mechanistic explanation for the localization pattern of the LCIB/C complex: when over 90% of Rubisco is aggregated in a CCM-induced WT cell, LCIB/C associates with Rubisco at the periphery of the pyrenoid where interaction surfaces are present. LCIB/C could be excluded from the pyrenoid interior simply by not being actively recruited to the pyrenoid, or by interactions that hold Rubisco in aggregation proceeding with higher affinities and thus outcompeting LCIB/C in gaining access to Rubisco surfaces. In CCM repressed conditions, the delocalization of a large proportion of Rubisco may be sufficient to cause an associated delocalization of the majority of LCIB/C. Localisation of LCIB/C

Chapter 4: A Rubisco interactome provides insight into the mechanism of pyrenoid assembly would, therefore, be directly informative about the localisation of Rubisco (Yamano et al., 2010). Consistent with this idea, mutants recovered in a screen for aberrant LCIB localisation also show pyrenoid anomalies (Yamano et al., 2014). Whilst perhaps not being a driving factor in the formation of a pyrenoid, LCIB and LCIC demonstrate that some of the factors equally interacting with Rubisco in WT and *pyr-* may associate with the pyrenoid *in vivo*.

4.4.2 Co-IP and BN-PAGE make specific contributions to the interactome analysis

To find the factors that drive pyrenoid assembly by binding to Rubisco, analysis needs to focus on those parts of the interactome that are different between WT and *pyr-*. The fact that differential abundance could only be found among proteins of lower abundance in BN-PAGE bands indicates that breaking the pyrenoid apart does not result in a high abundance of sub-complexes of a specific size. Any protein interactions that remain after pyrenoid breakdown likely form low abundance complexes at a range of different sizes.

With the high resolution of mass spectrometry, co-IP has a higher capacity for picking up these lower abundance sub-complexes than a BN-PAGE approach relying on silver staining and Western Blotting to identify complexes of interest. Correct identification of differences between WT and *pyr-* relies on a reasonable estimate of protein abundances. The fact that below 0.01 % *emPAI* a significant number of proteins were detected in a subset of conditions only (Fig. 4.10) suggests that the mass spectrometric identification is reaching a limit at such low abundances. When operating at this limit, proteins that are present may not be detected reliably, possibly resulting in a false assignment of which condition contains a particular protein most abundantly.

For example, a number of light harvesting proteins were detected only in WT/air replicate 1 (e.g. LHCA9, Cre07.g344950.t1.2), a replicate that contained a particularly high number of low abundance proteins (Fig. 4.9). These proteins were likely recovered as indirect interactors of Rubisco due to association with photosystems. Since several subunits of photosystems were detected at higher abundances in a number of samples from different conditions (see Fig. 4.12h), light harvesting complexes may have been present in these samples too but by chance were only detected in a single sample. The interaction signal may thus be genuine, however, to make the analysis of the interactome more reliable, rare and low abundance proteins were separated out (Fig. 4.12a) because of the high chance that

simple detection errors would lead to wrong conclusions about the behaviour of these proteins in the different experimental treatments.

4.4.3 A number of functional classes do show differences according to Rubisco aggregation state

Among those proteins showing a reliable difference between WT and *pyr-* were some of the factors involved in protein folding, such as a number of peptidyl-prolyl cis-trans isomerases. The clear bias towards *pyr-* indicates a greater requirement for factors aiding correct folding and dealing with misfolded Rubisco subunits. A large amount of dissociated SSU was found in *pyr-* BN-PAGE (Fig. 4.1, Fig. 4.4). These observations suggest *pyr-* cells may have some trouble correctly folding and incorporating this divergent (~46% sequence conservation, based on Spreitzer, 2003) heterologous SSU into functional holoenzymes.

All of the CBC enzymes are implicated in interacting with Rubisco as shown by co-IP, and to a lesser extent also by BN-PAGE. The finding that enzymes close to Rubisco in the metabolic pathway (Fig. 1.3) are more abundant (Fig. 4.12g) indicates that CBC enzymes likely associate or co-localise for substrate channelling, as has been suggested before (Anderson and Carol, 2004; Martin et al., 2006). The proteins show a subtle but consistent bias towards *pyr-*, supported by transketolase being significantly up in *pyr-* in the 600 kDa BN-band (Fig. 4.8). This suggests that the association occurs with delocalized Rubisco, consistent with the finding that CBC enzymes do not localize to the pyrenoid (McKay and Gibbs, 1991a, 1991b; Mettler, 2013). Metabolite exchange between Rubisco within and CBC enzymes outside the pyrenoid may rely on diffusive continuity provided by stromal minitubules enclosed in the thylakoid tubules that intersect the pyrenoid (Engel et al., 2015; Meyer and Griffiths, 2015). CBC enzymes such as aldolase and G3PDH are abundant in both the 600 kDa and the 720 kDa bands (Fig. 4.7), indicating complexes of a range of sizes are formed. In both BN-PAGE and co-IP, these elements are present at much higher abundance than Rubisco, suggesting CBC enzymes associate to multi-subunit complexes, which occasionally include a dissociated holoenzyme.

Plastid localized protein synthesis factors demonstrate a clear pyrenoid-related behaviour. The diagonal clustering dominated by purple circles in Fig. 4.12e shows that the composition of plastid translation complexes differs in the context of a fully assembly pyrenoid in CCM-induced WT/air from the other conditions. The contribution of the yellow circles demonstrates that the most contrasting condition is *pyr-* 5% CO₂ where the CCM is repressed and Rubisco is fully delocalized throughout the stroma. Co-IP data thus gives

Chapter 4: A Rubisco interactome provides insight into the mechanism of pyrenoid assembly evidence that the composition of the plastid translational complexes associated with Rubisco is altered by the aggregation state of Rubisco. This finding is consistent with reports that chloroplast translational machinery is localized in specific T-zones coordinated by the pyrenoid (Uniacke and Zerges, 2009).

4.4.4 The interactome supports Ca^{2+} - and redox-regulation of Rubisco aggregation

Regulatory factors associated with Rubisco clustering along the purple-yellow diagonal in Fig. 4.12i suggest redox-regulation is an important component of determining the aggregation state of Rubisco. 2-cys peroxiredoxins and thioredoxins bind to Rubisco most abundantly either in WT/air where most Rubisco is aggregated *in vivo*, or pyr-/5% CO_2 where Rubisco is fully delocalized with minimal physiological pressure for aggregation. The different redoxins may competitively promote aggregation and delocalization, creating a switch reactive to signals from the pETC.

Factors most abundantly binding to Rubisco in WT/5% CO_2 suggest that Ca^{2+} -calmodulin dependent protein phosphorylation may play a role in controlling aggregation. Most likely this Ca^{2+} -dependent kinase binds in a CCM-repressed context to aggregated Rubisco, since delocalized Rubisco would be more abundant in pyr-/5% CO_2 .

One interesting regulatory target abundantly present in the co-IP is CP12 (Fig. 4.12g). The intrinsically disordered protein is known to be redox-regulated through formation of disulphide bridges, inactivating CBC enzymes GAPDH and PRK at night when the chloroplast stroma is oxidizing (Gontero and Maberly, 2012). CP12 has been shown to interact with a number of other proteins including FBA (Erales et al., 2008), but not Rubisco. CP12 is thus likely an indirect interactor, present in the Rubisco co-IP by virtue of interacting with CBC enzymes.

That CP12 is present despite the fact that the cells were grown in continuous light suggests regulation of the CBC may be more subtle than a simple day-night switch. CP12 could form part of feedback regulation from the pETC, ensuring that CBC activity does not exceed photosynthetic supply of energy metabolites. Such a role would explain the high abundance of CP12 in 5% CO_2 , where high availability of substrate for Rubisco may require the cells to limit the turnover of the CBC.

4.4.5 The interactome offers mechanistic insight into pyrenoid assembly

A protein interaction profile thus emerges of how pyrenoid formation may be regulated, and what the effects are for chloroplast metabolism and protein turnover. To gain mechanistic insight into how Rubisco aggregation is achieved, however, requires closer analysis of the proteins not covered by the main functional annotation (Appendix 8.26). For co-IP, WT and *pyr-* cells were grown at CCM-repressing 5% CO₂ in addition to CCM-inducing air-levels of CO₂ to be able to better identify those parts of the Rubisco interactome that are relevant for pyrenoid formation.

Proteins abundant in WT irrespective of CO₂ but lower in *pyr-* may be informative about formation of the constitutive pyrenoid. The uncharacterized 10.7 kDa protein Cre16.g659700.t1.2 is the best candidate for this role. With no highly conserved homologues except for an equally uncharacterized protein in closely related *Volvox carteri*, the candidate is predicted to be disordered with a single helical stretch towards the C-terminal end, and perhaps a second short helix right at the N-terminus, by prediction programs Phyre2, Jpred and psipred (Kelley and Sternberg, 2009; Buchan et al., 2013; Drozdetskiy et al., 2015). This pattern is similar to a single LCI5 repeat (Fig. 3.1).

It will be interesting to see whether Cre16.g659700.t1.2 acts as a tether between holoenzymes, in which case it would seem unlikely that this protein would interact with more than two partners, as that would likely require multiple ordered regions. Should this constitutively associated candidate be a linker, such reduced ability to tether multiple partners at once, compared to LCI5, could be a mechanism to reduce the fraction of Rubisco within the pyrenoid at high CO₂. Alternatively, the short helix might act as a membrane anchor, or the small protein could fulfil a regulatory function.

Proteins binding to Rubisco within the fully assembled pyrenoid should be most abundant in WT grown in air. Among these candidates is linker protein LCI5 (Mackinder et al., 2015). Consistent with this proposed role as linker, LCI5 is present in the Rubisco co-IP most abundantly in the context of a fully assembled pyrenoid, in WT at low CO₂ (Appendix 8.26c). That LCI5 is more abundant in WT than *pyr-* even in high CO₂ (Appendix 8.26c) suggests an alternative to the notion of a constitutively active tether, which is that the minimal pyrenoid present in WT in CCM repressed conditions could be formed by reduced activity of the same linker proteins that aggregate Rubisco at low CO₂. It has been reported that LCI5 is a target for phosphorylation (Turkina et al., 2006) which might be able to modulate the ability to tether Rubisco, e.g. by obscuring the interface or participating in the

Chapter 4: A Rubisco interactome provides insight into the mechanism of pyrenoid assembly binding (see Chapter 3). However, *LCI5* expression is highly induced during CCM induction (Lavigne et al., 2001), suggesting that the activity of the linker is regulated on the level of protein abundance. A requirement for *de novo* expression of linker proteins would be consistent with Rubisco aggregation timescales observed pre-dawn and during CCM induction (Yamano et al., 2010; Mitchell et al., 2014).

Clustering alongside *LCI5* in Appendix 8.26c are the two uncharacterized proteins Cre02.g084000.t1.2 and Cre01.g050550.t1.2, which may thus play a similar role in tethering Rubisco. While the former is lacking any functional annotation, in striking similarity to *LCI5* it has no known homologue in other species except for *Volvox carteri*, a close relative of *Chlamydomonas*, and is resolved as three α -helices connected by unstructured domains by the structure prediction tool Phyre2 (Kelley and Sternberg, 2009). On Phytozome (Goodstein et al., 2012), Cre02.g084000.t1.2 is listed as co-expressing with a number of plastid ribosomal proteins, the functional class that showed the highest correlation with *in vivo* Rubisco aggregation (Fig. 4.12e). Co-expression is strongest with plastid ribosomal protein L31 (Cre08.g365400.t1.2), which is also significantly up in WT/air, strengthening the case for a pyrenoid-related function of candidate Cre02.g084000.t1.2.

The latter candidate, Cre01.g050550.t1.2, is annotated as carrying CDGSH-type zinc finger motif, which is a redox-active, pH-labile 2-Iron, 2-Sulfur cluster binding domain devoid of zinc (Wiley et al., 2007). Proteins carrying this domain are commonly tethered to the outer mitochondrial membrane by an N-terminal domain (Paddock et al., 2007). Should this candidate prove not to be a mitochondrial contaminant, it might provide pH- and redox-regulated tethering to the intra-pyrenoidal thylakoid membrane system, or prove to be the transmembrane tether between the pyrenoid and the cytoskeleton. Strong co-expression with CP12, according to Phytozome, supports a role associated with carbon assimilation.

The fact that α - and β -tubulin also cluster with *LCI5* in WT/air strongly suggests involvement of microtubules in pyrenoid assembly. Forming part of the cytoskeleton, α -tubulin 1 and β -tubulin 2 are excluded from the chloroplast. Nonetheless, as the localization of the eyespot demonstrates (Mittelmeier et al., 2013), cytoplasmic microtubules can play a role in determining the localization of chloroplast features. A role for cytoskeletal microtubules in organizing the pyrenoid would require molecular tethers that cross the chloroplast envelope. Involvement of cytoskeletal elements may go some way to explain the presence of a number of flagella-associated proteins in existing pyrenoid proteomes (Uniacke, 2009; Mackinder et al., 2015) as well as this co-IP dataset, which were classed as

contaminants for the purposes of the present analysis (Fig. 4.12b). Dyneins that could transport proteins along microtubules appear in the co-IP dataset as a flagella-associated outer dynein arm light chain 8 (Cre03.g181150.t1.1) up in WT 5% CO₂, and a dynein light chain-related protein (Cre12.g546400.t1.2) appearing in the pyr-/air candidate set, thus suggesting they may play a role in exerting delocalization and aggregation pressures. Kinesins were detected at very low abundances only.

4.4.6 The soluble protein interactome contains hints about the role of thylakoid membranes in pyrenoid formation

The identity of the factors driving the association between aggregated Rubisco and intra-pyrenoidal thylakoids (Engel et al., 2015) is yet another enticing enigma. Preliminary BN-PAGE analysis of membrane fractions did not yield any candidate complexes, after it was found that immuno-labelled bands were devoid of Rubisco according to mass-spec analysis (Appendix 8.24). Whilst the current co-IP was, for technical reasons, carried out on soluble proteins only, a number of thylakoid-associated were detected nonetheless.

Proteins interacting with Rubisco in pyr- in air could be informative about early steps in pyrenoid assembly, representing the only condition where Rubisco is present in a low-CO₂ atmosphere *in vivo* when pressure for aggregation should be maximal. In this condition, a general association of Rubisco with thylakoid membranes is demonstrated by the presence of various pETC components (Fig. 4.12h). By contrast, WT Rubisco shows specific binding to PSI-associated proteins, consistent with previous reports that intra-pyrenoidal thylakoids are devoid of PSII (Vallon et al., 1985; McKay and Gibbs, 1990; McKay et al., 1992), separating Rubisco from the production of oxygen.

Rubisco in pyr-/air further shows an association with vesicle inducing protein in plastids 1 (VIPP1 / Cre13.g583550.t1.2, 2nd largest red circle in Fig. 4.12i). VIPP1 localizes to both chloroplast inner membrane and thylakoids in pea and interacts with chloroplast stromal chaperone pair CDJ2 and HSP70B, which aid VIPP1 oligomerization (Li et al., 1994; Liu et al., 2005; Heide et al., 2009). The HSP70B chaperone appears abundantly in the co-IP (Cre06.g250100.t1.2, 4th largest magenta circle in Fig. 4.12f) clustering alongside chaperonin 60 subunits. VIPP1 is localized throughout the chloroplast (including intra-pyrenoidal thylakoids), is required for organization of thylakoid membranes and may play a role in thylakoid biogenesis in the vicinity of the pyrenoid (Nordhues et al., 2012). Pyrenoid-associated protein biosynthesis factors were found to be most abundant in WT/air (Fig. 4.12h), a behaviour that contrasts with proposed pyrenoid-associated thylakoid biogenesis

Chapter 4: A Rubisco interactome provides insight into the mechanism of pyrenoid assembly factor VIPP1 being most abundant in pyr-/air. This contrast supports the idea that VIPP1 could be among the proteins establishing a Rubisco-thylakoid interaction early in pyrenoid re-assembly as the CCM is induced, and could play a role in establishment of the intricate intra-pyrenoidal thylakoid architecture in WT.

4.5 Conclusion

A large fraction of protein interactions exhibited by Rubisco is not altered by the presence or absence of a pyrenoid. Such interactions include cytosolic protein translation complexes, chaperones and a range of metabolic enzymes. Pyr- cells do appear to have some issues with correctly incorporating the heterologous SSU gene, reflected by a greater presence of folding chaperones and a large amount of dissociated SSU. Plastid translation machinery is altered in the presence of a pyrenoid, consistent with reported localization of protein synthesis and complex assembly in T-zones (Uniacke and Zerges, 2009). The aggregation state of Rubisco appears to be redox-regulated, suggesting an involvement of feedback from the pETC, and may also be regulated through Ca^{2+} -signalling. An association of Rubisco with thylakoids may form part of the initial steps in pyrenoid re-assembly. The interactome supports a role for the cytoskeleton in pyrenoid organization and identifies novel pyrenoid assembly candidates alongside LCI5 that await further characterization.

5 IDENTIFICATION OF NOVEL PYRENOID MUTANTS THROUGH IF SCREENING

5.1 Introduction

All key genes composing the current *Chlamydomonas* CCM model (see Fig. 1.4) have been uncovered by screening random insertion libraries for strains impaired in growth under air-level CO₂, which could be rescued when grown photoautotrophically under elevated CO₂ or heterotrophically on a source of organic carbon. Surprisingly, only a very small number of mutations have been linked to a pyrenoid phenotype. The scarcity of detailed micrographs in the CCM literature suggests that the pyrenoid, despite being conspicuous, has been largely ignored. Other than the Rubisco SSU-less mutant (Khrebtukova and Spreitzer, 1996) and the acetate requiring mutant *ac-20*, a knock-down of an essential chloroplast ribosomal protein (Goodenough and Levine, 1970), only *cia6* has come out of a forward genetic screen, and has yet to be integrated as a *bona fide* CCM player. This mutant strain shows an altered pyrenoid structure and an associated defect in CCM operation (Ma et al., 2011), and the gene is somewhat homologous to SET-domain methyl transferases, but no transferase activity was measured when tested *in vitro*.

Whilst forward genetic screens remain an appropriate genetic tool to advance the understanding of the CCM in general (Jungnick et al., 2014; Zhang et al., 2014), there is now an urgent need to add screening tools to specifically single out pyrenoid mutants. Pyrenoids are easily visualized using electron microscopy (Griffiths, 1970; Pickett-Heaps,

1975), but the technique is too time and resource-intensive to present a viable screening option. Light microscopy of the pyrenoid is possible, especially when combined with mercury chloride staining (Fukuzawa et al., 2001), and can be enhanced by Differential Interference Contrast (DIC). However, such visualization can be ambiguous (Yamano et al., 2014) and provides no direct evidence that structures diagnosed as pyrenoids are indeed aggregates of Rubisco.

Given that Rubisco makes up a large fraction of the pyrenoid (Kuchitsu et al., 1988), and that pyrenoids can be lost entirely when mutating the Rubisco SSU (Genkov et al., 2010; Meyer et al., 2012), pyrenoids can be considered as large-scale aggregates of Rubisco. A novel mutant library could be generated with the specific aim of identifying pyrenoid mutants for example by GFP-tagging Rubisco LSU or SSU (Lauersen et al., 2015; Mackinder et al., 2015), and screening for pyrenoid defects using fluorescent microscopy. This being beyond the scope of the present research project, an existing library of *Chlamydomonas* high-CO₂ requiring mutants was screened instead. Immunofluorescence (IF) was successfully employed in a recent screen for aberrant localisation of LCIB in *Chlamydomonas* (Yamano et al., 2014) and has been applied previously for localizing Rubisco (Vladimirova et al., 1982; Uniacke et al., 2011).

Using antibodies to associate fluorescent tags with Rubisco provided the opportunity to harness existing mutant resources. By scaling up preparation and imaging, an IF-based screen was developed with potential to analyse several hundred mutant strains. The work presented here is the result of a collaboration with the research group of Martin Jonikas (Carnegie Institution, Stanford) who kindly provided access to a sub-set of their genome-saturating insertional mutant library. To achieve near genome-saturation, the library consisted of several hundred thousand strains, exceeding the scope of a microscopy-based manual screen. However, high-CO₂ requiring CCM mutant strains had previously been isolated from the library (Leif Pallesen, personal communication). Given that the pyrenoid is a crucial component of the CCM (Genkov et al., 2010) it was reasoned that mutants showing pyrenoid defects would also suffer a defective CCM. Thus screening among several hundred CCM mutants effectively represents a genome-saturating screen for pyrenoid defects.

5.2 Materials and Methods

5.2.1 IF mutant screen

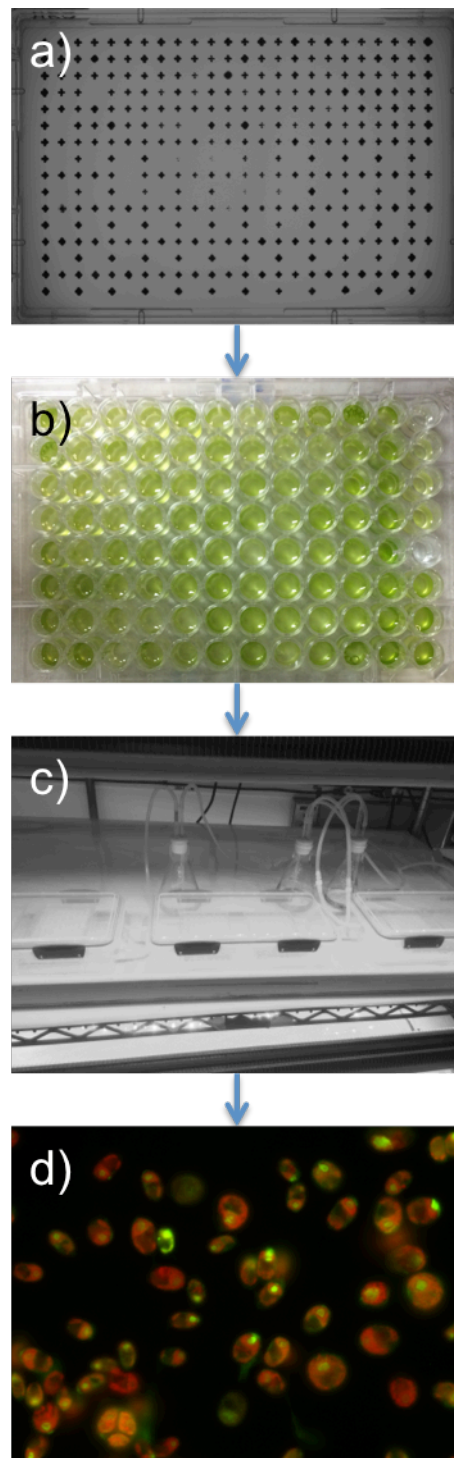


Fig. 5.1: Schematic of screening procedure

From robotically replated agar plates, (a), (picture credit: Leif Pallesen), cells were transferred to liquid culture (b) and grown under illumination in a controlled gaseous environment (c) before being prepared for IF (d).

CCM mutant lines and control strains (cMJ030 as positive control, SSU substitution WT and HelixAB lines as positive controls, and SSU substitution *Spinacia oleracea*, *Arabidopsis thaliana* and *Helianthus annuus* lines as negative controls) were replated robotically in a 96-colony format every 6 days for 3-4 times, grown on acetate-containing agar plates kept in the dark (Fig. 5.1a). From these agar plates, 96-well plates containing 200 μ l minimal medium (see 4.2.1) were inoculated robotically (Fig. 5.1b), placed in sealed transparent containers through which a gas mix of 5% CO₂/balance air was flown at 5 l/min, and subjected to constant illumination at \sim 50 μ E (Fig. 5.1c) for one day to grow the cells in CCM-repressive photoautotrophic conditions. Cells were subsequently grown in CCM-inducing conditions overnight by switching the gas supply to air, followed by transfer to 96-well imaging plates (μ -Plate 96 Well ibiTreat, ibidi GmbH, Martinsried, Germany) where cells were allowed to settle for \geq 10 min. Preparation thereafter followed the IF (Fig. 5.1d) protocol described in Chapter 3 (Section 3.2.1.2) except using 0.1% TBS-TT for permeabilisation of walled cMJ030 and cMJ030-derived CCM mutants.

5.2.2 IF optimisation

To increase quantitative diagnostic power and prevent fixation artefacts as far as possible, an optimized IF protocol for cMJ030 was developed. For this purpose, the protocol of Section 5.2.1 was compared to the protocol deemed to give the highest quality images in recent literature (Mittelmeier et al., 2013) as well as an ambiguous literature consensus protocol, collated based on recent publications using IF in *Chlamydomonas* (Sanders and Salisbury, 1995; Cole et al., 1998; Misamore et al., 2003; Yamano et al., 2010; Uniacke et al., 2011; Cusick et al., 2013; Huang et al., 2013; Lechtreck et al., 2013; Mittelmeier et al., 2013; Nguyen et al., 2013; Wood et al., 2013) and detailed below:

5.2.2.1 Cell attachment

Clean microscope slides were coated with poly-L-Lysine by adding a 10 μ l droplet to a slide and using another slide to smear the droplet across the first slide, generating a thin layer that was allowed to air-dry. 500 μ l mid-log phase cells, bulked up at 5% CO₂ under \sim 50 μ E continuous illumination in 50 ml liquid culture and adapted to air overnight, were spotted onto the slide and allowed to settle for 10 min after which excess media was removed.

5.2.2.2 Optional: formaldehyde fixation

A subset of slides was immersed in fixative (4% v/v Formaldehyde in PBS: 137 mM NaCl, 10 mM Na₂HPO₄, 2 mM KH₂PO₄, 2.7 mM KCl) in a coplin jar for 20 min at room temperature.

5.2.2.3 Optional: cold methanol combined fixation and permeabilisation

A subset of slides were (subsequently) immersed in 100% methanol, pre-cooled to -20°C, in a coplin jar for 10 min at -20°C.

5.2.2.4 PBS washes/rehydration

Following either fixation, or a combination of both, slides were washed three times by immersion in PBS for 5 min at room temperature in a coplin jar.

5.2.2.5 Optional: detergent permeabilisation

A subset of slides was immersed in Permeative (2% Triton X-100 in PBS) in a coplin jar for 10 min at room temperature, followed by 2 washes in PBS-Mg (5mM MgCl₂ in PBS) for 10 min each at room temperature in a coplin jar.

5.2.2.6 Block

Slides were removed from the coplin jar and allowed to air-dry. For each slide, 80µl block (1% w/v BSA, 1% cold water fish gelatin in PBS) ± detergent (0.05% Triton X100, 0.05% Tween20) were spotted onto a coverslip (width: 22 mm, length: 50 mm, depth: 0.16 – 0.19 mm) and inverted onto the cell-bearing face of the microscope slide. Slides were incubated with the block for 30 min at room temperature in a humid chamber, constructed by placing a tissue paper soaked with distilled water inside a petri dish.

5.2.2.7 Primary Antibody

Coverslips were removed and slides allowed to air-dry. Fresh coverslips were prepared with 80 µl 1° AB (Rabbit antibody raised against Rubisco purified from wheat in the research group of John Gray, bleed 2/7, diluted 1:2,000 in block ± detergent) and inverted onto slides, which were then incubated at 4°C overnight in a humid chamber.

5.2.2.8 Secondary Antibody

Coverslips were removed and slides were washed three times by immersion in PBS for 5 min at room temperature in a coplin jar. Slides were removed from the coplin jar and allowed to air-dry. Fresh coverslips were prepared with 80 µl 2° AB (1:1,000 dilution of

goat anti-rabbit Alexa 488 in block \pm detergent) and inverted onto slides, which were then incubated for 2 h at room temperature in a humid chamber.

5.2.2.9 Prolong Gold mounting

Coverslips were removed and slides were washed three times by immersion in PBS for 5 min at room temperature in a coplin jar. Slides were removed from the coplin jar and allowed to air-dry. Two drops of ProLong® Gold Antifade Mountant (Life Technologies) were spaced evenly along each slide and a clean coverslip was placed on top. Mountant was allowed to dry in the dark for at least 2h at room temperature. Slides were stored at 4°C in the dark.

5.2.2.10 The optimal protocol

Ideally, IF of Rubisco in WT *Chlamydomonas* strain cMJ030 should fulfil three criteria: (i) there should be a bright signal from the pyrenoid, where $\geq 90\%$ of Rubisco is known to be localized, (ii) the signal intensity from the rest of the chloroplast should be weak, (iii) the pattern described should be reliably apparent in every cell.

Fig. 5.2 shows the results of the IF protocol optimization. A view of 5-10 cells is shown for each protocol twice, firstly imaged using light microscopy, and secondly using epifluorescence of the Alexa 488 label. Of all the different combinations of consensus protocol aspects, Fig. 5.2j most closely resembles the “ideal” IF pattern, in that the pyrenoid is reliably labelled much more brightly than the rest of the cell in all cells. The optimal IF protocol for cMJ030 and derived CCM-mutant strains is thus to omit the formaldehyde fixation step (5.2.2.2), and instead combine cold methanol fixation (5.2.2.3) with detergent permeabilization (5.2.2.5), consistently using detergent in the block (5.2.2.6).

Use of formaldehyde (Fig. 5.2 c-h) appears to generate a more erratic labelling pattern, with some cells showing clear pyrenoid labelling and other cells showing a very diffuse signal. The effect of detergent on methanol-fixed cells seems to be a greater permeabilisation leading to greater antibody access: Methanol fixation alone (Fig. 5.2k) is sufficient to generate reliable pyrenoid labelling which is however very faint; increasing amounts of detergent (Fig. 5.2 l, i, j) lead to higher signal strength. Using Methanol instead of formaldehyde means that the fixed cells are devoid of chlorophyll, and thus cannot be used to record chlorophyll auto-fluorescence. The protocol of Mittelmeier et al. (2013) did give rise to high quality labelling (Fig. 5.2a) but seems to have had an adverse effect on cell integrity, possibly arising as a result of using cells that had been grown on plates and re-suspended in PBS, rather than cells grown in liquid culture.

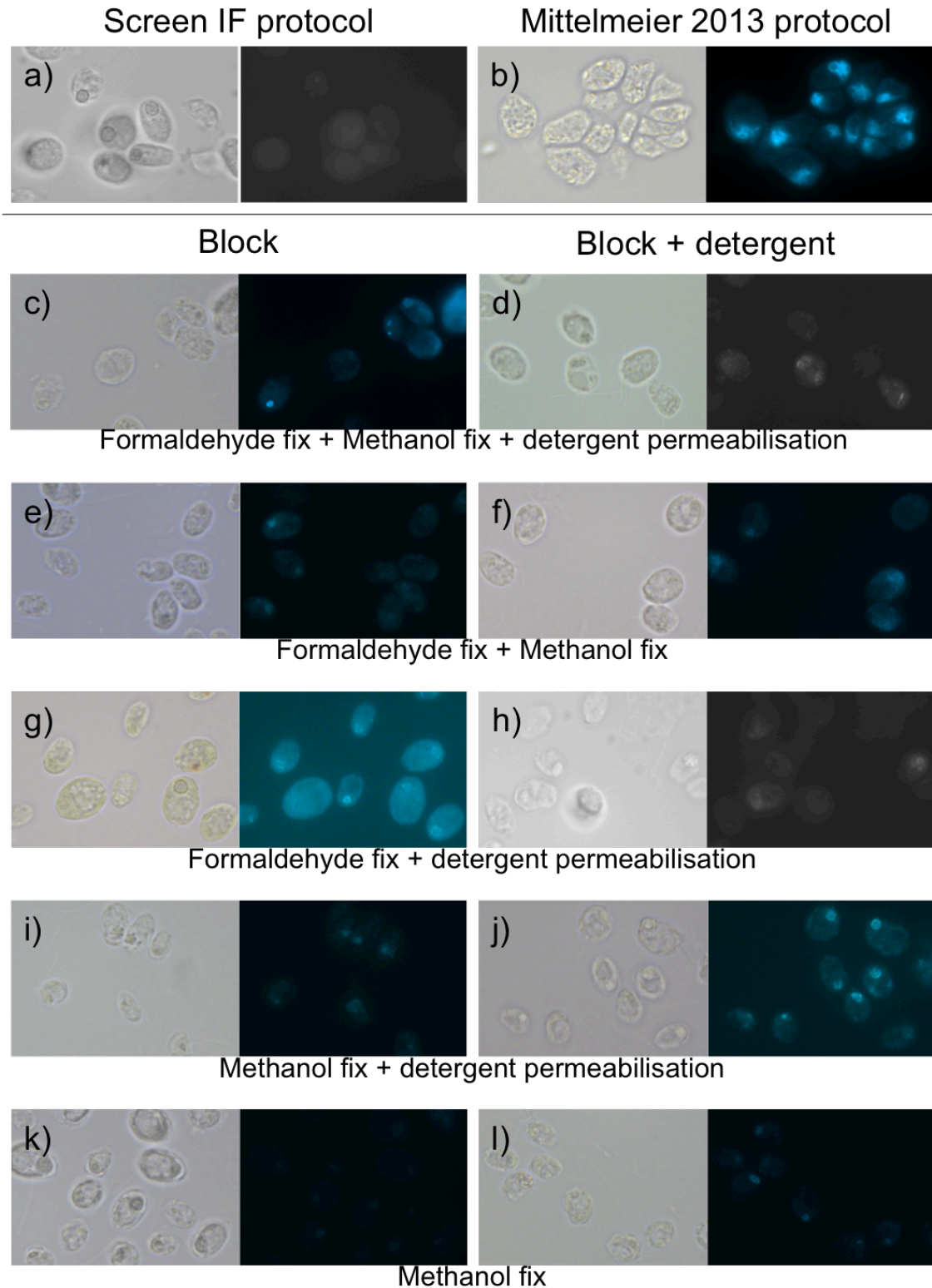


Fig. 5.2: Highest quality IF images are achieved when omitting the formaldehyde fixation step.

Light microscopy images, and epifluorescence images capturing Alexa 488 fluorescence, are shown side-by side for the same cells in (a)-(l) for different combinations of IF protocol aspects as detailed in image annotations.

5.2.3 Image acquisition

The initial mutant screen was conducted using a Leica microscope equipped with epifluorescence using Long Pass, GFP and Texas Red filters. A re-screen of previously identified pyrenoid-defective strains was imaged using an Axio Imager 2 (Carl Zeiss AG, Oberkochen, Germany) with a EC Plan-NeuFluar 100x/ 1.3 oil immersion objective under DIC and epifluorescence (FITC/GFP filter). Image z-stacks for quantitative analysis were taken with 488nm excitation lasers using a Leica SP5 with a 63x / 1.4 water immersion objective.

5.2.4 Image quantification

For quantitative analysis, Fiji (Schindelin et al., 2012) was used to generate a maximum intensity projection of z-stacks, on which background, cells and pyrenoid were outlined, recording areas, mean fluorescence intensities and integrated signal densities. Pyrenoids of all cells were outlined with a $4.6 \mu\text{m}^2$ circle, cells were outlined with freehand drawing, and multiple circles represented background across the entire image. Mean background intensity (b_m), extrapolated over pyrenoid (p_A) and whole cell (c_A) areas, was subtracted from integrated signal densities of pyrenoid (p_D) and whole cells (c_D), allowing the signal from outside the pyrenoid to be expressed either as percentage of whole cell fluorescence ($p\%$):

$$p\% = 100 \cdot \left(1 - \frac{p_D - (b_m \cdot p_A)}{c_D - (b_m \cdot c_A)}\right)$$

Or, alternatively, as fold-change relative to a (theoretical) uniform distribution of fluorescence throughout the cell (p_x):

$$p_x = \frac{\frac{p_D - (b_m \cdot p_A)}{p_A}}{\frac{c_D - (b_m \cdot c_A)}{c_A}}$$

5.3 Results

To identify mutant strains defective in pyrenoid formation, a selection of 352 CCM-defective mutants identified in a genome-saturating mutagenesis screen was sub-screened for defects in subcellular localisation of Rubisco using IF. The strategy assumes that strains defective in pyrenoid assembly would also be defective in the CCM, a hypothesis that is based on the finding that the CCM is not operational in mutants that cannot assemble a pyrenoid when expressing heterologous *RBCS* variants (Genkov et al., 2010; Meyer et al.,

2012). The strategy defines the pyrenoid as an aggregate of Rubisco, thereby making the localisation of Rubisco a reporter of the state of the pyrenoid.

5.3.1 IF can visualize pyrenoids with equal resolution to fluorescent-fusion techniques

Fig. 5.3 demonstrates the experimental approach of the screen using WT and pyr- control strains with previously characterized pyrenoid phenotypes. The cells were grown in CCM-inducing conditions to ensure maximal Rubisco aggregation. Rubisco was then immunolabelled with an Alexa 488 fluorophore that emits green light upon excitation, reporting on the subcellular localisation of the antigen. The specific fixation protocol used for the screen retains chlorophyll in the chloroplast, which is excited by the same wavelengths of light as the fluorophore, but can be distinguished from the label because the auto-fluorescence emission is in the red spectrum. As the screen was carried out using epifluorescence, the images shown in Fig. 5.3 (and subsequent figures) are in real-colour.

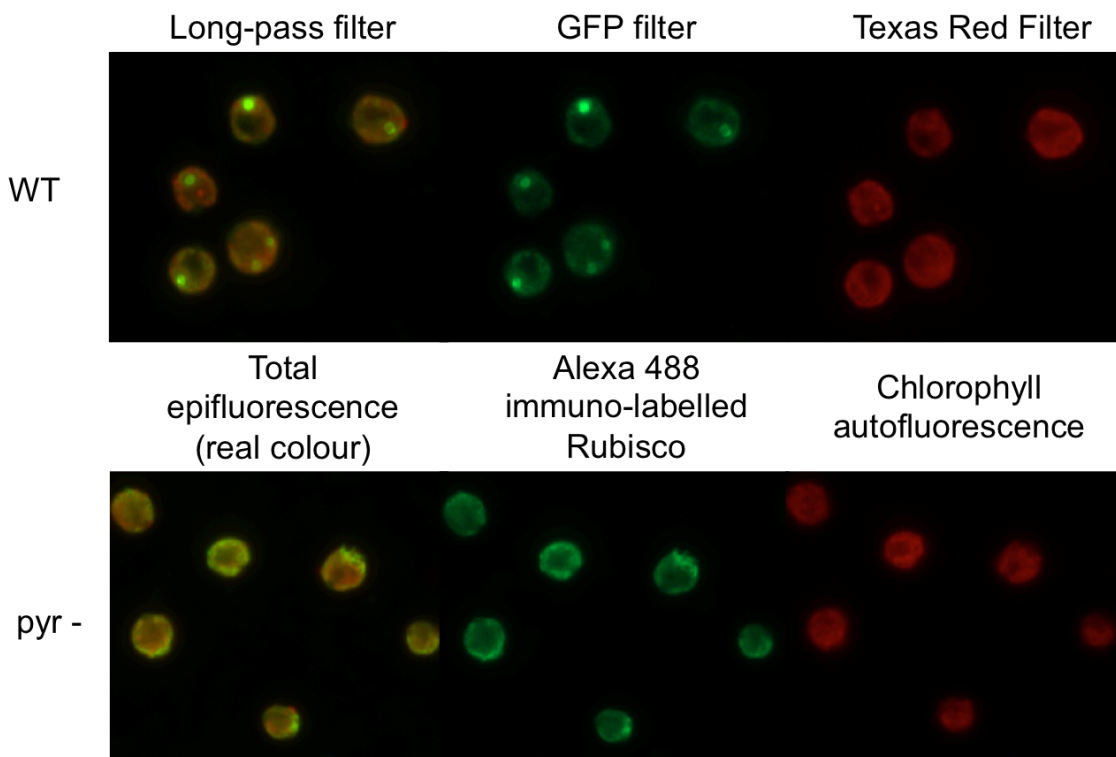


Fig. 5.3: IF labelling of Rubisco reveals pyrenoid presence and absence in controls.

Real-colour epifluorescence images are shown, using filters as indicated above the image to isolate fluorophore and auto-fluorescence. Control strains shown here are WT: WTint1,2 expressing *Chlamydomonas RBCS1*, and pyr- expressing *Spinacia oleracea RBCS*.

For WT, each of the three images shows the same five cells, viewed with different filters that exclude different emission wavelengths. The left-hand picture uses a long-pass filter

that allows most wavelengths above excitation to be recorded. In this picture, the cup shaped chloroplast can be made out in red around the periphery of each cell, whereas the cytoplasm shows very little labelling and thus appears as a dark centre. At the base of each chloroplast, a bright green spot indicates the presence of a dense Rubisco aggregate: the pyrenoid. This pattern is de-convoluted into contributions from Rubisco immuno-labelling and chlorophyll auto-fluorescence in the central and right-hand pictures respectively.

Pyr- on the other hand lacks a distinct region of intense Rubisco labelling, consistent with the absence of a pyrenoid from this strain. Instead Rubisco labelling and chlorophyll auto-fluorescence are both spread out over the whole of the chloroplast, leading to a more or less uniform yellow appearance of the chloroplast in the long-pass filter image on the left.

The labelling patterns clearly demonstrate pyrenoid presence in WT, and Rubisco delocalisation across the stroma in *pyr-*. There are, however, irregularities in the pattern that could lead to misidentification of mutants in a screen and are therefore important to keep in mind. For WT, one cell appears to have two pyrenoids. Most likely this is a result of a cell captured during mitotic division, as cells were grown asynchronously. For *pyr-*, two cells display more intense fluorescence at the base of the chloroplast than in the periphery. Assigning multiple, fragmented, or delocalised pyrenoid phenotypes to any mutant is ultimately a function of the frequency of the observation.

5.3.2 IF can diagnose pyrenoid presence in canonical localisation

Labelling of the WT pyrenoid in the parent strain (cMJ030) is shown in Fig. 5.4a. As a positive control, the parent strain cMJ030 was prepared alongside the mutant strains in the IF screen. The fluorescence signals of cMJ030 (Fig. 5.4a) are highly similar to the ones shown in Fig. 5.3. Pyrenoids can also be made out in DIC light microscopic images (Fig. 5.4a, Re-screen, top image). The only noticeable difference between the two WT strains is the shape of the cell, a likely consequence of the more severe wall-less phenotype of the SSU substitution strains, including *WTint1,2*, compared with cMJ030. This difference required an adjustment to the permeation protocol, with a higher amount of detergent required for cell lines based on cMJ030 (see Materials and Methods section 5.2.1).

Given that images which seem to support pyrenoid defects could be found even among controls, CCM mutants were screened instead for the presence of cells that unambiguously showed a single dense aggregate of Rubisco. These strains were then classed as containing WT-like pyrenoids, and removed from the pool of putative pyrenoid-defective strains.

Example images of strains with WT-like pyrenoids are shown in Fig. 5.4b. Strains with a putative pyrenoid defect were screened at least 2-3 times. Throughout the chapter, mutant strains are identified by replating position within the CCM screen as 96-well plate/row/column (see Fig. 5.1a): for example the position of strain 1A3 (Fig. 5.4b) within the CCM-screen was on 96-well plate 1, row A, column 3.

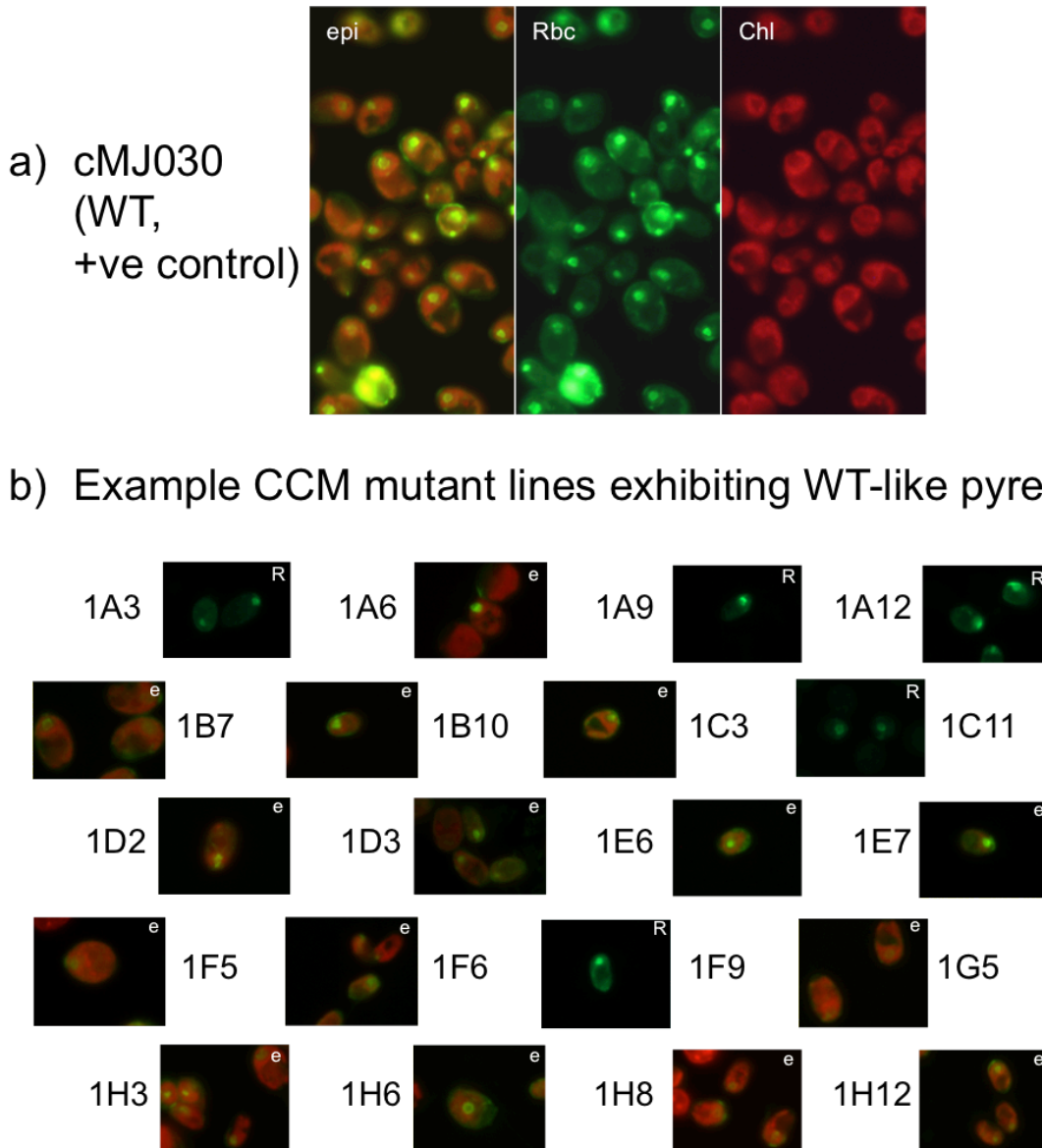


Fig. 5.4: Pyrenoid presence and canonical localisation is easily identified via IF

Epifluorescence images collected during IF mutant screen. The parent strain cMJ030, used for generating the library, serves as a positive control (a). Examples of strains classed as containing WT-like pyrenoids are shown in (b). Images are annotated by what they show as total epifluorescence (epi, e), Rubisco label (Rbc, R) or Chlorophyll auto-fluorescence (Chl).

5.3.3 Mutants with large amounts of delocalized Rubisco

Mutant strains where no cells could unambiguously be found to possess WT-like pyrenoids within at least 3 different planes of view, each containing usually 10-100 cells, were classed into different categories according to the recorded pyrenoid defect. Fig. 5.5 shows mutant strains where a pyrenoid can still be observed (white arrow) while large amounts of Rubisco are delocalized across the stroma, leading to high signal from all parts of the chloroplast and a diminished difference in intensity relative to the pyrenoid.

Mutant 1G10, now confirmed to be a *lci5* knock-down mutant, has a pyrenoid (mainly visible in DIC, Fig. 5.5a) but much of Rubisco is delocalised outside the pyrenoid, as evidenced by barely distinguishable signal strengths between the pyrenoid region and the stroma. Mutants 1G12 (Fig. 5.5b), 1H9 (Fig. 5.5c) and 1H10 (Fig. 5.5d) had somewhat similar patterns to 1G10, with pyrenoids discernible as somewhat more brightly labelled than the background, and at times most visible in chlorophyll auto-fluorescence images as fluorescence dark spots.

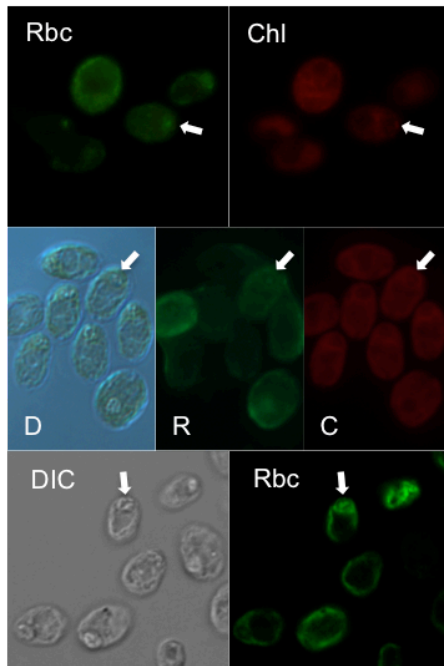
5.3.4 Mutants with a classical pyrenoid and additional Rubisco aggregates

A second class of mutants is shown in Fig. 5.6, where one or multiple Rubisco aggregates were observed (green arrows) in addition to a WT-like pyrenoid in the canonical position (white arrow). For 1A5 (Fig. 5.6a), punctate labelling indicates the presence of 2-4 additional Rubisco aggregates that are smaller than the structure identified as the main pyrenoid. This pattern is repeated in 1C4 (Fig. 5.6b) and 1C8 (Fig. 5.6c). Strain 1G6 (Fig. 5.6d) shows a smaller number of additional aggregates of similar size as the main pyrenoid, but in a distant location within the cell.

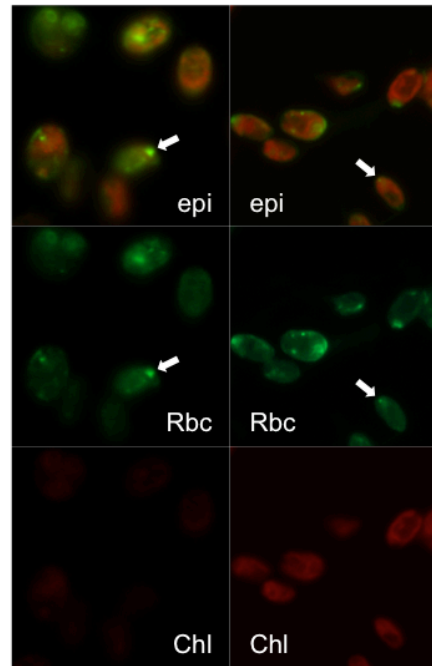
5.3.5 Some mutants show Rubisco aggregation, but lack a classical pyrenoid

Fig. 5.7 shows mutant strains that are similar to those of Fig. 5.6 in exhibiting some Rubisco aggregation, but differ in that there is generally no clear aggregate at the base of the chloroplast, i.e. no clear pyrenoid. Strain 1A7 (Fig. 5.6a), 1A8 (Fig. 5.6b), 1A11 (Fig. 5.6c) and 1D4 (Fig. 5.6d) all show usually 3-5 points of high Rubisco label intensity distributed throughout the chloroplast apparently randomly. Aggregates stand out bright green against the red auto-fluorescence in total epifluorescence images. The aggregates are smaller than a WT pyrenoid, making it difficult to determine whether there are corresponding dark spots in chlorophyll auto-fluorescence, which in any case are not obvious.

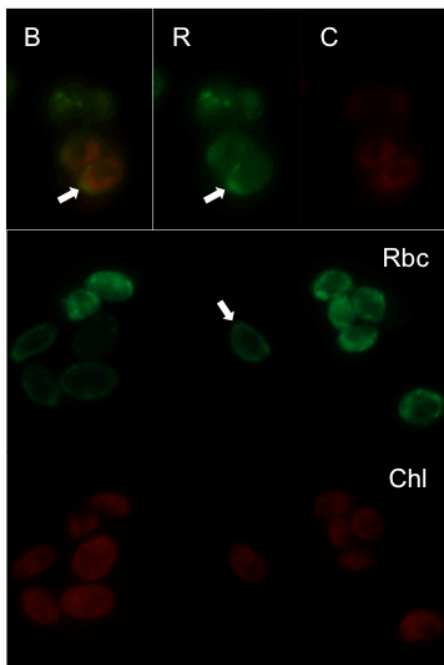
a) 1G10 (Lci5)



b) 1G12



c) 1H9



d) 1H10

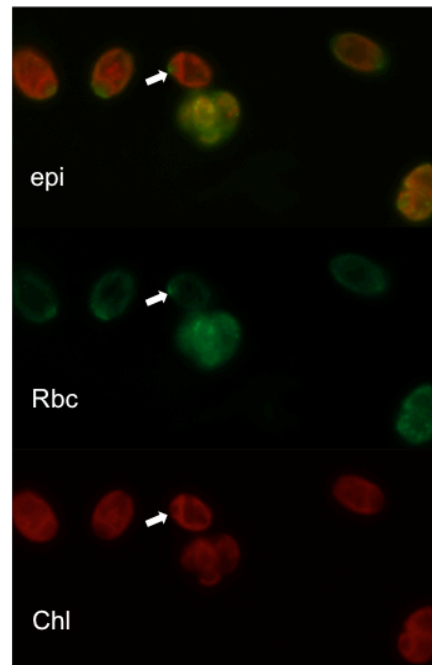
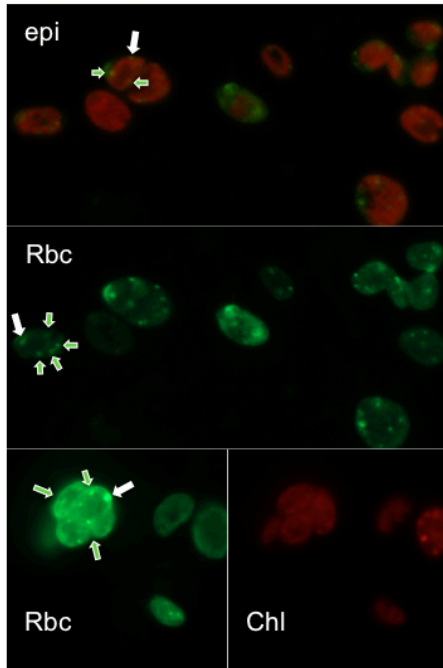


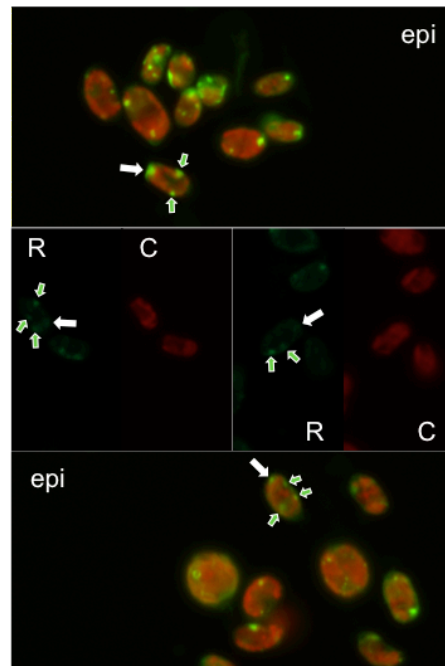
Fig. 5.5: Mutants with a large proportion of Rubisco delocalized outside the canonical pyrenoid location.

Epifluorescence images from the IF mutant screen. White arrows indicate position of the pyrenoid for one cell per view. Images are annotated by what they show as total epifluorescence (epi), **R**ubisco label (Rbc, R), **C**hlorophyll auto-fluorescence (Chl, C), **B**right Field (B) or **D**ifferential **I**nterference **C**ontrast (DIC, D).

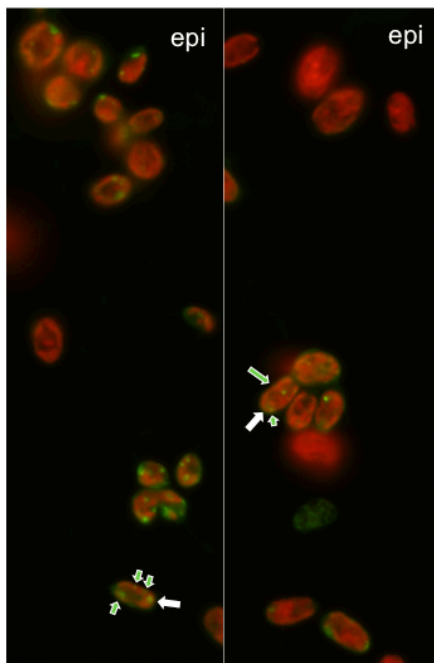
a) 1A5



b) 1C4



c) 1C8



d) 1G6

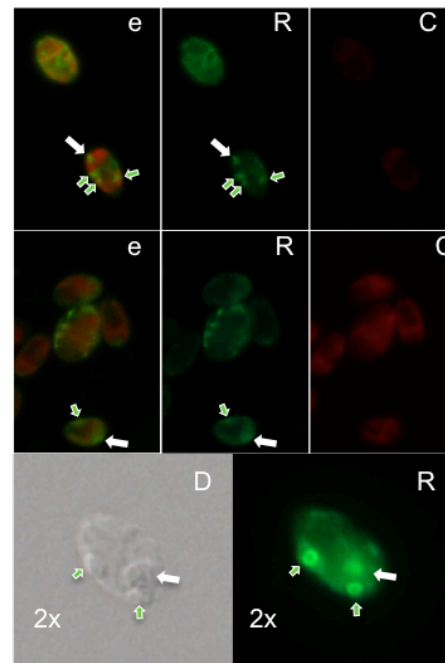
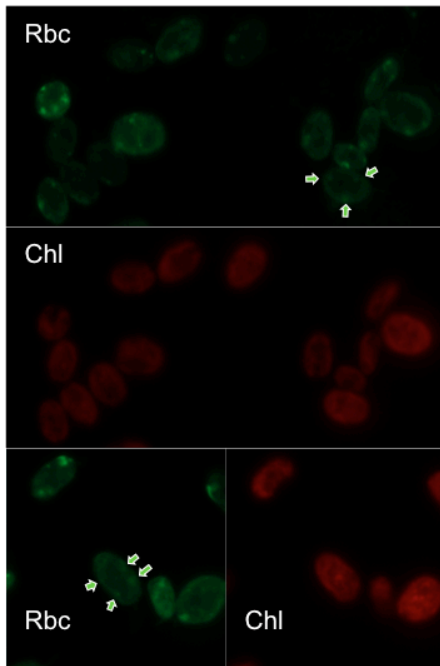


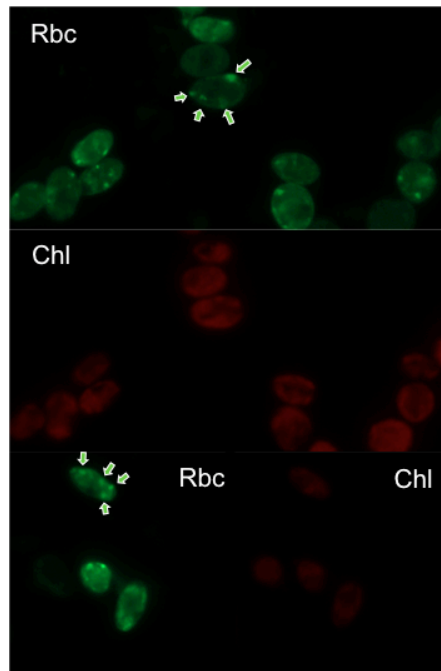
Fig. 5.6: Mutants with multiple Rubisco aggregates, in addition to a canonical pyrenoid

Epifluorescence images from the IF mutant screen. White arrows indicate the position of the pyrenoid, green arrows point out additional Rubisco aggregates for one cell per view. Images are annotated by what they show as total epifluorescence (epi, e), **R**ubisco label (Rbc, R), **C**hlorophyll auto-fluorescence (Chl, C) or **D**ifferential Interference Contrast (D).

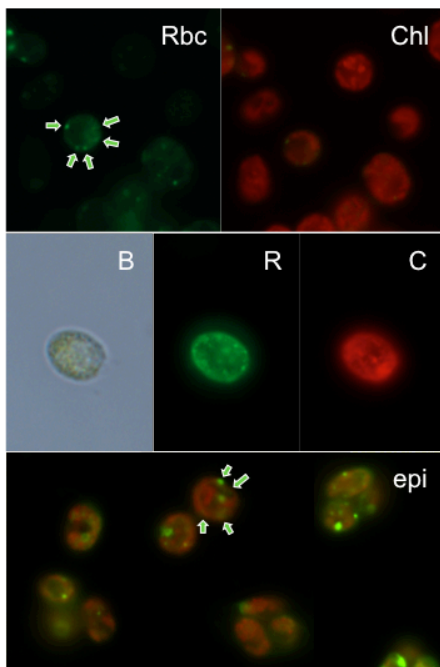
a) 1A7



b) 1A8



c) 1A11



c) 1D4

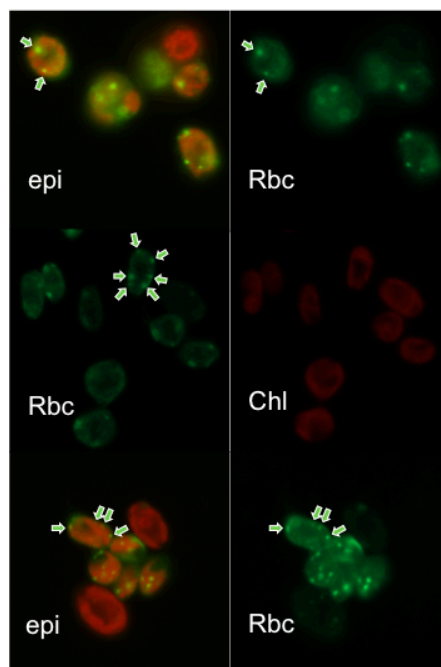


Fig. 5.7: Some mutants appear to contain Rubisco aggregates distributed across the chloroplast, while lacking a clear pyrenoid.

Epifluorescence images from the IF mutant screen. Green arrows point out additional Rubisco aggregates for one cell per view. Images are annotated by what they show as total epifluorescence (epi), Rubisco label (Rbc, R), Chlorophyll auto-fluorescence (Chl, C) or Bright Field (B).

5.3.6 Quantitative measure of Rubisco aggregation

The first mutant strain to have the insertion site characterized was 1G10. It carries a mutation in the *Lci5* gene (Leif Pallesen, personal communication). Characterization of the mutant included a quantitative analysis of Rubisco distribution (Fig. 5.8). An in-depth optimisation of the IF protocol previously used for the screening was therefore carried out (see Materials and Methods section 5.2.2).

Fig. 5.8a shows the analysis approach, depicting one typical cell for each growth condition. The *lci5* mutant was grown alongside parent WT-strain cMJ030 in both CCM-inducing conditions (air) that favour maximal Rubisco aggregation, and CCM-repressing conditions (5% CO₂) where a significant fraction of Rubisco delocalizes across the stroma even in WT.

For each cell, the pyrenoid was outlined using a circle of constant size, and the whole cell was outlined using the freehand drawing tool in Fiji (Schindelin et al., 2012). Qualitatively, cMJ030 grown in air has most of the IF signal originating from the pyrenoid, with low label intensities elsewhere in the chloroplast. Within the pyrenoid, the rim typically shows a higher intensity of labelling than the interior.

When grown at 5% CO₂, more of the label is distributed across the chloroplast, and the cup-shape is now visible. The pyrenoid itself appears more uniformly labelled than in air. The *lci5* mutant on the other hand shows high signal intensities across the whole chloroplast even in air. Qualitatively, the labelling pattern may suggest that the quantity of Rubisco retained in the pyrenoid is similar for cMJ030 at 5% CO₂ and *lci5* irrespective of CO₂ condition.

Quantitative analysis was conducted in two ways. Firstly, fluorescence was expressed as percentage of total cellular fluorescence outside the pyrenoid (Fig. 5.8b). According to this metric, WT grown in air has, with ~59%, by far the lowest amount of labelled Rubisco located outside the pyrenoid. The *lci5* mutant exhibits significantly ($p < 0.001$) more delocalized Rubisco labelling at ~78%. At high CO₂, WT and *lci5* have similar levels of delocalized signal ($p = 0.91$) at ~73%. *Lci5* actually appears less delocalized at high CO₂ than at low CO₂ ($p < 0.001$).

Secondly, quantitation was expressed as fold enrichment of fluorescence in the pyrenoid (Fig. 5.8c), where an enrichment of 1 corresponds to the theoretical case in which all measured fluorescence is distributed evenly across the cell. In contrast to the first proxy, which serves as a measure of delocalized Rubisco, this second proxy provides a measure of Rubisco aggregation into the pyrenoid.

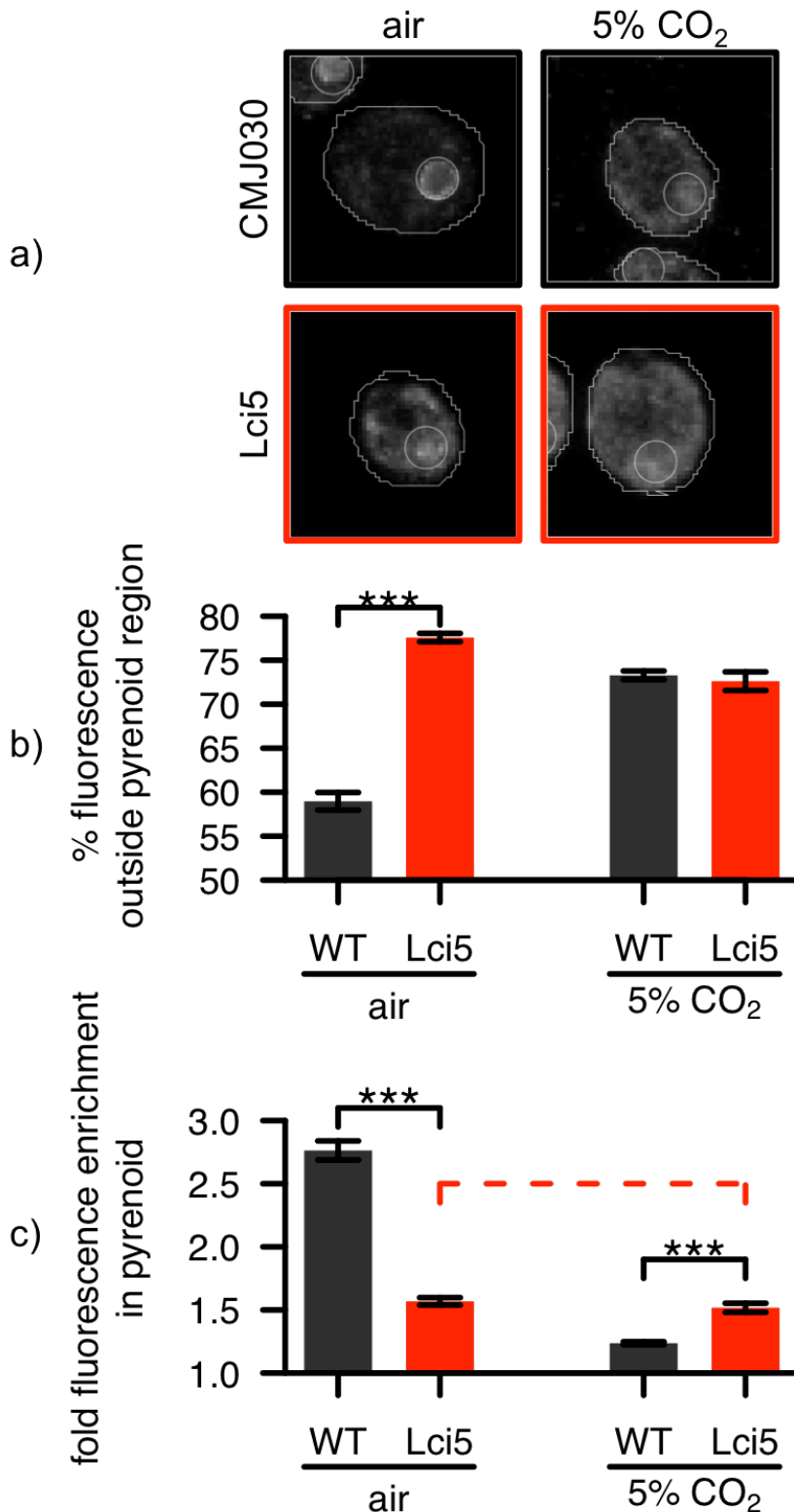


Fig. 5.8 Rubisco is quantifiably delocalised in the *lci5* mutant

Optimized IF images of *lci5* and positive control cMJ030 were quantified by recording fluorescence intensities of outlined cells and pyrenoids (a) using Fiji. Quantified values were expressed as % fluorescence originating outside the pyrenoid (b) or fold enrichment of fluorescence within the pyrenoid compared to a uniform distribution of fluorescence (c).

Fold enrichment reports that WT grown in air shows by far the highest aggregation of labelled Rubisco, with fluorescence originating from the pyrenoid 2.76 times higher than expected by chance. The *lci5* mutant shows a significantly lower 1.57-fold enrichment of fluorescence in the pyrenoid ($p < 0.001$). At high CO₂, WT actually shows significantly lower (1.2-fold) pyrenoid enrichment than *lci5*, which is at 1.52 ($p < 0.001$). However, fold enrichment of *lci5* is similar irrespective of CO₂ condition ($p = 0.76$).

The two metrics agree on a strong Rubisco delocalisation phenotype relative to WT exhibited by *lci5* grown in air. The disagreement about whether *lci5* grown at high CO₂ is equivalent to WT at high CO₂, or to *lci5* at low CO₂, effectively implies differences in cell size: fold enrichment in the pyrenoid (p_x) is equivalent to the percentage fluorescence originating from within the pyrenoid, i.e. the fraction not originating outside the pyrenoid ($p\%$), scaled by the ratio of cell area (c_A) to pyrenoid area (p_A): $p_x = \frac{c_A}{p_A} (1 - \frac{p\%}{100})$. Since pyrenoids were outlined using a circle of constant area of 4.6 μm^2 in all cells, a different area ratio is solely due to a difference in cell size.

Thus in order for *lci5* to have the same fold enrichment irrespective of CO₂ condition (Fig. 5.8c), but a higher delocalized signal in air (Fig. 5.8b), *lci5* cells are, at $\sim 26 \mu\text{m}^2$, on average smaller at 5% CO₂ than in air where the cell size is $\sim 32 \mu\text{m}^2$. For WT cells grown at 5% CO₂ to be on a par with *lci5* in terms of percentage of delocalized fluorescence, but to have the lowest fold enrichment, WT cells at 5% CO₂ are, at $\sim 21 \mu\text{m}^2$, even smaller than *lci5* cells at 5% CO₂. In air on the other hand WT cell are, with an average of $\sim 31 \mu\text{m}^2$, similar in size to *lci5*.

5.4 Discussion

The present study aimed to test if novel mutants affected in Rubisco targeting to the pyrenoid could be rapidly identified with a technique suited for screening large mutant libraries. For this purpose, the IF of Rubisco was optimized and 352 strains were screened over the course of 5 weeks. The screen recovered 23 candidates with some form of defect in Rubisco localisation or packaging. Such a high hit rate was the consequence of applying the IF screen only on mutants with a high CO₂-requiring phenotype, based on the fundamental observation that a defect in Rubisco aggregation renders the CCM non-operational (Genkov et al., 2010; Meyer et al., 2012). Using CCM-deficient strains as the basis of the screen thereby effectively enabled a near genome-saturating screen for pyrenoid-deficient mutants.

5.4.1 Assessing IF as high-throughput screening method

To minimize the number of false positives, i.e. strains identified as pyrenoid-deficient on the basis of staining artefacts or culture state, two precautions were taken. Firstly, screening focused on identifying unambiguously WT-looking strains, thereby limiting the effect staining artefacts could have on mutant categorisation. Secondly, strains that were classed as showing some form of pyrenoid defect were fixed and imaged independently at least 2-3 times.

In combination, these precautions reduced false positives at the expense of potentially increasing the number of false negatives, i.e. mutants falsely categorized as having a WT-like pyrenoid when pyrenoid assembly is actually affected by the mutation, especially where the phenotype is subtle. This was deemed the most appropriate strategy. Given that very little is known about pyrenoid assembly at the moment means that identification of the main contributing factors would be a significant advance. Having to deal with a large number of false positive strains on the other hand would be time and resource intensive.

As a result, the strategy was very successful in correctly identifying pyrenoid mutants: the twelve strains presented individually in this chapter were picked out again in a tertiary DIC-based screen (conducted independently by Dr Moritz Meyer, personal communication) and have since been further characterized ultrastructurally using TEM, confirming the existence of pyrenoid defects (conducted independently by Cindy Chan, personal communication).

5.4.2 No pyrenoid-less mutant strains were recovered

The screened library covered >90% of *Chlamydomonas* genes, with one out of three mutants having two or more alleles (Leif Pallesen, personal communication). All mutants singled out by the Rubisco IF screen had some level of Rubisco aggregation, unlike lines expressing a Rubisco small subunit from a foreign organism (Genkov et al. 2010). This, together with the observation that mutations leading to a complete loss of Rubisco aggregation are not lethal, reduces the likelihood of there being a single gene responsible for pyrenoid formation which would have escaped the present screen. Rubisco aggregation into the pyrenoid is more likely a multi-gene trait.

A mutant in a putative methyl transferase, *cia6*, has been shown to have an aberrant pyrenoid structure in addition to a high-CO₂ requiring phenotype (Ma et al., 2011), providing evidence that the assumption holds and a pyrenoid defect is associated with a CCM defect even when a partial pyrenoid remains. Further mutants, some of which seem to

show pyrenoid defects, were isolated in a screen for aberrant localisation of GFP-tagged LCIB, a protein that is targeted to the periphery of the pyrenoid in WT (Yamano et al., 2014).

Only two of the twelve mutants described in their study, however, showed a CCM-defect, one of which (*abl-1*) seemed to have a small pyrenoid possibly suggesting that much of Rubisco was delocalized, whereas the authors indicated that a second strain (*abl-3*) contained multiple pyrenoidal structures. Among the remaining ten aberrant LCIB localisation mutants, several were suggested to have pyrenoid phenotypes such as presence of multiple pyrenoid structures (*abl-10*, *abl-11*, *abl-12*) or mislocalization of the pyrenoid (*abl-2*). Thus some mutations affecting pyrenoid ultrastructure may not be associated with a simultaneous CCM-defect, in which case pyrenoids should remain functionally intact.

Amongst pyrenoid-bearing algae, a single pyrenoid is far from the norm (Pickett-Heaps, 1975; Nassoury et al., 2001). Multiple aggregates of Rubisco may therefore be able to function independently within a single cell, as long as each aggregate maintains certain fundamental pyrenoid characteristics. This idea could explain the fact that pyrenoid multiplicity is not always associated with a CCM defect (Yamano et al., 2014), and also why only a single mutant with a phenotype similar to pyrenoid multiplicity (1G6, Fig. 5.6) was detected in the present study. The smaller Rubisco aggregates found within some of the mutants (Fig. 5.6, Fig. 5.7) are thus most likely not functionally equivalent to pyrenoids.

Evidence for a link between possession of a functional pyrenoid and CCM operation is provided by the present IF screen. The 352 CCM mutants that formed the basis of the screen had been sorted into four groups of 88 mutants, based on severity of the high-CO₂ requiring phenotype and propagated on independent 96-well plates (Leif Pallesen, personal communication). Of the 23 pyrenoid-deficient lines identified, 15 originated from the group that showed the most severe CCM defects, 8 originated from group two, and no pyrenoid-mutant candidates were recovered from the other two groups. Defects in pyrenoid assembly thus correlate with a severe CCM phenotype, consistent with previously published results (Genkov et al., 2010; Ma et al., 2011; Meyer et al., 2012; Yamano et al., 2014). All the strains presented in this chapter belong to the most severe CCM phenotype group.

Hence it appears highly unlikely that a single Rubisco aggregation factor mutant would be present among the remainder of the library strains that do not exhibit CCM defects, or among the genes not captured by the library. As such it appears that Rubisco aggregation is a multi-gene trait, with multiple single gene mutants that show altered patterns of

aggregation, but none where aggregation is completely abolished. The fact that strains devoid of Rubisco aggregation can be produced experimentally by expressing a Rubisco small subunit with altered surface helices (Genkov et al., 2010; Meyer et al., 2012) demonstrates that while there may be multiple linker proteins encoded by different genes, all of them interact with Rubisco via the same interface.

5.4.3 Delocalized Rubisco mutants may include CCM induction regulators

The phenotype where a large fraction of Rubisco is delocalized across the chloroplast (Fig. 5.5) is reminiscent of WT grown in high CO₂ (Fig. 5.8a). Whilst only ~10% of Rubisco is found outside the pyrenoid in CCM-induced conditions in the WT, this fraction increases up to ~50% of cellular Rubisco when the CCM is repressed (Borkhsenius et al., 1998; Mitchell et al., 2014). A mutation in a gene controlling CCM induction could therefore lock the cells in a physiological state of CCM-repression with an associated delocalized Rubisco phenotype.

This effect has been documented before for *cia5/ccm1* (Fukuzawa et al., 2001). Nuclear localized CIA5/CCM1 has been dubbed the CCM “master regulator” and appears to be involved in regulation of almost all CCM-candidate genes during CCM induction despite showing no affinity for binding DNA (Xiang et al., 2001; Miura et al., 2004). It thus seems likely that a *cia5/ccm1* mutant could be among the delocalized Rubisco mutants identified in this work, possibly alongside additional regulatory factors operating at lower stages of the signalling cascade, or even upstream, at the level of inorganic carbon sensing.

5.4.4 The IF screen recovered a now well characterized pyrenoid factor

An alternative mechanism accounting for delocalisation of Rubisco would be a mutation affecting a protein that is responsible for linking Rubisco holoenzymes into higher order aggregates. *LCI5*, the gene mutated in strain 1G10, is the best characterized of such linker candidates to date (Mackinder et al., 2015). *LCI5* localizes to the pyrenoid in WT, and an interaction between *LCI5* and Rubisco was confirmed through reciprocal co-IP (also Chapter 4). The intrinsically disordered protein contains four almost exact amino-acid sequence repeats (Fig. 3.1), suggesting a mechanism where each repeat contains an independent Rubisco binding site, linking four holoenzymes together (Mackinder et al., 2015). This mode of action could account for hexagonal close packing with a spacing of 2-4.5 nm observed for holoenzymes within the pyrenoid matrix (Engel et al., 2015).

Here, quantitative analysis of the IF signal arising from 1G10 is used to demonstrate that the *lci5* mutant strain exhibits a pyrenoid defect where a large fraction of Rubisco is delocalized across the chloroplast (Fig. 5.8). This work forms part of a suite of experiments documenting the pyrenoid defect in the *lci5* mutant, supporting the notion of LCI5 as an essential pyrenoid component (Mackinder et al., 2015).

Compared with GFP-tagging and immuno-gold labelling experiments that document 10-20% of Rubisco signal arising from outside the pyrenoid in CCM-induced WT (Mackinder et al., 2015), IF generated a higher delocalized signal of almost 60% (Fig. 5.8b). The difference is most likely the result of limited antibody access to the pyrenoid interior that would arise from the close packing of proteins within the pyrenoid matrix as mentioned above (Engel et al., 2015). This exclusion of antibodies from much of the pyrenoid generates high intensity labelling on the outside surface of the pyrenoid where Rubisco is accessible, resulting in the observed bright rim of the WT pyrenoid in air (Fig. 5.8a). Judging from the absence of this bright rim in the *lci5* mutant as well as high-CO₂ grown WT (Fig. 5.8a) it seems likely that the pyrenoid matrix in these cells would be less dense and thus more accommodating for antibody penetration.

Thus antibody access issues would be expected to bias IF towards a higher apparent stromal signal, relative to fluorescent protein fusion or IGL methods. Quantitative IF should therefore not be taken as a direct measure of how much Rubisco is delocalized, but is nonetheless a very effective way of demonstrating differences in localization comparatively across strains or physiological conditions, as all three localisation techniques consistently captured the statistically significant differences between WT and mutant.

In striking similarity to what would be expected of CCM-induction regulator mutants, the delocalisation signal observed in *lci5* is highly similar to CCM-repressed WT (Fig. 5.8a). Larger cell size of the *lci5* mutant in air is consistent with slower growth in air, which would mean a larger proportion of the culture is arrested before cell division in a state of attempting to accumulate resources. That *lci5* cells are larger than WT cells even in 5% CO₂ thus suggests that a certain amount of stress resulting from the loss of the *LCI5* gene remains even when the CCM is repressed. Furthermore, while *lci5* shows a similar amount of fluorescence as WT arising from outside the (arbitrarily chosen) pyrenoid area in high CO₂ (Fig. 5.8b), when taking the different cell sizes into account *lci5* differs from WT in either CO₂ concentration (Fig. 5.8c). Thus it appears that the *lci5* mutant is not simply equivalent

to a CCM-repressed WT cell, consistent with the role of *lci5* as Rubisco linker rather than CCM regulator (Mackinder et al., 2015).

Pyrenoid assembly appears to be a multi-gene trait. While insertion sites remain to be characterized for nearly all the mutant strains presented in this chapter, a pooled analysis of all CCM-mutants used for screening indicates that there is only one *lci5* mutant in the set (Leif Pallesen, personal communication). It is thus very likely that further characterization of the pyrenoid mutants will reveal additional candidates important for Rubisco targeting to the pyrenoid or pyrenoid biogenesis.

5.4.5 Mutant phenotypes indicate the presence of organization factors, including a protein misannotated as E3 ubiquitin ligase

Finally, the presence of ectopic Rubisco aggregates in several mutant strains (Fig. 5.6, Fig. 5.7) suggests some of the genes affected play a role in correctly organizing the position of the single aggregate in WT. It will be very interesting to see whether there are links to the cytoskeleton among the mutants in this set. Direct mutations in cytoskeletal elements would likely be associated with strong pleiotropic effects and thus may not appear among CCM mutants. However, using the cytoskeleton could be a way to ensure that Rubisco aggregates are always located at the base of the pyrenoid in a single structure, thus intermediaries between Rubisco and the cytoskeleton could be flagged up in the present screen. By analogy, the *Chlamydomonas* eyespot is positioned the same way relative to the flagella in every cell via a chloroplast envelope-spanning connection to the microtubule cytoskeleton (Mittelmeier et al., 2013).

Gene insertion sites have been characterized for two strains with ectopic Rubisco aggregates (Moritz Meyer & Martin Jonikas, personal communication). 1A5 (Fig. 5.6) and 1C8 (Fig. 5.7) both contain insertions in Cre11.g467712, a protein labelled as E3 ubiquitin ligase involved in syntaxin degradation according to KOG (Koonin et al., 2004). However, this label appears to be a misannotation (Luke Mackinder, personal communication). The protein contains a starch binding domain according to PFAM (Finn et al., 2014), expression is induced at high CO₂, and Phytozome (Goodstein et al., 2012) reports co-expression with circadian clock-associated genes such as MAPK1 (ROC78 / Cre07.g317300.t1.1). Thus this protein may play a role during conditions where Rubisco is partially delocalized such as in elevated CO₂ or at night (Borkhsenius et al., 1998; Mitchell et al., 2014). The presence of ectopic Rubisco aggregates in the mutant during CCM-induced conditions suggests that the E3 ligase may act as a factor that antagonizes Rubisco aggregation. Low-

level expression of the protein in CCM-inducing conditions could therefore be one of the mechanisms to prevent Rubisco aggregation outside the pyrenoid. High-level expression at night (Mitchell et al., 2014) and in high CO₂ (Borkhsenius et al., 1998) could be sufficient to promote Rubisco delocalization even from within the pyrenoid, in which case the starch binding domain may serve as a guide, anchoring the protein to the pyrenoidal starch plates.

5.5 Conclusion

IF is a powerful tool for medium-throughput screening, suitable for processing hundreds of mutant strains. Phenotypes of the pyrenoid mutants detected suggest the presence of distinct Rubisco aggregation factors such as linker candidate *lci5*, and aggregate organisation factors ensuring appropriate localisation and unity of Rubisco aggregates, such as putative delocalisation promoting E3 ubiquitin ligase Cre11.g467712. The similarity of WT under CCM-repressed conditions to some of the observed mutant phenotypes suggests the presence of CCM induction regulatory factors among the mutated genes in this set. Only one strain contains a mutation in linker *LCI5*, and no strain was found to completely lack a pyrenoid, suggesting that pyrenoid assembly is a multi-gene trait and that further linker candidates are present among the mutants presented in this work.

6 CONCLUSIONS

The goal of this thesis was to provide novel insights into the molecular physiology of the *Chlamydomonas* CCM and functioning of the pyrenoid. In *Chlamydomonas*, a single pyrenoid is normally located at the base of a single chloroplast, and traversed by specialized thylakoid membrane tubules (Griffiths, 1970; Engel et al., 2015). Over 90% of Rubisco is localized to the pyrenoid when the CCM is active (Borkhsenius et al., 1998; Mitchell et al., 2014), making the pyrenoid the main site of CO₂ fixation within the cell and hence the focal point for C_i accumulation. Consequently, cells that are unable to form a pyrenoid due to expression of heterologous *RBCS* are also unable to operate a CCM (Genkov et al., 2010).

The Rubisco interface required for pyrenoid assembly to proceed had been identified as the SSU surface helices (Meyer et al., 2012). Since Rubisco is completely delocalized throughout the stroma in the absence of the native SSU helices, all interactions that keep Rubisco tethered within the pyrenoid must proceed via this interface. As the pyrenoid consists mostly of Rubisco (Kuchitsu et al., 1988) one major goal of this thesis was to determine whether Rubisco interacted directly to form supercomplexes within the pyrenoid, or via some linker protein candidate. Furthermore, it was not apparent whether the pyrenoid could be functionally defined solely in terms of the CCM, or whether additional roles were being fulfilled e.g. in coordinating chloroplast ultrastructure. The latter was implied in particular by the presence of T-zones around the pyrenoid (Uniacke and Zerges, 2007, 2009) and the intricate association with the thylakoid network (Goodenough and Levine, 1969; Engel et al., 2015) which seemed to be consistent with a suggested entropic effect of Rubisco aggregation on thylakoid stacking (Kim et al., 2005).

The current study aimed to address these open questions pertaining to functions beyond the CCM, and mechanism of assembly, of the *Chlamydomonas* pyrenoid. To address the former, a detailed physiological analysis of photosynthetic electron flow was conducted in Chapter 2. The latter was investigated by first analysing SSU interactions in Chapter 3, and then searching for candidate linker proteins and other assembly factors using a biochemical approach in Chapter 4, and a complementary genetic approach in Chapter 5. In these closing paragraphs, the findings of each chapter are first revisited sequentially before a synthesis is proposed and suggestions for future work are offered.

6.1 The pyrenoid is functionally defined as an aspect of the CCM

The present study firmly establishes the function of the pyrenoid as part of the CCM (Chapter 2). Originally hypothesized to be a Rubisco storage system (Griffiths, 1970), evidence had been accumulating for a role in the CCM (Kuchitsu et al., 1988; Villarejo et al., 1996; Borkhsenius et al., 1998; Duanmu et al., 2009) which was confirmed by CCM dysfunction in pyr- cells arising from SSU substitution experiments (Genkov et al., 2010; Meyer et al., 2012). However, given the involvement of the pyrenoid in chloroplast translation via T-zones (Uniacke and Zerges, 2007, 2009), the intricate structural arrangement of thylakoids (Engel et al., 2015) and the localization of CCM-unrelated proteins to the pyrenoid (McKay and Gibbs, 1991a; Süß et al., 1995; Uniacke, 2009; Shukla et al., 2012) it seemed likely that the pyrenoid fulfilled further functions beyond the CCM.

The current work found pyr- cells limited by CO₂ supply. As a result, increased *NPQ* (Fig. 2.7, Fig. 2.8, Appendix 8.6, Appendix 8.9, Appendix 8.16) and a reduction in functional PSII absorption cross-section (Fig. 2.11) were associated with a lower *LEF* (Fig. 2.6, Fig. 2.8, Fig. 2.9, Appendix 8.5, Appendix 8.9, Appendix 8.11, Appendix 8.12, Appendix 8.18) and *CEF* (Fig. 2.12, Appendix 8.14, Appendix 8.17) in the pETC. This way, supply of NADPH and ATP was balanced against demand in the context of a low CBC turnover (Fig. 2.1). Importantly however, all pyr- defects could be rescued immediately to WT-levels by establishing a high CO₂ environment and thereby removing any CO₂ limitation, demonstrating that pyrenoid presence is not required for any process other than CO₂ supply via the CCM.

The study also offers some interesting insight into the costs and benefits of the CCM for *Chlamydomonas*. It appears that the additional cost in ATP per revolution of the CBC caused by C_i accumulation is similar to, or even lower than the ATP cost of photorespiration, judging from the fact that the CEF/LEF ratio (measured as *LEF/ETR*) in

pyr- is at least as high as in WT (Fig. 2.12, Appendix 8.17). On the other hand, CCM operation allows WT to have significantly higher total rates of electron flow. Thus the chief benefit of the CCM seems to be an increase in overall CBC turnover, allowing pETC and CBC to be balanced at a higher rate of energy throughput. The CCM also effectively abolishes oxygenation and increases the quantum yield of CO₂ fixation without significantly altering the amount of energy processed. Thus the CCM allows for a higher efficiency of photosynthesis both in low light, when the quantum efficiency of carbon assimilation is important, and at higher light when the increased energy supply can be used effectively by a CBC with high turnover capacity, ideal for a plant or algal system adapted to growth in the shade under low and variable light intensities.

6.2 The pyrenoid is assembled by Rubisco tethering multiple linker proteins such as LCI5 via the SSU helices

Pyrenoid formation requires *Chlamydomonas* Rubisco SSU helices without which Rubisco does not aggregate (Genkov et al., 2010; Meyer et al., 2012). This current study demonstrates that the *Chlamydomonas* SSU helices present a formidable site for protein interaction (Chapter 3). Spontaneous aggregation of Rubisco, which had been suggested as a mechanism for pyrenoid assembly (Ma et al., 2011), is refuted (Fig. 3.3, Fig. 3.5, Fig. 3.6). That isolated Rubisco was found to repel itself (Fig. 3.3) demonstrates a need for a linking agent (Fig. 6.1a). Computational analysis supports growing evidence that LCI5 operates as a linker candidate (Mackinder et al., 2015), by docking to the SSU helix interface (Fig. 3.8). As the analysis resolved individual amino acids most likely to be involved in this interaction, an *in vivo* test could be performed via complementary SDM on *RBCS* and *LCI5* (Fig. 3.9) to regenerate the pyrenoid in a pyr- line.

By generating a differential interactome for Rubisco in WT and pyr- cells, novel insights into the mechanism of Rubisco aggregation could be obtained (Chapter 4). The case for LCI5 as a linker candidate (Mackinder et al., 2015) was strengthened by the finding that it not only binds to Rubisco, but does so specifically in conditions where Rubisco is fully aggregated in the pyrenoid (Appendix 8.26). Clustering alongside LCI5, new protein candidates were found to interact with Rubisco specifically in the context of a fully assembled pyrenoid associated, warranting further characterization. Like LCI5, both Cre02.g084000.t1.2 and Cre01.g050550.t1.2 are intrinsically disordered proteins, as is Cre16.g659700.t1.2, the candidate associated with the constitutive pyrenoid. Disordered regions may thus be a general feature of linker proteins as suggested by (Mackinder et al.,

2015) and supported by the fact that cyanobacteria also use intrinsically disordered proteins in an analogous fashion to tether Rubisco inside carboxysomes (Espie and Kimber, 2011; Rae et al., 2013; Cai et al., 2015).

The fact that α - and β -tubulin were found to be associated with WT Rubisco specifically in low CO₂ when the pyrenoid is fully assembled strongly implicates the microtubule cytoskeleton in pyrenoid organization (Fig. 6.1b). While microtubules are usually located in the cytoplasm outside the chloroplast, specific localisation of chloroplast features involving this cytoskeleton has a precedent in the positioning of the *Chlamydomonas* eyespot (Mittelmeier et al., 2013). Tubulins have been part of previous CCM and pyrenoid datasets but have so far been viewed with suspicion as contaminants (Miura et al., 2004; Yamano et al., 2008; Uniacke, 2009; Brueggeman et al., 2012; Mackinder et al., 2015).

Rubisco aggregation is known to be regulated in *Chlamydomonas* according to CO₂ in the environment (Borkhsenius et al., 1998) and the day/night cycle (Mitchell et al., 2014; Tirumani et al., 2014). This regulation has been suggested before to involve phosphorylation and redox-regulation (Turkina et al., 2006) and involving thylakoid membranes (Goodenough, 1970; Engel et al., 2015). Here, a number of redoxins were found to associate with Rubisco in an aggregation-state dependent manner. The apparent importance of specifically 2-cys-peroxiredoxins suggests feedback regulation from the pETC via reactive oxygen species (Eberhard et al., 2008; Hall et al., 2009). Phosphorylation control elements associated with Rubisco are likely regulated via Ca²⁺-signalling, which may provide a link to regulation of cytoskeletal elements (Wheeler and Brownlee, 2008). Both Ca²⁺ and redox signalling are also candidates for integration with the circadian clock (Lemaire et al., 1999; Mittag et al., 2005; Mitchell et al., 2014). Finally, there is evidence for regulatory feedback between the pyrenoid and the CCM.

Association with Rubisco irrespective of pyrenoid presence suggests a simple mechanistic explanation for the localization of the enigmatic LCIB/C complex (Wang and Spalding, 2014), which is that LCIB/C binds to Rubisco and therefore accumulates in the periphery of the pyrenoid (Fig. 6.1b) at low CO₂ when Rubisco is aggregated. In light of this evidence, the punctate pattern of LCIB localisation around the pyrenoid (Yamano et al., 2010, 2014) would suggest that LCIB/C is not localized within the starch sheath (Fig. 1.4), but rather at the junctions between starch plates where Rubisco is accessible from the stroma. A crucial component of the CCM, the LCIB/C complex has been suggested to play a role in limiting CO₂ leakage, possibly by acting as directional CA-analogue in facilitating recapture of CO₂

escaping from the pyrenoid (Duanmu et al., 2009; Yamano et al., 2010, 2014; Wang and Spalding, 2014; Wang et al., 2015). Localisation of a CO₂-recapture complex, specifically to the junctions between starch plates, would imply that CO₂ leakage through the starch sheath is limited. As the CCM appeared fully operational in a starch-less mutant (Villarejo et al., 1996) it had seemed unlikely that the starch sheath would function solely as a CO₂-diffusion barrier. However, it would be worth revisiting the localisation of LCIB in this starch-less mutant, as a uniform distribution of this putative CO₂ recapture complex around the pyrenoid might compensate for the loss of the physical diffusion barrier.

The proteins identified in the interactome were also consistent with previous reports of Rubisco being associated with chaperones, CBC enzymes, thylakoid membranes (Süss et al., 1995; Vitlin Gruber et al., 2013). Plastid protein synthesis components associated with Rubisco appear to be altered in conditions where the CCM is operational, consistent with the suggested organization of the translational machinery T-zones around the pyrenoid (Uniacke and Zerges, 2009). Finally, candidates such as VIPP1 (Nordhues et al., 2012) that might be involved in structuring the intra-pyrenoidal thylakoid network were recovered (Engel et al., 2015).

Identification of pyrenoid-defective mutants among CCM-mutants in a genome-wide insertional mutagenesis screen (Chapter 5) found a number of strains with pyrenoid defects, but no case where Rubisco aggregation was completely absent. Pyrenoid-deficient mutants identified, such as *lci5* (Mackinder et al., 2015), show pyrenoids reduced in size but retaining some degree of Rubisco aggregation (Chapter 5). This finding suggests the presence of multiple linker proteins (Fig. 6.1b). That single mutations, such as in the *lci5* mutant, lead to severe defects in pyrenoid ultrastructure (Fig. 5.8) and CCM operation (Mackinder et al., 2015) indicates that linking agents coded by different genes are unable to complement each other fully. All of these linkers will have to interact with Rubisco via the SSU helices (Fig. 6.1a), otherwise some residual aggregation would have been visible in the “Reciprocal” SSU substitution line, where Rubisco resembles the native *Chlamydomonas* holoenzyme except for the amino acid sequence of the SSU helices (Meyer et al., 2012).

The presence of multiple linker proteins may go some way to explain why it has been so difficult to unravel pyrenoid biogenesis (Wang et al., 2015). Individual linker proteins may be regulated in response to separate cues. For example, the fact that full Rubisco aggregation occurs over a timescale of 20-60 min (Yamano et al., 2010; Mitchell et al., 2014), which

suggests the involvement of *de novo* protein synthesis (Eberhard et al., 2008), is consistent with large scale upregulation of *LCI5* upon CCM induction (Lavigne et al., 2001).

The presence of ectopic Rubisco aggregates in some mutants suggests the presence of a factor promoting the delocalisation of Rubisco. One candidate for promoting delocalisation is Cre11.g467712, a protein misannotated as E3 ubiquitin ligase (Luke Mackinder, personal communication) which was recovered in the pyrenoid mutant screen (Chapter 5) as two independent mutant lines exhibiting ectopic Rubisco aggregates. This protein was not found to associate with Rubisco directly in the co-IP experiment (Chapter 4). Instead, the ligase might promote Rubisco delocalisation by disabling linker proteins such as *LCI5* (Fig. 6.1b). Given that in WT lines the pyrenoid never fully disassembles (Goodenough, 1970), perhaps only a subset of linker proteins would be targeted by this candidate.

This way, independent regulation of linker proteins would allow multiple environmental inputs to regulate the Rubisco aggregation state. Since the function of the pyrenoid is to increase CBC turnover capacity by supplying CO₂ to Rubisco as part of the CCM (Chapter 2), such regulation would likely involve complex trade-offs between the resource costs of photosynthesis in the presence and absence of CCM operation (Raven et al., 2012, 2014).

6.3 The Pyrenoid is functionally self-contained

Pyrenoid-negative cells are uniquely limited by internal availability of CO₂ (Chapter 2), demonstrating that the sole function of the pyrenoid is CO₂ delivery to Rubisco as part of the CCM (Fig. 6.1b). Interestingly, neither thylakoid ultrastructure (Fig. 2.5) nor expression of pETC components such as pigments or reaction centre complexes (Fig. 2.10) is altered in *pyr-* lines even when grown at low CO₂. While T-zones (Uniacke and Zerges, 2007, 2009) were not visualized directly, chloroplast protein import, translation and complex assembly must be working in order, in a *pyr-* context, to allow the pETC to be as present and functional, as in WT, once the CO₂ limitation is lifted. Despite a significant impairment of photosynthesis, the absence of a pyrenoid has thus very limited effects on directly associated aspects of cellular physiology. Similarly, a large part of the interactome associates with Rubisco, independently of pyrenoid presence or absence (Chapter 4), including pyrenoid-associated factors such as *LCIB/C* (Yamano et al., 2010). These findings are in line with recent whole-cell proteome (Mitchell, 2014) and transcriptome (Moritz Meyer, personal communication) analyses of *pyr-* cells showing expression profiles highly similar to WT. Thus a picture emerges of the pyrenoid as a functionally self-contained entity, with effects of perturbations largely limited to the pyrenoid itself and associated CCM functionality.

Presence of the pyrenoid is therefore not required for the thylakoid ultrastructure or the structural coordination of complex assembly in T-zones. On the other hand, both intra-pyrenoidal thylakoid lamellae and T-zones are intricate structures that likely require a dedicated suite of proteins and as such the presence of these structures must provide an adaptive advantage to *Chlamydomonas*. It is therefore likely that, rather than the pyrenoid presence being structurally required for thylakoids and T-zones, instead these associated structures are required for the pyrenoid to assemble and function within the CCM.

As such, it may be that thylakoids influence pyrenoid ultrastructure. In the interactome (Chapter 4), Rubisco was found to associate with thylakoid membrane proteins even in *pyr-*, particularly when the pressure for Rubisco aggregation was high, suggesting that thylakoids may play a role in early steps of Rubisco aggregation and thus pyrenoid assembly. Structures reminiscent of intra-pyrenoid tubules have been observed even in the absence of a pyrenoid, in the context of a cell unable to express Rubisco as a result of lacking plastid ribosomes (Goodenough and Levine, 1970). Thus, intra-pyrenoid tubule-like thylakoid structures may form independently of Rubisco aggregation and act as seed for pyrenoid formation (Fig. 6.1a). However, TEM analysis of the pyrenoid mutant strains recovered in Chapter 5 appears to show that some strains contain Rubisco aggregates devoid of thylakoids (Cindy Chan, personal communication). Rubisco aggregation may thus be able to proceed to some extent without a thylakoid seed, while the CCM phenotype of the strains suggests that thylakoid tubules are crucial for accumulation, or release, of CO₂ within the pyrenoid (Meyer and Griffiths, 2015).

The topic requires further clarification. Experiments to establish the presence or absence of intra-pyrenoid tubule-like thylakoid structures in *pyr-* lines are already under way (Moritz Meyer, personal communication). Furthermore, it will be interesting to see characterization of the mutant lines lacking pyrenoidal thylakoids, and also investigate what role putative thylakoid organization factors like VIPP1 that form part of the Rubisco interactome play.

6.4 Towards a molecular understanding of pyrenoid form and function

A model for the mechanism underlying Rubisco aggregation in the pyrenoid thus emerges (Fig. 6.1). While Rubisco holoenzymes in isolation repel each other (Chapter 3), they can be tethered together via linker proteins such as LCI5 (Fig. 6.1a). The interaction must involve the SSU helices and is likely to proceed via an ordered helical region within LCI5, which is repeated four times in the amino acid sequence (Chapter 3).

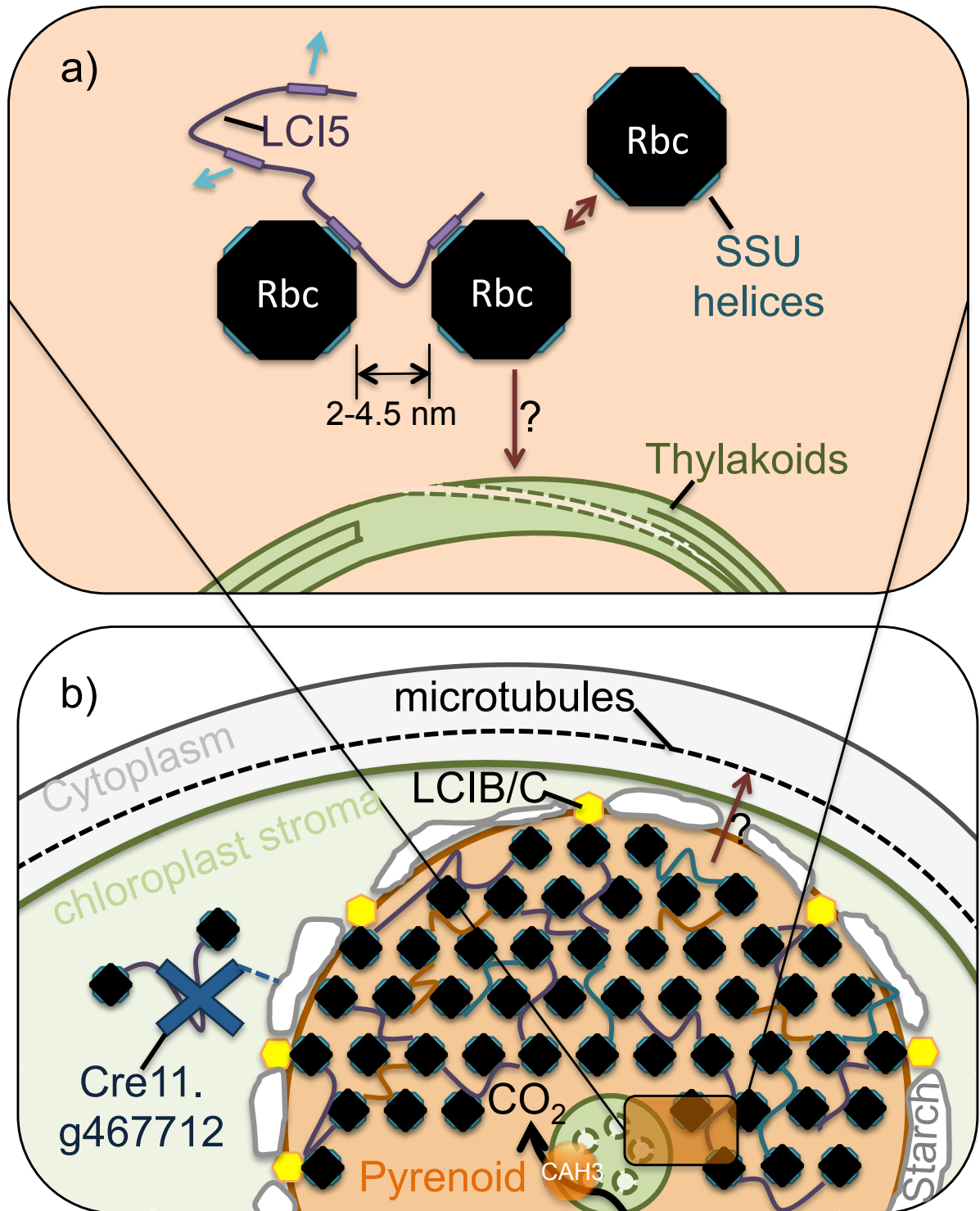


Fig. 6.1: A proposed mechanism for Rubisco aggregation within the pyrenoid

Rubisco holoenzymes repel each other, requiring linker proteins such as LCI5 as tethers to promote aggregation, which may form preferentially around specialized thylakoid tubules (a). A network of interactions between Rubisco and intrinsically disordered linker proteins forms the pyrenoid matrix, perhaps positioned relative to the microtubule cytoskeleton (b). Features such as LCIB/C may be excluded from the matrix and hence localize around the pyrenoid by binding to Rubisco. Aggregation outside the pyrenoid may be prevented by delocalisation factors, such as Cre11.g467712 misannotated as “E3 ligase” which contains a starch binding domain and does not interact with Rubisco itself, hence may act on the linkers.

This interaction between SSU helices and LCI5 could be demonstrated *in vitro* by showing that aggregates form when isolated LCI5 is mixed with Rubisco isolated from HelixAB (*Spinacia oleracea* SSU with *Chlamydomonas* helices), but not when mixed with Rubisco isolated from the Reciprocal strain (*Chlamydomonas* SSU with *Spinacia oleracea* helices). Intrinsically disordered parts of the LCI5 sequence repeats may act as flexible linkers between the helical interaction interfaces. That interaction proceeds via the ordered LCI5 helical stretch could be tested *in vivo* by rescue of a *pyr-* line via complementary SDM, as outlined in Chapter 3. Tethering this way could account for the hexagonal close packing (Fig. 6.1b) with a spacing of 2-4.5 nm (Fig. 6.1a) between holoenzymes that was established recently (Engel et al., 2015), as suggested by (Mackinder et al., 2015).

While the Rubisco aggregation does not affect thylakoid ultrastructure (Chapter 2), thylakoid tubules may play a role in organizing pyrenoid ultrastructure (Goodenough and Levine, 1970; Engel et al., 2015). Association with thylakoid membranes appears to be an early step in aggregation, although the molecular basis is not clear (Fig. 6.1a). LCI5 itself has been suggested to be membrane associated (Turkina et al., 2006) and may prove to be the linker in this respect, too. On the other hand, Rubisco has repeatedly been suggested to show some preference for thylakoid membranes in multiple species (Süss et al., 1995; Vitlin Gruber et al., 2013), and associates with thylakoid membrane proteins even in a *pyr-* context according to co-IP data (Chapter 4), suggesting the mechanism may be independent of SSU helices binding LCI5.

Rubisco tethered by linker proteins would thus form the pyrenoid interior. Given that pyrenoid assembly appears as a multi-gene trait (Chapter 5), linker proteins in addition to LCI5 should be involved. Should the candidates identified by co-IP (Chapter 4) prove to be additional linker proteins, then tethers would appear to generally contain intrinsically disordered regions, as suggested by (Mackinder et al., 2015). Pyrenoid positioning may be linked to the microtubule cytoskeleton (Chapter 4), although the transmembrane tether that this connection would require remains to be established.

Factors including T-zone ribosomes and the LCIB/C complex may localize to the periphery of the pyrenoid by binding to Rubisco (Chapter 4), whilst being excluded from the pyrenoid matrix. Given that LCIB/C binds to Rubisco equally in WT and *pyr-*, the interaction should proceed via an interface on the LSU.

Aggregation of Rubisco outside the pyrenoid appears to be prevented by delocalisation promoting factors such as Cre11.g467712, misannotated as E3 ubiquitin ligase (Chapter 5).

Chapter 6: Conclusions

Given that this protein does not appear to interact with Rubisco directly (Chapter 4), it may act through linker proteins, e.g. by targeting certain tethers for degradation. At night or at high CO₂, upregulation of factors like this candidate may lead to removal of linker proteins from the pyrenoid itself and hence a greater delocalisation of Rubisco. Such a mechanism would be consistent with the apparent requirement for *de novo* protein synthesis for full pyrenoid assembly, judging from aggregation timescales (Yamano et al., 2010; Mitchell et al., 2014). Expression of linker proteins such as LCI5 during CCM induction (Lavigne et al., 2001) would then act to replace previously degraded tethers.

The effect of Rubisco aggregation in the pyrenoid would be to allow a high CO₂ environment to be generated locally via the CCM (Chapter 2). The presence of thylakoid membranes within pyrenoidal aggregates appears to be important for CCM operation as well as pyrenoid ultrastructure (Chapter 5), consistent with the idea of CO₂ delivery via CAH3 associated with thylakoid tubules (Wang et al., 2015). Tubules may also be important in providing stromal connectivity for metabolite exchange (Engel et al., 2015; Meyer and Griffiths, 2015) with CBC enzymes located outside the pyrenoid (Tabea Mettler, personal communication; Chapter 4). A high CO₂ environment for Rubisco within the pyrenoid then leads to a suppression of photorespiration and enables pETC and CBC to balance at a higher energy throughput, decreasing *NPQ* and enabling photosynthesis to proceed with a higher quantum efficiency which in turn leads to higher growth rates (Chapter 2).

For further research, identification of the genes mutated in the strains identified in Chapter 5 should be of high priority. Should the candidates identified through the Rubisco interactome (Chapter 4) indeed be important for pyrenoid ultrastructure, there is a high chance that a corresponding mutant line would have been recovered. Such overlap between candidates of the biochemical and genetic searches for pyrenoid assembly candidates should be the first to be characterized in detail, perhaps following a similar approach as for *lci5* (Mackinder et al., 2015). Mutant lines that show no overlap to interactome candidates could still prove highly insightful, as these may e.g. include membrane proteins that would not have been available for detection via the co-IP. Proteins involved in organization of the thylakoid tubules may be identified this way. In addition to pyrenoid ultrastructure, the interactome also contains information about potential regulatory proteins, which may be worth following up on.

In addition, SDM of the SSU helices should continue to establish the set of amino acids sufficient to drive pyrenoid assembly starting from a *Spinacia oleracea* *RBCS* template. A SDM approach could also prove very useful for testing the interaction between LCI5 and

SSU, as detailed in Chapter 3. Finally, it would be interesting to follow up some of the ultrastructural implications of the present work. Further microscopic characterisation of the pyr- lines should reveal whether thylakoids form intra-pyrenoid tubule-like structures even in the absence of Rubisco aggregation, show whether T-zones persist in a pyr- cell and where they would be localized and provide a test for whether the localization of LCIB/C is determined by the localisation of Rubisco. The latter should also be investigated in a starch-less mutant.

Equipped with a greater mechanistic understanding of how the pyrenoid ultrastructure is assembled, the next challenge for successful incorporation of a CCM into any higher plant system will be an understanding of CCM regulation. In photosynthesis, complex feedback loops are active to control the flux of energy through the system (Eberhard et al., 2008; Foyer et al., 2012; Minagawa, 2013). Cellular response to environmental stresses is often associated with extensive regulatory changes (Mühlhaus et al., 2011; Mettler et al., 2014; Schmollinger et al., 2014; Schroda et al., 2015), and from what is known about the dynamic nature of pyrenoid and CCM, low CO₂ stress is no exception (Yamano et al., 2010; Brueggeman et al., 2012; Mitchell et al., 2014; Wang et al., 2015; Chapter 2). To address the issue of regulation, analysis of whole-cell transcriptome and proteome during CCM induction in SSU substitution lines is underway (Mitchell, 2014; Moritz Meyer, personal communication) to complement the interactome and the forward genetic screen presented here (Chapters 4&5). To get started, mutant lines of candidates identified by these approaches could be screened, pre-dawn (Mitchell et al., 2014) and under fluctuating CO₂ or light conditions, for photosynthetic aberrancies as described for pyr- in Chapter 2 using a CFimager to isolate key candidates for further analysis.

In this way, the work presented here contributes towards a molecular understanding of the pyrenoid in the model green alga *Chlamydomonas reinhardtii*. Functionally, the pyrenoid could be defined as an aspect of the CCM, with no effects on chloroplast ultrastructure found to be associated with pyrenoid loss. Pyrenoid formation was understood as a process of Rubisco aggregation. Progress has been made on the mechanism of this aggregation process and the factors that may be involved (Fig. 6.1), opening avenues for further research in this area. Ultimately, a molecular understanding of the CCM will allow transfer of genes or mechanistic principles to higher plants. The increased quantum efficiency of photosynthesis that a CCM operating in a low CO₂ atmosphere may allow yield increases of up to 50-60% (Hibberd and Weber, 2012; McGrath and Long, 2014; Long et al., 2015) and thereby form part of a wider effort to ensure food security for the future.

7 REFERENCES

- Akaike, H. A New Look at the Statistical Model Identification. *IEEE Trans. Automat. Contr.* **1974**, *19* (6).
- Allen, J. F. The Function of Genomes in Bioenergetic Organelles. *Philos. Trans. R. Soc. Lond. B. Biol. Sci.* **2003**, *358* (1429), 19–37; discussion 37–38.
- Allen, J. F.; de Paula, W. B. M.; Puthiyaveetil, S.; Nield, J. A Structural Phylogenetic Map for Chloroplast Photosynthesis. *Trends Plant Sci.* **2011**, No. L, 1–11.
- Alric, J. Cyclic Electron Flow around Photosystem I in Unicellular Green Algae. *Photosynth. Res.* **2010**, *106* (1-2), 47–56.
- Anderson, L. E.; Carol, A. A. Enzyme Co-Localization with Rubisco in Pea Leaf Chloroplasts. *Photosynth. Res.* **2004**, *82* (1), 49–58.
- Andersson, B.; Anderson, J. M. Lateral Heterogeneity in the Distribution of Chlorophyll-Protein Complexes of the Thylakoid Membranes of Spinach Chloroplasts. *Biochim. Biophys. Acta* **1980**, *593* (2), 427–440.
- Andersson, I. Large Structures at High Resolution: The 1.6 Å Crystal Structure of Spinach Ribulose-1,5-Bisphosphate Carboxylase/oxygenase Complexed with 2-Carboxyarabinitol Bisphosphate. *J. Mol. Biol.* **1996**, *259* (1), 160–174.
- Apweiler, R.; Bairoch, A.; Wu, C. H.; Barker, W. C.; Boeckmann, B.; Ferro, S.; Gasteiger, E.; Huang, H.; Lopez, R.; Magrane, M.; et al. UniProt: The Universal Protein Knowledgebase. *Nucleic Acids Res.* **2004**, *32* (Database issue), D115–D119.
- Badger, M. R.; Price, G. D. CO₂ Concentrating Mechanisms in Cyanobacteria: Molecular Components, Their Diversity and Evolution. *J. Exp. Bot.* **2003**, *54* (383), 609–622.
- Badger, M. R.; Hanson, D.; Price, G. D. Evolution and Diversity of CO₂ Concentrating Mechanisms in Cyanobacteria. *Funct. Plant Biol.* **2002**, *29* (3), 161–173.
- Bailleul, B.; Cardol, P.; Breyton, C.; Finazzi, G. Electrochromism: A Useful Probe to Study Algal Photosynthesis. *Photosynth. Res.* **2010**, *106* (1-2), 179–189.
- Batsanov, S. Van Der Waals Radii of Elements. *Inorg. Mater.* **2001**, *37* (9), 871–885.
- Bauwe, H.; Hagemann, M.; Fernie, A. R. Photorespiration: Players, Partners and Origin. *Trends Plant Sci.* **2010**, *15* (6), 330–336.
- Bauwe, H.; Hagemann, M.; Kern, R.; Timm, S. Photorespiration Has a Dual Origin and Manifold Links to

Molecular Physiology of the *Chlamydomonas* pyrenoid

- Central Metabolism. *Curr. Opin. Plant Biol.* **2012**, *15* (3), 269–275.
- Becker, B. Snow Ball Earth and the Split of Streptophyta and Chlorophyta. *Trends Plant Sci.* **2013**, *18* (4), 180–183.
- Bellasio, C.; Griffiths, H. Acclimation of C4 Metabolism to Low Light in Mature Maize Leaves Could Limit Energetic Losses during Progressive Shading in a Crop Canopy. *J. Exp. Bot.* **2014**, *65* (13), 1–12.
- Berman, H. M.; Westbrook, J.; Feng, Z.; Gilliland, G.; Bhat, T. N.; Weissig, H.; Shindyalov, I. N.; Bourne, P. E. The Protein Data Bank. *Nucleic Acids Res.* **2000**, *28* (1), 235–242.
- Blaszczyk, M.; Jamroz, M.; Kmiecik, S.; Kolinski, A. CABS-Fold: Server for the de Novo and Consensus-Based Prediction of Protein Structure. *Nucleic Acids Res.* **2013**, *41* (Web Server issue), 406–411.
- Bold, H. C.; Wynne, M. J. *Introduction to the Algae*, 1st ed.; Prentice-Hall International, Inc.: London, United Kingdom, 1978.
- Borkhsenius, O. N.; Mason, C. B.; Moroney, J. V. The Intracellular Localization of Ribulose-1,5-Bisphosphate Carboxylase/oxygenase in *Chlamydomonas Reinhardtii*. *Plant Physiol.* **1998**, *116* (4), 1585–1591.
- Borland, A. M.; Hartwell, J.; Weston, D. J.; Schlauch, K. a.; Tschaplinski, T. J.; Tuskan, G. a.; Yang, X.; Cushman, J. C. Engineering Crassulacean Acid Metabolism to Improve Water-Use Efficiency. *Trends Plant Sci.* **2014**, *19* (5), 327–338.
- Brueggeman, A. J.; Gangadharaiah, D. S.; Cserhati, M. F.; Casero, D.; Weeks, D. P.; Ladunga, I. Activation of the Carbon Concentrating Mechanism by CO₂ Deprivation Coincides with Massive Transcriptional Restructuring in *Chlamydomonas Reinhardtii*. *Plant Cell Online* **2012**, *24* (5), 1860–1875.
- Buchan, D. W. a; Minnici, F.; Nugent, T. C. O.; Bryson, K.; Jones, D. T. Scalable Web Services for the PSIPRED Protein Analysis Workbench. *Nucleic Acids Res.* **2013**, *41* (Web Server issue), 349–357.
- Von Caemmerer, S. Steady-State Models of Photosynthesis. *Plant, Cell Environ.* **2013**, *36* (9), 1617–1630.
- Cai, F.; Dou, Z.; Bernstein, S.; Leverenz, R.; Williams, E.; Heinhorst, S.; Shively, J.; Cannon, G.; Kerfeld, C. *Advances in Understanding Carboxysome Assembly in Prochlorococcus and Synechococcus Implicate CsoS2 as a Critical Component*; 2015; Vol. 5.
- Cardol, P.; Forti, G.; Finazzi, G. Regulation of Electron Transport in Microalgae. *Biochim. Biophys. Acta* **2011**, *1807* (8), 912–918.
- Chan, C. TEM of Pyrenoid Mutants. *Pers. Commun.* **2015**.
- Cheng, J.; Randall, a. Z.; Sweredoski, M. J.; Baldi, P. SCRATCH: A Protein Structure and Structural Feature Prediction Server. *Nucleic Acids Res.* **2005**, *33* (SUPPL. 2), 72–76.
- Chow, W. S. Grana Formation: Entropy-Assisted Local Order in Chloroplasts? *Funct. Plant Biol.* **1999**, *26* (7), 641–647.
- Chow, W. S.; Kim, E.-H.; Horton, P.; Anderson, J. M. Granal Stacking of Thylakoid Membranes in Higher Plant Chloroplasts: The Physicochemical Forces at Work and the Functional Consequences That Ensur. *Photochem. Photobiol. Sci.* **2005**, *4* (12), 1081–1090.
- Cole, D. G.; Diener, D. R.; Himelblau, A. L.; Beech, P. L.; Fuster, J. C.; Rosenbaum, J. L. Kinesin-II-dependent Intraflagellar Transport (IFT): IFT Particles Contain Proteins Required for Ciliary Assembly in. *J. Cell Biol.* **1998**, *141* (4), 993–1008.
- Cosgrove, J.; Borowitzka, M. A. Chlorophyll Fluorescence Terminology: An Introduction. In *Chlorophyll a Fluorescence in Aquatic Sciences*; Suggett, D. J., Prášil, O., Borowitzka, M. A., Eds.; Springer: Heidelberg London New York, 2010; pp 1–18.
- Crooks, G. E.; Hon, G.; Chandonia, J.; Brenner, S. E. WebLogo : A Sequence Logo Generator. *Genome Res.* **2004**, *14*, 1188–1190.

Chapter 7: References

- Cusick, K. D.; Wetzel, R. K.; Minkin, S. C.; Dodani, S. C.; Wilhelm, S. W.; Sayler, G. S. Paralytic Shellfish Toxins Inhibit Copper Uptake in *Chlamydomonas Reinhardtii*. *Environ. Toxicol. Chem.* **2013**, *32* (6), 1388–1395.
- Daum, B.; Nicastro, D.; Austin, J.; McIntosh, J. R.; Kühlbrandt, W. Arrangement of Photosystem II and ATP Synthase in Chloroplast Membranes of Spinach and Pea. *Plant Cell* **2010**, *22* (4), 1299–1312.
- Dominguez, C.; Boelens, R.; Bonvin, A. M. J. J. HADDOCK: A Protein-Protein Docking Approach Based on Biochemical And/or Biophysical Information. *J. Am. Chem. Soc.* **2003**, *125* (7), 1731–1737.
- Drop, B.; Webber-Birungi, M.; Yadav, S. K. N.; Filipowicz-Szymanska, A.; Fusetti, F.; Boekema, E. J.; Croce, R. Light-Harvesting Complex II (LHCII) and Its Supramolecular Organization in *Chlamydomonas Reinhardtii*. *Biochim. Biophys. Acta* **2014**, *1837* (1), 63–72.
- Drozdetskiy, a.; Cole, C.; Procter, J.; Barton, G. J. JPred4: A Protein Secondary Structure Prediction Server. *Nucleic Acids Res.* **2015**, 1–6.
- Duanmu, D.; Wang, Y.; Spalding, M. H. Thylakoid Lumen Carbonic Anhydrase (CAH3) Mutation Suppresses Air-Dier Phenotype of LCIB Mutant in *Chlamydomonas Reinhardtii*. *Plant Physiol.* **2009**, *149* (2), 929–937.
- Eberhard, S.; Finazzi, G.; Wollman, F.-A. The Dynamics of Photosynthesis. *Annu. Rev. Genet.* **2008**, *42*, 463–515.
- Ehleringer, J. R.; Cerling, T. E.; Helliker, B. R. C 4 Photosynthesis, Atmospheric CO₂, and Climate. *Oecologia* **1997**, *112* (3), 285–299.
- Ellis, R. J. Macromolecular Crowding: Obvious but Underappreciated. *Trends Biochem. Sci.* **2001**, *26* (10), 597–604.
- Engel, B. D.; Schaffer, M.; Kuhn Cuellar, L.; Villa, E.; Plitzko, J. M.; Baumeister, W. Native Architecture of the *Chlamydomonas* Chloroplast Revealed by in Situ Cryo-Electron Tomography. *Elife* **2015**, *4*, 1–29.
- Erales, J.; Avilan, L.; Lebreton, S.; Gontero, B. Exploring CP12 Binding Proteins Revealed Aldolase as a New Partner for the Phosphoribulokinase/glyceraldehyde 3-Phosphate dehydrogenase/CP12 Complex - Purification and Kinetic Characterization of This Enzyme from *Chlamydomonas Reinhardtii*. *FEBS J.* **2008**, *275* (6), 1248–1259.
- Espie, G. S.; Kimber, M. S. Carboxysomes: Cyanobacterial RubisCO Comes in Small Packages. *Photosynth. Res.* **2011**, *109* (1-3), 7–20.
- Eswar, N.; Webb, B.; Marti-Renom, M. a; Madhusudhan, M. S.; Eramian, D.; Shen, M.-Y.; Pieper, U.; Sali, A. *Comparative Protein Structure Modeling Using MODELLER.*; 2007; Vol. Chapter 2.
- Van Etten, J. L.; Dunigan, D. D. Chloroviruses: Not Your Everyday Plant Virus. *Trends Plant Sci.* **2012**, *17* (1), 1–8.
- Finazzi, G. The Central Role of the Green Alga *Chlamydomonas Reinhardtii* in Revealing the Mechanism of State Transitions. *J. Exp. Bot.* **2005**, *56* (411), 383–388.
- Finazzi, G.; Rappaport, F.; Furia, A.; Fleischmann, M.; Rochaix, J.-D.; Zito, F.; Forti, G. Involvement of State Transitions in the Switch between Linear and Cyclic Electron Flow in *Chlamydomonas Reinhardtii*. *EMBO Rep.* **2002**, *3* (3), 280–285.
- Finn, R. D.; Bateman, A.; Clements, J.; Coggill, P.; Eberhardt, R. Y.; Eddy, S. R.; Heger, A.; Hetherington, K.; Holm, L.; Mistry, J.; et al. Pfam: The Protein Families Database. *Nucleic Acids Res.* **2014**, *42* (D1), 222–230.
- Foyer, C. H.; Bloom, A. J.; Queval, G.; Noctor, G. Photorespiratory Metabolism: Genes, Mutants, Energetics, and Redox Signaling. *Annu. Rev. Plant Biol.* **2009**, *60*, 455–484.
- Foyer, C. H.; Neukermans, J.; Queval, G.; Noctor, G.; Harbinson, J. Photosynthetic Control of Electron Transport and the Regulation of Gene Expression. *J. Exp. Bot.* **2012**, *63* (4), 1637–1661.

Molecular Physiology of the *Chlamydomonas* pyrenoid

- Fukuzawa, H.; Miura, K.; Ishizaki, K.; Kucho, K.-I.; Saito, T.; Kohinata, T.; Ohyama, K. Ccm1, a Regulatory Gene Controlling the Induction of a Carbon-Concentrating Mechanism in *Chlamydomonas Reinhardtii* by Sensing CO₂ Availability. *Proc. Natl. Acad. Sci.* **2001**, *98* (9), 5347–5352.
- Genkov, T.; Meyer, M.; Griffiths, H.; Spreitzer, R. J. Functional Hybrid Rubisco Enzymes with Plant Small Subunits and Algal Large Subunits: Engineered rbcS cDNA for Expression in *Chlamydomonas*. *J. Biol. Chem.* **2010**, *285* (26), 19833–19841.
- Genty, B.; Briantais, J.; Baker, N. R. The Relationship between the Quantum Yield of Photosynthetic Electron Transport and Quenching of Chlorophyll Fluorescence. *Biochim. Biophys. Acta* **1989**, *990* (1), 87–92.
- Geourjon, C.; Deléage, G. SOPMA: Significant Improvements in Protein Secondary Structure Prediction by Consensus Prediction from Multiple Alignments. *Comput. Appl. Biosci.* **1995**, *11* (6), 681–684.
- Givnish, T. J.; Barfuss, M. H. J.; Ee, B. Van; Riina, R.; Schulte, K.; Horres, R.; Gonsiska, P. a.; Jabaily, R. S.; Crayn, D. M.; Smith, J. A. C.; et al. Adaptive Radiation, Correlated and Contingent Evolution, and Net Species Diversification in Bromeliaceae. *Mol. Phylogenet. Evol.* **2014**, *71* (1), 55–78.
- Gontero, B.; Maberly, S. C. An Intrinsically Disordered Protein, CP12: Jack of All Trades and Master of the Calvin Cycle. **2012**, 995–999.
- Goodenough, U. W. Chloroplast Division and Pyrenoid Formation in *Chlamydomonas Reinhardtii*. *J. Phycol.* **1970**, *6* (1), 1–6.
- Goodenough, U. W.; Levine, R. P. Chloroplast Ultrastructure in Mutant Strains of *Chlamydomonas Reinhardtii* Lacking Components of the Photosynthetic Apparatus. *Plant Physiol.* **1969**, *44* (7), 990–1000.
- Goodenough, U. W.; Levine, R. P. Chloroplast Structure and Function in Ac-20, a Mutant Strain of *Chlamydomonas Reinhardtii*. 3. Chloroplast Ribosomes and Membrane Organization. *J. Cell Biol.* **1970**, *44* (3), 547–562.
- Goodstein, D. M.; Shu, S.; Howson, R.; Neupane, R.; Hayes, R. D.; Fazo, J.; Mitros, T.; Dirks, W.; Hellsten, U.; Putnam, N.; et al. Phytozome: A Comparative Platform for Green Plant Genomics. *Nucleic Acids Res.* **2012**, *40* (D1), 1178–1186.
- Gorman, D. S.; Levine, R. P. Cytochrome F and Plastocyanin: Their Sequence in the Photosynthetic Electron Transport Chain of *Chlamydomonas Reinhardtii*. *Proc. Natl. Acad. Sci. U. S. A.* **1965**, *54* (6), 1665–1669.
- Griffiths, D. J. The Pyrenoid. *Bot. Rev.* **1970**, *36* (1), 29–58.
- Griffiths, H. Plant Venation: From Succulence to Succulents. *Curr. Biol.* **2013**, *23* (9), R340–R341.
- Grossman, A. R.; Croft, M.; Gladyshev, V. N.; Merchant, S. S.; Posewitz, M. C.; Prochnik, S.; Spalding, M. H. Novel Metabolism in *Chlamydomonas* through the Lens of Genomics. *Curr. Opin. Plant Biol.* **2007**, *10* (2), 190–198.
- Grossman, A. R.; Gonzalez-Ballester, D.; Bailey, S.; Karpowicz, S. J.; Merchant, S. S. Understanding Photosynthetic Electron Transport Using *Chlamydomonas*: The Path from Classical Genetics to High Throughput Genomics. In *Functional Genomics and Evolution of Photosynthetic Systems*; Burnap, R. L., Vermaas, W. F. J., Eds.; SPRINGER, PO BOX 17, 3300 AA DORDRECHT, NETHERLANDS, 2012; Vol. 33, pp 139–176.
- Gurevitz, M.; Somerville, C. R.; McIntosh, L. Pathway of Assembly of Ribulosebiphosphate Carboxylase/oxygenase from *Anabaena 7120* Expressed in *Escherichia Coli*. *Proc. Natl. Acad. Sci. U. S. A.* **1985**, *82* (19), 6546–6550.
- Gutman, J.; Zarka, A.; Boussiba, S. The Host-Range of *Paraphysoderma Sedebokerensis*, a Chytrid That Infects *Haematococcus Pluvialis*. *Eur. J. Phycol.* **2009**, *44* (4), 509–514.
- Haldrup, A.; Jensen, P. E.; Lunde, C.; Scheller, H. V. Balance of Power: A View of the Mechanism of Photosynthetic State Transitions. *Trends Plant Sci.* **2001**, *6* (7), 301–305.
- Hall, A.; Karplus, P. A.; Poole, L. B. Typical 2-Cys Peroxiredoxins: Structures, Mechanisms and Functions.

Chapter 7: References

- FEBS J.* **2009**, 276 (9), 2469–2477.
- Harris, E. H. *Chlamydomonas* as a Model Organism. *Annu. Rev. Plant Physiol.* **2001**, 52 (1), 363–406.
- Heikal, F. E.-T.; Hefny, M. M.; El-Tawab, A. M. A. Electrochemical Behavior of 304L Stainless Steel in High Saline and Sulphate Solutions Containing *Alga Dunaliella Salina* and β -Carotene. *J. Alloys Compd.* **2010**, 491 (1–2), 636–642.
- Heber, U. Irrungen, Wirrungen? The Mehler Reaction in Relation to Cyclic Electron Transport in C3 Plants. *Photosynth. Res.* **2002**, 73 (1–3), 223–231.
- Heide, H.; Nordhues, A.; Drepper, F.; Nick, S.; Schulz-Raffelt, M.; Haehnel, W.; Schroda, M. Application of Quantitative Immunoprecipitation Combined with Knockdown and Cross-Linking to *Chlamydomonas* Reveals the Presence of Vesicle-Inducing Protein in Plastids 1 in a Common Complex with Chloroplast HSP90C. *Proteomics* **2009**, 9 (11), 3079–3089.
- Hibberd, J. M.; Weber, A. P. M. Plant Metabolism and Physiology. *Curr. Opin. Plant Biol.* **2012**, 1–3.
- Hiyama, T.; Ke, B. Difference Spectra and Extinction Coefficients of p700*. *Biochim. Biophys. Acta* **1972**, 267 (459), 160–171.
- Holt, N. E.; Fleming, G. R.; Niyogi, K. K. Toward an Understanding of the Mechanism of Nonphotochemical Quenching in Green Plants. *Biochemistry* **2004**, 43 (26), 8281–8289.
- Horton, P.; Johnson, M. P.; Perez-Bueno, M. L.; Kiss, A. Z.; Ruban, A. V. Photosynthetic Acclimation: Does the Dynamic Structure and Macro-organisation of Photosystem II in Higher Plant Grana Membranes Regulate Light Harvesting States? *FEBS J.* **2008**, 275 (6), 1069–1079.
- Houtz, R. L.; Magnani, R.; Nayak, N. R.; Dirk, L. M. a. Co- and Post-Translational Modifications in Rubisco: Unanswered Questions. *J. Exp. Bot.* **2008**, 59 (7), 1635–1645.
- Huang, D. W.; Sherman, B. T.; Lempicki, R. a. Bioinformatics Enrichment Tools: Paths toward the Comprehensive Functional Analysis of Large Gene Lists. *Nucleic Acids Res.* **2009a**, 37 (1), 1–13.
- Huang, D. W.; Sherman, B. T.; Lempicki, R. a. Systematic and Integrative Analysis of Large Gene Lists Using DAVID Bioinformatics Resources. *Nat. Protoc.* **2009b**, 4 (1), 44–57.
- Huang, N.-L.; Huang, M.-D.; Chen, T.-L. L.; Huang, A. H. C. Oleosin of Subcellular Lipid Droplets Evolved in Green Algae. *Plant Physiol.* **2013**, 161 (4), 1862–1874.
- Hubbard, S. J.; Thornton, J. M. NACCESS. Department of Biochemistry and Molecular Biology, University College London: Computer Program 1993.
- Hutner, S.; Provasoli, L.; Schatz, A.; Haskins, C. Some Approaches to the Study of the Role of Metals in the Metabolism of Microorganisms. *Proc. Am. Philos. Soc.* **1950**, 94 (2), 152–170.
- IRRI, I. R. R. I. The C4 Rice Project c4rice.irri.org (accessed Sep 15, 2015).
- Ishihama, Y.; Oda, Y.; Tabata, T.; Sato, T.; Nagasu, T.; Rappsilber, J.; Mann, M. Exponentially Modified Protein Abundance Index (emPAI) for Estimation of Absolute Protein Amount in Proteomics by the Number of Sequenced Peptides per Protein. *Mol. Cell. Proteomics* **2005**, 4 (9), 1265–1272.
- Ivanov, A. G.; Sane, P. V.; Hurry, V.; Öquist, G.; Huner, N. P. a. Photosystem II Reaction Centre Quenching: Mechanisms and Physiological Role. *Photosynth. Res.* **2008**, 98 (1–3), 565–574.
- Iwai, M.; Kato, N.; Minagawa, J. Distinct Physiological Responses to a High Light and Low CO₂ Environment Revealed by Fluorescence Quenching in Photoautotrophically Grown *Chlamydomonas Reinhardtii*. *Photosynth. Res.* **2007**, 94 (2–3), 307–314.
- Iwai, M.; Takizawa, K.; Tokutsu, R.; Okamuro, A.; Takahashi, Y.; Minagawa, J. Isolation of the Elusive Supercomplex That Drives Cyclic Electron Flow in Photosynthesis. *Nature* **2010**, 464 (7292), 1210–1213.
- Jahns, P.; Holzwarth, A. R. The Role of the Xanthophyll Cycle and of Lutein in Photoprotection of Photosystem II. *Biochim. Biophys. Acta - Bioenerg.* **2012**, 1817 (1), 182–193.

Molecular Physiology of the *Chlamydomonas* pyrenoid

- Järvi, S.; Suorsa, M.; Paakkarinen, V.; Aro, E.-M. Optimized Native Gel Systems for Separation of Thylakoid Protein Complexes: Novel Super- and Mega-Complexes. *Biochem. J.* **2011**, *439* (2), 207–214.
- Jassby, A. D.; Platt, T. Mathematical Formulation of the Relationship between Photosynthesis and Light for Phytoplankton. *Limnol. Oceanogr.* **1976**, *21* (4), 540–547.
- Jayaram, B.; Bhushan, K.; Shenoy, S. R.; Narang, P.; Bose, S.; Agrawal, P.; Sahu, D.; Pandey, V. Bhageerath: An Energy Based Web Enabled Computer Software Suite for Limiting the Search Space of Tertiary Structures of Small Globular Proteins. *Nucleic Acids Res.* **2006**, *34* (21), 6195–6204.
- Johnson, X.; Alric, J. Interaction between Starch Breakdown, Acetate Assimilation, and Photosynthetic Cyclic Electron Flow in *Chlamydomonas Reinhardtii*. *J. Biol. Chem.* **2012**, *287* (31), 26445–26452.
- Joliot, P.; Delosme, R. Flash-Induced 519 Nm Absorption Change in Green Algae. *Biochim. Biophys. Acta* **1974**, *357* (2), 267–284.
- Joliot, P.; Joliot, A. Cyclic Electron Transfer in Plant Leaf. *Proc. Natl. Acad. Sci. U. S. A.* **2002**, *99* (15), 10209–10214.
- Joliot, P.; Joliot, A. How Plants Regulate the Photosynthetic Activity: Linear versus Cyclic Electron Flow and Non-Photochemical Quenching. *Biochim. Biophys. Acta - Bioenerg.* **2010**, *1797*, 2.
- Joliot, P.; Béal, D.; Joliot, A. Cyclic Electron Flow under Saturating Excitation of Dark-Adapted Arabidopsis Leaves. *Biochim. Biophys. Acta - Bioenerg.* **2004**, *1656* (2-3), 166–176.
- Jones, D. T. Protein Secondary Structure Prediction Based on Position-Specific Scoring Matrices. *J. Mol. Biol.* **1999**, *292* (2), 195–202.
- Jungnick, N.; Ma, Y.; Mukherjee, B.; Cronan, J. C.; Speed, D. J.; Laborde, S. M.; Longstreth, D. J.; Moroney, J. V. The Carbon Concentrating Mechanism in *Chlamydomonas Reinhardtii*: Finding the Missing Pieces. *Photosynth. Res.* **2014**, *121* (2-3), 159–173.
- Källberg, M.; Wang, H.; Wang, S.; Peng, J.; Wang, Z.; Lu, H.; Xu, J. Template-Based Protein Structure Modeling Using the RaptorX Web Server. *Nat. Protoc.* **2012**, *7* (8), 1511–1522.
- Kanehisa, M.; Goto, S.; Sato, Y.; Furumichi, M.; Tanabe, M. KEGG for Integration and Interpretation of Large-Scale Molecular Data Sets. *Nucleic Acids Res.* **2012**, *40* (D1), 109–114.
- Karlsson, J.; Clarke, A. K.; Chen, Z.-Y. Y.; Huggins, S. Y.; Park, Y.-I. I.; Husic, H. D.; Moroney, J. V.; Samuelsson, G. A Novel Alpha-Type Carbonic Anhydrase Associated with the Thylakoid Membrane in *Chlamydomonas Reinhardtii* Is Required for Growth at Ambient CO₂. *Eur. Mol. Biol. Organ. J.* **1998**, *17* (5), 1208–1216.
- Kaufmann, K. W.; Lemmon, G. H.; Deluca, S. L.; Sheehan, J. H.; Meiler, J. Practically Useful: What the R Osetta Protein Modeling Suite Can Do for You. *Biochemistry* **2010**, *49* (14), 2987–2998.
- Kautsky, H.; Hirsch, A. Neue Versuche Zur Kohlensäureassimilation. *Naturwissenschaften* **1931**, *19*, 964.
- Kelley, L. a; Sternberg, M. J. E. Protein Structure Prediction on the Web: A Case Study Using the Phyre Server. *Nat. Protoc.* **2009**, *4* (3), 363–371.
- Khrebtukova, I.; Spreitzer, R. J. Elimination of the *Chlamydomonas* Gene Family That Encodes the Small Subunit of Ribulose-1,5-Bisphosphate Carboxylase/oxygenase. *Proc. Natl. Acad. Sci. U. S. A.* **1996**, *93* (24), 13689–13693.
- Kim, E.-H.; Chow, W. S.; Horton, P.; Anderson, J. M. Entropy-Assisted Stacking of Thylakoid Membranes. *Biochim. Biophys. Acta* **2005**, *1708* (2), 187–195.
- Kirchhoff, H. Molecular Crowding and Order in Photosynthetic Membranes. *Trends Plant Sci.* **2008**, *13* (5), 201–207.
- Kochert, G.; Olson, L. W. Ultrastructure of *Volvox Carteri*. *Arch. Microbiol.* **1970**, *74* (1), 19–30.
- Kolber, Z. S.; Prášil, O.; Falkowski, P. G. Measurements of Variable Chlorophyll Fluorescence Using Fast

Chapter 7: References

- Repetition Rate Techniques: Defining Methodology and Experimental Protocols. *Biochim. Biophys. Acta - Bioenerg.* **1998**, 1367 (1–3), 88–106.
- Koonin, E. V.; Fedorova, N. D.; Jackson, J. D.; Jacobs, A. R.; Krylov, D. M.; Makarova, K. S.; Mazumder, R.; Mekhedov, S. L.; Nikolskaya, A. N.; Rao, B. S.; et al. A Comprehensive Evolutionary Classification of Proteins Encoded in Complete Eukaryotic Genomes. *Genome Biol.* **2004**, 5 (2), R7.
- Krause, G. H.; Weis, E. Chlorophyll Fluorescence and Photosynthesis: The Basics. *Annu. Rev. Plant Physiol. Plant Mol. Biol.* **1991**, 42 (1), 313–349.
- Kuchitsu, K.; Tsuzuki, M.; Miyachi, S. Characterization of the Pyrenoid Isolated from Unicellular Green Alga *Chlamydomonas Reinhardtii*: Particulate Form of RuBisCO Protein. *Protoplasma* **1988**, 144 (1), 17–24.
- Kügler, M.; Jansch, L.; Kruff, V.; Schmitz, U. K.; Braun, H. Analysis of the Chloroplast Protein Complexes by Blue-Native Polyacrylamide Gel Electrophoresis (BN-PAGE). *Photosynth. Res.* **1997**, 53, 35–44.
- Kumar, T. A. CFSSP : Chou and Fasman Secondary Structure Prediction Server. *Wide Spectr.* **2013**, 1 (9), 15–19.
- Lacoste-Royal, G.; Gibbs, S. P. Immunocytochemical Localization of Ribulose-1,5-Bisphosphate Carboxylase in the Pyrenoid and Thylakoid Region of the Chloroplast of *Chlamydomonas Reinhardtii*. *Plant Physiol.* **1987**, 83 (3), 602–606.
- Lambrev, P. H.; Schmitt, F.-J.; Kussin, S.; Schoengen, M.; Várkonyi, Z.; Eichler, H. J.; Garab, G.; Renger, G. Functional Domain Size in Aggregates of Light-Harvesting Complex II and Thylakoid Membranes. *Biochim. Biophys. Acta - Bioenerg.* **2011**, 1807 (9), 1022–1031.
- Lambrev, P. H.; Miloslavina, Y.; Jahns, P.; Holzwarth, A. R. On the Relationship between Non-Photochemical Quenching and Photoprotection of Photosystem II. *Biochim. Biophys. Acta - Bioenerg.* **2012**, 1817 (5), 760–769.
- Lane, N. Bioenergetic Constraints on the Evolution of Complex Life. *Cold Spring Harb. Perspect. Biol.* **2014**, 6, a015982.
- Lauersen, K. J.; Kruse, O.; Mussnug, J. H. Targeted Expression of Nuclear Transgenes in *Chlamydomonas Reinhardtii* with a Versatile, Modular Vector Toolkit. *Appl. Microbiol. Biotechnol.* **2015**, 3491–3503.
- Lavigne, A.; Pollock, S.; Somanchi, A.; Handley, E.; Moroney, J. Identification of *Lci5*, a Novel *Chlamydomonas Reinhardtii* Gene Induced under Low CO₂ Growth Conditions. *Photosynth. Res.* **2001**, 69 (1–3), 160–161.
- Lazár, D. Chlorophyll a Fluorescence Induction. *Biochim. Biophys. Acta - Bioenerg.* **1999**, 1412 (1), 1–28.
- Lehtreck, K.-F.; Gould, T. J.; Witman, G. B. Flagellar Central Pair Assembly in *Chlamydomonas Reinhardtii*. *Cilia* **2013**, 2 (1), 15.
- Leliaert, F.; Verbruggen, H.; Zechman, F. W. Into the Deep: New Discoveries at the Base of the Green Plant Phylogeny. *BioEssays* **2011**, 33 (9), 683–692.
- Leliaert, F.; Smith, D. R.; Moreau, H.; Herron, M. D.; Verbruggen, H.; Delwiche, C. F.; De Clerck, O. Phylogeny and Molecular Evolution of the Green Algae. *CRC. Crit. Rev. Plant Sci.* **2012**, 31 (1), 1–46.
- Lemaire, S. D.; Stein, M.; Issakidis-Bourguet, E.; Keryer, E.; Benoit, V.; Pineau, B.; Gérard-Hirne, C.; Miginiac-Maslow, M.; Jacquot, J. P. The Complex Regulation of Ferredoxin/thioredoxin-Related Genes by Light and the Circadian Clock. *Planta* **1999**, 209 (2), 221–229.
- Li, H. M.; Kaneko, Y.; Keegstra, K. Molecular Cloning of a Chloroplastic Protein Associated with Both the Envelope and Thylakoid Membranes. *Plant Mol. Biol.* **1994**, 25 (4), 619–632.
- Liu, C.; Willmund, F.; Whitelegge, J. P.; Hawat, S.; Knapp, B.; Lodha, M.; Schroda, M. J-Domain Protein CDJ2 and HSP70B Are a Pastidic Chaperone Pair That Interacts with Vesicle-Inducing Protein in Plastids 1. *Mol. Biol. Cell* **2005**, 16 (1), 1–13.

Molecular Physiology of the *Chlamydomonas* pyrenoid

- Liu, C.; Young, A. L.; Starling-Windhof, A.; Bracher, A.; Saschenbrecker, S.; Rao, B. V.; Rao, K. V.; Berninghausen, O.; Mielke, T.; Hartl, F. U.; et al. Coupled Chaperone Action in Folding and Assembly of Hexadecameric Rubisco. *Nature* **2010**, *463* (7278), 197–202.
- Lobley, A.; Sadowski, M. I.; Jones, D. T. pGenTHREADER and pDomTHREADER: New Methods for Improved Protein Fold Recognition and Superfamily Discrimination. *Bioinformatics* **2009**, *25* (14), 1761–1767.
- Long, B. M.; Rae, B. D.; Badger, M. R.; Price, G. D. Over-Expression of the β -Carboxysomal CcmM Protein in *Synechococcus* PCC7942 Reveals a Tight Co-Regulation of Carboxysomal Carbonic Anhydrase (CcaA) and M58 Content. *Photosynth. Res.* **2011**, *109* (1-3), 33–45.
- Long, S. P.; Marshall-Colon, A.; Zhu, X.-G. Meeting the Global Food Demand of the Future by Engineering Crop Photosynthesis and Yield Potential. *Cell* **2015**, *161* (1), 56–66.
- Lopez, D.; Casero, D.; Cokus, S. J.; Merchant, S. S.; Pellegrini, M. Algal Functional Annotation Tool: A Web-Based Analysis Suite to Functionally Interpret Large Gene Lists Using Integrated Annotation and Expression Data. *BMC Bioinformatics* **2011**, *12* (1), 282.
- Loseva, N. L.; Alyabyev, A. J.; Gordon, L. K.; Andreyeva, I. N.; Kolesnikov, O. P.; Ponomareva, A. A.; Chernov, V. M.; Kemp, R. B. The Energetic Stress Response of the Microalgal *Chlorella Vulgaris* to the Mycoplasma, *Acholeplasma Laidlawii* as a Model System for Plant–pathogen Interaction. *Thermochim. Acta* **2003**, *397* (1–2), 37–47.
- Losh, J. L.; Young, J. N.; Morel, F. M. M. Rubisco Is a Small Fraction of Total Protein in Marine Phytoplankton. *New Phytol.* **2013**, *198* (1), 52–58.
- Lucker, B.; Kramer, D. M. Regulation of Cyclic Electron Flow in *Chlamydomonas Reinhardtii* under Fluctuating Carbon Availability. *Photosynth. Res.* **2013**, *117* (1-3), 449–459.
- Ma, Y.; Pollock, S. V.; Xiao, Y.; Cunnusamy, K.; Moroney, J. V. Identification of a Novel Gene, CIA6, Required for Normal Pyrenoid Formation in *Chlamydomonas Reinhardtii*. *Plant Physiol.* **2011**, *156* (2), 884–896.
- Mackinder, L. C. M.; Meyer, M. T.; Mettler-Altmann, T.; Chen, V.; Mitchell, M. C.; Caspari, O. D.; Freeman Rosenzweig, E. S.; Pallesen, L.; Reeves, G.; Itakura, A.; et al. A Repeat Protein Links Rubisco to Form the Eukaryotic Carbon Concentrating Organelle. *Prep.* **2015**.
- Mackinder, L. Venus Tagged CCM Components. *Pers. Commun.* **2014**.
- Mallmann, J.; Heckmann, D.; Bräutigam, A.; Lercher, M. J.; Weber, A. P. M.; Westhoff, P.; Gowik, U. The Role of Photorespiration during the Evolution of C4 Photosynthesis in the Genus *Flaveria*. *Elife* **2014**, *2014* (3).
- Markelova, A. G.; Sinetova, M. P.; Kupriyanova, E. V.; Pronina, N. A. Distribution and Functional Role of Carbonic Anhydrase Cah3 Associated with Thylakoid Membranes in the Chloroplast and Pyrenoid of *Chlamydomonas Reinhardtii*. *Russ. J. Plant Physiol.* **2009**, *56* (6), 761–768.
- Martin, W.; Scheibe, R.; Schnarrenberger, C. The Calvin Cycle and Its Regulation. In *Photosynthesis: Physiology and Metabolism*; Leegood, R. C., Sharkey, T. D., von Caemmerer, S., Eds.; Springer Science & Business Media, 2006; pp 9–51.
- Mason, C. B.; Bricker, T. M.; Moroney, J. V. A Rapid Method for Chloroplast Isolation from the Green Alga *Chlamydomonas Reinhardtii*. *Nat. Protoc.* **2006**, *1* (5), 2227–2230.
- Maxwell, K.; Johnson, G. N. Chlorophyll Fluorescence--a Practical Guide. *J. Exp. Bot.* **2000**, *51* (345), 659–668.
- McGrath, J. M.; Long, S. P. Can the Cyanobacterial Carbon-Concentrating Mechanism Increase Photosynthesis in Crop Species? A Theoretical Analysis. *Plant Physiol.* **2014**, *164* (4), 2247–2261.
- McKay, R. M. L.; Gibbs, S. P. Phycoerythrin Is Absent from the Pyrenoid of *Porphyridium Cruentum*:

Chapter 7: References

- Photosynthetic Implications. *Planta* **1990**, *180* (2), 249–256.
- McKay, R. M. L.; Gibbs, S. P. Composition and Function of Pyrenoids - Cytochemical and Immunocytochemical Approaches. *Can. J. Bot. Can. Bot.* **1991a**, *69* (5), 1040–1052.
- McKay, R. M. L.; Gibbs, S. P. Immunocytochemical Localization of Phosphoribulokinase in Microalgae. *Bot. Acta* **1991b**, *104* (5), 367–373.
- McKay, R. M. L.; Gibbs, S. P.; Vaughn, K. C. RuBisCo Activase Is Present in the Pyrenoid of Green Algae. *Protoplasma* **1991**, *162* (1), 38–45.
- McKay, R. M. L.; Lichtlé, C.; Gibbs, S. P. Immunocytochemical Characterization of the Intraprenoid Thylakoids of Cryptomonads. *J. Phycol.* **1992**, *28*, 64–68.
- Merchant, S. S.; Prochnik, S. E.; Vallon, O.; Harris, E. H.; Karpowicz, S. J.; Witman, G. B.; Terry, A.; Salamov, A.; Fritz-Laylin, L. K.; Maréchal-Drouard, L.; et al. The Chlamydomonas Genome Reveals the Evolution of Key Animal and Plant Functions. *Science* (80-.). **2007**, *318* (October), 245–251.
- Mettler, T. Effect of Changed Ultrastructure on the Calvin-Benson Cycle in *C. Reinhardtii*. CCM8 conference: New Orleans 2013.
- Mettler, T.; Mühlhaus, T.; Hemme, D.; Schöttler, M.-A.; Rupprecht, J.; Idoine, A.; Veyel, D.; Pal, S. K.; Yaneva-Roder, L.; Winck, F. V.; et al. Systems Analysis of the Response of Photosynthesis, Metabolism, and Growth to an Increase in Irradiance in the Photosynthetic Model Organism *Chlamydomonas Reinhardtii*. *Plant Cell* **2014**, *26* (June), 2310–2350.
- Meyer, M. T.; Griffiths, H. The Internal Plumbing of Algal Chloroplasts. *Elife* **2015**, *4*, 1–3.
- Meyer, M. Fib-SEM and RNAseq of SSU Lines. *Pers. Commun.* **2015**.
- Meyer, M.; Griffiths, H. Origins and Diversity of Eukaryotic CO₂-Concentrating Mechanisms: Lessons for the Future. *J. Exp. Bot.* **2013**, *64* (3), 769–786.
- Meyer, M.; Seibt, U.; Griffiths, H. To Concentrate or Ventilate? Carbon Acquisition, Isotope Discrimination and Physiological Ecology of Early Land Plant Life Forms. *Philos. Trans. R. Soc. Lond. B. Biol. Sci.* **2008**, *363* (1504), 2767–2778.
- Meyer, M.; Genkov, T.; Skepper, J.; Jouhet, J.; Mitchell, M. C.; Spreitzer, R. J.; Griffiths, H. Rubisco Small Subunit Alpha-Helices Control Pyrenoid Formation in *Chlamydomonas*. *Proc. Natl. Acad. Sci.* **2012**.
- Minagawa, J. State transitions—The Molecular Remodeling of Photosynthetic Supercomplexes That Controls Energy Flow in the Chloroplast. *Biochim. Biophys. Acta - Bioenerg.* **2011**, *1807* (8), 897–905.
- Minagawa, J. Dynamic Reorganization of Photosynthetic Supercomplexes during Environmental Acclimation of Photosynthesis. *Front. Plant Sci.* **2013**, *4* (December), 513.
- Misamore, M. J.; Gupta, S.; Snell, W. J. The *Chlamydomonas* Fus1 Protein Is Present on the Mating Type plus Fusion Organelle and Required for a Critical Membrane Adhesion Event during Fusion with Minus Gametes. **2003**, *14* (June), 2530–2542.
- Mitchell, M. C.; Meyer, M. T.; Griffiths, H. Dynamics of Carbon-Concentrating Mechanism Induction and Protein Relocalization during the Dark-to-Light Transition in Synchronized *Chlamydomonas Reinhardtii*. *Plant Physiol.* **2014**, *166* (2), 1073–1082.
- Mitchell, M. Regulation of the Carbon-Concentrating Mechanism in *Chlamydomonas Reinhardtii*, University of Cambridge, 2014.
- Mitra, M.; Mason, C.; Xiao, Y.; Ynalvez, R.; Lato, S.; Moroney, J. The Carbonic Anhydrase Gene Families of *Chlamydomonas Reinhardtii*. *Can. J. Bot. Can. Bot.* **2005**, *83* (7), 780–795.
- Mittag, M.; Kiaulehn, S.; Johnson, C. H. The Circadian Clock in *Chlamydomonas Reinhardtii* . What Is It For ? What Is It Similar To ? 1. *Plant Physiol.* **2005**, *137* (February), 399–409.
- Mittelmeier, T. M.; Thompson, M. D.; Öztürk, E.; Dieckmann, C. L. Independent Localization of Plasma

Molecular Physiology of the *Chlamydomonas* pyrenoid

- Membrane and Chloroplast Components during Eyespot Assembly. *Eukaryot. Cell* **2013**, *12* (9), 1258–1270.
- Miura, K.; Yamano, T.; Yoshioka, S.; Kohinata, T.; Inoue, Y. Expression Profiling-Based Identification of CO₂-Responsive Genes Regulated by CCM1 Controlling a Carbon-Concentrating Mechanism in *Chlamydomonas Reinhardtii* 1. *Plant Physiol.* **2004**, *135* (July), 1595–1607.
- Morita, E.; Abe, T.; Tsuzuki, M.; Fujiwara, S.; Sato, N.; Hirata, a; Sonoike, K.; Nozaki, H. Presence of the CO₂-Concentrating Mechanism in Some Species of the Pyrenoid-Less Free-Living Algal Genus *Chloromonas* (Volvocales, Chlorophyta). *Planta* **1998**, *204* (3), 269–276.
- Moroney, J. V.; Jungnick, N.; Dimario, R. J.; Longstreth, D. J. Photorespiration and Carbon Concentrating Mechanisms: Two Adaptations to High O₂, Low CO₂ Conditions. *Photosynth. Res.* **2013**, *117* (1-3), 121–131.
- Moroney, J. V.; Ynalvez, R. A. Proposed Carbon Dioxide Concentrating Mechanism in *Chlamydomonas Reinhardtii*. *Eukaryot. Cell* **2007**, *6* (8), 1251–1259.
- Moroney, J. V.; Ma, Y.; Frey, W. D.; Fusilier, K. A.; Pham, T. T.; Simms, T. A.; DiMario, R. J.; Yang, J.; Mukherjee, B. The Carbonic Anhydrase Isoforms of *Chlamydomonas Reinhardtii*: Intracellular Location, Expression, and Physiological Roles. *Photosynth. Res.* **2011**, *109* (1-3), 133–149.
- Mühlhaus, T.; Weiss, J.; Hemme, D.; Sommer, F.; Schroda, M. Quantitative Shotgun Proteomics Using a Uniform 15-N-Labeled Standard to Monitor Proteome Dynamics in Time Course Experiments Reveals New Insights into the Heat Stress Response of *Chlamydomonas Reinhardtii*. *Mol. Cell. Proteomics* **2011**, *10* (9), M110.004739.
- Mullineaux, C. W. Function and Evolution of Grana. *Trends Plant Sci.* **2005**, *10* (11), 521–525.
- Mustárdy, L.; Buttle, K.; Steinbach, G.; Garab, G. G. The Three-Dimensional Network of the Thylakoid Membranes in Plants: Quasihelical Model of the Granum-Stroma Assembly. *Plant Cell* **2008**, *20* (10), 2552–2557.
- Nassoury, N.; Fritz, L.; Morse, D. Circadian Changes in Ribulose-1,5-Bisphosphate Carboxylase/oxygenase Distribution inside Individual Chloroplasts Can Account for the Rhythm in Dinoflagellate Carbon Fixation. *Plant Cell* **2001**, *13* (4), 923–934.
- Nelson, N.; Ben-Shem, A. The Complex Architecture of Oxygenic Photosynthesis. *Nat. Rev. Mol. Cell Biol.* **2004**, *5* (12), 971–982.
- Nguyen, H. M.; Cuiné, S.; Beyly-Adriano, A.; Légeret, B.; Billon, E.; Auroy, P.; Beisson, F.; Peltier, G.; Li-Beisson, Y. The Green Microalga *Chlamydomonas Reinhardtii* Has a Single ω -3 Fatty Acid Desaturase That Localizes to the Chloroplast and Impacts Both Plastidic and Extraplasmidic Membrane Lipids. *Plant Physiol.* **2013**, *163* (2), 914–928.
- Niyogi, K. K. Photoprotection and High Light Responses. In *The Chlamydomonas Sourcebook*; Harris, E. H., Stern, D. B., Witman, G. B., Eds.; Elsevier, 2009; pp 847–870.
- Niyogi, K. K.; Truong, T. B. Evolution of Flexible Non-Photochemical Quenching Mechanisms That Regulate Light Harvesting in Oxygenic Photosynthesis. *Curr. Opin. Plant Biol.* **2013**, *16* (3), 307–314.
- Nordhues, A.; Schöttler, M. A.; Unger, A.; Geimer, S.; Schönfelder, S.; Schmollinger, S.; Rütgers, M.; Finazzi, G.; Soppa, B.; Sommer, F.; et al. Evidence for a Role of VIPP1 in the Structural Organization of the Photosynthetic Apparatus in *Chlamydomonas*. *Plant Cell* **2012**, *24* (February), 637–659.
- Ong, S.-E.; Mann, M. Mass Spectrometry-Based Proteomics Turns Quantitative. *Nat. Chem. Biol.* **2005**, *1* (5), 252–262.
- Owen, N. A.; Griffiths, H. A System Dynamics Model Integrating Physiology and Biochemical Regulation Predicts Extent of Crassulacean Acid Metabolism (CAM) Phases. *New Phytol.* **2013**, *200*, 1116–1131.
- Paddock, M. L.; Wiley, S. E.; Axelrod, H. L.; Cohen, A. E.; Roy, M.; Abresch, E. C.; Capraro, D.; Murphy, A. N.; Nechushtai, R.; Dixon, J. E.; et al. MitoNEET Is a Uniquely Folded 2Fe 2S Outer Mitochondrial Membrane Protein Stabilized by Pioglitazone. *Proc. Natl. Acad. Sci. U. S. A.* **2007**, *104* (36), 14342–14347.

Chapter 7: References

- Pallesen, L.; Reeves, G. CCM Mutant Library. *Pers. Commun.* **2014**.
- Papageorgiou, G. C.; Govindjee. *Chlorophyll A Fluorescence: A Signature Of Photosynthesis*; Springer, 2004.
- Pickett-Heaps, J. D. *Green Algae*, 1st ed.; Sinauer Associates, Incorporated: Sunderland, Massachusetts, 1975.
- Pisareva, T.; Kwon, J.; Oh, J.; Kim, S.; Ge, C.; Wieslander, A.; Choi, J.-S.; Norling, B. Model for Membrane Organization and Protein Sorting in the Cyanobacterium *Synechocystis* Sp PCC 6803 Inferred from Proteomics and Multivariate Sequence Analyses. *J. Proteome Res.* **2011**, *10* (8), 3617–3631.
- Platt, T.; Gallegos, C.; Harrison, W. Photoinhibition of Photosynthesis in Natural Assemblages of Marine Phytoplankton. *J. Mar. Res.* **1980**, *38*, 687–701.
- Portis, A. R.; Li, C.; Wang, D.; Salvucci, M. E. Regulation of Rubisco Activase and Its Interaction with Rubisco. *J. Exp. Bot.* **2008**, *59* (7), 1597–1604.
- Price, G. D.; Badger, M. R.; von Caemmerer, S. The Prospect of Using Cyanobacterial Bicarbonate Transporters to Improve Leaf Photosynthesis in C-3 Crop Plants. *Plant Physiol.* **2011**, *155* (1), 20–26.
- Rae, B. D.; Long, B. M.; Badger, M. R.; Price, G. D. Functions, Compositions, and Evolution of the Two Types of Carboxysomes: Polyhedral Microcompartments That Facilitate CO₂ Fixation in Cyanobacteria and Some Proteobacteria. *Microbiol. Mol. Biol. Rev.* **2013**, *77* (3), 357–379.
- Raven, J. A. CO₂-Concentrating Mechanisms: A Direct Role for Thylakoid Lumen Acidification? *Plant. Cell Environ.* **1997**, *20* (2), 147–154.
- Raven, J. A. A Role for Mitochondrial Carbonic Anhydrase in Limiting CO₂ Leakage from Low CO₂ - Grown Cells of *Chlamydomonas Reinhardtii*. *Plant. Cell Environ.* **2001**, *24*, 261–265.
- Raven, J. A.; Giordano, M.; Beardall, J.; Maberly, S. C. Algal Evolution in Relation to Atmospheric CO₂: Carboxylases, Carbon-Concentrating Mechanisms and Carbon Oxidation Cycles. *Philos. Trans. R. Soc. B Biol. Sci.* **2012**, *367* (1588), 493–507.
- Raven, J. a.; Beardall, J.; Giordano, M. Energy Costs of Carbon Dioxide Concentrating Mechanisms in Aquatic Organisms. *Photosynth. Res.* **2014**, *121* (2-3), 111–124.
- Rochaix, J.-D. Assembly of the Photosynthetic Apparatus. *Plant Physiol.* **2011**, *155* (4), 1493–1500.
- Ross, C. a; Poirier, M. a. Protein Aggregation and Neurodegenerative Disease. *Nat. Med.* **2004**, *10* Suppl (July), S10–S17.
- Rozen, S.; Skaletsky, H. J. Primer3 on the WWW for General Users and for Biologist Programmers. In *Bioinformatics Methods and Protocols: Methods in Molecular Biology*; Krawetz, S., Misener, S., Eds.; Humana Press: Totowa, NJ, 2000; pp 365–386.
- Ruban, A. V.; Johnson, M. P. Dynamics of Higher Plant Photosystem Cross-Section Associated with State Transitions. *Photosynth. Res.* **2009**, *99* (3), 173–183.
- Ruban, A. V.; Murchie, E. H. Assessing the Photoprotective Effectiveness of Non-Photochemical Chlorophyll Fluorescence Quenching: A New Approach. *Biochim. Biophys. Acta - Bioenerg.* **2012**, *1817* (7), 977–982.
- Salvucci, M. E. Association of Rubisco Activase with Chaperonin-60 β : A Possible Mechanism for Protecting Photosynthesis during Heat Stress. *J. Exp. Bot.* **2008**, *59* (7), 1923–1933.
- Sanders, M.; Salisbury, J. Immunofluorescence Microscopy of Cilia and Flagella. *Methods Cell Biol.* **1995**, *47*, 163–169.
- Schägger, H.; von Jagow, G. Blue Native Electrophoresis for Isolation of Membrane Protein Complexes in Enzymatically Active Form. *Anal. Biochem.* **1991**, *199* (2), 223–231.
- Schindelin, J.; Arganda-Carreras, I.; Frise, E.; Kaynig, V.; Longair, M.; Pietzsch, T.; Preibisch, S.; Rueden, C.; Saalfeld, S.; Schmid, B.; et al. Fiji: An Open-Source Platform for Biological-Image Analysis. *Nat. Methods* **2012**, *9* (7), 676–682.

Molecular Physiology of the *Chlamydomonas* pyrenoid

- Schmollinger, S.; Mühlhaus, T.; Boyle, N. R.; Blaby, I. K.; Casero, D.; Mettler, T.; Moseley, J. L.; Kropat, J.; Sommer, F.; Strenkert, D.; et al. Nitrogen-Sparing Mechanisms in *Chlamydomonas* Affect the Transcriptome, the Proteome, and Photosynthetic Metabolism. *Plant Cell* **2014**, *26* (4), 1410–1435.
- Schroda, M. The *Chlamydomonas* Genome Reveals Its Secrets: Chaperone Genes and the Potential Roles of Their Gene Products in the Chloroplast. *Photosynth. Res.* **2004**, *82* (3), 221–240.
- Schroda, M.; Hemme, D.; Mühlhaus, T. The *Chlamydomonas* Heat Stress Response. *Plant J.* **2015**, *82*, 466–480.
- Schuck, P. Size-Distribution Analysis of Macromolecules by Sedimentation Velocity Ultracentrifugation and Lamm Equation Modeling. *Biophys. J.* **2000**, *78* (3), 1606–1619.
- Segovia, M.; Haramaty, L.; Berges, J. A.; Falkowski, P. G. Cell Death in the Unicellular Chlorophyte *Dunaliella Tertiolecta*. A Hypothesis on the Evolution of Apoptosis in Higher Plants and Metazoans. *Plant Physiol.* **2003**, *132* (1), 99–105.
- Sen, T. Z.; Jernigan, R. L.; Garnier, J.; Kloczkowski, A. GOR V Server for Protein Secondary Structure Prediction. *Bioinformatics* **2005**, *21* (11), 2787–2788.
- Shi, J.; Blundell, T. L.; Mizuguchi, K. FUGUE: Sequence-Structure Homology Recognition Using Environment-Specific Substitution Tables and Structure-Dependent Gap Penalties. *J. Mol. Biol.* **2001**, *310* (1), 243–257.
- Shimada, S.; Hiraoka, M.; Nabata, S.; Iima, M.; Masuda, M. Molecular Phylogenetic Analyses of the Japanese *Ulva* and *Enteromorpha* (Ulvales, Ulvophyceae), with Special Reference to the Free-Floating *Ulva*. *Phycol. Res.* **2003**, *51* (2), 99–108.
- Shukla, M.; Minda, R.; Singh, H.; Tirumani, S.; Chary, K. V. R.; Rao, B. J. UVI31+ Is a DNA Endonuclease That Dynamically Localizes to Chloroplast Pyrenoids in *C. Reinhardtii*. *PLoS One* **2012**, *7* (12).
- Simeoni, F.; Tasselli, L.; Tanaka, S.; Villanova, L.; Hayashi, M.; Kubota, K.; Isono, F.; Garcia, B. a; Michishita-Kioi, E.; Chua, K. F. Proteomic Analysis of the SIRT6 Interactome: Novel Links to Genome Maintenance and Cellular Stress Signaling. *Sci. Rep.* **2013**, *3*, 3085.
- Sinetova, M. a.; Kupriyanova, E. V.; Markelova, A. G.; Allakhverdiev, S. I.; Pronina, N. a. Identification and Functional Role of the Carbonic Anhydrase *Cah3* in Thylakoid Membranes of Pyrenoid of *Chlamydomonas Reinhardtii*. *Biochim. Biophys. Acta - Bioenerg.* **2012**.
- Söding, J. Protein Homology Detection by HMM-HMM Comparison. *Bioinformatics* **2005**, *21* (7), 951–960.
- Spreitzer, R. J. Role of the Small Subunit in Ribulose-1,5-Bisphosphate Carboxylase/oxygenase. *Arch. Biochem. Biophys.* **2003**, *414* (2), 141–149.
- Spreitzer, R. J.; Chastain, C. J. Heteroplasmic Suppression of an Amber Mutation in the *Chlamydomonas* Chloroplast Gene That Encodes the Large Subunit of Ribulosebisphosphate Carboxylase/oxygenase. *Curr. Genet.* **1987**, *11* (8), 611–616.
- Stock, J. B.; Zhang, S. The Biochemistry of Memory. *Curr. Biol.* **2013**, *23* (17), R741–R745.
- Stotz, M.; Mueller-Cajar, O.; Ciniawsky, S.; Wendler, P.; Hartl, F. U.; Bracher, A.; Hayer-Hartl, M. Structure of Green-Type Rubisco Activase from Tobacco. *Nat. Struct. Mol. Biol.* **2011**, *18* (12), 1366–1370.
- Suggett, D. J.; Oxborough, K.; Baker, N. R.; MacIntyre, H. L.; Kana, T. M.; Geider, R. J. Fast Repetition Rate and Pulse Amplitude Modulation Chlorophyll a Fluorescence Measurements for Assessment of Photosynthetic Electron Transport in Marine Phytoplankton. *Eur. J. Phycol.* **2003**, *38* (4), 371–384.
- Süss, K.-H.; Prokhorenko, I.; Adler, K. In Situ Association of Calvin Cycle Enzymes, Ribulose-1,5-Bisphosphate Carboxylase/Oxygenase Activase, Ferredoxin-NADP+ Reductase, and Nitrite Reductase with Thylakoid and Pyrenoid Membranes of *Chlamydomonas Reinhardtii* Chloroplasts as Revealed by Immunoe. *Plant Physiol.* **1995**, *107* (4), 1387–1397.
- Swamy, M.; Siegers, G. M.; Minguet, S.; Wollscheid, B.; Schamel, W. W. a. Blue Native Polyacrylamide Gel

Chapter 7: References

- Electrophoresis (BN-PAGE) for the Identification and Analysis of Multiprotein Complexes. *Sci. STKE* **2006**, 2006 (345), p14.
- Taylor, T. C.; Backlund, A.; Bjorhall, K.; Andersson, I.; Spreitzer, R. J. First Crystal Structure of Rubisco from a Green Alga, *Chlamydomonas Reinhardtii*. *J. Biol. Chem.* **2001**, 276, 48159.
- Tcherkez, G. G. B.; Farquhar, G. D.; Andrews, T. J. Despite Slow Catalysis and Confused Substrate Specificity, All Ribulose Bisphosphate Carboxylases May Be Nearly Perfectly Optimized. *Proc. Natl. Acad. Sci.* **2006**, 103 (19), 7246–7251.
- Thimm, O.; Bläsing, O.; Gibon, Y.; Nagel, A.; Meyer, S.; Krüger, P.; Selbig, J.; Müller, L. a.; Rhee, S. Y.; Stitt, M. MAPMAN: A User-Driven Tool to Display Genomics Data Sets onto Diagrams of Metabolic Pathways and Other Biological Processes. *Plant J.* **2004**, 37 (6), 914–939.
- Thoms, S.; Pahlow, M.; Wolf-Gladrow, D. a. Model of the Carbon Concentrating Mechanism in Chloroplasts of Eukaryotic Algae. *J. Theor. Biol.* **2001**, 208 (3), 295–313.
- Tirumani, S.; Kokkanti, M.; Chaudhari, V.; Shukla, M.; Rao, B. J. Regulation of CCM Genes in *Chlamydomonas Reinhardtii* during Conditions of Light-Dark Cycles in Synchronous Cultures. *Plant Mol. Biol.* **2014**, 85 (3), 277–286.
- Tolte, D.; Wittkopp, T. Analysis of JTS-10 Data. *Pers. Commun.* **2013**.
- Tolte, D.; Ghysels, B.; Alric, J.; Petroustos, D.; Tolstygina, I.; Krawietz, D.; Happe, T.; Auroy, P.; Adriano, J.; Beyly, A.; et al. Control of Hydrogen Photoproduction by the Proton Gradient Generated by Cyclic Electron Flow in *Chlamydomonas Reinhardtii*. *Plant Cell* **2011**.
- Trissl, H.-W.; Wilhelm, C. Why Do Thylakoid Membranes from Higher Plants Form Grana Stacks? *Trends Biochem. Sci.* **1993**, 18 (11), 415–419.
- Turkina, M. V; Blanco-Rivero, A.; Vainonen, J. P.; Vener, A. V; Villarejo, A. CO₂ Limitation Induces Specific Redox-Dependent Protein Phosphorylation in *Chlamydomonas Reinhardtii*. *Proteomics* **2006**, 6 (9), 2693–2704.
- Uniacke, J. Novel Chloroplast Compartments Are Sites of Photosystem II Biogenesis and mRNA Management during Stress in the Chloroplast of *Chlamydomonas Reinhardtii*, Concordia University Montréal, 2009.
- Uniacke, J.; Zerges, W. Photosystem II Assembly and Repair Are Differentially Localized in *Chlamydomonas*. *Plant Cell* **2007**, 19 (11), 3640–3654.
- Uniacke, J.; Zerges, W. Chloroplast Protein Targeting Involves Localized Translation in *Chlamydomonas*. *Proc. Natl. Acad. Sci. U. S. A.* **2009**, 106 (5), 1439–1444.
- Uniacke, J.; Colón-ramos, D.; Zerges, W. RNA Detection and Visualization: Methods and Protocols. In *Methods in Molecular Biology*, vol. 714; Gerst, J. E., Ed.; Methods in Molecular Biology; Humana Press: Totowa, NJ, 2011; Vol. 714, pp 15–29.
- Vallon, O.; Wollman, F. a.; Olive, J. Distribution of Intrinsic and Extrinsic Subunits of the PS II Protein Complex between Appressed and Non-Appressed Regions of the Thylakoid Membrane: An Immunocytochemical Study. *FEBS Lett.* **1985**, 183 (2), 245–250.
- Vertrees, J. InterfaceResidues.py <http://www.pymolwiki.org/index.php?title=InterfaceResidues&oldid=6949> (accessed May 24, 2015).
- Villarejo, A.; Martinez, F.; Pino Plumed, M.; Ramazanov, Z. The Induction of the CO₂ Concentrating Mechanism in a Starch-Less Mutant of *Chlamydomonas Reinhardtii*. *Physiol. Plant.* **1996**, 98 (4), 798–802.
- Villarreal, J. C.; Renner, S. S. Hornwort Pyrenoids, Carbon-Concentrating Structures, Evolved and Were Lost at Least Five Times during the Last 100 Million Years. *Proc. Natl. Acad. Sci.* **2012**, 109 (46), 18873–18878.
- Vitlin Gruber, A.; Nisemblat, S.; Azem, A.; Weiss, C. The Complexity of Chloroplast Chaperonins. *Trends Plant Sci.* **2013**, 18 (12), 688–694.

Molecular Physiology of the *Chlamydomonas* pyrenoid

- Vladimirova, M. G.; Markelova, A. G.; Semenenko, V. E. Identification of Ribulosebisphosphate Carboxylase Location in the Pyrenoids of Unicellular Algae by the Cyto-Immunofluorescent Method. *Fiziol. Rastenii* **1982**, *29* (5), 941–950.
- de Vries, S. J.; Bonvin, A. M. J. J. CPORT: A Consensus Interface Predictor and Its Performance in Prediction-Driven Docking with HADDOCK. *PLoS One* **2011**, *6* (3), e17695.
- de Vries, S. J.; van Dijk, M.; Bonvin, A. M. J. J. The HADDOCK Web Server for Data-Driven Biomolecular Docking. *Nat. Protoc.* **2010**, *5* (5), 883–897.
- Wang, Y.; Spalding, M. H. LCIB in the Chlamydomonas CO₂-Concentrating Mechanism. *Photosynth. Res.* **2014**, *121* (2-3), 185–192.
- Wang, Y.; Stessman, D. J.; Spalding, M. H. The CO₂ Concentrating Mechanism and Photosynthetic Carbon Assimilation in Limiting CO₂: How Chlamydomonas Works against the Gradient. *Plant J.* **2015**, *82* (3), 429–448.
- Watanabe, S.; Hirabayashii, S.; Boussiba, S.; Cohen, Z.; Vonshak, A.; Richmond, A. Parietochloris Incisa Comb. Nov. (Trebouxiophyceae, Chlorophyta). *Phycol. Res.* **1996**, *44* (January), 107–108.
- Wellburn, A. R. The Spectral Determination of Chlorophyll a and Chlorophyll B, as Well as Total Carotenoids, Using Various Solvents with Spectrophotometers of Different Resolution. *J. Plant Physiol.* **1994**, *144* (3), 307–313.
- Wheeler, G. L.; Brownlee, C. Ca²⁺ Signalling in Plants and Green Algae - Changing Channels. *Trends Plant Sci.* **2008**, *13* (9), 506–514.
- Wiley, S. E.; Murphy, A. N.; Ross, S. a; van der Geer, P.; Dixon, J. E. MitoNEET Is an Iron-Containing Outer Mitochondrial Membrane Protein That Regulates Oxidative Capacity. *Proc. Natl. Acad. Sci. U. S. A.* **2007**, *104* (13), 5318–5323.
- Williams, B. P.; Aubry, S.; Hibberd, J. M. Molecular Evolution of Genes Recruited into C₄ Photosynthesis. *Trends Plant Sci.* **2012**, *17* (4), 213–220.
- Wittig, I.; Braun, H.-P.; Schägger, H. Blue Native PAGE. *Nat. Protoc.* **2006**, *1* (1), 418–428.
- Wood, C. R.; Huang, K.; Diener, D. R.; Rosenbaum, J. L. The Cilium Secretes Bioactive Ectosomes. *Curr. Biol.* **2013**, *23* (10), 906–911.
- Worden, A. Z.; Lee, J.-H.; Mock, T.; Rouzé, P.; Simmons, M. P.; Aerts, A. L.; Allen, A. E.; Cuvelier, M. L.; Derelle, E.; Everett, M. V.; et al. Green Evolution and Dynamic Adaptations Revealed by Genomes of the Marine Picoeukaryotes Micromonas. *Science* (80-.). **2009**, *324* (5924), 268–272.
- Xiang, Y.; Zhang, J.; Weeks, D. P. The Cia5 Gene Controls Formation of the Carbon Concentrating Mechanism in Chlamydomonas Reinhardtii. *Proc. Natl. Acad. Sci. U. S. A.* **2001**, *98* (9), 5341–5346.
- Xu, D.; Zhang, Y. Ab Initio Protein Structure Assembly Using Continuous Structure Fragments and Optimized Knowledge-Based Force Field. *Proteins Struct. Funct. Bioinforma.* **2012**, *80* (7), 1715–1735.
- Yamano, T.; Miura, K.; Fukuzawa, H. Expression Analysis of Genes Associated with the Induction of the Carbon-Concentrating Mechanism in Chlamydomonas Reinhardtii. *Plant Physiol.* **2008**, *147* (1), 340–354.
- Yamano, T.; Tsujikawa, T.; Hatano, K.; Ozawa, S.-I.; Takahashi, Y.; Fukuzawa, H. Light and Low-CO₂-Dependent LCIB-LCIC Complex Localization in the Chloroplast Supports the Carbon-Concentrating Mechanism in Chlamydomonas Reinhardtii. *Plant Cell Physiol.* **2010**, *51* (9), 1453–1468.
- Yamano, T.; Asada, A.; Sato, E.; Fukuzawa, H. Isolation and Characterization of Mutants Defective in the Localization of LCIB, an Essential Factor for the Carbon-Concentrating Mechanism in Chlamydomonas Reinhardtii. *Photosynth. Res.* **2014**.
- Yang, J.; Yan, R.; Roy, A.; Xu, D.; Poisson, J.; Zhang, Y. The I-TASSER Suite: Protein Structure and Function Prediction. *Nat. Methods* **2014**, *12* (1), 7–8.

Chapter 7: References

- Yang, Y.; Faraggi, E.; Zhao, H.; Zhou, Y. Improving Protein Fold Recognition and Template-Based Modeling by Employing Probabilistic-Based Matching between Predicted One-Dimensional Structural Properties of Query and Corresponding Native Properties of Templates. *Bioinformatics* **2011**, *27* (15), 2076–2082.
- Zhang, R.; Patena, W.; Armbruster, U.; Gang, S. S.; Blum, S. R.; Jonikas, M. C. High-Throughput Genotyping of Green Algal Mutants Reveals Random Distribution of Mutagenic Insertion Sites and Endonucleolytic Cleavage of Transforming DNA. *Plant Cell* **2014**, *26* (4), 1398–1409.
- Zhu, X.-G.; Long, S. P.; Ort, D. R. Improving Photosynthetic Efficiency for Greater Yield. *Annu. Rev. Plant Biol.* **2010**, *61*, 235–261.

8 APPENDICES

DERIVATION OF JTS-10 CORRECTION FACTOR.....	199
CHAPTER 2 SUPPLEMENTARY FIGURES.....	200
CHAPTER 3 SUPPLEMENTARY FIGURES.....	217
CHAPTER 4 SUPPLEMENTARY FIGURES.....	218
TABULARIZED RUBISCO INTERACTOME.....	226

DERIVATION OF JTS-10 CORRECTION FACTOR

We measure $\Delta I/I$ with the JTS10. $\Delta A \approx \frac{1}{2.3} \times \frac{\Delta I}{I}$

Demonstration

By definition $A = \log_{10} (I/I_0)$ with I_0 incident intensity and I transmitted intensity.

At t_0 $M=R=I$ (M = measure, R = reference)

Under light $M=I+\Delta I$

$\Delta A = A_1 - A_0$

$$\Delta A = \log_{10} \left(\frac{I + \Delta I}{I_0} \right) - \log_{10} \left(\frac{I}{I_0} \right)$$

$$\Delta A = \log_{10} \left(\frac{I + \Delta I}{I_0} \times \frac{I_0}{I} \right)$$

$$\Delta A = \log_{10} \left(\frac{I + \Delta I}{I} \right)$$

$$\Delta A = \frac{1}{\ln(10)} \times \ln \left(1 + \frac{\Delta I}{I} \right)$$

By linear approximations $\ln(1+x) \approx x$ (if $x \approx 0$)

So $\Delta A \approx \frac{1}{2.3} \times \frac{\Delta I}{I}$

if $\Delta I \ll I$

$\Delta A = \epsilon_{P700} l$ [PSI] by the Beer-Lambert law

$\epsilon_{P700} = 64 \text{ mM}^{-1} \cdot \text{cm}^{-1}$ (from Hiyama and Ke BBA 1972, for Spinach. Sometimes Jean Alric use $50 \text{ mM}^{-1} \cdot \text{cm}^{-1}$)

So [PSI] = $\frac{\Delta I/I}{\epsilon_{P700} \times 2.3} \text{ mol} \cdot \text{L}^{-1}$

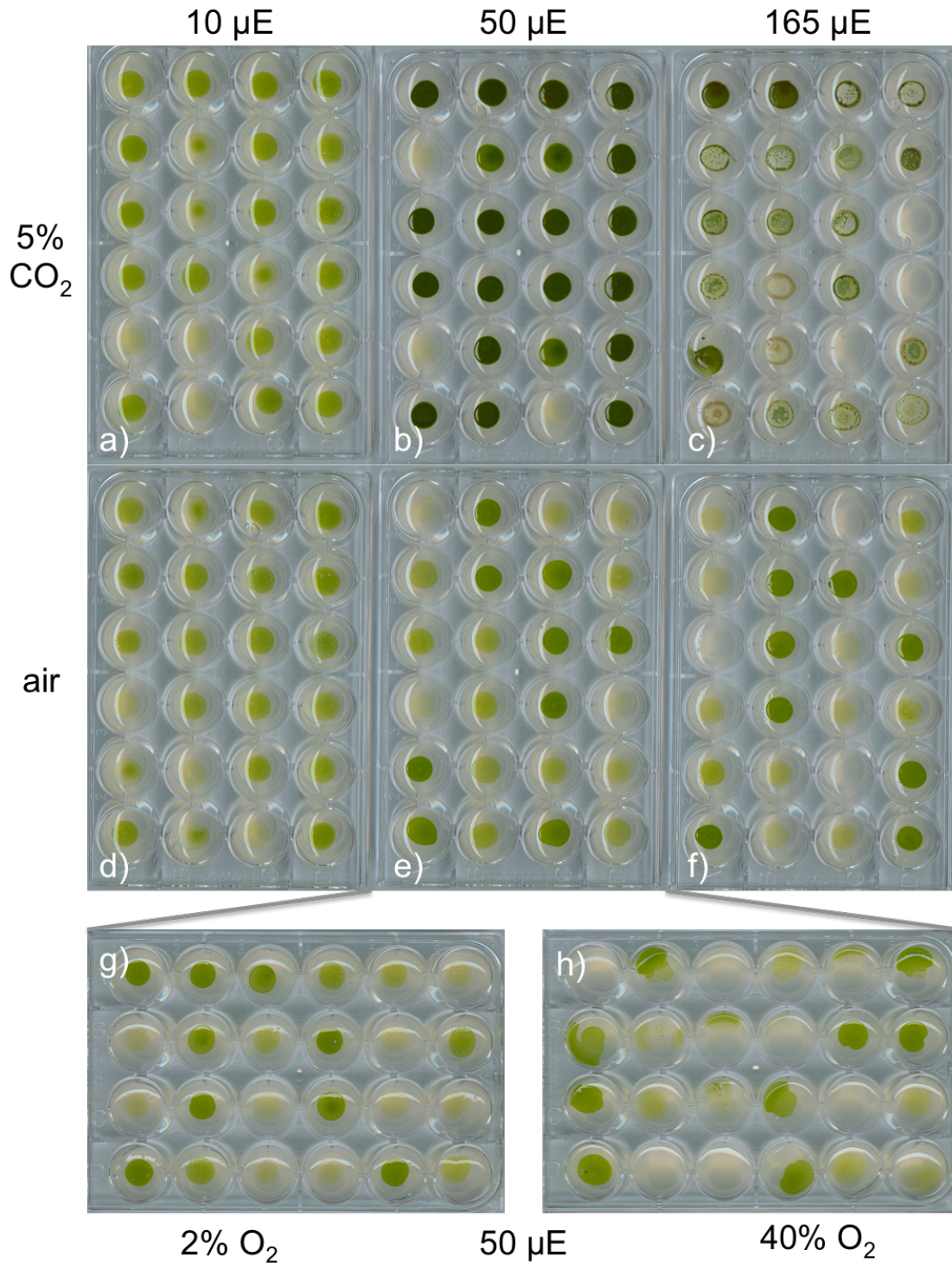
$n_{\text{chl}}/n_{P700} = \frac{[\text{Chl}]}{MW(\text{Chl})} \times \frac{\epsilon_{P700}}{\Delta I/I} \times 2.3 \times 10^6$

with [Chl] chlorophyll concentration in mg/mL, $MW(\text{Chl})$ molecular weight of chlorophyll a = $893.49 \text{ g} \cdot \text{mol}^{-1}$; n_{chl} quantity of chlorophyll in mol, n_{P700} quantity of PSI in mol.

Appendix 8.1: JTS-10 absorbance correction factor for calculation of [PSI] from p700 data

Made by Dimitri Tolleter, adapted from Jean Alric, June 2013

CHAPTER 2 SUPPLEMENTARY FIGURES



Appendix 8.2: CF screen colonies

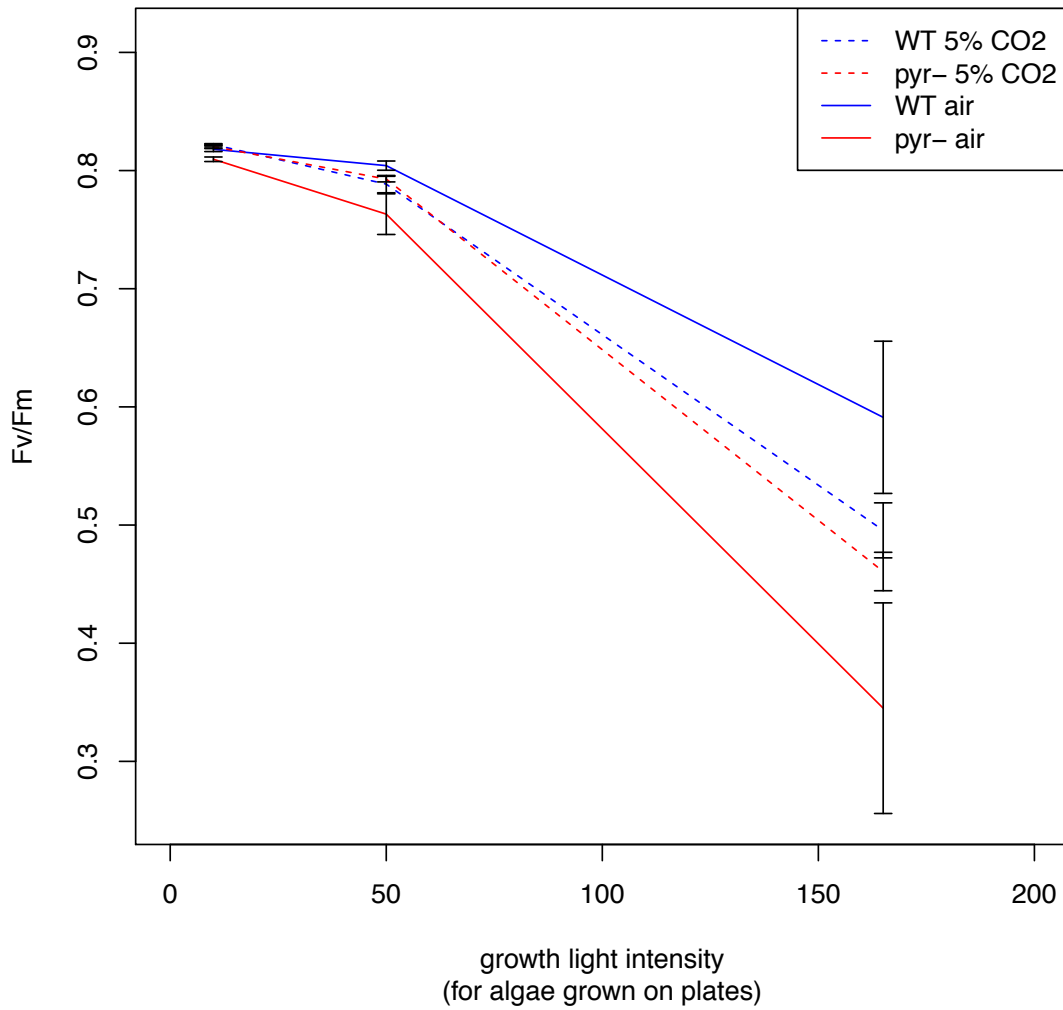
Data shown in main chapter is based on plates a-f which were grown at 21% O₂. Plates g-h were grown at air-levels of CO₂. Identity of randomly positioned colonies is listed in Appendix 8.3. Plates are oriented such that the label (a-h) is positioned closest to well A1.

Appendix 8.3: Colony positions for CF screen plates in Appendix 8.2

position	a	b	c	d	e	f	g	h
A 1	U	W1	1	W2	1	W1	W1	Q
A 2	Q	Q	T	1	W1	S	W2	W2
A 3	T	W2	W1	Q	Q	U	1	Q
A 4	W1	U	U	T	S	Q	2	S
A 5	W1	Q	1	2	2	2	S	U
A 6	W2	T	2	U	Q	T	U	W2
B 1	Q	U	1	1	S	2	T	1
B 2	Q	W2	S	Q	2	U	1	T
B 3	U	S	W1	S	S	W2	S	S
B 4	1	W1	2	S	U	1	W1	Q
B 5	1	1	2	W2	W2	W2	Q	W2
B 6	T	2	U	1	W1	W1	2	W1
C 1	2	Q	W2	Q	1	U	U	W1
C 2	S	1	W1	T	U	Q	W2	U
C 3	1	T	U	U	W1	T	Q	T
C 4	W1	S	S	W2	W2	2	1	1
C 5	W2	1	Q	2	1	W1	Q	2
C 6	T	2	T	T	T	Q	U	T
D 1	W2	S	W2	W1	2	1	W1	W1
D 2	S	W1	S	U	T	W2	2	2
D 3	U	2	Q	S	Q	S	T	2
D 4	2	W2	Q	2	W2	1	T	1
D 5	S	T	W2	W1	U	T	W2	S
D 6	2	U	T	W1	T	S	S	U

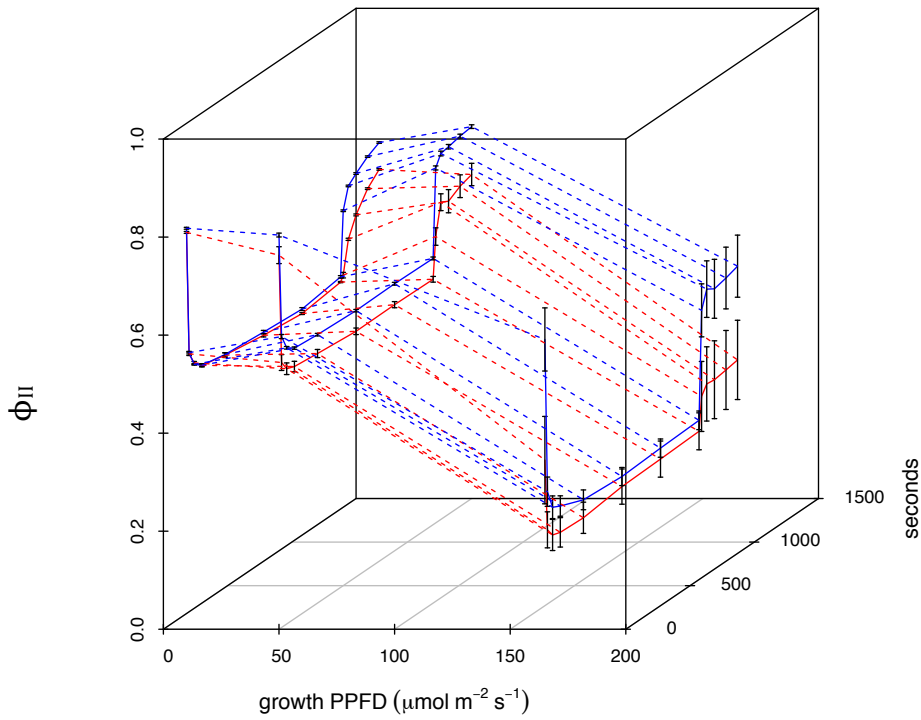
Plates identified in top row by label as per Appendix 8.2. For each position, the strain plated is indicated. SSU substitution strains used were: S – *Spinacia oleracea*, T – *Arabidopsis thaliana*, U – *Helianthus annuus*, W1 and W2 – independent native *Chlamydomonas* WTint1,2 insertion lines. Other strains were: Q – SSU substitution parent strain T-60 lacking *RBCS* from the genome (Khrebtukova and Spreitzer, 1996), 2 – *cia5/ccm1* knock-out mutant, 1 – parent strain 137c, used as WT control corresponding to strain 2.

dark adapted PSII quantum efficiency

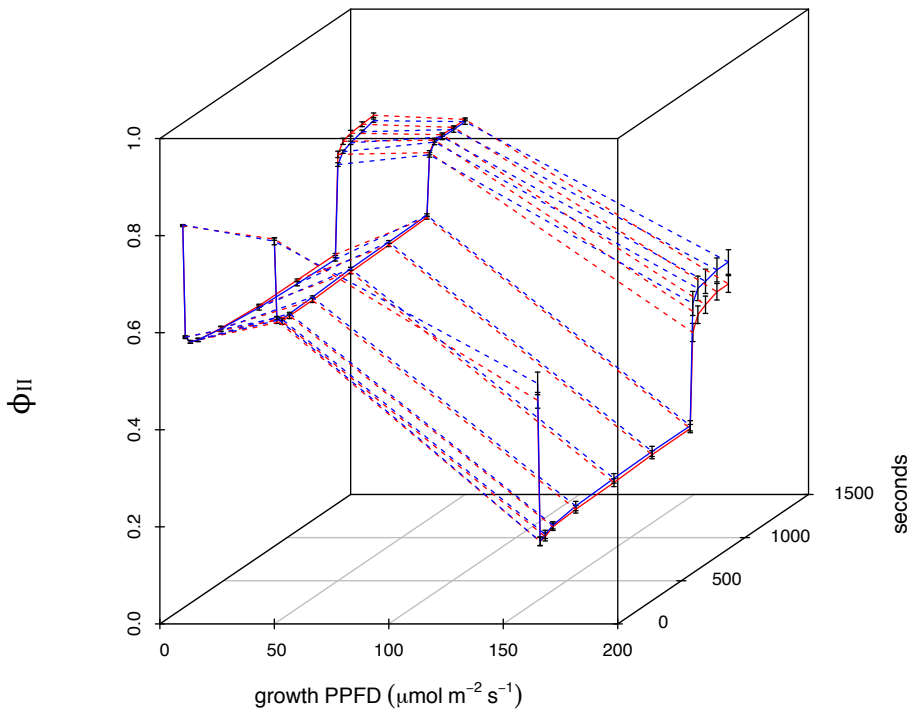


Appendix 8.4: High-throughput screen shows high CO₂ rescues pyr- Fv/Fm
CF imaging data.

air

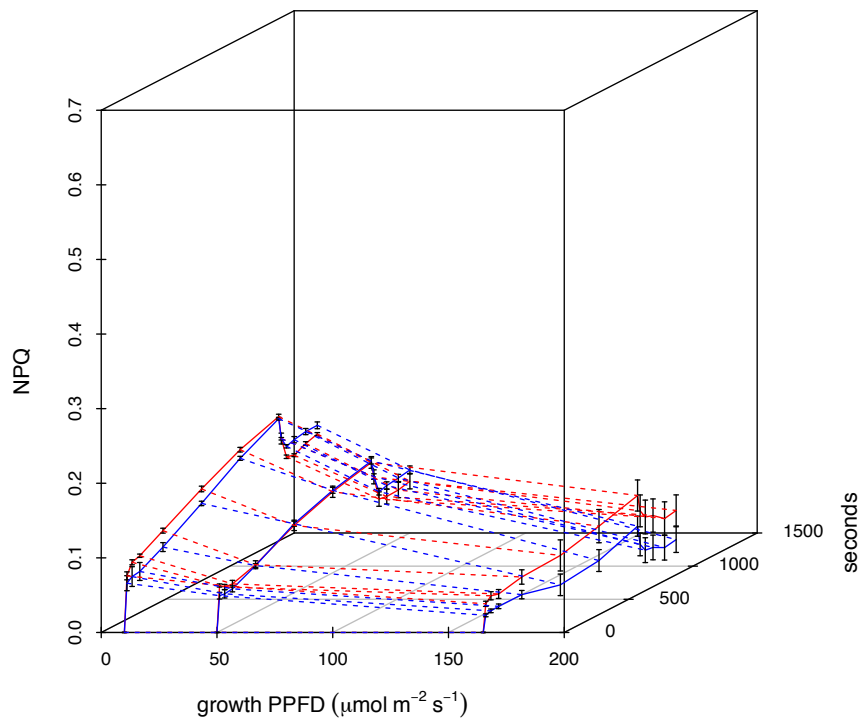
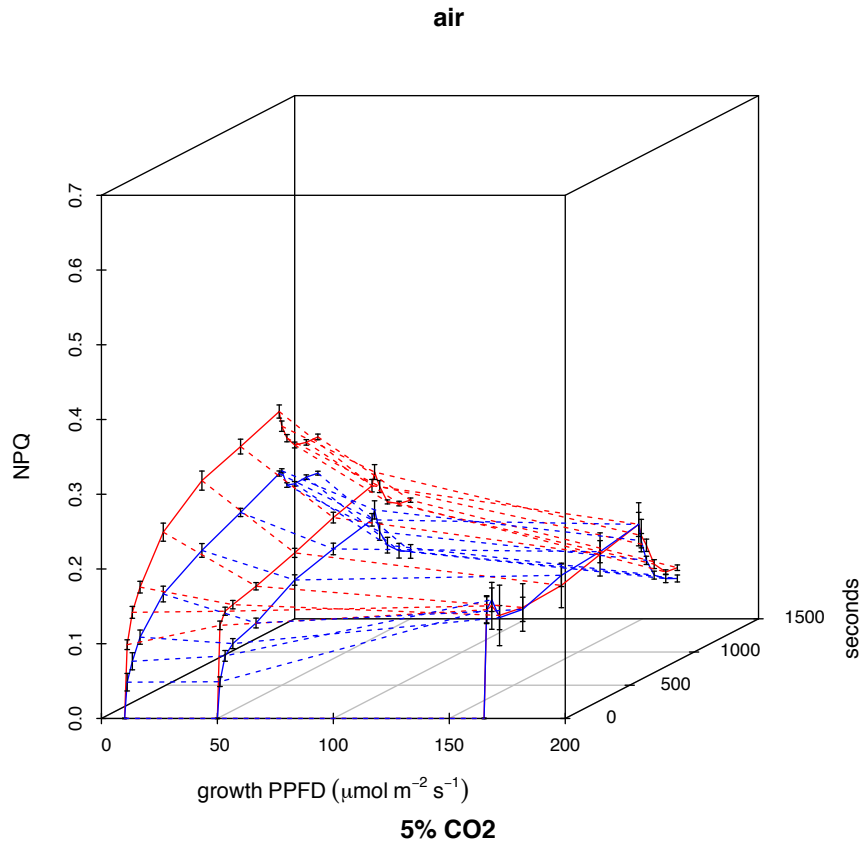


5% CO₂



Appendix 8.5 High CO₂ rescues pyr- ϕ_{II} during fluorescence induction (20 min at 106 μE) and dark relaxation (5 min)

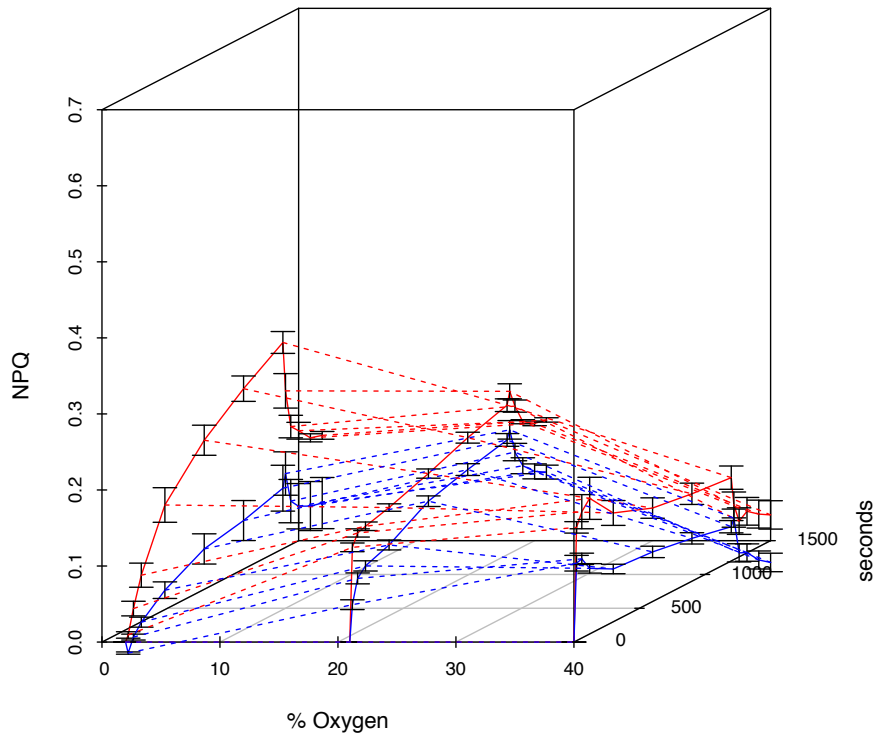
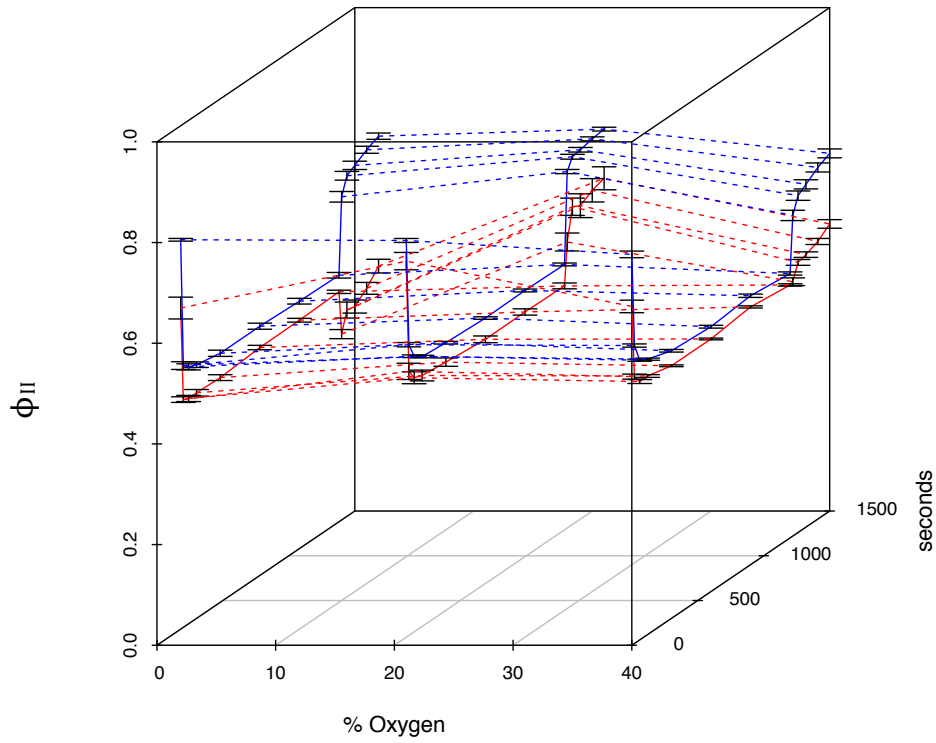
CF imaging data. Values stabilize after <2 min, meaning rapid light response curves (Fig. 2.6, Appendix 8.8) are indicative of steady-state.



Appendix 8.6 High CO₂ rescues pyr- NPQ during fluorescence induction (20 min at 106 μE) and dark relaxation (5 min)

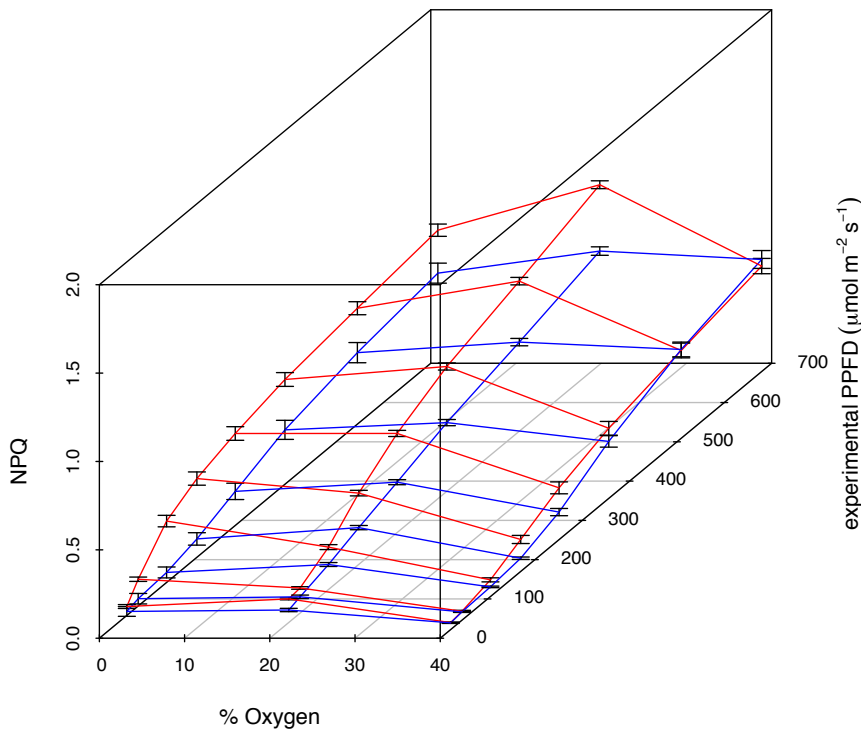
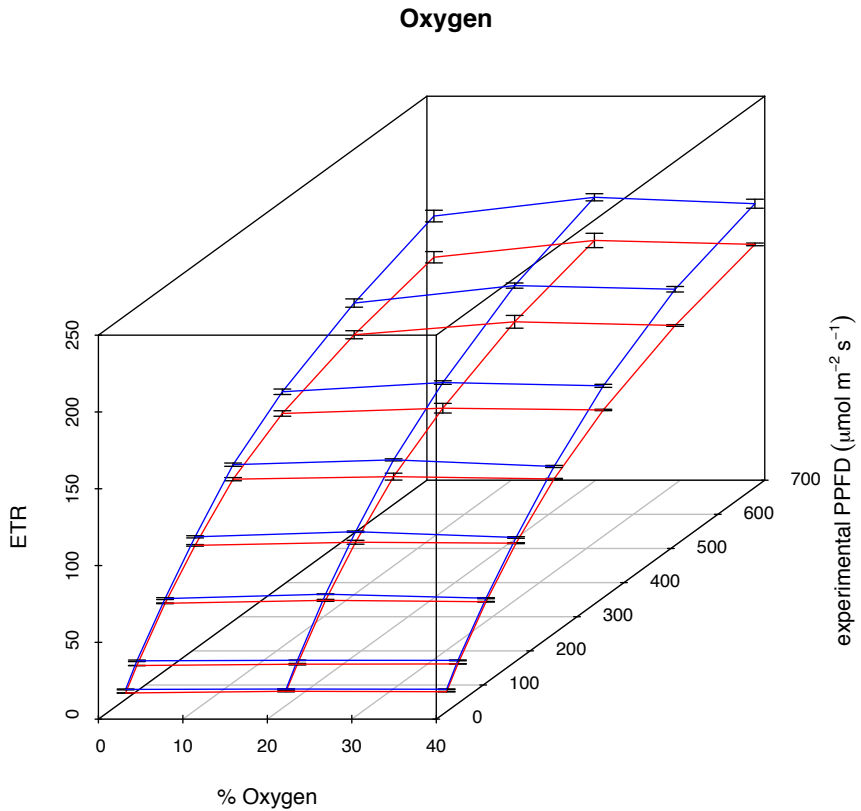
CF imaging data. Rapidly relaxing NPQ (qE) makes up high fraction for 165 μE samples and 50 μE WT, other samples show increased contributions of slower acting fractions (qT, possibly some qI) consistent with prior acclimation to a lower light intensity than used during this experiment.

Oxygen



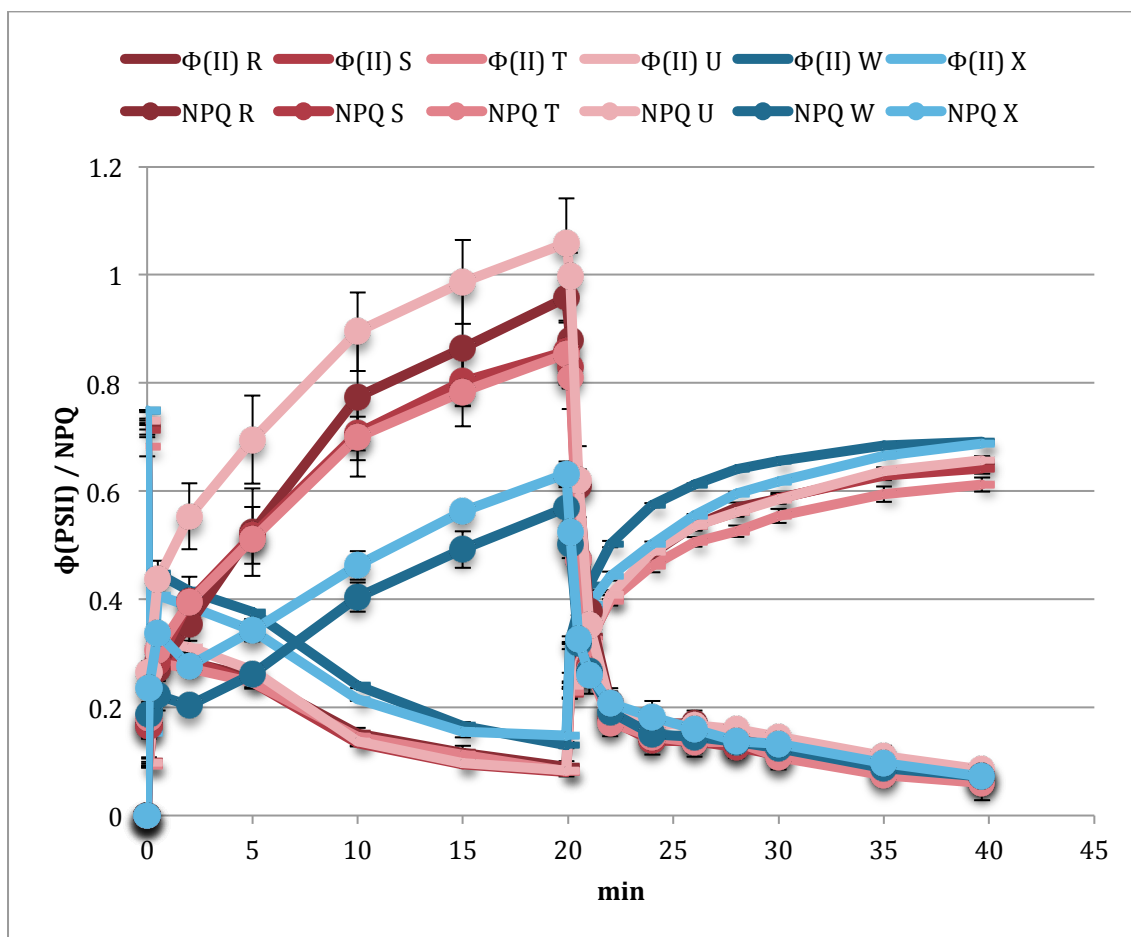
Appendix 8.7: Altered Oxygen levels (2%, 21%, 40%) have limited effect on ϕ_{II} but affect NPQ during fluorescence induction (20 min at 106 μ E) and dark relaxation (5 min)

CF imaging data. Pyr- NPQ, F_v/F_m (ϕ_{II} at 0 sec) and ϕ_{II} recovery in the dark are most severely affected in 2%, whereas ϕ_{II} difference between WT and pyr. is smallest at 40% suggesting O_2 may act as e^- sink, e.g. via photorespiration.



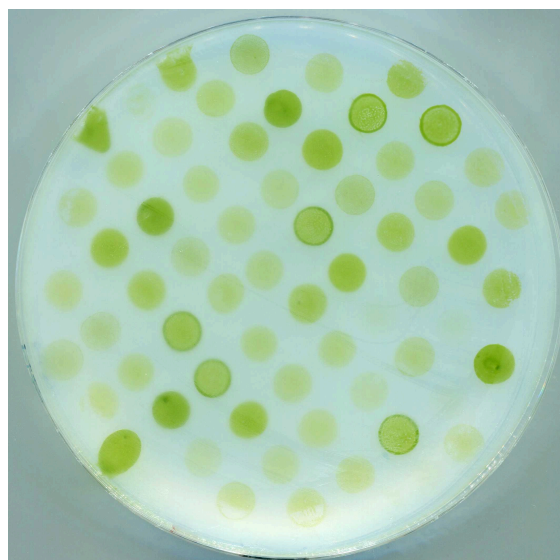
Appendix 8.8 Altered Oxygen levels (2%, 21%, 40%) have limited effect on *ETR* but affect *NPQ* during a light response curve

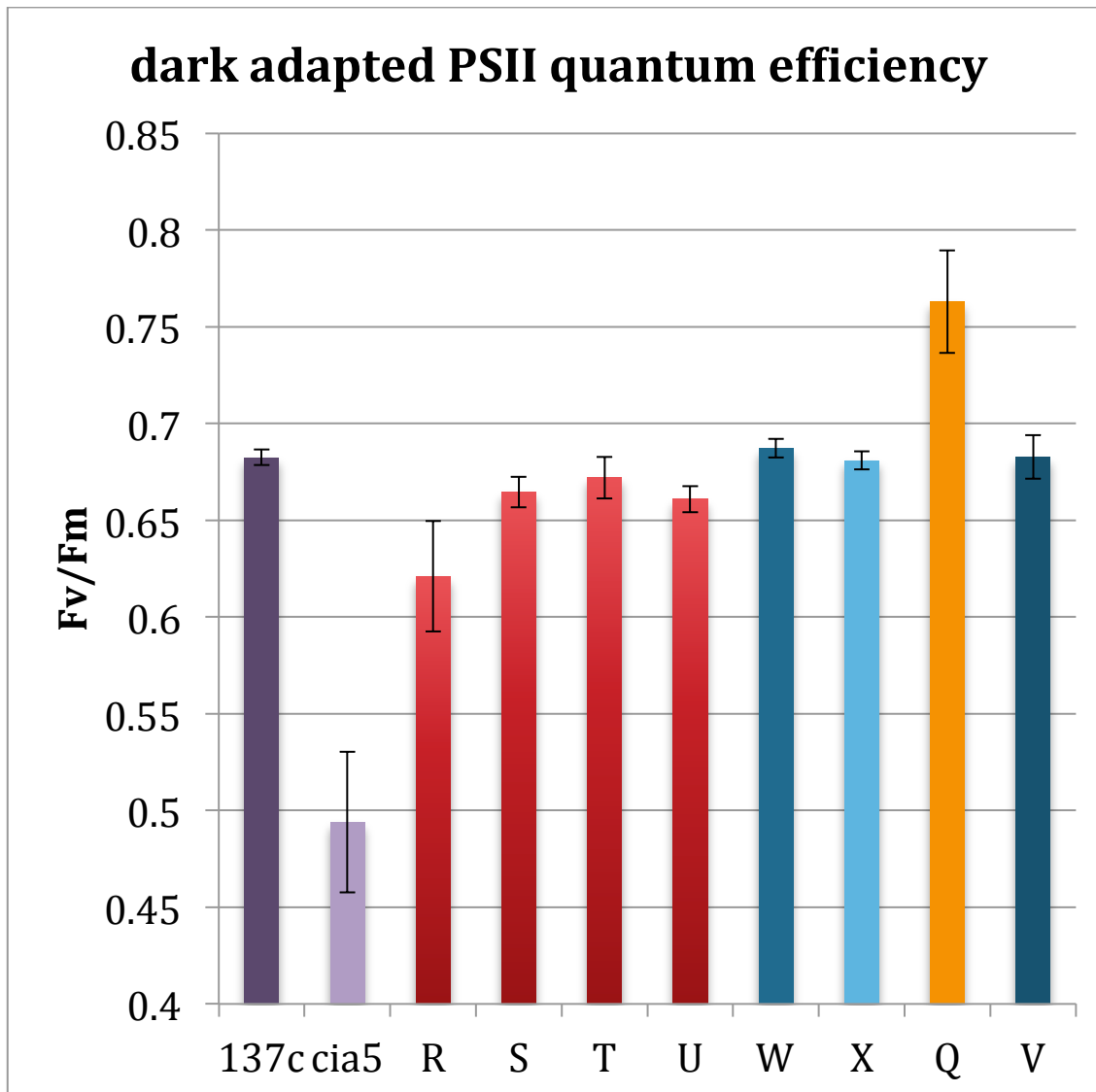
CF imaging data. Slight decrease in *ETR* at 2% suggests O_2 is used as e^- sink to a small extent even in WT. *NPQ* dynamic is altered, with pyr- saturating at lower irradiance at 2% compared to 21% and rescued to WT-levels at high irradiance at 40% O_2 .



Appendix 8.9: The majority of *NPQ* is fast relaxing qE

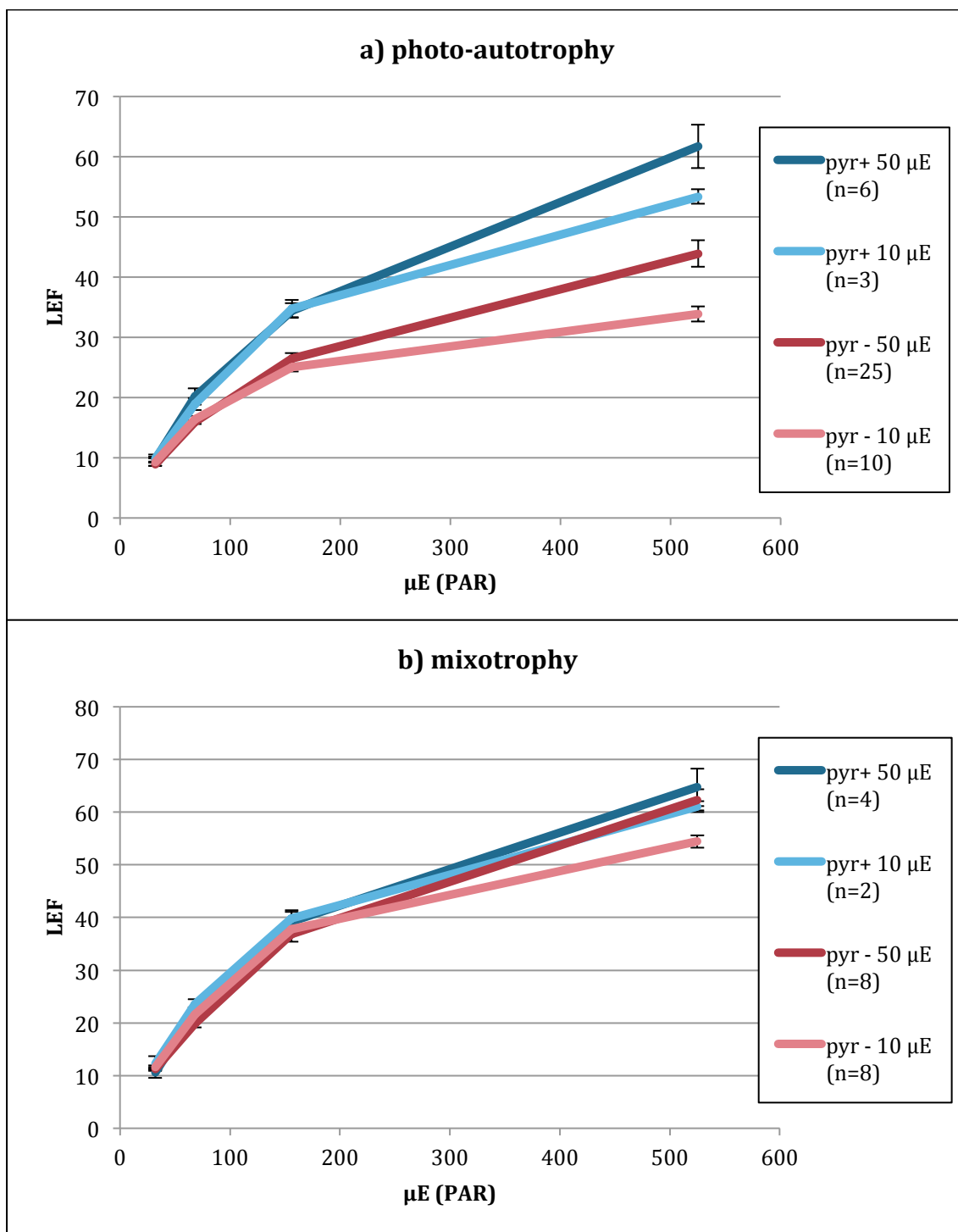
Cells were grown at $50\mu\text{E}$ and air on an agar plate and CF imaging was performed using a FluorCam (PSI, Brno, Czech Republic). Fluorescence induction at $525\mu\text{E}$ was recorded over 20min, after which relaxation was followed in the dark for another 20min. As before (Fig. 2.6, Fig. 2.7, Fig. 2.8), ϕ_{II} is higher and *NPQ* lower in WT than *pyr-* in the light. Dark relaxation data shows that up to $\sim 84\%$ of *NPQ* relaxes within 2min and is thus accounted for as qE.





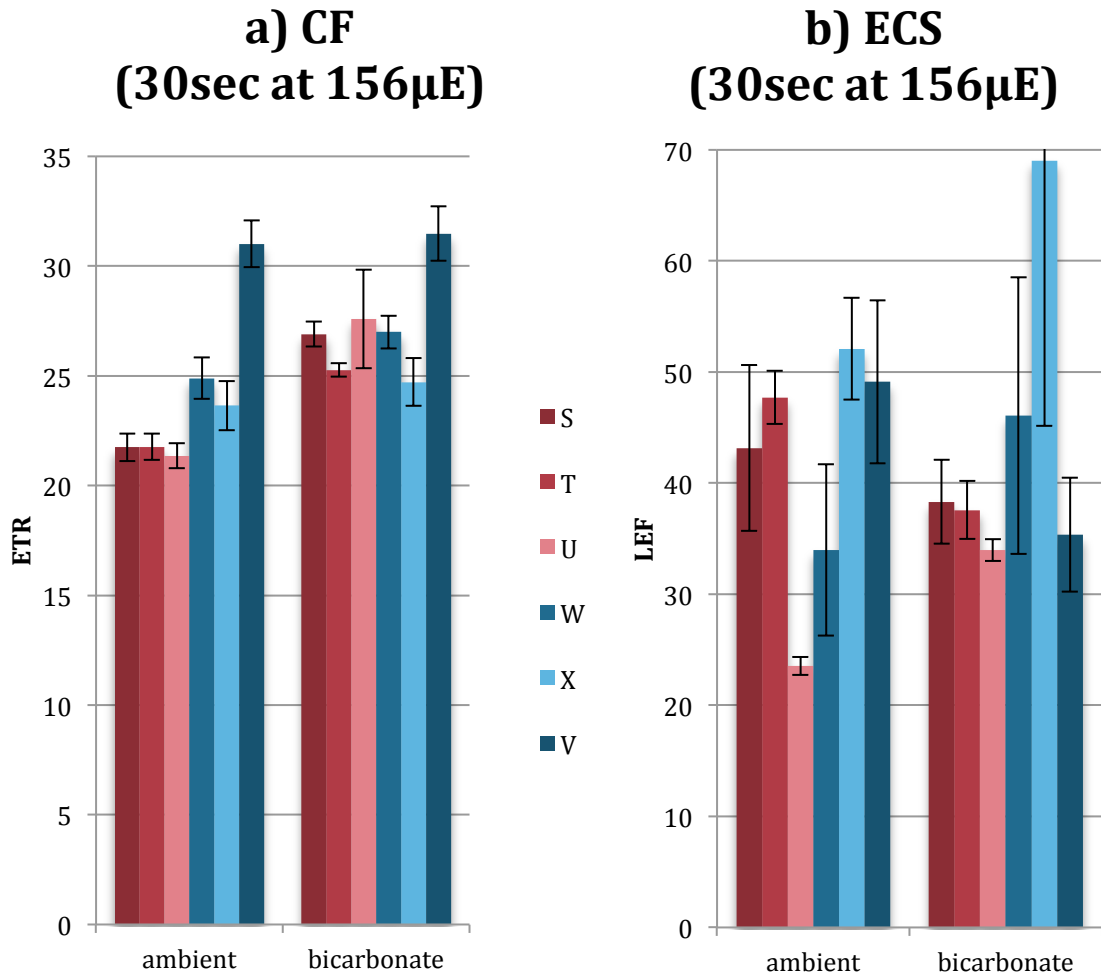
Appendix 8.10: High-resolution JTS-10 data shows pyr- F_v/F_m is lower than WT when grown at 50 μ E in air

J1 data. Positive control strain 137c is the WT parent strain corresponding to CCM mutant *cia5*, which shows that a CCM impairment leads to lower F_v/F_m . SSU substitution strains are labelled by the *RBCS* expressed as R – Reciprocal, S – *Spinacia oleracea*, T – *Arabidopsis thaliana*, U – *Helianthus annuus*, W – native *Chlamydomonas* construct WTint1,2, and X – HelixAB. Compared to strains W (=WT) and X (pyr+), pyr- strains R, S, T and U have lower F_v/F_m . Strains R and X, show a lower F_v/F_m than other pyr- strains and WT respectively, owing to the expression of chimeric SSU constructs that affect Rubisco catalysis kinetic properties in addition to any effect on pyrenoid assembly (Meyer et al., 2012). Strain Q is the *RBCS* knock out strain T-60 (Khrebtukova and Spreitzer, 1996) used to generate the SSU substitution lines (Genkov et al., 2010), and as the only strain was grown in the dark in acetate medium which may account for the high F_v/F_m . Strain V is the WT parent of T-60 (Q), a strain called CC-3395, which was used as positive control to test whether WT strain W fully complements the *RBCS* knock-out.

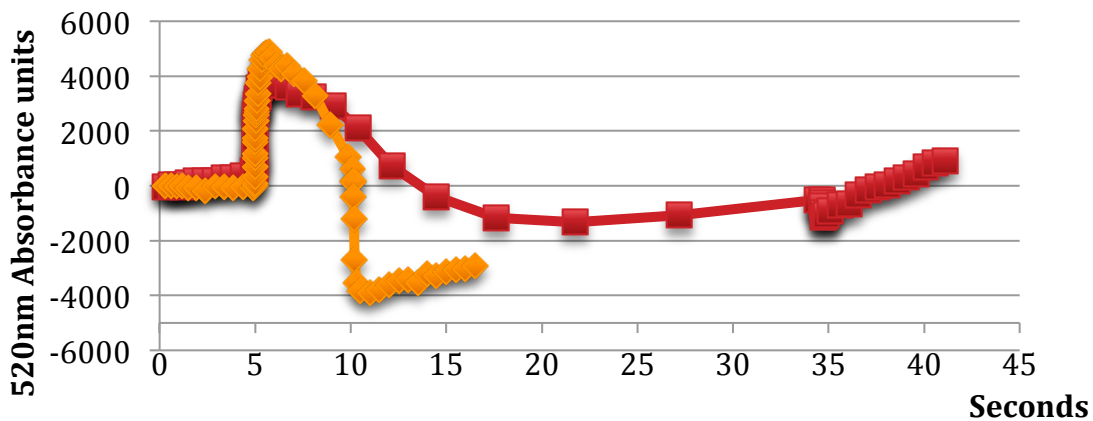


Appendix 8.11: ECS pilot study suggests organic carbon supply restores pyr- *LEF* at least partially

J1 data. Pyr+ (WT and HelixAB) and pyr- strains (Reciprocal, *Spinacia oleracea*, *Arabidopsis thaliana*, *Helianthus annuus* SSU lines) were grown in the absence of aeration either in minimal medium (a) or medium containing acetate (b) under 10 μE or 50 μE as per legend. All cells were measured in HF, which does not contain acetate. Growth on acetate restores pyr- *LEF* to levels similar as pyr+ in ECS light response curves (5s at each light intensity). Higher levels of respiration in mixotrophically grown cells may enrich CO₂ in the HF media during dark adaptation.

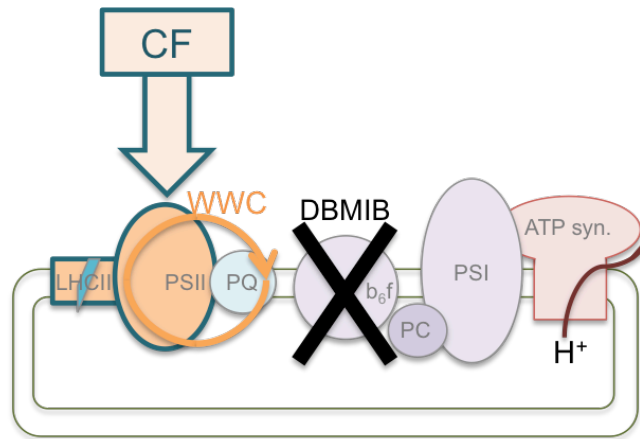


c) 30sec ECS traces show background drift

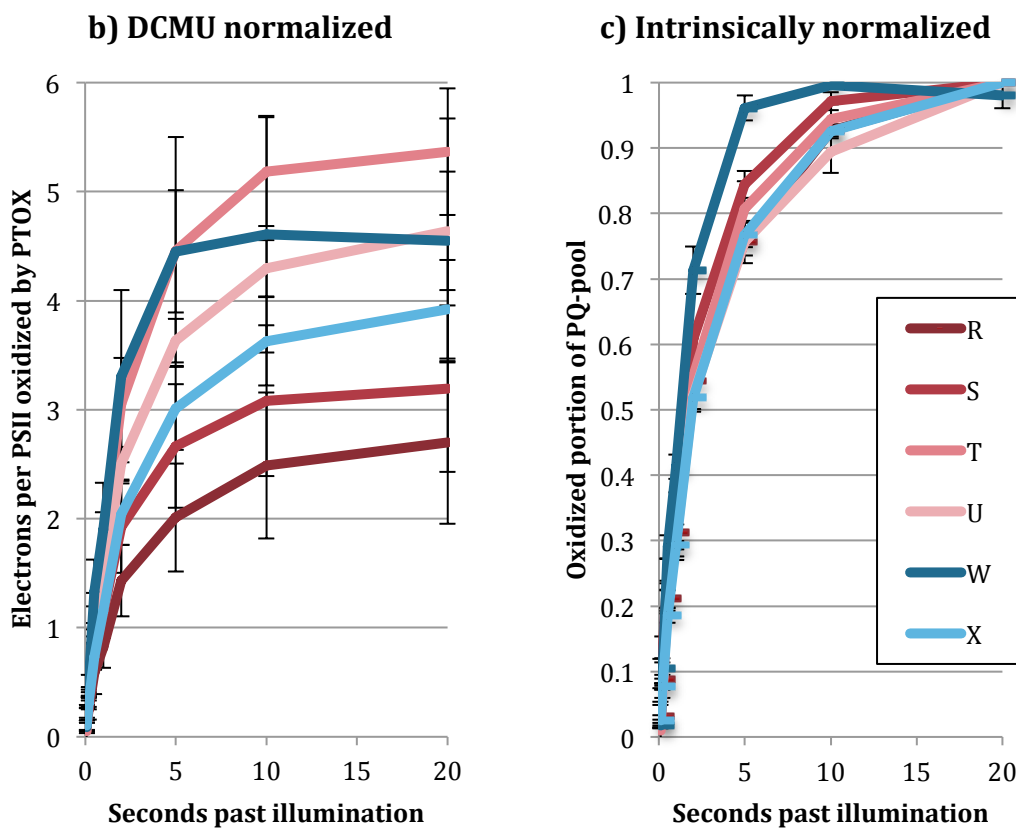


Appendix 8.12: Bicarbonate pilot experiment shows after 30s ECS is unreliable due to background drift

J1 data. Whereas measuring *ETR* using CF (a) after 30sec in the presence and absence of saturating (10mM) NaHCO_3 generates the same profile of pyr- defect and rescue as confirmed by a more in-depth study (Fig. 2.9). *LEF* measurements via ECS (b) generate highly variable results owing to high background drift in the original absorbance traces (c). See Appendix 8.10 for labels (V is CC-3395).

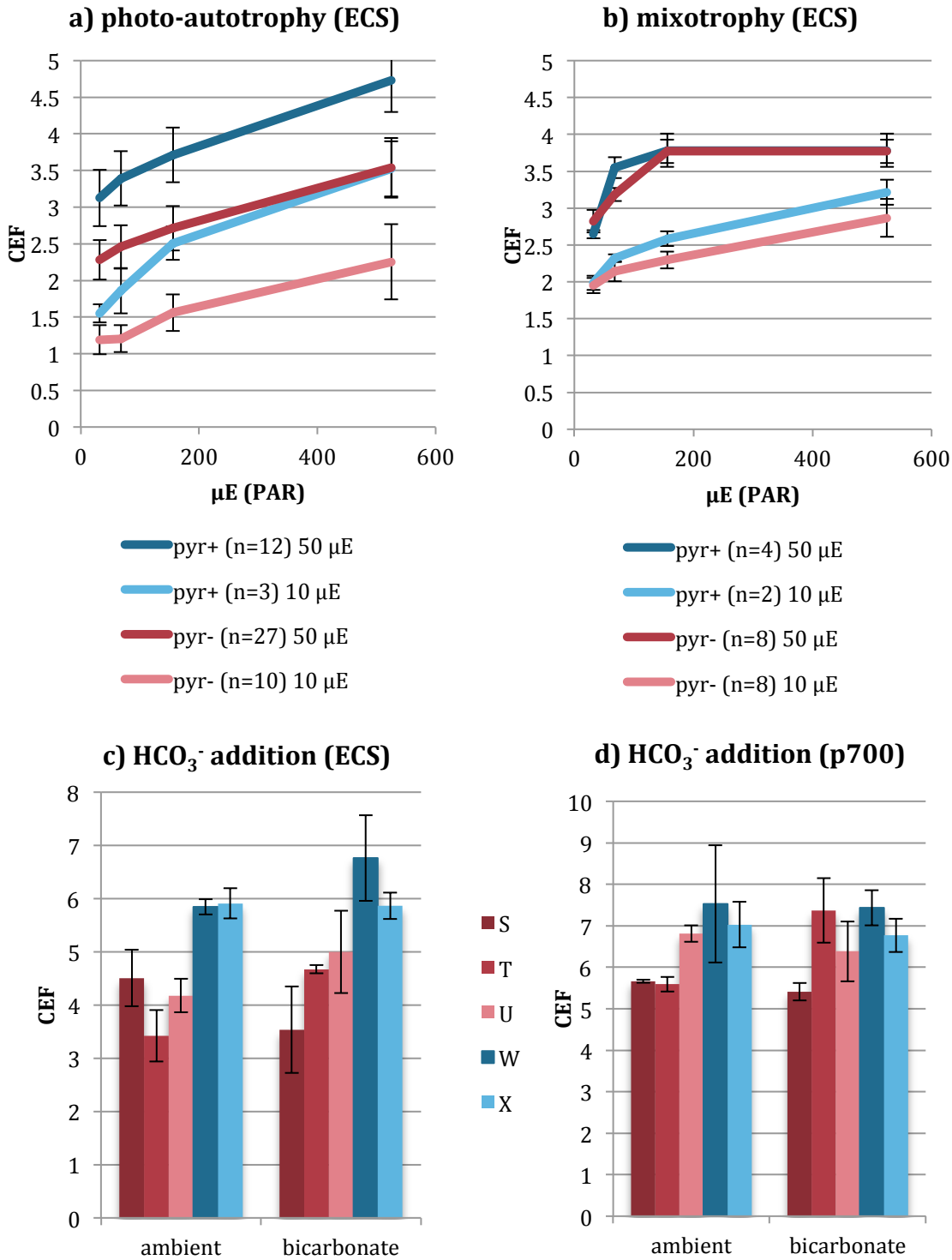


a) CF measures WWC in the presence of a b_6f inhibitor



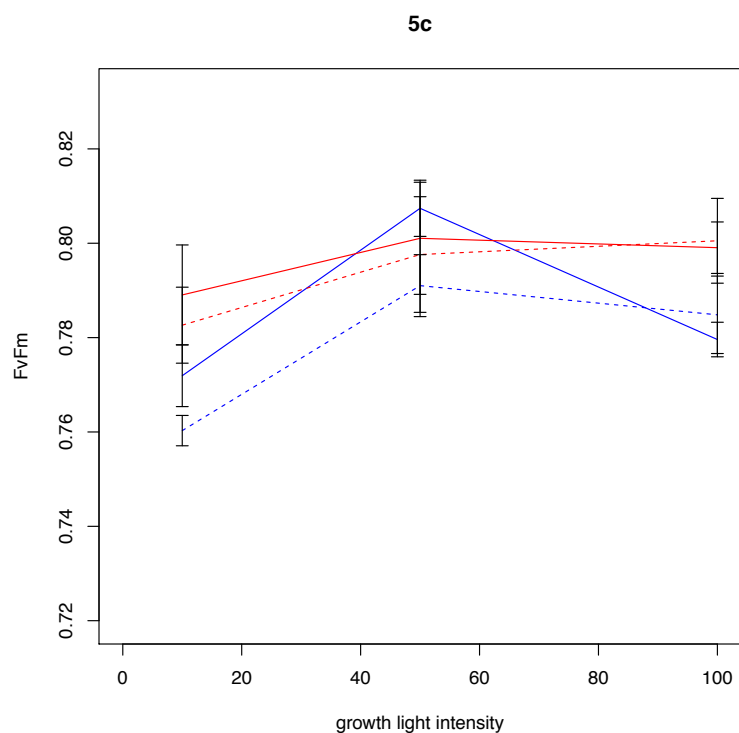
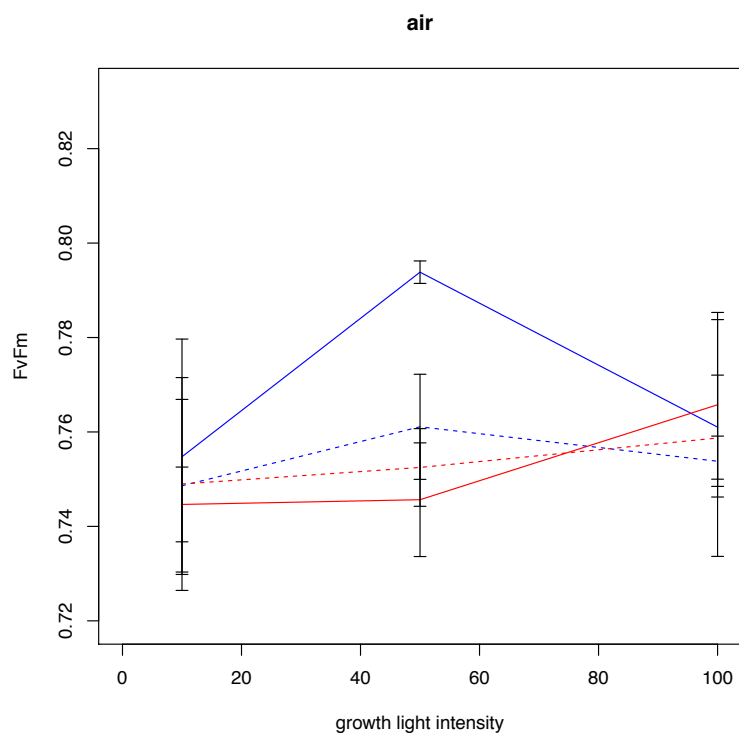
Appendix 8.13: Activity of the water-water cycle (WWC) around PSII is not affected by pyrenoid presence or absence

J1 data. Oxidation of the PQ pool by PTOX in the WWC can be inferred from CF (a) by measuring fluorescence saturation after increasing periods of dark recovery time, plotted on the x-axis in (b) & (c). The rate of electron flow (b) and PQ-pool oxidation (c) are similar between pyr- strains and HelixAB, showing that Rubisco aggregation state does not lead to a difference. Rates exhibited by WT are at the high end of the pyr- spectrum, refuting the idea that pyr- might use PTOX as an excess e^- valve. Strain labelling as in Appendix 8.10.



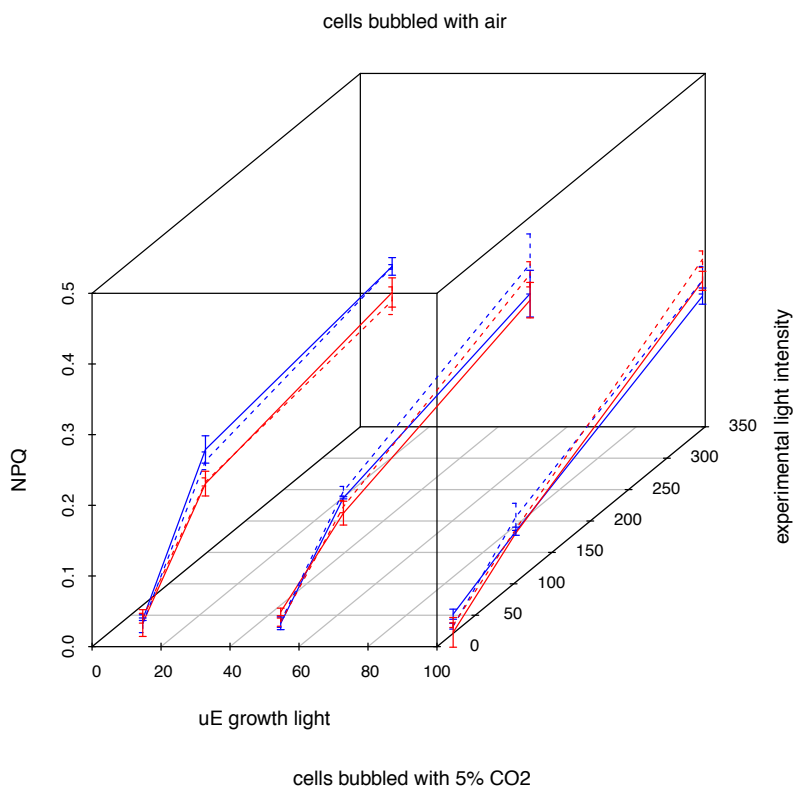
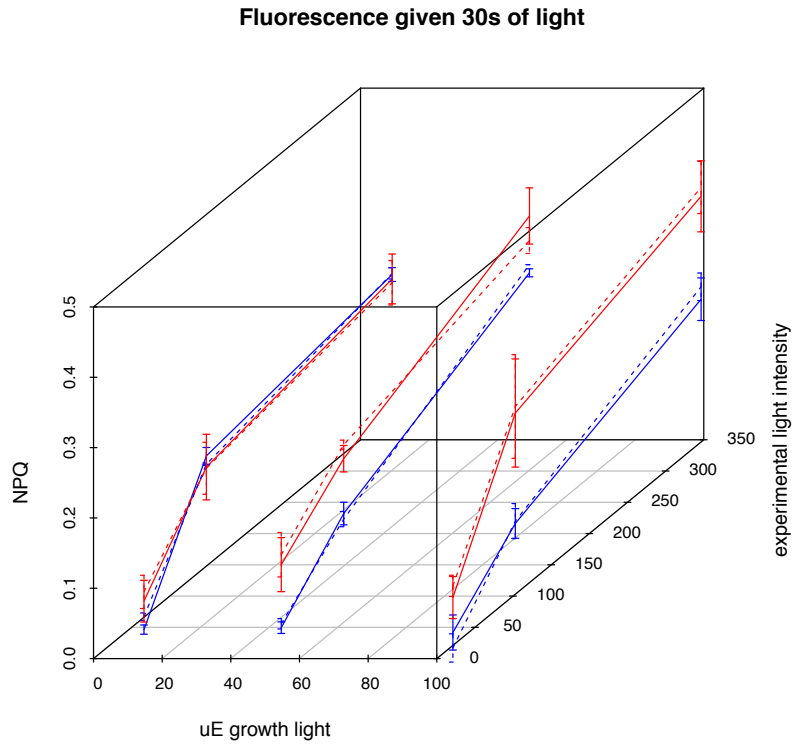
Appendix 8.14: CEF in pyr- can be rescued by long-term, but not instantaneous, supply of carbon.

J1 data. CEF is lower in pyr- than WT, and lower in 10 μE than 50 μE grown cells (a) for cultures grown in the absence of aeration in minimal medium (5sec light response curves). Growth in acetate medium rescues pyr- to WT levels (b), consistent with rescue of LEF (Appendix 8.11). In a 30 sec exposure to 156 μE, 10 mM bicarbonate has no effect on CEF (c)&(d) consistent with measurements conducted in the presence of PSII inhibitors that prevent LEF and thus CBC.



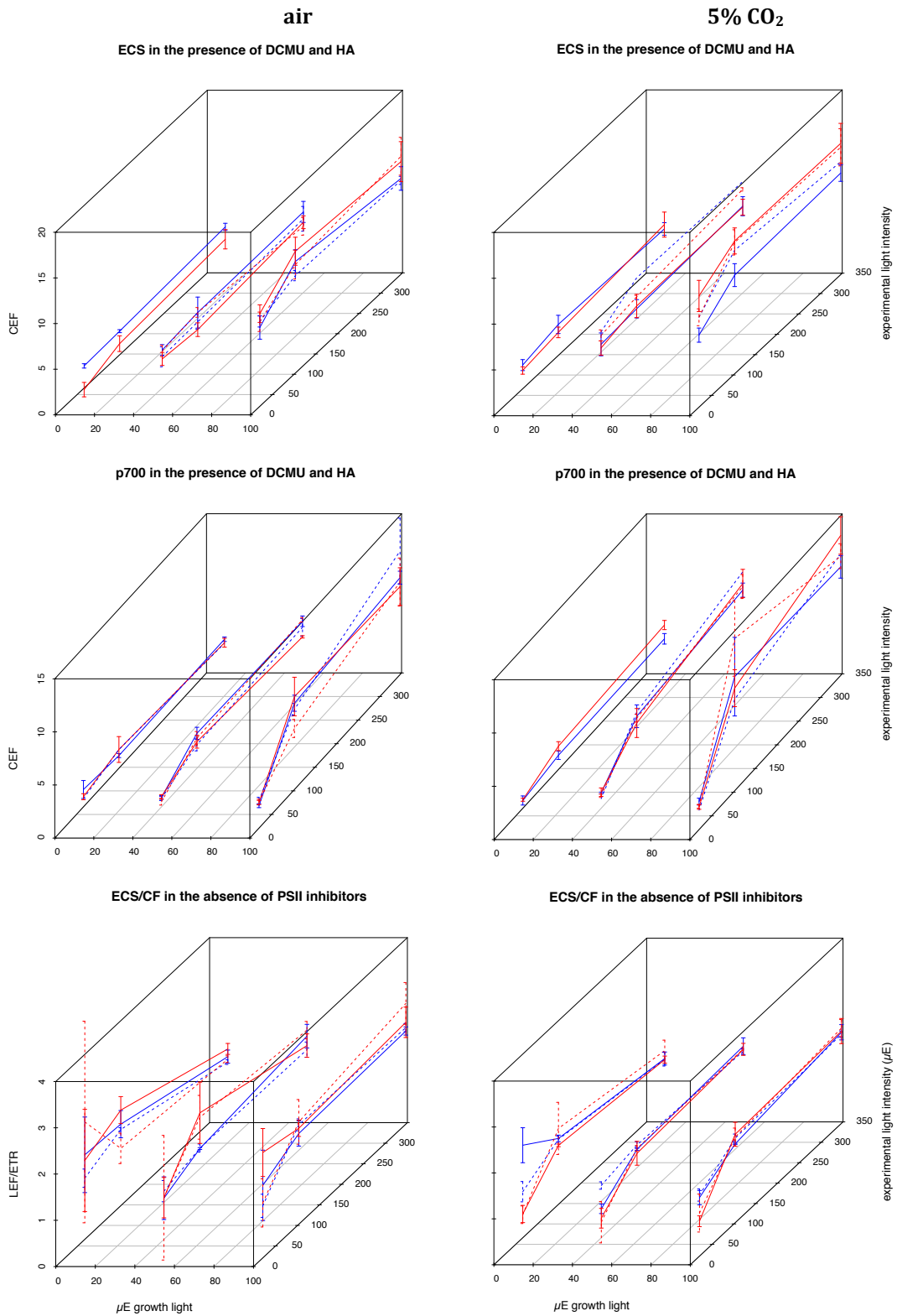
Appendix 8.15: Growth at high CO₂ but not addition of bicarbonate rescues pyr- F_v/F_m

J2 data, legend as in Fig. 2.9. That values are higher than in Appendix 8.10 is likely due to longer dark adaptation (≥ 40 min rather than ≥ 20 min). Thus F_v/F_m appears influenced by prior qI. Consistently, growth at 5% CO₂ (5c) rescues pyr- as higher CBC leads to less excess light experienced at PSII and hence lower qI. Bicarbonate added prior to measurements does not influence qI, hence no rescue. Instead, bicarbonate appears to have a small adverse effect on WT PSII.



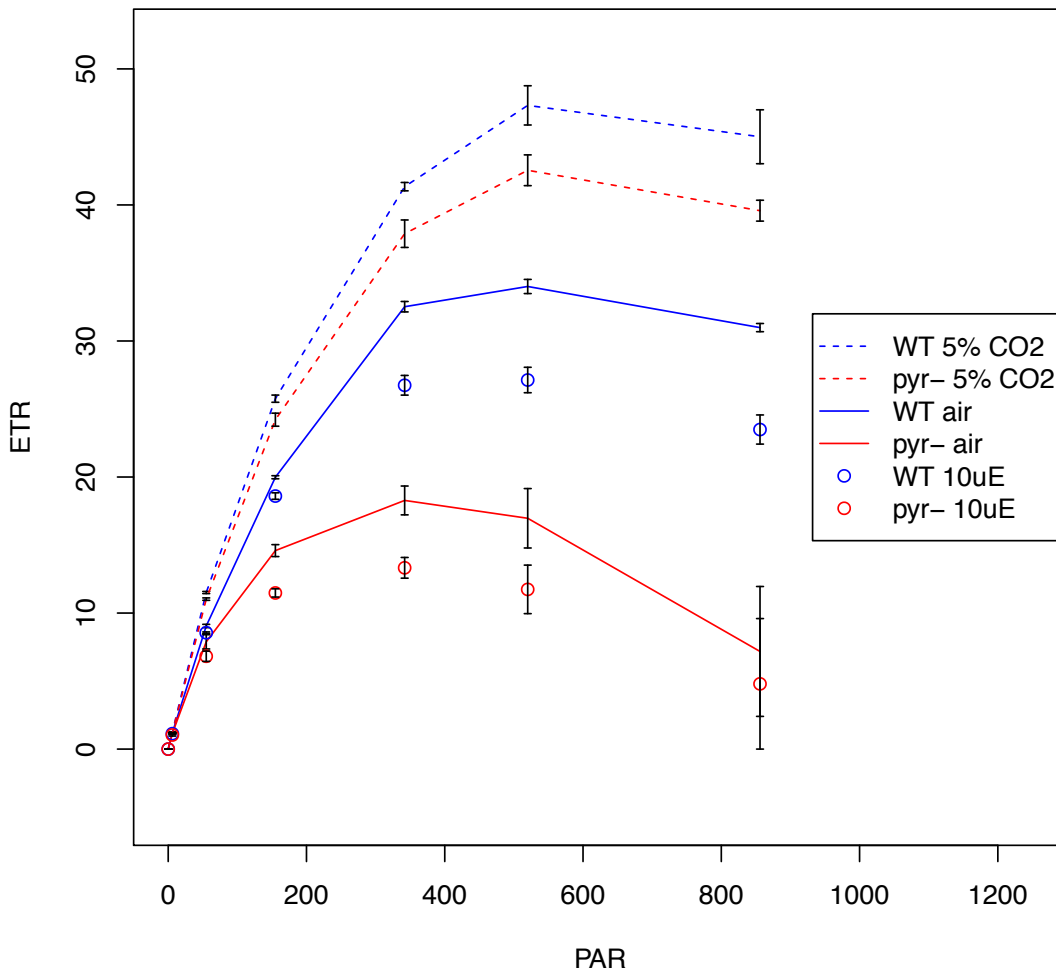
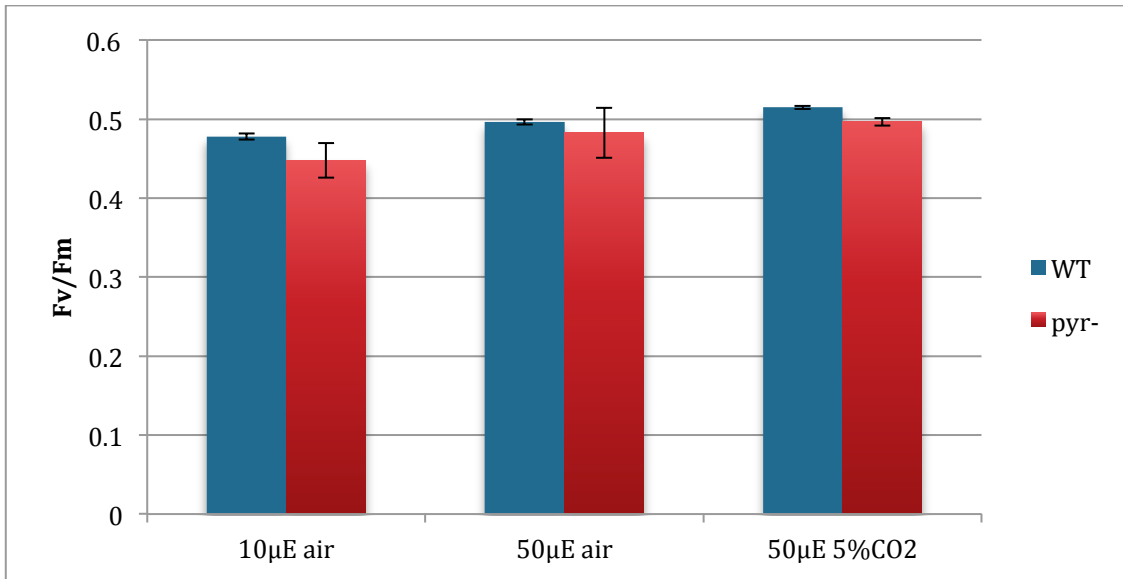
Appendix 8.16: *NPQ* of *pyr-* is rescued by growth at low light or high CO₂

JTS-10 data, legend as in Fig. 2.9. *NPQ* is similar between *pyr-* and WT grown at 5% CO₂, and when grown at 10 μ E in air. This observation is consistent with the notion of *NPQ* or CCM rebalancing pETC and CBC when light is plentiful (Fig. 2.1): WT operates a CCM whereas *pyr-* requires higher *NPQ*, except when grown at 10 μ E when light is not in excess.



Appendix 8.17: High CO₂ rescues pyr- CEF

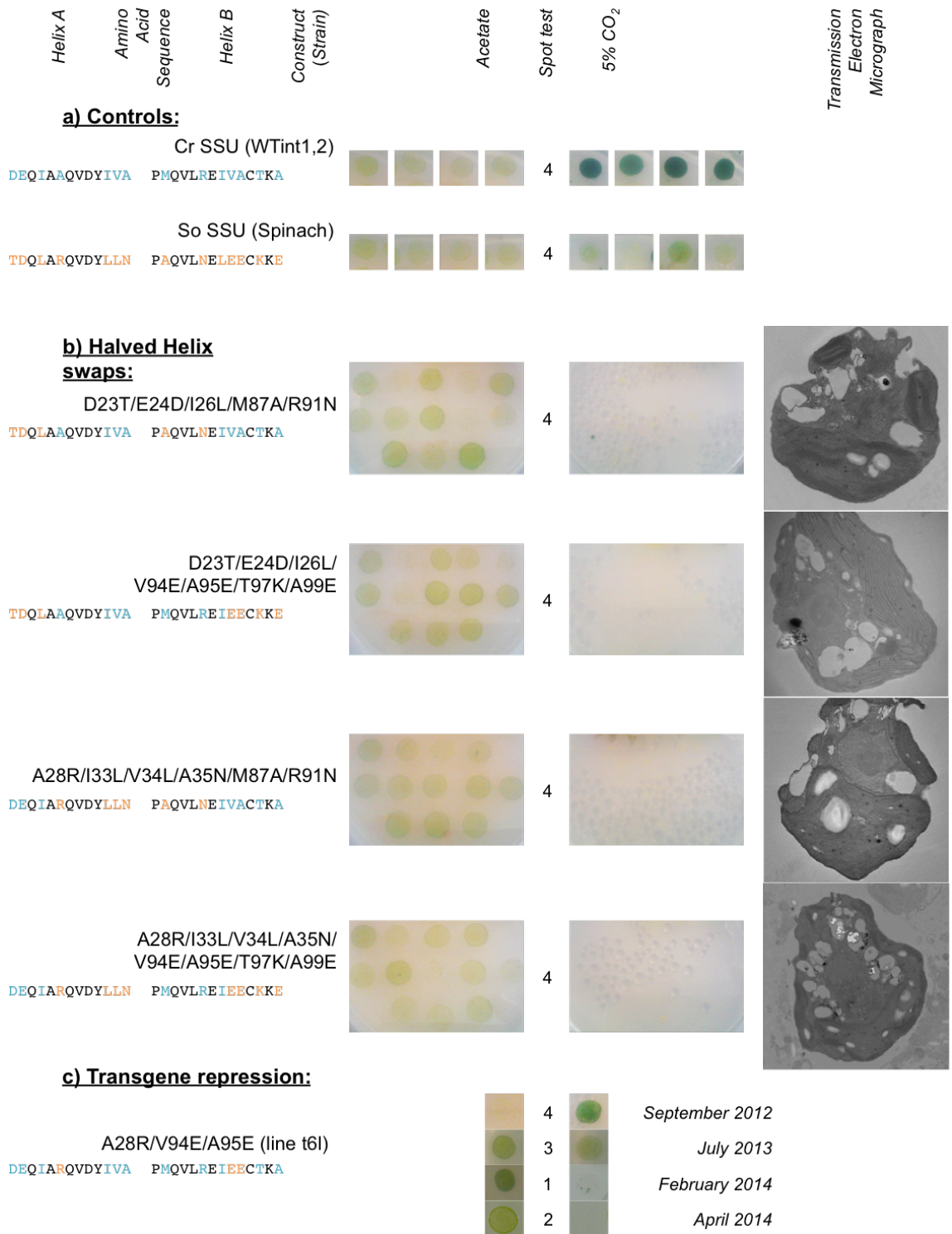
J2 data, legend as in Fig. 2.9. CEF is highly similar between pyr- and WT. Where differences were resolved (ECS, air), pyr- is lower than WT and rescued by high CO₂, consistent with the rescue of LEF (Fig. 2.9). LEF/ETR is higher in pyr- at air, suggesting higher CEF/LEF consistent with (Fig. 2.12), and equally rescued at 5% CO₂. Bicarbonate addition has no effect as the measurements are conducted over 5 sec only (Fig. 2.9) due to (Appendix 8.12).



Appendix 8.18: FRRf data are consistent with CFImager and JTS-10 data

FRRf data, associated with Fig. 2.11 d-f. F_v/F_m and ETR are lower in *pyr-* in air but rescued at 5% CO₂. That a small difference remains even at high CO₂ may be due to a partial loss of acclimation during the dark adaptation in the absence of high CO₂ aeration (see Section 2.2.5).

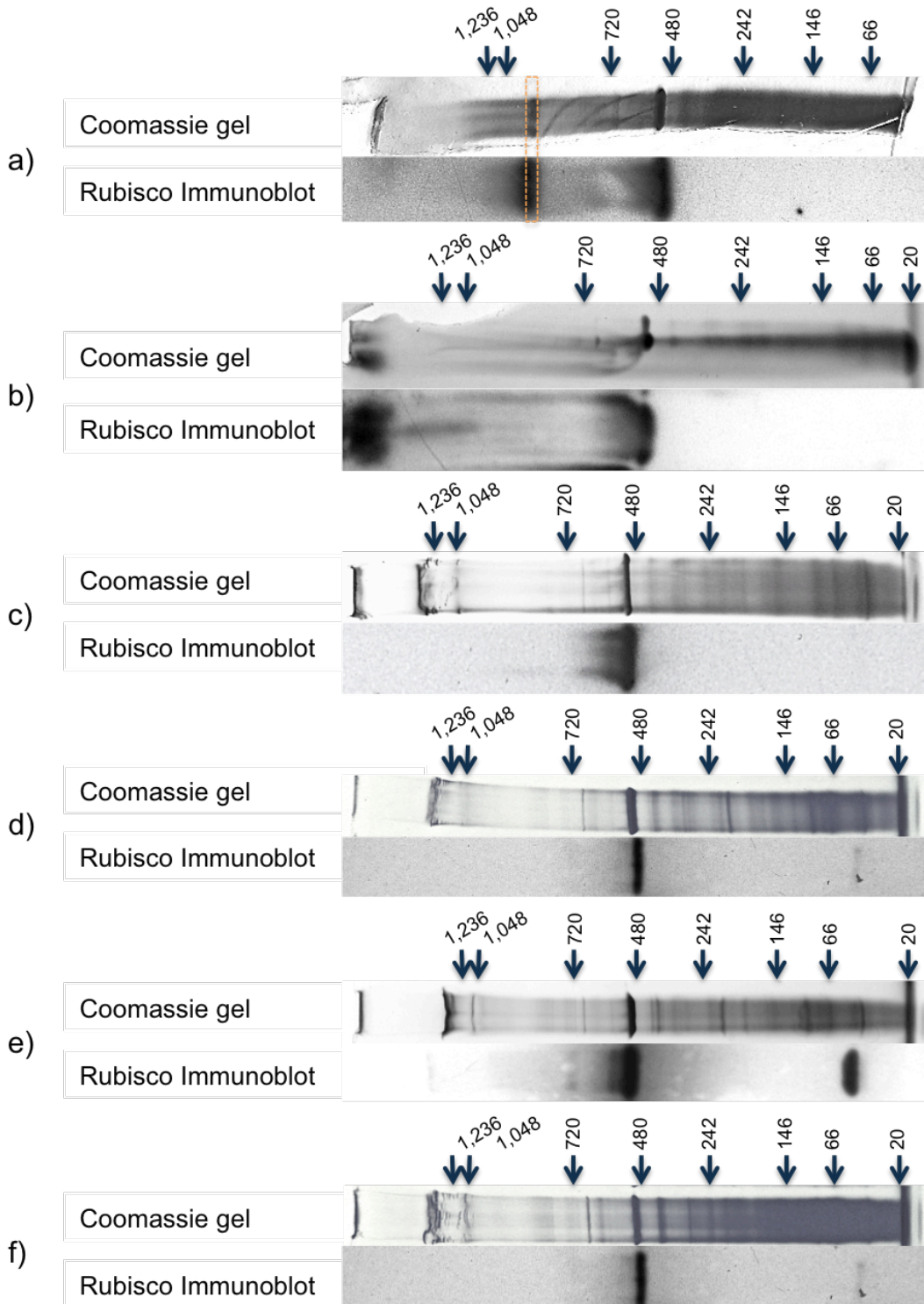
CHAPTER 3 SUPPLEMENTARY FIGURES



Appendix 8.19: Additional SDM constructs that did not recover photosynthetically competent lines

In contrast to controls (a), strains transformed with halved helix swap constructs and selected via photosynthetic growth (b) were unable to grow photoautotrophically. Unless selection failed, the effect may be due to transgene repression, which has been observed for other constructs (c).

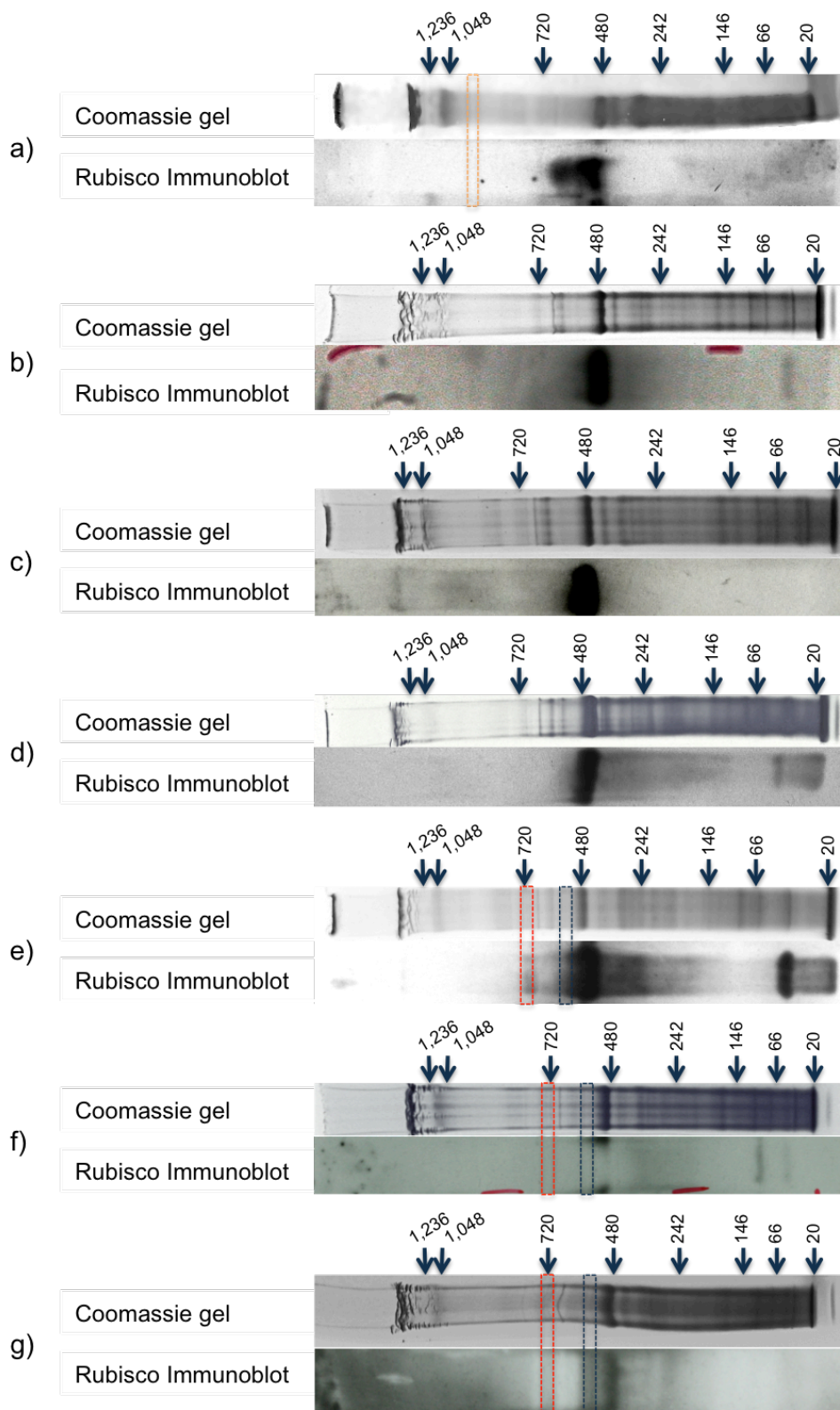
CHAPTER 4 SUPPLEMENTARY FIGURES



Appendix 8.20: 1st dimension Coomassie stained gel strips and Rubisco Westerns for positive control WT strains.

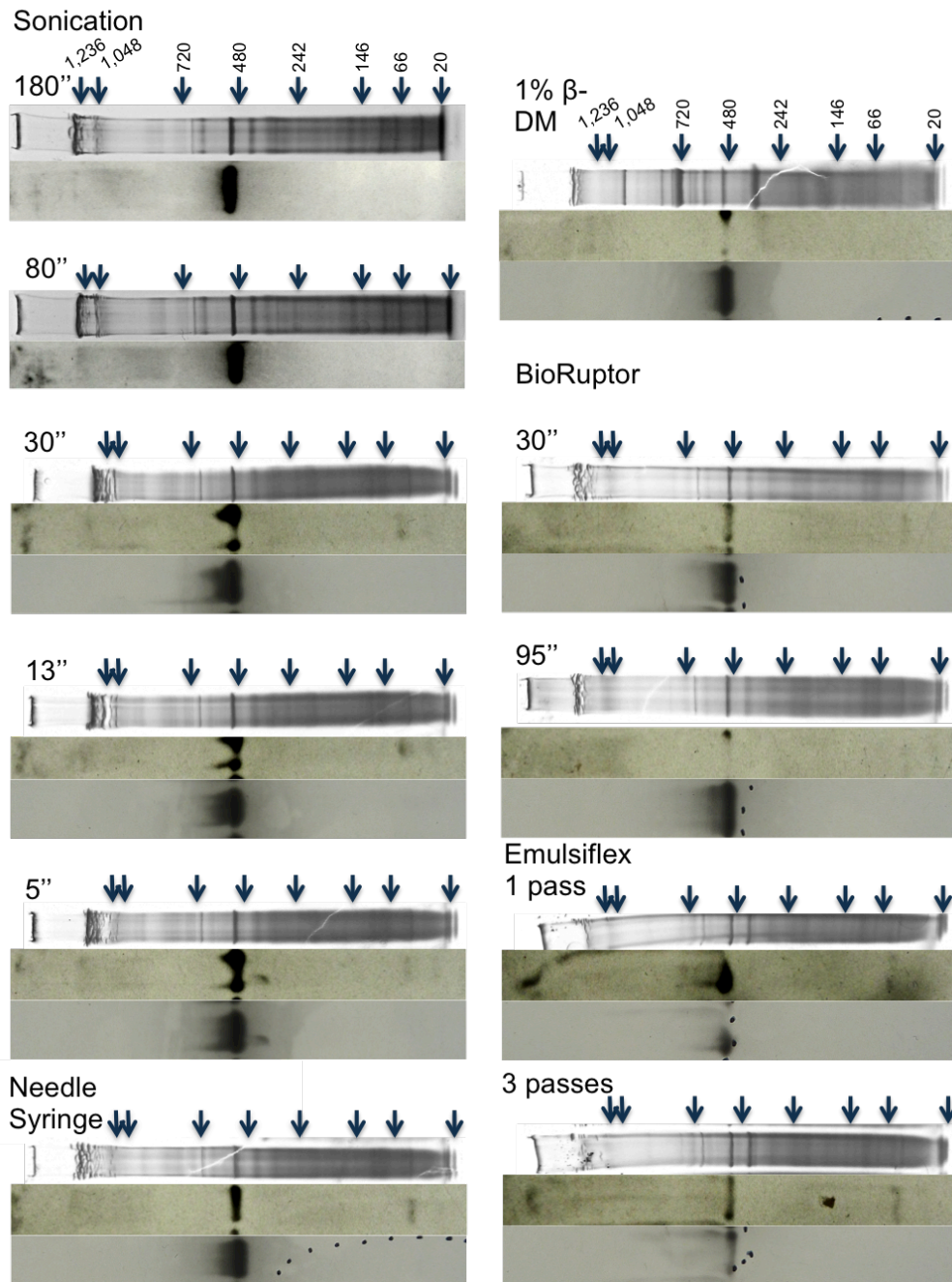
Shown are Coomassie stained gel strips and Rubisco Westerns for positive control WT strains 2137 (a)-(e) and CC-3395 (f), natively expressing *Chlamydomonas RBCS1* and *RBCS2*. The band highlighted in a yellow box was cut out from an equivalent gel for further analysis via mass spectrometry.

Chapter 8: Appendices



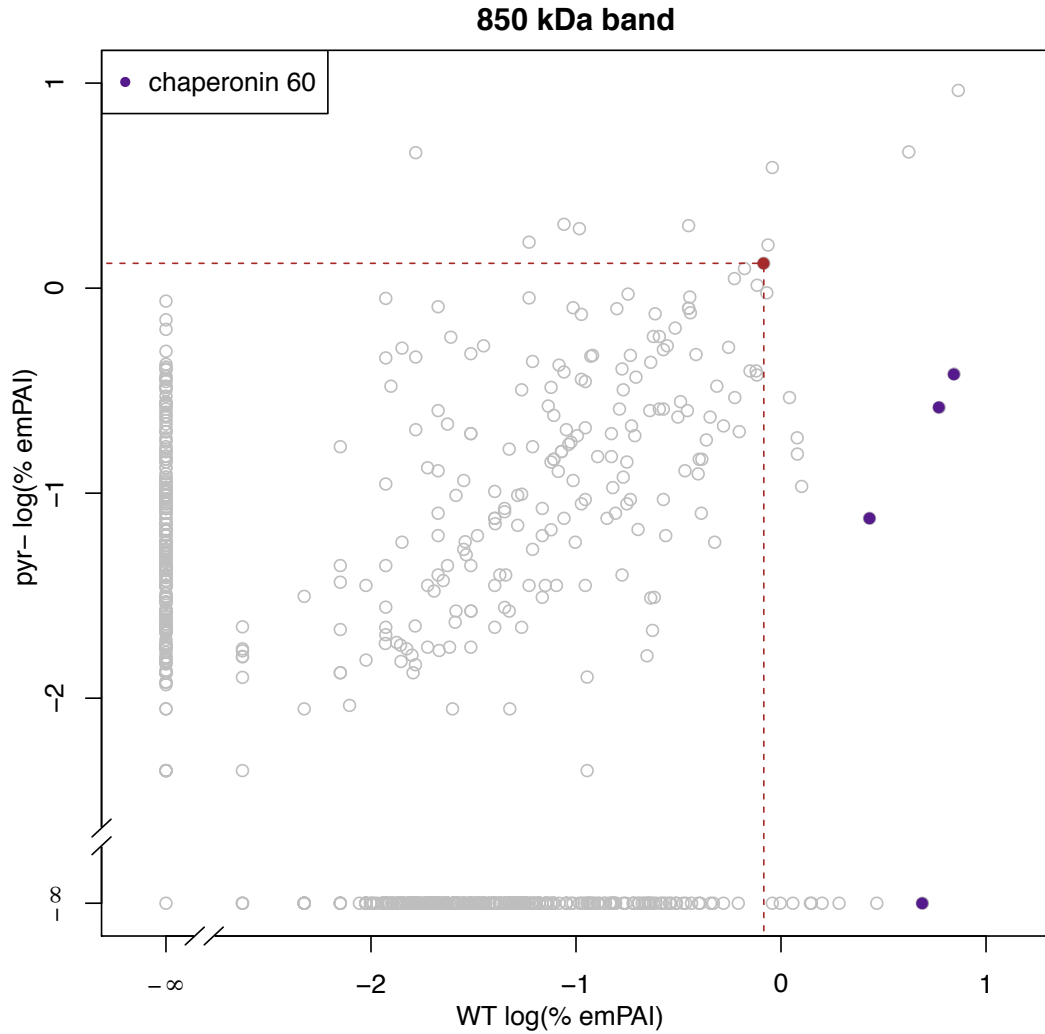
Appendix 8.21: 1st dimension Coomassie stained gel strips and Rubisco Westerns for the pyr- strain expressing *Spinacia oleracea* RBCS.

Shown are Coomassie stained gel strips and Rubisco Westerns for a pyr- strain expressing *Spinacia oleracea* RBCS. Bands highlighted in yellow (a), blue and red boxes (e)-(g) were analyzed via mass spectrometry. The yellow band (a) was taken from an equivalent gel.



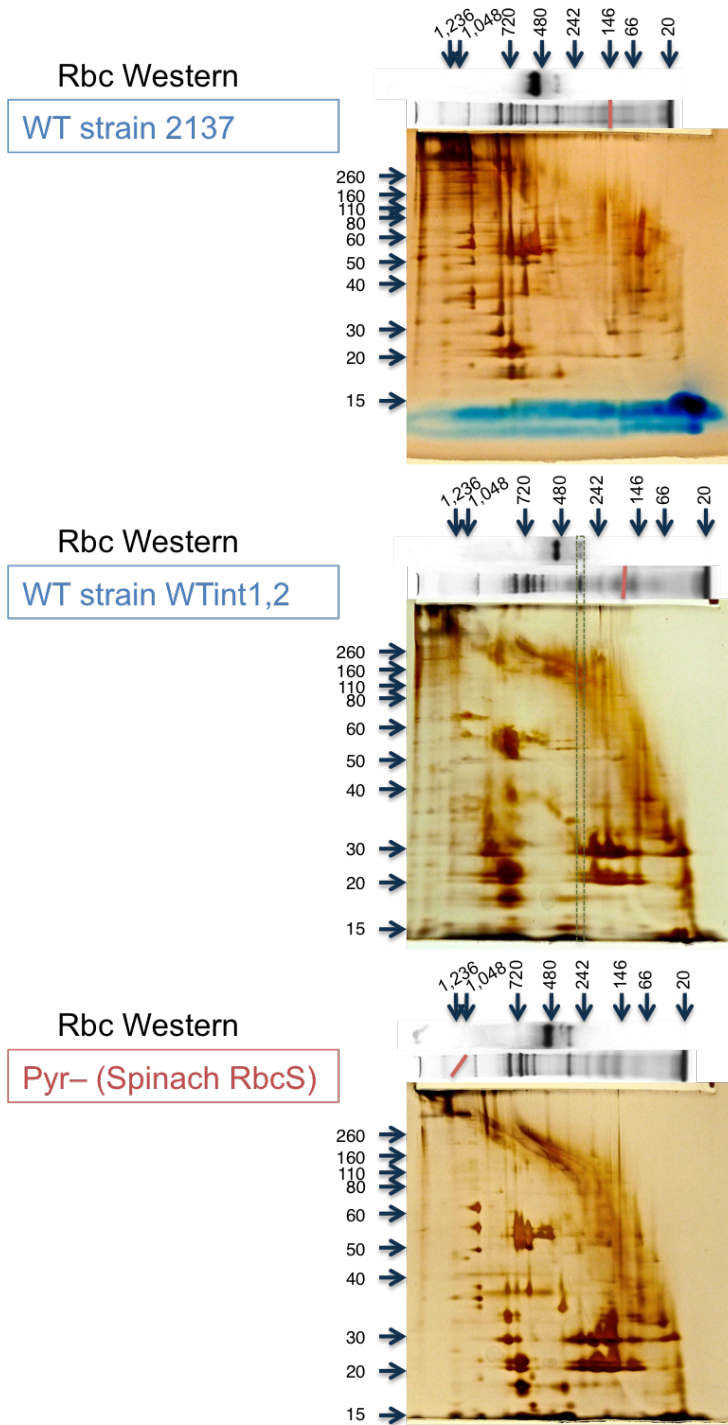
Appendix 8.22: 1st dimension BN-PAGE profile is independent of cell lysis method

Shown are Coomassie stained gel strips and Rubisco Westerns for WT strain WTint1,2 expressing *Chlamydomonas* *RBCS1*. To control for protein transfer through a single Western Blotting membrane (depicted adjacent to the gel), a second membrane was used in some cases (depicted below the first). Soluble protein was extracted using Sonication for 180, 80, 30, 13 or 5 seconds (Soniprep 150, MSE), needle and syringe (Mason et al., 2006), homogenisation by 1 or 3 passes through an Emulsiflex-C5 (Avestin Inc., Ottawa, Canada), or 30 or 95 seconds in a Bioruptor[®] Ultrasonicator (Diagenode, Liège, Belgium), followed by centrifugation to separate out membrane material. Total protein was extracted by cell lysis in 1% β -DM, analogous to membrane solubilisation. See Section 4.2.2 for experimental details.



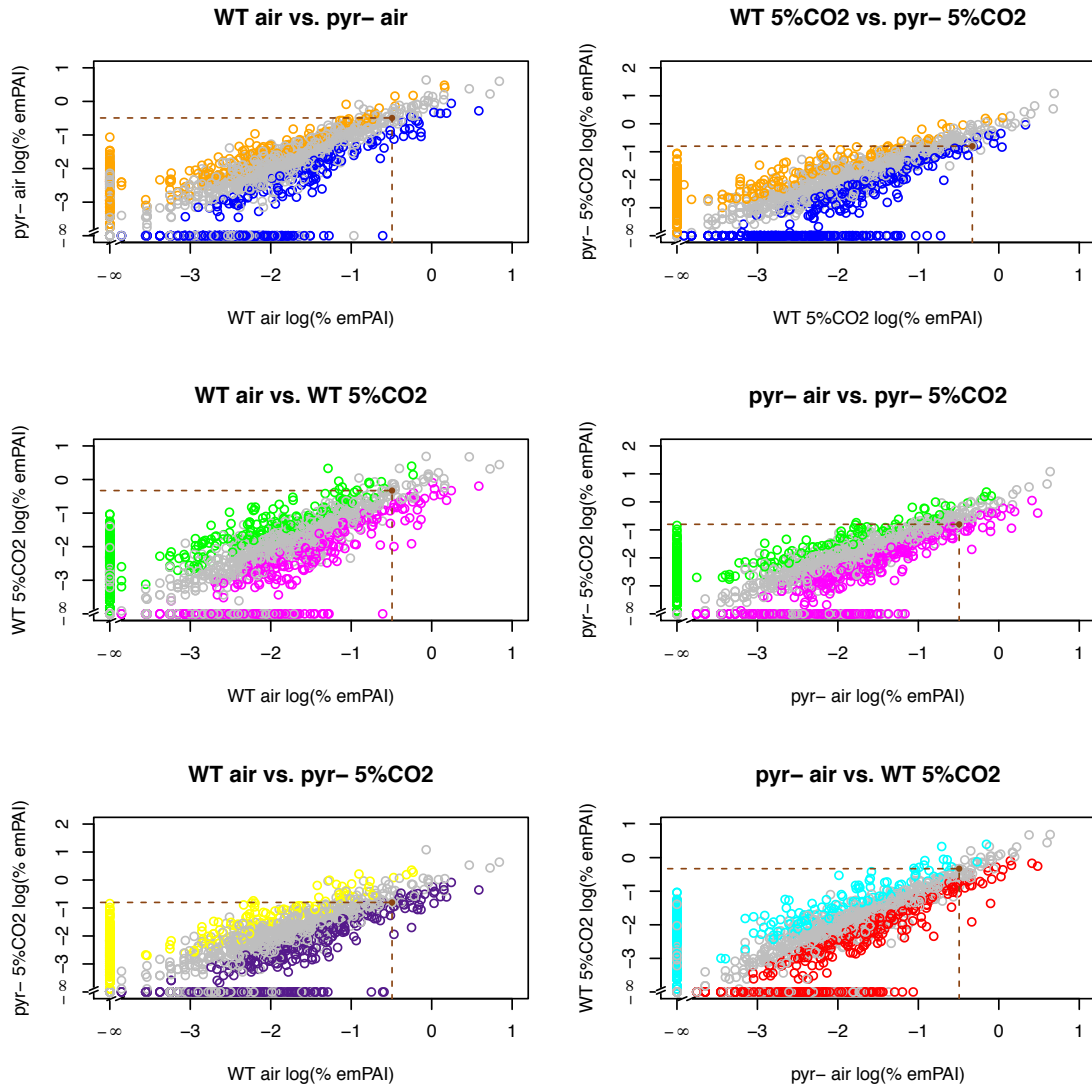
Appendix 8.23: Chaperonin 60 is the source of the non-reproducible, WT-specific, high-molecular weight band immuno-labelled as containing Rubisco.

Abundances of all detected proteins are shown for WT and pyr- samples, expressed as base 10 logarithm of the percentage of total protein content within a sample based on *emPAI* values. The position of the Large subunit of Rubisco is highlighted in brown. Note that due to a fault in ventilation, the incubator overheated shortly prior to extraction.



Appendix 8.24: The ~350 kDa band does not contain Rubisco despite immunolabelling in a preliminary BN-PAGE screen of membrane proteins for pyrenoid-relevant complexes.

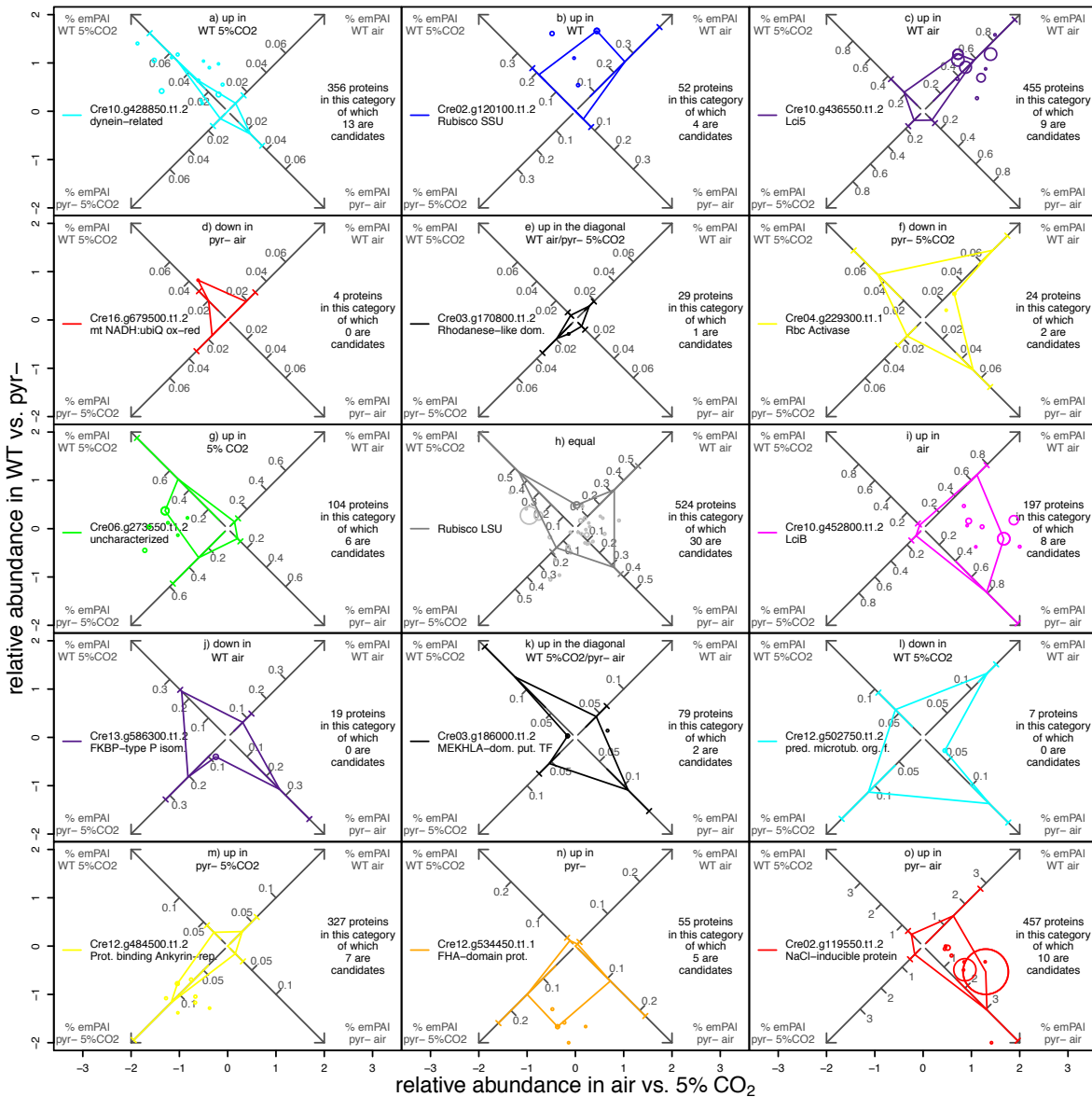
Red marks highlight positions where 1st dimension gel strips broke prior to running the 2nd dimension. Protein content of the ~350 kDa WTint1,2 band highlighted in green was analyzed using LC-MS/MS, but did not contain any Rubisco subunits.



Appendix 8.25: pairwise comparison of co-IP experimental conditions.

Protein abundances are shown as base 10 logarithm of % *emPAI* averages across three replicates for each experimental condition. Proteins that are not significantly different in abundance between the plotted conditions are coloured grey. Rubisco LSU is highlighted in brown.

Molecular Physiology of the *Chlamydomonas pyrenoid*



Appendix 8.26: The statistical groups inform which candidates show interesting behaviour.

For each statistical group, % *emPAI* averages and standard errors of an example protein are plotted for each condition on a cross-shaped spider plot overlaid onto a relative abundance plot of candidate proteins.

In addition to the remarks of the main text, the following observations are noteworthy: In a relative abundance plot, some of the proteins that fall in the same quadrant as those up in WT/air are actually equally abundant as in WT 5% CO₂ and pyr-/air, but are significantly less abundant in the opposite quadrant pyr- 5% CO₂, as shown in Appendix 8.26f. Besides Rubisco activase (Cre04.g229300.t1.1), the other protein in the set is predicted to be a universal stress protein A (Cre12.g542350.t1.2). All proteins detected as specifically down for any of the other three conditions (Appendix 8.26 d&j&l) could be accounted for based on annotation terms by a functional class (Fig. 4.12) other than ‘candidate’. That Rubisco activase less abundantly associated with Rubisco in pyr- 5% CO₂ (Appendix 8.26) is likely driven by lower demand (Portis et al., 2008). Aggregated Rubisco may require more activase if movement of the hexamer (Stotz et al., 2011) is restricted in a densely packed pyrenoid (Engel et al., 2015). Consistently, the highest abundance of activase was recovered from the sample containing the

Chapter 8: Appendices

most aggregated Rubisco: WT/air. Pyr- may contain more activase in air than at 5% CO₂ in an attempt to partially compensate for the lack of a CCM.

Of 356 proteins grouped as statistically most abundant in WT/5% CO₂, 13 were classed as potential candidates (Appendix 8.26a). The example protein, Cre10.g428850.t1.2 annotated as similar to dynein light chain, is present at 0.052±0.029 % *emPAI* in WT 5% CO₂, which is higher than in WT/air (0.008±0.008 % *emPAI*), pyr-/air (0.024±0.012 % *emPAI*) or pyr- 5% CO₂ (0.008±0.008 % *emPAI*). Proteins in this set are of reasonably low abundance, ranging between 4-63% of Rubisco LSU.

Proteins that were significantly more abundant in 5% CO₂ but equal across strains (Appendix 8.26g) were poorly characterized but contain at least one reasonably abundant candidate (Cre06.g273550.t1.2) at ~130% Rubisco LSU. Given that a considerable fraction of Rubisco delocalizes across the chloroplast stroma in high CO₂, some of the candidates that bind Rubisco in this condition may be factors that prevent aggregation or stabilize delocalization.

The largest group of candidates was found not to be significantly affected by experimental treatments (Appendix 8.26h). These included the large subunit of Rubisco which is shown as an example.

Pyr-/5% CO₂ (Appendix 8.26m) contained 7 reasonably low abundance candidates, of which the most abundant and best characterized is an Ankyrin-repeat domain containing protein (Cre12.g484500.t1.2).

Only a small number of candidates were higher in pyr- than in WT irrespective of CO₂ (Appendix 8.26n). The most abundant one (Cre12.g534450.t1.1) shows a Forkhead-associated (FHA) domain profile likely involved in the recognition of phosphorylated proteins. A thylakoid lumen protein (Cre16.g687300.t1.2) was found in this set.

Of the 11 candidates in pyr-/air (Appendix 8.26o), the three better characterized ones include a highly abundant NaCl-inducible protein (Cre02.g119550.t1.2), a dynein light chain-related roadblock/lc7 family protein (Cre12.g546400.t1.2) and a small protein predicted to be localized to the thylakoid lumen (Cre09.g404000.t1.1).

A small number of low abundance candidates was found to behave in a biologically counterintuitive fashion, being simultaneously most abundant in opposing quadrants of the relative abundance plots. With a Rhodanese-like domain carrying protein (Cre03.g170800.t1.2, Appendix 8.26e) and a MEKHLA-domain carrying protein (Cre03.g186000.t1.2, Appendix 8.26k), proteins behaving in this way are likely to be regulatory factors. The presence of RNA- and DNA-binding regulatory factors suggests feedback regulation of plastid protein expression. Candidates of Appendix 8.26 e&l are predicted regulatory elements showing the biologically counterintuitive behaviour of being up or down when either the pyrenoid is present while the CCM is repressed (WT 5%/CO₂), or the pyrenoid is absent in CCM-inducing conditions (pyr-/air). Regulators showing this behaviour may provide feedback between pyrenoid and CCM, and play a role during transition states. For example, such a factor could be expressed during CCM induction and provide feedback of the presence of delocalized Rubisco until pyrenoid assembly is complete.

TABULARIZED RUBISCO INTERACTOME

Appendix 8.27: Table of proteins detected via LC-MS/MS in co-IP

Proteins (column: c1) are listed by NCBI protein GI number reported by mascot (c2), as well as Phytozome JGI.v5 identifier (c3) where conversion was possible. Protein abundances (C4-7) are listed vertically as replicates 1, 2 and 3 with raw data and normalized data reported as *emPAI* and % *emPAI* respectively. The best model as per Table 4.1 is shown for each protein (c8) with the difference in *AIC* (ΔAIC) to the second best model listed as indication for statistical support. Statistical grouping (c9), as detailed in Appendix 8.26, is shown alongside (i) the probability that the grouping is correct, calculated as Akaike weights of all models that support the grouping, and (ii) a t-test based *p*-value reporting whether protein abundances of the indicated grouping are significantly higher than abundances seen in the remaining experimental conditions (ANOVA was used for model 15). An estimate of the average protein abundance in the set of conditions with highest abundance is shown as relative to LSU (c10), alongside fold change to the remaining experimental conditions (∞ is reported where abundance in remaining conditions is 0). Finally, the functional class as per Fig. 4.12 is reported (c11).

	mascot protein description	NCBI gene identifier	Phytozome v5 IDs (JGI version 5)	WT air emPAI / % emPAI	WT 5%CO2 emPAI / % emPAI	pyr- air emPAI / % emPAI	pyr- 5%CO2 emPAI / % emPAI	model fitted (ΔAIC)	Statistical grouping (Akaike w. / p-value) -colour coding-	abundance (fold)	functional class
1	predicted protein	gi 159489054	Cre10.g430501.t1.1	0.78 / 0.0677, 0.21 / 0.0456, 4.65 / 0.195	0 / 0, 7.3 / 0.268, 7.3 / 0.332	0.47 / 0.0519, 2.84 / 0.191, 2.84 / 0.15	0 / 0, 2.84 / 0.11, 2.17 / 0.137	12 (0.219)	a) up in WT 5%CO2 (0.356 / 0.226) -cyan-	0.63 (1.9)	i) candidates
2	predicted protein	gi 159469035	NA	0.44 / 0.0382, 0 / 0, 0 / 0	0.63 / 0.477, 0.83 / 0.0305, 0.83 / 0.0378	0.83 / 0.0916, 0.13 / 0.00874, 0.27 / 0.0143	0.63 / 0.163, 1.34 / 0.0519, 0.83 / 0.0524	12 (0.37)	a) up in WT 5%CO2 (0.408 / 0.229) -cyan-	0.573 (3.9)	i) candidates
3	hypothetical protein CHLREDRAFT_187415	gi 159485822	Cre05.g247950.t1.2	0.15 / 0.013, 0 / 0, 0.15 / 0.00628	0.54 / 0.409, 0.74 / 0.0272, 0.33 / 0.015	0.33 / 0.0364, 0.15 / 0.0101, 0.15 / 0.00792	0.33 / 0.0854, 0.15 / 0.00581, 0 / 0	12 (1.77)	a) up in WT 5%CO2 (0.518 / 0.207) -cyan-	0.474 (8.21)	i) candidates
4	predicted protein	gi 159484644	Cre01.g001100.t1.2	0 / 0, 0 / 0, 1.26 / 0.0528	0.06 / 0.0455, 0.31 / 0.0114, 0.72 / 0.0328	0.06 / 0.00662, 0.11 / 0.0074, 0.24 / 0.0127	0 / 0, 0.31 / 0.012, 0.24 / 0.0151	12 (0.335)	a) up in WT 5%CO2 (0.407 / 0.101) -cyan-	0.0941 (2.52)	i) candidates
5	hypothetical protein CHLREDRAFT_193202	gi 159480208	Cre16.g649350.t1.1	0.53 / 0.046, 0.09 / 0.0195, 0.53 / 0.0222	0.19 / 0.144, 0.67 / 0.0246, 0.53 / 0.0241	0.29 / 0.032, 0.67 / 0.0451, 0.82 / 0.0433	0.09 / 0.0233, 0.09 / 0.00349, 0.19 / 0.012	12 (0.154)	a) up in WT 5%CO2 (0.4 / 0.227) -cyan-	0.202 (2.34)	i) candidates
6	predicted protein	gi 159471698	Cre12.g549150.t1.1	0 / 0, 0 / 0, 0 / 0	0.2 / 0.152, 0.27 / 0.00991, 0.2 / 0.0091	0.06 / 0.00662, 0 / 0, 0 / 0	0.06 / 0.0155, 0.2 / 0.00775, 0 / 0	12 (1.92)	a) up in WT 5%CO2 (0.607 / 0.188) -cyan-	0.179 (17.1)	i) candidates
7	predicted protein	gi 159489436	Cre10.g428850.t1.2	0 / 0, 0 / 0, 0.59 / 0.0247	0 / 0, 1.53 / 0.0561, 2.19 / 0.0997	0 / 0, 0.59 / 0.0397, 0.59 / 0.0312	0 / 0, 0.59 / 0.0229, 0 / 0	12 (1.14)	a) up in WT 5%CO2 (0.581 / 0.155) -cyan-	0.164 (3.95)	i) candidates
8	hypothetical protein CHLREDRAFT_193449	gi 159481941	NA	0.5 / 0.0434, 0 / 0, 0 / 0	0.28 / 0.212, 0 / 0, 0 / 0	0.31 / 0.0342, 0 / 0, 0 / 0	0.12 / 0.0311, 0 / 0, 0.02 / 0.00126	12 (0.539)	a) up in WT 5%CO2 (0.395 / 0.248) -cyan-	0.223 (5.79)	i) candidates
9	predicted protein	gi 159487695	Cre02.g077800.t1.2	0.27 / 0.0235, 0 / 0, 0.08 / 0.00335	0.08 / 0.0606, 0.37 / 0.0136, 0.27 / 0.0123	0.27 / 0.0298, 0.17 / 0.0114, 0.17 / 0.00898	0.08 / 0.0207, 0.37 / 0.0143, 0.17 / 0.0107	12 (0.488)	a) up in WT 5%CO2 (0.38 / 0.221) -cyan-	0.0908 (2.11)	i) candidates
10	solute carrier protein	gi 159478234	Cre17.g722000.t1.1	0.07 / 0.00608, 0 / 0, 0 / 0	0.07 / 0.0531, 0.07 / 0.00257, 0.07 / 0.00319	0.07 / 0.00773, 0 / 0, 0.07 / 0.0037	0 / 0, 0.07 / 0.00271, 0.07 / 0.00442	12 (1.74)	a) up in WT 5%CO2 (0.518 / 0.21) -cyan-	0.0617 (7.16)	i) candidates
11	hypothetical protein CHLREDRAFT_187330	gi 159476672	Cre06.g249750.t1.1	0.11 / 0.00955, 0.05 / 0.0109, 0.05 / 0.00209	0.05 / 0.0379, 0.17 / 0.00624, 0.24 / 0.0109	0.17 / 0.0188, 0 / 0, 0.11 / 0.00581	0 / 0, 0.05 / 0.00194, 0 / 0	12 (0.565)	a) up in WT 5%CO2 (0.524 / 0.16) -cyan-	0.0578 (3.37)	i) candidates
12	predicted protein	gi 159489106	Cre10.g428050.t1.1	0.09 / 0.00782, 0 / 0, 0.09 / 0.00377	0.03 / 0.0227, 0.18 / 0.00661, 0.22 / 0.01	0.18 / 0.0199, 0 / 0, 0.03 / 0.00158	0.06 / 0.0155, 0.09 / 0.00349, 0 / 0	12 (0.312)	a) up in WT 5%CO2 (0.366 / 0.136) -cyan-	0.0413 (2.27)	i) candidates
13	predicted protein	gi 159473962	NA	0.04 / 0.00347, 0.07 / 0.0152, 0 / 0	0.04 / 0.0303, 0.07 / 0.00257, 0.11 / 0.00501	0.04 / 0.00442, 0.04 / 0.00269, 0.04 / 0.00211	0 / 0, 0.11 / 0.00426, 0.07 / 0.00442	12 (0.742)	a) up in WT 5%CO2 (0.408 / 0.218) -cyan-	0.0398 (3.11)	i) candidates
14	Rubisco small subunit 1, chloroplast precursor	gi 159488841	Cre02.g120100.t1.2	7.08 / 0.615, 0.35 / 0.076, 1.84 / 0.0771	0.16 / 0.121, 5.96 / 0.219, 4.99 / 0.227	1.11 / 0.123, 0 / 0, 0 / 0	0 / 0, 0 / 0, 0 / 0	8 (1.63)	b) up in WT (0.395 / 0.0295) -blue-	0.701 (2.9)	i) candidates
15	hypothetical protein CHLREDRAFT_193060	gi 159479554	Cre16.g659700.t1.2	0.32 / 0.0278, 1.3 / 0.282, 0.32 / 0.0134	0.74 / 0.561, 0.74 / 0.0272, 0.74 / 0.0337	0.32 / 0.0353, 0.32 / 0.0215, 0.32 / 0.0169	0 / 0, 0.74 / 0.0287, 0 / 0	8 (0.797)	b) up in WT (0.205 / 0.0917) -blue-	0.496 (1.96)	i) candidates
16	hypothetical protein CHLREDRAFT_192075	gi 159477179	Cre09.g409850.t1.2	1.41 / 0.122, 0.19 / 0.0413, 1.88 / 0.0787	0 / 0, 3.88 / 0.142, 3.09 / 0.141	0.7 / 0.0773, 1.02 / 0.0686, 0.7 / 0.037	0 / 0, 1.41 / 0.0546, 1.02 / 0.0644	8 (0.181)	b) up in WT (0.207 / 0.0998) -blue-	0.276 (1.35)	i) candidates
17	predicted protein	gi 159486699	Cre11.g467576.t1.1, Cre11.g467576.t3.1, Cre11.g467576.t2.1	0.1 / 0.00869, 0.48 / 0.104, 0.48 / 0.0201	0.1 / 0.0758, 0.79 / 0.029, 0.34 / 0.0155	0 / 0, 0.34 / 0.0229, 0.1 / 0.00528	0.1 / 0.0259, 0.34 / 0.0132, 0.1 / 0.00631	8 (1.48)	b) up in WT (0.301 / 0.0595) -blue-	0.133 (1.96)	i) candidates
18	predicted protein	gi 159487411	Cre02.g084000.t1.2	1.55 / 0.135, 9.37 / 2.03, 1.02 / 0.0427	0.6 / 0.455, 1.55 / 0.0569, 1.55 / 0.0706	1.02 / 0.113, 1.55 / 0.104, 1.02 / 0.0539	1.55 / 0.401, 2.22 / 0.086, 1.55 / 0.0978	11 (0.926)	c) up in WT air (0.432 / 0.234) -purple-	2.32 (4.62)	i) candidates
19	beta tubulin 2	gi 159471706	Cre12.g549550.t1.2	24.7 / 2.14, 0 / 0, 1.6 / 0.067	0 / 0, 1.77 / 0.065, 2.81 / 0.128	1.01 / 0.112, 1.6 / 0.108, 2.57 / 0.136	0.07 / 0.0181, 2.81 / 0.109, 2.14 / 0.135	11 (1.28)	c) up in WT air (0.47 / 0.227) -purple-	2.32 (8.19)	i) candidates

Chapter 8: Appendices

20	predicted protein	gi 159464032	Cre01.g050550.t1.2	0.75 / 0.0651, 2.08 / 0.452, 37.6 / 1.57	0.32 / 0.243, 4.4 / 0.161, 6.15 / 0.28	0 / 0, 3.07 / 0.206, 8.47 / 0.447	0.32 / 0.0828, 4.4 / 0.17, 2.08 / 0.131	11 (1.84)	c) up in WT air (0.565 / 0.19) -purple-	2.19 (3.64)	i) candidates
21	low-CO2-inducible protein 5	gi 159464709	Cre10.g436550.t1.2	1.82 / 0.158, 6.93 / 1.51, 1.82 / 0.0762	0.68 / 0.515, 1.82 / 0.0668, 1.47 / 0.0669	1.47 / 0.162, 0.68 / 0.0457, 1.82 / 0.0961	0.91 / 0.236, 1.17 / 0.0453, 0.47 / 0.0297	11 (1.09)	c) up in WT air (0.445 / 0.222) -purple-	1.83 (4.13)	i) candidates
22	alpha tubulin 1	gi 159467393	Cre03.g190950.t1.2	15.4 / 1.34, 0 / 0, 1.44 / 0.0603	0 / 0, 1.95 / 0.0716, 2.35 / 0.107	2.57 / 0.284, 1.6 / 0.108, 1.6 / 0.0845	0.14 / 0.0362, 1.6 / 0.062, 3.05 / 0.192	11 (0.626)	c) up in WT air (0.4 / 0.247) -purple-	1.47 (4.45)	i) candidates
23	predicted protein	gi 159468440	Cre07.g339000.t1.1, Cre07.g339050.t1.2	2.13 / 0.185, 0.1 / 0.0217, 0.33 / 0.0138	0 / 0, 1.59 / 0.0583, 0.61 / 0.0278	0.46 / 0.0508, 0.33 / 0.0222, 0.33 / 0.0174	0 / 0, 0.61 / 0.0236, 0.61 / 0.0385	11 (0.45)	c) up in WT air (0.384 / 0.244) -purple-	0.231 (2.77)	i) candidates
24	hypothetical protein CHLREDRAFT_182267	gi 159476758	Cre06.g272500.t1.2	0.87 / 0.0756, 0.52 / 0.113, 0.52 / 0.0218	0 / 0, 0.52 / 0.0191, 0.23 / 0.0105	0.52 / 0.0574, 0.23 / 0.0155, 0.87 / 0.046	0 / 0, 0.23 / 0.00891, 0.87 / 0.0549	11 (0.224)	c) up in WT air (0.616 / 0.107) -purple-	0.221 (2.97)	i) candidates
25	predicted protein	gi 159469662	Cre12.g536500.t1.2	0 / 0, 0.5 / 0.109, 0 / 0	0 / 0, 0.22 / 0.00807, 0.22 / 0.01	0 / 0, 0.22 / 0.0148, 0 / 0	0 / 0, 0 / 0, 0 / 0	11 (1.09)	c) up in WT air (0.448 / 0.232) -purple-	0.114 (9.91)	i) candidates
26	mago nashi-like protein	gi 159473236	Cre09.g392692.t1.1	1.03 / 0.0895, 0 / 0, 0 / 0	0 / 0, 0.19 / 0.00697, 0 / 0	0.19 / 0.021, 0 / 0, 0 / 0	0 / 0, 0.43 / 0.0167, 0 / 0	11 (0.548)	c) up in WT air (0.394 / 0.246) -purple-	0.0939 (6.02)	i) candidates
27	hypothetical protein CHLREDRAFT_135133	gi 159491046	Cre03.g170800.t1.2	0.11 / 0.00955, 0.11 / 0.0239, 0.23 / 0.00963	0 / 0, 0.11 / 0.00404, 0.23 / 0.0105	0 / 0, 0.11 / 0.0074, 0.23 / 0.0122	0 / 0, 0.23 / 0.00891, 0.77 / 0.0486	10 (0.428)	e) up in the diagonal WT air/ pyr- 5%CO2 (0.223 / 0.907)	0.0528 (2.95)	i) candidates
28	rubisco activase	gi 159468147	Cre04.g229300.t1.1	1.17 / 0.102, 0.24 / 0.0521, 1.5 / 0.0628	0 / 0, 1.5 / 0.055, 1.88 / 0.0856	0.15 / 0.0166, 1.02 / 0.0686, 1.33 / 0.0703	0 / 0, 0.42 / 0.0163, 0.53 / 0.0335	14 (0.451)	f) down in pyr- 5%CO2 (0.178 / 0.0127)	0.179 (3.44)	i) candidates
29	predicted protein	gi 159471556	Cre12.g542350.t1.2	0.66 / 0.0573, 0 / 0, 0.4 / 0.0168	0 / 0, 1.33 / 0.0488, 0.66 / 0.03	0.18 / 0.0199, 0.4 / 0.0269, 0.97 / 0.0512	0 / 0, 0.4 / 0.0155, 0.18 / 0.0114	14 (0.35)	f) down in pyr- 5%CO2 (0.156 / 0.0253)	0.0878 (3.11)	i) candidates
30	hypothetical protein CHLREDRAFT_182260	gi 159476730	Cre06.g273550.t1.2	1.28 / 0.111, 0 / 0, 2.44 / 0.102	1.8 / 1.36, 3.23 / 0.119, 1.28 / 0.0583	1.28 / 0.141, 1.8 / 0.121, 0.85 / 0.0449	3.23 / 0.836, 1.28 / 0.0496, 0.23 / 0.0145	9 (0.107)	g) up in 5%CO2 (0.193 / 0.112) -green-	1.28 (4.69)	i) candidates
31	predicted protein	gi 159484224	Cre07.g334600.t1.2	0.21 / 0.0182, 0 / 0, 0 / 0	0.46 / 0.349, 0 / 0, 0.21 / 0.00956	0.46 / 0.0508, 0 / 0, 0 / 0	2.1 / 0.544, 0 / 0, 0 / 0	9 (0.225)	g) up in 5%CO2 (0.212 / 0.106) -green-	0.473 (13.1)	i) candidates
32	hypothetical protein CHLREDRAFT_166860	gi 159483917	NA	0 / 0, 0 / 0, 0.45 / 0.0188	0.45 / 0.341, 0.45 / 0.0165, 0.45 / 0.0205	0 / 0, 0.45 / 0.0303, 0.45 / 0.0238	1.09 / 0.282, 0.45 / 0.0174, 0.45 / 0.0284	9 (1.05)	g) up in 5%CO2 (0.274 / 0.0745) -green-	0.37 (9.69)	i) candidates
33	predicted protein	gi 159478935	Cre03.g153450.t1.2	0 / 0, 0.23 / 0.00963	0 / 0, 1.78 / 0.0653, 1.78 / 0.081	0 / 0, 0.51 / 0.0343, 0.23 / 0.0122	0.23 / 0.0595, 0 / 0, 0.51 / 0.0322	9 (0.687)	g) up in 5%CO2 (0.265 / 0.0441) -green-	0.125 (4.25)	i) candidates
34	predicted protein	gi 159490032	Cre12.g513150.t1.2	0.61 / 0.053, 0 / 0, 0 / 0	0.06 / 0.0455, 0.61 / 0.0224, 0.61 / 0.0278	0.19 / 0.021, 0.06 / 0.00403, 0 / 0	0.06 / 0.0155, 0.52 / 0.0201, 0.92 / 0.0581	9 (0.818)	g) up in 5%CO2 (0.263 / 0.0621) -green-	0.0994 (2.43)	i) candidates
35	hypothetical protein CHLREDRAFT_179251	gi 159486539	Cre08.g372000.t1.2	0.1 / 0.00869, 0 / 0, 0.33 / 0.0138	0 / 0, 1.36 / 0.0499, 0.77 / 0.0351	0 / 0, 0.33 / 0.0222, 0.21 / 0.0111	0 / 0, 0.77 / 0.0298, 0.95 / 0.06	9 (1.5)	g) up in 5%CO2 (0.305 / 0.057) -green-	0.0917 (3.13)	i) candidates
36	predicted protein	gi 159480458	Cre10.g447100.t1.2	12.4 / 1.08, 0 / 0, 2.67 / 0.112	7.72 / 5.85, 7.72 / 0.283, 6.02 / 0.274	15.7 / 1.73, 3.55 / 0.239, 6.02 / 0.318	9.83 / 2.54, 7.72 / 0.299, 9.83 / 0.62	15 (0.248)	h) equal (0.149 / 0.679) -grey-	3.5	i) candidates
37	glycine-rich protein	gi 159471287	Cre13.g577900.t1.2	3.76 / 0.327, 0.48 / 0.104, 3.76 / 0.157	2.91 / 2.21, 3.76 / 0.138, 4.78 / 0.218	6.02 / 0.665, 2.22 / 0.149, 6.02 / 0.318	3.76 / 0.973, 6.02 / 0.233, 1.18 / 0.0745	15 (0.054)	h) equal (0.146 / 0.661) -grey-	1.46	i) candidates
38	Rubisco large subunit	gi 41179049	NA	8.24 / 0.716, 0.62 / 0.135, 2.75 / 0.115	1.46 / 1.11, 3.49 / 0.128, 3.77 / 0.172	3.77 / 0.416, 4.72 / 0.317, 4.38 / 0.231	0.72 / 0.186, 5.07 / 0.196, 1.46 / 0.0921	15 (0.732)	h) equal (0.16 / 0.728) -grey-	1	i) candidates
39	predicted protein	gi 159484358	NA	6.27 / 0.545, 0 / 0, 0.49 / 0.0205	0.35 / 0.265, 3.01 / 0.11, 2.63 / 0.12	3.43 / 0.379, 3.01 / 0.202, 2.29 / 0.121	1.21 / 0.313, 2.63 / 0.102, 1.44 / 0.0909	15 (1.65)	h) equal (0.211 / 0.964) -grey-	0.595	i) candidates
40	predicted protein	gi 159489052	NA	0.51 / 0.0443, 0.09 / 0.0195, 9.78 / 0.41	0 / 0, 6.15 / 0.226, 6.15 / 0.28	0.09 / 0.00994, 3.03 / 0.204, 5.07 / 0.268	0 / 0, 5.07 / 0.196, 2.42 / 0.153	15 (1.71)	h) equal (0.214 / 0.976) -grey-	0.475	i) candidates
41	predicted protein	gi 159469999	Cre03.g197500.t1.2, Cre03.g197500.t2.1	2.74 / 0.238, 0 / 0, 0.3 / 0.0126	0 / 0, 5.33 / 0.196, 3.86 / 0.176	2.27 / 0.251, 0.48 / 0.0323, 3.26 / 0.172	0 / 0, 1.52 / 0.0589, 6.22 / 0.393	15 (1.48)	h) equal (0.203 / 0.932) -grey-	0.401	i) candidates
42	nucleosome assembly protein	gi 159487615	Cre02.g073550.t1.2	1.62 / 0.141, 0 / 0, 1.42 / 0.0595	0.38 / 0.288, 0.49 / 0.018, 0.76 / 0.0346	1.06 / 0.117, 1.06 / 0.0713, 0.9 / 0.0475	1.42 / 0.368, 0.27 / 0.0105, 0.49 / 0.0309	15 (1.32)	h) equal (0.197 / 0.909) -grey-	0.311	i) candidates
43	predicted protein	gi 159483283	Cre02.g111800.t1.2	0.6 / 0.0521, 0.71 / 0.154, 2.35 / 0.0984	0 / 0, 3.68 / 0.135, 3.1 / 0.141	0.14 / 0.0155, 2.58 / 0.173, 1.56 / 0.0824	0.07 / 0.0181, 2.58 / 0.1, 1.24 / 0.0783	15 (1.35)	h) equal (0.199 / 0.915) -grey-	0.275	i) candidates
44	hypothetical protein CHLREDRAFT_106339	gi 159481977	Cre14.g615000.t1.1	0.48 / 0.0417, 0.22 / 0.0478, 2.95 / 0.124	0 / 0, 1.67 / 0.0613, 1.67 / 0.076	0.48 / 0.053, 0.22 / 0.0148, 3.81 / 0.201	0 / 0, 1.19 / 0.0461, 1.19 / 0.0751	15 (0.452)	h) equal (0.162 / 0.74) -grey-	0.194	i) candidates
45	predicted protein	gi 159468782	Cre07.g345500.t1.2	0 / 0, 0 / 0, 2.24 / 0.0938	0 / 0, 2.75 / 0.101, 1.42 / 0.0646	0.16 / 0.0177, 1.8 / 0.121, 1.8 / 0.0951	0 / 0, 1.42 / 0.055, 2.24 / 0.141	15 (0.871)	h) equal (0.172 / 0.792) -grey-	0.181	i) candidates
46	hypothetical protein CHLREDRAFT_188513	gi 159464455	Cre07.g328750.t1.2	0.48 / 0.0417, 0 / 0, 0.48 / 0.0201	0 / 0, 1.2 / 0.044, 1.2 / 0.0546	1.2 / 0.132, 0.48 / 0.0323, 0.48 / 0.0254	1.2 / 0.311, 0.48 / 0.0186, 0 / 0	15 (0.284)	h) equal (0.147 / 0.67) -grey-	0.178	i) candidates
47	membrane protein	gi 159488214	Cre01.g004450.t1.2	0 / 0, 0 / 0, 1.58 / 0.0662	0 / 0, 2.54 / 0.0932, 1.32 / 0.0601	0 / 0, 1.09 / 0.0733, 2.18 / 0.115	0 / 0, 1.32 / 0.0511, 2.93 / 0.185	15 (0.65)	h) equal (0.162 / 0.742) -grey-	0.169	i) candidates
48	predicted protein	gi 159469838	Cre13.g590650.t1.2	2.38 / 0.207, 0 / 0, 0.44 / 0.0184	0 / 0, 1.08 / 0.0396, 1.08 / 0.0492	1.08 / 0.119, 0.63 / 0.0424, 0.63 / 0.0333	0 / 0, 0.44 / 0.017, 0.84 / 0.053	15 (0.128)	h) equal (0.156 / 0.712) -grey-	0.152	i) candidates
49	predicted protein	gi 159468908	NA	0.97 / 0.0843, 0.31 / 0.0673, 0.15 / 0.00628	0 / 0, 2.87 / 0.105, 1.96 / 0.0892	0.97 / 0.107, 0.5 / 0.0336, 0.15 / 0.00792	0 / 0, 1.58 / 0.0612, 0.15 / 0.00947	15 (0.519)	h) equal (0.163 / 0.744) -grey-	0.15	i) candidates
50	hypothetical protein CHLREDRAFT_189410	gi 159468211	Cre04.g221400.t1.2	0.88 / 0.0764, 0 / 0, 0 / 0	0.23 / 0.174, 0 / 0, 0 / 0	1.86 / 0.205, 0 / 0, 0 / 0	0.23 / 0.0595, 0 / 0, 0.23 / 0.0145	15 (1.07)	h) equal (0.19 / 0.878) -grey-	0.139	i) candidates
51	predicted protein	gi 159484859	Cre17.g712300.t1.1	0 / 0, 0.11 / 0.0239, 0.89 / 0.0373	0 / 0, 2.05 / 0.0752, 1.46 / 0.0665	0 / 0, 1.1 / 0.074, 1.22 / 0.0645	0 / 0, 1.46 / 0.0566, 0.37 / 0.0234	15 (0.0269)	h) equal (0.152 / 0.694) -grey-	0.11	i) candidates
52	hypothetical protein CHLREDRAFT_95661	gi 159478443	Cre11.g478800.t1.2	0.27 / 0.0235, 0 / 0, 0.61 / 0.0256	0 / 0, 0.27 / 0.00991, 1.05 / 0.0478	0.82 / 0.0905, 0 / 0, 0.61 / 0.0322	0 / 0, 0.27 / 0.0105, 2.72 / 0.172	15 (0.524)	h) equal (0.162 / 0.742) -grey-	0.108	i) candidates

Molecular Physiology of the *Chlamydomonas pyrenoid*

53	hypothetical protein CHLREDRAFT_144348	gi 159464411	Cre07.g330750.t1.1	0.49 / 0.0426, 0 / 0, 0 / 0	0.31 / 0.235, 0 / 0, 0.07 / 0.00319	0.22 / 0.0243, 0 / 0, 0 / 0	0.4 / 0.104, 0 / 0, 0 / 0	15 (0.0352)	h) equal (0.145 / 0.659) -grey-	0.107	i) candidates
54	predicted protein	gi 159480638	Cre10.g458550.t1.2	0.72 / 0.0625, 0 / 0, 0.72 / 0.0302	1.06 / 0.0389, 0.72 / 0.0328	0.72 / 0.0795, 0.43 / 0.0289, 0.43 / 0.0227	0.43 / 0.0167, 1.06 / 0.0669	15 (1.07)	h) equal (0.187 / 0.863) -grey-	0.0994	i) candidates
55	hypothetical protein CHLREDRAFT_155527	gi 159483827	Cre02.g107150.t1.1	0.255 / 0.0221, 0 / 0, 0.19 / 0.00796	0.19 / 0.144, 0.19 / 0.00697, 0 / 0	0.19 / 0.021, 0.19 / 0.0128, 0.19 / 0.01	0.19 / 0.0492, 0 / 0, 0.42 / 0.0265	15 (0.121)	h) equal (0.148 / 0.675) -grey-	0.0788	i) candidates
56	predicted protein	gi 159467146	Cre17.g702200.t1.2	0.78 / 0.0677, 0 / 0, 0.1 / 0.00419	0 / 0, 0.74 / 0.0272, 0.96 / 0.0437	0.62 / 0.0685, 0.1 / 0.00672, 0.1 / 0.00528	0 / 0, 0 / 0, 1.16 / 0.0732	15 (1.98)	h) equal (0.225 / 0.999) -grey-	0.0778	i) candidates
57	hypothetical protein CHLREDRAFT_113182	gi 159485614	Cre07.g319950.t1.2	0.69 / 0.0599, 0 / 0, 0 / 0	0 / 0, 1.19 / 0.0437, 0.3 / 0.0137	0.69 / 0.0762, 0.3 / 0.0202, 0 / 0	0 / 0, 1.19 / 0.0461, 0.3 / 0.0189	15 (1.51)	h) equal (0.207 / 0.949) -grey-	0.0731	i) candidates
58	hypothetical protein CHLREDRAFT_185073	gi 159479996	Cre06.g278211.t1.1	0.75 / 0.0651, 0 / 0, 1.01 / 0.0423	0 / 0, 0.32 / 0.0117, 0.75 / 0.0341	0.15 / 0.0166, 0 / 0, 1.01 / 0.0534	0 / 0, 0.15 / 0.00581, 0.75 / 0.0473	15 (0.7)	h) equal (0.171 / 0.785) -grey-	0.0725	i) candidates
59	hypothetical protein CHLREDRAFT_144137	gi 159464189	Cre10.g444500.t1.2	0.47 / 0.0408, 0 / 0, 0.77 / 0.0323	0 / 0, 0.77 / 0.0283, 0.77 / 0.0351	0.21 / 0.0232, 0.47 / 0.0316, 0.47 / 0.0248	0 / 0, 0.77 / 0.0298, 0.47 / 0.0297	15 (1.61)	h) equal (0.209 / 0.958) -grey-	0.0723	i) candidates
60	thylakoid luminal protein	gi 159477050	Cre06.g256250.t1.2	0.16 / 0.0139, 0 / 0, 0.58 / 0.0243	0 / 0, 0.58 / 0.0213, 0.83 / 0.0378	0.58 / 0.064, 0 / 0, 0.35 / 0.0185	0 / 0, 0.58 / 0.0225, 0.83 / 0.0524	15 (1.25)	h) equal (0.19 / 0.877) -grey-	0.0668	i) candidates
61	predicted protein	gi 159482900	Cre11.g468750.t1.2	0.29 / 0.0252, 0.0974 / 0.0212, 0.13 / 0.00545	0 / 0, 0.65 / 0.0239, 0.46 / 0.0209	0.29 / 0.032, 0.46 / 0.0309, 0.29 / 0.0153	0.13 / 0.0337, 0.29 / 0.0112, 0.13 / 0.0082	15 (0.0341)	h) equal (0.15 / 0.685) -grey-	0.0598	i) candidates
62	predicted protein	gi 159471217	Cre13.g573250.t1.2	0.43 / 0.0373, 0 / 0, 0.61 / 0.0256	0 / 0, 0.27 / 0.00991, 0.27 / 0.0123	0 / 0, 0.13 / 0.0144, 0.27 / 0.0143	0 / 0, 0.43 / 0.0167, 0.81 / 0.0511	15 (0.315)	h) equal (0.15 / 0.683) -grey-	0.0524	i) candidates
63	hypothetical protein CHLREDRAFT_76641	gi 159483975	Cre02.g098250.t1.2	0.68 / 0.0591, 0 / 0, 0.3 / 0.0126	0 / 0, 0.68 / 0.025, 0.3 / 0.0137	0.09 / 0.00994, 0.19 / 0.0128, 0.54 / 0.0285	0 / 0, 0.19 / 0.00736, 0.42 / 0.0265	15 (1.07)	h) equal (0.183 / 0.846) -grey-	0.0512	i) candidates
64	predicted protein	gi 159462874	Cre01.g038950.t1.2	0.63 / 0.0547, 0 / 0, 0 / 0	0 / 0, 0.38 / 0.0139, 0.63 / 0.0287	0.18 / 0.0199, 0.38 / 0.0256, 0.18 / 0.00951	0 / 0, 0.38 / 0.0147, 0.38 / 0.024	15 (1.72)	h) equal (0.215 / 0.977) -grey-	0.0501	i) candidates
65	predicted protein	gi 159471882	Cre12.g544050.t1.1	0 / 0, 0.17 / 0.0369, 0.37 / 0.0155	0 / 0, 0.86 / 0.0316, 0.37 / 0.0168	0 / 0, 0.37 / 0.0249, 0.59 / 0.0312	0 / 0, 0.59 / 0.0229, 0.17 / 0.0107	15 (1.49)	h) equal (0.204 / 0.939) -grey-	0.05	i) candidates
66	low-CO2-inducible protein B	gi 159480548	Cre10.g452800.t1.2	10.3 / 0.898, 2.26 / 0.491, 14.7 / 0.617	0 / 0, 1.86 / 0.0683, 1.35 / 0.0615	2.72 / 0.3, 7.72 / 0.519, 29.4 / 1.55	0.07 / 0.0181, 1.06 / 0.0411, 3.24 / 0.204	9 (1.74)	i) up in air (0.63 / 0.00721) -magenta-	2.3 (11.1)	i) candidates
67	low-CO2 inducible protein C	gi 159466052	Cre06.g307500.t1.1	9.91 / 0.861, 1.89 / 0.41, 9.91 / 0.415	0 / 0, 0.39 / 0.0143, 0.49 / 0.0223	5.41 / 0.597, 3.31 / 0.223, 10.7 / 0.563	0 / 0, 0.22 / 0.00852, 0.82 / 0.0518	9 (1.2)	i) up in air (0.641 / 0.00122) -magenta-	1.61 (31.7)	i) candidates
68	predicted protein	gi 159468566	NA	7.79 / 0.677, 0 / 0, 2.27 / 0.0951	0 / 0, 3.86 / 0.142, 4.92 / 0.224	2.27 / 0.251, 2.99 / 0.201, 6.21 / 0.328	0 / 0, 4.92 / 0.191, 0 / 0	9 (0.668)	i) up in air (0.248 / 0.0796) -magenta-	0.814 (2.79)	i) candidates
69	hypothetical protein CHLREDRAFT_177330	gi 159481440	Cre11.g467682.t1.1	4.3 / 0.373, 0 / 0, 0.47 / 0.0197	0 / 0, 1.46 / 0.0536, 0.9 / 0.041	2.17 / 0.24, 0.9 / 0.0605, 1.46 / 0.0771	0 / 0, 0.9 / 0.0349, 0.9 / 0.0568	9 (0.733)	i) up in air (0.256 / 0.0837) -magenta-	0.404 (4.14)	i) candidates
70	hypothetical protein CHLREDRAFT_108674	gi 159490330	NA	1.13 / 0.0981, 0 / 0, 3.56 / 0.149	0 / 0, 2.12 / 0.0778, 1.13 / 0.0514	0.46 / 0.0508, 1.13 / 0.076, 1.13 / 0.0597	0 / 0, 0.46 / 0.0178, 0.46 / 0.029	9 (0.396)	i) up in air (0.248 / 0.0543) -magenta-	0.228 (2.46)	i) candidates
71	predicted protein	gi 159471602	Cre12.g544450.t1.2	1.42 / 0.123, 0 / 0, 0.17 / 0.00712	0 / 0, 0 / 0, 0 / 0	1.62 / 0.179, 0.17 / 0.0114, 0 / 0	0 / 0, 0 / 0, 0 / 0	9 (0.995)	i) up in air (0.259 / 0.0765) -magenta-	0.168 (∞)	i) candidates
72	hypothetical protein CHLREDRAFT_184643	gi 159477153	Cre09.g408300.t1.2	0.27 / 0.0235, 0 / 0, 1.03 / 0.0431	0 / 0, 0.27 / 0.00991, 0.27 / 0.0123	0.27 / 0.0298, 0.27 / 0.0182, 1.03 / 0.0544	0 / 0, 0.27 / 0.0105, 0.27 / 0.017	9 (0.694)	i) up in air (0.314 / 0.026) -magenta-	0.0887 (3.4)	i) candidates
73	predicted protein	gi 159473867	Cre09.g389393.t1.1	0.5 / 0.0434, 0 / 0, 0.72 / 0.0302	0 / 0, 0.5 / 0.0183, 0.5 / 0.0228	0.15 / 0.0166, 0.5 / 0.0336, 0.72 / 0.038	0 / 0, 0.5 / 0.0194, 0 / 0	9 (1.49)	i) up in air (0.339 / 0.0317) -magenta-	0.0849 (2.68)	i) candidates
74	hypothetical protein CHLREDRAFT_156884	gi 159467315	Cre03.g186000.t1.2	0.7 / 0.0608, 0 / 0, 1.64 / 0.0687	0 / 0, 4.83 / 0.177, 4.34 / 0.198	0.3 / 0.0331, 1.64 / 0.11, 3.48 / 0.184	0.09 / 0.0233, 2.44 / 0.0945, 0.7 / 0.0442	10 (1.53)	k) up in the diagonal WT 5%CO2/ pyr- air (0.301 / 0.945)	0.368 (2.41)	i) candidates
75	uncharacterized luminal polypeptide	gi 159464044	Cre01.g051500.t1.2	0 / 0, 0 / 0, 1.74 / 0.0729	0 / 0, 1.13 / 0.0415, 1.74 / 0.0792	0.29 / 0.032, 0.66 / 0.0444, 1.74 / 0.0919	0 / 0, 0 / 0, 0 / 0	10 (0.303)	k) up in the diagonal WT 5%CO2/ pyr- air (0.272 / 0.962)	0.152 (3.97)	i) candidates
76	hypothetical protein CHLREDRAFT_108580	gi 159490415	Cre12.g484500.t1.2	1.04 / 0.0903, 0 / 0, 0 / 0	0 / 0, 1.04 / 0.0382, 1.04 / 0.0473	0.43 / 0.0475, 0 / 0, 0 / 0	1.04 / 0.269, 0.43 / 0.0167, 1.04 / 0.0656	14 (1.9)	m) up in pyr- 5% CO2 (0.574 / 0.177) -yellow-	0.369 (4.72)	i) candidates
77	hypothetical protein CHLREDRAFT_184636	gi 159475288	Cre03.g143967.t1.1	0 / 0, 0.49 / 0.106, 0 / 0	0 / 0, 0.82 / 0.0301, 0.22 / 0.01	0 / 0, 0.49 / 0.0329, 0 / 0	0.22 / 0.057, 0.49 / 0.019, 3.06 / 0.193	14 (1.41)	m) up in pyr- 5% CO2 (0.542 / 0.158) -yellow-	0.282 (4.5)	i) candidates
78	predicted protein	gi 159469251	Cre14.g629550.t1.2	0.39 / 0.0339, 0 / 0, 0 / 0	0 / 0, 0.94 / 0.0345, 0.94 / 0.0428	0.39 / 0.0431, 0.65 / 0.0437, 0.65 / 0.0343	0 / 0, 0.39 / 0.0151, 3.46 / 0.218	14 (0.0398)	m) up in pyr- 5% CO2 (0.339 / 0.269) -yellow-	0.245 (3.02)	i) candidates
79	hypothetical protein CHLREDRAFT_194669	gi 159488793	Cre12.g497850.t1.2	0 / 0, 0 / 0, 0 / 0	0 / 0, 0.94 / 0.0345, 0.94 / 0.0428	0.3 / 0.0331, 0.3 / 0.0202, 0.14 / 0.0074	0.49 / 0.127, 0.3 / 0.0116, 0.94 / 0.0593	14 (0.529)	m) up in pyr- 5% CO2 (0.689 / 0.134) -yellow-	0.208 (4.3)	i) candidates
80	hypothetical protein CHLREDRAFT_163761	gi 159475040	Cre03.g144827.t1.1	0.53 / 0.046, 0 / 0, 0 / 0	0 / 0, 0.53 / 0.0194, 0 / 0	0.53 / 0.0585, 0 / 0, 0 / 0	0.53 / 0.137, 0.53 / 0.0205, 0.53 / 0.0335	14 (1.77)	m) up in pyr- 5% CO2 (0.588 / 0.154) -yellow-	0.201 (4.63)	i) candidates
81	predicted protein	gi 159468844	Cre07.g349250.t1.2	0.3 / 0.0261, 0 / 0, 0 / 0	0 / 0, 0 / 0, 0 / 0	0.3 / 0.0331, 0 / 0, 0 / 0	0.3 / 0.0777, 0 / 0, 0.14 / 0.00884	14 (0.414)	m) up in pyr- 5% CO2 (0.374 / 0.231) -yellow-	0.0908 (4.39)	i) candidates
82	predicted protein	gi 159489236	NA	0.12 / 0.0104, 0 / 0, 0 / 0	0 / 0, 0 / 0, 0.12 / 0.00546	0 / 0, 0.12 / 0.00807, 0.12 / 0.00634	0.25 / 0.0647, 0 / 0, 0.12 / 0.00757	14 (1.74)	m) up in pyr- 5% CO2 (0.516 / 0.209) -yellow-	0.0759 (7.16)	i) candidates
83	predicted protein	gi 159469692	Cre12.g534450.t1.1	0.22 / 0.0191, 0 / 0, 0 / 0	0 / 0, 0.8 / 0.0294, 0.48 / 0.0219	0 / 0, 0 / 0, 0 / 0	1.19 / 0.308, 0 / 0, 2.25 / 0.142	8 (1.5)	n) up in pyr- (0.291 / 0.0617) -orange-	0.407 (20.3)	i) candidates
84	hypothetical protein CHLREDRAFT_192969	gi 159479850	Cre06.g278195.t1.1	0.54 / 0.0469, 0 / 0, 0 / 0	0 / 0, 0 / 0, 0 / 0	1.38 / 0.152, 0 / 0, 0 / 0	0.91 / 0.236, 0 / 0, 0.24 / 0.0151	8 (0.157)	n) up in pyr- (0.201 / 0.108) -orange-	0.212 (4.3)	i) candidates
85	hypothetical protein CHLREDRAFT_185062	gi 159479818	Cre06.g278238.t1.1	0 / 0, 0 / 0, 0.58 / 0.0243	0 / 0, 0.58 / 0.0213, 0.58 / 0.0264	0.58 / 0.064, 0.58 / 0.039, 0.58 / 0.0306	0.58 / 0.15, 0.58 / 0.0225, 0.58 / 0.0366	8 (1.03)	n) up in pyr- (0.313 / 0.0342) -orange-	0.18 (7.06)	i) candidates

Chapter 8: Appendices

86	hypothetical protein CHLREDRAFT_115715	gi 159467845	Cre16.g687300.t1.2	0 / 0, 0 / 0, 0 / 0	0 / 0, 0 / 0, 0 / 0	0.58 / 0.064, 0.26 / 0.0175, 0 / 0	0.26 / 0.0673, 0.26 / 0.0101, 0.26 / 0.0164	8 (1.93)	n) up in pyr- (0.456 / 0.0281) -orange-	0.092 (∞)	i) candidates
87	hypothetical protein CHLREDRAFT_169691	gi 159465245	Cre12.g507150.t1.2	0 / 0, 0 / 0, 0.34 / 0.0142	0 / 0, 0 / 0, 0 / 0	0.55 / 0.0607, 0.16 / 0.0108, 0.16 / 0.00845	0.16 / 0.0414, 0 / 0, 0.55 / 0.0347	8 (1.86)	n) up in pyr- (0.44 / 0.028) -orange-	0.0819 (5.48)	i) candidates
88	NaCl-inducible protein	gi 159488909	Cre02.g119550.t1.2	1.76 / 0.153, 0.66 / 0.143, 96 / 4.02	0.308 / 0.233, 20.1 / 0.738, 15.4 / 0.7	1.76 / 0.194, 57.3 / 3.86, 96 / 5.07	0 / 0, 20.1 / 0.779, 6.64 / 0.419	13 (0.915)	o) up in pyr- air (0.557 / 0.131) -red-	9.57 (3.81)	i) candidates
89	predicted protein	gi 159466912	NA	7.22 / 0.627, 1.2 / 0.261, 3.85 / 0.161	1.2 / 0.909, 17.1 / 0.628, 5.32 / 0.242	29.6 / 3.27, 5.32 / 0.358, 12.9 / 0.682	0.3 / 0.0777, 3.85 / 0.149, 1.87 / 0.118	13 (1.45)	o) up in pyr- air (0.576 / 0.18) -red-	4.53 (4.08)	i) candidates
90	hypothetical protein CHLREDRAFT_154979	gi 159465102	NA	3.5 / 0.304, 0 / 0, 1.93 / 0.0808	0.24 / 0.182, 3.5 / 0.128, 2.63 / 0.12	3.5 / 0.386, 1.93 / 0.13, 2.63 / 0.139	0 / 0, 2.63 / 0.102, 1.36 / 0.0858	13 (0.309)	o) up in pyr- air (0.37 / 0.166) -red-	0.688 (1.96)	i) candidates
91	hypothetical protein CHLREDRAFT_184411	gi 159475687	Cre16.g676450.t1.2	0.79 / 0.0686, 0 / 0, 1.84 / 0.0771	0 / 0, 1.84 / 0.0675, 1.84 / 0.0838	0.26 / 0.0287, 1.53 / 0.103, 1.84 / 0.0972	0 / 0, 1.53 / 0.0593, 0.42 / 0.0265	13 (0.0743)	o) up in pyr- air (0.338 / 0.146) -red-	0.24 (1.79)	i) candidates
92	predicted protein	gi 159487947	Cre02.g092451.t1.1	0.74 / 0.0643, 0 / 0, 1 / 0.0419	0 / 0, 1 / 0.0367, 1.64 / 0.0747	1.3 / 0.144, 0.52 / 0.035, 0.52 / 0.0275	0 / 0, 1 / 0.0387, 0.32 / 0.0202	13 (0.395)	o) up in pyr- air (0.373 / 0.21) -red-	0.216 (2.24)	i) candidates
93	hypothetical protein CHLREDRAFT_142655	gi 159485858	Cre07.g313185.t1.1	0.72 / 0.0625, 0 / 0, 0.72 / 0.0302	0 / 0, 1.25 / 0.0459, 1.25 / 0.0569	0.31 / 0.0342, 0.72 / 0.0484, 1.25 / 0.066	0 / 0, 0.72 / 0.0279, 0.31 / 0.0196	13 (0.0341)	o) up in pyr- air (0.355 / 0.0601) -red-	0.156 (1.84)	i) candidates
94	hypothetical protein CHLREDRAFT_192655	gi 159477915	Cre12.g521300.t1.2	0 / 0, 0 / 0, 0 / 0	0 / 0, 0 / 0, 0 / 0	0.63 / 0.0696, 0.28 / 0.0188, 0.28 / 0.0148	0 / 0, 0 / 0, 0.28 / 0.0177	13 (1.6)	o) up in pyr- air (0.9 / 0.103) -red-	0.108 (17.5)	i) candidates
95	thylakoid luminal 17.4 kDa protein	gi 159474024	Cre09.g404000.t1.1	0.37 / 0.0321, 0 / 0, 0.37 / 0.0155	0 / 0, 0.61 / 0.0224, 0.17 / 0.00774	0.37 / 0.0409, 0.17 / 0.0114, 0.88 / 0.0465	0 / 0, 0.17 / 0.00659, 0.37 / 0.0234	13 (1.54)	o) up in pyr- air (0.644 / 0.0917) -red-	0.104 (2.75)	i) candidates
96	predicted protein	gi 159465813	Cre12.g489950.t1.2	0.25 / 0.0217, 0 / 0, 0.4 / 0.0168	0 / 0, 0.25 / 0.00917, 0.12 / 0.0114	0.57 / 0.0629, 0.12 / 0.00807, 0.12 / 0.00634	0 / 0, 0.12 / 0.00465, 0 / 0	13 (0.465)	o) up in pyr- air (0.436 / 0.21) -red-	0.0812 (3.64)	i) candidates
97	predicted protein	gi 159470227	Cre03.g193800.t1.1	0.3 / 0.0261, 0 / 0, 0.3 / 0.0126	0 / 0, 0.3 / 0.011, 0.3 / 0.0137	0.3 / 0.0331, 0.3 / 0.0202, 0.3 / 0.0158	0 / 0, 0 / 0, 0.3 / 0.0189	13 (1.14)	o) up in pyr- air (0.581 / 0.0452) -red-	0.0726 (2.52)	i) candidates
98	hypothetical protein CHLREDRAFT_156470	gi 159464481	Cre07.g327350.t1.2	1.78 / 0.155, 0 / 0, 0 / 0	8.48 / 6.43, 0.23 / 0.00844, 0 / 0	5.3 / 0.585, 0 / 0, 0 / 0	10.6 / 2.75, 0 / 0, 0 / 0	12 (0.226)	a) up in WT 5%CO2 (0.355 / 0.249) -cyan-	6.75 (5.53)	h) regulatory factors
99	predicted protein	gi 159478729	NA	4.03 / 0.35, 0 / 0, 8.61 / 0.361	2.64 / 2, 8.61 / 0.316, 5.95 / 0.271	3.28 / 0.362, 1.64 / 0.11, 4.03 / 0.213	1.64 / 0.425, 4.03 / 0.156, 0.38 / 0.024	12 (1.99)	a) up in WT 5%CO2 (0.575 / 0.189) -cyan-	3.72 (2.88)	h) regulatory factors
100	bi-ubiquitin	gi 159472951	Cre09.g396400.t1.2	0.71 / 0.0617, 0 / 0, 1.93 / 0.0808	1.45 / 1.1, 0.71 / 0.0261, 0.43 / 0.0196	0.71 / 0.0784, 0 / 0, 0 / 0	1.45 / 0.375, 0 / 0, 0 / 0	12 (0.69)	a) up in WT 5%CO2 (0.405 / 0.236) -cyan-	1.2 (5.76)	h) regulatory factors
101	predicted protein	gi 159469197	Cre14.g632767.t1.1	0.19 / 0.0165, 0 / 0, 0 / 0	0.19 / 0.144, 0.19 / 0.00697, 0.19 / 0.00865	0 / 0, 0 / 0, 0 / 0	0 / 0, 0 / 0, 0 / 0	12 (1.94)	a) up in WT 5%CO2 (0.608 / 0.188) -cyan-	0.168 (29)	h) regulatory factors
102	predicted protein	gi 159484701	Cre17.g715500.t1.2	0 / 0, 0 / 0, 0.13 / 0.00545	0.13 / 0.0985, 0.84 / 0.0308, 0 / 0	0.13 / 0.0144, 0 / 0, 0 / 0	0 / 0, 0 / 0, 0.44 / 0.0278	12 (1.85)	a) up in WT 5%CO2 (0.666 / 0.161) -cyan-	0.136 (8.16)	h) regulatory factors
103	2-cys peroxiredoxin	gi 159483223	Cre02.g114600.t1.2	6.45 / 0.56, 16.6 / 3.61, 26.1 / 1.09	0 / 0, 14.2 / 0.523, 19.3 / 0.879	4.59 / 0.507, 7.59 / 0.51, 30.2 / 1.6	0 / 0, 14.2 / 0.552, 30.2 / 1.91	11 (0.926)	c) up in WT air (0.426 / 0.193) -purple-	5.52 (2.44)	h) regulatory factors
104	thioredoxin m	gi 159464168	NA	8.05 / 0.699, 2.33 / 0.506, 2.33 / 0.0976	0.22 / 0.167, 2.33 / 0.0855, 3.06 / 0.139	5.06 / 0.559, 1.23 / 0.0827, 1.72 / 0.0909	0.82 / 0.212, 1.72 / 0.0666, 3.06 / 0.193	11 (1.05)	c) up in WT air (0.524 / 0.141) -purple-	1.37 (2.45)	h) regulatory factors
105	C1, subunit of the circadian RNA-binding protein CHLAMY 1	gi 159476646	Cre06.g250800.t1.1, Cre06.g250800.t2.1	0.13 / 0.0113, 1.67 / 0.363, 2.64 / 0.111	0 / 0, 1.84 / 0.0675, 2.87 / 0.131	0 / 0, 1.22 / 0.082, 1.09 / 0.0576	0 / 0, 0.85 / 0.0329, 2.03 / 0.128	11 (1.06)	c) up in WT air (0.446 / 0.209) -purple-	0.508 (2.91)	h) regulatory factors
106	protein phosphatase 2C	gi 159477373	Cre09.g410600.t1.1	0.08 / 0.00695, 0.5 / 0.109, 0.38 / 0.0159	0 / 0, 0.38 / 0.0139, 0.5 / 0.0228	0.18 / 0.0199, 0.28 / 0.0188, 0.5 / 0.0264	0 / 0, 0.38 / 0.0147, 0.63 / 0.0398	11 (0.265)	c) up in WT air (0.364 / 0.251) -purple-	0.138 (2.52)	h) regulatory factors
107	vasa intronic gene	gi 159473084	Cre09.g393358.t1.1	1.54 / 0.134, 0.18 / 0.0391, 2 / 0.0838	1.14 / 0.864, 3.58 / 0.131, 5.43 / 0.247	4.91 / 0.542, 1.76 / 0.118, 1.33 / 0.0703	2.56 / 0.663, 2.87 / 0.111, 7.29 / 0.46	9 (0.364)	g) up in 5%CO2 (0.258 / 0.0635) -green-	1.3 (2.51)	h) regulatory factors
108	calmodulin	gi 159490918	Cre03.g178150.t1.1	28.4 / 2.47, 0 / 0, 2.27 / 0.0951	16.7 / 12.7, 28.4 / 1.04, 20 / 0.909	113 / 12.4, 5.42 / 0.364, 4.42 / 0.233	134 / 34.6, 20 / 0.774, 14 / 0.88	15 (0.0705)	h) equal (0.145 / 0.657) -grey-	17.4	h) regulatory factors
109	hypothetical protein CHLREDRAFT_51996	gi 159476702	Cre06.g275100.t1.2	0.85 / 0.0738, 2.42 / 0.526, 3.65 / 0.153	0.36 / 0.273, 7.61 / 0.279, 7.61 / 0.346	0.85 / 0.0938, 5.33 / 0.358, 5.33 / 0.282	2.42 / 0.627, 0.85 / 0.0329, 5.33 / 0.336	15 (1.51)	h) equal (0.205 / 0.943) -grey-	0.887	h) regulatory factors
110	predicted protein	gi 159474730	Cre06.g285401.t1.1	2.72 / 0.236, 0.93 / 0.202, 2.72 / 0.114	0.39 / 0.296, 4.16 / 0.153, 6.16 / 0.28	4.16 / 0.459, 0.93 / 0.0625, 4.16 / 0.22	1.68 / 0.435, 4.16 / 0.161, 4.16 / 0.263	15 (0.982)	h) equal (0.178 / 0.819) -grey-	0.756	h) regulatory factors
111	polyadenylate-binding protein RB47	gi 159462882	Cre01.g039300.t1.2	2.05 / 0.178, 1.01 / 0.219, 4.58 / 0.192	0.05 / 0.0379, 13.1 / 0.482, 7.09 / 0.323	2.05 / 0.226, 2.85 / 0.192, 3.42 / 0.181	0.1 / 0.0259, 8.3 / 0.322, 2.85 / 0.18	15 (0.596)	h) equal (0.172 / 0.79) -grey-	0.671	h) regulatory factors
112	protein disulfide isomerase 1	gi 159487489	Cre02.g088200.t1.2	2.53 / 0.22, 0.06 / 0.013, 1.54 / 0.0645	0.55 / 0.417, 2.53 / 0.0928, 3.39 / 0.154	2.94 / 0.325, 1.28 / 0.0861, 1.54 / 0.0814	1.15 / 0.298, 0.47 / 0.0182, 4.78 / 0.302	15 (0.634)	h) equal (0.163 / 0.749) -grey-	0.543	h) regulatory factors
113	regulator of ribonuclease activity	gi 159470809	Cre13.g578150.t1.2	4.38 / 0.38, 0 / 0, 0 / 0	1.32 / 1, 0 / 0, 0 / 0	2.53 / 0.279, 0 / 0, 0 / 0	1.32 / 0.342, 0 / 0, 0 / 0	15 (0.597)	h) equal (0.173 / 0.8) -grey-	0.525	h) regulatory factors
114	nitrogen regulatory protein PII	gi 159491407	Cre07.g357350.t1.2	0.32 / 0.0695, 0.15 / 0.00628	3.08 / 0.113, 1.02 / 0.0464	0.76 / 0.576, 0.76 / 0.0511, 0.52 / 0.0275	0.76 / 0.0294, 1.02 / 0.0644	15 (0.342)	h) equal (0.141 / 0.636) -grey-	0.45	h) regulatory factors
115	ubiquitin-conjugating enzyme E2	gi 159485466	Cre05.g247600.t1.2	0.46 / 0.04, 0.46 / 0.0999, 3.57 / 0.15	0 / 0, 2.78 / 0.102, 4.52 / 0.206	0.46 / 0.0508, 1.14 / 0.0767, 3.57 / 0.189	0.21 / 0.0544, 0.77 / 0.0298, 8.76 / 0.553	15 (0.53)	h) equal (0.172 / 0.791) -grey-	0.407	h) regulatory factors
116	hypothetical protein CHLREDRAFT_119900	gi 159478386	Cre17.g729150.t1.2	0.79 / 0.0686, 0 / 0, 3.31 / 0.139	0 / 0, 4.77 / 0.175, 4.77 / 0.217	0.79 / 0.0872, 4.77 / 0.321, 2.22 / 0.117	0 / 0, 6.73 / 0.261, 0.34 / 0.0215	15 (0.495)	h) equal (0.157 / 0.716) -grey-	0.369	h) regulatory factors
117	RNA binding protein	gi 159491480	Cre04.g231124.t1.1	0.39 / 0.0339, 0.18 / 0.0391, 5.16 / 0.216	0 / 0, 2.18 / 0.08, 3.42 / 0.156	0 / 0, 1.7 / 0.114, 2.75 / 0.145	0 / 0, 1.7 / 0.0659, 0.94 / 0.0593	15 (0.903)	h) equal (0.181 / 0.835) -grey-	0.239	h) regulatory factors
118	peptidyl-prolyl cis-trans isomerase, parvulin-type	gi 159475603	Cre16.g671900.t1.1	0.12 / 0.0104, 0.25 / 0.0543, 2.37 / 0.0993	0.12 / 0.0909, 1.7 / 0.0624, 1.42 / 0.0646	0.94 / 0.104, 1.17 / 0.0787, 1.42 / 0.075	0.56 / 0.145, 0.94 / 0.0364, 0.56 / 0.0353	15 (1.03)	h) equal (0.178 / 0.821) -grey-	0.225	h) regulatory factors

Molecular Physiology of the *Chlamydomonas pyrenoid*

119	high light-induced nuclease	gi 159463980	Cre01.g048150.t1.2	0.7 / 0.0608, 0 / 0, 0.53 / 0.0222	0.38 / 0.288, 0.11 / 0.00404, 0.24 / 0.0109	0.89 / 0.0983, 0.24 / 0.0161, 0.38 / 0.0201	1.11 / 0.287, 0.11 / 0.00426, 0.24 / 0.0151	15 (0.683)	h) equal (0.176 / 0.81) -grey-	0.217	h) regulatory factors
120	hypothetical protein CHLREDRAFT_191517	gi 159475617	Cre16.g672750.t1.2	0.2 / 0.0174, 0.2 / 0.0434, 1.45 / 0.0607	0 / 0, 3.58 / 0.131, 2.5 / 0.114	0 / 0, 1.93 / 0.13, 1.45 / 0.0766	0 / 0, 3.19 / 0.124, 1.05 / 0.0663	15 (1.12)	h) equal (0.185 / 0.852) -grey-	0.2	h) regulatory factors
121	predicted protein	gi 159487321	Cre02.g079400.t1.2	0.79 / 0.0686, 0 / 0, 0.48 / 0.0201	0 / 0, 2.22 / 0.0815, 1.18 / 0.0537	0.79 / 0.0872, 0.48 / 0.0323, 1.18 / 0.0623	0.79 / 0.205, 0.79 / 0.0306, 0.22 / 0.0139	15 (0.686)	h) equal (0.163 / 0.744) -grey-	0.172	h) regulatory factors
122	hypothetical protein CHLREDRAFT_175227	gi 159474988	Cre03.g145967.t1.1, Cre03.g145947.t1.1	0.1 / 0.00869, 0.48 / 0.104, 0.98 / 0.041	0 / 0, 1.19 / 0.0437, 0.98 / 0.0446	0.1 / 0.011, 1.19 / 0.08, 0.98 / 0.0518	0 / 0, 0.98 / 0.038, 0.98 / 0.0619	15 (0.916)	h) equal (0.184 / 0.849) -grey-	0.127	h) regulatory factors
123	RNA binding protein	gi 159479752	Cre16.g662702.t1.1	0.2 / 0.0434, 1.48 / 0.062	1.27 / 0.0466, 1.72 / 0.0783	1.07 / 0.0719, 1.27 / 0.0671	1.72 / 0.0666, 0.31 / 0.0196	15 (1.53)	h) equal (0.204 / 0.938) -grey-	0.12	h) regulatory factors
124	predicted protein	gi 159471740	Cre12.g551900.t1.2	0.76 / 0.066, 0.21 / 0.0456, 0.76 / 0.0318	0 / 0, 1.13 / 0.0415, 1.13 / 0.0514	0.21 / 0.0232, 0.46 / 0.0309, 0.76 / 0.0401	0 / 0, 1.13 / 0.0438, 0.76 / 0.048	15 (0.0631)	h) equal (0.155 / 0.713) -grey-	0.111	h) regulatory factors
125	glutaredoxin, CGFS type	gi 159463028	Cre01.g047800.t1.1	0.36 / 0.0313, 0 / 0, 0.51 / 0.0214	0 / 0, 1.06 / 0.0389, 1.29 / 0.0587	0.11 / 0.0121, 0.86 / 0.0578, 1.06 / 0.056	0 / 0, 0.68 / 0.0263, 1.54 / 0.0972	15 (0.722)	h) equal (0.171 / 0.786) -grey-	0.105	h) regulatory factors
126	predicted protein	gi 159487261	Cre02.g077650.t1.2	0 / 0, 0.18 / 0.0391, 1.31 / 0.0549	0 / 0, 0.4 / 0.0147, 0.95 / 0.0432	0.4 / 0.0442, 0.4 / 0.0269, 0.95 / 0.0502	0.18 / 0.0466, 0 / 0, 0.4 / 0.0252	15 (0.34)	h) equal (0.15 / 0.682) -grey-	0.0905	h) regulatory factors
127	peroxiredoxin	gi 159465035	Cre17.g743897.t1.1	1.47 / 0.128, 0 / 0, 0.16 / 0.0067	0 / 0, 0.83 / 0.0305, 0.83 / 0.0378	0.57 / 0.0629, 0.16 / 0.0108, 0.35 / 0.0185	0 / 0, 0 / 0, 0.16 / 0.0101	15 (0.39)	h) equal (0.145 / 0.655) -grey-	0.08	h) regulatory factors
128	adenylylphosphosulfate reductase	gi 159477975	Cre12.g517150.t1.1	1.42 / 0.123, 0 / 0, 0 / 0	0 / 0, 0.15 / 0.0055, 0.15 / 0.00683	0.61 / 0.0673, 0 / 0, 0.07 / 0.0037	0 / 0, 0.15 / 0.00581, 0.72 / 0.0454	15 (0.817)	h) equal (0.166 / 0.758) -grey-	0.0677	h) regulatory factors
129	hypothetical protein CHLREDRAFT_205607	gi 159481692	Cre16.g688302.t1.1	0.55 / 0.0478, 0 / 0, 0.3 / 0.0126	0 / 0, 1.19 / 0.0437, 0.69 / 0.0314	0.55 / 0.0607, 0.09 / 0.00605, 0.09 / 0.00475	0 / 0, 0.84 / 0.0325, 0.19 / 0.012	15 (1.64)	h) equal (0.208 / 0.955) -grey-	0.066	h) regulatory factors
130	RNA-binding protein C3, CELF family	gi 159490942	Cre03.g177200.t1.2	0.09 / 0.00782, 0.18 / 0.0391, 0.63 / 0.0264	0 / 0, 0.5 / 0.0183, 1.26 / 0.0574	0 / 0, 0.28 / 0.0188, 0.77 / 0.0407	0 / 0, 0.5 / 0.0194, 0.18 / 0.0114	15 (0.698)	h) equal (0.171 / 0.789) -grey-	0.0628	h) regulatory factors
131	hypothetical protein CHLREDRAFT_182801	gi 159490962	Cre03.g176100.t1.2	0 / 0, 0 / 0, 0.99 / 0.0415	0 / 0, 0.41 / 0.015, 1.5 / 0.0683	0.2 / 0.0221, 0.26 / 0.0175, 0.41 / 0.0217	0 / 0, 0.26 / 0.0101, 0.58 / 0.0366	15 (1.28)	h) equal (0.192 / 0.886) -grey-	0.061	h) regulatory factors
132	nucleic acid binding protein	gi 159476838	Cre06.g268600.t1.2	1.57 / 0.136, 0.8 / 0.174, 4.22 / 0.177	0 / 0, 3.12 / 0.114, 2.25 / 0.102	1.28 / 0.141, 3.12 / 0.21, 2.66 / 0.141	0.42 / 0.109, 2.66 / 0.103, 0.6 / 0.0379	9 (1.86)	i) up in air (0.672 / 0.00257) -magenta-	0.513 (2.1)	h) regulatory factors
133	thioredoxin-related protein CITRX	gi 159473707	Cre02.g142800.t1.2	1.58 / 0.137, 0.61 / 0.132, 3.86 / 0.162	0.17 / 0.129, 3.15 / 0.116, 1.2 / 0.0546	1.2 / 0.132, 2.54 / 0.171, 2.02 / 0.107	0.61 / 0.158, 2.02 / 0.0783, 2.02 / 0.127	9 (0.0331)	i) up in air (0.241 / 0.0676) -magenta-	0.441 (1.27)	h) regulatory factors
134	hypothetical protein CHLREDRAFT_138215	gi 159474898	Cre03.g150300.t1.2	2.12 / 0.184, 0 / 0, 1.58 / 0.0662	0 / 0, 0.46 / 0.0169, 0.21 / 0.00956	2.78 / 0.307, 0.46 / 0.0309, 0.77 / 0.0407	0 / 0, 0.77 / 0.0298, 0.21 / 0.0133	9 (1.24)	i) up in air (0.293 / 0.0551) -magenta-	0.33 (9.05)	h) regulatory factors
135	adenosine 5'-phosphosulfate kinase	gi 159475705	Cre16.g677500.t1.2	0.79 / 0.0686, 0 / 0, 0.26 / 0.0109	0 / 0, 0.42 / 0.0154, 0.26 / 0.0118	0.59 / 0.0651, 0.12 / 0.00807, 0.42 / 0.0222	0 / 0, 0.26 / 0.0101, 0.12 / 0.00757	9 (1.13)	i) up in air (0.275 / 0.0701) -magenta-	0.0918 (3.9)	h) regulatory factors
136	hypothetical protein CHLREDRAFT_185446	gi 159483127	Cre17.g736900.t1.2	0.27 / 0.0235, 0.13 / 0.0282, 0.13 / 0.00545	0 / 0, 0.27 / 0.00991, 0.61 / 0.0278	0.43 / 0.0475, 0.27 / 0.0182, 0.13 / 0.00687	0 / 0, 0.27 / 0.0105, 0 / 0	9 (0.265)	i) up in air (0.25 / 0.0568) -magenta-	0.068 (2.69)	h) regulatory factors
137	hypothetical protein CHLREDRAFT_184902	gi 159477555	Cre12.g527450.t1.2	0.32 / 0.0278, 0.15 / 0.0326, 0.15 / 0.00628	0 / 0, 0.32 / 0.0117, 0.32 / 0.0146	0.32 / 0.0353, 0.15 / 0.0101, 0 / 0	0 / 0, 0 / 0, 0.15 / 0.00947	9 (0.798)	i) up in air (0.259 / 0.0505) -magenta-	0.0588 (3.13)	h) regulatory factors
138	predicted protein	gi 159473605	Cre09.g388726.t2.1, Cre09.g388726.t1.1, Cre09.g388726.t3.1	1.27 / 0.11, 0 / 0, 0.8 / 0.0335	0.12 / 0.0909, 4.79 / 0.176, 3.58 / 0.163	1.87 / 0.206, 0.6 / 0.0403, 2.62 / 0.138	1.02 / 0.264, 1.55 / 0.0601, 3.07 / 0.194	11 (1.32)	j) down in WT air (0.228 / 0.0314) -purple-	0.466 (3.09)	h) regulatory factors
139	subunit of the ESCRT-III complex	gi 159470807	Cre13.g577950.t1.2	0 / 0, 0 / 0, 0.39 / 0.0163	0 / 0, 1.26 / 0.0462, 2.14 / 0.0974	0.92 / 0.102, 0.63 / 0.0424, 0.63 / 0.0333	0 / 0, 0.39 / 0.0151, 2.7 / 0.17	11 (0.438)	j) down in WT air (0.166 / 0.0145) -purple-	0.177 (10.3)	h) regulatory factors
140	protein disulfide isomerase	gi 159482588	Cre16.g692751.t1.1	0 / 0, 0 / 0, 0.48 / 0.0201	0 / 0, 1.69 / 0.062, 1.69 / 0.0769	0.22 / 0.0243, 0.81 / 0.0545, 1.2 / 0.0634	0.22 / 0.057, 1.2 / 0.0465, 0.22 / 0.0139	11 (1.74)	j) down in WT air (0.289 / 0.00408) -purple-	0.139 (6.61)	h) regulatory factors
141	thioredoxin x	gi 159463112	Cre01.g052250.t1.2	0.47 / 0.0408, 0 / 0, 1.15 / 0.0482	0.21 / 0.159, 1.15 / 0.0422, 0.47 / 0.0214	0.77 / 0.085, 0.47 / 0.0316, 0.77 / 0.0407	0.21 / 0.0544, 0.77 / 0.0298, 0.21 / 0.0133	10 (0.152)	k) up in the diagonal WT 5%CO2/ pyr- air (0.195 / 0.89)	0.199 (2.04)	h) regulatory factors
142	coiled-coil domain 6-like protein	gi 159474686	Cre06.g282900.t1.2	0.09 / 0.00782, 0 / 0, 1.13 / 0.0473	0 / 0, 1.32 / 0.0484, 1.52 / 0.0692	0.4 / 0.0442, 0.8 / 0.0538, 0.96 / 0.0507	0 / 0, 0.52 / 0.0201, 0.29 / 0.0183	10 (1.54)	k) up in the diagonal WT 5%CO2/ pyr- air (0.396 / 0.981)	0.14 (2.85)	h) regulatory factors
143	serine hydroxymethyltransferase	gi 159486853	Cre16.g664550.t1.2	0.32 / 0.0278, 0 / 0, 0.48 / 0.0201	0 / 0, 1.31 / 0.0481, 2.06 / 0.0938	0.06 / 0.00662, 0.56 / 0.0377, 0.95 / 0.0502	0 / 0, 0 / 0, 0.56 / 0.0353	10 (0.412)	k) up in the diagonal WT 5%CO2/ pyr- air (0.229 / 0.93)	0.124 (2.84)	h) regulatory factors
144	tetratricopeptide repeat protein, circadian expression	gi 159483833	Cre02.g106850.t1.2	0 / 0, 0 / 0, 1.12 / 0.0469	0 / 0, 0.93 / 0.0341, 1.56 / 0.071	0 / 0, 0.6 / 0.0403, 0.93 / 0.0491	0 / 0, 0.21 / 0.00814, 0.21 / 0.0133	10 (0.556)	k) up in the diagonal WT 5%CO2/ pyr- air (0.235 / 0.92)	0.102 (2.85)	h) regulatory factors
145	COP signalosome subunit 5	gi 159473382	Cre09.g399178.t1.1	0.3 / 0.0261, 0 / 0, 0.3 / 0.0126	0 / 0, 1.21 / 0.0444, 1.21 / 0.0551	0 / 0, 0.42 / 0.0282, 1.02 / 0.0539	0 / 0, 0.55 / 0.0213, 0.3 / 0.0189	10 (0.486)	k) up in the diagonal WT 5%CO2/ pyr- air (0.232 / 0.913)	0.0953 (2.3)	h) regulatory factors
146	2-cys peroxiredoxin, chloroplastic	gi 159477024	Cre06.g257601.t1.2	8.85 / 0.769, 0.13 / 0.0282, 5.09 / 0.213	1.62 / 1.23, 11.5 / 0.423, 11.5 / 0.525	11.5 / 1.27, 3.78 / 0.254, 5.87 / 0.31	3.24 / 0.839, 6.74 / 0.261, 40.8 / 2.57	14 (0.42)	m) up in pyr- 5% CO2 (0.372 / 0.22) -yellow-	3.86 (2.19)	h) regulatory factors
147	14-3-3 protein	gi 159477028	Cre06.g257500.t1.2	5.73 / 0.498, 0 / 0, 0.4 / 0.0168	0.25 / 0.189, 10.8 / 0.396, 10.8 / 0.491	9.53 / 1.05, 1.45 / 0.0975, 1.45 / 0.0766	3.29 / 0.852, 2.84 / 0.11, 27.9 / 1.76	14 (1.52)	m) up in pyr- 5% CO2 (0.489 / 0.169) -yellow-	2.86 (2.9)	h) regulatory factors
148	chloroplast-targeted RNA-binding protein	gi 159490399	Cre12.g483700.t2.1, Cre12.g483700.t1.2	1.38 / 0.12, 0.16 / 0.0347, 3.56 / 0.149	0.66 / 0.5, 2.67 / 0.098, 3.24 / 0.147	1.96 / 0.216, 3.9 / 0.262, 3.24 / 0.171	7.74 / 2, 1.96 / 0.0759, 1.56 / 0.0985	14 (0.683)	m) up in pyr- 5% CO2 (0.406 / 0.245) -yellow-	2.29 (3.85)	h) regulatory factors
149	transcription factor	gi 159482727	Cre03.g213537.t1.1	0.71 / 0.0617, 0.2 / 0.0434, 0.2 / 0.00838	0 / 0, 4.03 / 0.148, 4.03 / 0.183	0.71 / 0.0784, 1.45 / 0.0975, 1.45 / 0.0766	0 / 0, 1.93 / 0.0748, 29.2 / 1.84	14 (1.35)	m) up in pyr- 5% CO2 (0.477 / 0.225) -yellow-	2.01 (8.26)	h) regulatory factors
150	14-3-3 protein	gi 159489655	Cre12.g559250.t1.2	2.59 / 0.225, 0 / 0, 0.7 / 0.0293	0.24 / 0.182, 1.11 / 0.0407, 1.34 / 0.061	2.59 / 0.286, 0.7 / 0.0471, 1.11 / 0.0586	1.34 / 0.347, 0.38 / 0.0147, 7.4 / 0.467	14 (1.62)	m) up in pyr- 5% CO2 (0.499 / 0.164) -yellow-	0.87 (2.67)	h) regulatory factors
151	ARF-like GTPase	gi 159468163	Cre04.g218250.t1.2	0.83 / 0.0721, 0 / 0, 0.83 / 0.0348	0 / 0, 1.47 / 0.0539, 1.13 / 0.0514	0.16 / 0.0177, 0.35 / 0.0235, 0.83 / 0.0438	0 / 0, 0.57 / 0.0221, 5.11 / 0.323	14 (0.344)	m) up in pyr- 5% CO2 (0.375 / 0.257) -yellow-	0.362 (3.48)	h) regulatory factors

Chapter 8: Appendices

152	predicted protein	gi 159473098	Cre09.g394065.t2.1, Cre09.g394065.t1.1	0.43 / 0.0373, 0 / 0, 1.04 / 0.0436	0 / 0, 1.92 / 0.0705, 1.44 / 0.0656	0 / 0, 0 / 0, 0 / 0	0.2 / 0.0518, 1.44 / 0.0558, 1.44 / 0.0909	2 (0.302)	m) up in pyr- 5% CO2 (0.495 / 0.0235) -yellow-	0.208 (2.74)	h) regulatory factors
153	predicted protein	gi 159489570	Cre10.g421200.t1.1	0.11 / 0.00955, 0 / 0, 0.54 / 0.0226	0 / 0, 0.54 / 0.0198, 0.71 / 0.0323	0.24 / 0.0265, 0.24 / 0.0161, 0.24 / 0.0127	0.11 / 0.0285, 1.12 / 0.0434, 0.38 / 0.024	14 (0.924)	m) up in pyr- 5% CO2 (0.611 / 0.0404) -yellow-	0.101 (2.06)	h) regulatory factors
154	predicted protein	gi 159489803	Cre07.g325734.t1.1	2.2 / 0.191, 0 / 0, 1.63 / 0.0683	0 / 0, 14 / 0.516, 3.71 / 0.169	9.21 / 1.02, 4.71 / 0.317, 21.2 / 1.12	0 / 0, 7.42 / 0.287, 14 / 0.887	13 (0.724)	o) up in pyr- air (0.716 / 0.0663) -red-	2.57 (3.47)	h) regulatory factors
155	vesicle inducing protein in plastids 1	gi 159471371	Cre13.g583550.t1.2	3.47 / 0.301, 0.11 / 0.0239, 1.71 / 0.0716	0.11 / 0.0834, 2.32 / 0.0851, 1.71 / 0.0778	2 / 0.221, 2.66 / 0.179, 5.67 / 0.3	0.11 / 0.0285, 1.22 / 0.0473, 5.04 / 0.318	13 (1.02)	o) up in pyr- air (0.433 / 0.0285) -red-	0.734 (2.02)	h) regulatory factors
156	hypothetical protein CHLREDRAFT_99772	gi 159464421	Cre07.g330300.t1.2	0.61 / 0.053, 0 / 0, 2.04 / 0.0854	0 / 0, 0.61 / 0.0224, 0.37 / 0.0168	0.37 / 0.0409, 1.6 / 0.108, 2.04 / 0.108	0 / 0, 0.89 / 0.0345, 0 / 0	5 (1.1)	o) up in pyr- air (0.722 / 0.0448) -red-	0.269 (3.62)	h) regulatory factors
157	glutaredoxin, CPYC type	gi 159490044	Cre12.g513750.t1.1	0.56 / 0.0486, 0 / 0, 0.25 / 0.0105	0 / 0, 0.56 / 0.0206, 0 / 0	1.43 / 0.158, 0 / 0, 0.56 / 0.0296	0 / 0, 0.25 / 0.00969, 0 / 0	13 (1.6)	o) up in pyr- air (0.524 / 0.196) -red-	0.197 (6.29)	h) regulatory factors
158	nucleoredoxin 2	gi 159487969	Cre02.g093750.t1.2	0 / 0, 0 / 0, 0 / 0	0 / 0, 0 / 0, 0.21 / 0.00956	0 / 0, 0.55 / 0.037, 1.25 / 0.066	0 / 0, 0 / 0, 0.28 / 0.0177	13 (1.8)	o) up in pyr- air (0.839 / 0.121) -red-	0.108 (11.3)	h) regulatory factors
159	poly(A) binding protein	gi 159476716	Cre06.g274500.t1.2	0 / 0, 0 / 0, 0.86 / 0.036	0 / 0, 0.51 / 0.0187, 0.23 / 0.0105	0 / 0, 0.86 / 0.0578, 0.51 / 0.0269	0 / 0, 0.51 / 0.0198, 0.23 / 0.0145	13 (0.455)	o) up in pyr- air (0.386 / 0.206) -red-	0.089 (2.56)	h) regulatory factors
160	thioredoxin-like protein	gi 159480598	Cre10.g456250.t1.2	0.14 / 0.0122, 0 / 0, 0.3 / 0.0126	0 / 0, 0.14 / 0.00514, 0 / 0	0.3 / 0.0331, 0.14 / 0.00941, 0.3 / 0.0158	0 / 0, 0.14 / 0.00542, 0.14 / 0.00884	13 (0.792)	o) up in pyr- air (0.82 / 0.0848) -red-	0.0613 (3.97)	h) regulatory factors
161	plastocyanin, chloroplast precursor	gi 159489946	Cre03.g182551.t1.2	1.8 / 0.156, 0 / 0, 1.28 / 0.0536	3.23 / 2.45, 3.23 / 0.119, 2.44 / 0.111	3.23 / 0.357, 2.44 / 0.164, 1.8 / 0.0951	3.23 / 0.836, 1.8 / 0.0697, 2.44 / 0.154	12 (0.704)	a) up in WT 5%CO2 (0.404 / 0.236) -cyan-	2.81 (4.26)	g) photos. electron transport chain
162	apoferreredoxin	gi 159469305	Cre14.g626700.t1.2	0.95 / 0.0825, 0.95 / 0.206, 0.95 / 0.0398	1.44 / 1.09, 2.05 / 0.0752, 2.05 / 0.0933	0.95 / 0.105, 0.95 / 0.0639, 2.05 / 0.108	1.44 / 0.373, 1.44 / 0.0558, 2.82 / 0.178	12 (0.576)	a) up in WT 5%CO2 (0.391 / 0.243) -cyan-	1.32 (3.12)	g) photos. electron transport chain
163	subunit H of photosystem I	gi 159464799	Cre07.g330250.t1.2	0.54 / 0.0469, 0 / 0, 0.24 / 0.0101	0.91 / 0.69, 0.24 / 0.00881, 0.54 / 0.0246	0.54 / 0.0596, 0.24 / 0.0161, 0 / 0	0.91 / 0.236, 0 / 0, 0.54 / 0.0341	12 (0.678)	a) up in WT 5%CO2 (0.401 / 0.237) -cyan-	0.759 (5.39)	g) photos. electron transport chain
164	photosystem I subunit VII	gi 41179066	NA	5.72 / 0.497, 0 / 0, 0.89 / 0.0373	0 / 0, 0 / 0, 1.59 / 0.0724	0.37 / 0.0409, 0.89 / 0.0598, 1.59 / 0.084	0 / 0, 0 / 0, 0 / 0	11 (1.08)	c) up in WT air (0.453 / 0.224) -purple-	0.56 (6.23)	g) photos. electron transport chain
165	photosystem I reaction center subunit II, 20 kDa	gi 159479282	Cre05.g238332.t1.1	1.39 / 0.121, 0.16 / 0.0347, 0.34 / 0.0142	0 / 0, 0.16 / 0.00587, 0.34 / 0.0155	0.34 / 0.0375, 0.16 / 0.0108, 0.34 / 0.018	0 / 0, 0.16 / 0.0062, 0.34 / 0.0215	11 (1.37)	c) up in WT air (0.663 / 0.156) -purple-	0.178 (4.72)	g) photos. electron transport chain
166	chloroplast ATP synthase delta chain	gi 159486703	Cre11.g467569.t1.1	1.17 / 0.102, 0 / 0, 0.68 / 0.0285	0 / 0, 0.47 / 0.0172, 0.47 / 0.0214	0 / 0, 0 / 0, 0.14 / 0.0074	0 / 0, 0.3 / 0.0116, 0.14 / 0.00884	11 (1.73)	c) up in WT air (0.609 / 0.178) -purple-	0.137 (5.87)	g) photos. electron transport chain
167	photosystem I reaction center subunit N	gi 159487379	NA	0.51 / 0.0443, 0.23 / 0.05, 0.23 / 0.00963	0 / 0, 0 / 0, 0.23 / 0.0105	0.23 / 0.0254, 0 / 0, 0.51 / 0.0269	0 / 0, 0 / 0, 0 / 0	5 (1.1)	c) up in WT air (0.716 / 0.075) -purple-	0.109 (4.96)	g) photos. electron transport chain
168	oxygen-evolving enhancer protein 2 of photosystem II	gi 159471964	Cre12.g550850.t1.2	11.5 / 1, 0 / 0, 0.69 / 0.0289	2.54 / 1.93, 2.93 / 0.108, 2.93 / 0.133	11.5 / 1.27, 0.52 / 0.035, 2.18 / 0.115	2.18 / 0.564, 2.18 / 0.0845, 2.54 / 0.16	15 (1.15)	h) equal (0.187 / 0.864) -grey-	1.42 (2.46)	g) photos. electron transport chain
169	oxygen-evolving enhancer protein 1 of photosystem II	gi 159473144	Cre09.g396213.t1.1	4.73 / 0.411, 0 / 0, 0.67 / 0.0281	0 / 0, 3.67 / 0.135, 1.52 / 0.0692	6.03 / 0.666, 0.85 / 0.0572, 1.79 / 0.0946	0.11 / 0.0285, 2.8 / 0.108, 2.43 / 0.153	15 (0.0556)	h) equal (0.145 / 0.661) -grey-	0.459 (2.46)	g) photos. electron transport chain
170	photosystem I 8.1 kDa reaction center subunit IV	gi 159489252	Cre10.g420350.t1.2	1.3 / 0.113, 0 / 0, 0.74 / 0.031	0.74 / 0.561, 0.32 / 0.0117, 1.3 / 0.0592	2.04 / 0.225, 0 / 0, 0.74 / 0.0391	1.3 / 0.337, 0.74 / 0.0287, 0.74 / 0.0467	15 (0.687)	h) equal (0.163 / 0.744) -grey-	0.381 (2.46)	g) photos. electron transport chain
171	photosystem II subunit 28	gi 159464615	Cre10.g440450.t1.2	1.16 / 0.101, 0.47 / 0.102, 0.78 / 0.0327	0.21 / 0.159, 1.16 / 0.0426, 1.16 / 0.0528	1.62 / 0.179, 0.78 / 0.0524, 0.47 / 0.0248	0.47 / 0.122, 1.16 / 0.0449, 1.16 / 0.0732	15 (1.96)	h) equal (0.224 / 0.998) -grey-	0.259 (2.46)	g) photos. electron transport chain
172	ferredoxin-nadp reductase	gi 159478523	Cre11.g476750.t1.2	1.9 / 0.165, 0 / 0, 0 / 0	0.28 / 0.212, 0.28 / 0.0103, 0.28 / 0.0127	2.15 / 0.237, 0.28 / 0.0188, 0.39 / 0.0206	0.51 / 0.132, 0 / 0, 0.39 / 0.0246	15 (1.59)	h) equal (0.209 / 0.956) -grey-	0.219 (2.46)	g) photos. electron transport chain
173	apoferreredoxin	gi 159484116	Cre07.g334800.t1.2, Cre07.g334800.t2.1	0.53 / 0.046, 0 / 0, 0.53 / 0.0222	0 / 0, 1.88 / 0.069, 1.88 / 0.0856	0 / 0, 0.89 / 0.0598, 1.33 / 0.0703	0 / 0, 1.88 / 0.0728, 1.88 / 0.119	15 (0.543)	h) equal (0.156 / 0.711) -grey-	0.143 (2.46)	g) photos. electron transport chain
174	OEE2-like protein of thylakoid lumen	gi 159465647	Cre12.g509050.t1.1	1.53 / 0.133, 0 / 0, 0.14 / 0.00586	0 / 0, 0.3 / 0.011, 0.49 / 0.0223	1.53 / 0.169, 0 / 0, 0.3 / 0.0158	0.49 / 0.127, 0.14 / 0.00542, 0.14 / 0.00884	15 (0.912)	h) equal (0.181 / 0.834) -grey-	0.131 (2.46)	g) photos. electron transport chain
175	predicted protein	gi 159471011	Cre13.g562150.t1.2	0.33 / 0.0287, 0 / 0, 1.19 / 0.0498	0 / 0, 0.77 / 0.0283, 0.9 / 0.041	0.15 / 0.0166, 0.65 / 0.0437, 1.52 / 0.0803	0 / 0, 0.53 / 0.0205, 1.52 / 0.0959	15 (0.791)	h) equal (0.176 / 0.812) -grey-	0.106 (2.46)	g) photos. electron transport chain
176	hypothetical protein CHLREDRAFT_187371	gi 159485408	Cre05.g243800.t1.2	0.63 / 0.0547, 0 / 0, 1.65 / 0.0691	0 / 0, 0.63 / 0.0231, 1.25 / 0.0569	0 / 0, 0.63 / 0.0424, 1.25 / 0.066	0 / 0, 0.38 / 0.0147, 0.63 / 0.0398	15 (0.789)	h) equal (0.173 / 0.795) -grey-	0.0962 (2.46)	g) photos. electron transport chain
177	photosystem I reaction center subunit III	gi 159477399	Cre09.g412100.t1.2	0.91 / 0.079, 0 / 0, 0.68 / 0.0285	0.14 / 0.106, 0 / 0, 0 / 0	0.47 / 0.0519, 0 / 0, 0.47 / 0.0248	0.14 / 0.0362, 0 / 0, 0 / 0	15 (1.19)	h) equal (0.189 / 0.873) -grey-	0.0857 (2.46)	g) photos. electron transport chain
178	ATP synthase CF1 beta subunit	gi 41179057	NA	6.24 / 0.542, 0 / 0, 1.94 / 0.0813	0 / 0, 3.22 / 0.118, 3.22 / 0.147	5.42 / 0.598, 2.13 / 0.143, 3.22 / 0.17	0.13 / 0.0337, 1.32 / 0.0511, 4.36 / 0.275	9 (0.0787)	i) up in air (0.193 / 0.107) -magenta-	0.805 (2.46)	g) photos. electron transport chain
179	chloroplast ATP synthase gamma chain	gi 159476472	Cre06.g259900.t1.2	0.5 / 0.0434, 0.08 / 0.0174, 0.5 / 0.0209	0 / 0, 0.5 / 0.0183, 0.77 / 0.0351	0.63 / 0.0696, 0.18 / 0.0121, 0.77 / 0.0407	0 / 0, 0.28 / 0.0108, 0.38 / 0.024	9 (0.145)	i) up in air (0.231 / 0.05) -magenta-	0.107 (2.31)	g) photos. electron transport chain
180	predicted protein	gi 159484630	Cre01.g000400.t1.2, Cre01.g000350.t1.1	0.78 / 0.0677, 0 / 0, 0.1 / 0.00419	0 / 0, 0.47 / 0.0172, 0.33 / 0.015	0.1 / 0.011, 0.33 / 0.0222, 0.47 / 0.0248	0 / 0, 0.62 / 0.024, 5.23 / 0.33	14 (1.3)	m) up in pyr- 5% CO2 (0.471 / 0.223) -yellow-	0.372 (6.55)	g) photos. electron transport chain
181	oxygen evolving enhancer protein 3	gi 159486609	Cre08.g372450.t1.2	3.2 / 0.278, 0.15 / 0.0326, 1.73 / 0.0725	0 / 0, 1.05 / 0.0385, 1.36 / 0.0619	4.59 / 0.507, 2.63 / 0.177, 1.73 / 0.0914	0 / 0, 1.73 / 0.067, 1.36 / 0.0858	13 (0.788)	o) up in pyr- air (0.601 / 0.137) -red-	0.813 (3.65)	g) photos. electron transport chain
182	ATP synthase CF1 alpha subunit	gi 41179050	NA	1.26 / 0.109, 0.06 / 0.013, 1.01 / 0.0423	0.06 / 0.0455, 1.01 / 0.0371, 0.59 / 0.0269	1.54 / 0.17, 0.79 / 0.0531, 1.13 / 0.0597	0.12 / 0.0311, 0.34 / 0.0132, 1.01 / 0.0637	13 (1.18)	o) up in pyr- air (0.518 / 0.152) -red-	0.297 (2.22)	g) photos. electron transport chain
183	ATP synthase CF1 epsilon subunit	gi 41179023	NA	0.49 / 0.0426, 0 / 0, 1.23 / 0.0515	0 / 0, 0.82 / 0.0301, 0.49 / 0.0223	0.82 / 0.0905, 0.22 / 0.0148, 1.72 / 0.0909	0 / 0, 0.49 / 0.019, 0.49 / 0.0309	13 (1.25)	o) up in pyr- air (0.699 / 0.111) -red-	0.206 (3)	g) photos. electron transport chain
184	photosystem II stability/assembly factor HCF136	gi 159476190	Cre06.g273700.t1.2	0.97 / 0.0843, 0 / 0, 0.34 / 0.0142	0 / 0, 0.97 / 0.0356, 0.79 / 0.036	0.97 / 0.107, 0.34 / 0.0229, 0.97 / 0.0512	0.21 / 0.0544, 0.21 / 0.00814, 0.62 / 0.0391	13 (0.265)	o) up in pyr- air (0.364 / 0.174) -red-	0.19 (2)	g) photos. electron transport chain

Molecular Physiology of the *Chlamydomonas pyrenoid*

185	glyceraldehyde 3-phosphate dehydrogenase,	gi 159490469	Cre12.g485150.t1.2	11.7 / 1.02, 0 / 0, 0 / 0	0 / 0, 0.49 / 0.018, 0.27 / 0.0123	2.04 / 0.225, 0 / 0, 0 / 0	0 / 0, 0.61 / 0.0236, 0.17 / 0.0107	11 (1.05)	c) up in WT air (0.443 / 0.231) -purple-	1.07 (10.6)	f) calvin cycle enzymes
186	CP12 (small protein associating with GAPDH and PRK)	gi 159472412	Cre08.g380250.t1.2	1.17 / 0.102, 0.3 / 0.0652, 36.4 / 1.52	6.92 / 5.24, 16.2 / 0.594, 36.4 / 1.66	2.64 / 0.291, 5.11 / 0.344, 27.8 / 1.47	16.2 / 4.19, 21.3 / 0.824, 27.8 / 1.76	9 (1.95)	g) up in 5%CO2 (0.371 / 0.0381) -green-	7.49 (3.76)	f) calvin cycle enzymes
187	phosphoglycerate kinase	gi 159482940	Cre11.g467770.t1.1	2.43 / 0.211, 0.21 / 0.0456, 4.07 / 0.17	0.68 / 0.515, 10.8 / 0.396, 16.4 / 0.746	9.35 / 1.03, 3.75 / 0.252, 9.35 / 0.494	0.58 / 0.15, 3.45 / 0.134, 39.4 / 2.49	15 (0.259)	h) equal (0.14 / 0.63) -grey-	1.74	f) calvin cycle enzymes
188	phosphoribulokinase	gi 159471788	Cre12.g554800.t1.2	3.88 / 0.337, 0 / 0, 6.11 / 0.256	0.08 / 0.0606, 2.61 / 0.0958, 7.91 / 0.36	2.89 / 0.319, 2.1 / 0.141, 7.27 / 0.384	0.16 / 0.0414, 0.97 / 0.0376, 5.59 / 0.353	15 (0.576)	h) equal (0.165 / 0.759) -grey-	0.626	f) calvin cycle enzymes
189	transketolase	gi 159487741	Cre02.g080200.t1.2	1.27 / 0.11, 0.18 / 0.0391, 1.09 / 0.0457	0 / 0, 2.42 / 0.0888, 4.6 / 0.209	1.01 / 0.112, 0.64 / 0.043, 5.87 / 0.31	0 / 0, 0.93 / 0.036, 10.7 / 0.676	15 (0.784)	h) equal (0.167 / 0.767) -grey-	0.438	f) calvin cycle enzymes
190	fructose-1, 6-bisphosphatase	gi 159465323	Cre12.g510650.t1.2	1.7 / 0.148, 0.15 / 0.0326, 4.48 / 0.188	0 / 0, 4.1 / 0.15, 3.43 / 0.156	0.89 / 0.0983, 1.9 / 0.128, 4.48 / 0.237	0.07 / 0.0181, 5.31 / 0.206, 4.48 / 0.283	15 (0.925)	h) equal (0.181 / 0.834) -grey-	0.431	f) calvin cycle enzymes
191	sedoheptulose-1, 7-bisphosphatase	gi 159467635	Cre03.g185550.t1.2	3.84 / 0.334, 0 / 0, 1.12 / 0.0469	0 / 0, 1.86 / 0.0683, 1.86 / 0.0847	4.21 / 0.465, 0.96 / 0.0646, 1.28 / 0.0676	0 / 0, 1.28 / 0.0496, 2.58 / 0.163	15 (0.239)	h) equal (0.145 / 0.657) -grey-	0.352	f) calvin cycle enzymes
192	ribose-5-phosphate isomerase	gi 159467673	Cre03.g187450.t1.2	0.38 / 0.033, 0 / 0, 0 / 0	0 / 0, 0.11 / 0.00404, 0.11 / 0.00501	0.11 / 0.0121, 0 / 0, 0 / 0	0 / 0, 0 / 0, 0.11 / 0.00694	15 (0.225)	h) equal (0.159 / 0.73) -grey-	0.016	f) calvin cycle enzymes
193	triose phosphate isomerase	gi 159463610	Cre01.g029300.t1.2	0.11 / 0.00955, 0 / 0, 0 / 0	0 / 0, 0.11 / 0.00404, 0 / 0	0.11 / 0.0121, 0 / 0, 0.11 / 0.00581	0 / 0, 0 / 0, 0.23 / 0.0145	15 (0.841)	h) equal (0.173 / 0.795) -grey-	0.0121	f) calvin cycle enzymes
194	glyceraldehyde-3-phosphate dehydrogenase	gi 159463282	Cre01.g010900.t1.2	9.53 / 0.828, 0.37 / 0.0804, 4.62 / 0.194	0 / 0, 5.08 / 0.186, 5.57 / 0.254	5.57 / 0.615, 4.62 / 0.311, 8.73 / 0.461	0.17 / 0.044, 5.57 / 0.216, 4.2 / 0.265	9 (1.63)	i) up in air (0.334 / 0.0393) -magenta-	1.31 (2.58)	f) calvin cycle enzymes
195	fructose-1, 6-bisphosphate aldolase	gi 159485250	Cre05.g234550.t1.2, Cre05.g234550.t2.1	6.41 / 0.557, 1.16 / 0.252, 5.86 / 0.245	0.36 / 0.273, 11.7 / 0.429, 17.7 / 0.804	7.64 / 0.844, 10.8 / 0.724, 11.7 / 0.618	0.47 / 0.122, 3 / 0.116, 16.3 / 1.03	13 (0.693)	o) up in pyr- air (0.399 / 0.0175) -red-	2.29 (1.71)	f) calvin cycle enzymes
196	ribulose phosphate-3-epimerase, chloroplast precursor	gi 159465721	Cre12.g511900.t1.2	0.12 / 0.0104, 0 / 0, 0 / 0	0 / 0, 0 / 0, 0 / 0	0.12 / 0.0132, 0 / 0, 0.12 / 0.00634	0 / 0, 0 / 0, 0.12 / 0.00757	13 (0.23)	o) up in pyr- air (0.354 / 0.18) -red-	0.0206 (3.27)	f) calvin cycle enzymes
197	peptidyl-prolyl cis-trans isomerase, FKBP-type	gi 159480568	Cre10.g454250.t1.2	0.78 / 0.0677, 0 / 0, 0 / 0	0.1 / 0.0758, 0.62 / 0.0228, 0.47 / 0.0214	0.33 / 0.0364, 0.1 / 0.00672, 0.1 / 0.00528	0 / 0, 0.33 / 0.0128, 0.21 / 0.0133	12 (0.376)	a) up in WT 5%CO2 (0.368 / 0.154) -cyan-	0.126 (2.53)	e) protein folding
198	chloroplast DnaJ-like protein	gi 159465259	Cre12.g507650.t1.2, Cre12.g507650.t2.1	0.07 / 0.00608, 0 / 0, 0.32 / 0.0134	0 / 0, 1.16 / 0.0426, 0.52 / 0.0237	0 / 0, 0.32 / 0.0215, 0.07 / 0.0037	0 / 0, 0.88 / 0.0341, 0 / 0	12 (0.112)	a) up in WT 5%CO2 (0.35 / 0.197) -cyan-	0.0695 (2.52)	e) protein folding
199	peptidyl-prolyl cis-trans isomerase, FKBP-type	gi 159469686	Cre12.g534700.t1.2	0.97 / 0.0843, 0 / 0, 0.57 / 0.0239	0.12 / 0.0909, 0.57 / 0.0209, 0.25 / 0.0114	0.76 / 0.0839, 0.41 / 0.0276, 0.76 / 0.0401	0 / 0, 0.12 / 0.00465, 0 / 0	14 (1.64)	f) down in pyr- 5%CO2 (0.222 / 0.00374)	0.134 (27.5)	e) protein folding
200	peptidyl-prolyl cis-trans isomerase, cyclophilin-type	gi 159484660	Cre01.g002300.t1.2	2.2 / 0.191, 2.2 / 0.478, 11.1 / 0.465	0 / 0, 4.27 / 0.157, 15.9 / 0.722	3.46 / 0.382, 1.71 / 0.115, 2.78 / 0.147	1.71 / 0.443, 2.78 / 0.108, 6.35 / 0.401	15 (1.25)	h) equal (0.187 / 0.864) -grey-	0.946	e) protein folding
201	calreticulin 2, calcium-binding protein	gi 159462862	Cre01.g038400.t1.2	3.7 / 0.321, 0 / 0, 0.71 / 0.0297	0.6 / 0.455, 3.39 / 0.124, 2.14 / 0.0974	4.38 / 0.484, 0.71 / 0.0477, 1.1 / 0.0581	2.36 / 0.611, 0.71 / 0.0275, 3.39 / 0.214	15 (1.2)	h) equal (0.185 / 0.851) -grey-	0.648	e) protein folding
202	peptidyl-prolyl cis-trans isomerase, cyclophilin-type	gi 159471594	Cre12.g544150.t1.2	6.09 / 0.529, 0 / 0, 2.4 / 0.101	0.28 / 0.212, 3.34 / 0.123, 2.01 / 0.0915	2.84 / 0.314, 1.36 / 0.0915, 0.84 / 0.0444	0.63 / 0.163, 1.66 / 0.0643, 0.84 / 0.053	15 (1.21)	h) equal (0.186 / 0.856) -grey-	0.468	e) protein folding
203	chaperonin 60B1	gi 159486163	Cre17.g741450.t1.2	2.27 / 0.197, 0.85 / 0.185, 2.1 / 0.088	0.11 / 0.0834, 3.68 / 0.135, 3.93 / 0.179	0.67 / 0.074, 2.81 / 0.189, 3.45 / 0.182	0 / 0, 2.62 / 0.102, 2.81 / 0.177	15 (0.107)	h) equal (0.148 / 0.672) -grey-	0.417	e) protein folding
204	peptidyl-prolyl cis-trans isomerase, FKBP-type	gi 159469556	Cre12.g530300.t1.2	1.7 / 0.148, 0 / 0, 0.53 / 0.0222	0.53 / 0.402, 1.34 / 0.0492, 0.76 / 0.0346	1.7 / 0.188, 0.76 / 0.0511, 1.03 / 0.0544	0.53 / 0.137, 1.03 / 0.0399, 0.76 / 0.048	15 (0.459)	h) equal (0.161 / 0.736) -grey-	0.308	e) protein folding
205	binding protein 1	gi 159487349	Cre02.g080700.t1.2	1.42 / 0.123, 0.09 / 0.0195, 0.56 / 0.0235	0 / 0, 1.12 / 0.0411, 1.76 / 0.0801	1.21 / 0.134, 0.63 / 0.0424, 0.86 / 0.0454	0.25 / 0.0647, 0.86 / 0.0333, 2.02 / 0.127	15 (0.818)	h) equal (0.175 / 0.807) -grey-	0.193	e) protein folding
206	peptidyl-prolyl cis-trans isomerase, cyclophilin-type	gi 159483401	Cre02.g106150.t1.2	1.36 / 0.118, 0 / 0, 0.68 / 0.0285	0 / 0, 1.36 / 0.0499, 2.96 / 0.135	0.99 / 0.109, 0 / 0, 0.19 / 0.01	0 / 0, 0.41 / 0.0159, 0.19 / 0.012	15 (0.329)	h) equal (0.154 / 0.7) -grey-	0.126	e) protein folding
207	peptidyl-prolyl cis-trans isomerase, FKBP-type	gi 159478565	Cre11.g447800.t1.2	1.38 / 0.12, 0 / 0, 0.24 / 0.0101	0 / 0, 0.54 / 0.0198, 0.54 / 0.0246	0.54 / 0.0596, 0.24 / 0.0161, 0 / 0	0 / 0, 0 / 0, 2.67 / 0.169	15 (0.998)	h) equal (0.183 / 0.844) -grey-	0.11	e) protein folding
208	peptidyl-prolyl cis-trans isomerase, FKBP-type	gi 159486302	NA	1.19 / 0.103, 0 / 0, 0.37 / 0.0155	0 / 0, 0.17 / 0.00624, 0.37 / 0.0168	0.87 / 0.0961, 0.17 / 0.0114, 0 / 0	0.17 / 0.044, 0.17 / 0.00659, 0.17 / 0.0107	15 (0.54)	h) equal (0.164 / 0.752) -grey-	0.0815	e) protein folding
209	heat shock protein 70E	gi 159475503	Cre16.g677000.t1.2	0.67 / 0.0582, 0 / 0, 0.08 / 0.00335	0 / 0, 0.24 / 0.00881, 0.29 / 0.0132	0.39 / 0.0431, 0.04 / 0.00269, 0.16 / 0.00845	0 / 0, 0 / 0, 2.1 / 0.133	15 (0.602)	h) equal (0.167 / 0.764) -grey-	0.0709	e) protein folding
210	chaperonin 60A	gi 159491478	Cre04.g231222.t1.1, Cre04.g231222.t2.1	6.92 / 0.601, 5.44 / 1.18, 31 / 1.3	0.17 / 0.129, 29.4 / 1.08, 26.4 / 1.2	3.72 / 0.411, 36.4 / 2.44, 25 / 1.32	0.3 / 0.0777, 17.1 / 0.663, 15.3 / 0.968	9 (0.102)	i) up in air (0.196 / 0.0864) -magenta-	3.81 (1.76)	e) protein folding
211	chaperonin 60B2	gi 159468684	Cre07.g339150.t1.1	5.8 / 0.504, 8.77 / 1.9, 20.3 / 0.849	0.11 / 0.0834, 18.2 / 0.667, 18.2 / 0.827	3.73 / 0.412, 19.2 / 1.29, 20.3 / 1.07	0.11 / 0.0285, 16.3 / 0.631, 8.28 / 0.523	9 (1.77)	i) up in air (0.341 / 0.0353) -magenta-	3.16 (2.19)	e) protein folding
212	heat shock protein 70B	gi 159476666	Cre06.g250100.t1.2	8.28 / 0.719, 1.91 / 0.415, 11.1 / 0.466	0.2 / 0.152, 9.61 / 0.353, 9.61 / 0.437	3.97 / 0.438, 5.22 / 0.351, 9.15 / 0.483	0.2 / 0.0518, 5.79 / 0.224, 6.77 / 0.427	9 (0.896)	i) up in air (0.334 / 0.0166) -magenta-	1.51 (1.75)	e) protein folding
213	heat shock protein 70C	gi 159472671	Cre09.g393200.t1.2	3.56 / 0.309, 0.63 / 0.137, 3.34 / 0.14	0.05 / 0.0379, 3.56 / 0.131, 3.34 / 0.152	1.8 / 0.199, 1.66 / 0.112, 5.43 / 0.287	0.16 / 0.0414, 0.55 / 0.0213, 0.98 / 0.0619	9 (0.335)	i) up in air (0.524 / 0.00754) -magenta-	0.621 (2.66)	e) protein folding
214	FKBP-type peptidyl-prolyl cis-trans isomerase	gi 159475463	Cre16.g675550.t1.2, Cre16.g675550.t2.1	3.59 / 0.312, 0.36 / 0.0782, 1.91 / 0.08	0.36 / 0.273, 8.83 / 0.324, 6.25 / 0.285	3.48 / 0.384, 4.34 / 0.292, 5.22 / 0.276	2.38 / 0.616, 7.44 / 0.288, 4.34 / 0.274	11 (0.569)	j) down in WT air (0.209 / 0.0655) -purple-	1.05 (2.14)	e) protein folding
215	peptidyl-prolyl cis-trans isomerase, FKBP-type	gi 159470941	Cre13.g586300.t1.2	1.81 / 0.157, 0 / 0, 1.81 / 0.0758	0.3 / 0.227, 6.92 / 0.254, 5.11 / 0.233	5.11 / 0.564, 0.68 / 0.0457, 3.72 / 0.197	0.3 / 0.0777, 2.64 / 0.102, 6.92 / 0.437	11 (0.561)	j) down in WT air (0.166 / 0.029) -purple-	0.748 (3.06)	e) protein folding
216	peptidyl-prolyl cis-trans isomerase, FKBP-type	gi 159475461	Cre16.g675500.t1.2	0 / 0, 0 / 0, 0.4 / 0.0168	0 / 0, 0.96 / 0.0352, 0.96 / 0.0437	0 / 0, 0.66 / 0.0444, 0.66 / 0.0349	0 / 0, 0.96 / 0.0372, 0.4 / 0.0252	11 (0.745)	j) down in WT air (0.176 / 0.0294) -purple-	0.0772 (4.39)	e) protein folding
217	peptidyl-prolyl cis-trans isomerase, FKBP-type	gi 159478449	Cre11.g479050.t1.2	0.48 / 0.0417, 0 / 0, 0.22 / 0.00921	0 / 0, 1.67 / 0.0613, 2.95 / 0.134	1.19 / 0.131, 0 / 0, 0.48 / 0.0254	0 / 0, 0 / 0, 0.48 / 0.0303	10 (1.12)	k) up in the diagonal WT 5%CO2 / pyr- air (0.271 / 0.932)	0.185 (4.34)	e) protein folding

Chapter 8: Appendices

218	peptidyl-prolyl cis-trans isomerase, cyclophilin-type	gi 159485018	Cre12.g495951.t1.1, Cre12.g495951.t2.1	2.2 / 0.191, 0 / 0, 3.29 / 0.138	0.16 / 0.121, 3.96 / 0.145, 2.71 / 0.123	2.71 / 0.299, 1.39 / 0.0935, 2.2 / 0.116	1.39 / 0.36, 2.2 / 0.0852, 4.73 / 0.299	14 (0.536)	m) up in pyr- 5% CO2 (0.439 / 0.155) -yellow-	0.78 (1.82)	e) protein folding
219	HSP70-HSP90 organizing protein	gi 159467379	Cre03.g189950.t1.2	0.05 / 0.00434, 0.05 / 0.0109, 0 / 0	0 / 0, 0.35 / 0.0128, 0.5 / 0.0228	0.29 / 0.032, 0 / 0, 0 / 0	0 / 0, 0.11 / 0.00426, 2.37 / 0.15	14 (0.731)	m) up in pyr- 5% CO2 (0.413 / 0.241) -yellow-	0.161 (5.57)	e) protein folding
220	peptide methionine sulfoxide reductase	gi 159463298	NA	0.83 / 0.0721, 0.08 / 0.0174, 1.66 / 0.0695	0 / 0, 1.66 / 0.0609, 1.29 / 0.0587	1.87 / 0.206, 1.47 / 0.0988, 1.47 / 0.0777	0.57 / 0.148, 0.97 / 0.0376, 1.29 / 0.0814	8 (0.695)	n) up in pyr- -orange-	0.341 (2.04)	e) protein folding
221	peptidyl-prolyl cis-trans isomerase, FKBP-type	gi 159475581	Cre16.g673953.t1.1	0.13 / 0.0113, 0 / 0, 0.13 / 0.00545	0 / 0, 0.28 / 0.0103, 0.13 / 0.00592	0.28 / 0.0309, 0.13 / 0.00874, 0.13 / 0.00687	0.13 / 0.0337, 0.13 / 0.00504, 0.28 / 0.0177	8 (1.78)	n) up in pyr- -orange-	0.054 (3.07)	e) protein folding
222	peptidyl-prolyl cis-trans isomerase, cyclophilin-type	gi 159467709	Cre03.g189800.t1.2	0.77 / 0.0669, 0 / 0, 0.07 / 0.00293	0 / 0, 0.15 / 0.0055, 0.15 / 0.00683	1.71 / 0.189, 0.07 / 0.00471, 0.15 / 0.00792	0 / 0, 0.07 / 0.00271, 0.77 / 0.0486	13 (0.453)	o) up in pyr- air -red-	0.211 (4.53)	e) protein folding
223	hypothetical protein CHLREDRAFT_127770	gi 159491000	Cre03.g173350.t2.1	0.28 / 0.0243, 0.18 / 0.0391, 0.78 / 0.0327	0 / 0, 0.93 / 0.0341, 0.93 / 0.0423	0.64 / 0.0707, 0.93 / 0.0625, 0.78 / 0.0412	0 / 0, 0.51 / 0.0198, 1.28 / 0.0808	13 (1.44)	o) up in pyr- air -red-	0.183 (1.92)	e) protein folding
224	organellar translation initiation factor	gi 159468169	Cre04.g218700.t1.2	1.18 / 0.102, 0 / 0, 6 / 0.251	0 / 0, 21.5 / 0.789, 14.2 / 0.649	0.48 / 0.053, 2.21 / 0.149, 1.18 / 0.0623	0 / 0, 6 / 0.232, 3.74 / 0.236	12 (1.84)	a) up in WT 5%CO2 (0.739 / 0.138) -cyan-	1.51 (3.97)	d) protein synthesis/turnover
225	non-discriminatory gln-glu-trna synthetase	gi 159485866	Cre07.g313700.t1.1	0 / 0, 0 / 0, 0.55 / 0.023	0 / 0, 1.04 / 0.0382, 0.64 / 0.0291	0.06 / 0.00662, 0.12 / 0.00807, 0.31 / 0.0164	0 / 0, 0.55 / 0.0213, 0.12 / 0.00757	12 (0.877)	a) up in WT 5%CO2 (0.427 / 0.185) -cyan-	0.0706 (2.43)	d) protein synthesis/turnover
226	ribosomal protein L36	gi 41179012	NA	5.18 / 1.12, 5.18 / 0.217	10.3 / 0.379, 10.3 / 0.471	0 / 0, 5.18 / 0.274	10.3 / 0.401, 0 / 0	8 (0.0385)	b) up in WT -blue-	1.15 (2.16)	d) protein synthesis/turnover
227	plastid ribosomal protein L3	gi 159485314	Cre48.g761197.t1.1	0.57 / 0.0495, 17.9 / 3.88, 15.8 / 0.664	0 / 0, 12.4 / 0.457, 5.82 / 0.265	0.97 / 0.107, 8.58 / 0.577, 12.4 / 0.657	0 / 0, 15.8 / 0.614, 2.09 / 0.132	11 (1.78)	c) up in WT air -purple-	4.82 (4.91)	d) protein synthesis/turnover
228	plastid ribosomal protein S17	gi 159488919	NA	12 / 1.04, 12 / 2.6, 5.02 / 0.21	0.67 / 0.508, 6.78 / 0.249, 6.78 / 0.309	9.05 / 0.999, 1.79 / 0.12, 3.66 / 0.193	1.16 / 0.3, 9.05 / 0.351, 1.79 / 0.113	11 (1.86)	c) up in WT air -purple-	4.04 (3.68)	d) protein synthesis/turnover
229	plastid ribosomal protein L24	gi 159480154	Cre16.g652550.t1.2	0.97 / 0.0843, 11.6 / 2.53, 14 / 0.584	0 / 0, 9.66 / 0.354, 14 / 0.635	1.33 / 0.147, 9.66 / 0.65, 11.6 / 0.614	0 / 0, 23.8 / 0.923, 1.76 / 0.111	11 (0.66)	c) up in WT air -purple-	3.35 (2.79)	d) protein synthesis/turnover
230	plastid ribosomal protein L31	gi 159476036	Cre08.g365400.t1.2	5.46 / 0.474, 1.29 / 0.28, 21.4 / 0.898	0 / 0, 11 / 0.405, 11 / 0.503	1.82 / 0.201, 6.95 / 0.467, 6.95 / 0.367	0 / 0, 13.8 / 0.535, 4.25 / 0.268	11 (0.733)	c) up in WT air -purple-	1.73 (1.8)	d) protein synthesis/turnover
231	plastid ribosomal protein L19	gi 159469822	Cre17.g734450.t1.2	0.74 / 0.0643, 3.4 / 0.738, 2.65 / 0.111	0 / 0, 5.37 / 0.197, 3.4 / 0.155	0.45 / 0.0497, 2.65 / 0.178, 3.4 / 0.18	0 / 0, 5.37 / 0.208, 1.1 / 0.0694	11 (0.546)	c) up in WT air -purple-	0.959 (2.64)	d) protein synthesis/turnover
232	plastid ribosomal protein L34	gi 159462702	Cre01.g030050.t1.2	0.26 / 0.0226, 3.02 / 0.656, 0.26 / 0.0109	0 / 0, 0.59 / 0.0217, 0.26 / 0.0118	0.26 / 0.0287, 0.26 / 0.0175, 0.26 / 0.0137	0.26 / 0.0673, 0.59 / 0.0229, 0.26 / 0.0164	11 (1.62)	c) up in WT air -purple-	0.723 (10.3)	d) protein synthesis/turnover
233	plastid ribosomal protein L33	gi 159481078	NA	0.3 / 0.0261, 1.84 / 0.4, 2.69 / 0.113	0 / 0, 1.84 / 0.0675, 1.19 / 0.0542	0.3 / 0.0331, 0.69 / 0.0464, 1.84 / 0.0972	0 / 0, 3.79 / 0.147, 0 / 0	11 (1.95)	c) up in WT air -purple-	0.565 (3.63)	d) protein synthesis/turnover
234	plastid ribosomal protein S10	gi 159470269	Cre03.g195650.t1.2	1.26 / 0.109, 0.18 / 0.0391, 2.14 / 0.0896	0 / 0, 1.67 / 0.0613, 1.67 / 0.076	0.18 / 0.0199, 0.92 / 0.0619, 0.92 / 0.0486	0 / 0, 1.67 / 0.0647, 0.63 / 0.0398	11 (1.66)	c) up in WT air -purple-	0.25 (1.92)	d) protein synthesis/turnover
235	ribosomal protein S18	gi 41179036	NA	1.57 / 0.136, 0 / 0, 0.21 / 0.0088	0 / 0, 0.46 / 0.0169, 0.46 / 0.0209	0.21 / 0.0232, 0.21 / 0.0141, 0.46 / 0.0243	0 / 0, 0.46 / 0.0178, 0 / 0	11 (0.438)	c) up in WT air -purple-	0.171 (3.12)	d) protein synthesis/turnover
236	SEC61-beta subunit of ER-translocon	gi 159485960	Cre07.g318450.t1.2	0 / 0, 0.38 / 0.0825, 0.9 / 0.0377	0 / 0, 0.9 / 0.033, 0.9 / 0.041	0 / 0, 0.38 / 0.0256, 0.38 / 0.0201	0 / 0, 0.9 / 0.0349, 0 / 0	11 (0.211)	c) up in WT air -purple-	0.126 (2.33)	d) protein synthesis/turnover
237	plastid ribosomal protein S21	gi 159462500	Cre01.g017300.t1.2	0.35 / 0.0304, 0.35 / 0.076, 0 / 0	0 / 0, 0 / 0, 0 / 0	0.16 / 0.0177, 0 / 0, 0 / 0	0 / 0, 0 / 0, 0 / 0	11 (1.74)	c) up in WT air -purple-	0.112 (18.1)	d) protein synthesis/turnover
238	ribosomal protein S4	gi 41179020	NA	1.08 / 0.0938, 0 / 0, 0.11 / 0.00461	0 / 0, 0.11 / 0.00404, 0.11 / 0.00501	0 / 0, 0 / 0, 0.11 / 0.00581	0 / 0, 0.11 / 0.00426, 0 / 0	11 (1.82)	c) up in WT air -purple-	0.103 (15.4)	d) protein synthesis/turnover
239	plastid ribosomal protein S5	gi 159479560	Cre16.g659950.t1.1	0.86 / 0.0747, 0 / 0, 0 / 0	0 / 0, 0 / 0, 0.14 / 0.00637	0.31 / 0.0342, 0 / 0, 0 / 0	0.25 / 0.0647, 0.09 / 0.00349, 0.77 / 0.0486	10 (0.608)	e) up in the diagonal WT air/ pyr- 5%CO2 (0.231 / 0.927)	0.1 (4.72)	d) protein synthesis/turnover
240	ribosomal protein S12	gi 41179059	NA	0.51 / 0.0443, 0.23 / 0.05, 0.23 / 0.00963	0 / 0, 0.23 / 0.00844, 0.23 / 0.0105	0 / 0, 0.23 / 0.0155, 0.23 / 0.0122	0.23 / 0.0595, 0.23 / 0.00891, 0.23 / 0.0145	10 (1.68)	e) up in the diagonal WT air/ pyr- 5%CO2 (0.42 / 0.974)	0.098 (4.02)	d) protein synthesis/turnover
241	plastid ribosomal protein L6	gi 159477461	Cre09.g415950.t1.2	0.52 / 0.0452, 8.39 / 1.82, 56.9 / 2.38	0 / 0, 56.9 / 2.09, 24 / 1.09	1.32 / 0.146, 42.8 / 2.88, 32.1 / 1.7	0 / 0, 27.8 / 1.08, 4.36 / 0.275	14 (0.0165)	f) down in pyr- 5%CO2 (0.138 / 0.0518)	4.25 (3)	d) protein synthesis/turnover
242	cysteine endopeptidase	gi 159479072	Cre09.g407700.t1.2	1.86 / 0.162, 0.64 / 0.139, 1.69 / 0.0708	0.45 / 0.341, 2.23 / 0.0818, 1.37 / 0.0624	1.69 / 0.187, 2.89 / 0.194, 2.04 / 0.108	0.06 / 0.0155, 2.04 / 0.079, 1.53 / 0.0966	14 (0.449)	f) down in pyr- 5%CO2 (0.164 / 0.0277)	0.471 (2.35)	d) protein synthesis/turnover
243	plastid ribosomal protein L32	gi 159468912	Cre07.g352850.t1.2	8.47 / 0.736, 6.15 / 1.34, 15.6 / 0.653	3.07 / 2.33, 15.6 / 0.572, 11.5 / 0.525	8.47 / 0.935, 21 / 1.41, 11.5 / 0.61	6.15 / 1.59, 15.6 / 0.604, 15.6 / 0.985	15 (1.74)	h) equal -grey-	3.22	d) protein synthesis/turnover
244	plastid ribosomal protein S15	gi 159476378	Cre06.g264300.t1.2	11.4 / 0.99, 0.47 / 0.102, 31.6 / 1.33	0 / 0, 38.6 / 1.42, 25.9 / 1.18	5.93 / 0.655, 11.4 / 0.767, 17.3 / 0.912	0 / 0, 25.9 / 1, 5.93 / 0.374	15 (0.701)	h) equal -grey-	2.29	d) protein synthesis/turnover
245	elongation factor Tu	gi 41179007	NA	9.69 / 0.842, 0.75 / 0.163, 22 / 0.922	0.15 / 0.114, 25.5 / 0.934, 31.6 / 1.44	3.32 / 0.367, 17.7 / 1.19, 17.7 / 0.933	0.23 / 0.0595, 17.7 / 0.685, 8.97 / 0.566	15 (0.491)	h) equal -grey-	2.15	d) protein synthesis/turnover
246	plastid ribosomal protein L10	gi 159476750	Cre06.g272850.t1.2	3.24 / 0.281, 2.76 / 0.599, 19.3 / 0.808	0.13 / 0.0985, 28.1 / 1.03, 19.3 / 0.878	1.62 / 0.179, 15 / 1.01, 13.1 / 0.694	0 / 0, 36 / 1.4, 11.5 / 0.728	15 (1.84)	h) equal -grey-	2.02	d) protein synthesis/turnover
247	plastid ribosomal protein L15	gi 159481831	Cre14.g612450.t1.2	0.28 / 0.0243, 6.15 / 1.34, 9.34 / 0.391	0 / 0, 15.9 / 0.583, 5.32 / 0.242	0.85 / 0.0938, 5.32 / 0.358, 12.2 / 0.646	0 / 0, 50.1 / 1.94, 2.02 / 0.127	15 (1.05)	h) equal -grey-	1.51	d) protein synthesis/turnover
248	plastid ribosomal protein L28	gi 159476894	Cre06.g265800.t1.2	1.33 / 0.116, 2.1 / 0.456, 7.33 / 0.307	0.15 / 0.114, 13.7 / 0.501, 15.9 / 0.723	0.76 / 0.0839, 5.28 / 0.355, 11.7 / 0.62	0.15 / 0.0388, 51.3 / 1.99, 1.03 / 0.065	15 (1.02)	h) equal -grey-	1.41	d) protein synthesis/turnover
249	plastid ribosomal protein L4	gi 159478579	Cre11.g479500.t1.2	0.63 / 0.0547, 2.4 / 0.521, 29.8 / 1.25	0 / 0, 12.1 / 0.443, 10.6 / 0.481	0.84 / 0.0927, 5.27 / 0.354, 13.8 / 0.728	0 / 0, 15.7 / 0.608, 2.84 / 0.179	15 (0.387)	h) equal -grey-	1.24	d) protein synthesis/turnover
250	plastid ribosomal protein L18	gi 159464052	Cre01.g052100.t1.2	0.47 / 0.0408, 2.17 / 0.471, 2.84 / 0.119	0 / 0, 20.7 / 0.76, 7.3 / 0.332	1.16 / 0.128, 4.65 / 0.313, 13.8 / 0.728	0 / 0, 20.7 / 0.803, 0.21 / 0.0133	15 (1.36)	h) equal -grey-	0.973	d) protein synthesis/turnover

Molecular Physiology of the *Chlamydomonas pyrenoid*

251	plastid ribosomal protein L9	gi 159472060	Cre12.g556050.t1.2	1.3 / 0.113, 0.74 / 0.161, 15 / 0.628	0 / 0, 9.56 / 0.351, 15 / 0.683	0.74 / 0.0817, 4.28 / 0.288, 7 / 0.37	0 / 0, 17.4 / 0.674, 1.3 / 0.082	15 (1.73)	h) equal (0.214 / 0.973) -grey-	0.9	d) protein synthesis/ turnover
252	plastid ribosomal protein S16	gi 159484984	Cre12.g494450.t1.2	0.53 / 0.046, 4.45 / 0.966, 5.73 / 0.24	0 / 0, 9.28 / 0.341, 9.28 / 0.422	0.24 / 0.0265, 5.73 / 0.385, 7.32 / 0.387	0 / 0, 9.28 / 0.36, 1.88 / 0.119	15 (0.748)	h) equal (0.168 / 0.772) -grey-	0.864	d) protein synthesis/ turnover
253	ribosomal protein S9	gi 41179039	NA	2.26 / 0.196, 0.34 / 0.0738, 8.17 / 0.342	0.16 / 0.121, 6.91 / 0.254, 8.17 / 0.372	0.81 / 0.0894, 4.08 / 0.274, 5.82 / 0.307	0 / 0, 24.8 / 0.961, 0.56 / 0.0353	15 (1.57)	h) equal (0.208 / 0.952) -grey-	0.794	d) protein synthesis/ turnover
254	acidic ribosomal protein P0	gi 159477927	Cre12.g520500.t1.1, Cre12.g520550.t1.2	6.48 / 0.563, 0 / 0, 1.08 / 0.0452	0 / 0, 5.23 / 0.192, 5.23 / 0.238	5.82 / 0.643, 2.94 / 0.198, 2.6 / 0.137	0.1 / 0.0259, 7.19 / 0.279, 7.19 / 0.454	15 (1.04)	h) equal (0.179 / 0.822) -grey-	0.728	d) protein synthesis/ turnover
255	ribosomal protein L5	gi 126165895	NA	1.16 / 0.101, 1.52 / 0.33, 6.4 / 0.268	0 / 0, 12.7 / 0.466, 5.34 / 0.243	0.59 / 0.0651, 5.34 / 0.359, 5.34 / 0.282	0 / 0, 10.7 / 0.416, 1.52 / 0.0959	15 (1.61)	h) equal (0.211 / 0.964) -grey-	0.689	d) protein synthesis/ turnover
256	plastid ribosomal protein S6	gi 159477657	Cre12.g520600.t1.2	4.92 / 0.427, 0.62 / 0.135, 0.91 / 0.0381	0 / 0, 4.03 / 0.148, 8.61 / 0.392	2.1 / 0.232, 0.62 / 0.0417, 2.1 / 0.111	0.38 / 0.0984, 8.61 / 0.334, 4.92 / 0.311	15 (1.22)	h) equal (0.183 / 0.842) -grey-	0.595	d) protein synthesis/ turnover
257	plastid ribosomal protein S13	gi 159485052	Cre12.g493950.t1.2	1.71 / 0.149, 0 / 0, 2.2 / 0.0921	0 / 0, 6.35 / 0.233, 1.3 / 0.0592	0.18 / 0.0199, 2.78 / 0.187, 3.46 / 0.183	0 / 0, 13.3 / 0.515, 0.18 / 0.0114	15 (1.39)	h) equal (0.197 / 0.906) -grey-	0.38	d) protein synthesis/ turnover
258	plastid ribosomal protein L27	gi 159466472	NA	0 / 0, 1.92 / 0.417, 1.92 / 0.0804	0 / 0, 4.95 / 0.182, 3.16 / 0.144	0 / 0, 1.92 / 0.129, 1.44 / 0.0761	0 / 0, 9.16 / 0.355, 0 / 0	15 (1.44)	h) equal (0.196 / 0.904) -grey-	0.363	d) protein synthesis/ turnover
259	ribosomal protein S19	gi 41179015	NA	0.33 / 0.0287, 0.77 / 0.167, 3.19 / 0.134	0 / 0, 3.19 / 0.117, 2.15 / 0.0979	0.33 / 0.0364, 3.19 / 0.215, 4.58 / 0.242	0 / 0, 6.43 / 0.249, 0 / 0	15 (0.323)	h) equal (0.154 / 0.703) -grey-	0.337	d) protein synthesis/ turnover
260	plastid ribosomal protein L17	gi 159483339	Cre02.g108850.t1.2	0.63 / 0.0547, 0.38 / 0.0825, 2.12 / 0.0888	0 / 0, 4.97 / 0.182, 4.08 / 0.186	0.38 / 0.042, 3.32 / 0.223, 2.67 / 0.141	0 / 0, 4.97 / 0.193, 1.25 / 0.0789	15 (0.767)	h) equal (0.176 / 0.812) -grey-	0.334	d) protein synthesis/ turnover
261	ribosomal protein L23	gi 41179013	NA	0.31 / 0.0269, 1.24 / 0.269, 0.71 / 0.0297	0 / 0, 7.54 / 0.277, 0.71 / 0.0323	0 / 0, 1.24 / 0.0834, 0.71 / 0.0375	0 / 0, 5.53 / 0.214, 0 / 0	15 (1.27)	h) equal (0.193 / 0.892) -grey-	0.255	d) protein synthesis/ turnover
262	plastid-specific ribosomal protein 3	gi 159487801	Cre02.g083950.t1.1	3.14 / 0.273, 0 / 0, 0.33 / 0.0138	0.1 / 0.0758, 1.13 / 0.0415, 0.94 / 0.0428	1.58 / 0.174, 0.61 / 0.041, 1.58 / 0.0835	0.33 / 0.0854, 1.13 / 0.0438, 1.13 / 0.0713	15 (1.16)	h) equal (0.193 / 0.889) -grey-	0.248	d) protein synthesis/ turnover
263	plastid ribosomal protein L35	gi 159486445	Cre04.g217932.t1.1	0 / 0, 1.1 / 0.239, 1.69 / 0.0708	0 / 0, 3.42 / 0.126, 0.28 / 0.0127	0 / 0, 1.1 / 0.074, 0.28 / 0.0148	0 / 0, 4.66 / 0.181, 0 / 0	15 (0.697)	h) equal (0.169 / 0.776) -grey-	0.188	d) protein synthesis/ turnover
264	ribosomal protein S8	gi 114812067	NA	0.8 / 0.0695, 0 / 0, 0.22 / 0.00921	0 / 0, 6.12 / 0.225, 0.48 / 0.0219	0 / 0, 0.8 / 0.0538, 0.48 / 0.0254	0 / 0, 6.12 / 0.237, 0 / 0	15 (0.619)	h) equal (0.175 / 0.807) -grey-	0.168	d) protein synthesis/ turnover
265	iron-sulfur cluster assembly protein	gi 159468454	Cre07.g339700.t1.2	0.5 / 0.0434, 0.11 / 0.0239, 2.73 / 0.114	0 / 0, 1.25 / 0.0459, 1.75 / 0.0797	0 / 0, 1.03 / 0.0693, 2.05 / 0.108	0 / 0, 0.5 / 0.0194, 1.49 / 0.094	15 (1.03)	h) equal (0.189 / 0.873) -grey-	0.16	d) protein synthesis/ turnover
266	chloroplast elongation factor G	gi 159487669	Cre02.g076250.t1.1	0.62 / 0.0539, 0.08 / 0.0174, 1.52 / 0.0637	0 / 0, 1.06 / 0.0389, 1.73 / 0.0788	0.38 / 0.042, 0.83 / 0.0558, 1.24 / 0.0655	0 / 0, 0.27 / 0.0105, 1.52 / 0.0959	15 (1.46)	h) equal (0.2 / 0.919) -grey-	0.137	d) protein synthesis/ turnover
267	ribosomal protein S7	gi 41179024	NA	2.1 / 0.182, 0 / 0, 0.91 / 0.0381	0 / 0, 0.62 / 0.0228, 0.91 / 0.0414	0 / 0, 0.18 / 0.0121, 0.62 / 0.0328	0 / 0, 4.03 / 0.156, 0 / 0	15 (0.202)	h) equal (0.153 / 0.695) -grey-	0.127	d) protein synthesis/ turnover
268	plastid ribosomal protein L21	gi 159466194	Cre06.g299000.t1.2	0 / 0, 0.89 / 0.0373	0 / 0, 1.21 / 0.0444, 1.6 / 0.0728	0 / 0, 0.61 / 0.041, 0.61 / 0.0322	0 / 0, 1.6 / 0.062, 0.37 / 0.0234	15 (0.759)	h) equal (0.159 / 0.726) -grey-	0.0821	d) protein synthesis/ turnover
269	ribosomal protein S3	gi 41179046	NA	0.8 / 0.0695, 0 / 0, 0.32 / 0.0134	0 / 0, 0.66 / 0.0242, 0.6 / 0.0273	0 / 0, 0.12 / 0.0132, 0.32 / 0.0215, 0.42 / 0.0222	0 / 0, 1.19 / 0.0461, 0.32 / 0.0202	15 (1.59)	h) equal (0.206 / 0.947) -grey-	0.0676	d) protein synthesis/ turnover
270	predicted protein	gi 159489554	Cre10.g422150.t1.1	0.42 / 0.0365, 0 / 0, 0 / 0	0.07 / 0.0531, 0.07 / 0.00257, 0 / 0	0.52 / 0.0574, 0.07 / 0.00471, 0.07 / 0.0037	0.15 / 0.0388, 0 / 0, 0.07 / 0.00442	15 (1.69)	h) equal (0.212 / 0.967) -grey-	0.0528	d) protein synthesis/ turnover
271	ribosomal protein S2	gi 41179035	NA	0.5 / 0.0434, 0 / 0, 0.16 / 0.0067	0 / 0, 0.58 / 0.0213, 0.5 / 0.0228	0.13 / 0.0144, 0.29 / 0.0195, 0.29 / 0.0153	0 / 0, 1.14 / 0.0442, 0.05 / 0.00316	15 (1.97)	h) equal (0.224 / 0.999) -grey-	0.05	d) protein synthesis/ turnover
272	plastid-specific ribosomal protein 7	gi 159477693	Cre12.g519180.t1.1	0.62 / 0.0539, 0 / 0, 0.06 / 0.00251	0 / 0, 0.19 / 0.00697, 0.23 / 0.0105	0.13 / 0.0144, 0.27 / 0.0182, 0.27 / 0.0143	0.17 / 0.044, 0.16 / 0.0062, 0.23 / 0.0145	15 (0.486)	h) equal (0.162 / 0.745) -grey-	0.0486	d) protein synthesis/ turnover
273	plastid ribosomal protein S1	gi 159472705	Cre09.g394750.t1.2	0.81 / 0.0704, 0 / 0, 0.07 / 0.00293	0 / 0, 0.22 / 0.00807, 0.22 / 0.01	0.14 / 0.0155, 0.07 / 0.00471, 0.3 / 0.0158	0.07 / 0.0181, 0.07 / 0.00271, 0.3 / 0.0189	15 (0.599)	h) equal (0.164 / 0.752) -grey-	0.0439	d) protein synthesis/ turnover
274	plastid ribosomal protein L11	gi 159489190	Cre10.g423650.t1.2	2.78 / 0.241, 11.1 / 2.41, 37.7 / 1.58	0 / 0, 15.9 / 0.582, 15.9 / 0.722	3.46 / 0.382, 26.8 / 1.8, 22.5 / 1.19	0 / 0, 37.7 / 1.46, 5.22 / 0.329	9 (1.39)	i) up in air (0.283 / 0.0507) -magenta-	3.99 (2.46)	d) protein synthesis/ turnover
275	acidic ribosomal protein P2	gi 159473469	Cre02.g143050.t1.2	2.97 / 0.258, 0.74 / 0.161, 19.8 / 0.827	0 / 0, 5.89 / 0.216, 8.07 / 0.367	8.07 / 0.891, 4.23 / 0.284, 11 / 0.578	0.32 / 0.0828, 11 / 0.424, 8.07 / 0.509	9 (0.0208)	i) up in air (0.193 / 0.0798) -magenta-	1.57 (1.87)	d) protein synthesis/ turnover
276	plastid ribosomal protein L1	gi 159487501	Cre02.g088900.t1.2	1.91 / 0.166, 2.9 / 0.63, 8.36 / 0.35	0.1 / 0.0758, 5.34 / 0.196, 4.75 / 0.216	2.54 / 0.28, 4.75 / 0.319, 3.74 / 0.198	0.1 / 0.0259, 8.36 / 0.324, 1.64 / 0.104	9 (0.211)	i) up in air (0.254 / 0.0352) -magenta-	1.02 (2.06)	d) protein synthesis/ turnover
277	plastid ribosomal protein L13	gi 159476924	Cre06.g264350.t1.2	1.15 / 0.0999, 0.89 / 0.193, 10.2 / 0.428	0 / 0, 4.23 / 0.155, 4.23 / 0.193	1.15 / 0.127, 6.65 / 0.447, 4.93 / 0.26	0 / 0, 10.2 / 0.396, 1.44 / 0.0909	9 (0.15)	i) up in air (0.211 / 0.0957) -magenta-	0.816 (1.86)	d) protein synthesis/ turnover
278	26S proteasome regulatory subunit	gi 159467022	Cre17.g708300.t1.2	3.03 / 0.263, 0 / 0, 1.62 / 0.0679	0 / 0, 1.36 / 0.0499, 1.92 / 0.0874	0.38 / 0.042, 1.36 / 0.0915, 2.25 / 0.119	0 / 0, 0.71 / 0.0275, 0.9 / 0.0568	9 (0.487)	i) up in air (0.224 / 0.0884) -magenta-	0.306 (2.63)	d) protein synthesis/ turnover
279	acidic ribosomal protein P1	gi 159483157	Cre17.g738300.t1.2	0.73 / 0.0634, 0.31 / 0.0673, 0.73 / 0.0306	0 / 0, 0.73 / 0.0268, 0.73 / 0.0332	0.73 / 0.0806, 0.73 / 0.0491, 0.73 / 0.0386	0 / 0, 0.73 / 0.0283, 0.73 / 0.0461	9 (1.88)	i) up in air (0.572 / 0.00661) -magenta-	0.173 (2.45)	d) protein synthesis/ turnover
280	iron-sulfur cluster assembly protein	gi 159490004	Cre12.g513950.t1.2	1.4 / 0.122, 0 / 0, 0.37 / 0.0155	0 / 0, 0.65 / 0.0239, 0.76 / 0.0346	0.65 / 0.0718, 0.21 / 0.0141, 0.46 / 0.0243	0 / 0, 0.28 / 0.0108, 0.28 / 0.0177	9 (0.0155)	i) up in air (0.204 / 0.113) -magenta-	0.13 (2.84)	d) protein synthesis/ turnover
281	ribosomal protein L2	gi 41179014	NA	0.66 / 0.0573, 0 / 0, 1.77 / 0.0741	0 / 0, 0.84 / 0.0308, 0.5 / 0.0228	0.11 / 0.0121, 0.5 / 0.0336, 0.84 / 0.0444	0 / 0, 1.26 / 0.0488, 0 / 0	9 (0.105)	i) up in air (0.193 / 0.0956) -magenta-	0.116 (2.16)	d) protein synthesis/ turnover
282	active subunit of chloroplast ClpP peptidase	gi 159465135	Cre12.g500950.t1.2	0.51 / 0.0443, 0 / 0, 0.78 / 0.0327	0 / 0, 0.51 / 0.0187, 0.28 / 0.0127	0.18 / 0.0199, 0.64 / 0.043, 0.29 / 0.0206	0 / 0, 0.18 / 0.00697, 0.18 / 0.0114	9 (1.79)	i) up in air (0.448 / 0.022) -magenta-	0.0842 (3.22)	d) protein synthesis/ turnover
283	plastid ribosomal protein L7/L12	gi 159470865	Cre13.g581650.t1.2	8.01 / 0.696, 0.93 / 0.202, 20.7 / 0.867	0.55 / 0.417, 51.3 / 1.88, 41 / 1.86	3.66 / 0.404, 20.7 / 1.39, 51.3 / 2.71	2 / 0.518, 80.2 / 3.11, 32.7 / 2.06	11 (0.963)	j) down in WT air (0.17 / 0.0134) -purple-	5.02 (2.71)	d) protein synthesis/ turnover

Chapter 8: Appendices

284	organelle elongation factor P	gi 159482564	Cre16.g691000.t1.2	1.46 / 0.127, 0 / 0, 3.48 / 0.146	0.16 / 0.121, 7.17 / 0.263, 7.17 / 0.326	1.46 / 0.161, 3.48 / 0.234, 6.03 / 0.319	0.57 / 0.148, 2.32 / 0.0899, 10 / 0.632	11 (0.804)	j) down in WT air -purple-	0.803 (2.81)	d) protein synthesis/turnover
285	plastid ribosomal protein S20	gi 159485040	Cre12.g494750.t1.2	1.33 / 0.116, 0 / 0, 2.87 / 0.12	0 / 0, 9.66 / 0.354, 6.6 / 0.3	0.66 / 0.0729, 4.42 / 0.297, 3.58 / 0.189	0 / 0, 6.6 / 0.256, 0.66 / 0.0417	10 (0.798)	k) up in the diagonal WT 5%CO2/ pyr- air (0.252 / 0.93)	0.637 (2.28)	d) protein synthesis/turnover
286	aspartyl aminopeptidase-like protein	gi 159464737	Cre10.g435300.t1.2, Cre10.g435300.t2.1	0.11 / 0.00955, 0.05 / 0.0109, 0.05 / 0.00209	0 / 0, 0.52 / 0.0191, 0.52 / 0.0237	0.13 / 0.0144, 0.11 / 0.0074, 0.37 / 0.0195	0 / 0, 0.17 / 0.00659, 0.11 / 0.00694	10 (1.66)	k) up in the diagonal WT 5%CO2/ pyr- air (0.335 / 0.958)	0.0441 (2.33)	d) protein synthesis/turnover
287	plastid-specific ribosomal protein 6	gi 159466322	Cre06.g308533.t2.1, Cre06.g308533.t1.1	1.23 / 0.107, 0 / 0, 6.39 / 0.268	2.32 / 1.76, 23.5 / 0.863, 15.4 / 0.702	1.23 / 0.136, 15.4 / 1.04, 23.5 / 1.24	10 / 2.59, 53.5 / 2.07, 3.95 / 0.249	7 (0.238)	m) up in pyr- 5% CO2 -yellow-	5.16 (2.41)	d) protein synthesis/turnover
288	hypothetical protein CHLREDRAFT_82920	gi 159488381	Cre05.g233800.t1.2	0.28 / 0.0243, 0 / 0, 0.39 / 0.0163	0 / 0, 0.28 / 0.0103, 0.18 / 0.00819	0.28 / 0.0309, 0.23 / 0.0155, 0.39 / 0.0206	0 / 0, 0.09 / 0.00349, 3.86 / 0.244	14 (0.807)	m) up in pyr- 5% CO2 -yellow-	0.259 (5.88)	d) protein synthesis/turnover
289	histone H2A	gi 159464886	Cre06.g276950.t1.2	0.25 / 0.0217, 0 / 0, 0 / 0	0 / 0, 0.25 / 0.00917, 0.25 / 0.0114	0 / 0, 0 / 0, 0 / 0	0.25 / 0.0647, 0.56 / 0.0217, 0 / 0	14 (1.54)	m) up in pyr- 5% CO2 -yellow-	0.0907 (6.13)	d) protein synthesis/turnover
290	20S proteasome alpha subunit D	gi 159462714	Cre01.g030850.t1.2	0.12 / 0.0104, 0 / 0, 0.26 / 0.0109	0 / 0, 0 / 0, 0.41 / 0.0187	0 / 0, 0.41 / 0.0276, 0.99 / 0.0523	0 / 0, 0.58 / 0.0225, 0.58 / 0.0366	8 (1.25)	n) up in pyr- -orange-	0.0729 (3.26)	d) protein synthesis/turnover
291	plastid-specific ribosomal protein 1	gi 159479306	Cre05.g237450.t1.2	1.7 / 0.148, 0.35 / 0.076, 8.79 / 0.368	0 / 0, 12.2 / 0.447, 6.27 / 0.285	1.98 / 0.219, 9.81 / 0.66, 8.79 / 0.464	0 / 0, 9.81 / 0.38, 1.7 / 0.107	13 (1.7)	o) up in pyr- air -red-	1.41 (2.22)	d) protein synthesis/turnover
292	ribosomal protein L14	gi 41179017	NA	1.46 / 0.127, 0.25 / 0.0543, 6.57 / 0.275	0 / 0, 8.48 / 0.311, 5.04 / 0.229	1.46 / 0.161, 8.48 / 0.57, 3.83 / 0.202	0 / 0, 8.48 / 0.329, 2.08 / 0.131	13 (0.323)	o) up in pyr- air -red-	0.98 (1.92)	d) protein synthesis/turnover
293	protein kinase C binding protein	gi 159476202	Cre06.g273000.t1.2	0.88 / 0.0764, 0 / 0, 3.36 / 0.141	0 / 0, 5.64 / 0.207, 4.38 / 0.199	1.86 / 0.205, 3.36 / 0.226, 7.19 / 0.38	0.23 / 0.0595, 5.64 / 0.219, 1.86 / 0.117	13 (0.755)	o) up in pyr- air -red-	0.851 (2.39)	d) protein synthesis/turnover
294	hypothetical protein CHLREDRAFT_192620	gi 159477837	Cre12.g524400.t1.2	0.37 / 0.0321, 0 / 0, 0 / 0	0.52 / 0.394, 0.11 / 0.00404, 0 / 0	0.69 / 0.0762, 0 / 0, 0 / 0	0.37 / 0.0958, 0 / 0, 0 / 0	12 (0.574)	a) up in WT 5%CO2 -cyan-	0.418 (5.85)	c) metabolic enzymes
295	magnesium chelatase subunit I	gi 159465325	Cre12.g510800.t1.2	0.73 / 0.0634, 0.15 / 0.0326, 1.79 / 0.075	0 / 0, 3.2 / 0.117, 3.82 / 0.174	0 / 0, 1.27 / 0.0854, 1.12 / 0.0592	0 / 0, 0.61 / 0.0236, 1.61 / 0.102	12 (0.152)	a) up in WT 5%CO2 -cyan-	0.306 (1.98)	c) metabolic enzymes
296	predicted protein	gi 159471069	NA	0 / 0, 0 / 0, 0.57 / 0.0239	0 / 0, 1.47 / 0.0539, 3.52 / 0.16	0 / 0, 0 / 0, 1.87 / 0.0988	0 / 0, 0 / 0, 1.13 / 0.0713	12 (0.463)	a) up in WT 5%CO2 -cyan-	0.225 (3.31)	c) metabolic enzymes
297	predicted protein	gi 159487689	Cre02.g077401.t1.1	0 / 0, 0 / 0, 0.39 / 0.0163	0.11 / 0.0834, 0.72 / 0.0264, 1.14 / 0.0519	0 / 0, 0.11 / 0.0074, 0 / 0	0 / 0, 0.24 / 0.0093, 0 / 0	12 (1.91)	a) up in WT 5%CO2 -cyan-	0.17 (14.7)	c) metabolic enzymes
298	predicted protein	gi 159476406	Cre06.g263250.t1.1	0.28 / 0.0243, 0 / 0, 0.16 / 0.0067	0.16 / 0.121, 0.22 / 0.00807, 0.28 / 0.0127	0.22 / 0.0243, 0.22 / 0.0148, 0.22 / 0.0116	0.22 / 0.057, 0.22 / 0.00852, 0.22 / 0.0139	12 (0.0634)	a) up in WT 5%CO2 -cyan-	0.149 (2.65)	c) metabolic enzymes
299	alanine aminotransferase	gi 159480896	Cre10.g451950.t1.2	0.12 / 0.0104, 0 / 0, 0.12 / 0.00503	0 / 0, 1.84 / 0.0675, 1.55 / 0.0706	0.06 / 0.00662, 0.12 / 0.00807, 0.47 / 0.0248	0 / 0, 0.12 / 0.00465, 0.73 / 0.0461	12 (1.52)	a) up in WT 5%CO2 -cyan-	0.145 (3.92)	c) metabolic enzymes
300	hypothetical protein CHLREDRAFT_145395	gi 159467637	Cre03.g185600.t1.1	0.62 / 0.0539, 0 / 0, 0 / 0	0.13 / 0.0985, 0.13 / 0.00477, 0.13 / 0.00592	0 / 0, 0 / 0, 0 / 0	0 / 0, 0.13 / 0.00504, 0.13 / 0.0082	12 (0.0219)	a) up in WT 5%CO2 -cyan-	0.115 (4.88)	c) metabolic enzymes
301	5, 10-methylenetetrahydrofolate dehydrogenase	gi 159489876	Cre03.g182450.t1.2	0.09 / 0.00782, 0 / 0, 0.55 / 0.023	0 / 0, 1.01 / 0.0371, 1.4 / 0.0637	0 / 0, 0.19 / 0.0128, 0.42 / 0.0222	0 / 0, 0.55 / 0.0213, 0.19 / 0.012	12 (1.99)	a) up in WT 5%CO2 -cyan-	0.106 (3.05)	c) metabolic enzymes
302	aspartate carbamoyltransferase	gi 159487733	Cre02.g079700.t1.2	0.23 / 0.02, 0 / 0, 0.51 / 0.0214	0 / 0, 1.06 / 0.0389, 1.06 / 0.0483	0 / 0, 0.23 / 0.0155, 0 / 0	0 / 0, 0.23 / 0.0145	12 (1.06)	a) up in WT 5%CO2 -cyan-	0.0915 (3.67)	c) metabolic enzymes
303	acetyl-coa biotin carboxyl carrier	gi 159484803	Cre17.g715250.t1.2	3.29 / 0.286, 1.53 / 0.332, 1.88 / 0.0787	0.94 / 0.712, 3.9 / 0.143, 1.88 / 0.0856	1.21 / 0.134, 0.94 / 0.0632, 1.53 / 0.0808	0.94 / 0.243, 0.7 / 0.0271, 1.53 / 0.0966	8 (0.782)	b) up in WT -blue-	0.859 (1.55)	c) metabolic enzymes
304	acetyl-coa biotin carboxyl carrier	gi 159463778	Cre01.g037850.t1.1	2.57 / 0.223, 4.23 / 0.919, 5.74 / 0.24	0 / 0, 6.65 / 0.244, 3.6 / 0.164	0.89 / 0.0983, 1.77 / 0.119, 4.23 / 0.223	0 / 0, 4.23 / 0.164, 3.6 / 0.227	11 (1.99)	c) up in WT air -purple-	1.45 (3.34)	c) metabolic enzymes
305	carbamoyl phosphate synthase, large subunit	gi 159464965	Cre08.g358580.t1.1	2.09 / 0.182, 0.06 / 0.013, 0.12 / 0.00503	0 / 0, 0.15 / 0.0055, 0.12 / 0.00546	0.28 / 0.0309, 0.15 / 0.0101, 0.25 / 0.0132	0 / 0, 0.39 / 0.0151, 0.43 / 0.0271	11 (1.35)	c) up in WT air -purple-	0.209 (5.57)	c) metabolic enzymes
306	phosphoribosylanthranilate isomerase	gi 159477699	Cre12.g519000.t1.1	0.58 / 0.126, 0.58 / 0.0243	0.12 / 0.0044, 0.12 / 0.00546	0 / 0, 0.41 / 0.0217	0 / 0, 0.12 / 0.00757	11 (1.95)	c) up in WT air -purple-	0.158 (11.5)	c) metabolic enzymes
307	predicted protein	gi 159485312	Cre15.g644051.t1.1	1.27 / 0.11, 0.12 / 0.0261, 0.34 / 0.0142	0 / 0, 0.34 / 0.0125, 0.42 / 0.0191	0.06 / 0.00662, 0.06 / 0.00403, 0.19 / 0.01	0 / 0, 0.6 / 0.0379	11 (1.92)	c) up in WT air -purple-	0.158 (5.01)	c) metabolic enzymes
308	mitochondrial ATP synthase subunit 5, OSCP subunit	gi 159475757	Cre16.g680000.t1.2	1.07 / 0.0929, 0 / 0, 0.13 / 0.00545	0 / 0, 0.27 / 0.00991, 0.27 / 0.0123	0.27 / 0.0298, 0 / 0, 0 / 0	0 / 0, 0.13 / 0.0082	11 (0.635)	c) up in WT air -purple-	0.103 (4.9)	c) metabolic enzymes
309	fructose-1, 6-bisphosphate aldolase	gi 159487573	Cre02.g093450.t1.2	0.91 / 0.079, 0 / 0, 0 / 0	0 / 0, 0.38 / 0.0139, 0.08 / 0.00364	0.08 / 0.00883, 0.08 / 0.00538, 0.08 / 0.00423	0 / 0, 0.08 / 0.0031, 0 / 0	11 (0.688)	c) up in WT air -purple-	0.0829 (6.06)	c) metabolic enzymes
310	2-C-methyl-D-erythritol 2, 4-cyclodiphosphate	gi 159465549	NA	0 / 0, 0.32 / 0.0695, 4.28 / 0.179	0 / 0, 3.6 / 0.132, 3.6 / 0.164	0.32 / 0.0353, 1 / 0.0672, 1.64 / 0.0866	0 / 0, 0 / 0, 1 / 0.0631	14 (0.352)	f) down in pyr- 5%CO2 (0.148 / 0.0442)	0.257 (3.88)	c) metabolic enzymes
311	hypothetical protein CHLREDRAFT_193467	gi 159481965	Cre14.g614300.t1.2	0.13 / 0.0113, 0.19 / 0.0413, 0.19 / 0.00796	0 / 0, 0.81 / 0.0297, 0.92 / 0.0419	0.06 / 0.00662, 0.61 / 0.041, 0.51 / 0.0269	0 / 0, 0.169 / 0.00653, 0.27 / 0.017	14 (0.342)	f) down in pyr- 5%CO2 (0.161 / 0.0404)	0.0723 (2.92)	c) metabolic enzymes
312	phosphoserine aminotransferase	gi 159464395	Cre07.g331550.t1.2	0.24 / 0.0208, 0.54 / 0.0226	0 / 0, 2.64 / 0.0969, 2.39 / 0.109	0.15 / 0.0166, 0.65 / 0.0437, 0.91 / 0.0481	0 / 0, 0.78 / 0.0302, 3.85 / 0.243	9 (0.189)	g) up in 5%CO2 -green-	0.251 (3.15)	c) metabolic enzymes
313	serine hydroxymethyltransferase 2	gi 159487140	NA	0.13 / 0.0113, 0 / 0, 0.13 / 0.00545	0 / 0, 0.73 / 0.0268, 1.5 / 0.0683	0 / 0, 0 / 0, 0.13 / 0.00687	0 / 0, 0 / 0, 2.19 / 0.138	9 (0.543)	g) up in 5%CO2 -green-	0.122 (9.88)	c) metabolic enzymes
314	acyl-carrier protein	gi 159471275	Cre13.g577100.t1.2	4.5 / 0.391, 1.08 / 0.235, 2.38 / 0.0997	1.65 / 1.25, 1.65 / 0.0606, 2.38 / 0.108	6.02 / 0.665, 1.65 / 0.111, 1.65 / 0.0872	4.5 / 1.17, 1.65 / 0.0639, 4.5 / 0.284	15 (1.06)	h) equal (0.19 / 0.877) -grey-	1.19	c) metabolic enzymes
315	isocitrate lyase	gi 159474436	Cre06.g282800.t1.2	7.01 / 0.609, 0 / 0, 2.25 / 0.0942	0.74 / 0.561, 2.03 / 0.0745, 3.29 / 0.15	4.66 / 0.515, 1.83 / 0.123, 3.93 / 0.208	0.63 / 0.163, 3.6 / 0.139, 2.49 / 0.157	15 (1.33)	h) equal (0.197 / 0.91) -grey-	0.733	c) metabolic enzymes
316	predicted protein	gi 159471802	Cre12.g555951.t1.1	0.27 / 0.0235, 1.04 / 0.226, 7.49 / 0.314	0 / 0, 7.49 / 0.275, 4.28 / 0.195	0 / 0, 5.69 / 0.383, 9.77 / 0.516	0.27 / 0.0699, 5.69 / 0.22, 2.28 / 0.144	15 (0.0815)	h) equal (0.151 / 0.692) -grey-	0.621	c) metabolic enzymes

Molecular Physiology of the *Chlamydomonas pyrenoid*

317	glutamate-1-semialdehyde aminotransferase	gi 159478861	Cre03.g158000.t1.2	2.39 / 0.208, 0 / 0, 3.98 / 0.167	0 / 0, 9.75 / 0.358, 7.87 / 0.358	1.03 / 0.114, 2.39 / 0.161, 4.31 / 0.228	0 / 0, 7.32 / 0.284, 3.98 / 0.251	15 (0.975)	h) equal (0.176 / 0.809) -grey-	0.558	c) metabolic enzymes
318	predicted protein	gi 159468534	Cre07.g344400.t1.2	0.68 / 0.0591, 0.16 / 0.0347, 3.12 / 0.131	0 / 0, 4.55 / 0.167, 12.6 / 0.571	0.16 / 0.0177, 2.82 / 0.19, 5.93 / 0.313	0 / 0, 0.95 / 0.0368, 7.05 / 0.445	15 (0.979)	h) equal (0.173 / 0.794) -grey-	0.516	c) metabolic enzymes
319	predicted protein	gi 159468766	Cre07.g344550.t1.2	0.99 / 0.086, 0 / 0, 3.27 / 0.137	0 / 0, 4.8 / 0.176, 9.69 / 0.441	0 / 0, 2.96 / 0.199, 5.26 / 0.278	0 / 0, 2.4 / 0.093, 6.29 / 0.397	15 (0.887)	h) equal (0.178 / 0.819) -grey-	0.474	c) metabolic enzymes
320	adenylate kinase 3	gi 159484978	Cre12.g494850.t1.2	2.27 / 0.197, 0.38 / 0.0825, 1.36 / 0.057	0 / 0, 2.27 / 0.0833, 3.51 / 0.16	3.51 / 0.388, 1.36 / 0.0915, 1.36 / 0.0718	0 / 0, 0.91 / 0.0353, 6.72 / 0.424	15 (1.11)	h) equal (0.187 / 0.861) -grey-	0.417	c) metabolic enzymes
321	adenylosuccinate synthase	gi 159469564	Cre17.g734100.t1.2	0.14 / 0.0122, 0.07 / 0.0152, 3.91 / 0.164	0 / 0, 5.33 / 0.196, 6.66 / 0.303	0.14 / 0.0155, 3.61 / 0.243, 4.23 / 0.223	0 / 0, 1.29 / 0.05, 4.94 / 0.312	15 (0.783)	h) equal (0.171 / 0.785) -grey-	0.402	c) metabolic enzymes
322	aspartate semialdehyde dehydrogenase	gi 159473875	Cre09.g389689.t1.1	1.21 / 0.105, 0.61 / 0.132, 4.27 / 0.179	0 / 0, 3.15 / 0.116, 8.16 / 0.371	0.61 / 0.0673, 1.8 / 0.121, 1.58 / 0.0835	0 / 0, 1.8 / 0.0697, 4.27 / 0.269	15 (1.29)	h) equal (0.194 / 0.893) -grey-	0.397	c) metabolic enzymes
323	malate dehydrogenase	gi 159469941	Cre03.g194850.t1.2	1.81 / 0.157, 0 / 0, 1.17 / 0.049	0 / 0, 4.59 / 0.168, 5.1 / 0.232	1.36 / 0.15, 1.58 / 0.106, 2.34 / 0.124	0.09 / 0.0233, 1.58 / 0.0612, 6.89 / 0.435	15 (1.01)	h) equal (0.179 / 0.822) -grey-	0.395	c) metabolic enzymes
324	magnesium chelatase subunit I	gi 159466070	NA	1.16 / 0.101, 1.01 / 0.219, 1.66 / 0.0695	0 / 0, 3.99 / 0.146, 2.06 / 0.0938	0.23 / 0.0254, 1.01 / 0.0679, 2.28 / 0.12	0 / 0, 0.88 / 0.0341, 5.59 / 0.353	15 (1.04)	h) equal (0.19 / 0.876) -grey-	0.323	c) metabolic enzymes
325	hypothetical protein CHLREDRAFT_184895	gi 159477543	Cre12.g528000.t1.2	1.05 / 0.0912, 0 / 0, 1.94 / 0.0813	0 / 0, 2.92 / 0.107, 3.87 / 0.176	0.54 / 0.0596, 2.4 / 0.161, 3.21 / 0.17	0 / 0, 3.21 / 0.124, 3.53 / 0.223	15 (0.557)	h) equal (0.159 / 0.724) -grey-	0.313	c) metabolic enzymes
326	aconitate hydratase	gi 159462944	Cre01.g042750.t1.2	1.82 / 0.158, 0.08 / 0.0174, 1.72 / 0.072	0.04 / 0.0303, 3.57 / 0.131, 3.24 / 0.147	1.1 / 0.121, 0.88 / 0.0592, 2.15 / 0.114	0.09 / 0.0233, 1.02 / 0.0395, 2.66 / 0.168	15 (1.54)	h) equal (0.207 / 0.951) -grey-	0.284	c) metabolic enzymes
327	dihydroliipoamide acetyltransferase	gi 159478837	Cre03.g158900.t1.2	3.06 / 0.266, 0 / 0, 0.34 / 0.0142	0.08 / 0.0606, 1.25 / 0.0459, 1.61 / 0.0733	1.81 / 0.2, 0.34 / 0.0229, 2.25 / 0.119	0.16 / 0.0414, 0.68 / 0.0263, 2.02 / 0.127	15 (1.13)	h) equal (0.189 / 0.874) -grey-	0.261	c) metabolic enzymes
328	cobalamin-independent methionine synthase	gi 159489910	Cre03.g180750.t1.2	1.61 / 0.14, 0.08 / 0.0174, 1.42 / 0.0595	0 / 0, 2.13 / 0.0782, 3.53 / 0.161	0.25 / 0.0276, 1.42 / 0.0955, 2.91 / 0.154	0 / 0, 0.74 / 0.0287, 3.36 / 0.212	15 (1.89)	h) equal (0.22 / 0.992) -grey-	0.255	c) metabolic enzymes
329	full-length thiazole biosynthetic enzyme	gi 159481205	NA	2.31 / 0.201, 0.19 / 0.0413, 1.16 / 0.0486	0 / 0, 1.79 / 0.0657, 2.31 / 0.105	1.16 / 0.128, 0.29 / 0.0195, 1.16 / 0.0613	0 / 0, 1.79 / 0.0693, 1.56 / 0.0985	15 (0.993)	h) equal (0.184 / 0.849) -grey-	0.22	c) metabolic enzymes
330	6, 7-dimethyl-8-ribityllumazine synthase	gi 159487499	Cre02.g088850.t1.2	0.95 / 0.0825, 0 / 0, 0.95 / 0.0398	0 / 0, 0.49 / 0.018, 1.91 / 0.0869	1.91 / 0.211, 0 / 0, 1.91 / 0.101	0 / 0, 0.31 / 0.012, 2.8 / 0.177	15 (0.345)	h) equal (0.155 / 0.708) -grey-	0.191	c) metabolic enzymes
331	enolase	gi 159489988	Cre12.g513200.t1.2	0.85 / 0.0738, 0 / 0, 2.02 / 0.0846	0 / 0, 1.36 / 0.0499, 1.09 / 0.0496	0.2 / 0.0221, 1.22 / 0.082, 1.51 / 0.0798	0 / 0, 0.63 / 0.0244, 3.36 / 0.212	15 (1.29)	h) equal (0.187 / 0.862) -grey-	0.178	c) metabolic enzymes
332	malate dehydrogenase	gi 159490405	Cre12.g483950.t1.2	1.89 / 0.164, 0 / 0, 0.28 / 0.0117	0.18 / 0.136, 0.77 / 0.0283, 0.63 / 0.0287	1.89 / 0.209, 0.18 / 0.0121, 0.28 / 0.0148	0.18 / 0.0466, 0.09 / 0.00349, 0.28 / 0.0177	15 (1)	h) equal (0.184 / 0.847) -grey-	0.176	c) metabolic enzymes
333	isopropylmalate synthase	gi 159477008	NA	1.53 / 0.133, 0 / 0, 1.07 / 0.0448	0 / 0, 3.02 / 0.111, 2.52 / 0.115	0.39 / 0.0431, 0.39 / 0.0262, 1.37 / 0.0724	0 / 0, 0.7 / 0.0271, 0.81 / 0.0511	15 (0.503)	h) equal (0.151 / 0.685) -grey-	0.163	c) metabolic enzymes
334	isopropylmalate dehydratase, small subunit	gi 159476606	Cre06.g252650.t1.2	0.69 / 0.0599, 0 / 0, 0.93 / 0.039	0 / 0, 1.51 / 0.0554, 1.86 / 0.0847	0.69 / 0.0762, 0.69 / 0.0464, 1.51 / 0.0798	0 / 0, 0.69 / 0.0267, 2.26 / 0.143	15 (1.07)	h) equal (0.18 / 0.831) -grey-	0.16	c) metabolic enzymes
335	hypothetical protein CHLREDRAFT_115042	gi 159466162	Cre06.g300700.t1.1	1.96 / 0.17, 0 / 0, 0.97 / 0.0406	0 / 0, 1.58 / 0.058, 1.25 / 0.0569	0.5 / 0.0552, 0.31 / 0.0208, 0.72 / 0.038	0 / 0, 0.31 / 0.012, 2.38 / 0.15	15 (1.39)	h) equal (0.198 / 0.911) -grey-	0.158	c) metabolic enzymes
336	predicted protein	gi 159484292	Cre01.g061077.t1.1	1.92 / 0.167, 0 / 0, 0 / 0	0 / 0, 1.36 / 0.0499, 1.12 / 0.051	0.71 / 0.0784, 0.38 / 0.0256, 0.9 / 0.0475	0 / 0, 0.24 / 0.0093, 2.25 / 0.142	15 (1.73)	h) equal (0.215 / 0.977) -grey-	0.15	c) metabolic enzymes
337	beta subunit of mitochondrial ATP synthase	gi 159466892	Cre17.g698000.t1.2	3.26 / 0.283, 0 / 0, 0.23 / 0.00963	0 / 0, 1.12 / 0.0513, 0.3 / 0.0137	1.67 / 0.184, 0.17 / 0.044, 0.05 / 0.00264	0 / 0, 0.11 / 0.00426, 0.3 / 0.0189	15 (0.1)	h) equal (0.145 / 0.659) -grey-	0.147	c) metabolic enzymes
338	glutamine synthetase	gi 159469782	Cre12.g530650.t2.1, Cre12.g530650.t1.1	0.36 / 0.0313, 0 / 0, 1.14 / 0.0478	0 / 0, 1.31 / 0.0481, 2.39 / 0.109	0.36 / 0.0397, 1.31 / 0.0881, 0.84 / 0.0444	0 / 0, 0.46 / 0.0178, 1.91 / 0.121	15 (1.01)	h) equal (0.185 / 0.852) -grey-	0.143	c) metabolic enzymes
339	acetolactate synthase, small subunit	gi 159484278	Cre01.g055453.t1.1	0.73 / 0.0634, 0.13 / 0.0282, 1.07 / 0.0448	0 / 0, 1.8 / 0.0661, 2.57 / 0.117	0 / 0, 0.95 / 0.0639, 1.2 / 0.0634	0 / 0, 1.34 / 0.0519, 0.27 / 0.017	15 (0.522)	h) equal (0.152 / 0.69) -grey-	0.135	c) metabolic enzymes
340	6-phosphogluconolactonase-like protein	gi 159463708	Cre01.g034400.t1.1	1.01 / 0.0877, 0 / 0, 0 / 0	0 / 0, 0.26 / 0.00954, 1.01 / 0.046	1.25 / 0.138, 0 / 0, 0.42 / 0.0222	0 / 0, 0.12 / 0.00465, 3.03 / 0.191	15 (0.955)	h) equal (0.183 / 0.845) -grey-	0.131	c) metabolic enzymes
341	UDP-glucose dehydrogenase	gi 159479860	Cre06.g278185.t1.1	1.77 / 0.154, 0 / 0, 0.72 / 0.0302	0 / 0, 1.18 / 0.0433, 1.18 / 0.0537	0.27 / 0.0298, 0.52 / 0.035, 0.93 / 0.0491	0 / 0, 0.52 / 0.0201, 0.82 / 0.0518	15 (0.642)	h) equal (0.169 / 0.774) -grey-	0.122	c) metabolic enzymes
342	hypothetical protein CHLREDRAFT_114298	gi 159491024	Cre03.g172000.t1.2	0.33 / 0.0287, 0 / 0, 0.94 / 0.0394	0 / 0, 1.35 / 0.0495, 1.84 / 0.0838	0.21 / 0.0141, 1.35 / 0.0713, 1.84 / 0.116	0 / 0, 1.14 / 0.0442, 1.84 / 0.116	15 (0.698)	h) equal (0.173 / 0.796) -grey-	0.117	c) metabolic enzymes
343	cysteine synthase	gi 159467511	Cre16.g685550.t1.2	0.65 / 0.0565, 0 / 0, 0.18 / 0.00754	0 / 0, 0.95 / 0.0349, 0.95 / 0.0432	0.52 / 0.0574, 0.29 / 0.0195, 0.4 / 0.0211	0 / 0, 0.4 / 0.0155, 2.81 / 0.177	15 (0.467)	h) equal (0.166 / 0.764) -grey-	0.114	c) metabolic enzymes
344	4-hydroxy-3-methylbut-2-enyl diphosphate	gi 159486551	Cre08.g372950.t1.2	0.64 / 0.0556, 0.2 / 0.0434, 0.85 / 0.0356	0 / 0, 1.22 / 0.0448, 1.37 / 0.0624	0.2 / 0.0221, 0.54 / 0.0363, 1.09 / 0.0576	0 / 0, 0.13 / 0.00504, 0.97 / 0.0612	15 (0.521)	h) equal (0.162 / 0.74) -grey-	0.111	c) metabolic enzymes
345	ADP-glucose pyrophosphorylase large subunit	gi 159470605	NA	0.68 / 0.0591, 0.12 / 0.0261, 0.19 / 0.00796	0 / 0, 0.78 / 0.0286, 0.99 / 0.0451	0.33 / 0.0364, 0.58 / 0.039, 0.78 / 0.0412	0 / 0, 0.12 / 0.00465, 2.15 / 0.136	15 (1.45)	h) equal (0.2 / 0.923) -grey-	0.111	c) metabolic enzymes
346	biotin carboxylase, acetyl-CoA carboxylase	gi 159488652	Cre08.g359350.t1.2	0.73 / 0.0634, 0.13 / 0.0282, 0.96 / 0.0402	0 / 0, 0.53 / 0.0194, 1.08 / 0.0492	0.13 / 0.0144, 0.63 / 0.0424, 1.21 / 0.0639	0 / 0, 0.53 / 0.0205, 0.96 / 0.0606	15 (0.0718)	h) equal (0.153 / 0.696) -grey-	0.106	c) metabolic enzymes
347	mitochondrial cytochrome c oxidase subunit	gi 159466404	Cre06.g304350.t1.2	1.43 / 0.124, 0 / 0, 0 / 0	0 / 0, 0.7 / 0.0257, 1.03 / 0.0469	1.03 / 0.114, 0 / 0, 0 / 0	0 / 0, 0.19 / 0.00736, 0.7 / 0.0442	15 (1.4)	h) equal (0.202 / 0.928) -grey-	0.095	c) metabolic enzymes
348	carbamoyl phosphate synthase, small subunit	gi 159466324	Cre06.g308500.t1.2	1.29 / 0.112, 0 / 0, 0.07 / 0.00293	0 / 0, 0.37 / 0.0136, 0.89 / 0.0405	0.66 / 0.0729, 0.14 / 0.00941, 0.37 / 0.0195	0 / 0, 0.21 / 0.00814, 1.15 / 0.0726	15 (1.55)	h) equal (0.204 / 0.939) -grey-	0.0922	c) metabolic enzymes
349	argininosuccinate synthase	gi 159477301	Cre09.g416050.t1.2	1.18 / 0.102, 0 / 0, 0.21 / 0.0088	0 / 0, 0.3 / 0.011, 0.38 / 0.0173	0.58 / 0.064, 0.14 / 0.00941, 0.3 / 0.0158	0 / 0, 0.48 / 0.0186, 1.18 / 0.0745	15 (0.798)	h) equal (0.178 / 0.821) -grey-	0.0845	c) metabolic enzymes

Chapter 8: Appendices

350	ADP-glucose pyrophosphorylase small subunit	gi 159467349	Cre03.g188250.t1.2	0.77 / 0.0669, 0 / 0, 0.33 / 0.0138	0 / 0, 0.49 / 0.018, 0.88 / 0.0401	0.19 / 0.021, 0.19 / 0.0128, 0.49 / 0.0259	0 / 0, 0.12 / 0.00465, 1.8 / 0.114	15 (1.33)	h) equal (0.197 / 0.907) -grey-	0.0831	c) metabolic enzymes
351	hypothetical protein CHLREDRAFT_137847	gi 159475539	Cre16.g679600.t1.2	0.76 / 0.066, 0 / 0, 0.12 / 0.00503	0 / 0, 1.48 / 0.0543, 0.76 / 0.0346	0 / 0, 0.57 / 0.0629, 0.57 / 0.0383, 0.41 / 0.0159, 0.25 / 0.0132	0 / 0, 0.41 / 0.0159, 0.41 / 0.0259	15 (0.713)	h) equal (0.161 / 0.737) -grey-	0.0829	c) metabolic enzymes
352	predicted protein	gi 159467048	Cre17.g706800.t1.2	1.31 / 0.114, 0 / 0, 0.32 / 0.0134	0 / 0, 0.75 / 0.0275, 0.32 / 0.0146	0.15 / 0.0166, 0 / 0, 1.01 / 0.0534	0 / 0, 0.75 / 0.0291, 0.52 / 0.0328	15 (0.69)	h) equal (0.172 / 0.792) -grey-	0.079	c) metabolic enzymes
353	hypothetical protein CHLREDRAFT_150548	gi 159478294	Cre17.g725050.t2.1, Cre17.g725050.t1.2	0 / 0, 1.8 / 0.0754	0 / 0, 0.99 / 0.0363, 1.8 / 0.0819	0 / 0, 0.41 / 0.0276, 0.41 / 0.0217	0 / 0, 0.41 / 0.0159, 0.41 / 0.0259	15 (0.626)	h) equal (0.165 / 0.756) -grey-	0.0747	c) metabolic enzymes
354	predicted protein	gi 159471067	NA	0.12 / 0.0104, 0.12 / 0.0261, 0 / 0	0 / 0, 0 / 0, 1.49 / 0.0678	0 / 0, 0.41 / 0.0276, 1.22 / 0.0645	0 / 0, 0 / 0, 1.22 / 0.077	15 (1.45)	h) equal (0.201 / 0.923) -grey-	0.0717	c) metabolic enzymes
355	light-dependent protochlorophyllide reductase	gi 159462468	Cre01.g015350.t1.1	0.46 / 0.04, 0 / 0, 0.97 / 0.0406	0 / 0, 1.29 / 0.0473, 0.83 / 0.0378	0 / 0, 0.35 / 0.0235, 0.57 / 0.0301	0 / 0, 0.97 / 0.0376, 0.25 / 0.0158	15 (1.07)	h) equal (0.191 / 0.881) -grey-	0.0715	c) metabolic enzymes
356	riboflavin kinase	gi 159463528	Cre01.g025250.t1.1	0 / 0, 0.08 / 0.0174, 0.45 / 0.0188	0 / 0, 1.43 / 0.0525, 0.68 / 0.031	0 / 0, 0.56 / 0.0377, 0.81 / 0.0428	0 / 0, 0.56 / 0.0217, 0.81 / 0.0353	15 (0.621)	h) equal (0.166 / 0.763) -grey-	0.0675	c) metabolic enzymes
357	dihydroipoamide dehydrogenase	gi 159463380	Cre01.g016500.t1.1, Cre01.g016514.t1.1	0.7 / 0.0608, 0.05 / 0.0109, 0.24 / 0.0101	0 / 0, 0.24 / 0.00881, 0.31 / 0.0141	0.24 / 0.0265, 0.17 / 0.0114, 0.8 / 0.0423	0 / 0, 0.24 / 0.0093, 0.9 / 0.0568	15 (0.128)	h) equal (0.153 / 0.7) -grey-	0.0658	c) metabolic enzymes
358	argininosuccinate lyase	gi 159462570	Cre01.g021251.t1.1	1.46 / 0.127, 0 / 0, 0 / 0	0 / 0, 0.14 / 0.00514, 0.29 / 0.0132	0.14 / 0.0155, 0 / 0, 0.14 / 0.0074	0 / 0, 0.14 / 0.00542, 1.16 / 0.0732	15 (0.286)	h) equal (0.153 / 0.697) -grey-	0.0647	c) metabolic enzymes
359	acetohydroxyacid dehydratase	gi 159470063	Cre03.g206600.t1.2	0.41 / 0.0356, 0.1 / 0.0217, 0.16 / 0.0067	0 / 0, 0.28 / 0.0103, 0.49 / 0.0223	0.1 / 0.011, 0.16 / 0.0108, 0.28 / 0.0148	0 / 0, 0.1 / 0.00387, 1.56 / 0.0985	15 (0.658)	h) equal (0.165 / 0.757) -grey-	0.0618	c) metabolic enzymes
360	UDP-glucose 4-epimerase	gi 159481273	Cre04.g214502.t1.1	0.08 / 0.00695, 0 / 0, 0.38 / 0.0159	0 / 0, 0.76 / 0.0279, 1.25 / 0.0569	0 / 0, 0.38 / 0.0256, 0.76 / 0.0401	0 / 0, 0.08 / 0.0031, 0.91 / 0.0574	15 (0.66)	h) equal (0.167 / 0.767) -grey-	0.0614	c) metabolic enzymes
361	prephenate dehydratase	gi 159476964	NA	0.65 / 0.0565, 0 / 0, 0.53 / 0.0222	0 / 0, 1.04 / 0.0382, 0.53 / 0.0241	0 / 0, 0.43 / 0.0289, 0.43 / 0.0227	0 / 0, 0.53 / 0.0205, 0.33 / 0.0208	15 (1.3)	h) equal (0.191 / 0.882) -grey-	0.0614	c) metabolic enzymes
362	hypothetical protein CHLREDRAFT_128624	gi 159467439	Cre16.g682100.t1.2	0.55 / 0.0478, 0 / 0, 0.39 / 0.0163	0 / 0, 0.55 / 0.0202, 0.55 / 0.025	0.12 / 0.0132, 0.55 / 0.037, 0.39 / 0.0206	0 / 0, 0.12 / 0.00465, 0.73 / 0.0461	15 (1.52)	h) equal (0.206 / 0.946) -grey-	0.0606	c) metabolic enzymes
363	phosphoenolpyruvate carboxykinase, splice variant	gi 159473683	Cre02.g141400.t1.2	1.45 / 0.126, 0 / 0, 0 / 0	0 / 0, 0.23 / 0.00844, 0.17 / 0.00774	0.59 / 0.0651, 0.05 / 0.00336, 0.11 / 0.00581	0 / 0, 0.05 / 0.00194, 0.17 / 0.0107	15 (0.0104)	h) equal (0.141 / 0.64) -grey-	0.0601	c) metabolic enzymes
364	malate dehydrogenase	gi 159489202	Cre10.g423250.t1.2	0.19 / 0.0165, 0 / 0, 0.19 / 0.00796	0 / 0, 0.42 / 0.0154, 0.69 / 0.0314	0.19 / 0.021, 0.3 / 0.0202, 0.69 / 0.0365	0 / 0, 0.3 / 0.0116, 0.69 / 0.0435	15 (0.23)	h) equal (0.129 / 0.573) -grey-	0.0535	c) metabolic enzymes
365	transaldolase	gi 159469019	Cre14.g630847.t1.1, Cre14.g630835.t1.1	0.58 / 0.0504, 0 / 0, 0.16 / 0.0067	0 / 0, 0.83 / 0.0305, 0.46 / 0.0209	0.35 / 0.0386, 0.16 / 0.0108, 0.46 / 0.0243	0 / 0, 0.26 / 0.0101, 0.16 / 0.0101	15 (0.192)	h) equal (0.146 / 0.664) -grey-	0.0531	c) metabolic enzymes
366	dual function alcohol dehydrogenase / acetaldehyde	gi 159491249	Cre17.g746997.t1.1	0.76 / 0.066, 0.03 / 0.00652, 0.13 / 0.00545	0 / 0, 0.17 / 0.00624, 0.65 / 0.0296	0.06 / 0.00662, 0.13 / 0.00874, 0.33 / 0.0174	0.03 / 0.00777, 0.06 / 0.00232, 0.33 / 0.0208	15 (0.222)	h) equal (0.16 / 0.737) -grey-	0.0466	c) metabolic enzymes
367	tryptophan synthase beta subunit	gi 159490872	NA	0.48 / 0.0417, 0 / 0, 0.07 / 0.00293	0 / 0, 0.8 / 0.0294, 0.48 / 0.0219	0.07 / 0.00773, 0.14 / 0.00941, 0.22 / 0.0116	0 / 0, 0.22 / 0.00852, 0.48 / 0.0303	15 (1.62)	h) equal (0.206 / 0.947) -grey-	0.0429	c) metabolic enzymes
368	rieske ferredoxin	gi 159487965	Cre02.g093650.t1.2	1.23 / 0.107, 0.22 / 0.0478, 43.9 / 1.84	0 / 0, 3.96 / 0.145, 5.06 / 0.23	1.23 / 0.136, 5.06 / 0.34, 12.5 / 0.661	0 / 0, 5.06 / 0.196, 1.23 / 0.0776	9 (0.12)	i) up in air (0.199 / 0.1) -magenta-	1.64 (4.82)	c) metabolic enzymes
369	predicted protein	gi 159484968	Cre12.g495850.t1.2	6.47 / 0.562, 1.44 / 0.313, 3.27 / 0.137	0 / 0, 7.35 / 0.27, 3.78 / 0.172	2.82 / 0.311, 6.47 / 0.435, 10.7 / 0.564	0.12 / 0.0311, 5.68 / 0.22, 1.44 / 0.0909	9 (1.05)	i) up in air (0.494 / 0.00601) -magenta-	1.22 (2.96)	c) metabolic enzymes
370	pyruvate kinase	gi 159469714	Cre12.g533550.t1.1	2 / 0.174, 0.59 / 0.128, 1.83 / 0.0767	0 / 0, 3.5 / 0.128, 2.37 / 0.108	0.89 / 0.0983, 2.18 / 0.147, 2.57 / 0.136	0 / 0, 2.57 / 0.0996, 1.67 / 0.105	9 (1.78)	i) up in air (0.325 / 0.0448) -magenta-	0.398 (1.72)	c) metabolic enzymes
371	glutamine synthetase	gi 159483707	Cre02.g113200.t1.1	1.84 / 0.16, 0 / 0, 0.35 / 0.0147	0 / 0, 0.81 / 0.0297, 1.11 / 0.0505	0.81 / 0.0894, 0.56 / 0.0377, 1.84 / 0.0972	0 / 0, 0.16 / 0.0062, 0.35 / 0.0221	9 (1.51)	i) up in air (0.289 / 0.0551) -magenta-	0.209 (3.67)	c) metabolic enzymes
372	acetyl CoA synthetase	gi 159488061	Cre07.g353450.t1.2	1.96 / 0.17, 0.09 / 0.0195, 0.48 / 0.0201	0 / 0, 0.54 / 0.0198, 0.84 / 0.0382	0.61 / 0.0673, 0.14 / 0.00941, 1.18 / 0.0623	0 / 0, 0.54 / 0.0209, 0.54 / 0.0341	9 (0.415)	i) up in air (0.218 / 0.0872) -magenta-	0.183 (3.09)	c) metabolic enzymes
373	pyruvate kinase	gi 159473557	Cre02.g147900.t4.1, Cre02.g147900.t3.1, Cre02.g147900.t2.1	1.95 / 0.169, 0 / 0, 0.18 / 0.00754	0 / 0, 0.31 / 0.0114, 0.46 / 0.0209	0.31 / 0.0342, 0.72 / 0.0484, 0.72 / 0.038	0 / 0, 0.18 / 0.00697, 0.54 / 0.0341	9 (0.3)	i) up in air (0.213 / 0.1) -magenta-	0.156 (4.06)	c) metabolic enzymes
374	anthranilate synthase, alpha subunit	gi 159466362	Cre06.g306601.t1.1	1.13 / 0.0981, 0.11 / 0.0239, 0.38 / 0.0159	0 / 0, 0.62 / 0.0228, 0.91 / 0.0414	0.24 / 0.0265, 0.91 / 0.0612, 0.91 / 0.0481	0 / 0, 0.46 / 0.0178, 0.24 / 0.0151	9 (1.67)	i) up in air (0.357 / 0.0363) -magenta-	0.144 (2.82)	c) metabolic enzymes
375	3-ketoacyl-CoA-synthase	gi 159486340	NA	0.99 / 0.086, 0 / 0, 0.11 / 0.00461	0 / 0, 0.3 / 0.011, 0.17 / 0.00774	0.61 / 0.0673, 0.05 / 0.00336, 0.24 / 0.0127	0 / 0, 0 / 0, 0.24 / 0.0151	9 (0.427)	i) up in air (0.236 / 0.0956) -magenta-	0.0913 (5.13)	c) metabolic enzymes
376	predicted protein	gi 159469361	Cre14.g623000.t1.1	1.06 / 0.0921, 0 / 0, 0.13 / 0.00545	0 / 0, 0.13 / 0.00477, 0.13 / 0.00592	0.44 / 0.0486, 0.13 / 0.00874, 0.13 / 0.00687	0 / 0, 0.13 / 0.00504, 0 / 0	9 (0.831)	i) up in air (0.243 / 0.0815) -magenta-	0.0848 (10.3)	c) metabolic enzymes
377	hypothetical protein CHLREDRAFT_120516	gi 159479888	Cre06.g278148.t1.1	0.36 / 0.0313, 0.11 / 0.0239, 0.11 / 0.00461	0 / 0, 0.23 / 0.00844, 0 / 0	0.67 / 0.074, 0.11 / 0.0074, 0.23 / 0.0122	0 / 0, 0 / 0, 0 / 0	9 (1.31)	i) up in air (0.347 / 0.0352) -magenta-	0.0804 (18.2)	c) metabolic enzymes
378	hypothetical protein CHLREDRAFT_194613	gi 159488208	Cre01.g004950.t1.1	0.66 / 0.0573, 0 / 0, 0.14 / 0.00586	0 / 0, 0.29 / 0.0106, 0.14 / 0.00637	0.46 / 0.0508, 0.29 / 0.0195, 0.29 / 0.0153	0 / 0, 0.29 / 0.0112, 0.29 / 0.0183	9 (0.99)	i) up in air (0.251 / 0.0722) -magenta-	0.0781 (3.2)	c) metabolic enzymes
379	3-dehydroquinate synthase	gi 159475948	Cre08.g368950.t1.2	0.06 / 0.00521, 0 / 0, 0.06 / 0.00251	0 / 0, 0.45 / 0.0165, 0.75 / 0.0341	0.2 / 0.0221, 0.13 / 0.00874, 0.36 / 0.019	0 / 0, 0.13 / 0.00504, 0.54 / 0.0341	11 (0.861)	j) down in WT air (0.181 / 0.01) -purple-	0.0488 (6.02)	c) metabolic enzymes
380	acetyl-CoA acyltransferase	gi 159478266	Cre17.g723650.t1.2	1.09 / 0.0947, 0 / 0, 2.34 / 0.098	0 / 0, 5.1 / 0.187, 3.36 / 0.153	0.83 / 0.0916, 2.57 / 0.173, 3.36 / 0.178	0 / 0, 1.39 / 0.0539, 1.73 / 0.109	10 (1.22)	k) up in the diagonal WT 5%CO2/ pyr- air (0.297 / 0.96)	0.41 (2.2)	c) metabolic enzymes
381	hypothetical protein CHLREDRAFT_82554	gi 159486443	Cre04.g217934.t1.1	0.13 / 0.0113, 0 / 0, 1.07 / 0.0448	0 / 0, 1.64 / 0.0602, 1.34 / 0.061	0.13 / 0.0144, 0.63 / 0.0424, 1.07 / 0.0565	0 / 0, 0.27 / 0.0105, 0.63 / 0.0398	10 (0.744)	k) up in the diagonal WT 5%CO2/ pyr- air (0.255 / 0.929)	0.123 (2.2)	c) metabolic enzymes
382	acetyl-CoA carboxylase	gi 159477697	Cre12.g519100.t1.2	0.27 / 0.0235, 0 / 0, 0.19 / 0.00796	0 / 0, 1.57 / 0.0576, 0.91 / 0.0414	0.13 / 0.0144, 0.91 / 0.0612, 0.42 / 0.0222	0 / 0, 0.8 / 0.031, 0 / 0	10 (1.87)	k) up in the diagonal WT 5%CO2/ pyr- air (0.334 / 0.956)	0.103 (3.15)	c) metabolic enzymes

Molecular Physiology of the *Chlamydomonas pyrenoid*

383	heme oxygenase	gi 159489196	Cre10.g423500.t1.2	0.1 / 0.00869, 0 / 0, 0.33 / 0.0138	0 / 0, 0.95 / 0.0349, 0.77 / 0.0351	0.21 / 0.0232, 0.33 / 0.0222, 0.61 / 0.0322	0 / 0, 0.46 / 0.0178, 0.46 / 0.029	10 (0.483)	k) up in the diagonal WT 5%CO ₂ / pyr- air (0.279 / 0.951)	0.0774 (2.13)	c) metabolic enzymes
384	isocitrate dehydrogenase, NADP-dependent	gi 159481269	NA	0.61 / 0.053, 0 / 0, 0.19 / 0.00796	0 / 0, 0.61 / 0.0224, 1.44 / 0.0656	0.27 / 0.0298, 0.13 / 0.00874, 0.27 / 0.0143	0 / 0, 0.19 / 0.00736, 3.68 / 0.232	14 (0.0839)	m) up in pyr- 5% CO ₂ (0.35 / 0.265) -yellow-	0.251 (3.56)	c) metabolic enzymes
385	ATP-sulfurylase	gi 159470391	Cre03.g203850.t1.2	0.17 / 0.0148, 0 / 0, 0 / 0	0 / 0, 0 / 0, 0.36 / 0.0164	0.47 / 0.0519, 0 / 0, 0 / 0	0 / 0, 0.08 / 0.0031, 2.15 / 0.136	14 (0.328)	m) up in pyr- 5% CO ₂ (0.369 / 0.248) -yellow-	0.146 (5.01)	c) metabolic enzymes
386	aspartate aminotransferase	gi 159483981	Cre02.g097900.t1.2	0 / 0, 0 / 0, 0.14 / 0.00586	0 / 0, 0 / 0, 0.07 / 0.00319	0 / 0, 0 / 0, 0.07 / 0.0037	0 / 0, 0 / 0, 1.58 / 0.0997	14 (1.53)	m) up in pyr- 5% CO ₂ (0.496 / 0.22) -yellow-	0.105 (23.5)	c) metabolic enzymes
387	predicted protein	gi 159472256	Cre08.g376100.t1.2	0 / 0, 0 / 0, 0.1 / 0.00419	0 / 0, 0.22 / 0.00807, 0.22 / 0.01	0.1 / 0.011, 0.1 / 0.00672, 0.22 / 0.0116	0 / 0, 0 / 0, 1.01 / 0.0637	14 (0.0546)	m) up in pyr- 5% CO ₂ (0.341 / 0.271) -yellow-	0.0669 (3.7)	c) metabolic enzymes
388	flagellar associated protein, nucleoside diphosphate kinase-	gi 159480348	Cre16.g650550.t2.1, Cre16.g650550.t1.2	1.54 / 0.134, 1.11 / 0.241, 4.35 / 0.182	0 / 0, 6.76 / 0.248, 3.44 / 0.157	2.06 / 0.227, 5.44 / 0.366, 5.44 / 0.287	0.45 / 0.117, 8.35 / 0.323, 6.76 / 0.427	8 (1.53)	n) up in pyr- (0.393 / 0.0241) -orange-	0.917 (1.57)	c) metabolic enzymes
389	predicted protein	gi 159487124	Cre06.g294950.t1.1	0.23 / 0.02, 0 / 0, 0 / 0	0 / 0, 0.11 / 0.00404, 0.11 / 0.00501	0.5 / 0.0552, 0.11 / 0.0074, 0.11 / 0.00581	0 / 0, 0.11 / 0.00426, 0.77 / 0.0486	8 (0.295)	n) up in pyr- (0.22 / 0.0985) -orange-	0.0636 (3.04)	c) metabolic enzymes
390	malate synthase	gi 159475042	Cre03.g144807.t1.1	1.31 / 0.114, 0.3 / 0.0652, 7.59 / 0.318	0 / 0, 6.34 / 0.233, 7.59 / 0.346	1.57 / 0.173, 8.06 / 0.542, 9.6 / 0.507	0 / 0, 2.34 / 0.0907, 2.91 / 0.184	13 (1.11)	o) up in pyr- air (0.741 / 0.0736) -red-	1.28 (2.72)	c) metabolic enzymes
391	hypothetical protein CHLREDRAFT_132881	gi 159488210	Cre01.g004900.t1.2	1.29 / 0.112, 0 / 0, 0.32 / 0.0134	0 / 0, 0.51 / 0.0187, 0.32 / 0.0146	2.46 / 0.272, 0.32 / 0.0215, 0.74 / 0.0391	0 / 0, 0.15 / 0.00581, 1.29 / 0.0814	13 (1.15)	o) up in pyr- air (0.449 / 0.205) -red-	0.349 (4.05)	c) metabolic enzymes
392	chorismate synthase	gi 159475000	Cre03.g145747.t1.1	1.16 / 0.101, 0.23 / 0.05, 1.48 / 0.062	0.07 / 0.0531, 1.85 / 0.0679, 1.66 / 0.0756	0.75 / 0.0828, 1.66 / 0.112, 1.85 / 0.0977	0.07 / 0.0181, 1.31 / 0.0508, 2.06 / 0.13	13 (0.469)	o) up in pyr- air (0.386 / 0.0291) -red-	0.307 (1.44)	c) metabolic enzymes
393	hypothetical protein CHLREDRAFT_80327	gi 159475703	NA	0.56 / 0.0486, 0 / 0, 0.87 / 0.0364	0 / 0, 0.43 / 0.0158, 0.56 / 0.0255	0.43 / 0.0475, 0.56 / 0.0377, 1.23 / 0.065	0 / 0, 0.56 / 0.0217, 0.87 / 0.0549	13 (0.874)	o) up in pyr- air (0.554 / 0.0226) -red-	0.158 (2.22)	c) metabolic enzymes
394	SOUL heme-binding protein	gi 159466186	Cre06.g299700.t1.2	0.18 / 0.0156, 0 / 0, 0.18 / 0.00754	0 / 0, 0.63 / 0.0231, 0.18 / 0.00819	0.92 / 0.102, 0 / 0, 0.39 / 0.0206	0 / 0, 0.39 / 0.0151, 0.63 / 0.0398	13 (0.744)	o) up in pyr- air (0.408 / 0.227) -red-	0.128 (3.35)	c) metabolic enzymes
395	phosphoribosylamino imidazole carboxylase,	gi 159465541	Cre12.g503300.t1.2	0.6 / 0.0521, 0 / 0, 0.53 / 0.0222	0 / 0, 0.84 / 0.0308, 0.46 / 0.0209	0.33 / 0.0364, 0.68 / 0.0457, 0.68 / 0.0359	0 / 0, 0.76 / 0.0294, 0.05 / 0.00316	13 (0.388)	o) up in pyr- air (0.499 / 0.0051) -red-	0.124 (2.23)	c) metabolic enzymes
396	bifunctional GTP cyclohydrolase II	gi 159472923	Cre09.g393900.t2.1, Cre09.g393900.t1.2	0.17 / 0.0148, 0 / 0, 0.62 / 0.026	0 / 0, 0.91 / 0.0334, 0.62 / 0.0282	0.27 / 0.0298, 0.38 / 0.0256, 0.62 / 0.0328	0 / 0, 0.17 / 0.00659, 0.62 / 0.0391	13 (0.095)	o) up in pyr- air (0.343 / 0.0221) -red-	0.0925 (1.79)	c) metabolic enzymes
397	aminoimidazolecarbo ximide ribonucleotide transformylase	gi 159469428	NA	0.07 / 0.00608, 0 / 0, 0.31 / 0.013	0 / 0, 0.23 / 0.00844, 0.51 / 0.0232	0.07 / 0.00773, 0 / 0, 0.41 / 0.0217	0 / 0, 0.23 / 0.00891, 0.23 / 0.0145	13 (0.633)	o) up in pyr- air (0.409 / 0.0946) -red-	0.0527 (2.03)	c) metabolic enzymes